frontiers | Research Topics

# High-performance computing in solid earth geohazards: Progresses, achievements and challenges for a safer world

**Edited by**
Alice-Agnes Gabriel, Marta Pienkowska, Manuela Volpe and Sara Barsotti

**Published in**
Frontiers in Earth Science

ISSN 1664-8714
ISBN 978-2-8325-2305-6
DOI 10.3389/978-2-8325-2305-6

## About Frontiers

Frontiers is more than just an open access publisher of scholarly articles: it is a pioneering approach to the world of academia, radically improving the way scholarly research is managed. The grand vision of Frontiers is a world where all people have an equal opportunity to seek, share and generate knowledge. Frontiers provides immediate and permanent online open access to all its publications, but this alone is not enough to realize our grand goals.

## Frontiers journal series

The Frontiers journal series is a multi-tier and interdisciplinary set of open-access, online journals, promising a paradigm shift from the current review, selection and dissemination processes in academic publishing. All Frontiers journals are driven by researchers for researchers; therefore, they constitute a service to the scholarly community. At the same time, the *Frontiers journal series* operates on a revolutionary invention, the tiered publishing system, initially addressing specific communities of scholars, and gradually climbing up to broader public understanding, thus serving the interests of the lay society, too.

## Dedication to quality

Each Frontiers article is a landmark of the highest quality, thanks to genuinely collaborative interactions between authors and review editors, who include some of the world's best academicians. Research must be certified by peers before entering a stream of knowledge that may eventually reach the public - and shape society; therefore, Frontiers only applies the most rigorous and unbiased reviews. Frontiers revolutionizes research publishing by freely delivering the most outstanding research, evaluated with no bias from both the academic and social point of view. By applying the most advanced information technologies, Frontiers is catapulting scholarly publishing into a new generation.

## What are Frontiers Research Topics?

Frontiers Research Topics are very popular trademarks of the *Frontiers journals series*: they are collections of at least ten articles, all centered on a particular subject. With their unique mix of varied contributions from Original Research to Review Articles, Frontiers Research Topics unify the most influential researchers, the latest key findings and historical advances in a hot research area.

Find out more on how to host your own Frontiers Research Topic or contribute to one as an author by contacting the Frontiers editorial office: frontiersin.org/about/contact

# High-performance computing in solid earth geohazards: Progresses, achievements and challenges for a safer world

**Topic editors**

Alice-Agnes Gabriel — Ludwig Maximilian University of Munich, Germany
Marta Pienkowska — ETH Zürich, Switzerland
Manuela Volpe — National Institute of Geophysics and Volcanology (INGV), Italy
Sara Barsotti — Icelandic Meteorological Office, Iceland

**Citation**

Gabriel, A.-A., Pienkowska, M., Volpe, M., Barsotti, S., eds. (2023). *High-performance computing in solid earth geohazards: Progresses, achievements and challenges for a safer world*. Lausanne: Frontiers Media SA. doi: 10.3389/978-2-8325-2305-6

# Table of contents

frontiers in Earth Science

ORIGINAL RESEARCH
published: 23 September 2021
doi: 10.3389/feart.2021.704797

# Simulating the Transport and Dispersal of Volcanic Ash Clouds With Initial Conditions Created by a 3D Plume Model

*Zhixuan Cao*[1,2], *Marcus Bursik*[3], *Qingyuan Yang*[4,5] *and Abani Patra* *[1,6]

[1]*Mechanical and Aerospace Engineering Department, SUNY Buffalo, Buffalo, NY, United States,* [2]*Fluids Business Unit, ANSYS Inc, Lebanon, NH, United States,* [3]*Center for Geohazards Studies, SUNY Buffalo, Buffalo, NY, United States,* [4]*Earth Observatory of Singapore, Singapore, Singapore,* [5]*The Asian School of the Environment, Nanyang Technological University, Singapore, Singapore,* [6]*Data Intensive Studies Center, Tufts University, Medford, MA, United States*

Volcanic ash transport and dispersion (VATD) models simulate atmospheric transport of ash from a volcanic source represented by parameterized concentration of ash with height. Most VATD models represent the volcanic plume source as a simple line with a parameterized ash emission rate as a function of height, constrained only by a total mass eruption rate (MER) for a given total rise height. However, the actual vertical ash distribution in volcanic plumes varies from case to case, having complex dependencies on eruption source parameters, such as grain size, speed at the vent, vent size, buoyancy flux, and atmospheric conditions. We present here for the first time the use of a three-dimensional (3D) plume model based on conservation laws to represent the ash cloud source without any prior assumption or simplification regarding plume geometry. By eliminating assumed behavior associated with a parameterized plume geometry, the predictive skill of VATD simulations is improved. We use our recently developed volcanic plume model based on a 3D smoothed-particle hydrodynamic Lagrangian method and couple the output to a standard Lagrangian VATD model. We apply the coupled model to the Pinatubo eruption in 1991 to illustrate the effectiveness of the approach. Our investigation reveals that initial particle distribution in the vertical direction, including within the umbrella cloud, has more impact on the long-range transport of ash clouds than does the horizontal distribution. Comparison with satellite data indicates that the 3D model-based distribution of ash particles through the depth of the volcanic umbrella cloud, which is much lower than the observed maximum plume height, produces improved long-range VATD simulations. We thus show that initial conditions have a significant impact on VATD, and it is possible to obtain a better estimate of initial conditions for VATD simulations with deterministic, 3D forward modeling of the volcanic plume. Such modeling may therefore provide a path to better forecasts lessening the need for user intervention, or attempts to observe details of an eruption that are beyond the resolution of any potential satellite or ground-based technique, or *a posteriori* creating a history of ash emission height via inversion.

**Keywords: volcano, 3D plume model, initial conditions, numerical simulation, SPH, Pinatubo, ash transport, ash dispersal**

OPEN ACCESS

***Edited by:***
*Sara Barsotti,*
*Icelandic Meteorological Office, Iceland*

***Reviewed by:***
*Frances Beckett,*
*Met Office, United Kingdom*
*Hans Schwaiger,*
*United States Geological Survey (USGS), United States*

***Correspondence:**
*Abani Patra*
*abani.patra@tufts.edu*

***Specialty section:***
*This article was submitted to Volcanology, a section of the journal Frontiers in Earth Science*

***Received:*** *03 May 2021*
***Accepted:*** *25 August 2021*
***Published:*** *23 September 2021*

***Citation:***
*Cao Z, Bursik M, Yang Q and Patra A (2021) Simulating the Transport and Dispersal of Volcanic Ash Clouds With Initial Conditions Created by a 3D Plume Model. Front. Earth Sci. 9:704797. doi: 10.3389/feart.2021.704797*

# 1 INTRODUCTION

Volcanic ash, the fine-grained fraction of tephra, can be widely dispersed to synoptic and global scales and can lead to a degradation of air quality and pose threats to aviation (Tupper et al., 2007). Identification, tracking, and modeling the future movement of volcanic ash help route and schedule flights to avoid ash clouds. Numerical estimation of ash distribution using known and forecast wind fields is necessary if we are to accurately predict ash cloud propagation and spread. Numerous volcanic ash transport and dispersion (VATD) forecast models have been developed by both civil and military aviation, and meteorological agencies, to provide forecasts of ash cloud motion (Witham et al., 2007), such as Puff (Tanaka, 1991; Searcy et al., 1998), NAME (Jones et al., 2007), HYSPLIT (Stein et al., 2015; Rolph et al., 2017), and Ash3d (Schwaiger et al., 2012). New techniques have been integrated into VATDs to satisfy increasing demands for different types of output, model accuracy, and forecast reliability. This contribution explores a forward modeling method for creating initial conditions for VATD simulations, which promises to reduce the need for inversion or user intervention and improve forecasting.

Fero et al. (2009) and Stohl et al. (2011) showed that initial source conditions have significant effects on the simulation of volcanic ash transport. Constantinescu et al. (2021) proved that an enhanced initial condition provides an overall better fit of the tephra deposit generated from an ash cloud than do models without a disk-like source, demonstrating the significant impact of initial condition on ash dispersion. Besides location of the eruption vent and timing of the release, traditional VATD simulation requires key global descriptors of the volcanic plume, especially plume height, grain size, eruption duration and mass loading, or alternatively, a mass eruption rate (MER). No matter how these global descriptors are obtained, they are used to furnish the initial conditions for VATDs in the form of a line-source term of a spatio-temporal distribution of particle mass. It is a common practice to pick values for these global descriptors using an empirical expression for the height-MER relation. The values for the descriptors can also be found by parameter calibration or inversion (e.g. Fero et al., 2008, 2009; Stohl et al., 2011; Zidikheri et al., 2017). One-dimensional (1D) plume models serve as an alternative option to provide these values. For example, Bursik et al. (2012) used the 1D model puffin (Bursik, 2001) to generate estimates of mass eruption rate and grain size. In some cases, an extra step is adopted to spread ash particles from the line source horizontally, resulting in an initial ash cloud in 3D space. The horizontal spreading depends on an empirical expression as well. For example, the VATD model Puff spreads particles from the line source uniformly in the horizontal direction within a given radius. Considering the complexities of volcanic eruptions, the actual ash distribution in the initial cloud should vary from case to case and with time, making it difficult to find one general expression that is suitable for all cases. It is useful therefore to investigate alternative ways for creating initial ash clouds without assumptions regarding plume geometry, or numerical inversion. This provides the major motivation for this study.

VATD models can be categorized into Lagrangian particle tracking and Eulerian advection/diffusion types. Among several available particle tracking models, such as, Hypact (Walko et al., 1995), Puff (Searcy et al., 1998), CANERM (D'amours, 1998), and HYSPLIT (Draxler and Hess, 1998) and advection/diffusion models, such as Fall3D (Folch et al., 2009), and Ash3D (Schwaiger et al., 2012), we adopt a particle tracking model, Puff, as the primary VATD model. Puff can accept a 3D point cloud description of the starting ash cloud as an initial condition, which makes it technically easier to couple with a 3D Lagrangian plume model. Puff initializes a discrete number of tracers that represent a sample of the eruption cloud and calculates transport, turbulent dispersion, and fallout for each representative tracer. A cylinder extending vertically from the volcano summit to a specified plume height is the standard approach to provide a simple model of the geometry of a typical ash column. Puff minimally requires horizontal wind field data. The "restart" feature of Puff makes it feasible to accommodate the hand-off between a plume simulation and the Puff simulation in terms of time and length scales. We use the hybrid single-particle Lagrangian integrated trajectory (HYSPLIT) model (Stein et al., 2015; Rolph et al., 2017) to better understand simulation results from Puff in this study.

Besides parameter calibration, 1D plume models have been used to obtain global descriptors of volcanic plumes. 1D plume models (e.g. Woods, 1988; Bursik, 2001; Mastin, 2007; de'Michieli Vitturi et al., 2015; Folch et al., 2016; Pouget et al., 2016b) solve the equations of motion in 1D using simplifying assumptions and hence depend on the estimation of certain parameters, especially those related to the entrainment of air, which is evaluated based on two coefficients: a coefficient due to turbulence in the rising buoyant jet and one due to the crosswind field. Different 1D models adopt different entrainment coefficients based on a specific formulation or calibration against well-documented case studies. The feedback from plume to atmosphere is usually ignored in 1D models. While these 1D models generate well-matched results with 3D models for plumes that are dominated by wind (often called weak plumes), much greater variability is observed for strong plume scenarios (Bursik et al., 2009; Costa et al., 2016). On the other hand, 3D numerical models for volcanic plumes based on first principles and having few parameterized coefficients (Oberhuber et al., 1998; Neri et al., 2003; Suzuki et al., 2005; Cerminara et al., 2016a; Cao et al., 2018) naturally create a 3D ash cloud, which could serve directly as an initial state of the volcanic material for VATDs. However, there is no VATD simulation using such 3D ash clouds as initial conditions. In this study, we will carry out VATD simulations using an initial state for the ash cloud based on 3D plume simulations, generated with Plume-SPH (Cao et al., 2018, 2017). The implementation techniques described in this study can be applied to any combination of VATD model and 3D plume model even though our investigation is based on a specific VATD model and plume model.

The 1991 eruption of Pinatubo volcano (Philippines) is used as a case study. Pinatubo erupted between June 12 and 16, 1991, after weeks of precursory activity. The climactic phase started on June 15 at 0441 UTC and ended around 1341 UTC (Holasek et al.,

1996a). The climactic phase generated voluminous pyroclastic flows and sent Plinian and co-ignimbrite ash and gas columns to great altitudes (Scott et al., 1996). The evolution of the Pinatubo ash and $SO_2$ clouds was tracked using visible (Holasek et al., 1996a), ultraviolet (Total Ozone Mapping Spectrometer; TOMS) (Guo et al., 2004a), and infrared sensors, including the advanced very high-resolution radiometer (AVHRR) (Guo et al., 2004b). There are sufficient observational data to estimate the eruption conditions for the climactic phase of the eruption (Suzuki and Koyaguchi, 2009). The availability of calibrated eruption conditions and extensive observational data regarding ash cloud transport make the Pinatubo eruption an ideal case study.

# 2 MATERIALS AND METHODS

## 2.1 Plume-SPH Model

Plume-SPH (Cao et al., 2018) is designed to describe an injection of well-mixed solid and volcanic gas from a circular vent above a flat surface into a stratified stationary atmosphere. The basic assumptions of the model are as follows:

1) Molecular viscosity and heat conduction are neglected since turbulent energy and momentum exchange are dominant;
2) Erupted material consisting of solid with different sizes and the mixture of gases is assumed to be well-mixed and behaves like a single-phase fluid (phase 2) which is valid for eruptions with fine particles and ash;
3) Air, which is assumed to be a well-mixed mixture of different gases, is assumed to be another phase (phase 1);
4) Assume thermodynamic equilibrium and dynamic equilibrium between the two phases. As a result, both phases share the common energy equation and momentum equations;
5) All other microphysical processes (such as the phase changes of $H_2O$, aggregation, disaggregation, absorption of gas on the surface of solids, solution of gas into a liquid) and chemical processes are not considered in this model;
6) The effect of wind is also not currently considered in this model.

Based on above assumptions, the governing equations of our model are given as:

$$\frac{\partial \rho}{\partial t} + \nabla \cdot (\rho \mathbf{v}) = 0 \tag{1}$$

$$\frac{\partial \rho \xi}{\partial t} + \nabla \cdot (\rho \xi \mathbf{v}) = 0 \tag{2}$$

$$\frac{\partial \rho \mathbf{v}}{\partial t} + \nabla \cdot (\rho \mathbf{v}\mathbf{v} + p\mathbf{I}) = \rho \mathbf{g} \tag{3}$$

$$\frac{\partial \rho E}{\partial t} + \nabla \cdot [(\rho E + p)\mathbf{v}] = \rho \mathbf{g} \cdot \mathbf{v} \tag{4}$$

where $\rho$ is the density, $\mathbf{v}$ is the velocity, $\xi$ is the mass fraction of ejected material, $\mathbf{g}$ is the gravitational acceleration, $\mathbf{I}$ is a unit tensor. $E = e + K$ is the total energy which is a summation of kinetic energy $K$ and internal energy $e$. An additional equation is required to close the system. In this model, the equation for closing the system is the following equation of state (EOS).

$$p = (\gamma_m - 1)\rho e \tag{5}$$

where

$$\gamma_m = R_m / C_{vm} + 1 \tag{6}$$

$$R_m = \xi_g R_g + \xi_a R_a \tag{7}$$

$$C_{vm} = \xi_s C_{vs} + \xi_g C_{vg} + \xi_a C_{va} \tag{8}$$

$$\xi_a = 1 - \xi \tag{9}$$

$$\xi_g = \xi \cdot \xi_{g0} \tag{10}$$

$$\xi_s = \xi - \xi_g \tag{11}$$

where $C_v$ is the specific heat with constant volume, $R$ is the gas constant. $\xi$ is the mass fraction of erupted material. The subscript $m$ represents the mixture of ejected material and air, $s$ represents solid portion in the ejected material, $g$ represents gas portion in the ejected material, $a$ represents air, 0 represents physical properties of erupted material. $\xi_{g0}$ is the mass fraction of vapor in the erupted material.

Three different boundary conditions are applied in this model. At the vent, temperature of erupted material $T$, eruption velocity $\mathbf{v}$, the mass fraction of vapor in erupted material $\xi_{g0}$, and mass discharge rate $\dot{M}$ are given. The pressure of erupted material $p$ is assumed to be the same as ambient pressure for pressure-balanced eruption. The radius of the vent is determined from $\rho$, $\dot{M}$ and $\mathbf{v}$. Nonslip wall boundary condition is applied to the flat ground, where we enforce the velocity to be zero. With further assumption that the ground is adiabatic, internal energy flux, which consists of heat flux and energy flux carried by mass flux, vanishes on the wall boundary. Pressure outlet boundary condition is applied to the surrounding atmosphere where the pressure is given. Except for the pressure, boundary values for density, velocity, and energy are determined by numerical calculation from the conservation laws. The initial condition for Plume-SPH is created based on the atmosphere profile before the eruption.

The governing equations, EOS, boundary conditions, and initial conditions establish a complete mathematical model. The model posed over the computational domain is then discretized using smoothed particle hydrodynamics (SPH) method (Gingold and Monaghan, 1977) available in the tool Plume-SPH (Cao et al., 2017, 2018) using two types of SPH particles: 1) particles of phase 1 to represent ambient air and 2) particles of phase 2 to represent erupted material. So before the eruption, the computational domain is fully occupied by particles of phase 1. During the eruption, particles of phase 2 are injected into the computational domain. The discretized model is then converted into a large computation task in the Plume-SPH tool based on a parallel data management framework (Cao et al., 2017).

The input parameters for Plume-SPH include the eruption condition at vent, the material properties, and a profile of the atmosphere. The eruption parameters, material properties, and atmosphere for the "strong plume–no wind" case in the recent

**TABLE 1 |** List of eruption condition and material properties for plume simulation.

| Parameters | Units | Plume |
|---|---|---|
| Vent Velocity | $m \cdot s^{-1}$ | 275 |
| Vent Gas Mass Fraction | – | 0.05 |
| Vent Temperature | K | 1053 |
| Vent Height | m | 1500 |
| Mass Discharge Rate | $kg \cdot s^{-1}$ | $1.5 \times 10^9$ |
| Specific Heat of Gas at Constant Volume | $J \cdot kg^{-1} \cdot K^{-1}$ | 717 |
| Specific Heat of Air at Constant Volume | $J \cdot kg^{-1} \cdot K^{-1}$ | 1340 |
| Specific Heat of Solid | $J \cdot kg^{-1} \cdot K^{-1}$ | 1100 |
| Specific Heat of Gas at Constant Pressure | $J \cdot kg^{-1} \cdot K^{-1}$ | 1000 |
| Specific Heat of Air at Constant Pressure | $J \cdot kg^{-1} \cdot K^{-1}$ | 1810 |
| Density of Air at Vent Height | $kg \cdot m^{-3}$ | 1.104 |
| Pressure at Vent Height | Pa | 84,363.4 |

comparison study on eruptive column models (Costa et al., 2016) are adopted. Eruption conditions and material properties are listed in **Table 1**. Note that the density of erupted material at the vent and radius of the vent can be computed from the given parameters. The eruption pressure is assumed to be the same as the atmospheric pressure at the vent; hence, it is not given in the table. The vertical profiles of atmospheric properties were based on the reanalysis data from European Centre for Medium-Range Weather Forecasts (ECMWF) for the period corresponding to the climactic phase of the Pinatubo eruption.

Running of Plume-SPH updates physical quantities, such as temperature, velocity, and the position of SPH particles in each time step. During Plume-SPH simulation, SPH particles of phase 2, which represent the erupted material, are injected from the eruption vent into the computation domain with an initial injection velocity. As they move upwards, these particles will get mixed with SPH particles of phase 1, which represent the air, during the whole simulation. Their physics quantities get updated as well. After the simulation, the computation domain will be filled with SPH particles of both phase 1 and phase 2. Removing all SPH particles of phase 1 from the computation domain, all of the remaining SPH particles represent the erupted material, which naturally forms a plume (see **Figure 1**).

## 2.2 Puff and Initial Ash Cloud

Puff (Tanaka, 1991; Searcy et al., 1998) is a dynamic pollutant tracer model. The model is based on a 3D Lagrangian form of the fluid mechanics, in which the material transport is represented by the fluid motion, and diffusion is parameterized by a stochastic process of random walk. Here, the model is constructed by a sufficiently large number of Lagrangian tracer particles with a random variables $\mathbf{R}_i(t) = (x(t), y(t), z(t))$, where $i = 1 \sim M$, which represents position vectors of particles from the origin of the ash source at the time $t$. $M$ is the total number of Lagrangian tracer particles, a sample of all the ash particles.

$$\mathbf{R}_i(t + \Delta t) = \mathbf{R}_i(t) + \mathbf{W}(t)\Delta t + \mathbf{Z}(t)\Delta t + \mathbf{S}_i(t)\Delta t \qquad (12)$$

Here, $\mathbf{W}$ accounts for local wind advection, $\mathbf{Z}$ is generated by Gaussian random numbers and accounts for turbulent dispersion, and $\mathbf{S}$ is the terminal gravitational fallout velocity or settling speed, which depends on a tracer's size.

A collection of tracer particles can be used to start a Puff simulation. The tracer particles have three basic properties: age, size, and position. The age of each particle is the elapsed time from when it was released. Ash particles in the initial ash cloud have zero age. Initial ash size distribution is assumed to be log-normal. According to a mean and standard deviation provided by the user, Puff assigns size to each particle. Puff initializes the position of each particle according to semiempirical expressions. The height of each particle is determined according to the specified distribution from the surface (1000 mbar ≅ 0 m) to

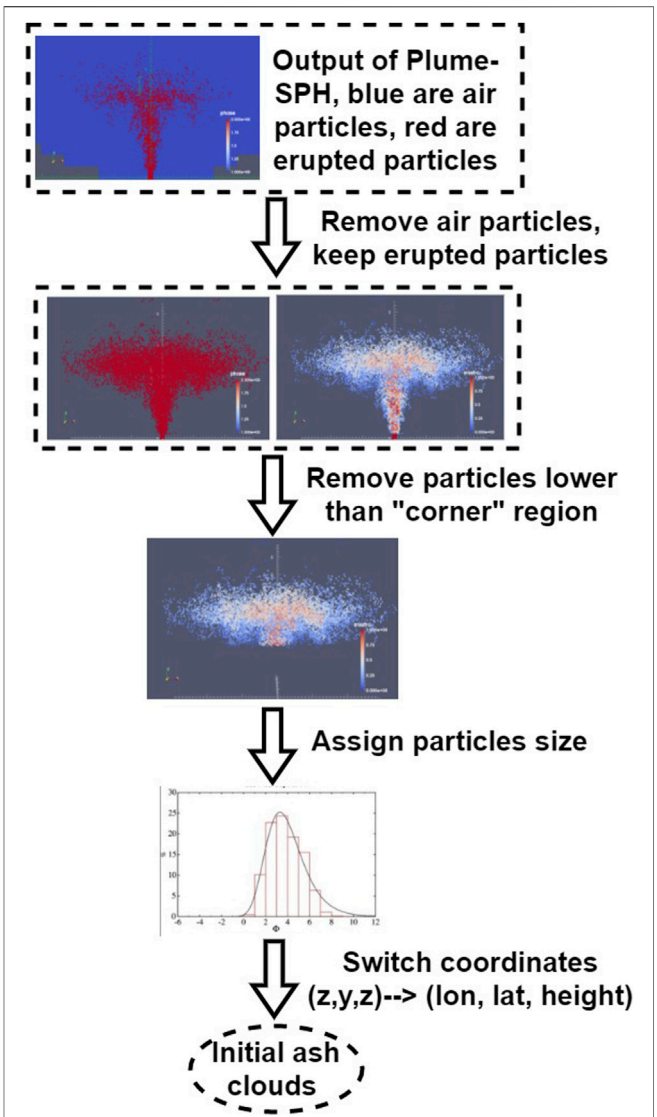


**FIGURE 1 |** Steps to create initial condition for Puff based on raw output of Plume-SPH (Cao et al., 2018). First row: raw output of Plume-SPH. Blue particles are phase 1 (ambient air), and red particles are phase 2 (erupted material). Second row: plume after removing SPH particles of phase 1. Picture at right is colored according to the mass fraction of erupted material. Third row: volcanic plume above the "corner" region after cutting off the lower portion. Fourth row: assign sizes to particles converting numerical discretization points into tracers. Fifth row: switch coordinates in local coordinate system into (*longitude*, *latitude*, *height*).

the top of the plume height, $H_{max}$, which is given by the user. Puff also supports reading predefined initial ash clouds from a file, containing the coordinates of all tracer particles.

Vertical particle distribution in Puff is usually based on the Poisson distribution. For the Poisson distribution, the vertical height of ash particles is given by **Eq. 13**:

$$H = H_{max} - 0.5H_{width}P + H_{width}R \tag{13}$$

where $P$ is an integral value drawn from a Poisson distribution of unit mean, $R$ is a uniformly distributed random number between 0 and 1, $H_{max}$ is the maximum plume height, $H_{width}$ represents an approximate vertical range over which the ash will be distributed. So for Poisson distribution, the user can specify two parameters, $H_{max}$ and $H_{width}$. Another commonly used vertical ash distribution in VATD simulation is Suzuki. For the Suzuki plume shape (Suzuki, 1983), the ash mass vertical distribution is assumed to follow the **Eq. 14**:

$$Q(z) = Q_m \frac{k^2(1 - z/H_{max})\exp(k(z/H_{max} - 1))}{H_{max}[1 - (1 + k)\exp(-k)]} \tag{14}$$

where $Q_m$ is the total mass of erupted material, $k$ is the shape factor, which is an adjustable constant that controls ash distribution with height. A low value of $k$ gives a roughly uniform distribution of mass with elevation, while high values of $k$ concentrate mass near the plume top. So for Suzuki distribution, besides the plume height $H_{max}$, there is another user-specified parameter, $k$.

Puff initializes the horizontal distribution of ash particles according to semiempirical expression as well. Puff uses a uniformly distributed random process to determine ash particle locations in a circle centered on the volcano site. The maximum radius (at plume top) at which a particle can be located is given as "horizontal spread". The horizontal displacement from a vertical line above the volcano is a random value within a circle of which the radius equals the "horizontal spread" multiplied by the ratio of the particle height $H$ to the maximum $H_{max}$, see **Eq. 15**. So the resulting shape of the particle distribution within the plume is an inverted cone in which particles are located directly over the volcano at the lowest level and extend out further horizontally with increasing plume height.

$$r(H) = r_{max}H/H_{max}R \tag{15}$$

where $r(H)$ is the radius of the horizontal circle, within which all particles at the height of $H$ are located. $r_{max}$ is the horizontal spread. $H$ is the height, and $R$ is an uniformly distributed random number between 0 and 1.

In summary, particle distributions in the initial ash cloud are controlled by several parameters, for example, $H_{max}$, $H_{width}$, and $r_{max}$ if the user chooses to use semiempirical expressions, **Eqs 13, 15**. Users can optimize or calibrate these parameters to adjust the initial condition for Puff so that the simulated results match better with observations. Besides the initial ash cloud, other input parameters for Puff are diffusivity in the vertical and horizontal directions, start and end time of the eruption, and eruption duration. When creating initial conditions from the output of Plume-SPH, the total number of Lagrangian tracers is the count of all SPH particles of phase 2 in the plume. The same total number of Lagrangian tracers is used when creating the initial ash cloud based on semiempirical expressions. All input parameters for Puff are listed in **Table 2**.

**TABLE 2 |** Parameters used in VATD simulation of the climactic phase of Pinatubo eruption on June 15, 1991. The first six parameters are used by semiempirical expression to create an initial ash cloud. When creating an initial condition based on the Plume-SPH model, these parameters are extracted from output of Plume-SPH model.

| Parameters | Unit | Semiempirical | Plume-SPH |
|---|---|---|---|
| Plume Height ($H_{max}$) | km | 40 | – |
| Horizontal Spread ($r_{max}$) | km | 103.808 | – |
| Vertical Spread ($H_{width}$) | km | 6.662 | – |
| Plume Shape | – | Poisson | – |
| Total Ash Particles | – | 1,768,500 | 1,768,500 |
| Elevation Threshold | m | – | 15,000 |
| Horizontal Diffusivity | $m^2/s$ | 10,000 | 10,000 |
| Vertical Diffusivity | $m^2/s$ | 10 | 10 |
| Grain Size Distribution | – | Gaussian | Gaussian |
| Mean of Grain Size (Radius) | mm | $3.5 \times 10^{-2}$ | $3.5 \times 10^{-2}$ |
| Standard Deviation of Grain Size | – | 1.0 | 1.0 |
| Start Time | UT | 0441 | 0441 |
| End Time | UT | 1341 | 1341 |
| Simulation Duration | hour | 72 | 72 |

## 2.3 Creation of Initial Ash Cloud From Plume-SPH Output

In this study, we convert the output of Plume-SPH into an initial ash cloud which serves as the initial condition for Puff. The method proposed consists of generating the initial ash cloud directly from Plume-SPH, foregoing assumptions and estimates, or inverse modeling, regarding ash injection height and timing. The steps to create an initial ash cloud based on the raw output of Plume-SPH are shown in **Figure 1**. The initial ash cloud is created from SPH particles of phase 2, which represents the erupted material in the model. After reaching the maximum rise height and starting to spread horizontally, particles of phase 2 form an initial umbrella cloud (**Figure 2**). The 3D plume simulation is considered complete once the umbrella cloud begins to form. Parcels that will be transported by the ambient wind are those above the "corner" region, where mean plume motion is horizontal rather than vertical. With such consideration, we introduce an elevation threshold, which is the lower elevation limit of the ash that will be transported by the VATD. All SPH particles with elevation lower than the threshold are excluded when creating the initial ash cloud. The inflection point from vertical raising to horizontal spreading happens around 15 km according to the averaged vertical velocity [(d) in **Figure 2**] and horizontal velocity [(e) in **Figure 2**]. Below this inflection point, particle trajectories are primarily vertical in the stalk-like eruption column. Above this level, particle trajectories are primarily horizontal, as they flow into the umbrella cloud gravity current. So we choose 15 km to be the elevation threshold in this study.

Considering that SPH particles are only discretization points, each is assigned a grain size according to a given total grain size distribution (TGSD) (Paladio-Melosantos

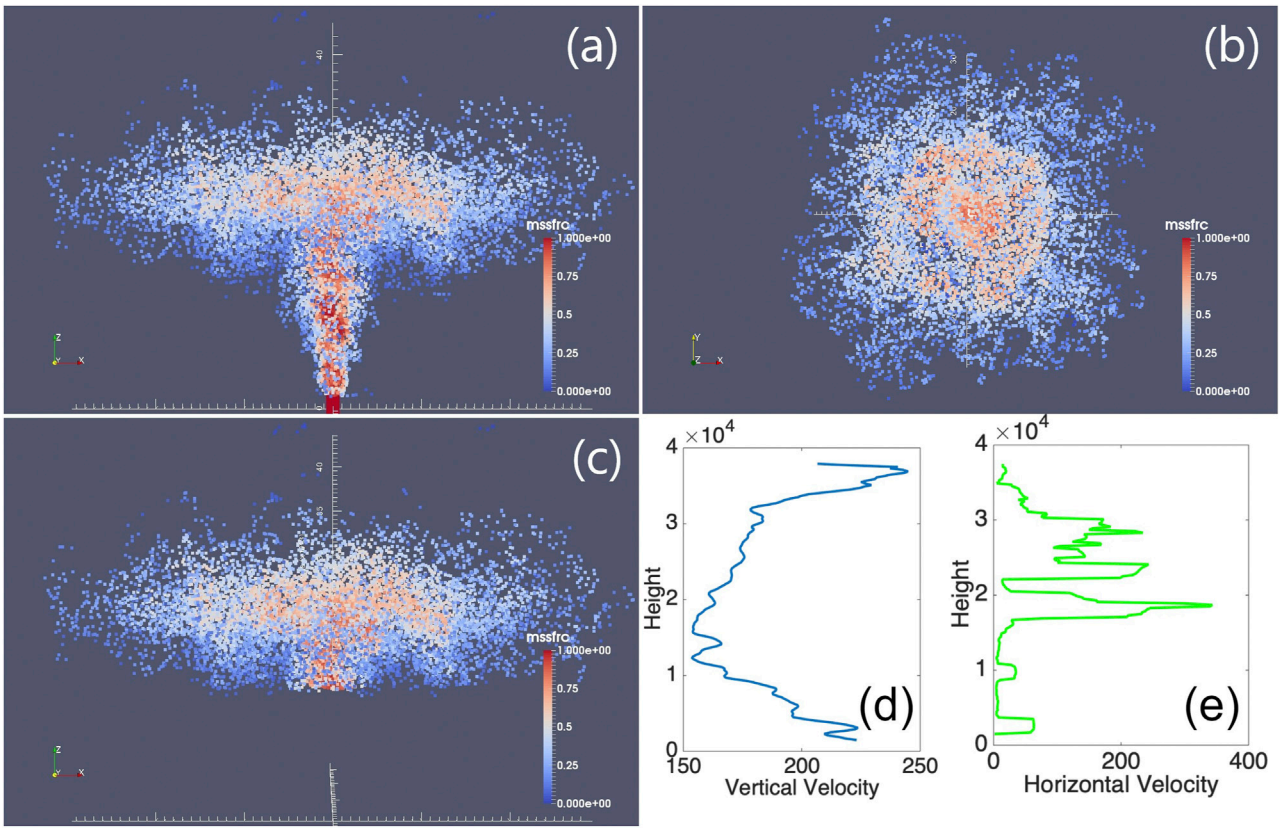


**FIGURE 2 |** Volcano plume from 3D plume model. All particles in the pictures are of phase 2 (particle of phase 1 has been removed) at 600s after eruption, at which time, the plume has already reached the plume height and started spreading radially. **(A)** is the front view of the whole plume. **(B)** is the top view of the plume. **(C)** is the front view of the initial ash cloud, which is essentially a portion of the whole plume whose elevation is higher than a given threshold (in this picture is 15 km). Particles are colored according to mass fraction of erupted material. Red represents high mass fraction while blue represents low mass fraction. **(D)** is the average vertical velocity of the plume. At elevations below 15 km, the average vertical velocity decreases. At elevations higher than 15 km, the averaged vertical velocity starts increasing. **(E)** is the average horizontal velocity of the plume. The averaged horizontal velocity becomes obviously larger when elevation is higher than15 km. So the reflection point is somewhere around 15 km.

et al., 1996), and a concentration according to the mass and volumetric eruption rate. The Plume-SPH discretization points are thus switched to Puff Lagrangian tracer particles having grain sizes and concentrations. The coordinates of these tracer particles, which are initially in the local Cartesian coordinate system of Plume-SPH, are converted into Puff's global coordinate system, which is given in terms of (*longitude*, *latitude*, *height*). Puff takes the initial ash cloud, consisting of the collection of Lagrangian tracer particles with grain size and concentration, and propagates from time $t$ to time $t + \Delta t$ via solution to an advection/diffusion equation (**Eq. 12**).

To summarize, there are four steps to create an initial ash cloud from the raw output of Plume-SPH:

1) filter by SPH particle type to select SPH particles that represent erupted material (phase 2);
2) filter by a mean velocity threshold to select the upper part (above the "corner" region) dominated by horizontal transport;
3) switch SPH discretization points to Lagrangian tracer particles, by assigning grain size to each particle;
4) convert coordinates of the SPH Lagrangian tracers into the VATDs geographic coordinate system.

The features of the volcanic plume and resulting initial ash cloud used in the case study are shown in **Figure 2**. It is important to point out that since both Plume-SPH and Puff are based on the Lagrangian method, there is no extra step of conversion between an Eulerian grid and Lagrangian particles.

## 2.4 Puff Restart

The plume and ash transport models are run at different time scales and length scales. The spatial and temporal resolutions of the plume simulations are much finer than those of the ash transport model. It takes tens of minutes (600 s in this case) for the Pinatubo plume to reach a steady height. However, the eruption persisted for a few hours (9 h for the climactic phase of Pinatubo eruption), and it may be necessary to track ash transport for days following an eruption. At present, it is too

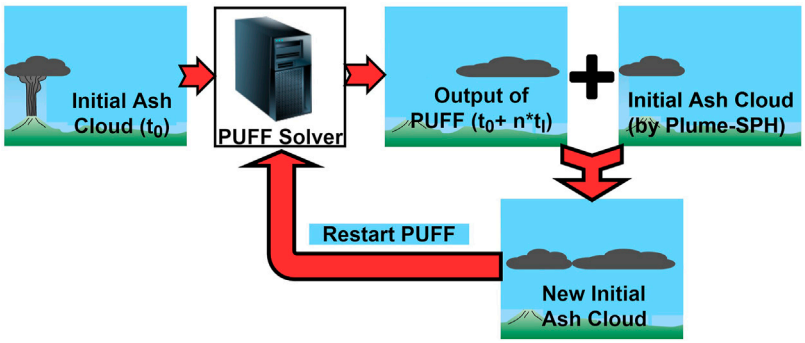


**FIGURE 3 |** Mimic successive eruption with intermittent pulsed releasing of ash particles. $t_l$ is the period of pulsing release. $t_l$ equals the physical time of 3D plume simulation.

computationally expensive to run 3D plume simulations for several hours in real time. In order to handle the difference in time scale, we mimic a continuing eruption with intermittent pulses releasing ash particles. In particular, we restart Puff at an interval of 600 s, i.e., the physical time of the plume simulation to reach a steady height. At every Puff restart, we integrate the output of the last Puff simulation and Plume-SPH into a new ash cloud. This new ash cloud serves as a new initial condition with which to restart a Puff simulation. A sketch demonstrating the overall restart process is shown in **Figure 3**. The total number of Lagrangian tracer particles used in Puff thus equals the summed number of particles in all releases. The total number of tracer particles is therefore no longer a user-selected parameter. Fero et al. (2008) proposed using more realistic time-dependent plume heights. We do not adopt that strategy here for simplicity, although the idea would be straightforward in execution, given time-dependent eruption conditions.

## 3 RESULTS

The transport of volcanic ash resulting from the Pinatubo eruption on June 15, 1991, is simulated using two different initial conditions. The first type of initial condition is created in a traditional way according to user-specified parameters ($H_{max}$, $H_{width}$, and $r_{max}$) and the semiempirical plume shape expressions (**Eqs 13, 15**). We use the observed plume height (40 km) as $H_{max}$ and take $H_{width}$ = 6.662 km, $r_{max}$ = 103.808 km, respectively, based on a previous study (Fero et al., 2008). The second type of initial condition is created by the new method proposed in this study. To create initial conditions using the new method described in this study, the plume rise is simulated first by Plume-SPH. Then, the initial ash cloud is obtained by processing the raw output of Plume-SPH following steps described in *Creation of Initial Ash Cloud From Plume-SPH Output* except for initial conditions, and the parameters that control the VATD simulation are the same for both simulations. Simulated ash transport results are compared against observations.

The simulation results using different initial conditions are compared with TOMS AI (Aerosol Index) and AVHRR BTD (brightness temperature difference) ash cloud map imagery (**Figure 4**). The Puff simulation results are post-processed by the following steps to calculate the relative concentration.

1) The 3D computational domain is discretized into a collection of cells (latitude, longitude, elevation), and each cell is of size 0.2 degree × 0.2 degree × 1 km;
2) Find the cell that has the maximum number of particles (tracer particles); say the maximum number of particles is $N_{max}$;
3) Exclude all cells that have fewer than five particles, and
4) Calculate the relative concentration of each cell by dividing the number of particles in the cell by $N_{max}$.

In contouring, we plot the relative concentration of the cell that has the maximum number of particles at a given (*latitude*, *longitude*). In addition to the relative concentration, we also plot the contours of the maximum height of the ash cloud (**Figure 5**), which is obtained by the following post-processing steps:

1) The 3D computational domain is discretized into a collection of cells (latitude, longitude, elevation), and each cell is of size 0.2 degree × 0.2 degree × 1 km;
2) Exclude all cells that have fewer than five particles, and
3) The maximum height is the cell center height of the top cell among all cells with the same (*latitude*, *longitude*).

We also calculated the Figure of Merit in Space (FMS) according to the definition:

$$FMS = \frac{(\text{area of intersection of Puff forecast footprint and satellite image extent})}{(\text{area of union})}$$

The differences between simulated ash transport by the "Semiempirical initial cloud + Puff" and "Plume-SPH + Puff" conditions are significant. We first check the maximum relative concentration in **Figure 4**. At 23 and 31 h after the beginning of

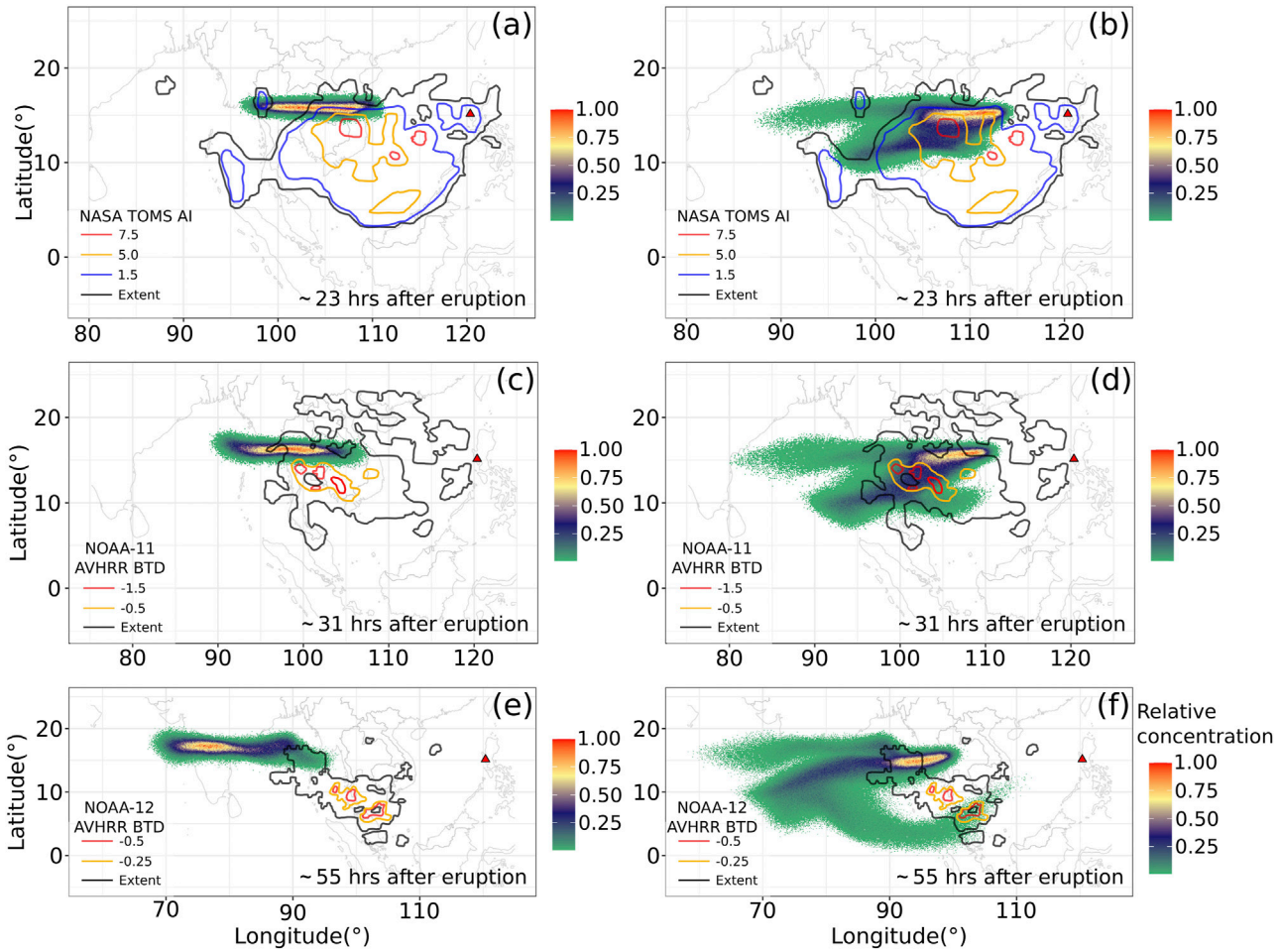


**FIGURE 4 |** Comparison between "Semiempirical initial cloud + Puff" and "Plume-SPH + Puff". Pictures to the left, **(A)**, **(C)** and **(E)**, are Puff simulation based on initial condition created according to semiempirical plume shape expression. Pictures to the right, **(B)**, **(D)** and **(F)**, are Puff simulation based on initial conditions generated by Plume-SPH. TOMS or AVHRR images of Pinatubo ash cloud are overlapped with the simulation results. Ash clouds at different hours after eruption are on different rows. From top to bottom, the images correspond to around 23 h after eruption (UT 199106160341), 31 h after eruption (UT 199106161141), 55 h after eruption (UT 199106171141). The observation data on the first row are TOMS AI (aerosol index) map. The observation data on the second and third row are AVHRR BTD (brightness temperature difference) ash cloud map with atmospheric correction method applied (Guo et al., 2004b). The contours of simulation results are maximum concentration at given (*longitude*, *latitude*). The colored dots are simulation results of relative concentrations whose values are between zero to one and have no unit, and the solid contours are observed in Dobson Units.

the climactic phase, the simulated ash concentration based on the initial conditions created from Plume-SPH is visibly closer to observation than that based on the initial condition generated from semiempirical expressions, especially in terms of the location of the highest concentration region. This is confirmed by the FMS, which is 0.249 (23 h) and 0.269 (31 h) for Plume-SPH results, and 0.063 (23 h) and 0.065 (31 h) for semiempirical initial clouds. Around 55 h after the beginning of the climactic phase, the disparity between observation and simulation becomes more obvious. Ash in the "Semiempirical initial cloud + Puff" simulation is located far west of the observed, with a FMS value equal to 0.058. The high concentration area of the "Plume-SPH + Puff" simulation, even though closer to observation, has also propagated further downwind than in the observation. The FMS goes down to 0.085.

While most of our work is based on the Puff VATD, it is useful to compare the maximum cloud height in **Figure 5** with the wind field indicated in the popular VATD, HYSPLIT's forward trajectory tracking (**Figure 6**). The comparison reveals that the ash cloud is being transported in two separate, main layers (directions) independently. From **Figure 6**, we can see that the wind between elevations of 10 and 15 km blew from north-east to south-west, while winds of higher elevation blew from east to west. This vertical wind shear naturally separated the ash cloud into two layers. In the "Semiempirical initial cloud + Puff" results, the lower elevation layer is missing, which is the most important factor causing differences between these two simulation results (**Figure 4**). Even for the upper layer, the maximum cloud height of the "Semiempirical initial cloud + Puff" simulation

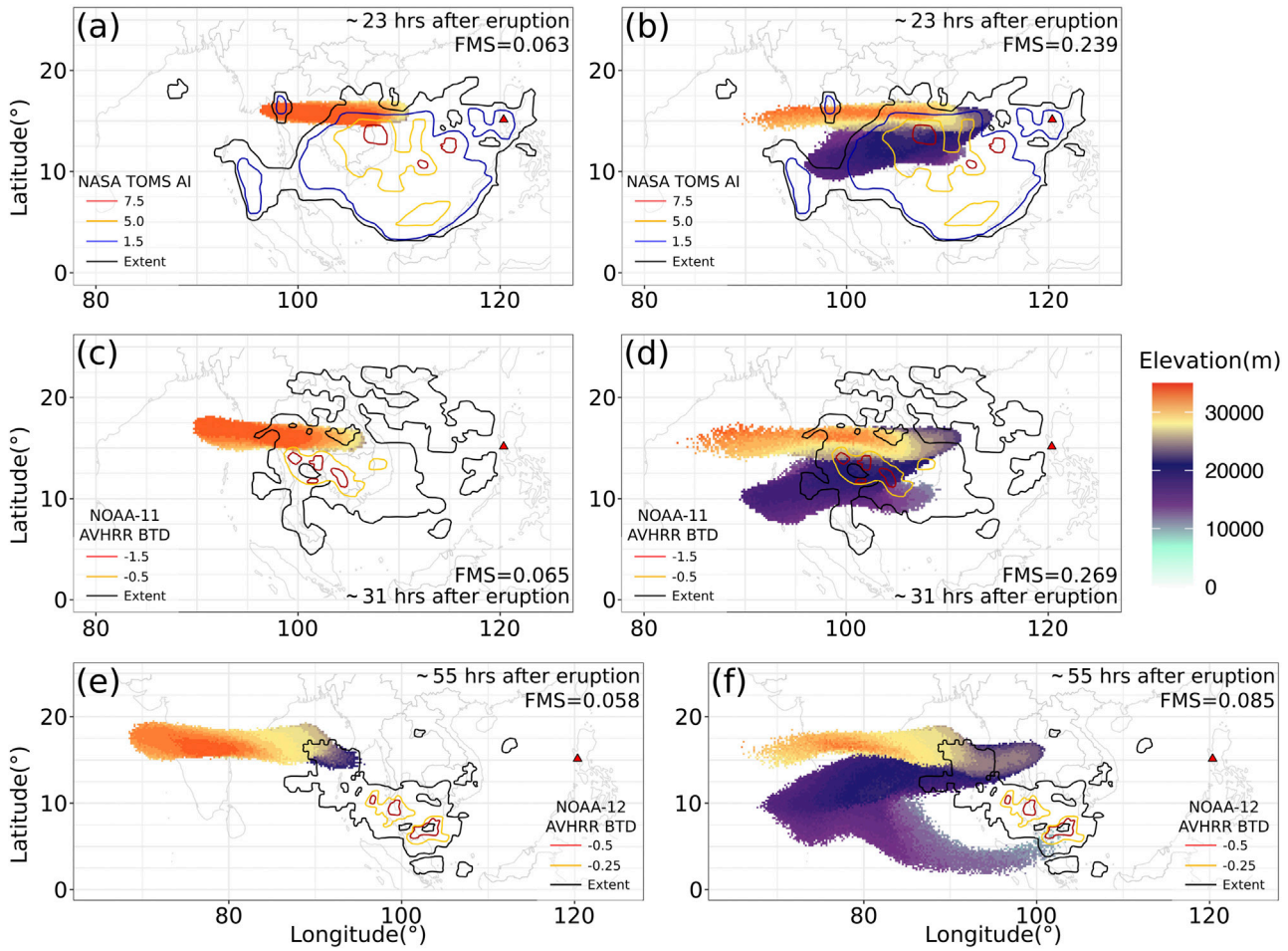


**FIGURE 5 |** Comparison between "Semiempirical initial cloud + Puff" and "Plume-SPH + Puff". Pictures to the left, **(A)**, **(C)** and **(E)**, are Puff simulation based on initial condition created according to semiempirical plume shape expression. Pictures to the right, **(B)**, **(D)** and **(F)**,are Puff simulation based on initial conditions generated by Plume-SPH. TOMS AI (aerosol index) or AVHRR BTD (brightness temperature difference) images of Pinatubo ash cloud are overlapped with the simulation results. Ash clouds at different hours after eruption are on different rows. From top to bottom, the images correspond to around 23 h after eruption (UT 199106160341), 31 h after eruption (UT 199106161141), 55 h after eruption (UT 199106171141). The observation data on the first row are TOMS AI (aerosol index) map. The observation data on the second and third row are AVHRR BTD (brightness temperature difference) ash cloud map with atmospheric correction method applied (Guo et al., 2004b). The colored dots are simulation, and the solid contours are observed in Dobson Units. The contours of simulation results are maximum height of ash cloud, whose unit is m. The FMS value for each simulation is on each contour.

results is higher than that of the "Plume-SPH + Puff" simulation. Such differences cannot be captured by metrics based on footprint, such as FMS. At 55 h after the eruption, the observed high concentration ash, which is at a relatively low elevation (inferred from the wind direction at different elevations in **Figure 6** and the eruption location), is missing in the "Plume-SPH + Puff" simulation results. This leads to the large decrease of FMS values from 0.269 to 0.085. One possibility is that these ash clouds are from eruptions after the climactic phase. In our current simulation, we use the eruption condition for the climactic phase generating plume height for the climactic phase, but satellites see ash and $SO_2$ from all eruption phases.

The only difference in initial conditions between these two simulations is the distribution of ash parcels. The main difference between simulation results from the "Plume-SPH + Puff" and the "Semiempirical initial cloud + Puff" runs can thus be directly attributed to the initial ash particle distribution, which we discuss further in the following section.

## 3.1 Effect of Plume Height ($H_{max}$)

In this section, we discuss the vertical distribution of ash particles in the initial ash cloud. The majority of volcanic ash particles are usually injected at an elevation lower than the plume height. For instance, Holasek et al. (1996a,b) reported the maximum Pinatubo volcanic plume, i.e., source height, as ~ 39 km while the distal volcanic cloud heights were estimated at ~ 20–25 km. Self et al. (1996) reported that the maximum plume height could have been >35 km, but that cloud height was ~23– 28 km after ~ 15–16 h. The neutral buoyancy height of the Pinatubo aerosol cloud was estimated with different methods at ~ 17–26 km (lidar) by DeFoor et al. (1992), ~ 20–23 km (balloon) by Deshler et al.

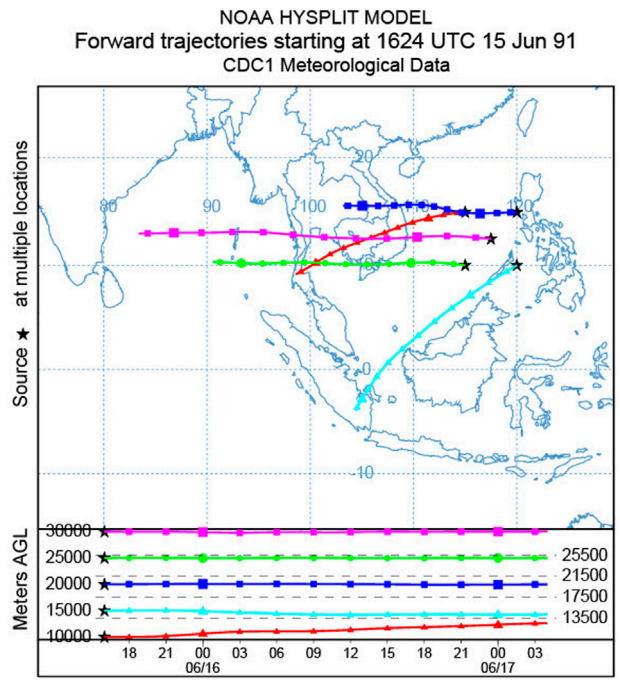


**FIGURE 6 |** Trajectories of particles starting from different heights indicating the wind directions of different evaluations. The trajectories are chosen to start at points that were on the perimeter of the umbrella cloud in *x*, *y*, and *z*, and in its center, right before it became affected by the wind to give an idea of the maximum possible spread of the trajectories from that initial condition.

(1992), ~ 17–28 km (lidar) by Jäger (1992), and ~ 17–25 km (lidar) by Avdyushin et al. (1993). Based on a comparison between simulated clouds with early infrared satellite imagery, Fero et al. (2008) reported that the majority of ash was transported between 16 and 18 km. These observations make good physical sense, as particles are concentrated or centered around the intrusion height of the umbrella cloud, not near the plume top, because the plume top is due to momentum overshoot. However, the empirical expressions for the height-MER relation, which are commonly adopted to create initial conditions for VATD simulations, tend to place the majority of ash particles closer to the top if one uses observed plume height in the empirical expressions.

Here, we investigate two commonly used plume shapes, the Poisson (see **Eq. 13**) and Suzuki (see **Eq. 14**). Particle distributions (in terms of mass percentage or particle number percentage) in the vertical direction in the initial ash cloud are shown in **Figure 7**. In that figure, the vertical particle distribution based on Plume-SPH output is compared with the vertical particle distribution based on semiempirical shape expressions. Both Poisson and Suzuki distributions in **Figure 7** take $H_{max}$ = 40 km, which is close to the reported observed plume height. When adopting the Poisson distribution [(c) in **Figure 7**], the majority of the particles are between 30 and ~ 40 km. Obviously, the Poisson function distributes the majority of ash at a higher elevation than was observed (e.g. Fero et al., 2008). As for the Suzuki distribution, (D) in **Figure 7**, the majority of ash particles also occur in a range that is significantly higher than 25 km. Note that in the plot (d), the Suzuki constant $k$ is set to 4, which is commonly used for Sub-Plinian and Plinian eruption columns (Pfeiffer et al., 2005). As for initial ash clouds in Plume-SPH simulations, most ash particles are distributed between ~ 17–28 km, which matches well with observations. The plume height is also consistent with observation.

For the Poisson distributions, the ash particles cannot be lower without changing the plume height. To distribute the majority of ash particles at a lower elevation, the plume height must be reduced to a value smaller than the observed plume height. Adjusting parameters such as plume height in the empirical expression is actually the traditional source term of calibration method. A set of initial ash clouds using different plume heights based on the Poisson distribution is shown in **Figure 8**. The plume heights adopted in plume shape expressions are not obtained from any plume model or observation of plume height, but by *a posteriori* calibration to later-observed ash cloud transport heights. For Suzuki distribution, adjusting the Suzuki constant can adjust the distribution of ash particles in vertical direction. As shown in **Figure 7**, when $k$ is equal to 1 [see (e)], the majority of ash particles are at a lower elevation than observation. With $k = 3$ and $k = 6$ [figure (g) and (h)], the majority of ash particles are at a higher elevation than observation. When $k$ is set to 2 [see (f)], we can see that the majority of ash particles are roughly distributed in the range 17–28 km. But the shape does not look like a typical plume, as particles are more uniformly distributed in the vertical direction. In addition, the "best fit" Suzuki constant is different from the typical value, which is 4 (Pfeiffer et al., 2005), for Sub-Plinian and Plinian eruptions, meaning that we can not apply previous experiences into the semiempirical expression for this eruption.

The ash clouds created by the Poisson distribution with different plume heights are used as initial conditions in Puff simulations, whose results are shown in **Figure 9**. Except for the plume height, all other parameters for creating an initial ash cloud are the same as those in **Table 2**. Of course, the range over which the majority of ash particles are located is lower when using lower plume heights. **Figure 9** thus shows that the plume height has a significant influence on the ash transport simulation. The maximum heights of the simulated ash cloud are completely different when using different $H_{max}$ values in the Poisson expression. When the plume height is 10 km, the ash lags behind that observed and its FMS is 0.055, which is very close to FMS when $H_{max}$ is 40 km. For the cases that $H_{max}$ is 20 and 30 km, the FMS values are 0.121 and 0.142, respectively. Taking 20 km as the plume height better represents the lower elevation portion of the ash cloud while taking 30 km as the plume height better represents the higher elevation portion of the ash cloud.

Simulation results based on a calibrated plume height of 30 km show a footprint similar to those of "Plume-SPH + Puff" although smaller in terms of area. However, the initial ash cloud created by a Poisson distribution with a plume height around 35 km generates the best match with observation in terms of FMS metric, with the FMS value reaching 0.227. That is to say, a

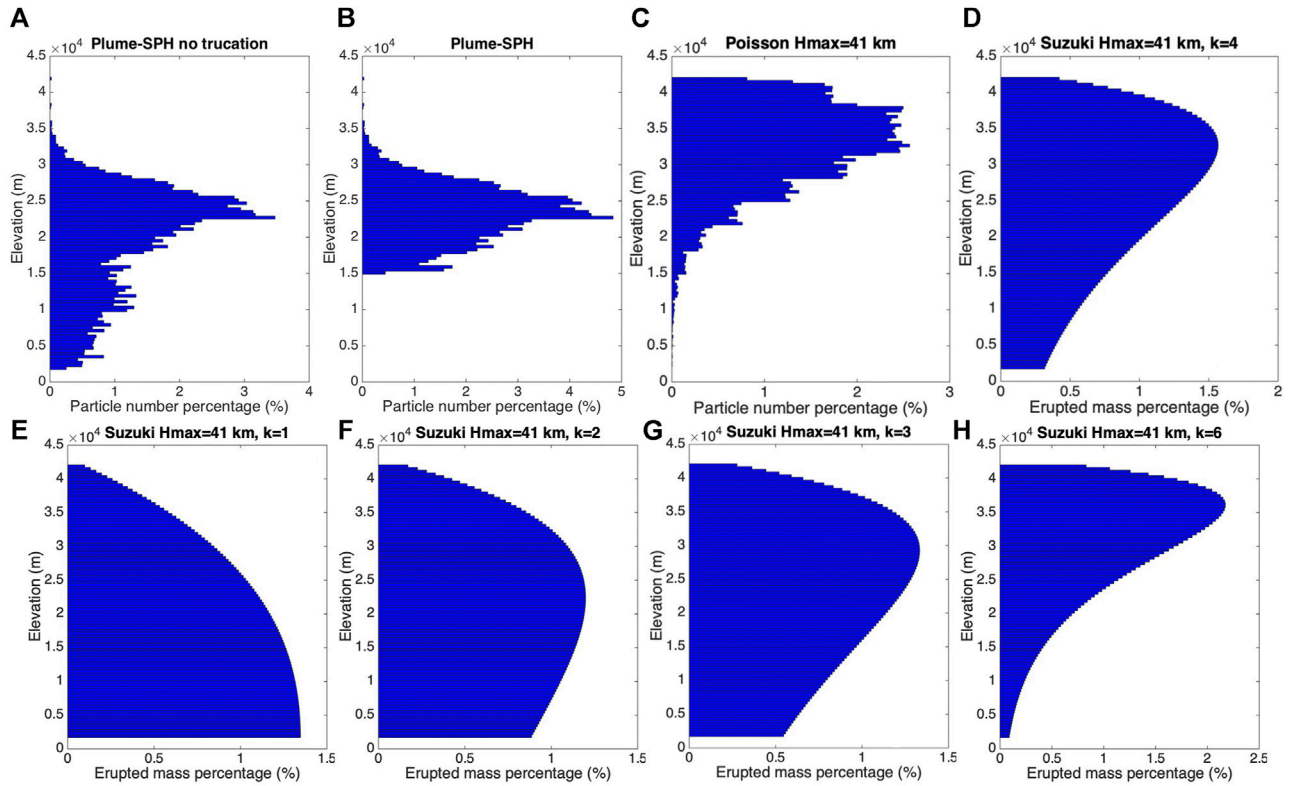


**FIGURE 7 |** First row, comparison of particle distribution of initial ash cloud in vertical direction. **(A)** is corresponding to the initial ash cloud obtained from Plume-SPH output. **(B)** is **(A)** truncated by a elevation threshold of 15 km. **(C)** is for vertical ash distribution based on Poisson distribution (**Eq. 13**) with $H_{max}$ equals to 40 km. Another parameter, $H_{width}$ is 6662 m. **(D)** is corresponding to Suzuki distribution (**Eq. 14**) with $H_{max}$ equals to 40 km and $k$ equals to 4 (Pfeiffer et al., 2005). The second row, Suzuki distribution with $H_{max}$ equals to 40 km but different values for $k$. The $x$ axis is the percentage of particle numbers for Plume-SPH and Poisson. For Suzuki, the $x$ axis is the mass percentage of erupted material.

plume height lower than the real plume height is required by the Poisson plume shape to distribute ash particles at elevations comparable to the "true" ash distribution. Even for the best-matched results, the high concentration area does not match with an observation well.

It is clear that the initial condition of vertical ash distribution has a dominant effect on VATD simulation, so it is critical for the forecast capability of VATD simulations to explore more accurate and adaptive ways for establishing the initial ash distribution, especially methods that do not rely on *a posteriori* parameter calibration or inversion.

## 3.2 Effect of Vertical Spread ($H_{width}$)

In the previous section, we explored the effects of adjusting the plume height to change the vertical ash distribution at the source. In this section, we investigate the importance of another parameter in the semiempirical Poisson expression (**Eq. 13**). We vary the "vertical spread", $H_{width}$, in the range ~ 3–10 km. A set of initial ash clouds with different vertical spreads are shown in **Figure 8**. Except for vertical spread, all other parameters for creating an initial ash cloud are the same as those in **Table 2**. The vertical range within which the majority of ash particles are located becomes narrower when a smaller value for the vertical spread parameter is used. The ash clouds based on different vertical spread parameters are then used as initial conditions in Puff simulations.

The VATD results are shown in **Figure 9**. Adjusting the vertical spread changes particle distribution in the vertical direction, and thus, not surprisingly, affects the VATD simulation results. None of the VATD simulations based on initial ash clouds with vertical spreads equal to 3 km or 5 km yield better results than do VATD simulations based on initial conditions created by Plume-SPH (see **Figure 9**). But when we take 10 km as the vertical spread, we get a FMS that is very close to Plume-SPH, even though the shape of the ash cloud footprint and the maximum height of the ash cloud are completely different.

The calibration tests on vertical spread, carried out here, are certainly not exhaustive. One could do a more comprehensive calibration throughout the multidimensional parameter space (for Poisson distribution, the parameter space is two-dimensional) and find better results. In addition, with a more complicated semiempirical plume shape expression, one could have more control over plume shape and might be able to get an initial condition that yields a more accurate ash transport forecast. However, more complicated and adaptable plume shape expressions imply a higher-dimensional parameter space, which requires more effort in calibration, even though the degrees of freedom to adjust plume shape are still limited.

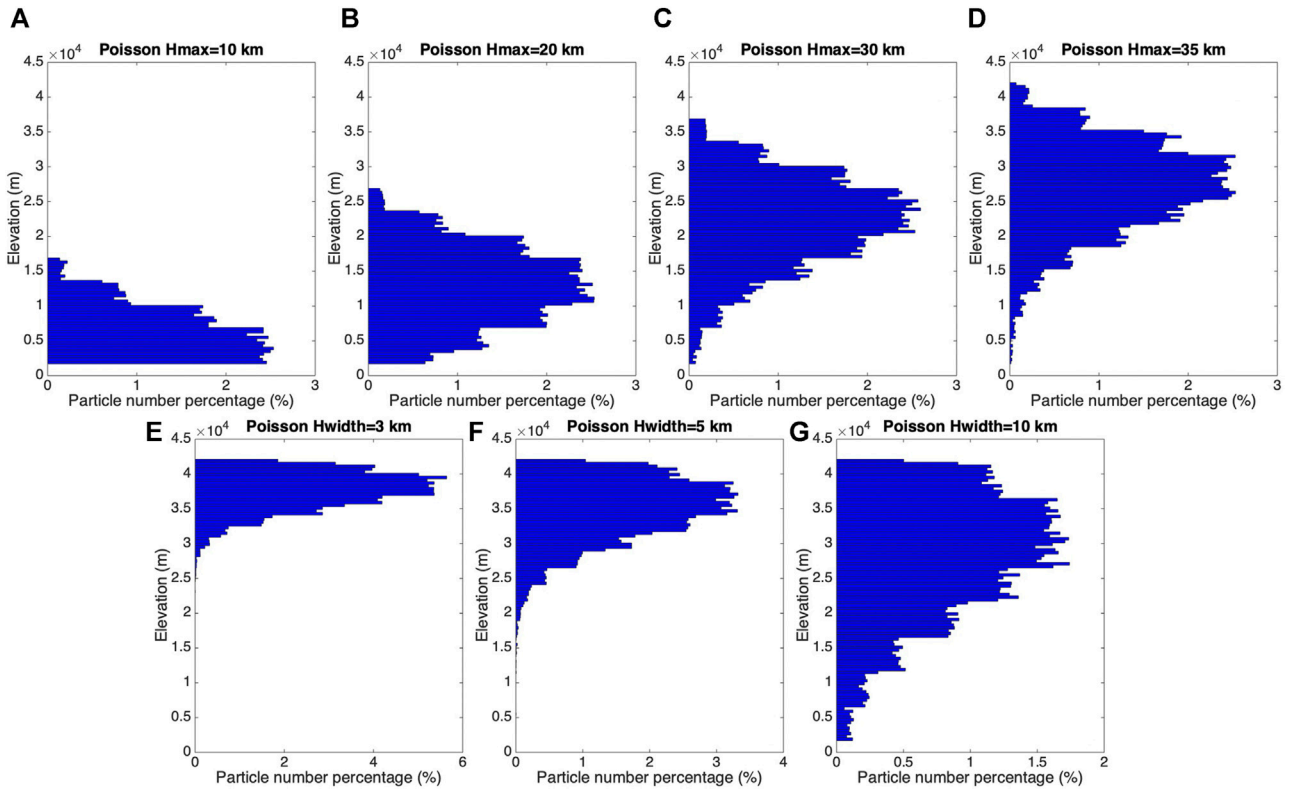


**FIGURE 8 |** Initial particle distribution in vertical direction based on Poisson plume shape (**Eq. 13**). The first row varies plume heights. **(A)** to **(D)** are corresponding to plume height of 10 km, 20 km, 30 km, 35 km. Another parameter, $H_{width}$ is 6662 m for all four figures in the first row. The second row varies "vertical spread", $H_{width}$. **(E)** to **(G)** are corresponding to vertical spread of 3 km, 5 km, and 10 km. The plume height, $H_{max}$, is set to 40 km for all three figures. The *x* axis is the percentage of particle numbers. See **Figure 7** for vertical ash distribution of Plume-SPH output.

Creating initial conditions based on 3D plume simulations avoids such parameter calibration.

## 3.3 Horizontal Ash Distribution

The differences between the semiempirical plume particle distribution and actual (or simulated by the 3D plume model) are not only in the vertical direction. The importance of the horizontal distance of each initial ash particle from a line extending upward from the volcano is investigated in this section. Puff uses a uniformly distributed random process to determine ash particle locations in a circle centered on the volcano site as described in *Puff and Initial Ash Cloud* for the output of Plume-SPH, and an effective (maximum) radius is determined according to a given threshold of ash concentration, following Cerminara et al. (2016b). A time-averaged, spatial integration of the dynamic 3D flow field is conducted to remove significant fluctuations in time and space. **Figure 10** compares the radius of the initial ash clouds created by 3D plume simulations with that assumed in the semiempirical plume shape expression adopted in Puff. It is impossible for the simple, assumed plume shapes to capture the complex and more realistic shapes developed by Plume-SPH. Additional parameterization may generate more reasonable shapes, but these would continue to be *ad hoc*; none would likely have the potential fidelity of the 3D simulation to reality, and adding a temporally changing distribution would be difficult.

Comparison between cross-sectional views of the initial ash clouds is shown in **Figure 11**. The cross-sectional view of horizontal particle distribution using the semiempirical method (last figure in **Figure 11**) is similar to a cross-sectional view of a simulated 3D plume, in a general sense. However, for simulated 3D plumes, the ash particle distribution in cross section varies with height, which factor would become increasingly important with increasing wind speed, where wind speed to be included in the estimate of initial plume shape. It is difficult for the semiempirical expressions to accommodate such a complex distribution.

Despite the obvious difficulty of correctly estimating ash distribution near the vent, or for short propagation times, assigning different values for the horizontal spread has a negligible effect on VATD simulation results at large time. We investigated horizontal spread values between 50 and 1600 km to create initial ash clouds; all of them generated similar results at large propagation times (> 1 day). **Figure 9** shows two different simulation results based on initial ash clouds with horizontal spread equal to 50 and 600 km, respectively. No visible differences are apparent between them. The FMS values, 0.073 and 0.074, respectively, are also very close. This implies that horizontal

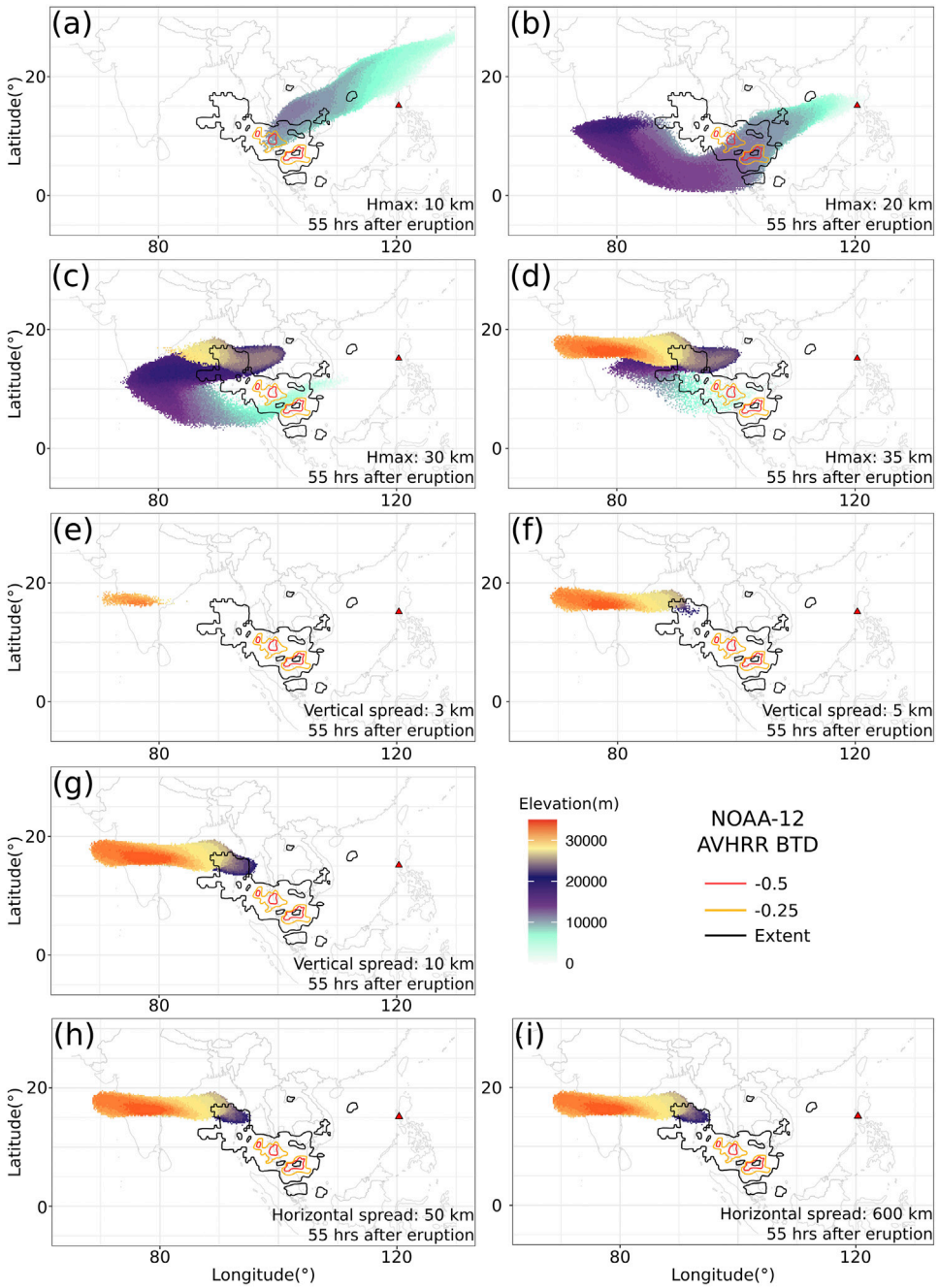


| Paramete | *Hmax* | | | | *Hwidth* | | | *rmax* | |
|---|---|---|---|---|---|---|---|---|---|
| Value | 10 km | 20 km | 30 km | 35 km | 3 km | 5 km | 10 km | 50 km | 600 km |
| Plot | (a) | (b) | (c) | (d) | (e) | (f) | (g) | (h) | (i) |
| FMS | 0.055 | 0.121 | 0.142 | 0.227 | 0 | 0.039 | 0.085 | 0.073 | 0.074 |

**FIGURE 9 |** Ash transport simulated by Puff using different initial ash clouds created according to the empirical expressions using different input parameters. All images are corresponding to 55 h after eruption (UT 199106171141). More details are in the table.

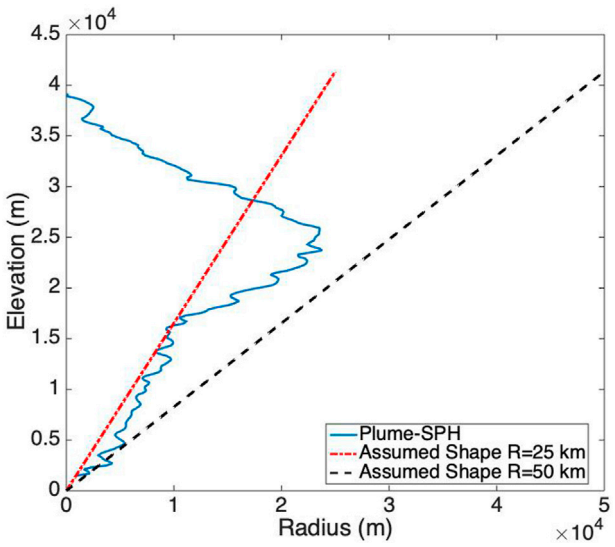


**FIGURE 10 |** Comparison between radius of initial ash clouds created by 3D plume model (Plume-SPH) and assumed initial ash cloud shape (**Eq. 15**) in Puff. The plume shape expression used in Puff defines an inverted cone whose actual shape changes when "horizontal spread" takes different values. $R$ = 25 km is corresponding to "horizontal spread" equals to 50 km. $R$ = 50 km is corresponding to "horizontal spread" equals to 100 km.

distribution has a less significant influence on VATD simulation results than does vertical distribution for long distance or large time. Perhaps, the most important ramification of this result is that it means the time at which the "handshake" is made between Plume-SPH and the VATD does not affect results significantly for relatively large distances and times.

# 4 DISCUSSION

## 4.1 Sentitivity of Other Input Parameters

Besides the initial ash cloud, other parameters for Puff simulations are horizontal diffusivity, vertical diffusivity, mean grain size, grain size standard deviation, and total number of tracers. We present in this subsection informal sensitivity studies on these parameters. We also investigate the influence of eruption duration. The sensitivity analyses will serve as the basis for identifying possible sources of disparities between simulation and observation.

Fero et al. (2008) simulated the volcanic ash transport in the Pinatubo eruption in 1991. He carried out systematic sensitivity analysis with respect to input parameters of Puff and found that all other parameters except for the plume height have negligible effect on long-term ash transportation of Pinatubo. Inspired by Fero et al. (2008), we carried out similar informal sensitivity analysis with much fewer sample points in the parameter space and got similar results. Among the parameters explored, the eruption duration and beginning time show the most obvious influence on simulated ash distribution although the effect is still small. To show the differences in an intuitive way, (a) - (c) in **Figure 12** shows simulated ash distribution corresponding to 4.9 h duration, 9 h duration, and 11 h duration, respectively. After 72 h, relative to the simulation starting time, these three cases

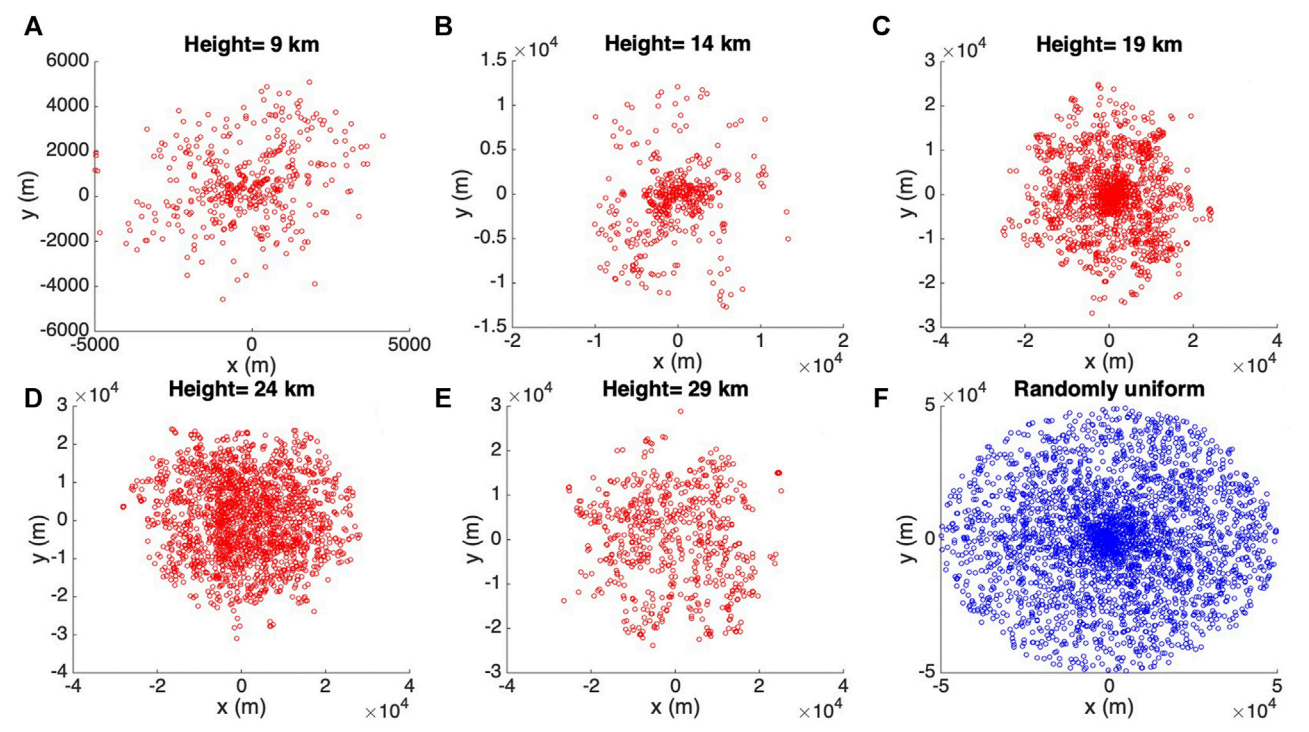


**FIGURE 11 |** Horizontal distribution of ash particles (tracers) on a cross section of initial ash cloud. Puff assumes a randomly uniform distribution of ash particles within a circle, as shown by blue dots in **(F)**. All other figures show the ash particle distribution of initial ash clouds created by Plume-SPH at different elevations.

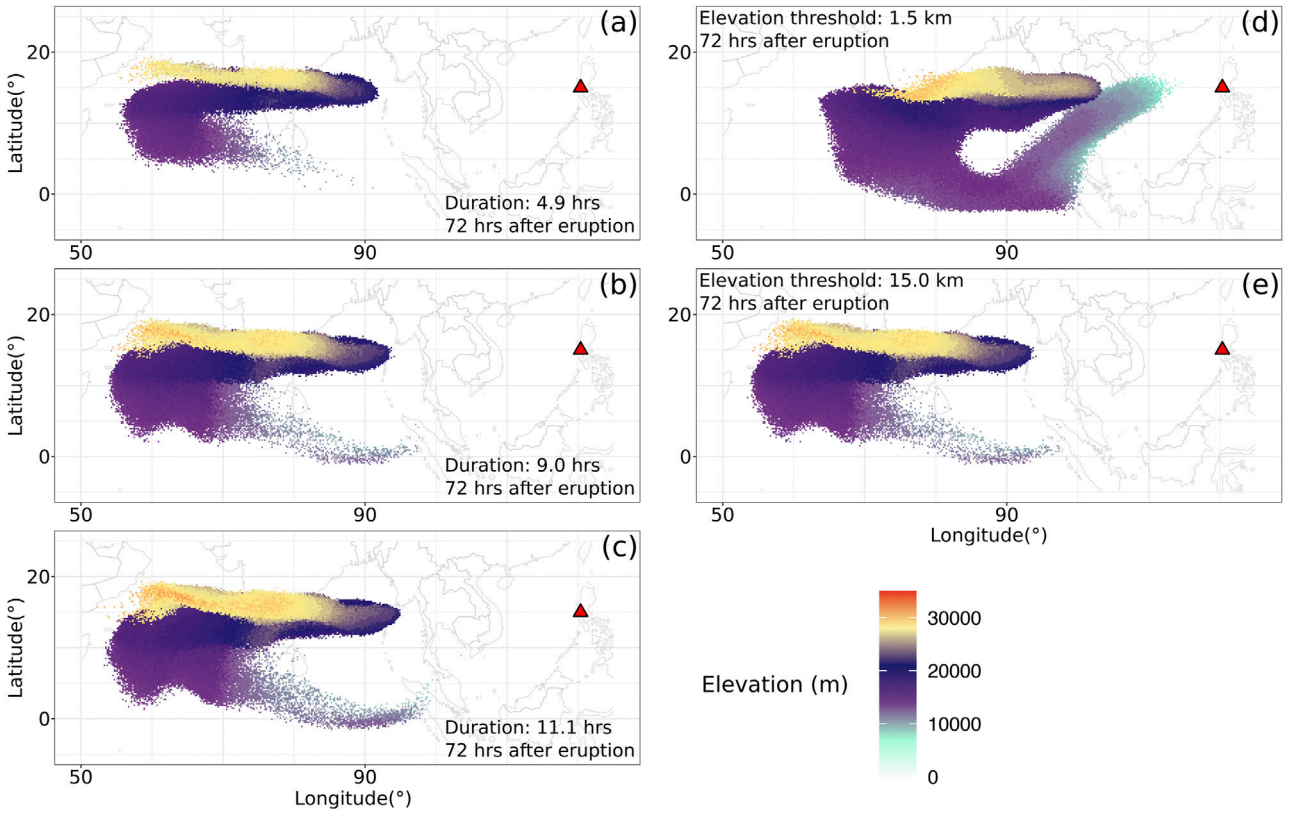


| Paramete | EruptionDuration | | | Elevation Threshold | |
|---|---|---|---|---|---|
| Value | 4.9 hour | 9 hour | 11.1 hour | 1500 m | 15 km |
| Plot | (a) | (b) | (c) | (d) | (e) |

**FIGURE 12 |** Sensitivity of Puff simulation with respect to eruption durations and initial ash cloud cutoff heights (elevation threshold). For different eruption durations, the starting and ending time for each case are in **Table 3**. The contours correspond to ash concentration at 72 h after eruption. Details are in the table.

**TABLE 3 |** The starting and ending time (UT) for simulating the climactic phase of Pinatubo eruption on June 15, 1991. Observed plume height (Holasek et al., 1996a) at different times is also listed in the table.

| Eruption Duration | 4.9 hours | 9 hours | 10 hours | 11.1 hours |
|---|---|---|---|---|
| Start Time | 0441 | 0441 | 0441 | 0334 |
| Height at Start Time | 37.5 km | 37.5 km | 37.5 km | 24.5 km |
| End Time | 0934 | 1341 | 1441 | 1441 |
| Height at End Time | 35 km | 26.5 km | 22.5 | 22.5 km |

generate very similar results with tiny visible differences. Daniele et al. (2009) did sensitivity analysis with respect to the input parameters of Puff on different volcanoes and found that for eruptive eruptions, the most dominant factors are the wind field and plume height, while all other input parameters are relatively less important. The significance of the wind field has been confirmed by other researchers (e.g. Stefanescu et al., 2014).

We conducted several simulations with eruption duration varying in the range of 5–11 h with slightly different starting time of climactic phase. **Table 3** lists all these simulations. However, only slight visible differences are observed among the simulated ash transport outputs. We can see that the eruption duration has negligible effects on long-term ash transport.

The new methodology for generating initial ash clouds introduces a new parameter: elevation threshold, which was specified based on averaged vertical velocity and horizontal velocity. We carry out a separate, informal sensitivity analysis on this parameter by varying the elevation threshold from 1.5 km (the height of the vent) to 25 km. The simulated ash distributions show obvious differences, especially when the elevation threshold is either very high or very low. However, varying the elevation threshold in the range of 12–18 km generates relatively small differences in ash transport simulation results. **Figure 12** (d) and (f) compare the simulated ash distributions corresponding to elevation thresholds of 1.5 and 15 km. Compared with the ash distribution for a threshold of 15 km, an extra-long tail appears when using an elevation threshold of 1.5 km. The maximum height of the tail is around 10 km. Adopting lower elevation

thresholds adds more tracer particles at lower elevation. As the winds at different elevations are different, the tracers at lower elevations propagate in different directions. The HYSPLIT forward trajectory tracking indicates that the wind between elevations of 10 and 15 km blew from north-east to south-west, while winds of higher elevation blew from east to west (see **Figure 6**).

## 4.2 Other Sources of Disparities

The full range of research issues raised by numerical forecasting of volcanic clouds is diverse. We focused on the effect of initial conditions in this study. During the plume modeling, secondary factors, such as microphysical processes, even though they play lesser roles, likely need to be included to improve accuracy for a particular eruption. Wind fields are not considered in the current version of Plume-SPH, but for weak plumes, wind plays an important enough role that it has to be considered in the plume model. In addition, eruption conditions are subject to change with time, even during the climactic phase of an eruption. For example, ash just west of Pinatubo observed in satellite images does not show up in "Plume-SPH + Puff" simulation results. This disparity is likely due to the fact that Pinatubo continued erupting (with smaller plume height) after the climactic phase, while we only simulate the climactic phase. In the future, time-dependent initial conditions for VATDs can be created from 3D plume simulations based on time-dependent eruption conditions. It is worth mentioning that the eruption conditions at the vent are usually inferred from observable information based on 1D plume models. Using a 3D plume model will not reduce uncertainties from the eruption conditions.

Additional assumptions made during computations in each VATD model or even measurements may also generate additional disparity. Analysis of the results (see large decrease in FMS shown in (f) in **Figure 5**) indicates that Puff underestimates the fallout of ash particles, which together with satellite pictures not capturing low-level ash clouds can explain the FMS decrease.

One implicit assumption in the current method is that ash transportation is dominated by wind advection (the passive dispersion approximation). However, during the growth of the volcanic umbrella, the dominant factors are various in different regimes (Pouget et al., 2016a) depending on the characteristics of a particular eruption. Webster et al. (2020) suggested that the lateral spread by the intrusive gravity current dominates the transport of the ash cloud in this stage. Studies by Mastin (Mastin et al., 2014; Mastin and Van Eaton, 2020) also showed that neglecting the umbrella cloud formation for larger eruptions led to significantly different footprints for the resulting VATD fallout maps. Their studies imply that including mapped velocities of the plume as a perturbation on the winds can better capture the radial spreading of an umbrella. In the current method, the 3D plume model generated initial ash cloud has a radius of around 25 km. For the Pinatubo 1991 eruption, the passive dispersion approximation can be reasonably applied when radius is greater than 450 km and can be fully valid only when the radius is greater than 1800 km (Costa et al., 2013). So the umbrella stage during the ash transportation is very likely oversimplified in the current simulation. It is computationally too expensive for the Plume-SPH model to continue simulation until the plume radius reaches, at least, for example, 450 km. An additional umbrella model, with a much coarser resolution and simplified physics, in between the plume model and the VATD model would presumably better model the whole ash transportation process.

Besides the errors from assumptions in the model, errors are also introduced from the reanalysis wind field data and the satellite observations, which are retrievals, with their associated errors, rather than the "truth". In addition, metrics based on footprint cannot account for the disparities at different heights and ash concentrations. Comparing the simulation and observation purely based on footprint-based metric sometimes is biased.

## 4.3 SUMMARY

Traditional VATD simulations use initial conditions created according to a semiempirical plume shape expression. This study presents, for the first time, VATD simulations using initial source conditions created by a 3D plume model. A case study of the 1991 Pinatubo eruption demonstrates that a 3D plume model can create more realistic initial ash cloud and ash parcel positions and therefore improve the accuracy of ash transport forecasts. Informal sensitivity analyses suggest that initial conditions, as expressed in the disposition of initial ash parcel positions in the vertical, have a more significant effect on a volcanic ash transport forecast than most other parameters. Comparison of initial ash parcel distributions among the 3D plume model, semiempirical expressions, and observations suggests that a major subpopulation of ash parcels should be placed at a much lower elevation than plume height to obtain a better VATD forecast. Comparing the effects of the plume height, vertical spread and horizontal spread show that ash particle distribution in the vertical direction has the strongest effect on VATD simulation results.

To summarize, we have presented a novel method for creating *a priori* initial source conditions for VATD simulations. We have shown that it might be possible to obtain initial positions of ash parcels with deterministic forward modeling of the volcanic plume, potentially obviating or lessening the need to attempt to somehow observe initial positions, or *a posteriori* create a history of release heights via inversion (Stohl et al., 2011). Although the method now suffers from the high computational cost associated with 3D forward modeling, there is the possibility that in future it might not only help overcome shortcomings of existing methods used to generate *a priori* input parameters but also overcome the need to carry out thousands of runs associated with inverse modeling. In addition, computational cost will continue to diminish as computing speed increases. As they are forward numerical models based on first principles, 3D plume models need little if any parameterization, and user intervention should not be required to improve forecast power; no assumption about the initial position of ash parcels is needed. Generation of the initial cloud of ash parcels directly by 3D simulation is potentially adaptable to a variety of volcanic and

atmospheric scenarios. In contrast, semiempirical expressions used to determine initial conditions require several parameters to control ash particle distribution along with a vertical line source or some simplified shape of the initial ash cloud, making it difficult in some cases to generate initial conditions that closely resemble a complex reality.

The plume-VATD coupling presented in this study is LagrangianLagrangian coupling. When coupling plume models and VATD models of different types, the interpolation will be different. For example, to couple a Lagarian plume model with an Eulerian VATD model, we must convert the particle distribution in the output of the plume model into ash concentration of cells (mesh grids). When coupling an Eulerian plume model to a Lagrangian VATD model, the mass fraction of the erupted material in the output of the 3D plume model should be converted into an ash cloud represented by a group of particles. The steps for coupling a 3D plume model with a VATD model also depend on features of the software, such as the inputs, the outputs, and file formats.

## DATA AVAILABILITY STATEMENT

The raw data supporting the conclusions of this article will be made available by the authors, without undue reservation.

## AUTHOR CONTRIBUTIONS

The idea of using a 3D plume model to start a VATD simulation originated from a conservation between AP and MB. ZC carried out the Plume-SPH simulations, Puff simulations, initial results analysis, and prepared the first draft. All authors worked together for further revisions. MB carried out the HYSPLIT simulation. QY post-processed the Puff simulation results, overlapped the simulation results with satellite observation, and calculated the FMS values. All authors contributed equally to the manuscript writing. AP and MB obtained funding to financially support the work.

## FUNDING

This work was supported by National Science Foundation awards 1521855, 1621853, and 1821311, 1821338, and 2004302 and by the National Research Foundation Singapore and the Singapore Ministry of Education under the Research Centres of Excellence initiative (project number: NRF2018NRF-NSFC003ES-010).

## ACKNOWLEDGMENTS

We are grateful to the two reviewers of the paper for their constructive comments and suggestions that improved the paper. Support for the Twentieth Century Reanalysis Project dataset is provided by the U.S. Department of Energy, Office of Science Innovative and Novel Computational Impact on Theory and Experiment (DOE INCITE) program, and Office of Biological and Environmental Research (BER), and by the National Oceanic and Atmospheric Administration Climate Program Office.

## REFERENCES

Avdyushin, S. I., Tulinov, G. F., Ivanov, M. S., Kuzmenko, B. N., Mezhuev, I. R., Nardi, B., et al. (1993). 1. Spatial and Temporal Evolution of the Optical Thickness of the Pinatubo Aerosol Cloud in the Northern Hemisphere from a Network of Ship-Borne and Stationary Lidars. *Geophys. Res. Lett.* 20, 1963–1966. doi:10.1029/93gl00485

Bursik, M. (2001). Effect of Wind on the Rise Height of Volcanic Plumes. *Geophys. Res. Lett.* 28, 3621–3624. doi:10.1029/2001gl013393

Bursik, M. I., Kobs, S. E., Burns, A., Braitseva, O. A., Bazanova, L. I., Melekestsev, I. V., et al. (2009). Volcanic Plumes and Wind: Jetstream Interaction Examples and Implications for Air Traffic. *J. Volcanology Geothermal Res.* 186, 60–67. doi:10.1016/j.jvolgeores.2009.01.021

Bursik, M., Jones, M., Carn, S., Dean, K., Patra, A., Pavolonis, M., et al. (2012). Estimation and Propagation of Volcanic Source Parameter Uncertainty in an Ash Transport and Dispersal Model: Application to the Eyjafjallajokull Plume of 14-16 April 2010. *Bull. Volcanol* 74, 2321–2338. doi:10.1007/s00445-012-0665-2

Cao, Z., Patra, A., Bursik, M., Pitman, E. B., and Jones, M. (2018). Plume-sph 1.0: a Three-Dimensional, Dusty-Gas Volcanic Plume Model Based on Smoothed Particle Hydrodynamics. *Geosci. Model. Dev.* 11, 2691–2715. doi:10.5194/gmd-11-2691-2018

Cao, Z., Patra, A., and Jones, M. (2017). Data Management and Volcano Plume Simulation with Parallel Sph Method and Dynamic Halo Domains. *Proced. Comp. Sci.* 108, 786–795. doi:10.1016/j.procs.2017.05.094

Cerminara, M., Esposti Ongaro, T., and Neri, A. (2016b). Large Eddy Simulation of Gas–Particle Kinematic Decoupling and Turbulent Entrainment in Volcanic Plumes. *J. Volcanology Geothermal Res.* 2016, 326. doi:10.1016/j.jvolgeores.2016.06.018

Cerminara, M., Esposti Ongaro, T., and Berselli, L. C. (2016a). Ashee-1.0: a Compressible, Equilibrium-Eulerian Model for Volcanic Ash Plumes. *Geosci. Model. Dev.* 9, 697–730. doi:10.5194/gmd-9-697-2016

Constantinescu, R., Hopulele-Gligor, A., Connor, C. B., Bonadonna, C., Connor, L. J., Lindsay, J. M., et al. (2021). The Radius of the Umbrella Cloud Helps Characterize Large Explosive Volcanic Eruptions. *Commun. Earth Environ.* 2, 1–8. doi:10.1038/s43247-020-00078-3

Costa, A., Folch, A., and Macedonio, G. (2013). Density-driven Transport in the Umbrella Region of Volcanic Clouds: Implications for Tephra Dispersion Models. *Geophys. Res. Lett.* 40, 4823–4827. doi:10.1002/grl.50942

Costa, A., Suzuki, Y., Cerminara, M., Devenish, B., Esposti Ongaro, T., Herzog, M., et al. (2016). Results of the Eruptive Column Model Inter-comparison Study. *J. Volcanology Geothermal Res.* 326, 2–25. doi:10.1016/j.jvolgeores.2016.01.017

D'amours, R. (1998). Modeling the Etex Plume Dispersion with the canadian Emergency Response Model. *Atmos. Environ.* 32, 4335–4341. doi:10.1016/S1352-2310(98)00182-4

Daniele, P., Lirer, L., Petrosino, P., Spinelli, N., and Peterson, R. (2009). Applications of the Puff Model to Forecasts of Volcanic Clouds Dispersal from etna and Vesuvio. *Comput. Geosciences* 35, 1035–1049. doi:10.1016/j.cageo.2008.06.002

DeFoor, T. E., Robinson, E., and Ryan, S. (1992). Early Lidar Observations of the June 1991 Pinatubo Eruption Plume at Mauna Loa Observatory, hawaii. *Geophys. Res. Lett.* 19, 187–190. doi:10.1029/91gl02791

de'Michieli Vitturi, M., Neri, A., and Barsotti, S. (2015). Plume-mom 1.0: A New Integral Model of Volcanic Plumes Based on the Method of Moments. *Geoscientific Model. Dev.* 8, 2447–2463. doi:10.5194/gmd-8-2447-2015

Deshler, T., Hofmann, D. J., Johnson, B. J., and Rozier, W. R. (1992). Balloonborne Measurements of the Pinatubo Aerosol Size Distribution and Volatility at laramie, wyoming during the Summer of 1991. *Geophys. Res. Lett.* 19, 199–202. doi:10.1029/91gl02787

Draxler, R. R., and Hess, G. (1998). An Overview of The HYSPLIT_4 Modelling System for Trajectories, Dispersion, and Deposition. *Aust. Meteorol. Mag.* 47, 295–308.

Fero, J., Carey, S. N., and Merrill, J. T. (2009). Simulating the Dispersal of Tephra from the 1991 Pinatubo Eruption: Implications for the Formation of Widespread Ash Layers. *J. Volcanology Geothermal Res.* 186, 120–131. doi:10.1016/j.jvolgeores.2009.03.011

Fero, J., Carey, S. N., and Merrill, J. T. (2008). Simulation of the 1980 Eruption of Mount St. Helens Using the Ash-Tracking Model Puff. *J. Volcanology Geothermal Res.* 175, 355–366. doi:10.1016/j.jvolgeores.2008.03.029

Folch, A., Costa, A., and Macedonio, G. (2009). Fall3d: A Computational Model for Transport and Deposition of Volcanic Ash. *Comput. Geosciences* 35, 1334–1342. doi:10.1016/j.cageo.2008.08.008

Folch, A., Costa, A., and Macedonio, G. (2016). Fplume-1.0: An Integral Volcanic Plume Model Accounting for Ash Aggregation. *Geosci. Model. Dev.* 9, 431–450. doi:10.5194/gmd-9-431-2016

Gingold, R. A., and Monaghan, J. J. (1977). Smoothed Particle Hydrodynamics: Theory and Application to Non-spherical Stars. *Monthly notices R. astronomical Soc.* 181, 375–389. doi:10.1093/mnras/181.3.375

Guo, S., Bluth, G. J., Rose, W. I., Watson, I. M., and Prata, A. (2004a). Re-evaluation of So2 Release of the 15 June 1991 Pinatubo Eruption Using Ultraviolet and Infrared Satellite Sensors. *Geochem. Geophys. Geosystems* 5, 1. doi:10.1029/2003gc000654

Guo, S., Rose, W. I., Bluth, G. J., and Watson, I. M. (2004b). Particles in the Great Pinatubo Volcanic Cloud of June 1991: The Role of Ice. *Geochem. Geophys. Geosystems* 5, 1. doi:10.1029/2003gc000655

Holasek, R. E., Self, S., and Woods, A. W. (1996a). Satellite Observations and Interpretation of the 1991 Mount Pinatubo Eruption Plumes. *J. Geophys. Res.* 101, 27635–27655. doi:10.1029/96jb01179

Holasek, R. E., Woods, A. W., and Self, S. (1996b). Experiments on Gas-Ash Separation Processes in Volcanic Umbrella Plumes. *J. volcanology geothermal Res.* 70, 169–181. doi:10.1016/0377-0273(95)00054-2

Jäger, H. (1992). The Pinatubo Eruption Cloud Observed by Lidar at Garmisch-Partenkirchen. *Geophys. Res. Lett.* 19, 191–194. doi:10.1029/92gl00071

Jones, A., Thomson, D., Hort, M., and Devenish, B. (2007). "The uk Met Office's Next-Generation Atmospheric Dispersion Model, Name Iii," in *Air Pollution Modeling and its Application XVII* (Springer), 580–589.

Mastin, L. G. (2007). A User-Friendly One-Dimensional Model for Wet Volcanic Plumes. *Geochem. Geophys. Geosystems* 8, 1. doi:10.1029/2006gc001455

Mastin, L. G., and Van Eaton, A. R. (2020). Comparing Simulations of Umbrella-Cloud Growth and Ash Transport with Observations from Pinatubo, Kelud, and Calbuco Volcanoes. *Atmosphere* 11, 1038. doi:10.3390/atmos11101038

Mastin, L. G., Van Eaton, A. R., and Lowenstern, J. B. (2014). Modeling Ash Fall Distribution from a Yellowstone Supereruption. *Geochem. Geophys. Geosyst.* 15, 3459–3475. doi:10.1002/2014gc005469

Neri, A., Esposti Ongaro, T., Macedonio, G., and Gidaspow, D. (2003). Multiparticle Simulation of Collapsing Volcanic Columns and Pyroclastic Flow. *J. Geophys. Res. Solid Earth* 1978–2012, 108. doi:10.1029/2001jb000508

Oberhuber, J. M., Herzog, M., Graf, H.-F., and Schwanke, K. (1998). Volcanic Plume Simulation on Large Scales. *J. Volcanology Geothermal Res.* 87, 29–53. doi:10.1016/s0377-0273(98)00099-7

Paladio-Melosantos, M. L. O., Solidum, R. U., Scott, W. E., Quiambao, R. B., Umbal, J. V., Rodolfo, K. S., et al. (1996). Tephra Falls of the 1991 Eruptions of Mount Pinatubo. *Fire and mud* 12000, 12030.

Pfeiffer, T., Costa, A., and Macedonio, G. (2005). A Model for the Numerical Simulation of Tephra Fall Deposits. *J. Volcanology Geothermal Res.* 140, 273–294. doi:10.1016/j.jvolgeores.2004.09.001

Pouget, S., Bursik, M., Johnson, C. G., Hogg, A. J., Phillips, J. C., and Sparks, R. S. J. (2016a). Interpretation of Umbrella Cloud Growth and Morphology: Implications for Flow Regimes of Short-Lived and Long-Lived Eruptions. *Bull. Volcanol* 78, 1–19. doi:10.1007/s00445-015-0993-0

Pouget, S., Bursik, M., Singla, P., and Singh, T. (2016b). Sensitivity Analysis of a One-Dimensional Model of a Volcanic Plume with Particle Fallout and Collapse Behavior. *J. Volcanology Geothermal Res.* 326, 18. doi:10.1016/j.jvolgeores.2016.02.018

Rolph, G., Stein, A., and Stunder, B. (2017). Real-time Environmental Applications and Display System: Ready. *Environ. Model. Softw.* 95, 210–228. doi:10.1016/j.envsoft.2017.06.025

Schwaiger, H. F., Denlinger, R. P., and Mastin, L. G. (2012). Ash3d: A Finite-Volume, Conservative Numerical Model for Ash Transport and Tephra Deposition. *J. Geophys. Res. Solid Earth* 117, 1. doi:10.1029/2011jb008968

Scott, W. E., Hoblitt, R. P., Torres, R. C., Self, S., Martinez, M. M. L., and Nillos, T. (1996). *Pyroclastic Flows of the June 15, 1991, Climactic Eruption of Mount Pinatubo*. Philippines: Fire and Mud: eruptions and lahars of Mount Pinatubo, 545–570.

Searcy, C., Dean, K., and Stringer, W. (1998). PUFF: A High-Resolution Volcanic Ash Tracking Model. *J. Volcanology Geothermal Res.* 80, 1–16. doi:10.1016/s0377-0273(97)00037-1

Self, S., Zhao, J.-X., Holasek, R. E., Torres, R. C., and King, A. J. (1996). *The Atmospheric Impact of the 1991 Mount Pinatubo Eruption*.

Stefanescu, E. R., Patra, A. K., Bursik, M., Jones, M., Madankan, R., Pitman, E. B., et al. (2014). Fast Construction of Surrogates for UQ Central to DDDAS-Application to Volcanic Ash Transport1. *Proced. Comp. Sci.* 29, 1227–1235. doi:10.1016/j.procs.2014.05.110

Stein, A. F., Draxler, R. R., Rolph, G. D., Stunder, B. J. B., Cohen, M. D., and Ngan, F. (2015). NOAA's HYSPLIT Atmospheric Transport and Dispersion Modeling System. *Bull. Am. Meteorol. Soc.* 96, 2059–2077. doi:10.1175/bams-d-14-00110.1

Stohl, A., Prata, A. J., Eckhardt, S., Clarisse, L., Durant, A., Henne, S., et al. (2011). Determination of Time- and Height-Resolved Volcanic Ash Emissions and Their Use for Quantitative Ash Dispersion Modeling: the 2010 Eyjafjallajökull Eruption. *Atmos. Chem. Phys.* 11, 4333–4351. doi:10.5194/acp-11-4333-2011

Suzuki, T. (1983). A Theoretical Model for Dispersion of Tephra. *Arc volcanism: Phys. tectonics* 95, 113.

Suzuki, Y. J., Koyaguchi, T., Ogawa, M., and Hachisu, I. (2005). A Numerical Study of Turbulent Mixing in Eruption Clouds Using a Three-Dimensional Fluid Dynamics Model. *J. Geophys. Res. Solid Earth* 110, 1. doi:10.1029/2004jb003460

Suzuki, Y., and Koyaguchi, T. (2009). A Three-Dimensional Numerical Simulation of Spreading Umbrella Clouds. *J. Geophys. Res. Solid Earth* 1978–2012, 114. doi:10.1029/2007jb005369

Tanaka, H. (1991). "Development of a Prediction Scheme for the Volcanic Ash Fall from Redoubt Volcano," in *First Int'l. Symp. On Volcanic Ash and Aviation Safety*, 58.

Tupper, A., Itikarai, I., Richards, M., Prata, F., Carn, S., and Rosenfeld, D. (2007). Facing the Challenges of the International Airways Volcano Watch: the 2004/05 Eruptions of Manam, papua new guinea. *Weather Forecast.* 22, 175–191. doi:10.1175/waf974.1

Walko, R., Tremback, C., and Bell, M. (1995). *Hypact: The Hybrid Particle and Concentration Transport Model*. User's guide. Available at: https://scholar.google.com/scholar?hl=en&as_sdt=0%2C30&q=Hypact%3A+The+Hybrid+Particle+and+Concentration+Transport+Model.+User%E2%80%99s+guide.&btnG=

Webster, H. N., Devenish, B. J., Mastin, L. G., Thomson, D. J., and Van Eaton, A. R. (2020). Operational Modelling of Umbrella Cloud Growth in a Lagrangian Volcanic Ash Transport and Dispersion Model. *Atmosphere* 11, 200. doi:10.3390/atmos11020200

Witham, C. S., Hort, M. C., Potts, R., Servranckx, R., Husson, P., and Bonnardot, F. (2007). Comparison of VAAC Atmospheric Dispersion Models Using the 1 November 2004 Grimsvötn Eruption. *Met. Apps* 14, 27–38. doi:10.1002/met.3

Woods, A. W. (1988). The Fluid Dynamics and Thermodynamics of Eruption Columns. *Bull. Volcanol* 50, 169–193. doi:10.1007/bf01079681

Zidikheri, M. J., Lucas, C., and Potts, R. J. (2017). Estimation of Optimal Dispersion Model Source Parameters Using Satellite Detections of Volcanic Ash. *J. Geophys. Res. Atmos.* 122, 8207–8232. doi:10.1002/2017jd026676

**Conflict of Interest:** ZC was employed by ANSYS Inc.

The remaining authors declare that the research was conducted in the absence of any commercial or financial relationships that could be construed as a potential conflict of interest.

**Publisher's Note:** All claims expressed in this article are solely those of the authors and do not necessarily represent those of their affiliated organizations, or those of the publisher, the editors and the reviewers. Any product that may be evaluated in this article, or claim that may be made by its manufacturer, is not guaranteed or endorsed by the publisher.

frontiers in Earth Science

ORIGINAL RESEARCH
published: 21 October 2021
doi: 10.3389/feart.2021.713175

# Modelling Settling-Driven Gravitational Instabilities at the Base of Volcanic Clouds Using the Lattice Boltzmann Method

*Jonathan Lemus*[1,2]*, *Allan Fries*[1], *Paul A. Jarvis*[1], *Costanza Bonadonna*[1], *Bastien Chopard*[2] *and Jonas Lätt*[2]

[1]*Department of Earth Sciences, University of Geneva, Geneva, Switzerland,* [2]*Department of Computer Science, University of Geneva, Carouge, Switzerland*

Field observations and laboratory experiments have shown that ash sedimentation can be significantly affected by collective settling mechanisms that promote premature ash deposition, with important implications for dispersal and associated impacts. Among these mechanisms, settling-driven gravitational instabilities result from the formation of a gravitationally-unstable particle boundary layer (PBL) that grows between volcanic ash clouds and the underlying atmosphere. The PBL destabilises once it reaches a critical thickness characterised by a dimensionless Grashof number, triggering the formation of rapid, downward-moving ash fingers that remain poorly characterised. We simulate this process by coupling a Lattice Boltzmann model, which solves the Navier-Stokes equations for the fluid phase, with a Weighted Essentially Non Oscillatory (WENO) finite difference scheme which solves the advection-diffusion-settling equation describing particle transport. Since the physical problem is advection dominated, the use of the WENO scheme reduces numerical diffusivity and ensures accurate tracking of the temporal evolution of the interface between the layers. We have validated the new model by showing that the simulated early-time growth rate of the instability is in very good agreement with that predicted by linear stability analysis, whilst the modelled late-stage behaviour also successfully reproduces quantitative results from published laboratory experiments. The results show that the model is capable of reproducing both the growth of the unstable PBL and the non-linear dependence of the fingers' vertical velocity on both the initial particle concentration and the particle diameter. Our validated model is used to expand the parameter space explored experimentally and provides key insights into field studies. Our simulations reveal that the critical Grashof number for the instability is about ten times larger than expected by analogy with thermal convection. Moreover, as in the experiments, we found that instabilities do not develop above a given particle threshold. Finally, we quantify the evolution of the mass of particles deposited at the base of the numerical domain and demonstrate that the accumulation rate increases with time, while it is expected to be constant if particles settle individually. This suggests that real-time measurements of sedimentation rate from volcanic clouds may be able to distinguish finger sedimentation from individual particle settling.

**Keywords: volcanic ash, ash sedimentation, tephra, weighted essentially non-oscillatory, finite-difference, high performance computing**

OPEN ACCESS

***Edited by:***
*Sara Barsotti,*
*Icelandic Meteorological Office,*
*Iceland*

***Reviewed by:***
*Stephen Solovitz,*
*Washington State University*
*Vancouver, United States*
*Tushar Mittal,*
*Massachusetts Institute of*
*Technology, United States*
*Benjamin James Andrews,*
*Smithsonian Institution, United States*

****Correspondence:***
*Jonathan Lemus*
*jonathan.lemus@unige.ch*

***Specialty section:***
*This article was submitted to*
*Volcanology,*
*a section of the journal*
*Frontiers in Earth Science*

***Received:*** *21 May 2021*
***Accepted:*** *07 October 2021*
***Published:*** *21 October 2021*

***Citation:***
*Lemus J, Fries A, Jarvis PA,*
*Bonadonna C, Chopard B and Lätt J*
*(2021) Modelling Settling-Driven*
*Gravitational Instabilities at the Base of*
*Volcanic Clouds Using the Lattice*
*Boltzmann Method.*
*Front. Earth Sci. 9:713175.*
*doi: 10.3389/feart.2021.713175*

## INTRODUCTION

Explosive volcanic eruptions can inject large quantities of ash into the atmosphere, generating multiple hazards at various spatial and temporal scales (Blong, 2000; Bonadonna et al., 2021). Subsequent volcanic ash dispersal and sedimentation can strongly disrupt air traffic (Guffanti et al., 2008; Prata and Rose, 2015), affect inhabited areas (Spence et al., 2005; Jenkins et al., 2015), and impact ecosystems and public health (Gudmundsson, 2011; Wilson et al., 2011). A good understanding of ash dispersal is critical for effective forecasting and management of the response to these hazards. Modern volcanic ash transport and dispersal models have now reached high levels of sophistication (Jones et al., 2007; Bonadonna et al., 2012; Folch, 2012; Folch et al., 2020; Prata et al., 2021) but do not include all of the physical processes affecting ash transport, such as particle aggregation and settling-driven gravitational instabilities (e.g., Durant, 2015). Various studies have highlighted the need to take these processes into account by revealing discrepancies between field measurements and numerical models (Scollo et al., 2008), premature sedimentation of fine ash leading to bimodal grainsize distributions not only related to particle aggregation (Bonadonna et al., 2011; Manzella et al., 2015; Watt et al., 2015) and significant depletion of airborne fine ash close to the source (Gouhier et al., 2019).

Alongside particle aggregation, settling-driven gravitational instabilities contribute to the early deposition of fine ash with similar outcomes (e.g., grainsize bimodality, premature sedimentation of fine ash). These instabilities generate downward-moving ash columns (fingers) which grow from the base of the ash cloud (**Figure 1**) (Carazzo and Jellinek, 2012; Manzella et al., 2015; Scollo et al., 2017). This phenomenon has the potential to enhance the sedimentation rate of fine ash beyond the terminal fall velocity of individual particles, reducing the residence time of fine ash in the atmosphere. Thus, a rigorous understanding of these processes is important in order to build a comprehensive parametrisation that can be included in dispersal models (Scollo et al., 2010; Bonadonna et al., 2012; Folch, 2012; Durant, 2015).

Settling-driven gravitational instabilities should be fully characterized as they also have the potential to impact other ash-related processes. First, the high particle concentration and the turbulence induced by fingers (i.e., the intrinsic turbulence within fingers as well as the shear generated during the downward motion) may enhance particle aggregation by increasing the collision rate of particles (Costa et al., 2010; Scollo et al., 2017). This process could happen regardless of plume height and atmospheric conditions contrary to ice-nucleation for example, which requires specific conditions (Maters et al., 2020). Second, as settling-driven gravitational instabilities trigger premature deposition of fine ash, this may affect the residence time of other elements in the plume. Indeed, fine ash is involved in some geochemical processes such as the adsorption of volatiles (e.g., sulphur or halogens) (Bagnato et al., 2013; Zhu et al., 2020). Considering that the sedimentation rate of volatiles depends on the sedimentation rate of fine ash, the possible premature deposition of volatiles can be explained by the presence of both settling-driven gravitational instabilities and particle aggregation. Finally, fine ash has been shown to play an important role in the volcanic cloud heating through radiative processes that may affect the dynamics (Niemeier et al., 2009; Stenchikov et al., 2021). Thus, in order to model the large-scale transport of volcanic clouds, there is a need to estimate accurately the amount of fine ash within the cloud, and, therefore, to constrain all size-selective sedimentation processes such as settling-driven gravitational instabilities.

Settling-driven gravitational instabilities occur at the interface between an upper, buoyant particle suspension, e.g., a volcanic ash cloud, and a lower, denser fluid, e.g., the underlying atmosphere (Hoyal et al., 1999; Burns and Meiburg, 2012; Manzella et al., 2015; Davarpanah Jazi and Wells, 2016). Whilst the initial density configuration is stable, particle settling across the density interface creates a narrow unstable region called the particle boundary layer (PBL) (Carazzo and Jellinek, 2012). Once this attains a critical thickness (Hoyal et al., 1999), a Rayleigh-Taylor-like instability (Chandrasekhar, 1961; Sharp, 1984) can form on the interface between the PBL and the lower layer, generating finger-like structures which propagate downwards. A further critical condition for instability is that the particle settling velocity $V_s$ must be smaller than the finger propagation velocity $V_f$ (Carazzo and Jellinek, 2012). Thus, the

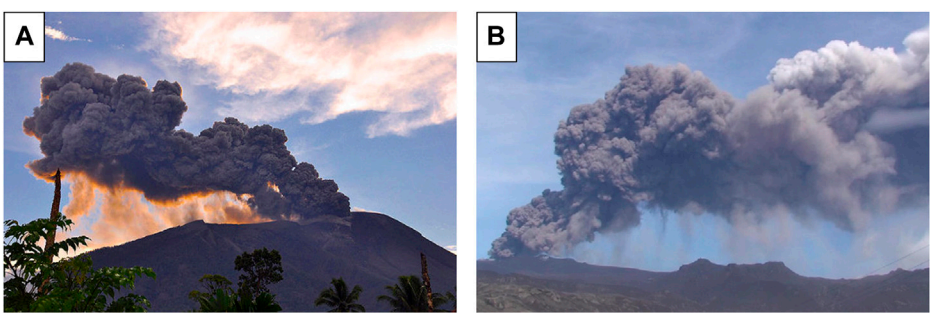


**FIGURE 1 |** Gravitational instabilities observed at the base of a volcanic plume during **(A)** the 2011 Gamalama eruption (Indonesia) (Credit: AP) and **(B)** the 2010 eruption of Eyjafjallajökull (Iceland) (Manzella et al., 2015).

occurrence of the instability enhances the sedimentation rate (Manzella et al., 2015; Scollo et al., 2017). Alternatively, if $V_s$ is greater than the propagation velocity of fingers $V_f$, then particles settle individually before a PBL can form and no instability occurs.

Settling-driven gravitational instabilities have been widely studied in laboratory experiments that simulate various natural settings. Many experiments have considered an initial two-layer system, where the particle suspension is initially separated from the underlying denser layer by a removable horizontal barrier (Hoyal et al., 1999; Harada et al., 2013; Manzella et al., 2015; Davarpanah Jazi and Wells, 2016; Scollo et al., 2017; Fries et al., 2021) whilst other experiments have involved injection of the suspension into a density-stratified fluid at its neutral buoyancy level (Cardoso and Zarrebini, 2001; Carazzo and Jellinek, 2012). Similar instabilities can also be studied by allowing fine particles to sediment through the free surface between water and air (Carey, 1997; Manville and Wilson, 2004). Additionally, dimensional analysis has been used to predict that the downward propagation velocity of the generated fingers is given by (Hoyal et al., 1999; Carazzo and Jellinek, 2012)

$$V_f = \left[ g\left( \frac{\rho_{PBL} - \rho_f}{\rho_f} \right) \right]^{\frac{2}{5}} \left[ \frac{\pi V_s \delta_{PBL}^2}{4} \right]^{\frac{1}{5}}, \tag{1}$$

where $\rho_{PBL}$ is the PBL bulk density, $\rho_f$ the underlying fluid density, $g = 9.81\ \mathrm{m.s^{-2}}$ the gravitational acceleration and $\delta_{PBL}$ the PBL thickness, which by analogy with thermal convection (Turner, 1973) is taken to be (Hoyal et al., 1999)

$$\delta_{PBL} = \left( \frac{Gr_c \nu^2}{g'} \right)^{\frac{1}{3}}, \tag{2}$$

where $g' = g(\rho_{PBL} - \rho_f)/\rho_f$, $\nu$ the kinematic viscosity and $Gr_c$ a critical Grashof number which estimates the ratio of the buoyancy to viscous forces on the fluid (see **Supplementary Table S1** for all acronyms and symbols used in this paper). The reduced gravity $g'$ describes the change in the gravitational acceleration due to buoyancy forces. Continuing the analogy with thermal convection, it has been proposed that $Gr_c = 10^3$ (Hoyal et al., 1999), although recent experimental observations suggests $Gr_c \approx 10^4$ may be more accurate (Fries et al., 2021). Therefore, for known particle and fluid properties, it is possible to predict whether collective settling will occur and fingers subsequently form using the condition $V_f > V_s$ (Hoyal et al., 1999). According to this relation, the limit between collective and individual settling occurs when $V_f = V_s$. However, the transition is likely to be smooth, with a transitionary regime where both fluid-like and particle-like settling occur at the same time, as suggested by Harada et al. (2013).

For the initial two-layer configuration, Hoyal et al. (1999) also developed a series of analytical mass-balance models predicting the average particle concentration in the lower layer depending on whether the upper and lower layers were convecting or not. In the case of a quiescent upper layer and a convective lower layer (convection initiated by finger propagation), the evolution of the mass of particles in the lower layer $M_2$ depends on the balance between the mass flux of particles arriving from the upper layer $\dot{M}_{in}$ and the mass flux of particle leaving by sedimentation $\dot{M}_{out}$

$$\frac{dM_2}{dt} = \dot{M}_{in} - \dot{M}_{out}\,, \tag{3}$$

where $t$ is time. Assuming that $M_2(t) = Ah_2C_2(t)$, where $C_2(t)$ is the average particle concentration in the lower layer, Hoyal et al. (1999) solved this equation using $\dot{M}_{in} = AV_sC_1(0)$, $\dot{M}_{out} = AV_sC_2(t)$ and the initial condition $C_2(0) = 0$. Thus

$$C_2(t) = C_1(0)\left[1 - e^{-\frac{V_s}{h_2}t}\right], \tag{4}$$

where $C_1(0)$ is the initial particle concentration in the upper layer, $h_2$ the lower layer thickness and $A$ the horizontal cross section of the tank.

Further studies of settling-driven gravitational instabilities have taken theoretical approaches, such as using linear stability analyses to predict the growth rate and characteristic wavelengths of the instability at very early stages (Burns and Meiburg, 2012; Yu et al., 2013; Alsinan et al., 2017). Moreover, various numerical models simulating settling-driven gravitational instability have also been developed (Jacobs et al., 2013; Burns and Meiburg, 2014; Yamamoto et al., 2015; Chou and Shao, 2016; Keck et al., 2021). Most numerical approaches to this problem have used continuum-phase models, where the coupling between particles and fluid is strong enough to describe them as a single-phase (Burns and Meiburg, 2014; Yu et al., 2014; Chou and Shao, 2016). This Eulerian description is valid under the assumptions of sufficiently small particles and a large enough number of particles such that the drag and gravitational forces are in equilibrium. The condition on the particle size can be quantified through the Stokes number (Burgisser et al., 2005; Roche and Carazzo, 2019), one possible definition of which is

$$St = \frac{\rho_p D_p^2 U}{18\mu L}, \tag{5}$$

where $\rho_p$ is the particle density, $D_p$ the particle diameter, $\mu$ the dynamic viscosity and $U$ and $L$ characteristic velocity and length scales of the flow. For $St < 1$, the particles and fluid can be considered coupled and, providing there are enough particles, the continuum approach is valid.

The Eulerian description can be extended to multiple phases in order to simulate their interaction (e.g., gas-liquid interaction) using adaptive mesh refinements to resolve the phase interfaces (Jacobs et al., 2013). However, for large particle diameters and small particle volume fractions, collective behaviour no longer occurs and the continuum-phase method cannot be applied. In this case, there is a need to explicitly model particle motion, taking the drag force into consideration (Yamamoto et al., 2015; Chou and Shao, 2016).

This paper presents an innovative method to implement a continuum model by coupling the Lattice Boltzmann Method (LBM) with a low-diffusivity finite difference (FD) scheme. This model takes advantage of the LBM capabilities to simulate complex flows through uniform grids and thus, the ease of coupling with finite difference methods. This hybrid model has been validated by comparing the results with those from linear stability analysis and laboratory experiments (Fries et al., 2021). The validated model then allows us to gain new insights into the fundamental processes by exploring experimentally-inaccessible regions of the parameter space. We first describe the general framework and governing equations that describe settling-driven gravitational instabilities, then the configuration of the validatory experiments to which we apply the model. Next, we propose a numerical strategy involving a hybrid model in order to solve the system of equations. We then go on to present the linear stability analysis before finally describing and discussing the results of our simulations.

# MATERIALS AND METHODS

## Problem Formulation

The model consists of a three-way coupling between fluid momentum, fluid density, and particle volume fraction, based on the assumption that the particle suspension can be represented by a continuum concentration field. Moreover, the particle drag force is in equilibrium with the gravitational force such that the forcing term in the fluid momentum equation is equivalent to a buoyant force term (Boussinesq approximation), which depends on the particle volume fraction $\varnothing(\vec{x},t)$ (Burns and Meiburg, 2014; Yu et al., 2014; Chou and Shao, 2016). $\varnothing(\vec{x},t)$ satisfies the advection-diffusion-settling equation

$$\frac{\partial \varnothing}{\partial t} + \vec{\nabla}.\left[\varnothing\left(\vec{u}_f - V_s\overrightarrow{e_z}\right)\right] = D_c\nabla^2\varnothing, \tag{6}$$

where $\vec{u}_f(\vec{x},t)$ is the fluid velocity, $D_c$ the particle diffusion coefficient, $\overrightarrow{e_z}$ the vertical unit vector and $\vec{x} = (x, y, z)$ the position coordinate. The particle settling velocity $V_s$ can be fixed or allowed to be a function of other parameters. Its formulation will be set later according to the assumptions of the flow configuration. The fluid is considered incompressible, meaning $\vec{\nabla}.\vec{u}_f = 0$. Thus, **Eq. 6** becomes

$$\frac{\partial \varnothing}{\partial t} + \left(\vec{u}_f - V_s\overrightarrow{e_z}\right).\vec{\nabla}\varnothing - \varnothing\vec{\nabla}.\left(V_s\overrightarrow{e_z}\right) = D_c\nabla^2\varnothing. \tag{7}$$

The particle settling velocity depends on the ambient fluid density $\rho$, which in turn depends on any transported density-altering properties, such as temperature or the concentration of a chemical species, e.g., the sugar in our validatory experiments (Fries et al., 2021). We incorporate the effect of a single density-altering property on the fluid density through a classical advection-diffusion equation

$$\frac{\partial \rho(\rho_0,S)}{\partial t} + \vec{u}_f.\vec{\nabla}\rho(\rho_0,S) = D\nabla^2\rho(\rho_0,S), \tag{8}$$

where $\rho_0$ is a reference density of the carrier fluid, $S$ the density-altering quantity (temperature or concentration), and $D$ the associated diffusion coefficient. Additionally, under the Boussinesq approximation, we assume that the density depends linearly on $S$. The fluid momentum is modelled with the incompressible Navier-Stokes momentum equation

$$\frac{\partial \vec{u}_f}{\partial t} + \left(\vec{u}_f.\vec{\nabla}\right)\vec{u}_f = -\frac{1}{\rho_0}\vec{\nabla}p + \nu\nabla^2\vec{u}_f + \vec{F}, \tag{9}$$

where $p$ is the pressure and $\vec{F}$ the buoyant body force term. We complete the system of equations by taking this force term to be a function of $\varnothing$ and $\rho$

$$\vec{F} = \left[\left(\frac{\rho_p - \rho_0}{\rho_0}\right)\varnothing + \left(\frac{\rho}{\rho_0} - 1\right)(1-\varnothing)\right]\vec{g}. \tag{10}$$

The system of equations presented so far assumes that all particles are of uniform size. In order to generalise to systems with polydisperse particle size distributions, we consider $N$ different particle concentration fields $\varnothing_i$, where each one is associated with a different size class and individually satisfies **Eq. 7**. Furthermore, the body force term becomes

$$\vec{F} = \left[\left(\frac{\rho_p - \rho_0}{\rho_0}\right)\varnothing_{tot} + \left(\frac{\rho}{\rho_0} - 1\right)(1-\varnothing_{tot})\right]\vec{g}, \tag{11}$$

where

$$\varnothing_{tot} = \sum_{i=1}^{N}\varnothing_i. \tag{12}$$

## Flow Configuration and Experiment Description

Full details of the validatory laboratory experiments can be found in Fries et al. (2021) but we summarise the essential details here. The experiments are performed in a configuration identical to that of Manzella et al. (2015) and Scollo et al. (2017) (**Figure 2**) and consist of a water tank divided into two horizontal layers, initially separated by a removable barrier. The upper layer is an initially mixed particle suspension, which represents the ash cloud, and the lower layer is a dense sugar solution, analogue to the underlying atmosphere. The particles are spherical glass beads with a median diameter of 41.5 ± 0.5 μm (measured using laser diffraction with a Bettersizer S3 Plus) and a density $\rho_p$ of 2519.24 ± 0.09 kg/m$^3$ (measured using helium pycnometry UltraPyc 1200e), and are sufficiently small to be well-coupled with the fluid, whilst the initial particle concentration $C_1(0)$ of the upper layer is varied from 1 to 10 g/l (see **Table 1** for the conversion to particle volume fraction $\varnothing_0$). The lower layer density is kept constant at $\rho_f$ = 1008.4 kg/m$^3$ (corresponding to a sugar concentration of $S_0$ = 35 g/l), always ensuring an initially stable density configuration.

Before starting an experiment, the upper layer is manually and carefully stirred using a brush. Then the barrier separating the two layers is immediately removed, allowing particle settling through the interface. A PBL subsequently forms and finger formation is initiated. Experiments are illuminated from the side of the water tank with a planar laser and recorded with a high-contrast camera. We measure the vertical finger velocity by tracking the progression

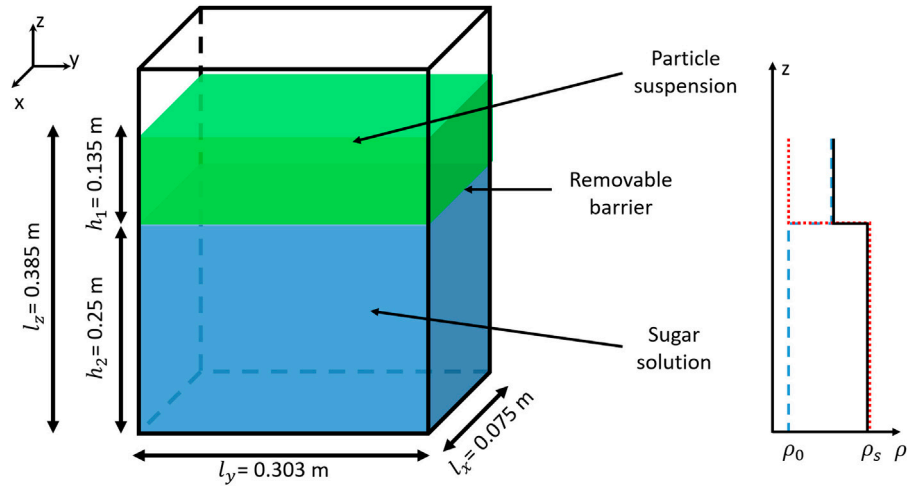


**FIGURE 2 |** Experimental setup used by (Fries et al., 2021) and the initial density profiles associated with the contributions from particles (blue dashed) and sugar (red dotted), as well as the bulk density (black solid). The density of fresh water is given by $\rho_0$.

**TABLE 1 |** List of simulations performed. All the simulations have been performed using an initial lower layer fluid density of 1008.4 kg/m$^3$. $z_H$, $z_\varnothing$ and $z_s$ are parameters used in the linear stability analysis (LSA) in order to describe the different base states associated with the particle and sugar profiles in **Eqs 39**, **40**. The LSA has been performed only for a constant particle size of 40 μm in order to study the effect of the particle volume fraction.

| Initial particle concentration (g/L) | Volume fraction | Particle diameter (μm) | $z_H = V_s T$ (mm) | $z_o$ (mm) | $z_s$ (mm) |
|---|---|---|---|---|---|
| 1 | $3.97 \times 10^{-4}$ | 40 | 12.11 | 2.59 | 0.67 |
| 2 | $7.94 \times 10^{-4}$ | 40 | 7.37 | 2.20 | 0.63 |
| 3 | $1.19 \times 10^{-3}$ | 40 | 5.47 | 1.99 | 0.61 |
| 4 | $1.59 \times 10^{-3}$ | 40 | 5.01 | 1.99 | 0.61 |
| 5 | $1.98 \times 10^{-3}$ | 40 | 4.20 | 1.84 | 0.60 |
| 6 | $2.38 \times 10^{-3}$ | 40 | 3.45 | 1.72 | 0.59 |
| 7 | $2.78 \times 10^{-3}$ | 40 | 3.25 | 1.70 | 0.60 |
| 8 | $3.18 \times 10^{-3}$ | 40 | 3.17 | 1.72 | 0.61 |
| 9 | $3.57 \times 10^{-3}$ | 40 | 3.01 | 1.71 | 0.62 |
| 10 | $3.97 \times 10^{-3}$ | 40 | 2.54 | 1.58 | 0.61 |
| 3 | $1.19 \times 10^{-3}$ | 25 | — | — | — |
| 3 | $1.19 \times 10^{-3}$ | 55 | — | — | — |
| 3 | $1.19 \times 10^{-3}$ | 70 | — | — | — |
| 3 | $1.19 \times 10^{-3}$ | 85 | — | — | — |
| 3 | $1.19 \times 10^{-3}$ | 100 | — | — | — |
| 3 | $1.19 \times 10^{-3}$ | 115 | — | — | — |
| 3 | $1.19 \times 10^{-3}$ | 130 | — | — | — |
| 9 | $3.57 \times 10^{-3}$ | 25 | — | — | — |
| 9 | $3.57 \times 10^{-3}$ | 55 | — | — | — |
| 9 | $3.57 \times 10^{-3}$ | 70 | — | — | — |
| 9 | $3.57 \times 10^{-3}$ | 85 | — | — | — |
| 9 | $3.57 \times 10^{-3}$ | 100 | — | — | — |
| 9 | $3.57 \times 10^{-3}$ | 115 | — | — | — |
| 9 | $3.57 \times 10^{-3}$ | 130 | — | — | — |
| 9 | $3.57 \times 10^{-3}$ | 145 | — | — | — |
| 9 | $3.57 \times 10^{-3}$ | 160 | — | — | — |

of the finger front with time. Additionally, Planar Laser Induced Fluorescence (PLIF) (Koochesfahani, 1984; Crimaldi, 2008) and particle imaging are used to quantify the spatial distribution of the fluid phase density and particle concentration.

## Application to Flow Configuration

We apply the general system of equations presented in *Problem Formulation section* to the configuration of the validatory experiments. The particles are spherical and sufficiently small

that their terminal settling velocity in water is given by the Stokes velocity (Stokes, 1851)

$$V_s = \frac{D_p^2 g\left[\rho_p - \rho(S)\right]}{18\mu}, \tag{13}$$

where $S$ is the sugar concentration and $\rho = \rho_0(1 + \alpha S)$, with $\alpha$ the sugar solution expansion coefficient.

The diluted system ensures the Boussinesq assumption is valid as the ratio $\Delta\rho/\rho_0$ is much less than 1 (about $6 \times 10^{-3}$ for the highest initial particle volume fraction).

We simulate the solid walls of the tank around our domain with a no-slip boundary condition for the fluid velocity. Neumann boundary conditions are employed for $\varnothing$ and $\rho$ to avoid any flux of particles or sugar across the walls. Thus we impose

$$\frac{\partial \varnothing}{\partial x} = 0, \tag{14}$$

and

$$\frac{\partial \rho}{\partial x} = 0, \tag{15}$$

on the wall nodes. Furthermore, we define the following initial states for $\varnothing$ and $S$:

$$\varnothing\left(\vec{x},\, t = 0\right) = \begin{cases} 0 & , z < H_0 \\ \varnothing_0 & , z > H_0 \end{cases}, \tag{16}$$

and

$$S\left(\vec{x},\, t = 0\right) = \begin{cases} S_0, & z < H_0 \\ 0 & , z > H_0 \end{cases}, \tag{17}$$

where $\varnothing_0$ and $S_0$ are the initial particle volume fraction in the upper layer and initial sugar concentration in the lower layer, respectively, and $H_0 = 0.25$ m the initial height of the interface ($z = 0$ corresponds to the base of the tank). We also add a small perturbation to the particle volume fraction field in order to initiate the instability. Finally, the system is initially stationary so $\vec{u}_f(\vec{x},\, t = 0) = 0$.

## Numerical Methods

The 3D numerical model is implemented using a hybrid strategy where a LBM solves the fluid motion and is coupled with finite difference schemes that solve the advection-diffusion equations for $\varnothing$ and $S$.

### Fluid Motion

The LBM is an efficient alternative to conventional Computational Fluid Dynamics (CFD) methods that explicitly solve the Navier-Stokes equations at each node of a discretised domain (He and Luo, 1997; Succi et al., 2010). It is a well-established approach for simulating complex flows, including multiphase fluids (Leclaire et al., 2017) and thermal and buoyancy effects (Parmigiani et al., 2009; Noriega et al., 2013). The LBM originates from the kinetic theory of gases and provides a description of gas dynamics at the mesoscopic scale. This scale exists between the microscopic, which describes molecular dynamics, and the macroscopic, which gives a continuum description of the system with variables such as density and velocity. Thereby, the mesoscopic scale considers a probability distribution function of molecules described by the Lattice Boltzmann equation. This model reduces the process to two main steps: streaming (i.e., displacement of populations between consecutive calculation nodes), and collision (i.e., interaction of populations on a node). The Bhatnagar-Gross-Krook (BGK) model (Bhatnagar et al., 1954) provides a simple collision process based on a fundamental property given by kinetic theory which describes gas motion as a perturbation around the equilibrium state. Then, the LBM-BGK model solves the equation

$$f_i\left(\vec{x} + \vec{c}_i\delta t,\, t + \delta t\right) - f_i\left(\vec{x},\, t\right) = -\frac{\delta t}{\tau}\left(f_i\left(\vec{x},\, t\right) - f_i^{eq}\right), \tag{18}$$

where the particle population $f_i$ is a discrete representation of the probability distribution function, $\delta t$ is the time step, $f_i^{eq}(\rho, \vec{u}_f)$ the equilibrium distribution function, $\tau$ the relaxation time associated with the flow viscosity and $\vec{c}_i$ the local particle velocity. The LBM is applied to specific types of lattices that describe how the populations move through the calculation nodes (Kruger et al., 2017). These types of lattice are commonly summarized in the form $DrQm$ where $r$ denotes the dimension of the system and $m$ the number of directions in which populations can propagate. **Figure 3** shows the scheme $D3Q19$ used for our 3D simulations and the associated set of local velocities.

The macroscopic fluid state is described through the usual macroscopic variables such as density, velocity and kinematic viscosity. These variables are related to the moments of the populations $f_i$ through

$$\rho = \sum_i f_i, \tag{19}$$

and

$$\rho\vec{u}_f = \sum_i f_i\vec{c}_i, \tag{20}$$

whilst the kinematic viscosity controls the relaxation to equilibrium through the relaxation time

$$\tau = \frac{\nu}{c_s^2} + \frac{\delta t}{2}. \tag{21}$$

The variable $c_s$ is commonly called the speed of sound and is equal to $(1/\sqrt{3})\delta x/\delta t$ where $\delta x$ is the spatial step. However, the classical LBM-BGK model described above does not take into account any forcing term. One way to include forcing is to rewrite **Eq. 18** as

$$f_i\left(\vec{x} + \vec{c}_i\delta t,\, t + \delta t\right) - f_i\left(\vec{x},\, t\right) = -\frac{1}{\tau}\left(f_i\left(\vec{x},\, t\right) - f_i^{eq}\right) + F_i\delta t, \tag{22}$$

where $F_i$ is the forcing term, which can be expressed by a power series in the local particle velocities, and the equilibrium distribution is now given by $f_i^{eq} = f_i^{eq}(\rho, \vec{u}_f^*)$, where $\rho\vec{u}_f^* = \sum_i f_i\vec{c}_i + b\vec{F}\delta t$. The determination of the coefficient $b$, as

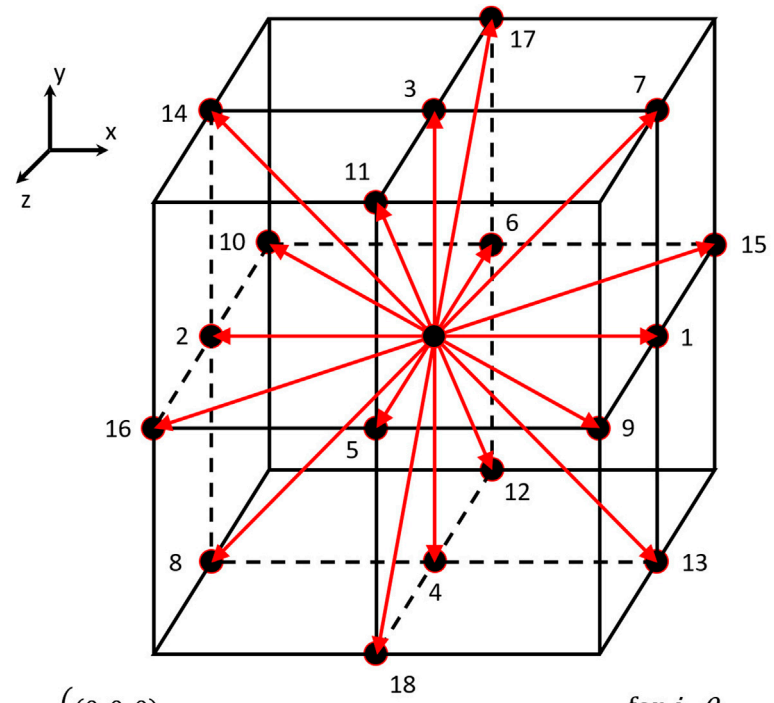


$$\vec{c}_i = \begin{cases} (0,0,0) & \text{for } i=0 \\ (\pm 1,0,0),(0,\pm 1,0),(0,0,\pm 1) & \text{for } i=1,\ldots,6 \\ (\pm 1,\pm 1,0),(\pm 1,0,\pm 1),(0,\pm 1,\pm 1) & \text{for } i=7,\ldots,18 \end{cases}$$

**FIGURE 3 |** Depiction of the D3Q19 lattice. The red arrows show the different possible directions of propagation. The associated local velocities are summarised in the velocity set $\vec{c}_i$.

well as the power series expansion of $F_i$ are described by Guo et al. (2002). Finally, no-slip boundary conditions in the LBM, to simulate walls for example, can be implemented using the classical *bounce-back* boundary condition (Kruger et al., 2017) where the populations arriving on a wall node during the streaming step are simply reflected back to their previous nodes.

## Transport of Particles and Other Density-Altering Quantities

The particles and other density-altering quantities are described by continuum fields that follow an advection-diffusion law coupled with the fluid motion as simulated with the LBM. The numerical solution of the advection equation is particularly challenging for methods which, like ours, are Eulerian (i.e., mesh-based). Indeed, such methods exhibit numerical diffusion which may strongly reduce model accuracy and, in some cases, even exceed the amplitude of the actual, physical diffusion term. The lack of physical diffusion in our problem and the presence of sharp interfaces restrict our ability to solve the advection equations with the LBM. In fact, the advection-diffusion equation can be solved by the LBM with a BGK approach in analogous fashion to the fluid motion by modifying the equilibrium distribution and the relaxation time to depend on the diffusion coefficient $D$ rather than $\nu$

$$\tau = \frac{D}{c_s^2} + \frac{\delta t}{2}. \tag{23}$$

However, a stability condition for a LBM-BGK algorithm is $\tau/\delta t > 1/2$. Thus, since the problem is convection dominated, the low diffusion coefficient ($D \ll 1$) drives the model towards the stability limit, introducing strong numerical errors near sharp concentration gradients (Hosseini et al., 2017). For this reason, we solve the advection term using two finite-difference schemes which are selected depending on the required accuracy: the classical first-order upwind finite difference and the third-order Weighted Essentially Non Oscillatory (WENO) finite difference scheme (Liu et al., 1994; Jiang and Shu, 1996).

Coupling the LBM with an upwind finite difference scheme allows us to avoid the stability problem. First-order FD schemes however, still suffer from the problem of numerical diffusion due to the truncation error associated with terminating the Taylor expansion after the first spatial derivative. The induced numerical error $NE$ for the convective term in the advection-diffusion equation is given by

$$NE \sim u\frac{\delta x}{2}\frac{\partial^2 \varnothing}{\partial x^2}, \tag{24}$$

where $u$ is the transport velocity. $NE$ acts like an additional diffusion term because of the presence of the second-order

derivative. (A quantitative estimate of the numerical diffusion for both 1st order and WENO procedure is available in section 1.3 of the **Supplementary Figure S2**). The numerical diffusion associated with the solution of $S$ is negligible due to the low fluid velocity and consequently the use of the first order FD scheme does not significantly affect the accuracy. However, in the solution of $\varnothing$, which includes an additional velocity contribution due to the settling, the truncation error associated with the first-order scheme becomes non-negligible. Whilst decreasing $\delta x$ would reduce numerical diffusion, we would require an unpractically small value in order to get a sufficiently accurate solution. Additionally, simply increasing the order of the scheme introduces dispersion (spurious oscillations) near regions of high gradient, according to the Godunov theorem (Godunov, 1954, 1959). Therefore, we choose here to implement the low diffusive WENO procedure for the solution of $\varnothing$, thus achieving a stable and high-resolution scheme without dispersion.

Further information on how we discretise the convective term in the advection-diffusion equation using the first order upwind and the third order WENO finite difference schemes is detailed in Section 1 of the **Supplementary Figure S1**.

### Numerical Implementation

Our model is implemented using *Palabos* (Parallel Lattice Boltzmann Solver), a Computational Fluid Dynamics (CFD) solver based on the Lattice Boltzmann Method and developed by the Scientific Parallel Computing group of the Computer Science Department, University of Geneva (Latt et al., 2020). *Palabos* is designed to perform calculations on massively parallel computers, thus allowing very small spatial resolutions for accurate simulation of the finger dynamics.

## Linear Stability Analysis

In order to validate our model, we compare the early-time simulated behaviour against predictions from linear stability analysis (LSA). LSA is applied to the onset of the physical instability at the interface between layers of different particle concentration. It involves defining a field equation-satisfying base state for each of the unknown fields in a problem and then applying an infinitesimally small perturbation to each of these fields. The equations are then expanded to linear order in the perturbation, with higher order terms assumed to be negligible. By assigning the perturbation to have the form of a complex waveform, the system of equations reduces to an eigenvalue problem, which can be solved to determine which wavelengths will grow or decay (Chandrasekhar, 1961). In this section, we assume that the system is invariant under translation in the $x-y$ plane, thus reducing the analysis to a 2D problem. We strongly follow the procedure described by (Burns and Meiburg, 2012) in order to solve our problem.

### Nondimensionalisation

We nondimensionalise our system of equations by defining

$$l^c = \left(\frac{\nu^2}{g}\right)^{1/3}, \tag{25}$$

$$t^c = \left(\frac{\nu}{g^2}\right)^{1/3}, \tag{26}$$

and

$$p^c = \rho_0 (\nu g)^{2/3}, \tag{27}$$

where $l^c$, $t^c$ and $p^c$ are characteristic quantities. We also define the dimensionless parameters

$$S^* = \alpha S_0, \tag{28}$$

$$\varnothing^* = \varnothing_0, \tag{29}$$

$$Fr = \frac{1}{t^c}\sqrt{\frac{l^c}{g}}, \tag{30}$$

and

$$Sc_i = \frac{\nu}{D_i}, \tag{31}$$

noting that $Fr$ is a Froude number and $Sc_i$ are Schmidt numbers. Furthermore, the stream function $\psi$ is defined such that $\vec{u}_f = (\partial\psi/\partial z,\ -\partial\psi/\partial x)$ and the vorticity as $\vec{\omega} = \vec{\nabla} \times \vec{u}_f$. Then, applying the characteristic quantities to the vorticity formulation and **Eqs 7–9**, we obtain the dimensionless system (for the rest of the analysis, all the symbols used represent dimensionless quantities):

$$\omega = -\nabla^2\psi. \tag{32}$$

$$\frac{\partial\omega}{\partial t} + \left(\vec{u}_f.\vec{\nabla}\right)\omega = \nabla^2\omega + \frac{\partial\varnothing}{\partial y}\frac{\varnothing^*}{Fr^2}\left[SS^* - \left(\frac{\rho_p - \rho_0}{\rho_0}\right)\right] - \frac{\partial S}{\partial y}\frac{S^*}{Fr^2}(1 - \varnothing\varnothing^*), \tag{33}$$

$$\frac{\partial S}{\partial t} + \vec{u}_f.\vec{\nabla}S = \frac{1}{Sc_s}\nabla^2 S, \tag{34}$$

and

$$\frac{\partial\varnothing}{\partial t} + \left(\vec{u}_f - V_s\overrightarrow{e_z}\right).\vec{\nabla}\varnothing = \frac{1}{Sc_c}\nabla^2\varnothing. \tag{35}$$

Note that here we have neglected the term $-\varnothing\vec{\nabla}.(V_s\overrightarrow{e_z})$ in **Eq. 7** assuming the fluid density variation across the interface is sufficiently small that it does not affect the particle settling velocity.

### Variable Expansion and Eigenvalue Problem

We linearise the system of equations by expanding each variable in terms of a base state and a perturbation

$$\varphi(y,z,t) = \bar{\varphi}(z) + \varphi'(y,\ z,\ t), \tag{36}$$

where $\varphi(y,z,t) = \{\psi,\ \omega,\ \varnothing,\ S\}$, $\bar{\varphi}(z) = \{\bar{\psi}, \bar{\omega}, \bar{\varnothing}, \bar{S}\}$ the associated base state and $\varphi'(y,\ z,\ t) = \{\psi', \omega', \varnothing',\ S'\}$ the perturbation. We choose the following base states

$$\bar{\psi} = 0, \tag{37}$$

$$\bar{\omega} = 0, \tag{38}$$

$$\bar{\varnothing}\ (z,\ t) = \frac{1}{2}\left(1 + \mathrm{erf}\left(\frac{z}{z_{\varnothing}(T)}\right)\right), \tag{39}$$

and

$$\bar{S}(z,\,t) = \frac{1}{2}\left(1 - \mathrm{erf}\left(\frac{z - V_s t}{z_S(T)}\right)\right), \tag{40}$$

where $z_{\varnothing}(T)$ and $z_S(T)$ are coefficients fitted in order to have similar base states to the profiles observed in the simulations prior to the onset of the instability which starts growing at the time $T$. We choose these base states to represent the initial conditions of the validatory experiments; **Eqs 37**, **38** ensure an initially-zero velocity field whilst the error functions in **Eqs 39**, **40** ensure sigmoidal distributions for $\bar{S}$ and $\bar{\varnothing}$.

Solutions for the perturbation are assumed to have the form of normal modes

$$\varphi'(y,\,z,\,t) = \hat{\varphi}(z) exp(iky + \sigma t), \tag{41}$$

where $\hat{\varphi}(z)$ is the perturbation amplitude, $k$ the wavenumber and $\sigma$ the instability growth rate. The linearised system of equations is then formulated in matrix form so that the problem is reduced to the eigenvalue problem $K\vec{x} = \sigma W\vec{x}$ where

$$\vec{x} = \begin{pmatrix} \hat{\psi}(z) \\ \hat{\omega}(z) \\ \hat{S}(z) \\ \hat{\varnothing}(z) \end{pmatrix}, \tag{42}$$

and, in a reference frame moving downward at $V_s$, the matrices $K$ and $W$ are given by

$$K = \begin{pmatrix} M & I & 0 & 0 \\ 0 & M - V_s D_z & -ik\frac{S^*}{Fr^2}(1 - \bar{\varnothing}\varnothing^*)I & ik\frac{\varnothing^*}{Fr^2}\left[\bar{S}S^* - \left(\frac{\rho_p - \rho_0}{\rho_0}\right)\right]I \\ ik\frac{d\bar{S}}{dz}I & 0 & \frac{1}{Sc_s}M - V_s D_z & 0 \\ ik\frac{d\bar{\varnothing}}{dz}I & 0 & 0 & \frac{1}{Sc_c}M \end{pmatrix}, \tag{43}$$

and

$$W = \begin{pmatrix} 0 & 0 & 0 & 0 \\ 0 & I & 0 & 0 \\ 0 & 0 & I & 0 \\ 0 & 0 & 0 & I \end{pmatrix}, \tag{44}$$

where $D_z = \partial/\partial z$, $M = -k^2 + D_z^2$ and $I$ is the identity operator.

The eigenvalues $\sigma$ determine the stability of the system:

- If all the eigenvalues have negative real parts, the system remains stable
- If at least one eigenvalue has a positive real part, the system is unstable.

In order to solve the eigenvalue problem, the spatial derivatives are discretised using the linear rational collocation method with a grid transformation allowing a fine resolution around narrow interfacial regions (Baltensperger and Berrut, 2001; Berrut and Mittelmann, 2004).

The key result of the LSA is the dispersion relation between $\sigma$ and $k$. **Figure 4** presents the growth rate as a function of the wavenumber, for different initial particle volume fractions. The parameters for the different base states used to produce these curves are summarised in **Table 1**. We use this result in *Comparison of Model Results With Predictions From Linear Stability Analysis Section* in order to compare the predictions of the LSA with the results of our numerical model. Additionally, a comparison with the 2D Fourier analysis of the interface is given in **Supplementary Figures S3–S5**.

# RESULTS

We validate our numerical model by comparing the results with predictions from LSA and experimental observations. The LSA predicts the growth rates of different perturbation wavenumbers during the very early stage of the instability, which can be compared with the spectrum of wavenumbers present in the particle concentration interface in the numerical model. Additionally, the experiments of Fries et al. (2021) employ imaging techniques to measure quantities, such as the particle concentration field and finger velocity, at times beyond the linear regime. Finally, our results are compared with some results of previous analyses on settling-driven gravitational instabilities (Hoyal et al., 1999; Carazzo and Jellinek, 2012).

## Comparison of Model Results With Predictions From Linear Stability Analysis

In order to compare our 3D simulations with the 2D linear stability analysis, we consider just the central plane of the simulation domain, i.e., a slice in the $(y,\,z)$ plane located at $x = l_x/2$ ($l_x$ being the tank depth) (**Figure 2**). We define the front of the particle field to be the lowest position where $\varnothing = \varnothing_0/2$ and also define $H(y)$ to be the separation between $z = 0$ and this front. Our study has shown that the front position is only weakly affected when using other possible thresholds, i.e., $\varnothing_0/10$ or $\varnothing_0/5$ (relative change ~3%). **Figure 5A** shows an example of a space-time diagram showing the evolution of $H(y)$ through time. Furthermore, by calculating the Fourier transform $\tilde{H}(k,\,t)$ of $H(y)$ at different times, we can identify different dominant wavenumbers and their associated amplitudes as shown in the space diagram of the power spectral density (PSD) $\Gamma_H(k,t) = (1/(k_S L_S))|\tilde{H}(k,t)|^2$ (**Figure 5B**), where $k_S$ is the sampling wavenumber and $L_S$ the number of samples. We extract the dominant mode and its associated growth rate from $\Gamma_H(k,\,t)$ and compare the results with the predicted growth rates from LSA. We apply this analysis during a period when the amplitude $|\tilde{H}(k,t)|$ of any given mode does not exceed 40% of its wavelength, thus ensuring we are still in the linear regime (Lewis, 1950).

During the linear regime, we can assume that the growth of the spectral amplitude can be described as (Völtz et al., 2001)

$$\left|\tilde{H}(k,t)\right| = \left|\widetilde{H_i}(k)\right| \exp(\sigma_{sim}(k)t), \tag{45}$$

with $|\widetilde{H_i}(k)|$ the initial amplitude and $\sigma_{sim}(k)$ the instability growth rate as determined from the simulations. Thus, the PSD can be expressed as

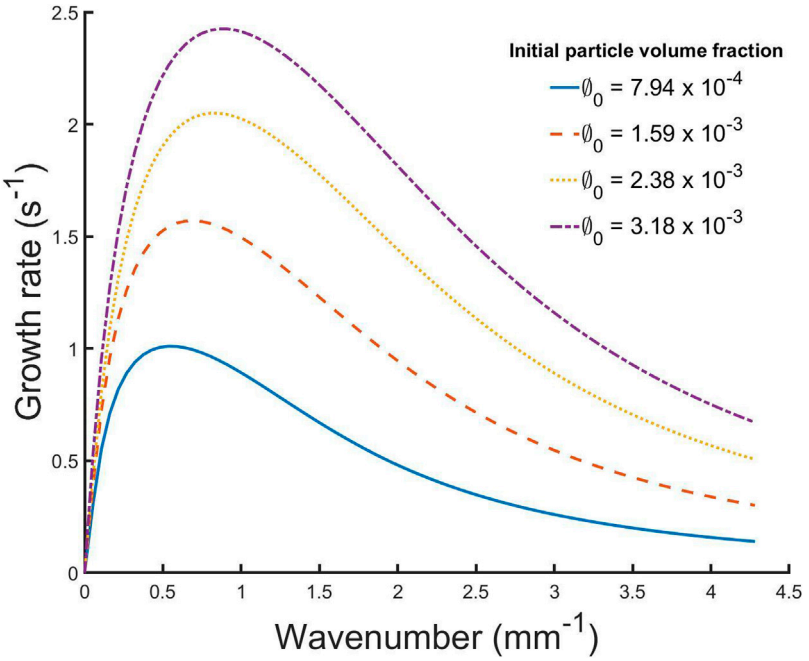


**FIGURE 4 |** Dispersion relation obtained from LSA for several initial particle volume fractions.

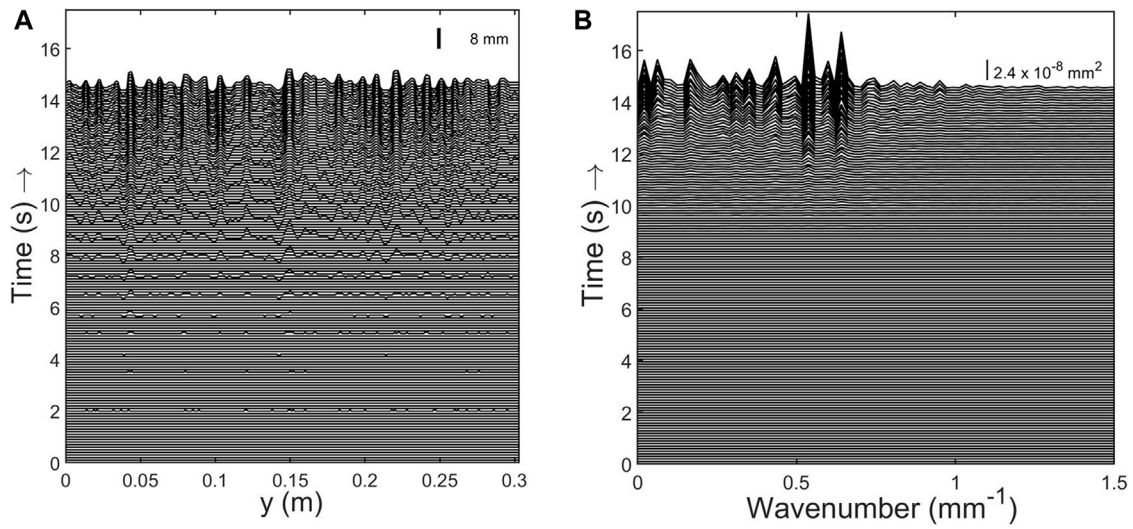


**FIGURE 5 | (A)** Space-time diagram of the particle front height $H(y, t)$. **(B)** Evolution of the power spectral density of the particle interface over time. Initial particle volume fraction: $\varnothing_0 = 3.97 \times 10^{-4}$

$$\Gamma_H(k, t) = \Gamma_{Hi} \exp(2\sigma_{sim}(k)t), \tag{46}$$

where $\Gamma_{H\,i}$ is the initial spectral density. At each time step, we extract the PSD and the wavenumber $k_{sim}$ associated with the dominant mode as shown in **Figure 6**. However, we observe that the dominant mode remains at the same wavenumber during instability growth except for three cases ($\varnothing_0 = 1.59 \times 10^{-3}$, $2.38 \times 10^{-3}$ and $3.97 \times 10^{-3}$) where we observed that the dominant mode changed its position in the spectral space. For these simulations only, we have a set of several wavenumbers $k_{sim,i}$, $(i = 1, 2, 3)$ associated with the dominant mode. With the computed PSD of the dominant mode as a function of time $\Gamma_H(k_{sim}, t)$, we apply our exponential fitting (**Eq. 46**) to determine the growth rate $\sigma_{sim,i}$ (**Figure 6B**). For the simulations which resulted in several values

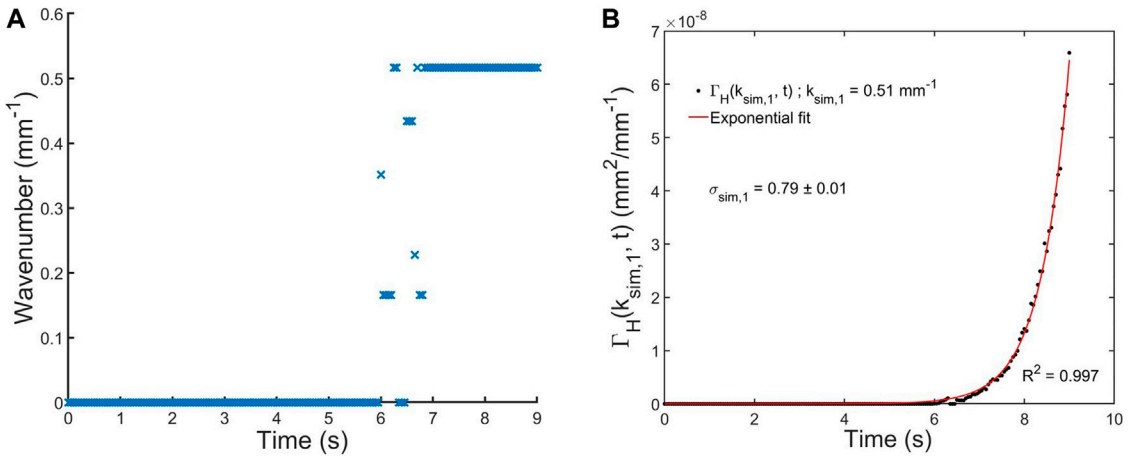


**FIGURE 6 | (A)** Example of dominant wavenumbers extracted from the maximum of the PSD. Initial particle volume fraction $\varnothing_0 = 7.94 \times 10^{-4}$. **(B)** Exponential fitting to the temporal evolution of the PSD for the first maximum in **(A)**, $k_{sim,1} = 0.517$ mm$^{-1}$.

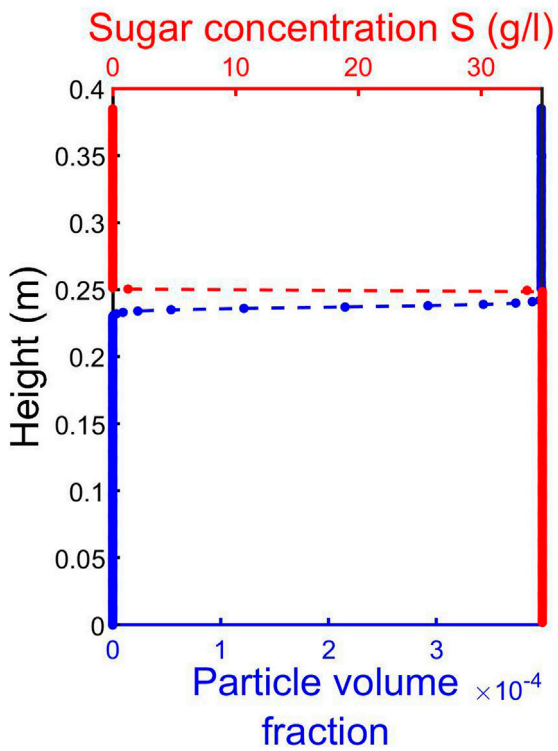


**FIGURE 7 |** Example of LSA base states extracted from the simulations for $\varnothing_0 = 3.97 \times 10^{-4}$. Dots: profiles extracted from the simulations at T = 9.55s (start of the instability growth). Dotted lines: Fit with **Eqs 39**, **40**. i.e., base states used for the LSA. Blue: particle volume fraction. Red: Sugar concentration.

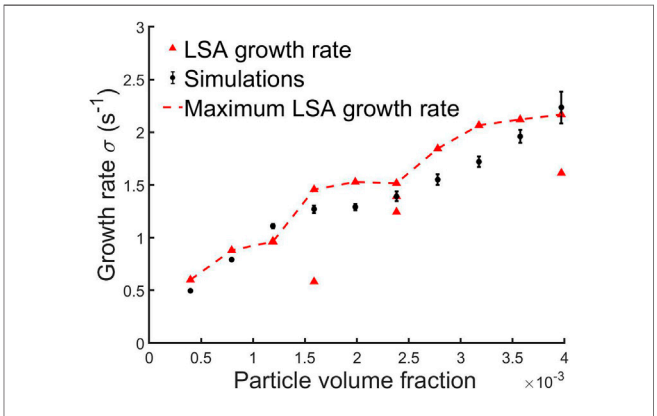


**FIGURE 8 |** Comparison of the instability growth rate measured in the simulations (black circles) and that predicted by the linear stability analysis (red triangles).

of $k_{sim,i}$ for the dominant mode, we measured the growth rates of each mode $\sigma_{sim,i}$ and found identical values, up to a precision of 5%. Additionally, for each simulation, we find the time $T$ when the instability starts growing easily identified as the time at which the modal wavenumber becomes non-zero (e.g., in **Figure 6A** this is at approximately 6 s). At this time, we extract the associated vertical profiles of particle and sugar concentration which are used to find the coefficients $z_{\varnothing}(T)$ and $z_S(T)$ (**Eqs 39**, **40**) and thus determine the base states of $\bar{\varnothing}(z, T)$ and $\bar{S}(z, T)$ (**Figure 7**). We then perform the LSA for each $\varnothing_0$, using the appropriate base states, and obtain a dispersion relation $\sigma = f(k)$. Using this relation, we predict the different growth rates $\sigma = \sigma_{LSA,i}$ associated with $k = k_{sim,i}$ and we compare with $\sigma_{sim}(k_{sim,i})$ as measured in our simulations. **Figure 8** shows the comparison between $\sigma_{sim}$ (black dots) and $\sigma_{LSA,i}$ (red triangles), as predicted from the LSA, for the dominant wave mode. The error bars associated with the simulation data show the uncertainty on the fitted results of $\sigma_{sim}$ (given by the 95% confidence interval). For the cases including a moving dominant mode, we plotted the growth rates associated with the different measured

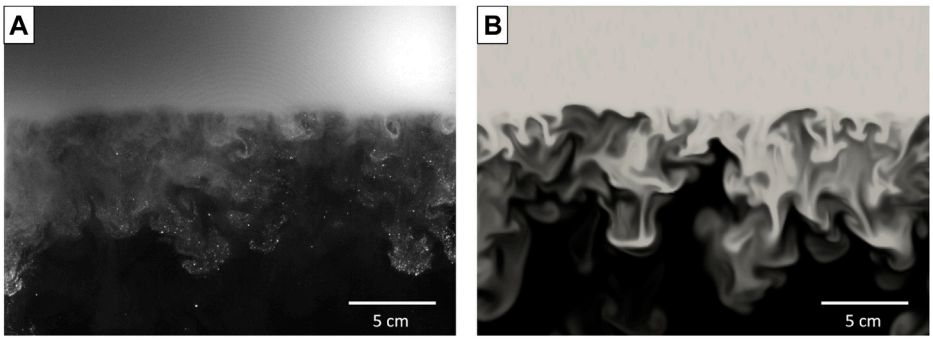


**FIGURE 9 |** Settling-driven gravitational instabilities observed 19.5 s after the barrier removal **(A)** in the laboratory (Fries et al., 2021) and **(B)** in numerical simulations. Particle size: 40 μm and initial volume fraction: $\varnothing_0 = 2.78 \times 10^{-3}$.

wavenumbers. We see that the dependence of the largest value of $\sigma_{LSA,i}$ on the initial particle concentration is in good agreement with the simulated growth rate.

## Comparison With Experimental Investigations

**Figures 9A,B** show a qualitative comparison between snapshots taken from experiments (Fries et al., 2021) and simulations (slice in the numerical domain). First, we note that our model is able to qualitatively reproduce the shape and size of fingers, especially their fronts where we observe the formation of lobes and eddies due to the Kelvin-Helmholtz instability (Chou and Shao, 2016). Second, we provide a quantitative validation of the non-linear regime by comparing our model with experiments, through measurements of the PBL thickness and the vertical finger velocity as functions of the particle volume fraction and size.

### Characterisation of the PBL and Effect of the Initial Particle Volume Fraction on the Finger Velocity

The bulk density profile $\rho_{\mathrm{blk}}$, derived from the contributions of the particle concentration and sugar profiles, is given everywhere by the relation

$$\rho_{blk} = \varnothing\rho_p + (1 - \varnothing)\rho_f. \tag{47}$$

**Figure 10** shows the profiles of $\varnothing$, $\rho_f$ and $\rho_{\mathrm{blk}}$ in the numerical simulations as well as in the experiments 8 s after the barrier removal for the same initial conditions ($\varnothing_0 = 3.18 \times 10^{-3}$ ). Despite some differences associated with limitations in achieving idealised initial conditions in the experiments, as well as the experimental data collection method, it can be seen that, in both the model and the experiments, there is an increase of the bulk density below the initial interface, owing to the particle front moving downwards. This zone of excess density corresponds to the unstable PBL from which instabilities occur, generating fingers. To calculate the finger velocity using the same method as in experiments, we extract slices from the 3D numerical domain and manually track the fronts of several fingers (6–15 fingers) from when they become fully developed until just before they become too diluted (the duration of this phase is $\sim 5\,s$). For each simulation with different volume fraction, we then average the velocity of all tracked fingers and the uncertainty is the standard deviation associated with each set of fingers used for the measurements. **Figure 11A** shows the average finger velocity $V_f$ as a function of $\varnothing_0$, for both experiments (Fries et al., 2021) and simulations. Our simulation results are in good agreement with the experimental measurements and highlight that the increase of $V_f$ with $\varnothing_0$ is non-linear.

By analogy with thermal convection, it has previously been assumed that $Gr_c = 10^3$ (Hoyal et al., 1999), but this is only an order of magnitude estimate and its application to settling-driven gravitational instabilities remains uncertain (Fries et al., 2021). **Figure 11A** shows good agreement between the simulations and **Eq. 1** for a fitted $Gr_c$ of $1.2 \pm 0.4 \times 10^4$ ($R^2 = 0.92$), which is an order of magnitude higher than the value previously assumed (Hoyal et al., 1999; Carazzo and Jellinek, 2012). This agrees reasonably with the experiments, where the best fit is obtained for $Gr_c = 1.9 \pm 0.7 \times 10^4$ ($R^2 = 0.75$), but the experimental results show more scatter. However, neither of these fits have completely satisfactory values of $R^2$. We therefore further investigate the applicability of **Eq. 1** by examining the dependence of $V_f$ on $\varnothing_0$, assuming a more general power law of the form $V_f \propto \varnothing_0^q$. According to **Eq. 1**, $q = 4/15 \cong 0.27$. However, from the experiments, we obtain $q = 0.50 \pm 0.16$ (with $R^2 = 0.95$) while for our simulations $q = 0.37 \pm 0.08$ (with $R^2 = 0.98$). Here $Gr_c$, $q$ and their associated uncertainties have been calculated accounting for the uncertainty on $V_f$ with the SciPy (Python-based ecosystem) procedure *scipy. optimize.curve_fit*.

### Effect of Particle Size on the Finger Vertical Velocity

Since gravitational instabilities cause particles to sediment faster than their settling velocity, it is of interest to explore the transition from collective to individual settling, since this has implications for which grain sizes may prematurely sediment from a volcanic cloud (Scollo et al., 2017). **Figure 11B** shows the effect of particle size on the finger velocity as measured from the model, for two different initial volume fractions, in the experiments configuration (i.e., in the tank filled with water). We clearly observe two regimes:

- For particle sizes less than or equal to 115 μm (for $\varnothing_0 = 1.19 \times 10^{-3}$) and 145 μm (for $\varnothing_0 = 3.57 \times 10^{-3}$), we

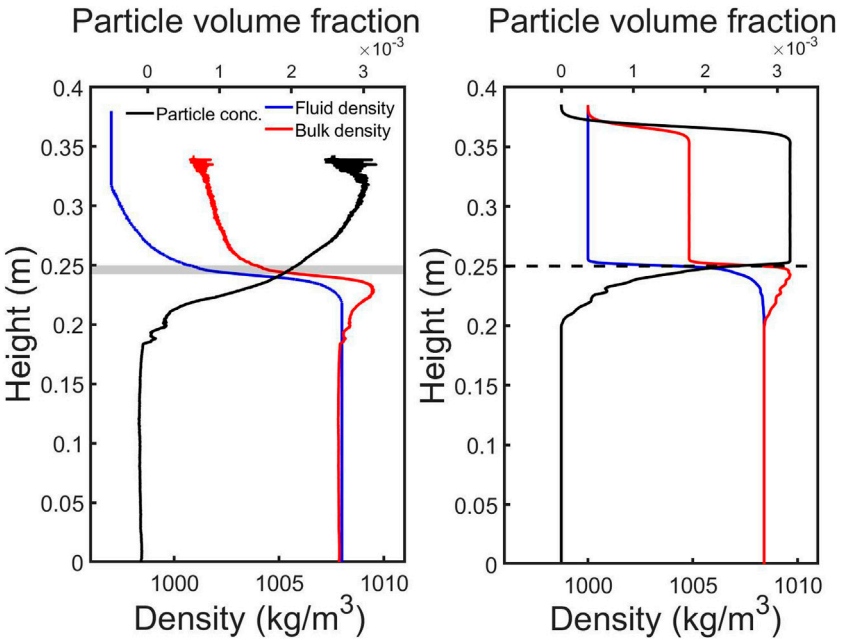


**FIGURE 10 |** Density profile after 8 s for experiments (left) (Fries et al., 2021) and simulations (right) with $\varnothing_0 = 3.18 \times 10^{-3}$ and a particle size of 40 μm. For clarity, the uncertainty on the experimental fluid density are not displayed on the figure and correspond to 0.8 kg m$^{-3}$.

observe fingers, with the finger velocity increasing with particle size.
- For greater particle sizes, no fingers are observed to form.

From our simulations, we constrain the transition between the two regimes to occur at a critical particle diameter around 115 and 145 μm respectively for $\varnothing_0 = 1.19 \times 10^{-3}$ and $\varnothing_0 = 3.57 \times 10^{-3}$. We also note that this size range corresponds to the particle size at which the Stokes velocity exceeds the predicted finger velocity. This result agrees with the experimental observations of Scollo et al. (2017), who observed that no fingers form for particles with diameter larger than ~125 μm with an initial particle volume fraction of $\varnothing_0 = 1.19 \times 10^{-3}$. We also compare the dependence of $V_f$ on the particle diameter with that predicted by **Eq. 1** and find a best fit for $Gr_c = 7.6 \pm 3.6 \times 10^3$ (with $R^2 = 0.91$) and $Gr_c = 2.7 \pm 0.8 \times 10^4$ (with $R^2 = 0.87$) respectively for the two initial volume fractions (**Figure 11B**). We observe again that the values for the fitted $Gr_c$ are greater than the one proposed by Hoyal et al. (1999) by analogy with thermal convection, whilst they also substantially differ from one another. We therefore also fit the results to a power law $V_f \propto Dp^{\eta}$ finding $\eta = 0.38 \pm 0.13$ ($R^2 = 0.94$) and $\eta = 0.42 \pm 0.10$ ($R^2 = 0.88$) respectively to the two volume fractions which is in very good agreement with the analytical formulation (**Eq. 1**) that suggests $\eta = 0.4$.

## Particle Mass Flux, Particle Concentration in the Lower Layer and Accumulation Rate

Given the excellent agreement between the proposed model and both LSA analysis and analogue experiments described above, we take advantage of having 3D data from the numerical simulations in order to extract other parameters which are difficult to obtain otherwise (Fries et al., 2021). Three interesting parameters are the particle mass flux across a plane, the particle concentration in the lower layer and the amount of particles accumulated at the bottom of the tank, which can be related to the accumulation rate. The latter is especially interesting as, when the model is applied to volcanic clouds, it could eventually be compared with field data (Bonadonna et al., 2011).

We calculate the mass flux across a horizontal plane (actually a thin box of thickness $\delta x$) as shown in **Figure 12A** with

$$J = \frac{\Delta m}{A \Delta t}, \tag{48}$$

where $\Delta m$ is the mass crossing the yellow plane of area $A$ in time $\Delta t$, and is given by the mass difference in the volume below the plane between $t$ and $t - \Delta t$. The mass below at each time is calculated by summing the mass of particles in each cell $i$ of volume $\Delta V$, which is individually given by $m_i = \Delta V \varnothing_i \rho_p$. **Figure 12B** shows the temporal evolution of the particle mass flux settling through the yellow plane (located at 0.15 m below the barrier), for several initial particle volume fractions. The vertical black dashed line indicates the theoretical time $T_i$ when particles would be expected to reach the plane if they were settling individually at their Stokes velocity. For the different simulations, we clearly observe that the moments when the flux starts initially increasing (i.e., the arrival of the fastest finger) are much earlier than $T_i$ and this shows the extent to which the collective settling enhances the premature sedimentation. After the initial increase, the fluxes exhibit strong oscillations around a high plateau. These oscillations are associated with the intermittent

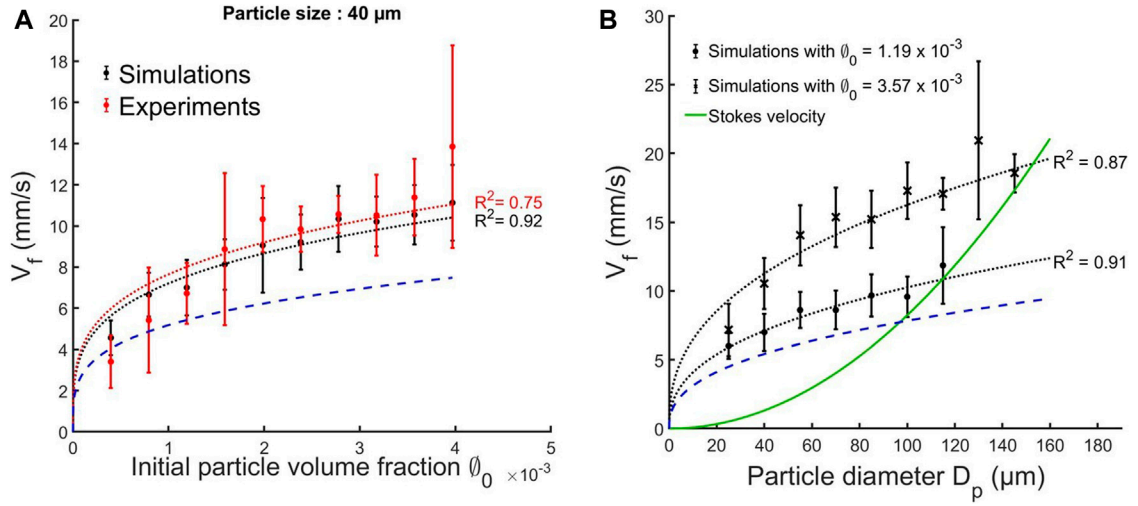


**FIGURE 11 | (A)** Average finger speed ($V_f$) as a function of the initial volume fraction ($\varnothing_0$) for a particle diameter of 40 µm. Red and black dotted lines show the best fits to the experiments (Fries et al., 2021) and simulations, respectively, using **Eq. 1** with $Gr_c$ as the fit parameter. For the simulations, we find $Gr_c = 1.2 \pm 0.4 \times 10^4$ whilst for the experiments $Gr_c = 1.9 \pm 0.7 \times 10^4$. **(B)** Average finger speed ($V_f$) as a function of the initial particle diameter ($D_p$), for two different particle volume fractions. The green line is the Stokes velocity for individual particles. The black dotted lines show the best fits to the simulations using **Eq. 1** with $Gr_c$ as the fit parameter. For $\varnothing_0 = 1.19 \times 10^{-3}$, the best fit gives $Gr_c = 7.6 \times 10^3$ and no fingers are observed to form for particle sizes higher than 115 µm. For $\varnothing_0 = 3.57 \times 10^{-3}$, the best fit gives $Gr_c = 2.7 \times 10^4$ and no fingers are observed to form for particle sizes higher than 145 µm. In the two plots, the blue dashed line shows **Eq. 1** using $Gr_c = 10^3$ from the analogy with thermal convection (Hoyal et al., 1999).

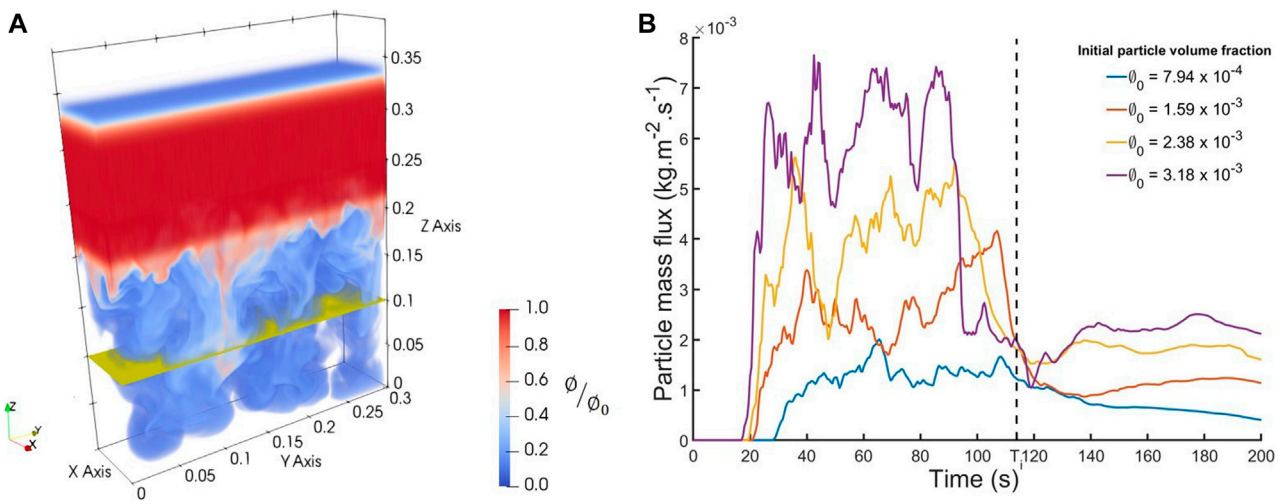


**FIGURE 12 | (A)** Horizontal planar surface (yellow slice) located 0.15 m below the barrier, across which the particle mass flux is computed in the simulation domain. **(B)** Temporal evolution for the particle mass flux crossing the plane. Black dashed line: theoretical time for the particles to reach the plane at their individual Stokes velocity.

nature of PBL detachment and the strong convection generated by fingers in the lower layer. Indeed, we observe that as soon as fingers reach the bottom of the tank, convection cells appear re-entraining some particles upward. The results show the net downward flux of particles and when particles are entrained upward, this consequently decreases the flux value. Interestingly, the different peaks show that we have some oscillatory convection and not steady convection. Finally, the particle mass flux reaches a plateau after some time which shows the end of convection and a transition to individual settling. Throughout, the average mass flux, as well as the amplitude of the oscillations increases with the initial volume fraction.

Another way to highlight the enhancement of the sedimentation rate by collective settling is to study the spatial distribution of particles beneath the interface. Assuming a quiescent upper layer and a convective lower layer, akin to our

simulations, Hoyal et al. (1999) derived **Eq. 4** for the evolution of the particle concentration in the lower layer. The derivation of this formulation assumes that $\dot{M}_{out} \neq 0$ since $t = 0$ but in fact, $\dot{M}_{out} = 0$ for $t < t_a$ where $t_a$ is the time when the first particles reach the bottom of the tank. Also, **Eq. 4** only remains valid for $t < t_{lim}$, where $t_{lim} = h_1/V_s$, $h_1$ being the height of the upper layer. After this time, there are no longer any particles remaining in the upper layer and $\dot{M}_{in} = 0$. We therefore propose an extension for the solution of the problem (see section 2.1 in **Supplementary Material**) which becomes

$$C_2(t) = \frac{V_s}{h_2} C_1(0) t, \quad \text{for } t < t_a, \tag{49}$$

$$C_2(t) = C_1(0)\left[1 + \left(\frac{V_s}{h_2} t_a - 1\right) e^{-\frac{V_s}{h_2}(t - t_a)}\right], \quad \text{for } t_a \le t < t_{lim}, \tag{50}$$

$$C_2(t) = C_1(0)\left[1 + \left(\frac{V_s}{h_2} t_a - 1\right) e^{-\frac{V_s}{h_2}(t_{lim} - t_a)}\right]\left(1 + \frac{h_1}{h_2} - \frac{V_s}{h_2} t\right), \quad \text{for } t \ge t_{\text{lim}}, \tag{51}$$

where $h_2$ is the thickness of the lower layer. **Equation 51** assumes that the convection stops at $t_{lim}$, which suggests a quiescent settling in the lower layer after that time with a constant flux $\dot{M}_{out} = AV_sC_2(t_{lim})$.

An interesting result coming out of the previous analytical study is the mass of particles accumulating at the bottom of the tank and the associated accumulation rate. We can derive an analytical prediction for the mass of particles $m_b$ accumulated at the bottom of the tank for the different regimes highlighted above. Thus, by integration of the flux (see Section 2.2 in **Supplementary Material**) we have

$$m_b = 0, \quad \text{for } t < t_a, \tag{52}$$

$$m_b = m_0 \frac{V_s}{h_1}\left[t + \left(\frac{h_2}{V_s} - t_a\right) e^{-\frac{V_s}{h_2}(t - t_a)} - \frac{h_2}{V_s}\right], \quad \text{for } t_a \le t < t_{lim}, \tag{53}$$

$$m_b = m_0 \frac{V_s}{h_1}\left\{t_{lim} - \frac{h_2}{V_s}\left[1 + \left(\frac{V_s}{h_2} t_a - 1\right) e^{-\frac{V_s}{h_2}(t_{lim} - t_a)}\right]\left(1 + \frac{h_1}{h_2} - \frac{V_s}{h_2} t\right)\right\}, \quad \text{for } t \ge t_{lim}, \tag{54}$$

where $m_0$ is the initial mass of particles injected in the upper layer. Finally, at the time $t_{lim} + h_2/V_s$, all the particles have settled through the lower layer, thus $m_b = m_0$. **Figure 13A** shows the simulated particle accumulation at the bottom of the tank through time, for different particle sizes as well as the analytical prediction (**Eqs 52–54**). We compare as well with the analytical formulation of the mass which assumes that the lower is still turbulently convective even after the time $t_{lim}$ (Eq. S43 in **Supplementary Material**, dashed lines in **Figure 13A**). In order to compare between this prediction and the model results, $t_a$ is fitted in order to have the best agreement between the numerical data and **Eqs 52–54**. The results show clearly that the quiescent model of the lower layer for $t \ge t_{lim}$ agrees very well with the simulations and suggest that the entirely convective model underestimates the accumulation rate. Additionally, the fitted parameter $t_a$ is coherent with the time for the first fingers to reach the bottom of the tank in the simulations. **Figure 13B** shows the instantaneous accumulation rate computed from the numerical data for several initial volume fractions, as estimated by

$$\frac{1}{A}\frac{dm_b}{dt}, \tag{55}$$

We observe, for each initial particle volume fraction, an initial increase of the accumulation rate with time which reflects the enhancement of the sedimentation process due to convection. Interestingly, the accumulation rate then reaches a plateau at around $t = t_{lim}$, indicating that the system switches to a steady settling regime once all particles have left the upper layer. We compare also with the analytical relations which again have very good agreement with our simulations.

Finally, using the determined $t_a$, we can also calculate the concentration $C_2(t)$, as calculated with the analytical expressions in **Eqs 49–51**. **Figure 14** shows a comparison with the average $C_2(t)$ as measured in simulations for a particle size of 40 μm and three different initial upper layer concentrations, finding very good agreement.

# DISCUSSION

## Model Caveats

Our numerical model has been validated by comparing various outputs with results from linear stability analysis, lab experiments (Fries et al., 2021) and theoretical predictions from previous studies (Hoyal et al., 1999; Carazzo and Jellinek, 2012). Even though these comparisons are good (**Figures 9–14**), the results provided by the model inherits the caveats of the experiments. Indeed, the static and confined configuration, as well as the fact that we performed the simulations in water, mean that we cannot fully extend the results to the volcanic case yet. Thus, further investigations are necessary to better simulate the volcanic environment (e.g., in air, with wind, etc.). Additionally, it is necessary to consider the limits of validity of the different assumptions. In our study, particles are small enough that they have no inertia and thus the fluid-particle interaction force is governed by the buoyant force term in the fluid momentum equation. However, as soon as the particle size increases, we need to consider some other dynamics. Indeed, a rigid particle moving in a fluid produces locally a disturbance flow which generates other contributions to the fluid-particle force terms. The assumption that particles settle at their Stokes velocity will then no longer be valid as the created local flow affects $V_S$ (Maxey and Riley, 1983; Cartwright et al., 2010; Patočka et al., 2020).

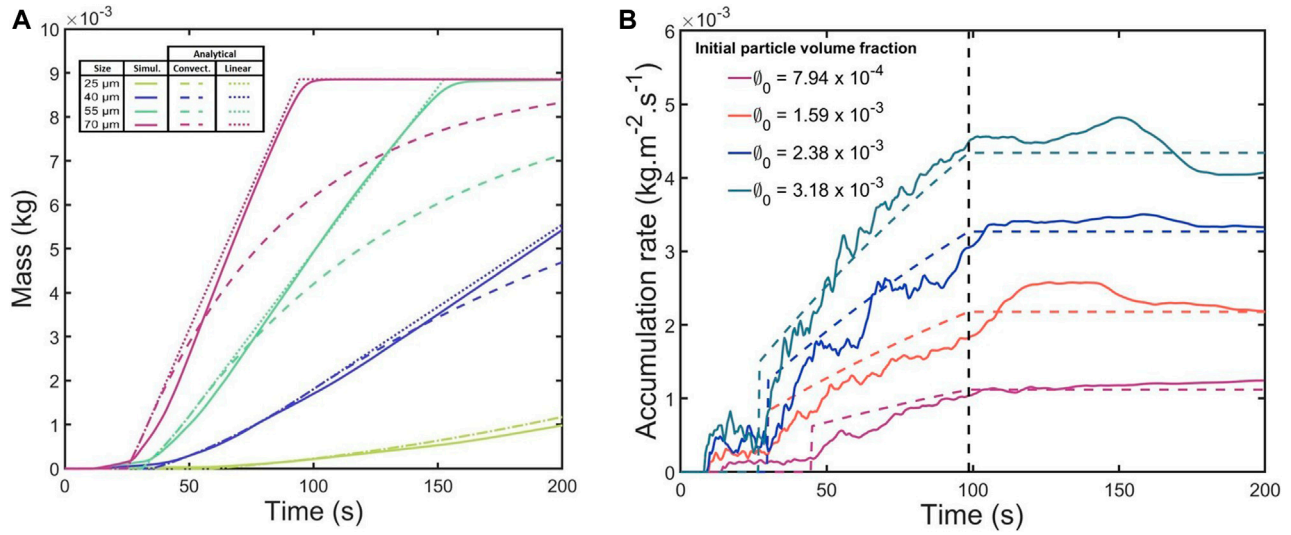


**FIGURE 13 | (A)** Temporal evolution of the mass of particles accumulating at the bottom of the tank for several particle sizes. The dashed and dotted lines represent the extended analytical model of (Hoyal et al., 1999). Particle volume fraction $\varnothing_0 = 1.19 \times 10^{-3}$. **(B)** Accumulation rate calculated at the bottom of the tank for several particle volume fractions and a particle size of 40 µm. The coloured dashed lines are the rate derived from the analytical model. The black dashed line is the theoretical time at which all particles have settled across the interface.

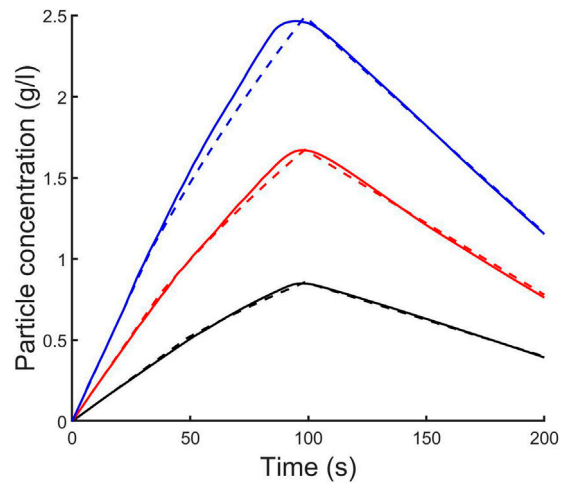


**FIGURE 14 |** Evolution of the average particle volume fraction in the lower layer for particle of size 40 µm. Black: $C_0$ = 2 g/L ($\varnothing_0 = 7.94 \times 10^{-4}$), Red: $C_0$ = 4 g/L ($1.59 \times 10^{-3}$) and Blue: $C_0$ = 6 g/L ($2.38 \times 10^{-3}$). Solid lines: numerical model. Dashed lines: modified (Hoyal et al., 1999) model **(Eqs 49–51)**.

Whilst the condition on the particle coupling is given by the Stokes number ($St < 1$), there is also a condition on the particle volume fraction to take in account. Harada et al. (2013) and Yamamoto et al. (2015) derived a dimensionless number in order to characterise the transition between fluid-like and particle-like settling. Although this number is only valid for narrow channel configurations, which are considerably different from ours, it highlights the fact that the particle size, volume fraction and characteristic length scale of the flow are critical parameters to define the validity of the continuum assumption. Thus, the transition from fluid-like to particle-like behaviour is achieved by decreasing the volume fraction and characteristic length scale and increasing the particle size. Near this transition, the use of a single-phase model, such as that presented here, should be treated with caution and this reveals the need for a comparison with future models which explicitly account for the drag contribution of individual particles. In multiphase models this contribution has been commonly represented through a force term involving the ratio between the phases differential velocities and the relaxation time (drag timescale) (Laibe and Price, 2014; Chou and Shao, 2016).

Another related caveat concerns the numerical diffusion underlying the use of an Eulerian approach to describe the transport of particles. Compared to classical first order finite difference methods, the use of the third order WENO procedure has drastically reduced the numerical diffusion. It is also possible to further reduce the induced numerical diffusion by increasing the order of the WENO scheme (i.e. increase also the computational cost). However, for problems purely related to advection, where the presence of any diffusion is critical, another strategy, such as two-phase models (using a Lagrangian approach where individual particles are explicitly modelled), has to be considered.

## Vertical Finger Velocity

We have compared the simulated vertical velocity of fingers with experimental observations (Fries et al., 2021) and a theoretical prediction (**Eq. 1**) from (Hoyal et al., 1999; Carazzo and Jellinek, 2012) (**Figure 11**). This expression depends on a critical Grashof number, which by analogy with thermal convection (Turner, 1973) has previously been assumed to be $10^3$ (Hoyal et al., 1999).

This value effectively corresponds to a dimensionless critical PBL thickness at which point the PBL can detach and form fingers. However, both the model results and experimental observations summarised in **Figure 11** suggest that $Gr_c > 10^3$ for our configuration. Furthermore, as seen in **Figure 11B**, the curve for $V_f$ using $Gr_c = 10^3$ (blue dotted line) crosses the Stokes velocity curve around 95 μm for instance with an initial particle volume fraction of $\varnothing_0 = 1.19 \times 10^{-3}$, suggesting this value should be the upper particle size limit for finger formation. However, in agreement with experiments (Scollo et al., 2017; Fries et al., 2021), we observe a larger threshold for the finger formation to be in the size range [115 − 125] μm, for $\varnothing_0 = 1.19 \times 10^{-3}$, and in the range [145 − 160] μm for $\varnothing_0 = 3.57 \times 10^{-3}$, in this particular configuration. We also showed that **Eq. 1** poorly predicts the observed dependence of the finger velocity on the initial particle volume fraction. Indeed, our studies suggests an alternative power law that better describes the dependence of $V_f$ on $\varnothing_0$. **Equation 1** has been derived by a scaling theory that involves $\delta_{PBL}$ as characteristic length of the problem (Hoyal et al., 1999; Carazzo and Jellinek, 2012) and the discrepancies highlighted in this paper (**Figure 11**) may suggest that $\delta_{PBL}$ actually has a slightly different dependence on the initial particle volume fraction. Moreover, the use of the Grashof number as an appropriate scaling for the PBL thickness remains uncertain. On the one hand, our results suggest that if instability does occur once a critical Grashof number is reached, the critical value taken from the thermal convection analogy is not valid. On the other hand, the Grashof number may simply not be the correct dimensionless form of the PBL thickness, and different flow configurations will produce different critical values. The fact that both the experiments and simulations agree very well shows that the "true" value for $Gr_c$, if it exists, is an order of magnitude higher than in the thermal case. However, **Figure 11B** shows that we find a ratio of $\sim 3.5$ between the two fitted $Gr_c$ which is interestingly close to the ratio of three between the two associated particle volume fractions. Whilst the variability of $Gr_c$ might come from the measurement itself (fitting of the numerical and experimental data), this behaviour is coherent considering the definition of $Gr_c$ (ratio between buoyancy and viscous forces) and the fact that the buoyancy force is a function of the particle volume fraction. Obviously, this is only the case so long as the particle concentration does not affect the bulk viscosity, which is the case in our study. Therefore, we highlight here that the order of magnitude found for $Gr_c$ is valid for the flow configuration presented in this study and also that there is a dependence on the initial particle volume fraction. Further analyses with different flow configurations (i.e., different buoyancy and viscous conditions) are required to constrain the variability of $Gr_c$ and confirm that it may not be a rigorous scaling for the PBL thickness. A study involving settling-driven gravitational instabilities in air and in the presence of shear is currently performed and will certainly provide some insights on the dependence of $Gr_c$ on the flow configuration.

The predicted dependence of the finger velocity on the particle diameter by **Eq. 1** shows a very good agreement with our simulated results, as confirmed by a power-law fitting between $V_f$ and $D_p$. Thus, whilst we have demonstrated the need for a better scaling of $\delta_{PBL}$, **Eq. 1** can still provide a good estimate for the particle size threshold to form fingers. Consequently, if the size threshold to form fingers is given when **Eq. 1** equals the Stokes velocity (**Eq. 13**) we can derive a formulation for the threshold

$$D_p^* = \left[\frac{(18\mu)^2 \varnothing \delta_{PBL}}{g(\rho_p - \rho_f)\rho_f}\sqrt{\left(\frac{\pi}{4}\right)}\right]^{\frac{1}{4}}. \quad (56)$$

The main caveats for this formulation are that it strongly depends on having a correct scaling for $\delta_{PBL}$ and obviously this estimation is valid under the assumption that particles settle at their Stokes velocity, which is reasonable for our study but might be uncertain in nature where the ambient fluid is air and for non-spherical particles.

## Particle Concentration in the Lower Layer and Mass Accumulation Rate

We have proposed a modified analytical formulation for the particle concentration in the lower layer $C_2(t)$ and consequently for the mass of particles accumulated at the bottom of the tank $m_b(t)$. Despite some numerical artefacts that can be seen on **Figure 13B** where the computed accumulation rate seems to be non-zero before $t_a$, there is very good agreement between the simulations and the analytical model. The artefacts themselves are due to fluctuating numerical errors that do not affect the final results.

The analytical predictions for $C_2(t)$ and $m_b(t)$ are step-wise functions depending on $t_a$, the time it takes for the first particles to reach the bottom. For $t < t_a$, the analytical model predicts that $C_2(t)$ increases linearly with time since the formulation assumes that, during this period, particles are settling individually. In fact, our numerical results show that convective settling does occur for $t < t_a$ but, since this time period is short, the linear law seems to be a satisfactory approximation for the early-time average lower layer particle concentration. However, in order to compare our simulated results with the analytical prediction, we fitted the parameter $t_a$ in this study. Although we are able to obtain excellent agreement between model and theory, it would be better to develop a fully independent formulation. To achieve this, it is necessary to also provide an analytical estimation for $t_a$. One possible approach would be to assume the decomposition $t_a = t_a' + t_a''$ where $t_a'$ is the time during which the PBL initially grows beneath the interface at the individual particle settling velocity, i.e., $t_a' = \delta_{PBL}/V_s$, and $t_a''$ is the time between the PBL detachment and the first arrival of particles at the base of the domain. If, during this stage, we assume that the particles are advected at the finger velocity then $t_a'' = (h_2 - \delta_{PBL})/V_f$). We therefore see that $t_a$ strongly depends on $\delta_{PBL}$, which highlights once again the need for a correct scaling of the PBL thickness, as discussed in the previous section.

Another interesting result concerns the accumulation rate of particles at the base of the domain in the presence of fingers. **Figure 13B** shows the accumulation rate increases with time for $t_a < t < t_{lim}$, in agreement with the analytical prediction (i.e., combination of **Eqs 53**, **55** which provides an exponential

increase of $m_b$). Conversely, if the particles had settled individually, the accumulation rate would be temporally constant. However, there is no denying that the effect as a function of position is also interesting in order to characterise especially the consequences of the oscillatory convection on the sedimentation rate. We computed an animated map (**Supplementary Material**) showing the spatial distribution of the sedimentation rate at the tank floor through time, for an initial particle volume fraction of $1.98 \times 10^{-3}$. As expected, the convection in the lower layer initiated by fingers generates a spatially inhomogeneous sedimentation rate which strongly evolves in time. Furthermore, we also observe that the temporal evolution stops a time around the theoretical time when we expect all particle have left the upper layer (i.e., end of convection). Generally, all these aspects show that temporally resolved measurements of the accumulation rate of particles from volcanic clouds may record temporal signatures of sedimentation *via* settling-driven gravitational instabilities. Whilst there is already a spatial deposit signature of settling-driven gravitational instabilities (i.e. bimodal grainsize distribution) (Bonadonna et al., 2011; Manzella et al., 2015), this is not unique and can be generated by other mechanisms such as particle aggregation (Brown et al., 2012). Accumulation rate data from the field may therefore provide a powerful tool for distinguishing the efficiency of convective sedimentation beneath volcanic clouds.

## CONCLUSION

We have presented an innovative hybrid Lattice Boltzmann-Finite Difference 3D model in order to simulate settling-driven gravitational instabilities at the base of volcanic ash clouds. Such instabilities occur when particles settle through a density interface at the base of a suspension, leading to the formation of an unstable particle boundary layer (Hoyal et al., 1999; Carazzo and Jellinek, 2012; Manzella et al., 2015), and also occur in other natural settings, such as river plumes (Davarpanah Jazi and Wells, 2016). Our numerical model makes use of a low-diffusive WENO procedure to solve the advection-diffusion-settling equation for the particle volume fraction. The use of such a routine allows us to minimise errors associated with numerical diffusion and has the advantage of being applied to simple uniform meshes, which makes the coupling with the LBM easier. This innovative use of the WENO scheme, therefore, represents an effective tool for the solving of advection-dominated problems. Our implementation of the third order WENO finite difference scheme will be integrated in a future release of the open-source *Palabos* code. Our model has been successfully validated by comparing the results with 1) predictions from linear stability analysis where we show that the model is able to simulate settling-driven gravitational instabilities from the initial disturbance through the linearly-unstable regime, 2) analogue experiments (Fries et al., 2021) and 3) theoretical models (Hoyal et al., 1999; Carazzo and Jellinek, 2012) in order to reproduce the non-linear regime which describes the downward propagation of fingers. We also confirmed the premature sedimentation process through collective settling compared to individual settling.

Our model provides new insights into:

- The value of the critical Grashof number. From measurements of the vertical finger speed, we have found $Gr_c \sim 10^4$ in our configuration. This value differs from the one suggested by analogy with thermal convection ($Gr_c \sim 10^3$) (Hoyal et al., 1999). Our results suggest that either the critical Grashof number for settling-driven gravitational instabilities is greater than in the thermal convection case or that the Grashof number may not be the correct dimensionless form of the PBL thickness. In any case, this highlights the need for further investigation of the scaling of the PBL thickness $\delta_{PBL}$.
- The presence of a particle size threshold for the finger formation. Using our results, we have proposed an analytical formulation for this threshold depending on the density of particles, the viscosity of the medium and also the bulk density difference between the two fluid layers.
- The signature of settling-driven gravitational instabilities (i.e., accumulation rate). We show that the accumulation rate of particles at the tank base initially increases with time before reaching a plateau. This contrasts with the constant accumulation rate associated with individual particle settling. This suggests that accumulation rate data could be used during tephra fallout to distinguish between sedimentation through settling-driven gravitational instabilities and individual-particle sedimentation.

We have also demonstrated how our numerical model can be used to expand the initial conditions and configuration settings that can be explored through experimental investigations. The results presented so far in an aqueous media permitted model validation but have also opened fundamental questions that will be addressed in future works involving configurations more similar to the natural system. Indeed, thanks to the strengths of the LBM, the model can easily be applied to more complex systems and provides a robust tool for the transition from the laboratory studies to volcanic systems, as well as other environmental flows.

## DATA AVAILABILITY STATEMENT

The raw data supporting the conclusions of this article will be made available by the authors, without undue reservation.

## AUTHOR CONTRIBUTIONS

JL integrated the WENO procedure in the Palabos framework, conducted the simulations and data analysis under the supervision of PJ, JLä, CB, and BC. JL drafted the manuscript. JLä and BC were involved in the development of the Palabos code. All authors have contributed to data

interpretation as well as the editing and finalising of the paper.

## FUNDING

The study has been funded by the Swiss National Science Foundation #200021_169463.

## ACKNOWLEDGMENTS

All the simulations presented in this paper have been performed using the High Performance Computing (HPC) facilities *Baobab* and *Yggdrasil* of the University of Geneva. We would like to thank Amanda B. Clarke and Jeremy C. Phillips for constructive discussions. The authors are grateful to SS, TM, BA and the Editor for their constructive reviews. A preprint of this work has been submitted on the arXiv server in the Fluid Dynamics category on the June 14, 2021: arXiv:2106.07694 (Lemus et al., 2021).

## SUPPLEMENTARY MATERIAL

The Supplementary Material for this article can be found online at: https://www.frontiersin.org/articles/10.3389/feart.2021.713175/full#supplementary-material.

## REFERENCES

Alsinan, A., Meiburg, E., and Garaud, P. (2017). A Settling-Driven Instability in Two-Component, Stably Stratified Fluids. *J. Fluid Mech.* 816, 243–267. doi:10.1017/jfm.2017.94

Bagnato, E., Aiuppa, A., Bertagnini, A., Bonadonna, C., Cioni, R., Pistolesi, M., et al. (2013). Scavenging of sulphur, Halogens and Trace Metals by Volcanic Ash: The 2010 Eyjafjallajökull Eruption. *Geochimica et Cosmochimica Acta* 103, 138–160. doi:10.1016/j.gca.2012.10.048

Baltensperger, R., and Berrut, J.-P. (2001). The Linear Rational Collocation Method. *J. Comput. Appl. Math.* 134, 243–258. doi:10.1016/s0377-0427(00)00552-5

Berrut, J.-P., and Mittelmann, H. D. (2004). Adaptive point Shifts in Rational Approximation with Optimized Denominator. *J. Comput. Appl. Math.* 164-165, 81–92. doi:10.1016/S0377-0427(03)00485-0

Bhatnagar, P. L., Gross, E. P., and Krook, M. (1954). A Model for Collision Processes in Gases. *Phys. Rev.* 94, 515–525. doi:10.1103/physrev.94.511

Blong, R. (2000). "Volcanic Hazards and Risk Management," in *Encyclopedia of Volcanoes* (Cambridge: Academic Press), 1215–1227.

Bonadonna, C., Biass, S., Menoni, S., and Gregg, C. E. (2021). Assessment of Risk Associated with Tephra-Related Hazards. *Forecasting and Planning for Volcanic Hazards, Risks, and Disasters* 2, 329–378. doi:10.1016/b978-0-12-818082-2.00008-1

Bonadonna, C., Folch, A., Loughlin, S., and Puempel, H. (2012). Future Developments in Modelling and Monitoring of Volcanic Ash Clouds: Outcomes from the First IAVCEI-WMO Workshop on Ash Dispersal Forecast and Civil Aviation. *Bull. Volcanol.* 74, 1–10. doi:10.1007/s00445-011-0508-6

Bonadonna, C., Genco, R., Gouhier, M., Pistolesi, M., Cioni, R., Alfano, F., et al. (2011). Tephra Sedimentation during the 2010 Eyjafjallajökull Eruption (Iceland) from deposit, Radar, and Satellite Observations. *J. Geophys. Res.* 116. doi:10.1029/2011JB008462

Brown, R. J., Bonadonna, C., and Durant, A. J. (2012). A Review of Volcanic Ash Aggregation. *Phys. Chem. Earth* 45–46, 67–78. doi:10.1016/j.pce.2011.11.001

Burgisser, A., Bergantz, G. W., and Breidenthal, R. E. R. (2005). Addressing Complexity in Laboratory Experiments: The Scaling of Dilute Multiphase Flows in Magmatic Systems. *J. Volcanology Geothermal Res.* 141, 245–265. doi:10.1016/j.jvolgeores.2004.11.001

Burns, P., and Meiburg, E. (2012). Sediment-laden Fresh Water above Salt Water: Linear Stability Analysis. *J. Fluid Mech.* 691, 279–314. doi:10.1017/jfm.2011.474

Burns, P., and Meiburg, E. (2014). Sediment-laden Fresh Water above Salt Water: Nonlinear Simulations. *J. Fluid Mech.* 762, 156–195. doi:10.1017/jfm.2014.645

Carazzo, G., and Jellinek, A. M. (2012). A New View of the Dynamics, Stability and Longevity of Volcanic Clouds. *Earth Planet. Sci. Lett.* 325-326, 39–51. doi:10.1016/j.epsl.2012.01.025

Cardoso, S. S. S., and Zarrebini, M. (2001). Convection Driven by Particle Settling Surrounding a Turbulent Plume. *Chem. Eng. Sci.* 56, 3365–3375. doi:10.1016/S0009-2509(01)00028-8

Carey, S. (1997). Influence of Convective Sedimentation on the Formation of Widespread Tephra Fall Layers in the Deep Sea. *Geol* 25, 839–842. doi:10.1130/0091-7613(1997)025<0839:iocsot>2.3.co;2

Cartwright, J. H. E., Feudel, U., Károlyi, G., De Moura, A., Piro, O., and Tél, T. (2010). Dynamics of Finite-Size Particles in Chaotic Fluid Flows. *Nonlinear Dynamics and Chaos: Advances and Perspectives* 51(1), 87. doi:10.1007/978-3-642-04629-2_4

Chandrasekhar, S. (1961). *Hydrodynamic and Hydromagnetic Stability*. Oxford: Oxford University Press.

Chou, Y.-J., and Shao, Y.-C. (2016). Numerical Study of Particle-Induced Rayleigh-Taylor Instability: Effects of Particle Settling and Entrainment. *Phys. Fluids* 28, 043302. doi:10.1063/1.4945652

Costa, A., Folch, A., and Macedonio, G. (2010). A Model for Wet Aggregation of Ash Particles in Volcanic Plumes and Clouds: 1. Theoretical Formulation. *J. Geophys. Res.* 115, 1–14. doi:10.1029/2009JB007175

Crimaldi, J. P. (2008). Planar Laser Induced Fluorescence in Aqueous Flows. *Exp. Fluids* 44, 851–863. doi:10.1007/s00348-008-0496-2

Davarpanah Jazi, S., and Wells, M. G. (2016). Enhanced Sedimentation beneath Particle-Laden Flows in Lakes and the Ocean Due to Double-Diffusive Convection. *Geophys. Res. Lett.* 43, 10,883–10,890. doi:10.1002/2016GL069547

Durant, A. J. (2015). RESEARCH FOCUS: Toward a Realistic Formulation of fine-ash Lifetime in Volcanic Clouds. *Geology* 43, 271–272. doi:10.1130/focus032015.1

Folch, A. (2012). A Review of Tephra Transport and Dispersal Models: Evolution, Current Status, and Future Perspectives. *J. Volcanology Geothermal Res.* 235-236, 96–115. doi:10.1016/j.jvolgeores.2012.05.020

Folch, A., Mingari, L., Gutierrez, N., Hanzich, M., Macedonio, G., and Costa, A. (2020). FALL3D-8.0: A Computational Model for Atmospheric Transport and Deposition of Particles, Aerosols and Radionuclides - Part 1: Model Physics and Numerics. *Geosci. Model. Dev.* 13, 1431–1458. doi:10.5194/gmd-13-1431-2020

Fries, A., Lemus, J., Jarvis, P. A., Clarke, A. B., Phillips, J. C., Manzella, I., et al. (2021). The Influence of Particle Concentration on the Formation of Settling-Driven Gravitational Instabilities at the Base of Volcanic Clouds. *Front. Earth Sci.* 9. doi:10.3389/feart.2021.640090

Godunov (1959). A Difference Scheme for Numerical Solution of Discontinuous Solution of Hydrodynamic Equations. *Math. Sb.* 47, 271–306.

Godunov (1954). *Different Methods for Shock Waves*. Moscow, Russia: Moscow State Univ.

Gouhier, M., Eychenne, J., Azzaoui, N., Guillin, A., Deslandes, M., Poret, M., et al. (2019). Low Efficiency of Large Volcanic Eruptions in Transporting Very fine Ash into the Atmosphere. *Sci. Rep.* 9, 1–12. doi:10.1038/s41598-019-42489-z

Gudmundsson, G. (2011). Respiratory Health Effects of Volcanic Ash with Special Reference to Iceland. A Review. *Clin. Respir. J.* 5, 2–9. doi:10.1111/j.1752-699X.2010.00231.x

Guffanti, M., Mayberry, G. C., Casadevall, T. J., and Wunderman, R. (2008). Volcanic Hazards to Airports. *Nat. Hazards* 51, 287–302. doi:10.1007/s11069-008-9254-2

Guo, Z., Zheng, C., and Shi, B. (2002). Discrete Lattice Effects on the Forcing Term in the Lattice Boltzmann Method. *Phys. Rev. E* 65, 1–6. doi:10.1103/PhysRevE.65.046308

Harada, S., Kondo, M., Watanabe, K., Shiotani, T., and Sato, K. (2013). Collective Settling of fine Particles in a Narrow Channel with Arbitrary Cross-Section. *Chem. Eng. Sci.* 93, 307–312. doi:10.1016/j.ces.2013.01.054

He, X., and Luo, L.-S. (1997). Theory of the Lattice Boltzmann Method: From the Boltzmann Equation to the Lattice Boltzmann Equation. *Phys. Rev. E* 56, 6811–6817. doi:10.1103/PhysRevE.56.6811

Hosseini, S. A., Darabiha, N., Thévenin, D., and Eshghinejadfard, A. (2017). Stability Limits of the Single Relaxation-Time Advection-Diffusion Lattice Boltzmann Scheme. *Int. J. Mod. Phys. C* 28, 1750141. doi:10.1142/S0129183117501418

Hoyal, D. C. J. D., Bursik, M. I., and Atkinson, J. F. (1999). Settling-driven Convection: A Mechanism of Sedimentation from Stratified Fluids. *J. Geophys. Res.* 104, 7953–7966. doi:10.1029/1998jc900065

Jacobs, C. T., Collins, G. S., Piggott, M. D., Kramer, S. C., and Wilson, C. R. G. (2013). Multiphase Flow Modelling of Volcanic Ash Particle Settling in Water Using Adaptive Unstructured Meshes. *Geophys. J. Int.* 192, 647–665. doi:10.1093/gji/ggs059

Jenkins, S. F., Wilson, T. M., Magill, C., Miller, V., Stewart, C., Blong, R., et al. (2015). Volcanic Ash Fall hazard and Risk. *Global Volcanic Hazards and Risk*, 173–222. doi:10.1017/CBO9781316276273.005

Jiang, G.-S., and Shu, C.-W. (1996). Efficient Implementation of Weighted ENO Schemes. *J. Comput. Phys.* 126, 202–228. doi:10.1006/jcph.1996.0130

Jones, A., Thomson, D., Hort, M., and Devenish, B. (2007). The U.K. Met Office's Next-Generation Atmospheric Dispersion Model, NAME III. *Air Pollut. Model. Its Appl. XVII* 1, 580–589. doi:10.1007/978-0-387-68854-1_62

Keck, J.-B., Cottet, G.-H., Meiburg, E., Mortazavi, I., and Picard, C. (2021). Double-diffusive Sedimentation at High Schmidt Numbers: Semi-lagrangian Simulations. *Phys. Rev. Fluids* 6, 1–10. doi:10.1103/PhysRevFluids.6.L022301

Koochesfahani, M. M. (1984). Experiments on Turbulent Mixing and Chemical Reactions in a Liquid Mixing Layer. *Journal of Fluid Mechanics*. doi:10.7907/Y7BR-C556

Kruger, T., Kusumaatmaja, H., Kuzmin, A., Shardt, O., Goncalo, S., and Viggen, E. M. (2017). The Lattice Boltzmann Method. *Principles and Practice* 1. doi:10.1191/0265532206lt326oa

Laibe, G., and Price, D. J. (2014). Dusty Gas with One Fluid. *Mon. Not. R. Astron. Soc.* 440, 2136–2146. doi:10.1093/mnras/stu355

Latt, J., Malaspinas, O., Kontaxakis, D., Parmigiani, A., Lagrava, D., Brogi, F., et al. (2021). Palabos: Parallel Lattice Boltzmann Solver. *Comput. Math. Appl.* 81, 334–350. doi:10.1016/j.camwa.2020.03.022

Leclaire, S., Parmigiani, A., Malaspinas, O., Chopard, B., and Latt, J. (2017). Generalized Three-Dimensional Lattice Boltzmann Color-Gradient Method for Immiscible Two-phase Pore-Scale Imbibition and Drainage in Porous media. *Phys. Rev. E* 95, 33306. doi:10.1103/PhysRevE.95.033306

Lemus, J., Fries, A., Jarvis, P. A., Bonadonna, C., Chopard, B., and Latt, J. (2021). Modelling Settling-Driven Gravitational Instabilities at the Base of Volcanic Clouds Using the Lattice Boltzmann Method. Available at: https://arxiv.org/abs/2106.07694.

Lewis, D. J. (1950). The Instability of Liquid Surfaces when Accelerated in a Direction Perpendicular to Their Planes. II. *Proc. R. Soc. Lond. A.* 202, 81–96. doi:10.1098/rspa.1950.0086

Liu, X.-D., Osher, S., and Chan, T. (1994). Weighted Essentially Non-oscillatory Schemes. *J. Comput. Phys.* 115(1), 1–32. doi:10.1006/jcph.1994.1187

Manville, V., and Wilson, C. J. N. (2004). Vertical Density Currents: A Review of Their Potential Role in the Deposition and Interpretation of Deep-Sea Ash Layers. *J. Geol. Soc.* 161, 947–958. doi:10.1144/0016-764903-067

Manzella, I., Bonadonna, C., Phillips, J. C., and Monnard, H. (2015). The Role of Gravitational Instabilities in Deposition of Volcanic Ash. *Geology* 43, 211–214. doi:10.1130/G36252.1

Maters, E. C., Cimarelli, C., Casas, A. S., Dingwell, D. B., and Murray, B. J. (2020). Volcanic Ash Ice-Nucleating Activity Can Be Enhanced or Depressed by Ash-Gas Interaction in the Eruption Plume. *Earth Planet. Sci. Lett.* 551, 116587. doi:10.1016/j.epsl.2020.116587

Maxey, M. R., and Riley, J. J. (1983). Equation of Motion for a Small Rigid Sphere in a Nonuniform Flow. *Phys. Fluids* 26, 883–889. doi:10.1063/1.864230

Niemeier, U., Timmreck, C., Graf, H.-F., Kinne, S., Rast, S., Self, S., et al. (2009). Initial Fate of fine Ash and Sulfur from Large Volcanic Eruptions. *Atmos. Chem. Phys.* 9, 9043–9057. doi:10.5194/acp-9-9043-2009

Noriega, H., Reggio, M., and Vasseur, P. (2013). Natural Convection of Nanofluids in a Square Cavity Heated from below. *Comput. Therm. Sci. Int. J.* 5. doi:10.1615/computthermalscien.2013006652

Parmigiani, A., Huber, C., Chopard, B., Latt, J., and Bachmann, O. (2009). Application of the Multi Distribution Function Lattice Boltzmann Approach to thermal Flows. *Eur. Phys. J. Spec. Top.* 171, 37–43. doi:10.1140/epjst/e2009-01009-7

Patočka, V., Calzavarini, E., and Tosi, N. (2020). Settling of Inertial Particles in Turbulent Rayleigh-Bénard Convection. *Phys. Rev. Fluids* 5, 1–36. doi:10.1103/PhysRevFluids.5.114304

Prata, A. T., Mingari, L., Folch, A., Macedonio, G., and Costa, A. (2021). FALL3D-8.0: A Computational Model for Atmospheric Transport and Deposition of Particles, Aerosols and Radionuclides - Part 2: Model Validation. *Geosci. Model. Dev.* 14, 409–436. doi:10.5194/gmd-14-409-2021

Prata, F., and Rose, B. (2015). *Volcanic Ash Hazards to Aviation*, ed. H. B. T.-T. E. of V. (Second E. Sigurdsson (Amsterdam: Academic Press), 911–934. doi:10.1016/B978-0-12-385938-9.00052-3

Roche, O., and Carazzo, G. (2019). The Contribution of Experimental Volcanology to the Study of the Physics of Eruptive Processes, and Related Scaling Issues: A Review. *J. Volcanology Geothermal Res.* 384, 103–150. doi:10.1016/j.jvolgeores.2019.07.011

Scollo, S., Bonadonna, C., and Manzella, I. (2017). Settling-driven Gravitational Instabilities Associated with Volcanic Clouds: New Insights from Experimental Investigations. *Bull. Volcanol.* 79, 1–14. doi:10.1007/s00445-017-1124-x

Scollo, S., Folch, A., Coltelli, M., and Realmuto, V. J. (2010). Three-dimensional Volcanic Aerosol Dispersal: A Comparison between Multiangle Imaging Spectroradiometer (MISR) Data and Numerical Simulations. *J. Geophys. Res.* 115, 1–14. doi:10.1029/2009JD013162

Scollo, S., Tarantola, S., Bonadonna, C., Coltelli, M., and Saltelli, A. (2008). Sensitivity Analysis and Uncertainty Estimation for Tephra Dispersal Models. *J. Geophys. Res. Solid Earth* 113, 1–17. doi:10.1029/2006jb004864

Sharp, D. H. (1984). An Overview of Rayleigh-Taylor Instability. *Physica D: Nonlinear Phenomena* 12, 3–18. doi:10.1016/0167-2789(84)90510-4

Spence, R. J. S., Kelman, I., Baxter, P. J., Zuccaro, G., and Petrazzuoli, S. (2005). Residential Building and Occupant Vulnerability to Tephra Fall. *Nat. Hazards Earth Syst. Sci.* 5, 477–494. doi:10.5194/nhess-5-477-2005

Stenchikov, G., Ukhov, A., Osipov, S., Ahmadov, R., Grell, G., Cady-Pereira, K., et al. (2021). How Does a Pinatubo-Size Volcanic Cloud Reach the Middle Stratosphere. *Geophys. Res. Atmos.* 126. doi:10.1029/2020JD033829

Stokes, G. G. (1851). On the Theories of the Internal Friction of Fluids in Motion, and of the Equilibrium and Motion of Elastic Solids. *Math. Phys. Pap.* 19, 75–129. doi:10.1017/CBO9780511702242.005

Succi, S., Sbragaglia, M., and Ubertini, S. (2010). Lattice Boltzmann Method. *Scholarpedia* 5, 9507. doi:10.4249/scholarpedia.9507

Turner, J. S. (1973, *Buoyancy Effects in Fluids*. Cambridge: Cambridge University Press. doi:10.1017/CBO9780511608827

Völtz, C., Pesch, W., and Rehberg, I. (2001). Rayleigh-Taylor Instability in a Sedimenting Suspension. *Phys. Rev. E* 65, 011404. doi:10.1103/PhysRevE.65.011404

Watt, S. F. L., Gilbert, J. S., Folch, A., Phillips, J. C., and Cai, X. M. (2015). An Example of Enhanced Tephra Deposition Driven by Topographically Induced Atmospheric Turbulence. *Bull. Volcanol.* 77, 35. doi:10.1007/s00445-015-0927-x

Wilson, T. M., Cole, J. W., Stewart, C., Cronin, S. J., and Johnston, D. M. (2011). Ash Storms: Impacts of Wind-Remobilised Volcanic Ash on Rural Communities and Agriculture Following the 1991 Hudson Eruption, Southern Patagonia, Chile. *Bull. Volcanol.* 73, 223–239. doi:10.1007/s00445-010-0396-1

Yamamoto, Y., Hisataka, F., and Harada, S. (2015). Numerical Simulation of Concentration Interface in Stratified Suspension: Continuum-Particle Transition. *Int. J. Multiphase Flow* 73, 71–79. doi:10.1016/j.ijmultiphaseflow.2015.03.007

Yu, X., Hsu, T.-J., and Balachandar, S. (2014). Convective Instability in Sedimentation: 3-D Numerical Study. *J. Geophys. Res. Ocean.*, 3868–3882. doi:10.1002/2014jc010123

Yu, X., Hsu, T.-J., and Balachandar, S. (2013). Convective Instability in Sedimentation: Linear Stability Analysis. *J. Geophys. Res. Oceans* 118, 256–272. doi:10.1029/2012JC008255

Zhu, Y., Toon, O. B., Jensen, E. J., Bardeen, C. G., Mills, M. J., Tolbert, M. A., et al. (2020). Persisting Volcanic Ash Particles Impact Stratospheric SO2 Lifetime and Aerosol Optical Properties. *Nat. Commun.* 11, 1–11. doi:10.1038/s41467-020-18352-5

**Conflict of Interest:** The authors declare that the research was conducted in the absence of any commercial or financial relationships that could be construed as a potential conflict of interest.

**Publisher's Note:** All claims expressed in this article are solely those of the authors and do not necessarily represent those of their affiliated organizations, or those of the publisher, the editors and the reviewers. Any product that may be evaluated in this article, or claim that may be made by its manufacturer, is not guaranteed or endorsed by the publisher.

frontiers in Earth Science

ORIGINAL RESEARCH
published: 07 December 2021
doi: 10.3389/feart.2021.765610

# Fast High-Resolution S-PTHA Along the Western Mediterranean Sea Coastlines. Application to the Bay of Cannes

*Viviane Souty* *† *and Audrey Gailler*

*CEA, DAM, DIF, Bruyères-le-Châtel, France*

Probabilistic Tsunami Hazard Assessment (PTHA) is a fundamental framework for producing time-independent forecasts of tsunami hazards at the coast, taking into account local to distant tsunamigenic earthquake sources. If high resolution bathymetry and topography data at the shoreline are available, local tsunami inundation models can be computed to identify the highest risk areas and derive evidence-based evacuation plans to improve community safety. We propose a fast high-resolution Seismic-PTHA approach to estimate the tsunami hazard at a coastal level using the Bay of Cannes as test site. The S-PTHA process is firstly fastened by performing seismic and tsunami hazards separately to allow for quick updates, either from seismic rates by adding new earthquakes, or from tsunami hazard by adding new scenarios of tsunamis. Furthermore, significant tsunamis are selected on the basis of the extrapolation of a tsunami amplitude collected offshore from low-resolution simulations to an a priori amplitude nearshore using Green's law. This allows a saving in computation time on high-resolution simulations of almost 85%. The S-PTHA performed in the Bay of Cannes exhibits maximum expected tsunami waves that do not exceed 1 m in a 2500-year period, except in some particular places such as the Old Port of Cannes. However, the probability to experience wave heights of 30 cm in this same period exceeds 50% along the main beach of Cannes and these results need to be considered in risk mitigation plans given the high touristic attraction of the area, especially in summer times.

**Keywords: Bay of Cannes (France), earthquake tsunamis, amplification-law filter, high-resolution simulations, probabilistic assessment**

OPEN ACCESS

***Edited by:***
*Manuela Volpe, Istituto Nazionale di Geofisica e Vulcanologia (INGV), Italy*

***Reviewed by:***
*Roberto Tonini, Istituto Nazionale di Geofisica e Vulcanologia (INGV), Italy*
*Natalia ZamoraS, Barcelona Supercomputing Center, Spain*

***Correspondence:**
*Viviane Souty*
*viviane.souty@gmail.com*

*†Present address: EMSC/CSEM, Bruyères-le-Châtel, France*

***Specialty section:***
*This article was submitted to Geohazards and Georisks, a section of the journal Frontiers in Earth Science*

***Received:*** *27 August 2021*
***Accepted:*** *12 November 2021*
***Published:*** *07 December 2021*

***Citation:***
*Souty V and Gailler A (2021) Fast High-Resolution S-PTHA Along the Western Mediterranean Sea Coastlines. Application to the Bay of Cannes. Front. Earth Sci. 9:765610. doi: 10.3389/feart.2021.765610*

## 1 INTRODUCTION

The determination of the tsunami hazard is a key challenge worldwide, since the major tsunamigenic earthquakes at Sumatra in December 2004 and Tohoku in March 2011. The Sumatra tsunami is known as the deadliest one within living memory (death toll of 250,000–300,000; Okal, 2011). The failure to warn is essentially due to a deficiency of communication and is partly responsible for the

**Abbreviations:** ETA, estimated time arrival; MCT, maximum considered tsunami; PCTA, peak coastal tsunami amplitude; POI, point of interest; POTA, peak offshore tsunami amplitude; ROI, region of interest; S-PTHA, seismic probabilistic tsunami hazard assessment; WM, western mediterranean.

high number of causualities (Okal, 2011). The 2011 Tohoku tsunami caused a great deal of attention, strengthened by the Fukushima Nuclear Power Plant accident. The reactors were stopped after the Mw9.0 earthquake, but the elevation of the structures were too low in altitude to be preserved from tsunami waves exceeding 10 m in height at the site location (IAEA, 2015, p. 6, 12). Indeed, earthquakes up to Mw 8.0 were expected in this region and studies were performed to prevent the risks from these large earthquakes, but a mega-thrust earthquake was not considered in the tsunami hazard (and risk) studies (Stein and Okal, 2011, and reference within). These two events illustrate well the interest of accurately determine the tsunami hazard order to make better decisions based on reliable results of hazard studies.

Moreover, the above examples also highlight that the management of the tsunami hazard must be done dealing with two timescales. The warning timescale starts with a triggering event in real time such as an earthquake. The historical timescale studies past events to extrapolate to future events. For instance, the operating procedure at warning time scale can be based on a decision matrix, which defines the alert level (e.g., Schindelé et al., 2015). The Deterministic Tsunami Hazard Assessment or the Probabilistic Tsunami Hazard Assessment (PTHA), on the other hand, are two approaches that are usually conducted, at historical scale, for prevention purposes. The Deterministic Tsunami Hazard Assessment appears as the most conservative approach and is used in most of the forecasting tools in operational context. The results obtained merely account for the effects of the worst probable scenario on a few points of interest (POI, e.g., TANDEM, 2020) and do not consider smallest events that could also be significant, especially since they are more frequent. On the contrary, PTHA aggregates numerous scenarios in order to account for a range of tsunami sources as wide as possible (location, intensity, geometry, temporality). The resulting products allow identifying the most affected areas with recurrence possibilities. Then, PTHA provides key outcomes for long-term coastal management (Behrens et al., 2021). Furthermore, in the case of near-field triggering tsunamis that would reach the closest coasts within a few minutes, the real-time warning process is not always fast enough (e.g., Park et al., 2018) even so efforts are made to improve the speed of real-time forecast (e.g., Giles et al., 2021b; Selva et al., 2021). In this particular case, the disaggregation allows to ascertain the most dangerous tsunamigenic sources for a given area considering that the catalogs of seismicity is quite complete. PTHA studies performed using efficient numerical inundation simulations also provide a key upstream complementary information for site-specific hazard assessment (e.g., Gibbons et al., 2020) and evacuation planning (Tonini et al., 2021).

Tsunamis of seismic origin that can spread throughout the Western Mediterranean (WM) basin are not as large, nor as destructive as tsunamis that can be triggered by megathrust earthquakes originated along the subduction zone of the Pacific Rim. The seismicity within the WM can be considered as moderate, and quantifying the associated tsunami hazards remains a key point for planning of integrated community-level preparedness. Some historical earthquakes, indeed, have generated tsunamis with wave heights exceeding 1 m nearshore (**Figure 1A**). The Imperia earthquake (Mw 6.3–7.5, Italy) of the February 23, 1887 is one of these tsunamigenic-earthquakes and generated waves reaching heights between 1 and 2 m at Cannes and Antibes cities (France, e.g., Eva and Rabinovich, 1997; Larroque et al., 2012). The Boumerdes-Zemmouri tsunamigenic-earthquake (Mw 6.9, Algeria) in the night of the May 21, 2003 induced a rapid draw-down (−1.5 m) along the French Riviera coastlines (e.g., Sahal et al., 2009). This draw-down was accompanied by strong currents and eddies in several harbours, including the Old Port of Cannes. In both cases, the tsunami fortunately did not occur when beaches and harbours were crowed (e.g., summer day-time).

Since the 2010s, several PTHA studies aiming at constraining the tsunami hazard along the European coastlines can be cited. Most of them simulate tsunamis of seismic origin using a quite coarse long-wave model to extract a Peak Offshore Tsunami Amplitude (POTA), often located at a water depth between 50 and 100 m. Then, the Green's law (Green, 1838) is used to extrapolate the POTA close to the shore, usually around 1 m (e.g., Selva et al., 2016; Grezio et al., 2020; Selva et al., 2021). The extrapolated value expresses the Peak Coastal Tsunami Amplitude (PCTA). Sørensen et al. (2012) quantify the tsunami hazard due to earthquakes in the Mediterranean Sea this way by building numerous synthetic catalogues based on seismic rates in order to process the PTHA. Lorito et al. (2015) perform a linear approximation of the tsunami propagation in order to build a preliminary S-PTHA. They apply then a two-stage filter to reduce the number of significant sources and then perform non-linear tsunami propagation using the selected sources. A recent regional project, the TSUMAPS-NEAM updates tsunami hazard outcomes along the European coastlines (e.g., Basili et al., 2018; Basili et al., 2021). The POTAs are here extrapolated to PCTAs, using an amplification factor that depends on the POI and the tsunami period (Glimsdal et al., 2019).

These studies relying on S-PTHA use regional approaches, meaning that POTAs are extracted from low resolution simulations throughout the basin thereby reducing the computational cost. The PCTAs are then obtained from empirical amplification laws, that unfortunately results in estimates of wave heights at the coast within a factor of 2 at best (e.g., Gailler et al., 2018), partly because local effects are not taken into account (i.e., resonance in harbours and bays) and there is no distinction between direct and reflected waves. The estimates obtained from the extrapolation of a POTA are therefore a good approximation when used for warning scale forecasting (e.g., Selva et al., 2021). Besides, with such approaches based on amplification laws, the horizontal inundation and the currents are missing. In order to overcome these gaps, recent papers propose a high-resolution S-PTHA with a pre-selection of significant scenarios to simulate inundations at specific coastal sites efficiently (Volpe et al., 2019; Gibbons et al., 2020). Such local S-PTHA compared to more conservative approaches underlines the importance to perform local studies using the proper level of data resolution, to best serve specific risk mitigation actions, without neglecting the quantification of epistemic uncertainties (Tonini et al., 2021).

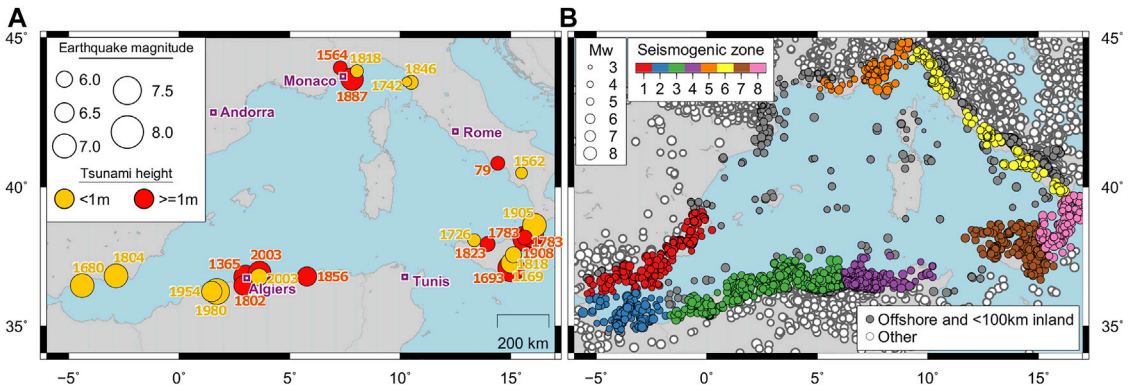


**FIGURE 1 | (A)** Historical tsunamigenic seismicity in the WM basin. Adapted from Figure 1 in Gailler et al. (2013). **(B)** Repartition of the earthquakes (Mw⩾3) within the WM basin (catalogue obtained from the synchronization of the datasets in **Table 1**, see also **Supplementary Table S1**). White circles show earthquakes located more than 100 km inland (non-tsunamigenic locations) and earthquakes discarded from the analysis (e.g., within the Adriatic and Ionian Seas). Gray circles show earthquakes located offshore or less than 100 km inland (tsunamigenic locations) that are not inside any seismogenic zone of Sørensen et al. (2012). Colored circles show earthquakes located in the seismogenic zones (one color per zone). The size of the circles is proportional to the magnitude of the earthquake. z01: South Eastern Spain; z02: Northern Morocco; z03: Northern Algeria; z04: Northern Tunisia; z05: Ligurian Coast; z06: Western Italy; z07: Sicily; z08: Calabria.

The aim of this study is to develop an efficient high-resolution S-PTHA proof of concept with sensitivity study to quantify the tsunami hazard associated with earthquakes, based on the a priori knowledge provided by the active fault database of the French tsunami warning center (CENALT). The method will then be operable into any area providing the data availability. The Bay of Cannes (France) is selected as a test case, because this region can be threatened by tsunamis and hosts many inhabitants and tourists. Moreover, Cannes is not a targeted POI in the TSUMAPS-NEAM project despite the historical events such as 1887 Imperia and 2003 Boumerdes earthquakes, whose tsunamis effects were observed at Cannes (e.g., Sahal et al., 2009; Larroque et al., 2012).

A classical S-PTHA scheme is used to design the method (e.g., Grezio et al., 2012; Sørensen et al., 2012; Grezio et al., 2017; Glimsdal et al., 2019; Behrens et al., 2021). The annual probability of the triggering-event is given to the induced tsunami. The effects of the tsunami, i.e., the PCTA, are aggregated with those of other tsunamis and weighted by the annual probability of the triggering-event. The PCTAs are directly extracted from high-resolution simulations (down to 10 m space step accuracy at the coastal level) instead of being extrapolated from POTAs. A selection of the significant tsunami is therefore necessary in order to reduce the computational time.

In this paper, we first present the details of the method, organized such that the seismic rates (**Section 2.1**) and the tsunami hazard (**Section 2.2**) are treated independently to perform a fast high-resolution S-PTHA. Especially, we propose a selection of significant tsunamis for which the high-resolution simulations are required (**Section 2.2.2**). Moreover, a sensitivity study is performed on various epistemic and aleatory uncertainties due to input data and methods, analysed all along the process (**Section 2.4**). We then show the results of the method applied to the Bay of Cannes (**Section 3.2**). Finally we discuss the uncertainties and the sensitivity regarding the seismic and tsunami hazards (**Sections 4.2**, **4.3**) and summarize the main outcomes in **Section 5**.

# 2 MATERIALS AND METHODS

## 2.1 Seismic Rates

### 2.1.1 Seismogenic Zones

The occurrence of earthquakes depends on the seismotectonic context (e.g., the Sicily region triggers more earthquakes and stronger earthquakes than the Ligurian region). In this study, the WM basin is split into sub-regions depending on their seismic regime in order to determine with higher accuracy the annual rates of earthquakes. These zones are thus defined consistently with the seismic rate and the faulting regime of each region. We choose to follow the partition proposed by Sørensen et al. (2012), where the WM basin is split into eight seismogenic zones (**Figure 1B**) small enough to represent areas of homogeneous activity (rates and faulting regime) and large enough to contain sufficient earthquakes to characterize the activity (i.e., to build a distribution law).

### 2.1.2 Earthquake Catalogues Used

Several earthquake catalogues are available, such as the USGS or EMSC ones (European-Mediterranean Seismological Centre, 2020; U.S. Geological Survey, 2020). They are large databases that concatenate earthquake records from several institutes throughout the world and use various magnitude estimates (moment magnitude, body wave magnitude, surface wave magnitude, local magnitude...). These catalogues mostly cover instrumental earthquakes (since ~1960). Larger and less frequent earthquakes might not have occurred during this instrumental period, creating a temporal incompleteness.

Compiled catalogues such as FCAT-17 (France) and SHARE (Europe) contain historical events directly giving the moment magnitude (Grünthal and Wahlström, 2012; Giardini et al., 2013;

**TABLE 1 |** Earthquake catalogues of reference. Catalogues in **bold** record only instrumental earthquakes.

| Catalogue | Number[a] | Date range | Ref[b] |
|---|---|---|---|
| **CMT** | 182 | 1977–2017 | [1] |
| EMEC (ext) | 5,442 | 1005–2006 | [2] |
| **EMEC(online)** | 40,261 | 2005–2019 | [3] |
| ISC | 42,870 | 1904–2015 | [4] |
| NOAA | 97 | 1783–2018 | [5] |
| SHARE | 3,508 | 1000–2006 | [6] |
| **USGS** | 46,650 | 1905–2019 | [7] |
| FCAT-17 | 25,214 | 463–2009 | [8] |

[a]*Number of seismic events (all* Mw*) within the WM basin (6°W to 17°E, 34°N to 45°N).*
[b]*[1] Dziewonski et al. (1981), Ekström et al. (2012); [2] Giardini et al. (2013); [3] European-Mediterranean Seismological Centre (2020); [4] International Seismological Centre (2020); [5] National Geophysical Data Center NOAA (2020); [6] Stucchi et al. (2013), Grünthal and Wahlström (2012), Grünthal et al. (2013), Giardini et al. (2013); [7] U.S., Geological Survey (2020); [8] Manchuel et al. (2018).*

Grünthal et al., 2013; Stucchi et al., 2013; Manchuel et al., 2018). The FCAT-17 and SHARE catalogues are not sufficient either, since the records stop in 2009 and 2006, respectively. The occurrence of strong earthquakes during the remaining period until now might also lead to temporal incompleteness. In this study, additional earthquake datasets are also synchronized in order to overcome this drawback and constrain the seismic rates as best as possible (i.e., **Table 1**).

The completeness of the resultant catalogue (time, magnitude and space) must still be carefully considered. For instance, the moment magnitude is rarely estimated for the smallest earthquakes. Also, the moment magnitude of historical earthquakes is mostly derived from macro-seismicity by experts and the date and time of the historical earthquakes can be slightly inaccurate. The date-and-time accuracy, fortunately, does not have a heavy influence on the results because annual rates are needed at a long time scale (>100 y).

### 2.1.3 Magnitude Conversion

The moment magnitudes Mw associated with the earthquakes catalogues depicted above are often derived from several conversion laws, depending on the time, place and magnitude range such as the one in Wason et al. (2012) which used General Orthogonal Regression on data from 1976 to 2007 to convert surface wave magnitude and body wave magnitude to Mw at global scale; Lolli et al. (2014) which proposed Exponential Regression Models to convert surface- and body-wave magnitudes to Mw at global, regional and local scales between 1976 and 2011; Cara et al. (2017) which proposed conversion relationships from local magnitude $M_{l,LDG}$ recorded between 1962 and 2009 by the Laboratoire de Détection et de Géophysique (LDG, CEA) to Mw. Nevertheless, the catalogues also record non-Mw which not fit the time and magnitude constraints to be converted using the above conversion laws. We did not convert these events as they represent less than 5% of additional earthquakes of Mw lower than 5.4 in 99% of cases, after synchronization. We are therefore confident in the collected Mw, the non-Mw records being part of the incompleteness of the catalogue.

### 2.1.4 Synchronization of the Earthquake Catalogues

This study requires building a recent and complete earthquake catalogue for the WM basin. Thus, earthquakes records were downloaded from several databases up to the December 31, 2018 (**Table 1**) in order to synchronize them as best as possible. A crude concatenation of the catalogs is first performed, keeping the earthquakes that are located in the WM basin (6°W—17°E, 34°N—45°N) and recorded using the moment magnitude. At this step of the process, the whole magnitude range is kept in order to have truthful distributions.

The transition from a fragile stress regime (upper crust) to a ductile regime (lower crust) enables the removal of deep earthquakes, as they cannot activate a large enough vertical motion of the water column. We assume this transition at 100 km, taking into account a potential error on the earthquake depths provided by the catalogues. Thus, earthquakes deeper than 100 km are considered as non-tsunamigenic and are ignored. In addition, in accordance with the WM basin decision matrix for tsunami warning, earthquakes located farther than 100 km inland are also ignored (Schindelé et al., 2015; **Figure 1B**).

Finally, earthquakes closer than 60 s in time and 10 km in distance are considered as replicated records. They are mainly due to duplicates between catalogues and are automatically removed, followed by a manual selection refinement. The automatic deletion of the duplicates might also remove some aftershocks despite the fact we want to keep them. Indeed, the strongest aftershocks can also trigger tsunamis and need to be taken into account for the determination of the seismic rates. The resultant catalogue records 5,015 earthquakes spreading from 1048 A.D. to 2018 (see also the supplementary materials). Among them only 73 earthquakes have a Mw 6.0 or above.

### 2.1.5 Determination of the Seismic Rates

The earthquake magnitude and occurrence are constrained by the tectonic settings. Furthermore, the aftershocks are strongly correlated to their main-shock. The use of a time-dependent approach would have been appropriate to determine the seismic rates. However, the speed of execution being a key factor in this study, the choice was made to handle all earthquakes as random Poissonian processes.

Then, we assume that the cumulative distribution of the earthquake magnitudes within a seismogenic zone follows a Gutenberg-Richter law and can be expressed, for the magnitude $M$, in terms of the annual rate $\lambda_M$, by

$$\lambda_M = \lambda_{M_0} e^{-\beta(M-M_0)}, \quad (1)$$

where $\lambda_{M_0}$ is the annual rate of the magnitude of completeness $M_0$ and $\beta$ an adjustable parameter. The resultant distribution laws mainly depend on the completeness of the dataset, but also on the method chosen to determine the parameters $\beta$, $\lambda_{M_0}$ and $M_0$.

The establishment of seismic monitoring networks on one hand, and the improvement of instruments and methods on the other hand, make possible the detection of smaller earthquakes, lowering the magnitude of completeness of the more recent periods. The magnitude of completeness is then a

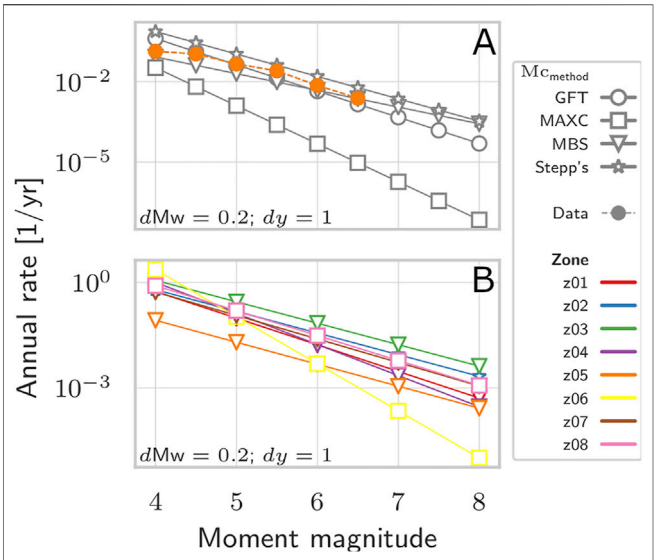


**FIGURE 2 |** Distribution law per seismogenic zone. **(A)** Comparison of the law of distributions obtained using earthquakes that occured within the Ligurian Coast seismogenic zone (z05), using a 0.2 magnitude step (*d*Mw) and a 1-year time step (*dy*). **(B)** Best law of distribution per seismogenic zone (*d*Mw = 0.2, *dy* =1 y). The markers show the method used to find the magnitude of completeness. The colors show the seismogenic zones.

key parameter because it sets up the magnitude for which we are confident to count every earthquake that actually occurred. The magnitude of completeness corresponds to an earthquake detection threshold and depends on the period of observation and the location. The magnitude of completeness of a period of observation can be determined using 1) the Maximum Curvature method (MAXC, Woessner and Wiemer, 2005), 2) the Goodness of Fit method (GFT, Wiemer and Wyss, 2000), 3) the *b*-value stability method (MBS, Woessner and Wiemer, 2005; Cao and Gao, 2002), applied with the stability criterion of Shi and Bolt (1982) and 4) the Stepp's method (Stepp, 1972). All these methods were performed for each seismogenic zone and yield to similar or different results depending on the selected datasets and the values used for the Mw interval and the time interval (**Section 3.1.1**). This reflects that uncertainties exist and must be taken into account.

The method of Weichert (1980) is used to determine the coefficient values of the annual rate expression (**Eq. 1**) and is based on the maximum likelihood. This method includes seismic rates determined for periods of time that depend on the magnitude such that:

$$\frac{\sum_i t_i M_i \exp\left(-\beta M_i\right)}{\sum_j t_j \exp\left(-\beta M_j\right)} = \frac{\sum_i n_i M_i}{N} = \bar{M}, \qquad (2)$$

where $t_i$ is the period of completeness of the magnitude $M_i$ ($M \in [M_i - \delta; M_i + \delta]$) with $n_i$ events and $N$ the number of all events ($N = \sum n_i$). The $\beta$ value is found by iterations. Weichert's method then allows to determine accurate seismic rates even if the historical period is less documented than the instrumental period.

The time and magnitude steps in this study are fixed to 1 year and 0.2, respectively. The method to determine the magnitude of completeness is chosen for each seismogenic zone, such as the annual rates from Weichert's method fit the data at best (**Figure 2A**). The distribution laws obtained varies depending on the seismogenic zone (**Figure 2B**). The North Algerian zone presents the highest annual rates, while the Ligurian coast have the lowest rates. These various distributions reflect well the necessity of processing by seismogenic zone.

## 2.2 Tsunami Hazard

### 2.2.1 Rupture Scenarios

The fault database of the French Tsunami Warning Center (CENALT) is used to build a catalogue of ruptures at the scale of the WM basin. The database consists in a unit source function system which follows the major structural trends of the seismogenic context of the WM basin (Gailler et al., 2013). To be conservative, the top of all faults in the database reach the seafloor. The length, width, slip and rigidity of each unit segment are set constant (respectively 25 km, 20 km, 1 m, and 35 GPa. For instance, the rupture of a unit source generates a Mw 6.76 earthquake.

One or several unit sources can be combined linearly to build a rupture of any moment magnitude Mw, the lengths and widths of the combined unit sources observing Wells and Coppersmith (1994) laws (fixing $L$ = 200 km for Mw = 8.0), and the slip being scaled by a factor $F_S$ (Gailler et al., 2013). The unit sources combination is controlled geometrically by the distance between two units (18.5–37.5 km) and the azimuth difference between them (≤40°). Combinations can be performed with various fault types. The available maximal combination of unit sources within a seismogenic zone gives the maximum magnitude in that zone. More details on the CENALT fault database and the method of construction of the rupture scenarios are available in Gailler et al. (2013).

Following the WM decision matrix used in operational context, an earthquake between Mw 5.5 and Mw 5.9 does not lead to a warning tsunami message. In such cases, an information message only is sent to the civil protection authorities Schindelé et al. (2015). As this study is aimed at probabilistic purposes, we opt to consider events of Mw from 5.5 to be conservative.

**TABLE 2 |** Number of unit sources and scenarii per seismogenic zone. The number of significant tsunamis are given for the Bay of Cannes region (gr03, **Figure 3**).

| Zone | | Sources | Scenarios | $Mw_{max}$ | Significant[a] |
|---|---|---|---|---|---|
| z01 | South Eastern Spain | 403 | 3,940 | 8.0 | 930 |
| z02 | Northern Moroco | 277 | 3,090 | 8.0 | 366 |
| z03 | Northern Algeria | 259 | 2,288 | 7.9 | 587 |
| z04 | Northern Tunisia | 165 | 1344 | 7.4 | 127 |
| z05 | Ligurian Coast | 93 | 1577 | 7.4 | 939 |
| z06 | Western Italy | 114 | 1899 | 7.4 | 460 |
| z07 | Sicily | 45 | 423 | 7.8 | 0 |
| z08 | Calabria | 101 | 942 | 7.8 | 13 |

[a]*Bay of Cannes region.*

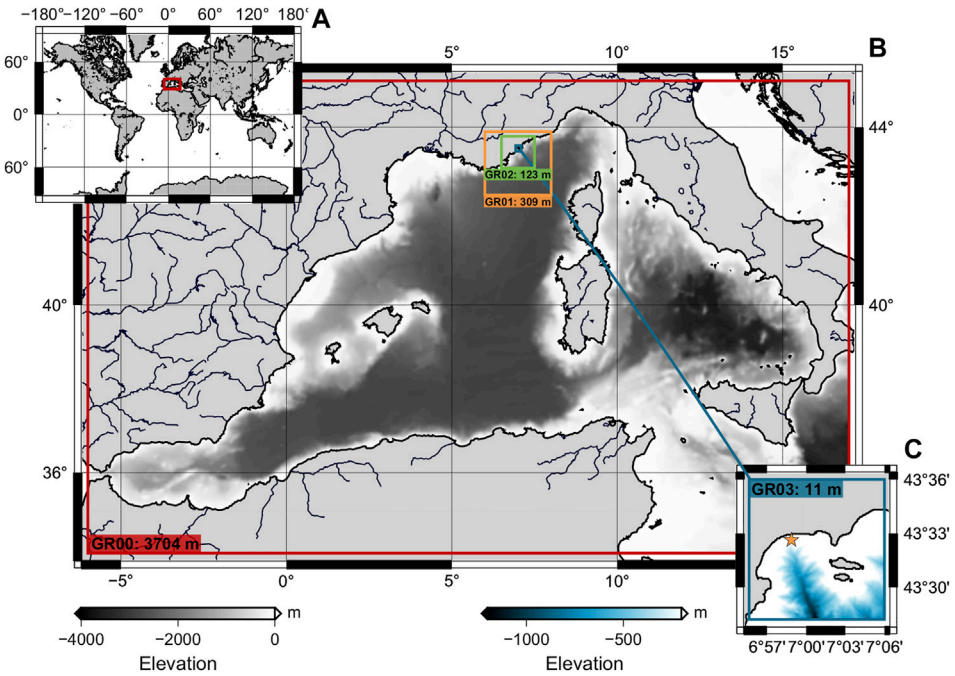


**FIGURE 3 |** Nested grids for high resolution simulations of the tsunami down to the Bay of Cannes. **(A)** GR00 location (red). **(B)** Seismic ROI within GR00 boundaries. **(C)** PTHA ROI within GR03 boundaries (blue). GR00: 691 × 331 nodes, 1.8 Mb. GR01: 721 × 505 nodes, 2.8 Mb. GR02: 901 × 631 nodes, 4.4 Mb. GR03: 1731 × 1301 nodes, 18 Mb. The yellow star, in GR03, shows the location of POTA to estimate $\eta_{\max,\text{apriori}}$ in the Bay of Cannes.

The construction of the rupture scenarios is conducted only one time independently of the ROI. From the 1457 unit sources of the CENALT database located inside or closer than 30 km from the seismogenic zones of Sørensen et al. (2012), 15,503 rupture scenarios with Mw between 5.5 and 8.0 are obtained (**Table 2**). Depending on the resultant combinations, the fault ruptures have length from 25 to 200 km and width from 20 to 40 km. The slip, which is scaled by the factor $F_S$ is then ranging from 0.01 to 4.5 m.

### 2.2.2 Tsunami Simulations

The objective of our method is to generate a S-PTHA down to the coastal level. The ROI of the S-PTHA is then smaller than the region of the likely sources of tsunamis (**Figure 3**). For instance, we use a ten-metre resolution topo-bathymetry grid focused on the Bay of Cannes (spreading over 14.8 × 9.8 km$^2$), which was built thanks to the Digital Elevation Models produced within the Litto3d® program.

The high-resolution nested grids tsunami simulations are performed with TAITOKO, the code developed at CEA which solves the shallow water equations from rupture properties (Heinrich et al., 2021, CEA). TAITOKO is there set to use a Runge-Kutta scheme, with second order in time and first order in space. The high-resolution simulations are performed using 4 nested grids from 2 min resolution at basin scale to 10 m space step at the local scale (**Figure 3**). Running more than 15,000 scenarios this way is expensive in term of computational time. So the choice is made to optimize each simulation duration $t_s$ as best as possible, taking as reference the Estimated Time Arrival (ETA) of the first wave (obtained using the program TTT from Geoware (GEOWARE, 2007)) plus 30 min. This limitation using the ETA preserves digital artefacts related to the propagation scheme which is robust for earlier waves. More performance schemes exist, but they head to a high increase of the computational time while speed is demanded. This choice implies that maximum wave heights information is only retrieved for the first waves. With the same aim of saving calculation time, the number of high-resolution runs to perform is also reduced by selecting scenarios able to produced a minimum wave height threshold in the bay of Cannes at least. To achieve this, the tsunami simulation for each rupture scenario is first performed in the coarse grid (basin scale, low-resolution) only, in order to collect a POTA where the water depth is about 100 m. The POI offshore is located 6.981031° E; 43.543846° N in the Bay of Cannes, with a depth of 94 m (Yellow star, **Figure 3**). Second, the Green's law (Green, 1838) is used to extrapolate each POTA $\eta_{\text{offshore}}$ to a wave height peak nearshore $\eta_{\max,\text{apriori}}$ at one-metre water depth

$$\begin{aligned}\eta_{\max,\text{apriori}} &= \eta_{\text{offshore}} \times \left(\frac{h_{\text{offshore}}}{h_{\text{nearshore}}}\right)^{1/4} \\ &= \eta_{\text{offshore}} \times h_{\text{offshore}}^{1/4} \quad (h_{\text{nearshore}} = 1),\end{aligned} \tag{3}$$

where $h_{\text{offshore}}$ and $h_{\text{nearshore}}$ are the water depths offshore and nearshore, respectively. The peak nearshore is assimilated to an priori PCTA $\eta_{\max,\text{apriori}}$, derived from the coarse grid models. Third, the rupture scenarios for which $\eta_{\max,\text{apriori}}$ exceeds a

chosen threshold at the POI are selected as significant. Assuming that a tsunami is significant if the a priori PCTAs exceed 5 cm, the threshold applied in the Bay of Cannes is set from the Northern Algerian and Ligurian zones at 1 cm. We assume that threshold is consistent for every seismogenic zone because the Northern Algerian and Ligurian zones are the most impacting areas. Finally, the high-resolution simulations are performed for this relevant selection.

Following the threshold chosen, 22.1% of the 15,503 tsunami scenarios are significant for the Bay of Cannes, matching with 17.6% of the number of hours of tsunami propagation to simulate (**Table 2**). About 75% of the computational time can subsequently be saved thanks to this selection process of significant tsunami scenarios (**Supplementary Figure S1**).

## 2.3 Probabilistic Tsunami Hazard Assessment

### 2.3.1 Scenario Probability

Synchronized earthquakes are extrapolated to future events over a period of observation by using a distribution law per seismogenic zone (**Figure 2B**). The extrapolation of the earthquake catalogue to a rupture catalogue spreading over a larger period of observation is made exhaustive. This means that the rupture catalogue is built such that all the $N_{\text{Mw–scenarios}}$ rupture scenarios that can generate a given magnitude are associated to each event of this magnitude, happening during the period of observation with the probability $P_{\text{Mw}} = 1/N_{\text{Mw–scenarios}}$. Then the annual probability of a scenario of magnitude Mw is independent of the ROI and given by

$$P_{\text{scenario}} = \lambda_{\text{Mw}} P_{\text{Mw}} \tag{4}$$

where $\lambda_{\text{Mw}}$ is the annual rate of a event of magnitude Mw. The annual probability of a scenario is equal to the annual rate if the annual rate is lower than 1. Otherwise, the annual probability equals 1.

### 2.3.2 Aggregation

The tsunami hazard is obtained by the aggregation of the seismic rates and the PCTAs. The annual probability of a scenario, as given by **Eq. 4**, is applied to each PCTA of the scenario. The annual probability $P_{s,h}$ of exceedance of a PCTA, $h$, at a place $s$ along the coastline, is then estimated by the union of all probabilities of scenarios that can produce a PCTA equal to or greater than $h$ at this place $s$:

$$P_{s,h} = P\left( \bigcup_{\text{scenario } \mathcal{S}} \{\mathcal{S}:\ PCTA_s \geq h\} \right) \tag{5}$$

and the probability $\mathcal{P}_{s,h,T}$ to exceed $h$ in a period $T$ at the place $s$ is then given by

$$\mathcal{P}_{s,h,T} = 1 - \left(1 - P_{s,h}\right)^T. \tag{6}$$

## 2.4 Sensitivity Analyses

Sensitivity analyses were performed in order to determine which parameters influence the most 1) the distribution law determination and 2) which rupture parameters influence the most the PCTAs. In both cases, the Morris' algorithm (Morris, 1991; Campolongo et al., 2007) is chosen rather than the Sobol's one (Sobol, 2001). Some parameters sets do not allow determining the parameters of the distribution law using the available earthquakes records. Then, the features cannot be distributed to fulfill the Sobol's algorithm requirements. The rupture parameters cannot satisfy the required distribution of the Sobol's feature either because they are constrained by the fault system.

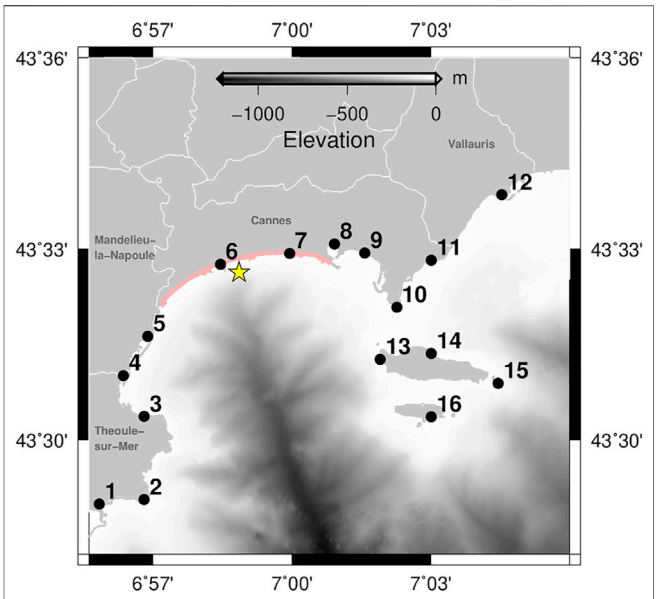


**FIGURE 4 |** Location of the POIs used for the deaggregation and the sensitivity analyses. Yellow star: location of the POTA. Pink line: Boulevard du Midi Louise Moreau at Cannes. White lines inland: city boundaries.

### 2.4.1 Seismic Rates

The features, that are tested, to perform the sensitivity analysis on the distribution law are.

- the method to determine the magnitude of completeness (`Mc method`),
- the magnitude interval $d$Mw,
- the period interval $dy$,
- the error on the moment magnitude $dm$,
- the turning year $t_i$ between historical and instrumental records
- the number of earthquakes $N_{\text{eq}}$ randomly chosen in the earthquake catalogue (keeping at least 90% of the records).

The $N_{\text{eq}}$ parameter is set up to mimic the incompleteness we can have in the catalogue. The effect of the random selection of the earthquakes within the records is also tested. The sensitivity analysis is performed on the parameters $\beta$, $\lambda_0$ and $M_0$ of the distribution law (**Eq. 1**) and on the annual rate of given magnitudes.

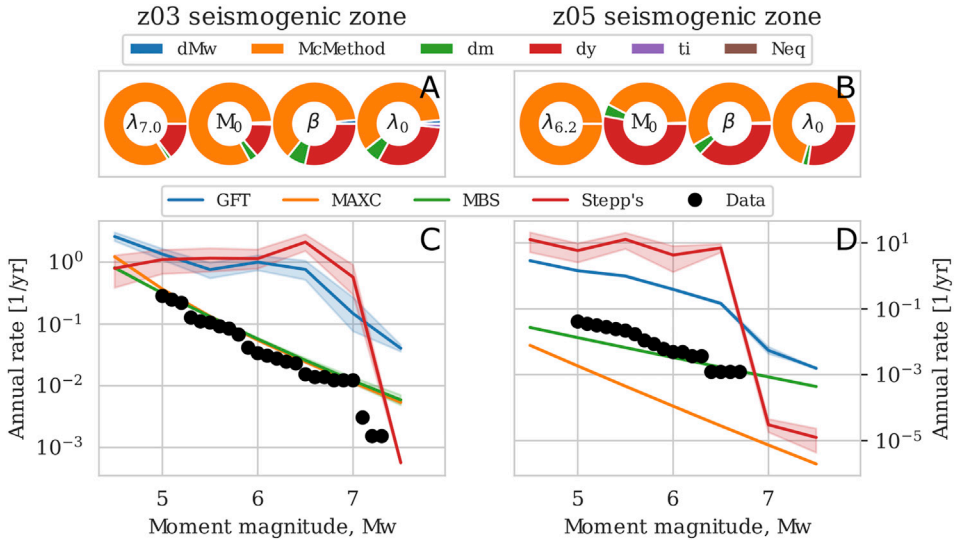


**FIGURE 5 |** Sensitivity on the distribution laws performed on the two most contributing seismogenic zones (z03 and z05). Contribution of the input features to $\lambda_{6.2}$, $\beta$, $\lambda_0$ and to $M_0$ of the distribution law in the **(A)** North Algerian (z03) and **(B)** Ligurian (z05) seismogenic zones. Mean distribution law per `Mc method` determined using variable input features for the **(C)** North Algerian (z03) and **(D)** Ligurian (z05) seismogenic zones. The shadows show the 95% confidence interval of the mean distribution law. Input data are superimposed as black circles.

### 2.4.2 PCTAs

The sensitivity on the PCTAs is analyzed by using the high-resolution simulations. Then, the Morris' sensitivity analysis tested the features of the rupture scenarios such as their location depending on the coastal POIs (distance and azimuth), the geometry of the rupture (strike, dip, rake angle), the size of the rupture (surface) and the slip of the rupture. The depth of the rupture is not part of the sensitivity analysis as the simulations consider faults reaching the sea floor.

## 3 RESULTS

The method described above is applied to obtain a high-resolution ( ~10 m) S-PTHA in the Bay of Cannes. Sixteen representative POIs are selected along the shoreline (**Figure 4**) to ease the analysis and the discussion about the deaggregation (**Figure 9**) and the sensitivity analysis of the PCTA (**Figure 6**).

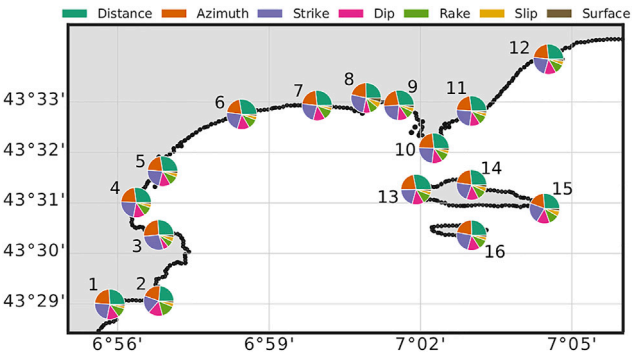


**FIGURE 6 |** Sensitivity of the source parameters on the PCTAs. The pie charts show the sensitivity of each source parameters. The larger is the section, the more the feature is sensitive.

## 3.1 Sensitivity Analyses

### 3.1.1 Annual Rates

We performed a sensitivity analysis for the distribution law within the North Algerian (z03) and Ligurian (z05) seismogenic zones (**Figure 5**). The random selection of the earthquakes itself has no effect on the results, only the number of earthquakes to be selected influences the results. The results of the analysis vary between the two seismogenic zones, but they highlight several common conclusions. The choice of the method to determine the magnitude of completeness is the key parameter (**Figures 5A,B**), while other parameters have minor effects on the distribution laws when using MAXC and MBS methods (**Figures 5C,D**). Then, the parameters to determine the distribution law can be set constant and the best distribution can be found by only testing the various methods to find the magnitude of completeness. The results also support the non-linearity of the distribution law.

### 3.1.2 PCTAs

The analysis is performed on the 16 POIs in **Figure 4** to map the coastal variability of the most sensitive features (**Figure 6**). The three most sensitive parameters on PCTA results are the distance, the strike and the azimuth considering rupture scenarios from all seismogenic zones. The influence of these parameters however varies depending on the place along the coastline. The distance is the most sensitive parameter at each POI except at POIs 3 and 8

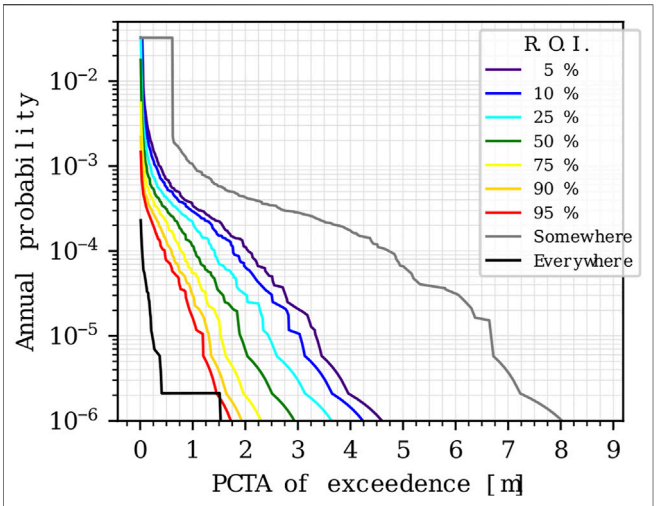


**FIGURE 7 |** Annual probability that a PCTA is being exceeded along a portion of the Bay of Cannes coast. Somewhere: at least at one place; everywhere: at all places (i.e., at all shoreline nodes of the grid).

(La Petite Fontaine beach in Théoule-sur-Mer and Old Port of Cannes) where the strike becomes more sensitive. This is due to the spread direction of the tsunami, essentially governed by the strike of the rupture. These two POIs are also naturally better protected, allowing a significant tsunami hazard for a few preferential orientations of the main tsunami energy axis only. The slip and the surface of the rupture, (i.e., the moment magnitude) are the least sensitive parameters, because they are strongly constrained to each other by empirical laws (Wells and Coppersmith, 1994).

## 3.2 S-PTHA in the Bay of Cannes

The analysis focuses on the tsunami hazard in terms of the maximum water elevation of the first waves at the coastline (PCTA). The main outcomes of this study indicate that an earthquake generating a tsunami with waves exceeding 1 m locally along the coast in the Bay of Cannes can be expected every 961 years (annual probability of $1.04 \times 10^{-3}$, **Figure 7**). However, the probability of occurrence of a tsunamigenic earthquake with waves exceeding 1 m along 50% of the coastline drops to $1.14 \times 10^{-4}$, hence a 8766-year period. These observations alone do not allow establishing a spatial planning strategy with regard to tsunamis and therefore require a closer look at the hazards.

Then, the above outcomes is analysed at small scale to account for the geometry of the coastline. The hazard maps show the maximum expected PCTAs in 50-, 500- and 2500-year periods (**Figures 8A–C**), and provide an accurate overview of local PTHA with systematically amplifying coastal POIs compared to the rough regional PTHA estimates of Sørensen et al. (2012). The PCTAs remain below 20 cm for periods shorter than 50 years, and the distribution of the PCTAs provides homogeneous wave heights all along the coastline (**Figure 8A**). The PCTAs then increase with the period in a non-homogeneous manner (**Figures 8A–C** and focus in **Figure 8I**). Indeed, some places, such as the Old Port of Cannes (POI 8), amplify the effects of the tsunami; whereas some other places, such as La Petite Fontaine beach at Théoule-sur-mer (POI 3), are protected from most of the tsunamis effects.

The S-PTHA also provides information on the maximum expected PCTA in a period of time. The probability to exceed a PCTA in a given period is shown in **Figures 8E–H**. These probability maps are complementary to deterministic hazard maps generally built from the most impacting scenarios for a given area. They highlight the greater occurrence of the hazard linked to smaller waves (e.g., 50 cm, **Figure 8F**), from which we cannot preclude potential damages. These probability maps show that a wave height of 1 m has a low probability to be exceeded in a period of 2,500 years (**Figure 8G**). The probability that a tsunami wave exceeds 1 m in a 2500-year period along the Boulevard du Midi Louise Moreau (pink line on **Figure 4**) is below 20%. The Midi beach (East to POI 7) is the most exposed area along the Boulevard and also the most crowed in the summer holidays. The probability to exceed 1 m in a 2500-year period along the coast of Vallauris is higher and can reach up to 50%. The most exposed places face directly the basin (POIs 1–2, 15–16). The greatest hazard is obtained for the Old Port of Cannes, probably due to resonance effects which amplify the waves. Here, the probability to exceed 1 m in a 2500-year period reaches 70% (POI 8). Naturally, the probability to exceed a PCTA in a period increases with decreasing PCTAs and increasing the periods.

The Maximum Considered Tsunami (MCT), as proposed by the national standard of practice for engineers in the United States, has 2% probability of being exceeded in a 50-year period (corresponding to a return time of 2500 years). The resultant hazard map can help the work of decision for the prioritization of the prevention (**Figure 8D**). For instance, in the Old Port of Cannes (POI 8), tsunami waves greater than 1 m can be expected every 50 years with a probability of 2%, making this place a priority in terms of preparedness. The preparedness along the Midi beach, crowded in summer times, is not to be omitted either, because waves can reach there 30 cm with 2% probability in 50 years.

The seismogenic zones that contribute the most to the tsunami hazard within the Bay of Cannes are the North Algerian (z03) and the Ligurian (z05) areas (**Figure 9**). Especially, earthquakes from the Ligurian zone only are able to impact POIs 3 and 8. It is worth noting that among the rupture scenarios selected as significant in the Ligurian seismogenic zone (z05), some ruptures have a moment magnitude below 6.0 (**Supplementary Figure S2**). This study focuses on PCTAs because there is little flooding in Cannes. However, 41 rupture scenarios generate an inundation above 5 m of altitude, all belonging to the Ligurian seismogenic zone (z05) and with a moment magnitude of 6.7 or above.

# 4 DISCUSSION

## 4.1 Resulting PTHA

The results of the sensitivity analysis on the PCTAs and the high resolution S-PTHA confirm that the coastal geometry influences the tsunami hazard in the Bay of Cannes, with POIs at local scale that are more are less protected depending on the earthquake

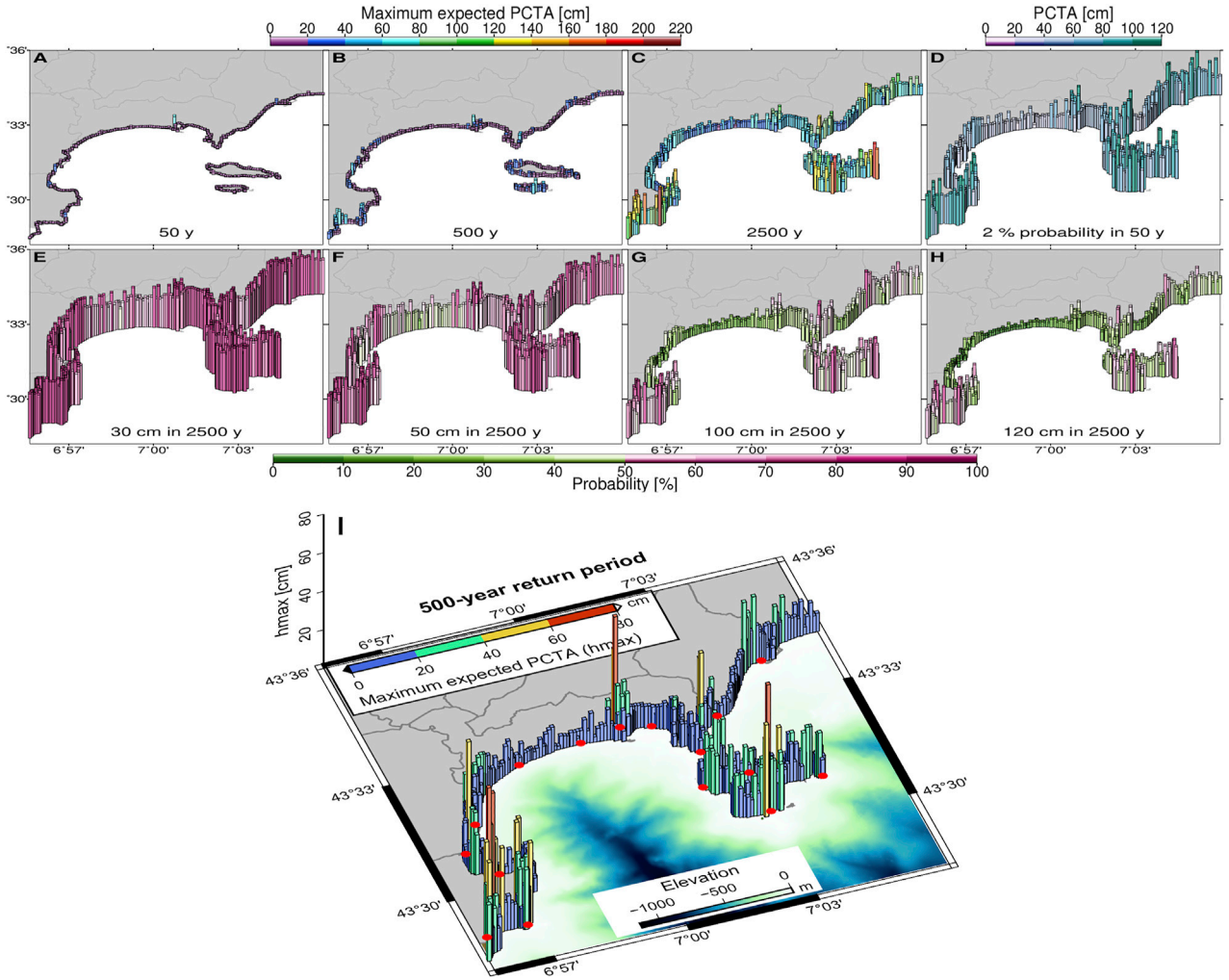


**FIGURE 8 |** Hazard ma+ps: maximum expected PCTAs in **(A)** a 50-year period, **(B)** a 500-year period, **(C)** a 2500-year period. **(D)** Maximum Considered Tsunami (MCT): The MCT has 2% probability of being exceeded in a 50-year period. This MCT is the reference of engineering in U.S.A. Probability maps: probability to exceed **(E)** 30 cm, **(F)** 50 cm, **(G)** 1 m, **(H)** 1.2 m in a 2500-year period. **(I)** Focus on the maximum expected PCTAs in 500-year period. The red dots remind the location of the POIs.

sources. Furthermore, a recent study of the tsunami hazard in the Bay of Cannes showed that the extended Green's laws method reproduce high resolution simulation with relative errors up to 25% (Giles et al., 2021a), and concluded that the extrapolation is adequate to rapidly predict a PCTA estimate. This validates the necessity of applying high-resolution PTHA rather than PTHA using offshore extrapolations in order to capture the effects at specific places (bay, harbours, beaches. . .).

## 4.2 Actual Tsunami-Earthquake Sources and Seismogenic Zones Definition

The assumption of separated and tsunami-independent basins has relevant implications, such as the effects on the definition of the domain for seismic sources selection and numerical simulations. Regarding the hazard within the WM, it was highlighted that straits like Gibraltar act as a natural barrier for tsunamis generated in the Atlantic, that attenuate strongly while crossing this strait. In addition, the broad and relatively shallow Sicily channel, despite being a less effective barrier, prevents the free propagation of tsunamis between eastern and western Mediterranean (Sørensen et al., 2012). However, the Hellenic arc seismogenic zone should also be added as the strongest earthquakes occurring there can generate a trans-Mediterranean tsunami, i.e., tsunami crossing from the Eastern to the Western Mediterranean basins (e.g., Gailler et al., 2016). One should also note that the earthquake datasets used do not contain any strong pre-historical earthquakes. It would be difficult to integrate them to the study as the seismic rates cannot be validated at geological scales.

Looking at a smaller scale, the seismogenic zones, which are taken from Sørensen et al. (2012) should be updated in order to integrate the earthquakes (for the seismic rates) and the faults (for the rupture scenarios) up to 100 km inland and then join the strategy implemented at the CENALT with the decision matrix of the WM basin (**Figure 1B**; Schindelé et al., 2015). Additional

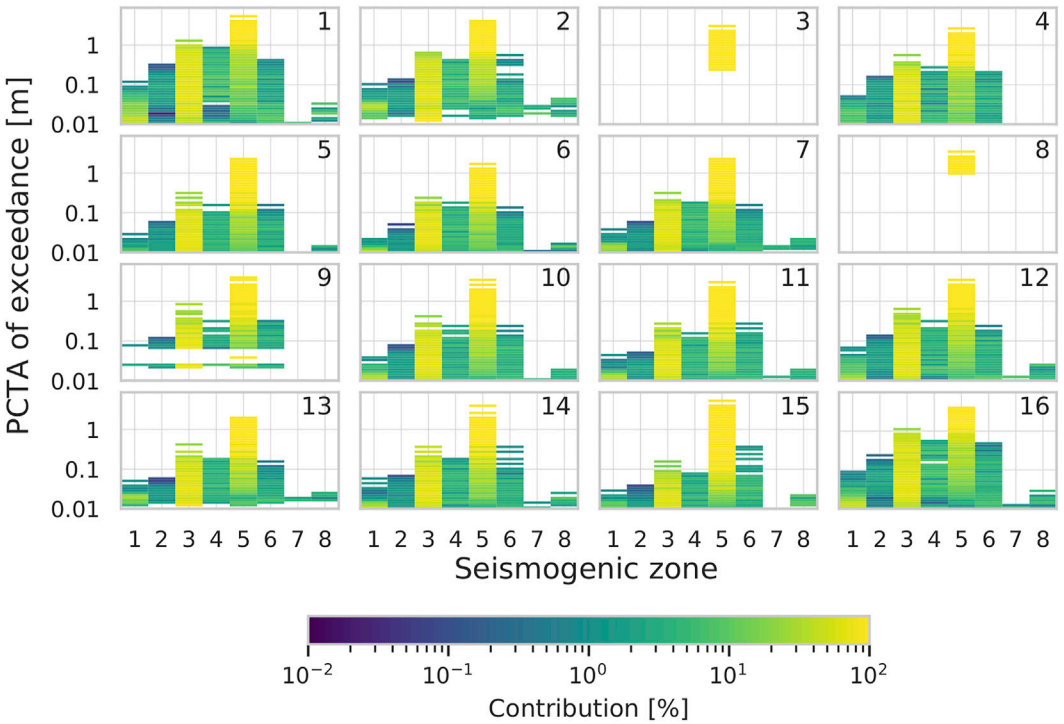


**FIGURE 9 |** Contribution of the seismogenic zones to the tsunami hazard. The number at the upper right of each subplots is the POI reference (**Figure 4**).

zones should also be added for spatial completeness in Eastern Spain, Southwestern France (Gulf of Lion area), the Balearic Islands, the Corsica and Sardinia Islands and the Strait of Sicily. The absence of records of earthquakes of Mw>5.5 in these areas does not means it cannot occur. The determination of the seismic law allows extrapolating the seismic rates within an area and the fault combination, as described in Gailler et al. (2013), allows to estimate the maximum moment magnitude that possibly can occur within the same area. Then additional tsunami sources might be available for PTHA processes in the WM basin.

## 4.3 Faults and Ruptures

The CENALT database of unit sources in some regions might need further investigation to be completed, because the model of the complex fault system of the WM basin may be incomplete, especially far offshore, where active structures are still poorly known (**Supplementary Figure S2**). We assume that the model is quite complete for the North Algerian and Ligurian seismogenic zones (z03 and z05). An advantage of our method is that we can easily add new unit sources to the fault system and thus new rupture scenarios. The simulation of tsunamis generated by new ruptures has only to be performed once for a given ROI.

Some rupture scenarios, located outside of the seismogenic zones (**Supplementary Figure S2**), were also selected as being able to generate a significant tsunami in the Bay of Cannes. Their high magnitude lead to low annual rates, and then account for low probability within the tsunami hazards. However, it would be valuable to extend the seismogenic zones to better cover the seismicity further inland.

One should also reminds that all the ruptures scenarios used to process this S-PTHA follow a static and uniform-slip model, reach the seafloor and have a constant shear modulus. Even though introducing more complexity in the rupture dynamic might not have much effects on the PTHA (e.g., An et al., 2018), it would be interesting to test the impact of including heterogeneous slip and rigidity models in the rupture sources dataset through a stochastic approach (e.g., Davies and Griffin, 2019).

## 4.4 Tsunami Simulations

The tsunami simulation itself is a source of uncertainty. The accuracy of the simulations depends on the choice of the models used to generate and propagate the tsunami (e.g., transfer law used for the tsunami generation that is induced by the rupture motion; shallow water, Boussinesq for the propagation, etc., Heinrich et al., 2021).

The water level fluctuations, related to the atmospheric condition or tides (high tide, low tide, tide coefficient), are also not taken into account in the present study. The tides, in spite of the fact that they are not significant in the WM basin, could be implemented as a source of aleatory uncertainty (e.g., González et al., 2009).

The use of the threshold to select significant tsunamis and the choice of the location of the POTA of reference also impact the results of the S-PTHA. The use of complex amplification laws (e.g., Gailler et al., 2018; Glimsdal et al., 2019) to select significant tsunami can be useful when it's suitably calibrating for the studied ROI. However, it is not necessary if performing a calibration of the threshold to be a significant tsunami when using a classic

Green's law. A comparison of the tsunami selection and final outcomes using the classic Green's law and the embedded Green's law for the area of Cannes (Giles et al., 2021a) can however be performed.

The use of a different threshold for near-fiel and far-field sources should also be explored (Volpe et al., 2019) in order to improve the selection of the significant tsunamis. Indeed, the energy of the near-field tsunami is less dissipated when arriving within the ROI than the energy of the far-field tsunamis, leading to inadequate height extrapolations.

## 5 CONCLUSION

The base of a modular procedure to perform high-resolution S-PTHA at the coastal level is proposed. An effort is made to save time on this computationally expensive approach by the use of independent processes for the determination of the seismic and tsunami hazards, by the selection of significant tsunamis for a place using Green's law, and by the use of an exhaustive rupture catalogue. The low resolution simulations performed first to select significant tsunamis can be re-used to apply the same approach to other coastal ROIs in the WM and save time too. The method is thought such that it is easy to add new a priori knowledge such as additional earthquakes to improve annual rates and new unit faults to build up new ruptures.

This study provides, for the first time, high resolution S-PTHA for the french metropolitan coastlines using the CENALT fault database. Specially, the study supplies an accurate overview of S-PTHA in the Bay of Cannes, both in terms of spacial resolution and wave heights modeling (i.e., based on high resolution tsunami simulations down to 10 m space step), compared to previous rough regional PTHA estimates. Magnitudes 5.5 to 8.0 are covered with annual rates determined from an improved earthquake catalogue spreading from 463 A.D. to 2018. The results highlight that the tsunami hazard in the Bay of Cannes remains low when considering the available data and the limitations of our approach. Indeed, we do not expect that a tsunami which generates PCTAs exceeding 50 cm along more than 50% of the coastlines to happen more than once every 3189 years. The evaluation of the MCT also underlines the portions of the coast where waves are systematically amplified the most and where priority should be given to preparedness. In particular, the Old Port of Cannes shows a MCT exceeding 1 m and beaches can still have MCT locally exceeding 30 cm. The disaggregation highlights that further analysis efforts, such as a confidence analysis, could focus on the Ligurian and North Algerian margins.

In the case of a risk-based study, consideration should be given to extending simulation times to ensure the highest wave in the PTHA. The extension of the simulation time must, however, be reasonable in order not to introduce multiple resonances that can artificially increase the maximum water height. The effects of a tsunami are, also characterized by other parameters such as the wave velocity, the run-up elevation, the inundation distance, the minimum water elevation associated to sea withdrawals, etc. The choice of the parameters of interest depends on why the S-PTHA is needed for, though all these parameters could have been extracted from high-resolution simulations at the same time.

The sensitivity analysis performed in this study shows that the most sensitive parameter to determine the annual rates of a magnitude is the `Mc method`. The distance, the azimuth and the strike of the source rupture are the three most sensitive parameters on the PCTAs, while the slip and the surface of the rupture are the least sensitive because constrained empirically.

Some limitations could be overcome in future developments of the proposed approach, for instance, by implementing stochastic sources (with heterogeneous slip and rigidity), by considering water level fluctuation either due to tides or atmospheric conditions, or by perfecting the definition of the seismogenic zones. The use of numerous catalogues of random ruptures instead of a unique exhaustive catalogue should also be considered to determine the confidence interval of the results and therefore give truthful hazard models for tsunami risk mitigation. The modular build of this approach allows to easily implement these ideas in order to improve the relevance of the high-resolution S-PTHA.

## DATA AVAILABILITY STATEMENT

The data analyzed in this study is subject to the following licenses/restrictions: Earthquake data are available as described in **Table 1**. Seismogenic zones are taken from Sørensen et al. (2012). The other raw data supporting the conclusions of this article will be made available by the authors on request. Requests to access these datasets should be directed to audrey.gailler@cea.fr.

## AUTHOR CONTRIBUTIONS

VS and AG contributed to conception and methodology of the study. VS organized data, produced tools and validated them, produced visuals, processed to analyses, wrote the first draft of the manuscript. AG found resources and founding, supervised the study. All authors contributed to manuscript revision, read, and approved the submitted version.

## FUNDING

This study was founded by NARSIS (New Approach to Reactor Safety Improvments, Horizon 2020) H2020 project (http://www.narsis.eu/), with the grant agreement No. 755439.

## ACKNOWLEDGMENTS

The Service Hydrographique et Oceanographique de la Marine (SHOM) is gratefully acknowledged for making bathymetry and topography data available free of charge on their portal data.shom.fr. City boundaries were collected under the ODbL licence

from OpenStreetMap (http://openstreetmap.fr/36680-communes). We want to acknowledge Francois Shindelé and Hélène Hébert for their relevant pre-review. We are thankful to the two reviewers for their questions and comments that enabled us to provide this enhanced manuscript.

## REFERENCES

An, C., Liu, H., Ren, Z., and Yuan, Y. (2018). Prediction of Tsunami Waves by Uniform Slip Models. *J. Geophys. Res. Oceans* 123, 8366–8382. doi:10.1029/2018JC014363

Basili, R., Brizuela, B., Herrero, A., Iqbal, S., Lorito, S., Maesano, F. E., et al. (2018). *NEAM Tsunami hazard Model 2018 (NEAMTHM18): Online Data of the Probabilistic Tsunami hazard Model for the Neam Region from the Tsumaps-Neam Project*. Available at: https://www.earth-prints.org/bitstream/2122/12739/1/NEAMTHM18_OnlineDataCover.pdf.

Basili, R., Brizuela, B., Herrero, A., Iqbal, S., Lorito, S., Maesano, F. E., et al. (2021). The Making of the NEAM Tsunami hazard Model 2018 (NEAMTHM18). *Front. Earth Sci.* 8, 753. doi:10.3389/feart.2020.616594

Behrens, J., Løvholt, F., Jalayer, F., Lorito, S., Salgado-Gálvez, M. A., Sørensen, M., et al. (2021). Probabilistic Tsunami Hazard and Risk Analysis: A Review of Research Gaps. *Front. Earth Sci.* 9, 114. doi:10.3389/feart.2021.628772

Campolongo, F., Cariboni, J., and Saltelli, A. (2007). An Effective Screening Design for Sensitivity Analysis of Large Models. *Environ. Model. Softw.* 22, 1509–1518. doi:10.1016/j.envsoft.2006.10.004

Cao, A., and Gao, S. S. (2002). Temporal Variation of Seismic b-Values beneath Northeastern Japan Island Arc. *Geophys. Res. Lett.* 29, 48-1–48-3. doi:10.1029/2001GL013775

Cara, M., Denieul, M., Sèbe, O., Delouis, B., Cansi, Y., and Schlupp, A. (2017). Magnitude M W in Metropolitan France. *J. Seismol.* 21, 551–565. doi:10.1007/s10950-016-9617-1

Davies, G., and Griffin, J. (2019). Sensitivity of Probabilistic Tsunami Hazard Assessment to Far-Field Earthquake Slip Complexity and Rigidity Depth-Dependence: Case Study of Australia. *Pure Appl. Geophys.* 177, 1521–1548. doi:10.1007/s00024-019-02299-w

Dziewonski, A. M., Chou, T.-A., and Woodhouse, J. H. (1981). Determination of Earthquake Source Parameters from Waveform Data for Studies of Global and Regional Seismicity. *J. Geophys. Res.* 86, 2825–2852. doi:10.1029/JB086iB04p02825

Ekström, G., Nettles, M., and Dziewoński, A. M. (2012). The Global CMT Project 2004-2010: Centroid-Moment Tensors for 13,017 Earthquakes. *Phys. Earth Planet. Inter.* 200-201, 1–9. doi:10.1016/j.pepi.2012.04.002

European-Mediterranean Seismological Centre (2020). *EMSC, Search for Earthquakes*. [Dataset].

Eva, C., and Rabinovich, A. B. (1997). The February 23, 1887 Tsunami Recorded on the Ligurian Coast, Western Mediterranean. *Geophys. Res. Lett.* 24, 2211–2214. doi:10.1029/97GL02110

Gailler, A., Hébert, H., Loevenbruck, A., and Hernandez, B. (2013). Simulation Systems for Tsunami Wave Propagation Forecasting within the French Tsunami Warning center. *Nat. Hazards Earth Syst. Sci.* 13, 2465–2482. doi:10.5194/nhess-13-2465-2013

Gailler, A., Schindelé, F., and Hébert, H. (2016). "Impact of Hellenic Arc Tsunamis on Corsica (France)," in *Global Tsunami Science: Past and Future* (Springer), Vol. I, 3847–3862. doi:10.1007/978-3-319-55480-8_10

Gailler, A., Hébert, H., Schindelé, F., and Reymond, D. (2018). Coastal Amplification Laws for the French Tsunami Warning Center: Numerical Modeling and Fast Estimate of Tsunami Wave Heights along the French Riviera. *Pure Appl. Geophys.* 175, 1429–1444. doi:10.1007/s00024-017-1713-9

GEOWARE (2007). *A Tsunami Travel-Time Calculator*. [Dataset]. Available at: http://www.geoware-online.com/tsunami.html.

Giardini, D., Grünthal, G., Shedlock, K. M., Zhang, P., and Giardini, D. (2013). *Seismic Hazard Harmonization in Europe (SHARE)*. [Dataset]. Available at: http://www.efehr.org/en/Documentation/specific-hazard-models/europe/overview/. doi:10.12686/SED-00000001-SHARE

## SUPPLEMENTARY MATERIAL

The Supplementary Material for this article can be found online at: https://www.frontiersin.org/articles/10.3389/feart.2021.765610/full#supplementary-material.

Gibbons, S. J., Lorito, S., Macías, J., Løvholt, F., Selva, J., Volpe, M., et al. (2020). Probabilistic Tsunami hazard Analysis: High Performance Computing for Massive Scale Inundation Simulations. *Front. Earth Sci.* 8, 623. doi:10.3389/feart.2020.591549

Giles, D., Gailler, A., Souty, V., Chouli, A., and Dias, F. (2021a). Automative Approaches for Capturing Localised Tsunami Response - Application to the French Coastlines. *J. Geophys. Res. – Oceans (Preprint)*. doi:10.1002/essoar.10506015.1

Giles, D., Gopinathan, D., Guillas, S., and Dias, F. (2021b). Faster Than Real Time Tsunami Warning with Associated hazard Uncertainties. *Front. Earth Sci.* 8, 560. doi:10.3389/feart.2020.597865

Glimsdal, S., Løvholt, F., Harbitz, C. B., Romano, F., Lorito, S., Orefice, S., et al. (2019). A New Approximate Method for Quantifying Tsunami Maximum Inundation Height Probability. *Pure Appl. Geophys.* 176, 1–20. doi:10.1007/s00024-019-02091-w

González, F. I., Geist, E. L., Jaffe, B., Kâno\\uglu, U., Mofjeld, H., Synolakis, C. E., et al. (2009). Probabilistic Tsunami hazard Assessment at seaside, Oregon, for Near-And Far-Field Seismic Sources. *J. Geophys. Res. Oceans* 114, 1–19. doi:10.1029/2008jc005132

Green, G. (1838). On the Motion of Waves in a Variable Canal of Small Depth and Width. *Trans. Cambridge Philos. Soc.* 6, 457.

Grezio, A., Sandri, L., Marzocchi, W., Argnani, A., Gasparini, P., and Selva, J. (2012). Probabilistic Tsunami hazard Assessment for Messina Strait Area (Sicily, Italy). *Nat. Hazards* 64, 329–358. doi:10.1007/s11069-012-0246-x

Grezio, A., Babeyko, A., Baptista, M. A., Behrens, J., Costa, A., Davies, G., et al. (2017). Probabilistic Tsunami hazard Analysis: Multiple Sources and Global Applications. *Rev. Geophys.* 55, 1158–1198. doi:10.1002/2017rg000579

Grezio, A., Cinti, F. R., Costa, A., Faenza, L., Perfetti, P., Pierdominici, S., et al. (2020). Multisource Bayesian Probabilistic Tsunami hazard Analysis for the Gulf of Naples (Italy). *J. Geophys. Res. Oceans* 125, e2019JC015373. doi:10.1029/2019jc015373

Grünthal, G., and Wahlström, R. (2012). The European-Mediterranean Earthquake Catalogue (EMEC) for the Last Millennium. *J. Seismol.* 16, 535–570. doi:10.1007/s10950-012-9302-y

Grünthal, G., Wahlström, R., and Stromeyer, D. (2013). The SHARE European Earthquake Catalogue (SHEEC) for the Time Period 1900–2006 and its Comparison to the European-Mediterranean Earthquake Catalogue (EMEC). *J. Seismol.* 17, 1339–1344. doi:10.1007/s10950-013-9379-y

Heinrich, P., Jamelot, A., Cauquis, A., and Gailler, A. (2021). Taitoko, an Advanced Code for Tsunami Propagation, Developed at the French Tsunami Warning Centers. *Eur. J. Mechanics-B/Fluids* 88, 72–88. doi:10.1016/j.euromechflu.2021.03.001

IAEA (2015). *The Fukushima Daiichi Accident*. Tech. rep., Volume 1/5. Vienna: International Atomic Energy Agency. Description and context of the accident.

International Seismological Centre (2020). *ISC-GEM Earthquake Catalogue*. [Dataset]. doi:10.31905/d808b825

Larroque, C., Scotti, O., Ioualalen, M., Oona, S., and Mansour, I. (2012). Reappraisal of the 1887 Ligurian Earthquake (Western Mediterranean) from Macroseismicity, Active Tectonics and Tsunami Modelling. *Geophys. J. Int.* 190, 87–104. doi:10.1111/j.1365-246X.2012.05498.x

Lolli, B., Gasperini, P., and Vannucci, G. (2014). Empirical Conversion between Teleseismic Magnitudes ($M_b$ and $M_s$) and Moment Magnitude ($M_w$) at the Global, Euro-Mediterranean and Italian Scale. *Geophys. J. Int.* 199, 805–828. doi:10.1093/gji/ggu264

Lorito, S., Selva, J., Basili, R., Romano, F., Tiberti, M., and Piatanesi, A. (2015). Probabilistic hazard for Seismically Induced Tsunamis: Accuracy and Feasibility of Inundation Maps. *Geophys. J. Int.* 200, 574–588. doi:10.1093/gji/ggu408

Manchuel, K., Traversa, P., Baumont, D., Cara, M., Nayman, E., and Durouchoux, C. (2018). The French Seismic CATalogue (FCAT-17). *Bull. Earthquake Eng.* 16, 2227–2251. doi:10.1007/s10518-017-0236-1

Morris, M. D. (1991). Factorial Sampling Plans for Preliminary Computational Experiments. *Technometrics* 33, 161–174. doi:10.1080/00401706.1991.10484804

National Geophysical Data Center NOAA (2020). *NCEI/WDS Global Significant Earthquake Database, 2150 BC to Present*. [Dataset]. doi:10.7289/V5TD9V7K

Okal, E. A. (2011). Tsunamigenic Earthquakes: Past and Present Milestones. *Pure Appl. Geophys.* 168, 969–995. doi:10.1007/s00024-010-0215-9

Park, H., Cox, D. T., and Barbosa, A. R. (2018). Probabilistic Tsunami Hazard Assessment (PTHA) for Resilience Assessment of a Coastal Community. *Nat. Hazards* 94 (3), 1117–1139. doi:10.1007/s11069-018-3460-3

Sahal, A., Roger, J., Allgeyer, S., Lemaire, B., Hébert, H., Schindelé, F., et al. (2009). The Tsunami Triggered by the 21 May 2003 Boumerdès-Zemmouri (Algeria) Earthquake: Field Investigations on the French Mediterranean Coast and Tsunami Modelling. *Nat. Hazards Earth Syst. Sci.* 9, 1823–1834. doi:10.5194/nhess-9-1823-2009

Schindelé, F., Gailler, A., Hébert, H., Loevenbruck, A., Gutierrez, E., Monnier, A., et al. (2015). Implementation and Challenges of the Tsunami Warning System in the Western Mediterranean. *Pure Appl. Geophys.* 172, 821–833. doi:10.1007/s00024-014-0950-4

Selva, J., Tonini, R., Molinari, I., Tiberti, M. M., Romano, F., Grezio, A., et al. (2016). Quantification of Source Uncertainties in Seismic Probabilistic Tsunami hazard Analysis (SPTHA). *Geophys. J. Int.* 205, 1780–1803. doi:10.1093/gji/ggw107

Selva, J., Lorito, S., Volpe, M., Romano, F., Tonini, R., Perfetti, P., et al. (2021). Probabilistic Tsunami Forecasting for Early Warning. *Nat. Commun.* 12, 1–14. doi:10.1038/s41467-021-25815-w

Shi, Y., and Bolt, B. A. (1982). The Standard Error of the Magnitude-Frequency *B* Value. *Bull. Seismol. Soc. Am.* 72, 1677–1687. doi:10.1785/bssa0720051677

Sobol, I. M. (2001). Global Sensitivity Indices for Nonlinear Mathematical Models and Their Monte Carlo Estimates. *Math. Comput. Simul.* 55, 271–280. doi:10.1016/s0378-4754(00)00270-6

Sørensen, M. B., Spada, M., Babeyko, A., Wiemer, S., and Grünthal, G. (2012). Probabilistic Tsunami hazard in the Mediterranean Sea. *J. Geophys. Res. Solid Earth* 117, 2465–2482. doi:10.5194/nhess-13-2465-2013

Stein, S., and Okal, E. A. (2011). The Size of the 2011 Tohoku Earthquake Need Not Have Been a surprise. *Eos, Trans. Am. Geophys. Union* 92, 227–228. doi:10.1029/2011eo270005

Stepp, J. C. (1972). "Analysis of Completeness of the Earthquake Sample in the Puget Sound Area and its Effect on Statistical Estimates of Earthquake hazard," in Proceeding of the 1st International Conference on Microzonazion, Seattle. 897–910.

Stucchi, M., Rovida, A., Capera, A. G. A. G., Alexandre, P., Camelbeeck, T., Demircioglu, M. B., et al. (2013). The SHARE European Earthquake Catalogue (SHEEC) 1000–1899. *J. Seismol.* 17, 523–544. doi:10.1007/s10950-012-9335-2

TANDEM (2020). *TANDEM : Tsunamis in the Atlantic and the English ChaNnel Definition of the Effects through Numerical Modeling*. [Dataset]. Available at: http://www-tandem.cea.fr/.

Tonini, R., Di Manna, P., Lorito, S., Selva, J., Volpe, M., Romano, F., et al. (2021). Testing Tsunami Inundation Maps for Evacuation Planning in Italy. *Front. Earth Sci.* 9, 82. doi:10.3389/feart.2021.628061

U.S. Geological Survey (2020). *Search Earthquake Catalog*. [Dataset].

Volpe, M., Lorito, S., Selva, J., Tonini, R., Romano, F., and Brizuela, B. (2019). From Regional to Local SPTHA: Efficient Computation of Probabilistic Tsunami Inundation Maps Addressing Near-Field Sources. *Nat. Hazards Earth Syst. Sci.* 19, 455–469. doi:10.5194/nhess-19-455-2019

Wason, H. R., Das, R., and Sharma, M. L. (2012). Magnitude Conversion Problem Using General Orthogonal Regression. *Geophys. J. Int.* 190, 1091–1096. doi:10.1111/j.1365-246X.2012.05520.x

Weichert, D. H. (1980). Estimation of the Earthquake Recurrence Parameters for Unequal Observation Periods for Different Magnitudes. *Bull. Seismol. Soc. Am.* 70, 1337–1346. doi:10.1785/bssa0700041337

Wells, D. L., and Coppersmith, K. J. (1994). New Empirical Relationships Among Magnitude, Rupture Length, Rupture Width, Rupture Area, and Surface Displacement. *Bull. Seismol. Soc. Am.* 84, 974–1002.

Wiemer, S., and Wyss, M. (2000). Minimum Magnitude of Completeness in Earthquake Catalogs: Examples from Alaska, the Western United States, and Japan. *Bull. Seismol. Soc. Am.* 90, 859–869. doi:10.1785/0119990114

Woessner, J., and Wiemer, S. (2005). Assessing the Quality of Earthquake Catalogues: Estimating the Magnitude of Completeness and its Uncertainty. *Bull. Seismol. Soc. Am.* 95, 684–698. doi:10.1785/0120040007

**Conflict of Interest:** The authors declare that the research was conducted in the absence of any commercial or financial relationships that could be construed as a potential conflict of interest.

frontiers in Earth Science

ORIGINAL RESEARCH
published: 05 January 2022
doi: 10.3389/feart.2021.741841

# Ensemble-Based Forecast of Volcanic Clouds Using FALL3D-8.1

*Arnau Folch*[1,2]*, *Leonardo Mingari*[2] *and Andrew T. Prata*[2,3]

[1]Geociencias Barcelona (GEO3BCN-CSIC), Barcelona, Spain, [2]Barcelona Supercomputing Center (BSC), Barcelona, Spain, [3]Sub-Department of Atmospheric, Oceanic and Planetary Physics, University of Oxford, Oxford, United Kingdom

Operational forecasting of volcanic ash and $SO_2$ clouds is challenging due to the large uncertainties that typically exist on the eruption source term and the mass removal mechanisms occurring downwind. Current operational forecast systems build on single-run deterministic scenarios that do not account for model input uncertainties and their propagation in time during transport. An ensemble-based forecast strategy has been implemented in the FALL3D-8.1 atmospheric dispersal model to configure, execute, and post-process an arbitrary number of ensemble members in a parallel workflow. In addition to intra-member model domain decomposition, a set of inter-member communicators defines a higher level of code parallelism to enable future incorporation of model data assimilation cycles. Two types of standard products are automatically generated by the ensemble post-process task. On one hand, deterministic forecast products result from some combination of the ensemble members (e.g., ensemble mean, ensemble median, etc.) with an associated quantification of forecast uncertainty given by the ensemble spread. On the other hand, probabilistic products can also be built based on the percentage of members that verify a certain threshold condition. The novel aspect of FALL3D-8.1 is the automatisation of the ensemble-based workflow, including an eventual model validation. To this purpose, novel categorical forecast diagnostic metrics, originally defined in deterministic forecast contexts, are generalised here to probabilistic forecasts in order to have a unique set of skill scores valid to both deterministic and probabilistic forecast contexts. Ensemble-based deterministic and probabilistic approaches are compared using different types of observation datasets (satellite cloud detection and retrieval and deposit thickness observations) for the July 2018 Ambae eruption in the Vanuatu archipelago and the April 2015 Calbuco eruption in Chile. Both ensemble-based approaches outperform single-run simulations in all categorical metrics but no clear conclusion can be extracted on which is the best option between these two.

**Keywords: ensemble forecast, volcanic clouds, FALL3D model, categorical metrics, Ambae eruption, Calbuco eruption**

OPEN ACCESS

***Edited by:***
*Nico Fournier,*
*GNS Science, New Zealand*

***Reviewed by:***
*Meelis Zidikheri,*
*Bureau of Meteorology, Australia*
*Larry Garver Mastin,*
*United States Geological Survey (USGS), United States*

***Correspondence:**
*Arnau Folch*
*afolch@geo3bcn.csic.es*

***Specialty section:***
*This article was submitted to Volcanology, a section of the journal Frontiers in Earth Science*

***Received:*** *15 July 2021*
***Accepted:*** *06 December 2021*
***Published:*** *05 January 2022*

***Citation:***
*Folch A, Mingari L and Prata AT (2021) Ensemble-Based Forecast of Volcanic Clouds Using FALL3D-8.1. Front. Earth Sci. 9:741841. doi: 10.3389/feart.2021.741841*

## 1 INTRODUCTION

Numerical modelling of volcanic plumes, including the atmospheric dispersal of volcanic particles and aerosols and its ultimate fallout on the ground, is challenging due to a number of reasons that include, among others, the multiplicity of scales involved, the complex underlying physical phenomena, the characterisation of the emitted particles and aerosols, and the quantification of the strength, vertical distribution, and evolution in time of the source term (volcanic plume) and related uncertainties (Folch, 2012). The latter two aspects are particularly critical in operational forecast scenarios where, in addition to larger source term uncertainties, requirements exist also on the forecast time-to-solution that constrain the space-time resolutions of operational model setups depending on the computational resources available.

Ensemble-based modelling is well recognised as the proper strategy to characterise uncertainties in model inputs, in model physics and its parameterisations, and in the underlying model-driving meteorological data. In the fields of meteorology and atmospheric dispersal, the use of ensemble-based approaches to improve predictions and quantify model-related uncertainties has long been considered, first in the context of numerical weather forecast (e.g., Mureau et al., 1993; Bauer et al., 2015), and afterwards for toxic dispersal (e.g., Dabberdt and Miller, 2000; Maurer et al., 2021), air quality (e.g., Galmarini et al., 2004; Galmarini et al., 2010), or volcanic clouds (e.g., Bonadonna et al., 2012; Madankan et al., 2014; Stefanescu et al., 2014) among others. Ensemble-based approaches can give a deterministic product based on some combination of the single ensemble members (*e.g.*, the ensemble mean) and, as opposed to single deterministic runs, attach to it an objective quantification of the forecast uncertainty. On the other hand, ensemble runs can also furnish probabilistic products based on the fraction of ensemble members that verify a certain (threshold) condition, *e.g.,* the probability of cloud being detected by satellite-based instrumentation, the probability that the cloud mass concentration compromises the safety of air navigation, the probability of particle fallout or of aerosol concentration at surface to exceed regulatory values for impacts on infrastructures or on air quality, etc. Added to these, ensembles can also be used as multiple trial simulations, e.g., in optimal source term inversions by calculating correlations between the different members and observations (e.g., Zidikheri et al., 2017; Zidikheri et al., 2018; Harvey et al., 2020) or to make more robust in flight-planning decisions (Prata et al., 2019). Finally, ensembles are also the backbone of most modern data assimilation techniques, which require estimates of forecast uncertainty to merge a priori forecasts with observations during data assimilation cycles (e.g., Fu et al., 2015; Fu et al., 2017; Osores et al., 2020; Pardini et al., 2020).

At a research level, forecasting of volcanic clouds using ensemble-based approaches has been considered in several models including, for example, ASH3D (Denlinger et al., 2012a; Denlinger et al., 2012b), COSMO-ART (Vogel et al., 2014), HYSPLIT (Dare et al., 2016; Zidikheri et al., 2018; Pardini et al., 2020), NAME (Dacre and Harvey, 2018; Beckett et al., 2020), FALL3D (Osores et al., 2020) or, more recently, even tackling multi-model ensemble approaches (Plu et al., 2021). Despite promising results, implementations at operational level are still limited to a few cases, *e.g.* the Dispersion Ensemble Prediction System (DEPS) of the Australian Bureau of Meteorology (Dare et al., 2016). Such a slow progress can be explained by the inertia of operational frameworks to go beyond single-run scenarios, the limited pool of validation studies supporting this approach, the computational overhead of ensemble-based forecast methodologies, the reluctance of some end-users to incorporate probabilistic scenarios in their decision-making operations, or even the difficulties to interpret and communicate ensemble-based products. Here we present FALL3D-8.1, the last version release of this atmospheric transport model that includes the option of ensemble-based simulations. Developments are being done in the frame of the EU Center of Excellence for Exascale in Solid Earth (ChEESE) and, more precisely, within the Pilot Demonstrator (PD) number 12 (PD12) that considers an ensemble-based data assimilation workflow combining the FALL3D dispersal model with high-resolution latest-generation geostationary satellite retrievals. The ultimate goal of this pilot is to have a km-resolution short and long-range automated forecast system with edge-to-end latencies compatible with early-warning and crisis management requirements. We limit our discussion here to the ensemble modelling module, leaving the data assimilation component to another publication linked to the upcoming v8.2 model release (Mingari et al., 2021). In this scenario, the objectives of this manuscript are three-fold:

1. To introduce FALL3D-8.1, including the novel model tasks to generate ensemble members from an unperturbed reference member, merge and post-process the single-member simulations, and validate model forecasts against satellite-based and ground deposit observations (**Section 2**). The ensemble generation in FALL3D-8.1 can consider uncertainties in the emissions (*i.e.,* the so-called Eruption Source Parameters for volcanic species), particle properties, and meteorological fields (wind velocity).
2. To define quantitative forecast-skill metrics applicable to both ensemble-based deterministic and ensemble-based probabilistic forecasts simultaneously. Note that, typically, only ensemble-based deterministic outputs are compared against observations, *e.g.,* by means of categorical metrics. However, the question on whether a probabilistic approach is more (or less) skilled than a deterministic one is rarely tackled. Generalised categorical metrics are proposed in **Section 3** of this paper in order to explicitly address this question.
3. To validate the ensemble-based deterministic and probabilistic approaches using different types of observation datasets for ash/$SO_2$ clouds (satellite detection and satellite retrieval) and ground deposits (scattered points and isopach contours). This is done in two different contexts, the July 2018 Ambae eruption for $SO_2$ clouds, and the April 2015 Calbuco eruption for ash clouds and tephra fallout (**Section 4**). In both cases, computational capacity requirements are

**TABLE 1 |** List of model input parameters that can be perturbed in FALL3D-8.1 to generate ensemble runs. The related task and the species category affected are also indicated (see Folch et al. (2020), for details).

| Parameter | Related task | Species category | Comments |
|---|---|---|---|
| Fi-mean $\Phi_m$ | *SetTgsd* | Particles and radionuclides | Mean of the Gaussian particle Grain Size Distribution (GSD) |
| Column height $H$ | *SetSrc* | All species | Maximum source term injection height [(1)] |
| Mass flow rate $\dot{M}$ | *SetSrc* | All species | Source term strength. Applies to configurations in which $\dot{M}$ is explicitly given and not derived from height $H$[(1)] |
| Source start | *SetSrc* | All species | Source start time [(1)] |
| Source duration | *SetSrc* | All species | Source duration time [(1)] |
| Top-hat thickness | *SetSrc* | All species | Source thickness in the *HAT* source type option[(1)] |
| Suzuki $A$ | *SetSrc* | Tephra and aerosols | Parameter $A$ in the *SUZUKI* source type option[(1)] |
| Suzuki $\lambda$ | *SetSrc* | Tephra and aerosols | Parameter $\lambda$ in the *SUZUKI* source type option[(1)] |
| Aggregate size | *SetSrc* | Tephra | Size of the aggregate bins |
| Aggregate density | *SetSrc* | Tephra | Density of the aggregate bins |
| Wind speed | *FALL3D* | All species | Horizontal wind components |
| Insertion height | *FALL3D* | Tephra and aerosols | Cloud height if the model initial condition is given from data insertion |
| Insertion thickness | *FALL3D* | Tephra and aerosols | Cloud thickness if the model initial condition is given from data insertion |

[(1)] *In case of time-dependent parameters the same perturbation is applied to all phases of the source term.*

considered in the context of urgent (super)-computing, including constraints in the forecast time-to-solution.

## 2 FALL3D-8.1

During its latest major version release (v8.0), the FALL3D model (Costa et al., 2006; Folch et al., 2009) was rewritten and refactored in order to incorporate dramatic improvements in model physics, spectrum of applications, numerics, code scalability, and overall code performance on large supercomputers (for details see Folch et al., 2020; Prata et al., 2021). This included also the parallelisation and embedding of former pre-process auxiliary programmes to run either as independent model tasks (specified by a call argument) or concatenated in a single execution workflow. In FALL3D-8.1, three new model tasks have been added to automatically generate an ensemble of members (task *SetEns*), post-process ensemble-based simulations (task *PosEns*) and, finally, validate the model against different types of observation datasets (task *PosVal*). Ensemble members in FALL3D-8.1 run concurrently in parallel, with a dedicated MPI communicator for the master ranks of each ensemble member. However, because this code version does not handle data assimilation cycles yet (something planned for the next version release v8.2), the individual ensemble members run actually as an embarrassingly parallel workload (e.g., Herlihy et al., 2020), *i.e.,* with no dependency among parallel tasks.

### 2.1 Ensemble Generation Task

The task *SetEns*, which must be run first in the case of ensemble runs, generates and sets the ensemble members from a unique input file by perturbing a reference case (the so-called central or reference member). This task also creates a structure of sub-folders, one for each ensemble member, where successive model tasks will be pointed to locate the necessary input and dump the output files generated by the execution of each member. In case of ensemble-based simulations, a new block in the FALL3D-8.1 input file allows to set which model input parameters will be perturbed, its perturbation amplitude (given as a percentage of the reference value or in absolute terms), and the perturbation sampling strategy, which in FALL3D-8.1 can follow either a constant or a Gaussian Probability Density Function (PDF). Note that this block in the input file is simply ignored if the ensemble option is not activated, ensuring backwards compatibility with previous versions of the code. **Table 1** shows which model input parameters can be perturbed and to which category and related sub-category of species each perturbation can be applied. Note that this manuscript pertains to volcanic particles and aerosols but, nonetheless, the ensemble-based approach is also possible for other types of species available in FALL3D-8. x (for details on the species category types see Table 3 in Folch et al., 2020).

The ensemble generation starts with an unperturbed central member, which typically is set with the observed or "best-guess" input values and that, by construction, coincides with the "standard" single-run. For each parameter to be perturbed, the ensemble spread is then generated by sampling on the corresponding PDF around the unperturbed central value and within a range (amplitude) that spans the parameter uncertainty. For example, a perturbation of the source duration $S_d$ by ± 1 h samples using either a linear or a Gaussian (centred at $S_d$) PDF within the interval $[S_d - 1, S_d + 1]$. For $n$ ensemble members and $m$ parameters (dimensions) perturbations result on a combination of $n \times m$ possible values that are then sub-sampled to define the $n$ ensemble members using a classical Latin hypercube sampling algorithm (e.g., Husslage et al., 2006). This strategy guarantees that the spread across each of the $m$ dimensions is maintained in the final member's sub-sample. It is clear that the a priori generation of an ensemble requires expert judgement and involves some degree of subjectivity. The question on how an ensemble can be optimally generated is complex and falls beyond the scope of this manuscript. Nonetheless, a good practice if forecast observations exist is to check (a posteriori) that the ensemble-based forecast is statistically indistinguishable from observations by looking at the shape of the ensemble rank histogram.

**TABLE 2 |** Four types of observation datasets that can be used for model validation by task *PosVal*. The satellite detection and the satellite retrieval observation types stand, respectively, for detection (*i.e.* "yes/no" categorical observation) and quantitative column mass retrievals. The deposit contours observation type refers to isopach/isopleth deposit contours (*e.g.* from shape files or gridded maps). Finally, the deposit points stands for deposit thickness/load observations at scattered points. For each type of forecast, deterministic (D) or probabilistic (P), the Table indicates which validation metrics apply to each combination of observation-forecast types. The different generalised categorical and quantitative scores are defined in **Section 3**.

| **Observation dataset** | **Satellite Detection** | | **Satellite Retrieval** | | **Deposit Contours** | | **Deposit Points** | |
|---|---|---|---|---|---|---|---|---|
| **Observation type** | **Categorical** | | **Quantitative** | | **Categorical** | | **Quantitative** | |
| **Forecast type** | **D** | **P** | **D** | **P** | **D** | **P** | **D** | **P** |
| Generalised categorical metrics | ✓ | ✓ | ✓ | ✓ | ✓ | ✓ | – | – |
| Brier Score (BS) | – | ✓ | – | ✓ | – | ✓ | – | ✓ |
| Quantitative scores | – | – | ✓ | – | – | – | ✓ | – |
| Rank histogram | – | – | - | ✓ | – | – | – | ✓ |

## 2.2 Ensemble Postprocess Task

Once the model has run, the task *PosEns* merges all outputs from individual ensemble members in a single netCDF file containing ensemble-based deterministic and/or probabilistic outputs for all variables of interest (*e.g.,* concentration at native model levels or at flight levels, cloud column mass, ground deposit load, etc). Options for ensemble-based deterministic outputs include the ensemble mean, the ensemble median, and values of user-defined percentiles. The standard deviation can be attached to any variable as a measure of the uncertainty of the deterministic outputs. On the other hand, ensemble-based probabilistic outputs can also be built by counting, at each grid point and time step, the fraction of ensemble members that verify a given condition, typically the exeedance of some threshold. For example, a probabilistic output for airborne volcanic ash can be defined based on the 2 $mg/m^3$ concentration threshold in case of aviation-targeted products and counting, at each grid cell and time step, the fraction of members that overcome this value.

## 2.3 Model Validation Task

FALL3D-8.1 includes a third new task *PosVal* to validate both single-run (compatible with previous code versions) and ensemble-based deterministic and/or probabilistic outputs against various types of gridded and scattered observation datasets (see **Table 2**). Observation datasets include satellite-based observations and quantitative retrievals (to validate against cloud column mass), deposit isopach/isopleth maps, and point-wise deposit observations (to validate against deposit thickness or mass load). In all cases, this model task reads the required files, interpolates model and observations into the same grid and computes a series of categorical and quantitative validation metrics that are detailed in the following section. This model validation task inherits the model domain decomposition structure and, consequently, all metrics are first computed (in parallel) over each spatial sub-domain and then gathered and added to get global results over the whole computational domain.

# 3 ENSEMBLE FORECAST DIAGNOSTIC METRICS

This section defines the different types of metrics computed by task *PosVal*, summarised in **Table 3**. These include: i) generalised categorical metrics, ii) quantitative metrics for deterministic forecasts and, iii) the ensemble rank histogram for ensemble-based probabilistic scenarios.

## 3.1 Generalised Categorical Metrics

Categorical metrics (e.g., Jolliffe and Stephenson, 2012) apply to variables that take a limited number of values or "categories". For example, in a deterministic forecast context it is common to define dichotomic categories (yes/no) for model and observations based on the occurrence (or not) of a given condition. At each observation point, this results on a 2 × 2 model-observations "contingency table" (true positives, true negatives, false positives, false negatives), from which a series of "geometric-based" or "contour-based" categorical metrics can be constructed, *e.g.,* the probability of detection, the false alarm rate, etc. (Marti and Folch, 2018; Pardini et al., 2020). In this section, several classical categorical metrics widely used in deterministic forecast contexts are generalised to probabilistic forecasts with the objective of having a same set of forecast skill scores usable in both contexts.

Consider an ensemble-based model realisation with $n$ ensemble members in a computational domain $\Omega$. At each point and time instant, the forecasts of the $n$ ensemble members can be ranked and the discrete probability of occurrence of a certain condition or threshold can be computed by simply counting how many ensemble members verify the condition (note that this results on $n + 1$ categories or probability bins). Let's denote by $P_m\ (x, t)$ the resulting discrete probability function defined in the domain $\Omega$, where the subscript $m$ stands for model and $0 \leq P_m\ (x, t) \leq 1$. Clearly, $P_m\ (x, t) = 0$ implies that no ensemble member satisfies the condition at $(x, t)$, whereas $P_m(x, t) = 1$ implies that all members do. In general, $P_m\ (x, t)$ will be a function with finite support, that is, it will take non-zero values only over a sub-domain $\Omega_m(t) = \{x \in \Omega \mid P_m(x, t) > 0\}$

**TABLE 3 |** Summary of metrics. GMFS: Generalised Figure Merit of Space, GFAR: Generalised False Alarm Rate, GPPV: Generalised Positive Predictive Value, GPOD: Generalised Probability of Detection, GCCM: Generalised Composite Categorical Metric, BS: Brier Score, NRMSE: Normalised Root Mean Square Error.

| Metric | Metrics type | Metrics definition | Optimal value | Worst Value | Comment |
|---|---|---|---|---|---|
| GFMS | Categorical | (3) or (5) | 1 | 0 | Gives FMS in the deterministic limit (4) |
| GFAR | Categorical | (8) or (10) | 0 | 1 | Gives FAR in the deterministic limit (9) |
| GPPV | Categorical | (13) or (14) | 1 | 0 | Gives PPV in the deterministic limit (15) |
| GPOD | Categorical | (18) or (20) | 1 | 0 | Gives POD in the deterministic limit (19) |
| GCCM | Categorical | (22) | 1 | 0 | |
| BS | Categorical | (24) or (25) | 0 | 1 | Only for probabilistic forecasts |
| NRMSE | Quantitative | (27) | 0 | $\infty$ | Only for deterministic forecasts |
| Histogram | Rank | | Flat | — | Only for probabilistic forecasts |

where at least one ensemble member satisfies the condition. Let's denote by $\delta_m(x, t)$ the step function defined from the support of $P_m(x, t)$, that is:

$$\delta_m(x,t) = \begin{cases} 1 & \text{if } x \in \Omega_m(t) \\ 0 & \text{if } x \notin \Omega_m(t) \end{cases} \quad (1)$$

Note that the definitions of $P_m(x, t)$ and $\delta_m(x, t)$ are also valid in a deterministic context. In fact, the deterministic forecast scenario represents the limit in which $P_m(x, t)$ can take only two discrete values (0 or 1) and one simply has that $\Omega_m(t) = \{x \in \Omega \mid P_m(x, t) = 1\}$ and $P_m(x, t) = \delta_m(x, t)$. From a geometrical point of view, $\delta_m(x, t)$ can be interpreted as the union of the $n$ probability contours that define the discrete probability function $P_m(x, t)$. In the deterministic limit, only one contour exists and, consequently, one has $P_m(x, t) = \delta_m(x, t)$.

Similar arguments can be followed regarding observations. In general, one could consider $m$ different sources of observations and apply the same condition (threshold) to obtain a discrete probability function of observations $P_o(x, t)$, define the subdomain $\Omega_o(t) = \{x \in \Omega \mid P_o(x, t) > 0\}$ as the subset of $\Omega$ where at least one observation verifies the condition and, finally, define the resulting observations step function $\delta_o x, t)$ analogous to **Eq. 1** but using $\Omega_o(t)$. Following with the analogy, this would result on a $(n + 1) \times (m + 1)$ model-observations "contingency table" for the most general case. In what follows, generalised categorical metrics will be defined for an arbitrary number of members/observations and grid projection. However, and for the sake of simplicity, only cases in which observations come from a single source ($m = 1$) will be considered here. As a result, it will be implicitly assumed that $\Omega_o(t) = \{x \in \Omega \mid P_o(x, t) = 1\}$ and $P_o(x, t) = \delta_o(x, t)$. The following generalised categorical metrics are introduced:

### 3.1.1 Generalised Figure Merit of Space

The Generalised Figure Merit of Space (GFMS) is defined as:

$$\mathrm{GFMS}(t) = \frac{\int_\Omega \delta_o \delta_m P_o P_m d\Omega}{\int_\Omega [(1-\delta_o)P_m + (1-\delta_m)P_o + \delta_o \delta_m P_o P_m] d\Omega} \quad (2)$$

which, for the single-observation case considered here ($P_o = \delta_o$) and using that $\delta_o^2 = \delta_o$, simplifies to:

$$\mathrm{GFMS}(t) = \frac{\int_\Omega \delta_o \delta_m P_m d\Omega}{\int_\Omega [(1-\delta_o)P_m + (1-\delta_m)\delta_o + \delta_o \delta_m P_m] d\Omega} \quad (3)$$

Note that in the deterministic forecast limit (*i.e.,* $P_m = \delta_m$), the GFMS reduces to:

$$\mathrm{GFMS}(t) = \frac{\int_\Omega \delta_o \delta_m d\Omega}{\int_\Omega [\delta_m + \delta_o - \delta_m \delta_o] d\Omega} = \frac{\Omega_o \cap \Omega_m}{\Omega_m + \Omega_o - \Omega_o \cap \Omega_m} = \frac{\Omega_o \cap \Omega_m}{\Omega_o \cup \Omega_m} = \mathrm{FMS}(t) \quad (4)$$

which is the classical definition of the Figure Merit of Space (FMS), also known as the Jaccard coefficient (e.g., Levandowsky and Winter 1971; Galmarini et al., 2010). From a geometric point of view, the FMS is interpreted as the ratio between the intersection of model-observations contours and its union. The GFMS introduced here has the same interpretation but using a weight-average with model/observations probability contours. The GFMS ranges from 0 (worst) to 1 (optimal). The continuous integrals over $\Omega$ in the expressions above are in practice computed by projecting observations into the model grid and summing the discrete probability bins over all grid cells. For example, in the case of **Eq. 3**, the discrete computation would be as:

$$\mathrm{GFMS}(t) = \frac{\sum_j H_j \delta_{oj} \delta_{mj} P_{mj}}{\sum_j H_j (1-\delta_{oj}) P_{mj} + \sum_j H_j (1-\delta_{mj}) \delta_{oj} + \sum_j H_j \delta_{oj} \delta_{mj} P_{mj}} \quad (5)$$

where $H_j = m_{1j} m_{2j} m_{3j} V_j$ is the grid mapping factor of the $j$ grid cell, $V_j$ is the cell volume, and $m_{xj}$ are the mapping factors depending on the coordinate system (see Tables 8 and 9 in Folch et al., 2020). Note that in the deterministic limit and for the particular case of a regular Cartesian grid (*i.e.,* all cells equal, unit map factors) this further simplifies to:

$$\mathrm{FMS}(t) = \frac{\sum_j \delta_{oj} \delta_{mj}}{\sum_j (1-\delta_{oj}) \delta_{mj} + \sum_j (1-\delta_{mj}) \delta_{oj} + \sum_j \delta_{oj} \delta_{mj}} = \frac{\mathrm{TP}}{\mathrm{FP} + \mathrm{FN} + \mathrm{TP}} \quad (6)$$

and coincides with the number of True Positives (TP) divided by the number of False Positives (PF) + False Negatives (FN) + True Positives (TP), which is also the classical non-geometric interpretation of the FMS (e.g., Pardini et al., 2020). However, in general, the computation of the GFMS in non-regular

coordinate systems (5) takes into account a cell-dependent weight proportional to the cell volume (area) through the grid mapping factors $H_j$.

### 3.1.2 Generalised False Alarm Rate

The Generalised False Alarm Rate (GFAR) is defined as:

$$\mathrm{GFAR}(t) = \frac{\int_\Omega (1-\delta_o)\delta_m P_m d\Omega}{\int_\Omega [(1-\delta_o)\delta_m P_m + \delta_o \delta_m P_o P_m] d\Omega} \tag{7}$$

which, for the case of single set of observations ($P_o = \delta_o$), reduces to:

$$\mathrm{GFAR}(t) = \frac{\int_\Omega (1-\delta_o)\delta_m P_m d\Omega}{\int_\Omega [(1-\delta_o)\delta_m P_m + \delta_o \delta_m P_m] d\Omega} \tag{8}$$

In the deterministic forecast limit ($P_m = \delta_m$), the definition of the GFAR further simplifies to:

$$\mathrm{GFAR}(t) = \frac{\int_\Omega (1-\delta_o)\delta_m d\Omega}{\int_\Omega \delta_m d\Omega} = \frac{\Omega_m - \Omega_o \cap \Omega_m}{\Omega_m} = 1 - \frac{\Omega_o \cap \Omega_m}{\Omega_m} = \mathrm{FAR}(t) \tag{9}$$

which is the classical definition of the False Alarm Rate (FAR) (e.g., Kioutsioukis et al., 2016). In the geometric interpretation, the GFAR can be viewed as the fraction of $\Omega_m$ with false positives but generalised to probabilistic contours, and it ranges from 0 (optimal) to 1 (worst). Again, the continuous integrals in **Eq. 8** are computed in practice over the model grid as:

$$\mathrm{GFAR}(t) = \frac{\sum_j H_j \left(1-\delta_{oj}\right)\delta_{mj} P_{mj}}{\sum_j H_j \left(1-\delta_{oj}\right)\delta_{mj} P_{mj} + \sum_j H_j \delta_{oj}\delta_{mj} P_{mj}} \tag{10}$$

which, in the deterministic limit and for a regular grid ($H_j = 1$), further simplifies to:

$$\mathrm{FAR}(t) = \frac{\sum_j \left(1-\delta_{oj}\right)\delta_{mj}}{\sum_j \left(1-\delta_{oj}\right)\delta_{mj} + \sum_j \delta_{oj}\delta_{mj}} = \frac{\mathrm{FP}}{\mathrm{FP} + \mathrm{TP}} \tag{11}$$

and therefore coincides, in a non-geometric interpretation, with the number of False Positives (FP) divided by the number of False Positives (FP) + True Positives (TP).

### 3.1.3 Generalised Positive Predictive Value

The Generalised Positive Predictive Value (GPPV) is defined as the complement of the GFAR:

$$\mathrm{GPPV}(t) = 1 - \mathrm{GFAR}(t) = \frac{\int_\Omega \delta_o \delta_m P_o P_m d\Omega}{\int_\Omega [(1-\delta_o)\delta_m P_m + \delta_o \delta_m P_o P_m] d\Omega} \tag{12}$$

Analogously, for the single-observation case ($P_o = \delta_o$):

$$\mathrm{GPPV}(t) = \frac{\int_\Omega \delta_o \delta_m P_m d\Omega}{\int_\Omega [(1-\delta_o)\delta_m P_m + \delta_o \delta_m P_m] d\Omega} \tag{13}$$

or

$$\mathrm{GPPV}(t) = \frac{\sum_j H_j \delta_{oj}\delta_{mj} P_{mj}}{\sum_j H_j \left(1-\delta_{oj}\right)\delta_{mj} P_{mj} + \sum_j H_j \delta_{oj}\delta_{mj} P_{mj}} \tag{14}$$

In the deterministic limit **Eq. 13** yields to the classical Positive Predictive Value (PPV), also known as the model precision (Pardini et al., 2020):

$$\mathrm{GPPV}(t) = \frac{\int_\Omega \delta_o \delta_m d\Omega}{\int_\Omega \delta_m d\Omega} = \frac{\Omega_o \cap \Omega_m}{\Omega_m} = \mathrm{PPV}(t) \tag{15}$$

The GPPV ranges from 0 (worst) to 1 (optimal) and geometrically can be interpreted as the fraction of $\Omega_m$ with true positives (model hits) but for probabilistic contours. Again, in a regular Cartesian grid the discrete version of **Eq. 15** coincides with the number of True Positives (TP) divided by the number of False Positives (FP) + True Positives (TP):

$$\mathrm{PPV}(t) = \frac{\sum_j \delta_{oj}\delta_{mj}}{\sum_j \left(1-\delta_{oj}\right)\delta_{mj} + \sum_j \delta_{oj}\delta_{mj}} = \frac{\mathrm{TP}}{\mathrm{FP} + \mathrm{TP}} \tag{16}$$

### 3.1.4 Generalised Probability of Detection

The Generalised Probability of Detection (GPOD) is defined as:

$$\mathrm{GPOD}(t) = \frac{\int_\Omega \delta_o \delta_m P_o P_m d\Omega}{\int_\Omega [(1-\delta_m)\delta_o P_o + \delta_o \delta_m P_o P_m] d\Omega} \tag{17}$$

which, for the single-observation case ($P_o = \delta_o$), reduces to:

$$\mathrm{GPOD}(t) = \frac{\int_\Omega \delta_o \delta_m P_m d\Omega}{\int_\Omega [(1-\delta_m)\delta_o + \delta_o \delta_m P_m] d\Omega} \tag{18}$$

As with the other metrics, in the deterministic limit ($P_m = \delta_m$) the GPOD simplifies to:

$$\mathrm{GPOD}(t) = \frac{\int_\Omega \delta_o \delta_m d\Omega}{\int_\Omega \delta_o d\Omega} = \frac{\Omega_o \cap \Omega_m}{\Omega_o} = \mathrm{POD}(t) \tag{19}$$

and coincides with the Probability of Detection (POD), also known as the model sensitivity (Pardini et al., 2020). The GPOD ranges from 0 (worst) to 1 (optimal) and, geometrically, is interpreted as the fraction of $\Omega_o$ with true positives. Again, in the discrete space (18) yields to:

$$\mathrm{GPOD}(t) = \frac{\sum_j H_j \delta_{oj}\delta_{mj} P_{mj}}{\sum_j H_j \left(1-\delta_{mj}\right)\delta_{oj} + \sum_j H_j \delta_{oj}\delta_{mj} P_{mj}} \tag{20}$$

that in a regular grid and deterministic limit coincides with the number of True Positives (TP) divided by the number of False Negatives (FN) + True Positives (TP):

$$\mathrm{POD}(t) = \frac{\sum_j \delta_{oj}\delta_{mj}}{\sum_j \left(1-\delta_{mj}\right)\delta_{oj} + \sum_j \delta_{oj}\delta_{mj}} = \frac{\mathrm{TP}}{\mathrm{FN} + \mathrm{TP}} \tag{21}$$

### 3.1.5 Generalised Composite Categorical Metric

It can be anticipated that some generalised categorical metrics can vary oppositely when comparing single-run and ensemble-based

simulations. For example, one may expect that a large ensemble spread yields to a larger GPOD but, simultaneously, also to larger GFAR. In order to see how different metrics counterbalance we introduce the Generalised Composite Categorical Metric (GCCM) as:

$$\mathrm{GCCM} = \frac{\mathrm{GFMS} + \mathrm{GPPV} + \mathrm{GPOD}}{3} = \frac{\mathrm{GFMS} + (1 - \mathrm{GFAR}) + \mathrm{GPOD}}{3} \quad (22)$$

where the factor 3 is introduced to normalise GCCM in the range 0 (worst) to 1 (optimal). This multi-composite definition is analogous to what is done for the SAL, defined as the sum of Structure, Amplitude and Location (e.g., Marti and Folch, 2018).

### 3.1.6 Brier Score

The Brier Score (BS) is defined as:

$$\mathrm{BS} = \frac{\int_{\Omega_o} (P_m - P_o)^2 d\Omega}{\int_{\Omega_o} d\Omega} \quad (23)$$

which, for the single-observation case, reduces to:

$$\mathrm{BS} = \frac{\int_{\Omega_o} (P_m - \delta_o)^2 d\Omega}{\int_{\Omega_o} d\Omega} \quad (24)$$

Note that the above integrals are constrained to the subdomain $\Omega_o$ where observations exist. The Brier score is the averaged squared error of a probabilistic forecast and ranges from 0 (optimal) to 1 (worst). In the discrete space, **Eq. 24** is computed as:

$$\mathrm{BS} = \frac{\sum_j H_j \delta_{oj} \left(P_{mj} - 1\right)^2}{\sum_j H_j \delta_{oj}} \quad (25)$$

which, in a regular Cartesian grid, reduces to the more standard definition of the Brier score (Brier, 1950):

$$\mathrm{BS} = \frac{1}{n_o} \sum_{j=1}^{n_o} \left(P_{mj} - 1\right)^2 \quad (26)$$

where $n_o$ is the total number of observation points.

## 3.2 Quantitative Scores

As a quantitative metric for deterministic forecasts we consider the Normalised Root Mean Square Error (NRMSE), defined as:

$$\mathrm{NRMSE} = \frac{\sqrt{\frac{1}{n_o}\sum (M_i - O_i)^2}}{O_{max} - O_{min}} \quad (27)$$

where $O_i$ are the $n_o$ observation values, $M_i$ is the model value at the $i$th observation point, and $O_{\max}$ and $O_{\min}$ are, respectively, the maximum and minimum of the observations (at the considered time step). Note that, as opposed to the previous categorical metrics, this quantitative score is valid only for deterministic forecasts (single-run or ensemble-based).

## 3.3 Ensemble Rank Metrics

The observations rank histogram or Talagrand diagram (Talagrand et al., 1997) is commonly used a posteriori to measure the consistency of an ensemble forecast and to assess whether observations are statistically indistinguishable from the ensemble members. The histogram can be used to recalibrate ensemble forecasts and it is constructed as follows. For each observation (grid point and time), the $n$ ensemble members are ranked from lowest to highest using the variable of interest (column mass, deposit thickness, etc.) and the rank of the observation with respect to the forecast is identified and added to the corresponding bin (points with zero observation values are not counted). Flat histograms indicate a consistent forecast, with an observed probability distribution well represented by the ensemble. Asymmetric histograms indicate positive/negative forecast bias, as most observations often rank below/above the extremes respectively. Finally, dome-shaped/U-shaped histograms indicate over/under forecast dispersion and reflect too large/small ensemble spread respectively. Other common metrics to evaluate ensembles, *e.g.,* the spread-skill relationship (e.g., Scherrer et al., 2004), are not considered at this stage but will be incorporated in future code versions.

# 4 APPLICATION CASES

## 4.1 The July 2018 Ambae $SO_2$ Cloud

In April and July 2018 the Ambae volcano (Vanuatu archipelago) produced two paroxysm eruptions that injected large amounts of $SO_2$ reaching the tropopause (Moussallam et al., 2019). According to Himawari-8 satellite observations, the July 26, 2018 phase started before 12 UTC (23:00 LT) and lasted for about 4 h. Kloss et al. (2020) estimated an atmospheric $SO_2$ injection height of either 18 or 14 km a.s.l. by co-locating ERA5 temperature profiles and Brightness Temperature observations. To generate our $SO_2$ validation dataset we apply the 3-band interpolation procedure proposed by Prata et al. (2004) to measurements made by the Advanced Himawari Imager (AHI) aboard Himawari-8. Details of the method can be found in Appendix B of Prata et al. (2021). To estimate the total mass we only considered pixels containing more than 20 DU within a spatial domain from 160–200°E to 5–25°S. We also applied a Gaussian filter to generate smoothed contours around the $SO_2$ clouds to filter out pixels greater than 20 DU that were far from source (*i.e.,* false detections). Our results show that, during our satellite analysis period (from 26 July at 09:00 UTC to 31 July at 09:00 UTC), maximum total mass of 323005E;86_90 kt was injected into the upper atmosphere, where 86 and 90 kt are asymmetric errors around the best estimate (323 kt). The first significant injection of $SO_2$ occurred at around 10:00 UTC on 26 July and reached its maximum (253 kt) at 23:00 UTC. A second eruption occurred at around on 27 July at 01:00 UTC, and added a further 70 kt of $SO_2$. These $SO_2$ mass estimates are in broad agreement with independent TROPOMI $SO_2$ standard product mass retrievals (360 ± 40 kt), that assume a 15 km high $SO_2$ layer with 1 km thickness (Malinina et al., 2020).

**TABLE 4 |** Model setup for the July 26, 2018 single-run and ensemble-based (64 members) Ambae $SO_2$ simulations.

| | | Single-run (1 member) | Ensemble-run (64 members) |
|---|---|---|---|
| Source term (plume) | Start time | 26 July 10:00 UCT | perturbation range ±1 h |
| | Duration | 4 h | perturbation range ±1 h |
| | Plume height $H$ | 16 km a.s.l | perturbation range ±2 km |
| | Top-hat thickness $T$ | 1.5 km | perturbation range ±1 km |
| | $SO_2$ emission rate $\dot{M}^{(1)}$ | 2 × 104 kg/s | perturbation range ±30% |
| Source term (insertion) | Insertion time | 26 July 16:00 UCT | same |
| | Cloud height $H$ | 16 km a.s.l | perturbation range ±1 km |
| | Cloud thickness $T$ | 1.5 km | perturbation range ±0.5 km |
| Model grid | Horizontal resolution | $0.05^o$ | same |
| | Vertical resolution | 250 m | same |
| | Domain top | 22 km | same |
| | Grid size | 600 × 400 × 84 cells | same |
| Meteorology | | ERA5 (137 model levels) | winds $^{(2)}$ perturbed by ± 20% |

*$^{(1)}$ For the reference member, the total $SO_2$ emitted mass is 290 kt. For the other members it varies due to perturbations in $\dot{M}$ and duration.*
*$^{(2)}$ Horizontal wind components are perturbed globally (same perturbation in all grid cells).*

Based on the observations available during or shortly after the eruption, a single-run FALL3D-8.1 simulation was configured considering one $SO_2$ (aerosol) bin and an emission starting on 26 July at 10:00 UTC (21:00 LT) lasting for 4 h, assuming a top-hat plume vertical profile with the top at 16 km a.s.l. and a total emitted mass of 290 kt (emission rate 2 × 104 kg/s). This reference run represents a typical operational procedure during or shortly after an eruption, when model inputs are set with the uncertain available information. From this "best-guess" central member, an ensemble with 64 members was defined by perturbing the eruption start time (perturbation range of ±1 h), the eruption duration (±1 h), the cloud injection height $H$ (±2 km), the thickness $T$ of the top-hat emission profile (±2 km), the eruption rate (±30%), and the driving ERA-5 wind field as shown in **Table 4**. For both single-run and ensemble-based forecasts, the model grid resolution is $0.05^o$ in the horizontal and 250 m in the vertical, with the top of the computational domain placed at 22 km a.s.l.

Model runs generate hourly outputs concurrent with the AHI cloud mass retrievals over the forecast period. **Figure 1** compares AHI $SO_2$ column mass retrievals with different deterministic forecast outputs, namely the single-run, the ensemble mean, and the ensemble median at one particular instant (July 28, 2018 at 00:00 UTC). The ensemble mean and median produce a more diffused cloud, partly due to wind shear effects. Time series of quantitative scores, *e.g.,* using the NRMSE (**Eq. 27**), are automatically generated by the FALL3D-8.1 model task *PosVal*. **Figure 2** shows time series of NRMSE for different deterministic forecast options (single run, ensemble mean, and ensemble median). As observed, this metric follows a similar trend in all cases but the gain from the ensemble-based approaches is very clear: the deterministic ensemble-based options reduce the forecast NRMSE by a factor between two and three in most time instants. For comparative purposes, **Figure 2** also shows what happens if the data insertion mechanism is used to initialise the model runs instead of the source option. Data insertion consists of initialising a model run with an effective virtual source inserted away from the source, and FALL3D admits this initialisation option from column load satellite retrievals (Prata et al., 2021). This represents a case with better constrained input data (initial conditions) and, as expected, the data insertion option yields lower values of the NRMSE and shows little differences among the single-run and ensemble-based approaches.

As discussed in **Section 2.2**, probabilistic outputs can be generated from a given condition by counting the fraction of ensemble members that exceed a threshold value. For example, **Figure 3** shows 20 Dobson Units (DU) contours of $SO_2$ column mass for deterministic and probabilistic forecasts, where the value of 20 is assumed as representative of the $SO_2$ detection threshold in the AHI retrievals. These contours can be used for forecast validation using generalized categorical metrics that allow, on one side, to quantify the gain in the ensemble-based cases with respect to the reference single-run and, on the other side, to compare objectively the different ensemble-based approaches. To these purposes, **Figure 4** plots the time series of different generalised categorical metrics, GFMS (**Eq. 5**), GPOD (**Eq. 20**), and GCCM (**Eq. 22**) together with the BS (**Eq. 25**), the latter for the probabilistic case only. As expected, the ensemble mean outperforms the reference run in all the metrics, with substantial gain in GFMS and GPOD, yielding to better generalised composite metric GCCM. This is not true for the ensemble median, which presents similar forecast skills than those of the single run. On the other hand, the probabilistic approach behaves similarly to the ensemble mean in terms of GCCM because the larger false alarm rate is counterbalanced by a higher probability of detection. No conclusion can be extracted from this example on whether the probabilistic forecast option outperforms the deterministic ensemble mean or not. Finally, the observations rank histogram over the considered period (see **Figure 5A**) shows an acceptably flat histogram (reflecting good ensemble spread) although with a slight bias towards members having larger $SO_2$ mass. This skewing can be due to errors in cloud location, errors in amplitude, or to a combination of both. However, an inspection to the time series of AHI total retrieved mass (**Figure 5B**) suggests that the ensemble spread in cloud mass is adequate, indicating co-location as the reason for skewing. In fact, we performed successive ensemble redefinition

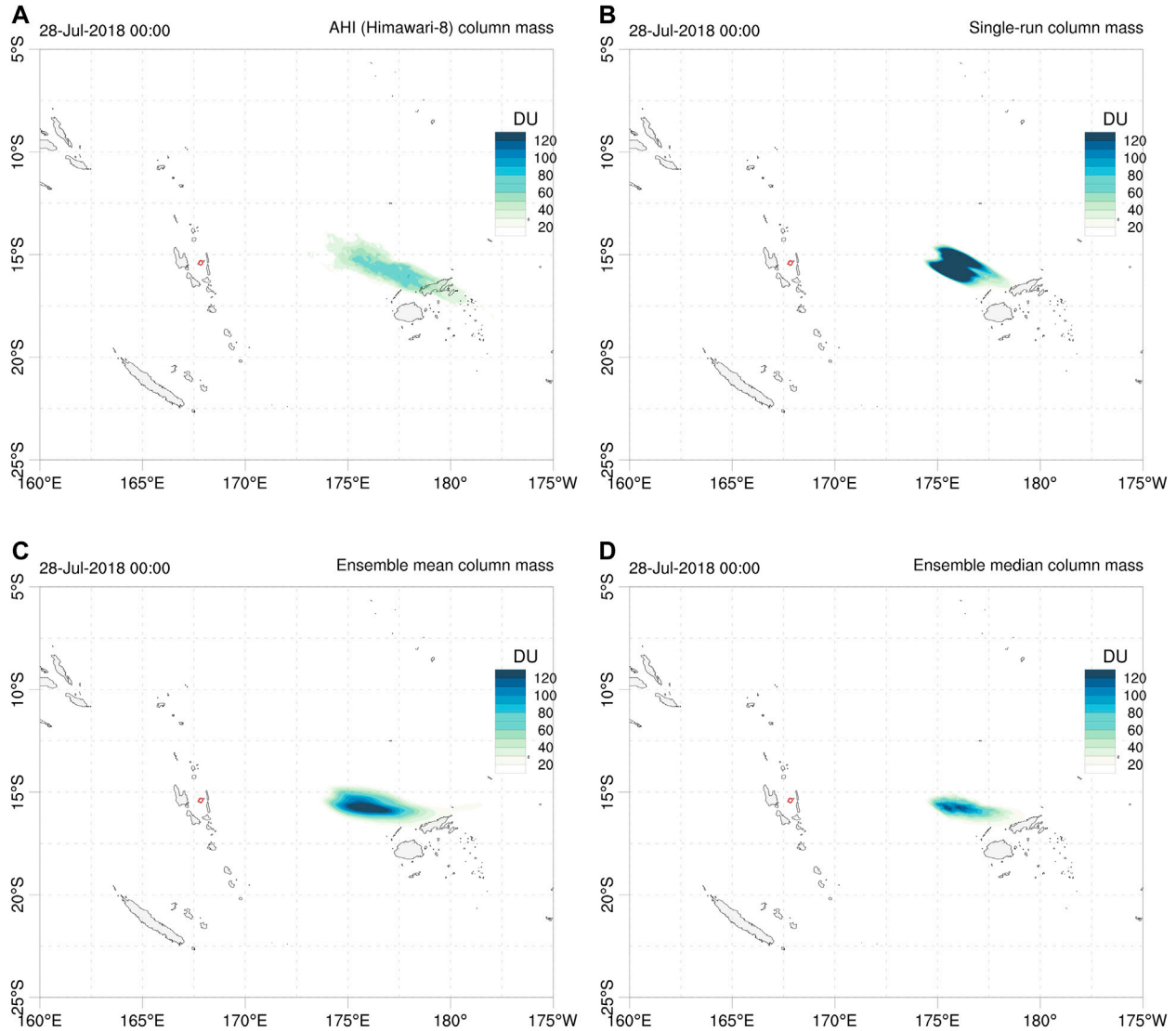


**FIGURE 1 |** Comparison between: **(A)** Ambae AHI $SO_2$ column mass retrievals, **(B)** single-run (unperturbed central member), **(C)** ensemble mean deterministic forecast, **(D)** ensemble median deterministic forecast. All snapshots correspond to July 28, 2018 at 00:00 UTC. Contours in Dobson Units (DU). Red circle shows the location of Ambae volcano.

runs (increasing mass in the reference run) and observed that the ensemble histogram flattened but, at the same time, this did not imply better values of the generalized metrics.

## 4.2 The April 2015 Calbuco Ash Cloud and Deposit

The Calbuco volcano (Chile) reawakened in 2015 with two major eruptive pulses on 22 April at 21:08 UTC and 23 April at about 04:00 UTC respectively, followed by a third minor event on the following day (e.g., Reckziegel et al., 2016). According to C-band dual-polarisation radar observations, the maximum ash plume heights exceeded 20 km above sea level in the surrounding area of the Calbuco volcano (Vidal et al., 2017). Subsequent plume modelling and field studies on the tephra fallout deposits indicated that the sub-Plinian phases, with similar column heights exceeding 15 km a.s.l. blanked the region with a total erupted volume ranging between 0.28 and 0.58 $km^3$ and a deposit mass in the range 2–7 × 1011 kg depending on different estimations (Romero et al., 2016; Van Eaton et al., 2016). On the other hand, ash cloud mass estimations from Moderate Resolution Imaging Spectroradiometer (MODIS) and Visible Infrared Imaging Radiometer Suite (VIIRS) indicated 1–3 × 109 kg of distal airborne material (e.g., Marzano et al., 2018), suggesting $< 1\%$ of remaining fine ash in the distal cloud. The comparison with field-based reconstructed particle grain size distributions, entailing a much larger fraction of mass in the fine tail (Reckziegel et al., 2016), point at the occurrence of substantial fine ash aggregation, as corroborated also by *in-situ* deposit observations. The Calbuco eruptions also entailed

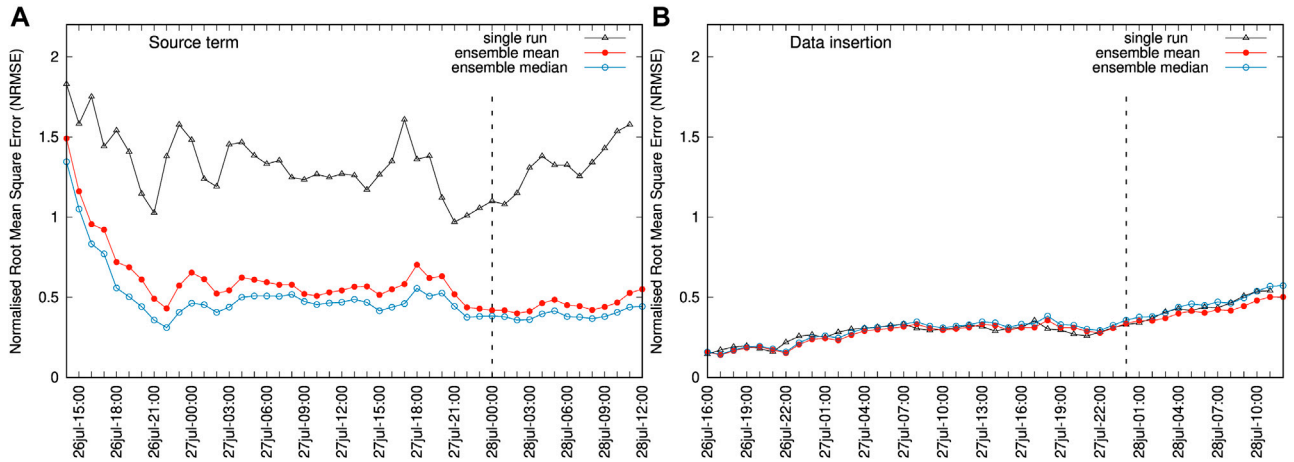


**FIGURE 2 | (A)** Time series of Normalised Root Mean Square Error (NRMSE) for the Ambae single-run (black line), ensemble mean (red line), and ensemble median (blue line). The vertical dashed line marks the instant of the snapshot shown in **Figure 1**. Symbols indicate the hourly AHI retrievals. **(B)** Same but with the source term given by a data insertion mechanism. In this case, the ensemble is defined by perturbing only the height and thickness of the injected cloud as indicated in **Table 4**. Plots on the same vertical scale.

substantial co-located emissions of $SO_2$ at 15 km a. v.l. in the range of 300 kt for the two phases according to GOME-2 satellite images (Pardini et al., 2017).

To show how ensemble ash simulations can be validated at high temporal resolution with qualitative ash cloud observations, we use satellite data collected from the SEVIRI instrument aboard Meteosat-10. Following the ash detection method presented in Appendix A of Prata et al. (2021), we generated binary (ash/no ash) fields at 1 h time-steps from 22 April at 23:00 UTC to 26 April at 23:00 UTC within a domain from 0–75°W to 15–55°S. We did not consider quantitative retrievals for this eruption as Calbuco is located outside of the SEVIRI field of view, which meant that many of the pixels detected as ash at the beginning of the eruption were associated with high satellite zenith angles ( > 75°) where retrievals can be unreliable. On the other hand, thickness measurements of fallout deposits from the 22–23 April 2015 eruption of Calbuco volcano were reported at 163 sites by Van Eaton et al. (2016) within a radius of 500 km. Romero et al. (2016) used thickness measurements to reconstruct the fallout deposit distribution by hand-drawing the corresponding isopach maps. A remarkable feature of the distal deposit is the presence of a secondary thickness maximum in the region around Junín de los Andes and Piedra del Aguila (Argentina, around 300 km downwind), indicating the occurrence of a complex plume dynamics involved during the eruption. Here, two independent deposit datasets are used to validate the Calbuco simulations: i) the deposit contours (isopachs) generated by Romero et al. (2016) for 0.1, 0.5, 1 and 2 mm (Van Eaton, personal communication) and, ii) the deposit point thickness at 159 sites reported by Van Eaton et al. (2016). Note that ambiguous data from 4 sites were removed from the original dataset.

For the Calbuco case, the ensemble reference run was configured with 20 tephra bins ranging in size from $\Phi = -2$ (4 mm) to $\Phi = 7$ (8 $\mu$m) and including one bin of aggregates. The plume source term consists of 2 phases lasting 1.5 and 6 h respectively, with a Suzuki vertical profile ($A = 5$, $\lambda = 3$) reaching 16 km a.s.l. and a total emitted mass of $6 \times 10^{11}$ kg. The 64-member ensemble was built by perturbing the most relevant source, granulometry and wind parameters as shown in **Table 5**. As for the previous Ambae case, the model grid resolution is $0.05^o$ in the horizontal and 250 m in the vertical, with the top of the computational domain placed at 20 km a.s.l. An ensemble with 64 members was defined by perturbing the starting time of the phases (±1 h), its duration (±1 h), the plume height $H$ (±2 km), the dimensionless Suzuki parameters $A$ (±3) and $\lambda$ (±2), the mean of the particle size distribution $\Phi_m$ (±1), and the size (±100 $\mu$m) and density (±100 kg/m$^3$) of the aggregates.

**Figure 6** compares single-run and ensemble-based deterministic runs at 159 deposit observation points that span almost 4 orders of magnitude in tephra thickness. On a point-by-point basis, the ensemble mean run reduces the differences with observations in 107 out of 159 points (67%), whereas the single-run reference still gives a closer fit in 52 points (33%). In contrast, the ensemble median can only improve on 64 points (40%), outperforming the reference run values only in the proximal (**Figure 6B**). In terms of overall NRMSE, the ensemble mean gives 0.11 as opposed to a 0.13 for the other two deterministic options, *i.e.* a 16% of overall improvement (**Table 6**).

In addition to the deposit points, the deposit isopach contours provide a second dataset for deposit validation based on generalised categorical metrics (see **Table 2**). **Figure 7** shows the different deterministic forecast contours compared with the 0.1, 0.5, 1, and 2 mm isopachs reported by Romero et al. (2016), characteristic of intermediate (few hundreds of km) to more proximal (up to around 100 km) distances to source. On the other hand, **Figure 8** shows the probabilistic counterpart, with the ensemble probability contours giving the probability to exceed each corresponding isopach value. The resulting values for generalised metrics and Brier score are reported in **Table 7**, which includes also an additional more proximal contour of 4 mm (not shown in the previous Figures). For deterministic

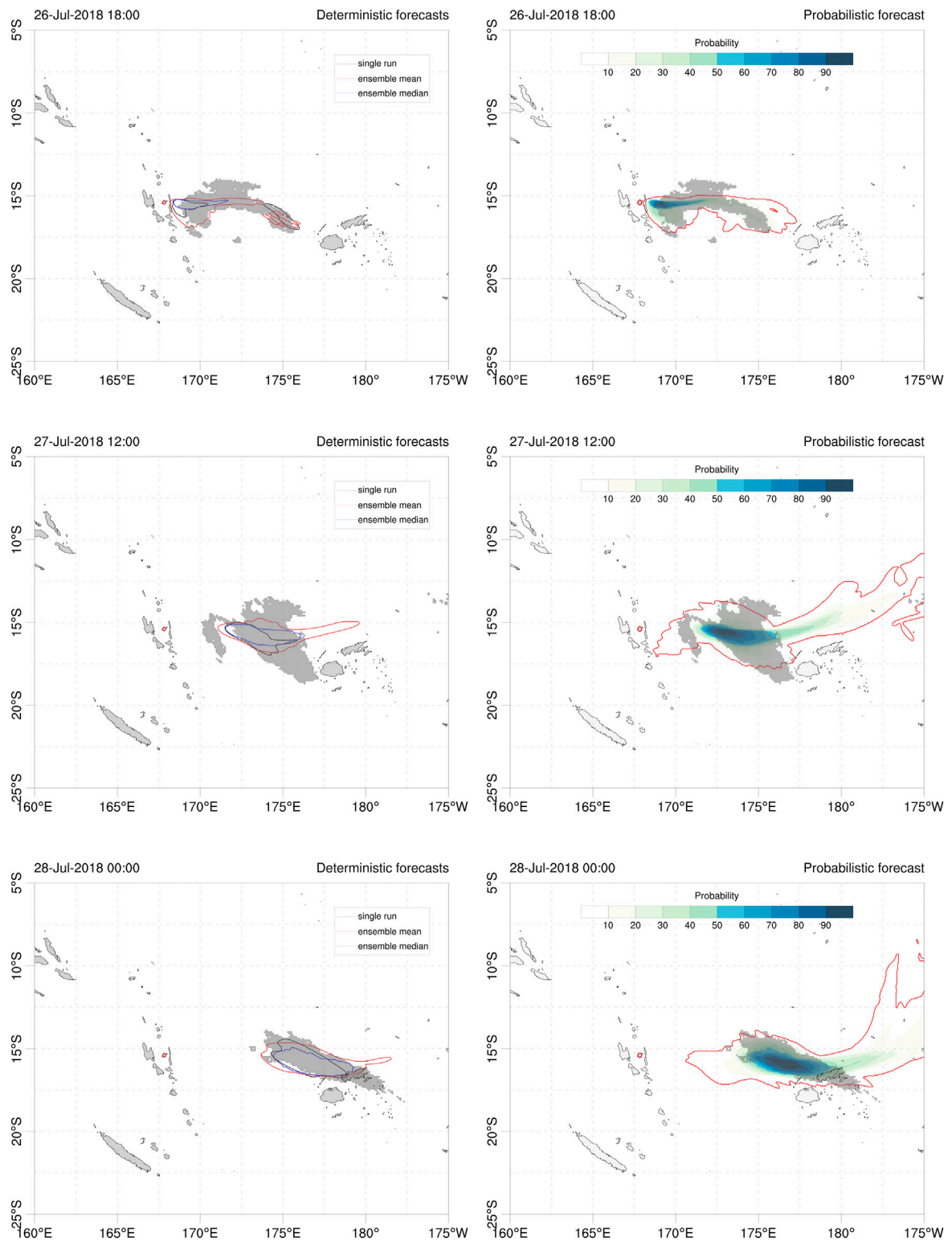


**FIGURE 3 |** Contours of 20 DU $SO_2$ column mass for deterministic **(left)** and probabilistic **(right)** Ambae forecasts at three different instants; 26 July at 18:00UTC **(top)**, 27 July at 12:00 UTC **(middle)** and 28 July at 00:00UTC **(bottom)**. In the probabilistic approach, contours give the probability (in %) to exceed 20 DU. The outer red contour indicates the 1.56% (1/64) probability. The grey shaded area shows the corresponding 20 DU from AHI retrievals. Red circle shows the location of Ambae volcano.

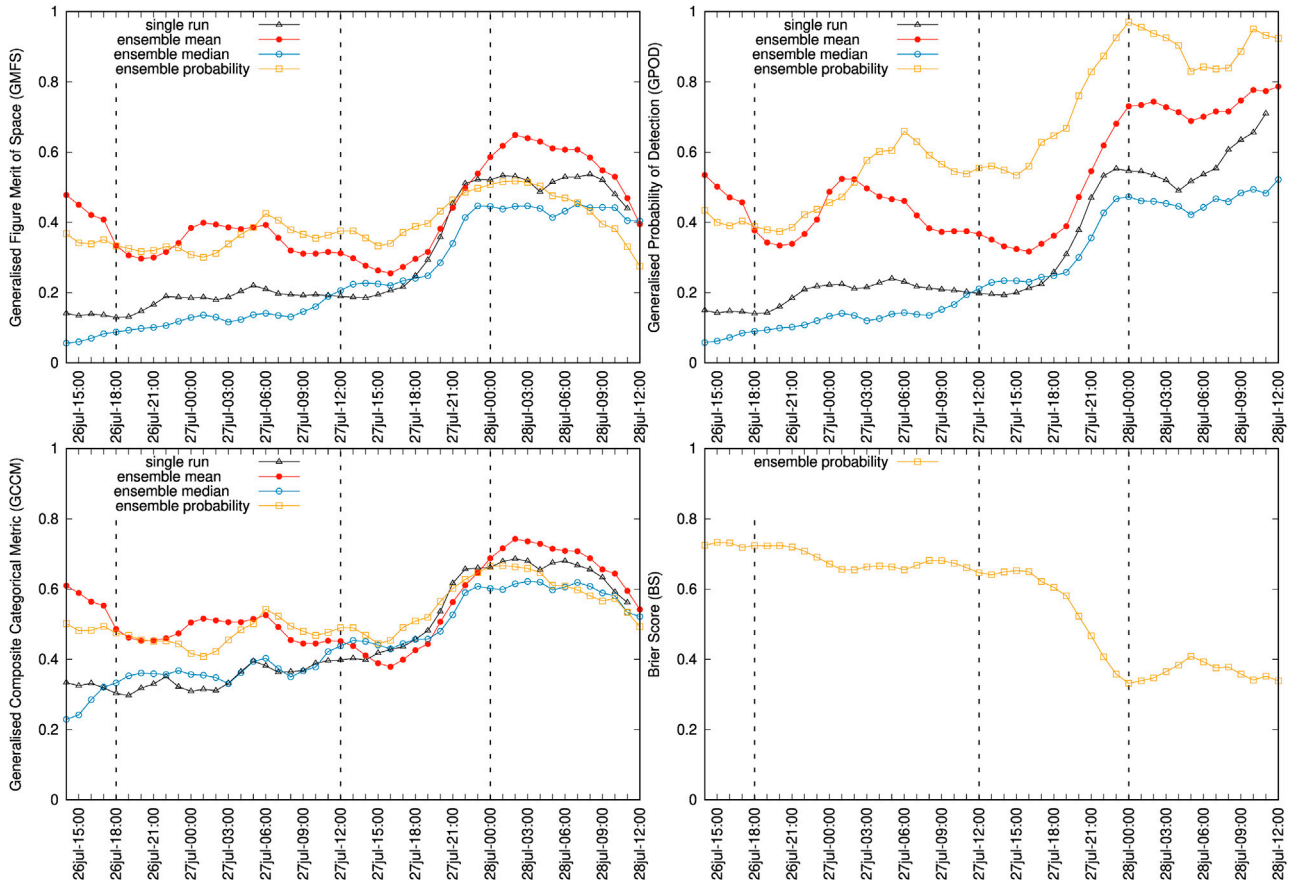


**FIGURE 4 |** Time series of generalised categorical metrics for deterministic (single run and ensemble-based) and probabilistic Ambae forecasts using the 20 DU $SO_2$ column mass contours. Plots show GFMS **(top left)**, GPOD **(top right)**, GCCM (bottom left) and BS **(bottom right)**. Symbols indicate the instants of the AHI retrievals. The three vertical dashed lines mark the instants of the snapshots shown in **Figure 3**. Note that for the BS only the probabilistic option applies.

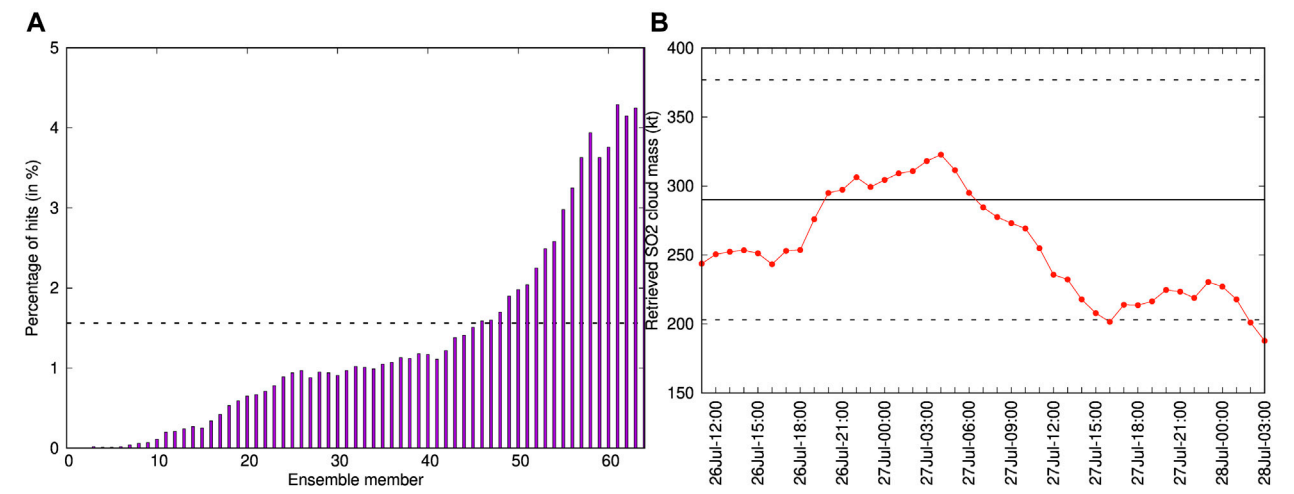


**FIGURE 5 | (A)** Observations rank histogram (Talagrand diagram) for the 64-member Ambae ensemble run. The horizontal dashed line at 1/64 = 1.56% indicates a perfectly consistent forecast, with all its members being equally represented against observations. **(B)** time series of $SO_2$ AHI retrieved cloud mass. The solid horizontal line at 290 kt shows the reference run and the dashed lines indicate the ±30% ensemble spread in emission rate.

**TABLE 5 |** Model setup for the April 22, 2015 single-run and ensemble-based (64 members) Calbuco tephra simulations.

| | | Single-run (1 member) | Ensemble-run (64 members) |
|---|---|---|---|
| Source term | Phase 1 start time | 22 April 21:00 UCT | perturbation range ±1 h |
| | Phase 1 duration | 1.5 h | perturbation range ±1 h |
| | Phase 2 start time | 23 April 04:00 UCT | perturbation range ±1 h |
| | Phase 2 duration | 6.0 h | perturbation range ±1 h |
| | column height $H$ | 16 km a.s.l. (both phases) | perturbation range ±2 km |
| | Suzuki parameter $A$ | 5 | perturbation range ±3 |
| | Suzuki parameter $\lambda$ | 3 | perturbation range ±2 |
| | eruption rate $\dot{M}$ | estimated from height [(1)] | perturbed through $H$ |
| | erupted mass | $6 \times 10^{11}$kg (2 phases) | perturbed through $\dot{M}$ and duration |
| Granulometry | Gaussian $\Phi_m$ | $\Phi_m = 4$ | perturbation range ±1 |
| | Gaussian $\sigma_\Phi$ | $\sigma_\Phi = 1.5$ | same |
| | upper bin size | $\Phi = -2$ (4 mm) | same |
| | lower bin size | $\Phi = 7$ (8 $\mu$m) | same |
| | bin interval | $0.5\Phi$ | same |
| Aggregates | size | 300 $\mu$m | perturbation range ±100 $\mu$m |
| | density | 400 kg/m$^3$ | perturbation range ±100 kg/m$^3$ |
| | fraction | 25% | same |
| Model grid | horizontal resolution | $0.05^o$ | same |
| | vertical resolution | 250 m | same |
| | domain top | 20 km | same |
| | Meteorological data | ERA5 (137 model levels) | winds [(2)] perturbed by ± 20% |

[(1)] *Parameterisation as in Degruyter and Bonadonna (2012).*
[(2)] *Horizontal wind components are perturbed globally (same perturbation in all grid cells).*

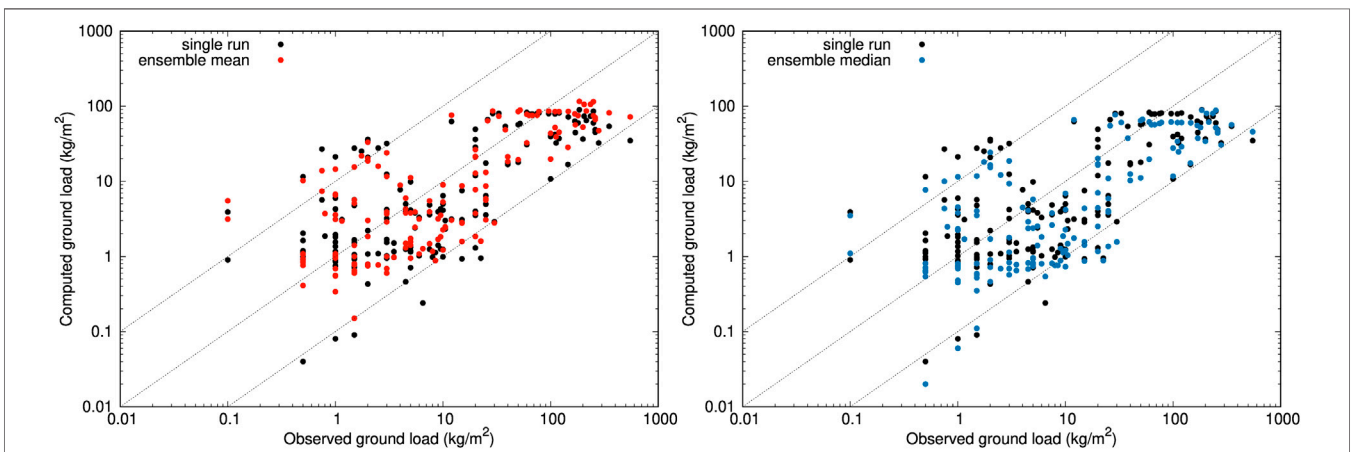


**FIGURE 6 |** Validation of Calbuco runs in 159 deposit points. Deposit thicknesses are converted to deposit loads (kg/m$^2$) assuming an averaged density of 1,000 kg/m$^3$. Left: single-run (black points) versus ensemble mean (red points). Right: single-run (black points) versus ensemble median (blue points). For reference, the three dashed lines show the perfect fit and the 10 model over and under-estimation bounds. The resulting global values of the NRMSE are reported in **Table 6**.

**TABLE 6 |** Validation of the April 22, 2015 Calbuco simulations with deposit thickness at scattered deposit points. Percentage means the fraction of points that reduce differences with observations with respect to the reference single-run. Best values highlighted in green.

| Metric | Deterministic single-run | Deterministic ensemble-mean | Deterministic ensemble-median |
|---|---|---|---|
| NRMSE | 0.13 | 0.11 | 0.13 |
| Percentage | — | 67% | 40% |

approaches, the ensemble mean clearly outperforms the reference run and the ensemble median (with the only exception of GFAR) across all distances. However, best overall results are obtained by probabilistic forecasts, particularly for GFMS and GPOD. In terms of the composite metric (GCCM), the ensemble mean is slightly better in the distal and the probabilistic in the proximal but, again, it is not clear which of these two options performs better.

Finally, the Calbuco ash cloud can also be validated with satellite imagery. Given the limitations of the dataset (as

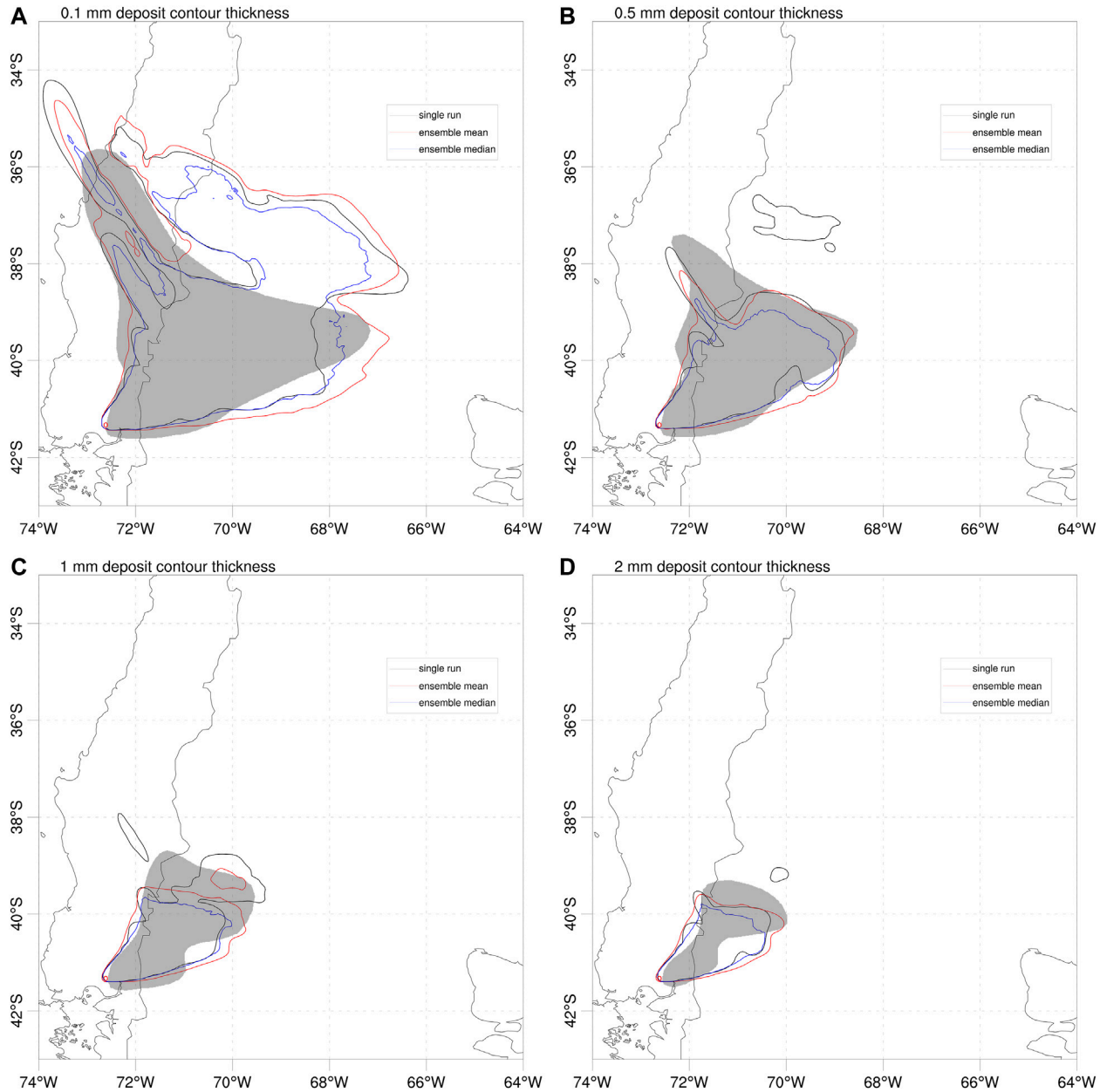


**FIGURE 7 |** Validation of Calbuco deterministic forecasts using deposit isopach contours of 0.1, 0.5, 1, and 2 mm. Model results for single-run (black line), ensemble mean (red line) and ensemble median (blue line). Grey-filled areas show the corresponding isopachs estimated by Romero et al. (2016) from extrapolation of deposit point measurements. Red circle shows the location of Calbuco volcano. The resulting values of generalised categorical metrics are reported in **Table 7**.

explained above) we do not consider ash retrievals as reliable and use the SEVIRI ash detection option instead. **Figures 9**, **10** show, respectively, snapshots of deterministic and probabilistic cloud mass contours (0.1 g/m$^2$ is assumed as a detection threshold) and time series of generalised categorical metrics. Model to observations miss-matches are more evident than for the Ambae case, partly due to the aforementioned reasons. However, similar conclusions can be extracted about the improvements in the ensemble mean and probabilistic cases. Again, the ensemble median (blue curves) worsens the single-run forecast skills.

## 5 SUMMARY AND DISCUSSION

The last version release (v8.1) of FALL3D allows configuring, running, post-processing and eventually validating ensemble-based forecasts in a single embarrassingly parallel workflow.

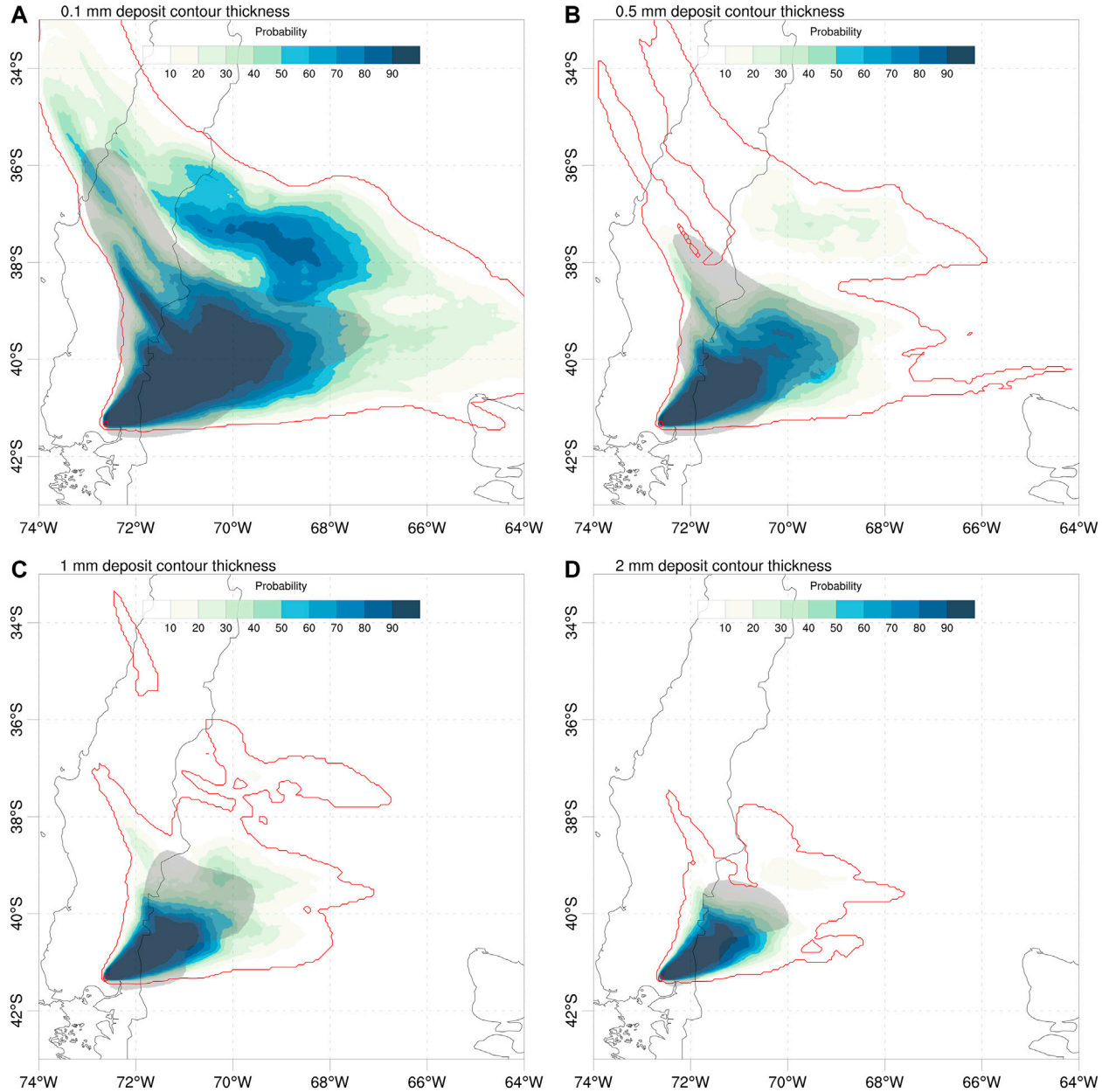


**FIGURE 8 |** Validation of Calbuco probabilistic forecasts with deposit isopach contours. Color contours give the model probability (in %) for deposit thickness to exceed 0.1, 0.5, 1, and 2 mm. Grey-filled areas show the corresponding isopachs estimated by Romero et al. (2016) from extrapolation of deposit point measurements. The outer red contour indicates the 1.56% (1/64) probability. Red circle shows the location of Calbuco volcano. The resulting values of generalised categorical metrics and Brier Score (BS) are reported in **Table 7**.

The ensemble runs, built from perturbing the most uncertain input parameters of a reference ensemble member, can furnish an array of deterministic forecasts with an associated uncertainty and/or probabilistic products based on the occurrence (or not) of certain exeedance or threshold conditions. Different types of metrics can be considered in FALL3D-8.1 for model validation (see **Table 2**), including novel categorical metrics resulting from the generalisation to probabilistic scenarios of classic geometric-based indicators (FMS, POD, FAR, etc). The skills of the ensemble-based modelling approaches have been compared against single-runs (and among them) using different types of observations. On one hand, satellite retrievals of cloud mass have been considered for validation of the July 2018 Ambae $SO_2$ clouds (**Table 4**). On the other, tephra deposit thickness observations at 159 locations and resulting deposit isopach contours have been used, together with satellite ash cloud detection, *i.e.* yes/no ash flagged pixels, for the April 2015 Calbuco eruption (**Table 5**). An ensemble of 64 members with a model spatial resolution of 0.05$^o$

**TABLE 7 |** Validation of the April 22, 2015 Calbuco simulations with deposit isopach contours from Romero et al (2016). Five deposit isopach values of 0.1, 0.5, 1, 2, and 4 mm are considered. Best values for each metric and contour are highlighted in green. The Brier Score (BS) applies only to the probabilistic approach.

| Metric | Contour thickness (mm) | Deterministic single-run | Deterministic ensemble-mean | Deterministic ensemble-median | Probabilistic |
|---|---|---|---|---|---|
| GFMS | 0.1 | 0.41 | 0.47 | 0.47 | 0.40 |
| | 0.5 | 0.58 | 0.70 | 0.54 | 0.67 |
| | 1 | 0.56 | 0.60 | 0.45 | 0.62 |
| | 2 | 0.48 | 0.50 | 0.40 | 0.56 |
| | 4 | 0.26 | 0.24 | 0.21 | 0.40 |
| GFAR | 0.1 | 0.49 | 0.49 | 0.38 | 0.59 |
| | 0.5 | 0.18 | 0.07 | 0.02 | 0.30 |
| | 1 | 0.23 | 0.18 | 0.12 | 0.35 |
| | 2 | 0.34 | 0.36 | 0.33 | 0.43 |
| | 4 | 0.57 | 0.64 | 0.60 | 0.58 |
| GPOD | 0.1 | 0.69 | 0.86 | 0.67 | 0.96 |
| | 0.5 | 0.67 | 0.72 | 0.55 | 0.96 |
| | 1 | 0.68 | 0.68 | 0.48 | 0.95 |
| | 2 | 0.64 | 0.70 | 0.51 | 0.98 |
| | 4 | 0.41 | 0.41 | 0.32 | 0.96 |
| GCCM | 0.1 | 0.53 | 0.61 | 0.58 | 0.59 |
| | 0.5 | 0.69 | 0.78 | 0.69 | 0.77 |
| | 1 | 0.67 | 0.70 | 0.60 | 0.74 |
| | 2 | 0.59 | 0.61 | 0.52 | 0.70 |
| | 4 | 0.36 | 0.33 | 0.31 | 0.59 |
| BS | 0.1 | — | — | — | 0.46 |
| | 0.5 | — | — | — | 0.30 |
| | 1 | — | — | — | 0.30 |
| | 2 | — | — | — | 0.33 |
| | 4 | — | — | — | 0.46 |

was considered in both cases. Main findings from these two applications can be summarised as follows:

- For ensemble-based deterministic forecasts, the ensemble mean gives the overall best scores for all typologies of datasets considered. However, the probabilistic approach also gives very similar results in terms of generalised categorical metrics. No conclusion can be extracted about which is "the best" option among these two but, clearly, both outperform the single-run reference run. Note that, in general, a gain in the ensemble-based approaches can be expected when some single-run inputs are uncertain. However, a consistent outperform cannot be guaranteed a priori as a well-chosen single-value run set with accurate "true" values is expected to outperform the ensemble mean.
- For the Ambae case, ensemble-based deterministic approaches improved the single-run time series of the quantitative NRMSE metric by a factor of 2-3 in most time instants (**Figure 2**). In terms of categorical metrics based on the 20 DU column mass contours, the ensemble-mean and the probabilistic approach also outperform substantially the single-run forecasts (**Figure 4**). This is not true for the ensemble median, which worsens all metrics, and most notably the probability of detection (GPOD).
- For the Calbuco case, the ensemble mean improves the averaged NRMSE of the deposit points by a 16%, with better skills in 67% of the single points (**Figure 6** and **Table 6**). Considering the validation with deposit isopach contours from Romero et al. (2016) (**Table 7**), the ensemble mean also outperforms the reference run and the ensemble median (with the only exception of GFAR) across all range of distances. However, best overall results are obtained by probabilistic forecasts, particularly for the GFMS. Finally, validation of the Calbuco ash cloud with satellite detection data (**Figure 7**) compared against 0.1 g/m$^2$ column mass model contours yields similar conclusions to the Ambae case.

A relevant aspect in operational forecast contexts is to consider the computational overhead of ensemble-based runs and, linked to this, its feasibility in the context of urgent (super)-computing. The simulations shown here were run at the Skylake-Irene partition of the Joliot-Curie supercomputer using only 24 processors per ensemble member (*i.e.,* 1536 processors for the whole ensemble run in this particular machine). The total computing times were of 460 s (7.6 min) and 2,650 s (44 min) for the Ambae (1 bin, 48 h forecast window) and the Calbuco (20 bins, 72 h forecast window) cases respectively. In terms of time-to-solution and due to the embarrassingly parallel workflow, the ensemble runs only add a little penalty if computational capacity is provided. In fact, this is actually a good example of capacity

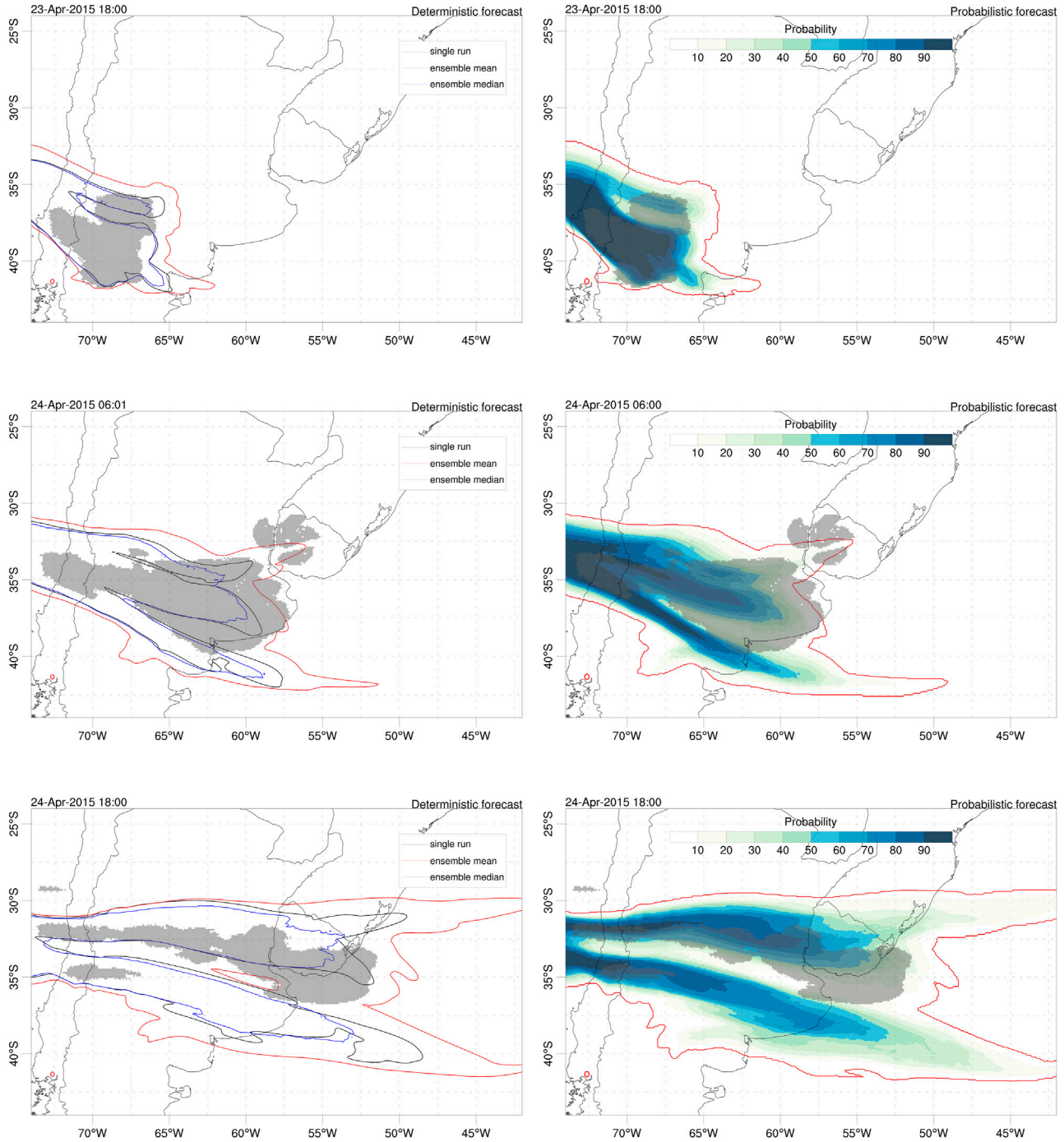


**FIGURE 9 |** Validation of Calbuco ash cloud with the satellite detection (SEVIRI ash flag) observation dataset. Model column mass contours of 0.1 g/m$^2$ for deterministic **(left)** and probabilistic **(right)** forecasts at three different instants; 23 April at 18:00UTC **(top)**, 24 April at 06:00 UTC **(middle)** and 24 April at 18:00UTC **(bottom)**. In the probabilistic plots, the outer red contour indicates the 1.56% (1/64) probability. The shaded areas show the contours encompassing SEVIRI ash flagged pixels. Red circle shows the location of Calbuco volcano.

computing, in which High Performance Computing (HPC) is needed to solve problems with uncertain inputs (entailing multiple model realisations) and constrains in computing time. On the other hand, FALL3D has been proved to have strong scalability (above 90% of parallel efficiency) up to several thousands of processors. Given that each ensemble member was run on only half computing node, times-to-solution could easily be lowered by at least one order of magnitude if enough computational capability is provided. Finally, it is worth mentioning that further study is needed on

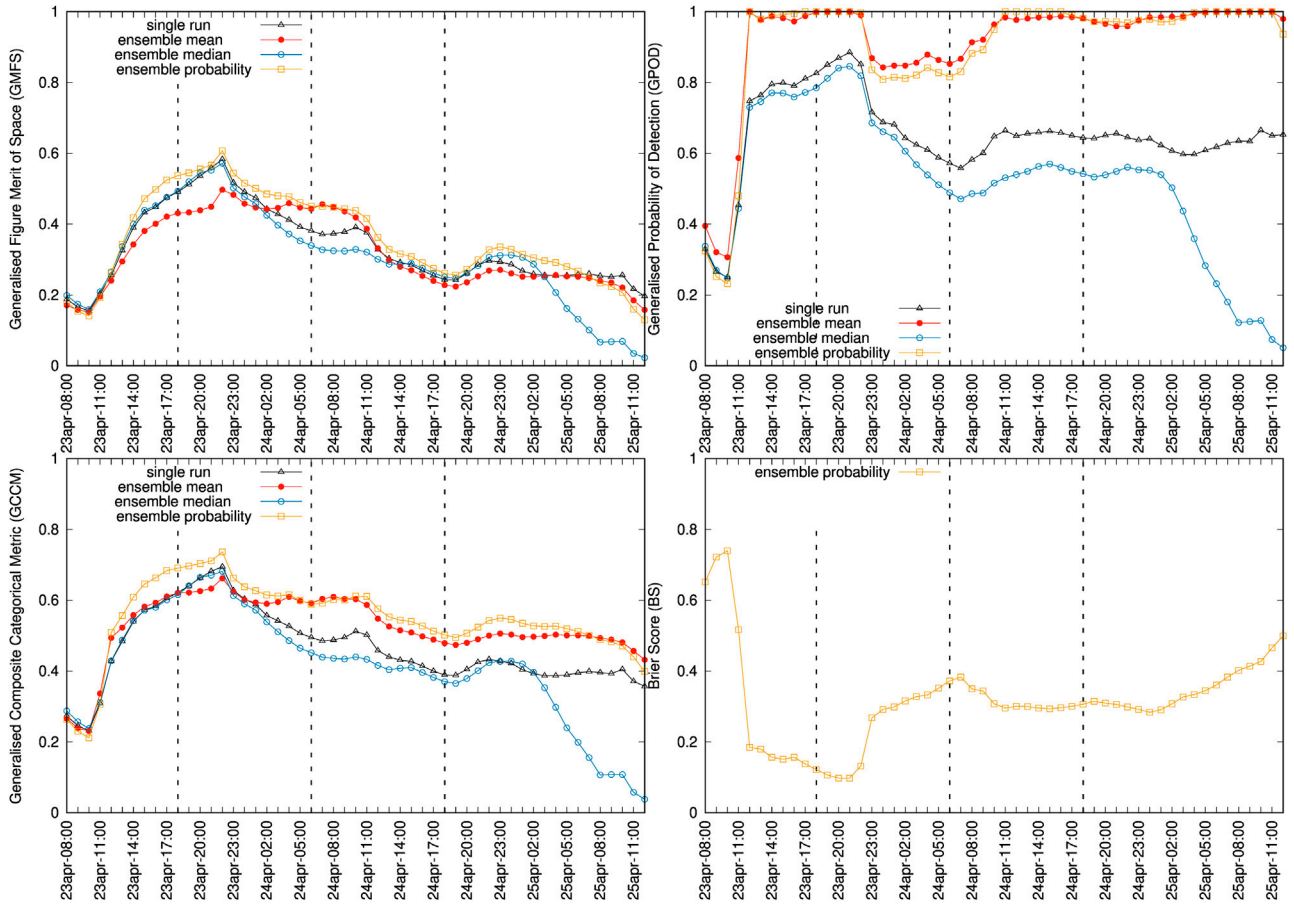


**FIGURE 10 |** Time series of generalised categorical metrics for deterministic (single run and ensemble-based) and probabilistic forecasts using the 0.1 g/m$^2$ ash column mass contours. Plots show GFMS **(top left)**, GPOD **(top right)**, GCCM **(bottom left)** and BS **(bottom right)**. Symbols indicate the instants of SEVIRI retrievals. The vertical dashed lines mark the three instants plot in **Figure 9**. Note that for the BS only the probabilistic option applies.

some aspects of the ensemble-based forecasts not explicitly addressed in this paper. Future work needs to consider:

- Optimal a priori configuration of the ensemble, including the number of members.
- Ensemble-based deterministic forecasts have been considered only for ensemble mean, ensemble median, and other percentiles. Future works will show how, in practice, it is possible to determine the best linear estimator compatible with the observational data. This optimal state should outperform the deterministic forecast presented here, which pertains to specific cases of linear combinations (single member or ensemble mean) or showed a poor performance when compared to linear estimators (ensemble median).
- Efforts to implement ensemble capabilities on FALL3D not only allow the improvement of forecast quality and to quantify model uncertainties, but also set the foundations for the incorporation of data assimilation techniques in the next release of FALL3D (v8.2). The use of ensemble Kalman filter methods, such as the Local Ensemble Transform Kalman filter (LETKF), will provide a further improvements in the quality of volcanic aerosol forecasts.

## DATA AVAILABILITY STATEMENT

The original contributions presented in the study are included in the article, further inquiries can be directed to the corresponding author.

## AUTHOR CONTRIBUTIONS

AF and LM have written the bulk of the FALL3D-8.1 code, including the implementation of the validation metrics. ATP conducted the satellite retrievals and planned the test cases. LM, AF have run model executions and validations. All authors have contributed to the writing of the text.

## FUNDING

This work has been partially funded by the H2020 Center of Excellence for Exascale in Solid Earth (ChEESE) under the Grant Agreement 823 844 and the multi-year PRACE Project Access “Volcanic Ash Hazard and Forecast” (ID 2019 215 114).

## ACKNOWLEDGMENTS

We acknowledge the use of the ERA5 Fifth generation of ECMWF atmospheric data from the Copernicus Climate Change Service; neither the European Commission nor ECMWF is responsible for the use made of the Copernicus Information and Data. We thank Alexa Van Eaton from USGS for providing us with digitalised Calbuco isopach contours. Finally, we acknowledge the constructive reviews from Larry Mastin and two reviewers.

## REFERENCES

Bauer, P., Thorpe, A., and Brunet, G. (2015). The Quiet Revolution of Numerical Weather Prediction. *Nature* 525, 47–55. doi:10.1038/nature14956

Beckett, F. M., Witham, C. S., Leadbetter, S. J., Crocker, R., Webster, H. N., Hort, M. C., et al. (2020). Atmospheric Dispersion Modelling at the London VAAC: A Review of Developments since the 2010 Eyjafjallajökull Volcano Ash Cloud. *Atmosphere* 11, 352. doi:10.3390/atmos11040352

Bonadonna, C., Folch, A., Loughlin, S., and Puempel, H. (2012). Future Developments in Modelling and Monitoring of Volcanic Ash Clouds: Outcomes from the First IAVCEI-WMO Workshop on Ash Dispersal Forecast and Civil Aviation. *Bull. Volcanol.* 74, 1–10. doi:10.1007/s00445-011-0508-6

Brier, G. W. (1950). Verification of Forecasts Expressed in Terms of Probability. *Mon. Wea. Rev.* 78, 1–3. doi:10.1175/1520-0493(1950)078<0001:vofeit>2.0.co;2

Costa, A., Macedonio, G., and Folch, A. (2006). A Three-Dimensional Eulerian Model for Transport and Deposition of Volcanic Ashes. *Earth Planet. Sci. Lett.* 241, 634–647. doi:10.1016/j.epsl.2005.11.019

Dabberdt, W. F., and Miller, E. (2000). Uncertainty, Ensembles and Air Quality Dispersion Modeling: Applications and Challenges. *Atmos. Environ.* 34, 4667–4673. doi:10.1016/S1352-2310(00)00141-2

Dacre, H. F., and Harvey, N. J. (2018). Characterizing the Atmospheric Conditions Leading to Large Error Growth in Volcanic Ash Cloud Forecasts. *J. Appl. Meteorol. Climatol.* 57, 1011–1019. doi:10.1175/JAMC-D-17-0298.1

Dare, R. A., Smith, D. H., and Naughton, M. J. (2016). Ensemble Prediction of the Dispersion of Volcanic Ash from the 13 February 2014 Eruption of Kelut, indonesia. *J. Appl. Meteorol. Climatol.* 55, 61–78. doi:10.1175/JAMC-D-15-0079.1

Degruyter, W., and Bonadonna, C. (2012). Improving on Mass Flow Rate Estimates of Volcanic Eruptions. *Geophys. Res. Lett.* 39, 16308. doi:10.1029/2012GL052566

Denlinger, R. P., Pavolonis, M., and Sieglaff, J. (2012a). A Robust Method to Forecast Volcanic Ash Clouds. *J. Geophys. Res.* 117, 1–10. doi:10.1029/2012JD017732

Denlinger, R. P., Webley, P., Mastin, L. G., and Schwaiger, H. F. (2012b). "A Bayesian Method to Rank Different Model Forecasts of the Same Volcanic Ash Cloud," in *Lagrangian Modeling of the Atmosphere*. 2 edn (American Geophysical Union), Chap. 24, 200. Geophysical Monograph Series. doi:10.1029/2012GM001249

Folch, A. (2012). A Review of Tephra Transport and Dispersal Models: Evolution, Current Status, and Future Perspectives. *J. Volcanol. Geothermal Res.* 235-236, 96–115. doi:10.1016/j.jvolgeores.2012.05.020

Folch, A., Costa, A., and Macedonio, G. (2009). Fall3d: A Computational Model for Transport and Deposition of Volcanic Ash. *Comput. Geosci.* 35, 1334–1342. doi:10.1016/j.cageo.2008.08.008

Folch, A., Mingari, L., Gutierrez, N., Hanzich, M., Macedonio, G., and Costa, A. (2020). FALL3D-8.0: a Computational Model for Atmospheric Transport and Deposition of Particles, Aerosols and Radionuclides - Part 1: Model Physics and Numerics. *Geosci. Model. Dev.* 13, 1431–1458. doi:10.5194/gmd-13-1431-2020

Fu, G., Lin, H. X., Heemink, A. W., Segers, A. J., Lu, S., and Palsson, T. (2015). Assimilating Aircraft-Based Measurements to Improve Forecast Accuracy of Volcanic Ash Transport. *Atmos. Environ.* 115, 170–184. doi:10.1016/j.atmosenv.2015.05.061

Fu, G., Prata, F., Lin, H. X., Heemink, A., Segers, A., and Lu, S. (2017). Data Assimilation for Volcanic Ash Plumes Using a Satellite Observational Operator: a Case Study on the 2010 Eyjafjallajökull Volcanic Eruption. *Atmos. Chem. Phys.* 17, 1187–1205. doi:10.5194/acp-17-1187-2017

Galmarini, S., Bianconi, R., Klug, W., Mikkelsen, T., Addis, R., Andronopoulos, S., et al. (2004). Ensemble Dispersion Forecasting-Part I: Concept, Approach and Indicators. *Atmos. Environ.* 38, 4607–4617. doi:10.1016/j.atmosenv.2004.05.030

Galmarini, S., Bonnardot, F., Jones, A., Potempski, S., Robertson, L., and Martet, M. (2010). Multi-model vs. Eps-Based Ensemble Atmospheric Dispersion Simulations: A Quantitative Assessment on the Etex-1 Tracer experiment Case. *Atmos. Environ.* 44, 3558–3567. doi:10.1016/j.atmosenv.2010.06.003

Harvey, N. J., Dacre, H. F., Webster, H. N., Taylor, I. A., Khanal, S., Grainger, R. G., et al. (2020). The Impact of Ensemble Meteorology on Inverse Modeling Estimates of Volcano Emissions and Ash Dispersion Forecasts: Grímsvötn 2011. *Atmosphere* 11, 1022. doi:10.3390/atmos11101022

Herlihy, M., Shavit, N., Luchangco, V., and Spear, M. (2020). *The Art of Multiprocessor Programming*. 2 edn. Elsevier. doi:10.1016/C2011-0-06993-4

Husslage, B. G. M., Rennen, G., van Dam, E. R., and den Hertog, D. (2011). Space-filling Latin Hypercube Designs for Computer Experiments. *Optim. Eng.* 12, 611–630. doi:10.1007/s11081-010-9129-8

Jolliffe, I. T., and Stephenson, D. B. (2012). *Forecast Verification: A Practitioner's Guide in Atmospheric Science*. 2 edn. Chichester, U.K.: John Wiley & Sons.

Kioutsioukis, I., Im, U., Solazzo, E., Bianconi, R., Badia, A., Balzarini, A., et al. (2016). Insights into the Deterministic Skill of Air Quality Ensembles from the Analysis of Aqmeii Data. *Atmos. Chem. Phys.* 16, 15629–15652. doi:10.5194/acp-16-15629-2016

Kloss, C., Sellitto, P., Legras, B., Vernier, J. P., Jégou, F., Venkat Ratnam, M., et al. (2020). Impact of the 2018 Ambae Eruption on the Global Stratospheric Aerosol Layer and Climate. *J. Geophys. Res. Atmos.* 125, e2020JD032410. doi:10.1029/2020JD032410

Levandowsky, M., and Winter, D. (1971). Distance between Sets. *Nature* 234, 34–35. doi:10.1038/234034a0

Madankan, R., Pouget, S., Singla, P., Bursik, M., Dehn, J., Jones, M., et al. (2014). Computation of Probabilistic hazard Maps and Source Parameter Estimation for Volcanic Ash Transport and Dispersion. *J. Comput. Phys.* 271, 39–59. doi:10.1016/j.jcp.2013.11.032

Malinina, E., Rozanov, A., Niemeier, U., Peglow, S., Arosio, C., Wrana, F., et al. (2020). Changes in Stratospheric Aerosol Extinction Coefficient after the 2018 Ambae Eruption as Seen by Omps-Lp and Echam5-Ham. *Atmos. Chem. Phys. Discuss.* 2020, 1–25. doi:10.5194/acp-2020-749

Marti, A., and Folch, A. (2018). Volcanic Ash Modeling with the Nmmb-Monarch-Ash Model: Quantification of Offline Modeling Errors. *Atmos. Chem. Phys.* 18, 4019–4038. doi:10.5194/acp-18-4019-2018

Marzano, F. S., Corradini, S., Mereu, L., Kylling, A., Montopoli, M., Cimini, D., et al. (2018). Multisatellite Multisensor Observations of a Sub-plinian Volcanic Eruption: The 2015 Calbuco Explosive Event in chile. *IEEE Trans. Geosci. Remote Sensing* 56, 2597–2612. doi:10.1109/TGRS.2017.2769003

Maurer, C., Arias, D. A., Brioude, J., Haselsteiner, M., Weidle, F., Haimberger, L., et al. (2021). Evaluating the Added Value of Multi-Input Atmospheric Transport Ensemble Modeling for Applications of the Comprehensive Nuclear Test-Ban Treaty Organization (Ctbto). *J. Environ. Radioactivity* 237, 106649. doi:10.1016/j.jenvrad.2021.106649

Mingari, L., Folch, A., Prata, A. T., Pardini, F., Macedonio, G., and Costa, A. (2021). Data Assimilation of Volcanic Aerosols Using Fall3d+pdaf. *Atmos. Chem. Phys. Discuss.* 2021, 1–30. doi:10.5194/acp-2021-747

Moussallam, Y., Rose-Koga, E., Koga, K., Medard, E., Bani, P., Devidal, J., et al. (2019). Fast Ascent Rate during the 2017-2018 Plinian Eruption of Ambae (Aoba) Volcano: a Petrological Investigation. *Contrib. Mineral. Petrol.* 174, 90. doi:10.1007/s00410-019-1625-z

Mureau, R., Molteni, F., and Palmer, T. N. (1993). Ensemble Prediction Using Dynamically Conditioned Perturbations. *Q. J. R. Meteorol. Soc.* 119, 299–323. doi:10.1002/qj.49711951005

Osores, S., Ruiz, J., Folch, A., and Collini, E. (2020). Volcanic Ash Forecast Using Ensemble-Based Data Assimilation: an Ensemble Transform Kalman Filter

Coupled with the FALL3D-7.2 Model (ETKF-FALL3D Version 1.0). *Geosci. Model. Dev.* 13, 1–22. doi:10.5194/gmd-13-1-2020

Pardini, F., Burton, M., Arzilli, F., La Spina, G., and Polacci, M. (2017). Satellite-derived SO2 Flux Time-Series and Magmatic Processes during the 2015 Calbuco Eruptions. *Solid Earth Discuss.* 2017, 1–25. doi:10.5194/se-2017-64

Pardini, F., Corradini, S., Costa, A., Esposti Ongaro, T., Merucci, L., Neri, A., et al. (2020). Ensemble-based Data Assimilation of Volcanic Ash Clouds from Satellite Observations: Application to the 24 December 2018 Mt. etna Explosive Eruption. *Atmosphere* 11, 359. doi:10.3390/atmos11040359

Plu, M., Scherllin-Pirscher, B., Arnold Arias, D., Baro, R., Bigeard, G., Bugliaro, L., et al. (2021). A Tailored Multi-Model Ensemble for Air Traffic Management: Demonstration and Evaluation for the Eyjafjallajökull Eruption in May 2010. *Nat. Hazards Earth Syst. Sci. Discuss.* 2021, 1–32. doi:10.5194/nhess-2021-96

Prata, A. J., Rose, W. I., Self, S., and O'Brien, D. M. (2004). "Global, Long-Term sulphur Dioxide Measurements from TOVS Data: A New Tool for Studying Explosive Volcanism and Climate," in *Volcanism and the Earths Atmosphere* (American Geophysical Union, AGU), 75–92. doi:10.1029/139GM05

Prata, A. T., Dacre, H. F., Irvine, E. A., Mathieu, E., Shine, K. P., and Clarkson, R. J. (2019). Calculating and Communicating Ensemble-based Volcanic Ash Dosage and Concentration Risk for Aviation. *Meteorol. Appl.* 26, 253–266. doi:10.1002/met.1759

Prata, A. T., Mingari, L., Folch, A., Macedonio, G., and Costa, A. (2021). FALL3D-8.0: a Computational Model for Atmospheric Transport and Deposition of Particles, Aerosols and Radionuclides - Part 2: Model Validation. *Geosci. Model. Dev.* 14, 409–436. doi:10.5194/gmd-14-409-2021

Reckziegel, F., Bustos, E., Mingari, L., Báez, W., Villarosa, G., Folch, A., et al. (2016). Forecasting Volcanic Ash Dispersal and Coeval Resuspension during the April-May 2015 Calbuco Eruption. *J. Volcanol. Geothermal Res.* 321, 44–57. doi:10.1016/j.jvolgeores.2016.04.033

Romero, J. E., Morgavi, D., Arzilli, F., Daga, R., Caselli, A., Reckziegel, F., et al. (2016). Eruption Dynamics of the 22-23 April 2015 Calbuco Volcano (Southern chile): Analyses of Tephra Fall Deposits. *J. Volcanol. Geothermal Res.* 317, 15–29. doi:10.1016/j.jvolgeores.2016.02.027

Scherrer, S. C., Appenzeller, C., Eckert, P., and Cattani, D. (2004). Analysis of the Spread-Skill Relations Using the ECMWF Ensemble Prediction System over Europe. *Wea. Forecast.* 19, 552–565. doi:10.1175/1520-0434(2004)019<0552:aotsru>2.0.co;2

Stefanescu, E. R., Patra, A. K., Bursik, M. I., Madankan, R., Pouget, S., Jones, M., et al. (2014). Temporal, Probabilistic Mapping of Ash Clouds Using Wind Field Stochastic Variability and Uncertain Eruption Source Parameters: Example of the 14 April 2010 Eyjafjallajökull Eruption. *J. Adv. Model. Earth Syst.* 6, 1173–1184. doi:10.1002/2014MS000332

Talagrand, O., Vautard, R., and Strauss, B. (1997). "Evaluation of Probabilistic Prediction Systems," in Workshop on Predictability, Shinfield Park, Reading, 20-22 October, 1997 (ECMWF), 1–26.

Van Eaton, A. R., Amigo, Á., Bertin, D., Mastin, L. G., Giacosa, R. E., González, J., et al. (2016). Volcanic Lightning and Plume Behavior Reveal Evolving Hazards during the April 2015 Eruption of Calbuco Volcano, chile. *Geophys. Res. Lett.* 43, 3563–3571. doi:10.1002/2016GL068076

Vidal, L., Nesbitt, S. W., Salio, P., Farias, C., Nicora, M. G., Osores, M. S., et al. (2017). C-band Dual-Polarization Radar Observations of a Massive Volcanic Eruption in South america. *IEEE J. Sel. Top. Appl. Earth Obs. Remote Sensing* 10, 960–974. doi:10.1109/JSTARS.2016.2640227

Vogel, H., Förstner, J., Vogel, B., Hanisch, T., Mühr, B., Schättler, U., et al. (2014). Time-lagged Ensemble Simulations of the Dispersion of the Eyjafjallajökull Plume over Europe with COSMO-ART. *Atmos. Chem. Phys.* 14, 7837–7845. doi:10.5194/acp-14-7837-2014

Zidikheri, M. J., Lucas, C., and Potts, R. J. (2017). Estimation of Optimal Dispersion Model Source Parameters Using Satellite Detections of Volcanic Ash. *J. Geophys. Res. Atmos.* 122, 8207–8232. doi:10.1002/2017JD026676

Zidikheri, M. J., Lucas, C., and Potts, R. J. (2018). Quantitative Verification and Calibration of Volcanic Ash Ensemble Forecasts Using Satellite Data. *J. Geophys. Res. Atmos.* 123, 4135–4156. doi:10.1002/2017JD027740

**Conflict of Interest:** The authors declare that the research was conducted in the absence of any commercial or financial relationships that could be construed as a potential conflict of interest.

frontiers in Earth Science

METHODS
published: 14 January 2022
doi: 10.3389/feart.2021.744655

# Workflows for Construction of Spatio-Temporal Probabilistic Maps for Volcanic Hazard Assessment

*Renette Jones-Ivey*[1]*, *Abani Patra*[2] *and Marcus Bursik*[3]

[1]Institute for Computational and Data Sciences, University at Buffalo, Buffalo, NY, United States, [2]Data Intensive Studies Center (DISC), Tufts University, Medford, MA, United States, [3]Center for Geohazards Studies, University at Buffalo, Buffalo, NY, United States

Probabilistic hazard assessments for studying overland pyroclastic flows or atmospheric ash clouds under short timelines of an evolving crisis, require using the best science available unhampered by complicated and slow manual workflows. Although deterministic mathematical models are available, in most cases, parameters and initial conditions for the equations are usually only known within a prescribed range of uncertainty. For the construction of probabilistic hazard assessments, accurate outputs and propagation of the inherent input uncertainty to quantities of interest are needed to estimate necessary probabilities based on numerous runs of the underlying deterministic model. Characterizing the uncertainty in system states due to parametric and input uncertainty, simultaneously, requires using ensemble based methods to explore the full parameter and input spaces. Complex tasks, such as running thousands of instances of a deterministic model with parameter and input uncertainty require a High Performance Computing infrastructure and skilled personnel that may not be readily available to the policy makers responsible for making informed risk mitigation decisions. For efficiency, programming tasks required for executing ensemble simulations need to run in parallel, leading to twin computational challenges of managing large amounts of data and performing CPU intensive processing. The resulting flow of work requires complex sequences of tasks, interactions, and exchanges of data, hence the automatic management of these workflows are essential. Here we discuss a computer infrastructure, methodology and tools which enable scientists and other members of the volcanology research community to develop workflows for construction of probabilistic hazard maps using remotely accessed computing through a web portal.

**Keywords: uncertainty quantification, volcanology, hazard mapping, volcanic hazard assessment, Pegasus Workflow Management System, ash cloud, pyroclastic flow**

OPEN ACCESS

***Edited by:***
*Sara Barsotti,*
*Icelandic Meteorological Office, Iceland*

***Reviewed by:***
*Warner Marzocchi,*
*University of Naples Federico II, Italy*
*Stuart Mead,*
*Massey University, New Zealand*

***Correspondence:**
*Renette Jones-Ivey*
*renettej@buffalo.edu*

***Specialty section:***
*This article was submitted to Geohazards and Georisks, a section of the journal Frontiers in Earth Science*

***Received:*** *20 July 2021*
***Accepted:*** *20 December 2021*
***Published:*** *14 January 2022*

***Citation:***
*Jones-Ivey R, Patra A and Bursik M (2022) Workflows for Construction of Spatio-Temporal Probabilistic Maps for Volcanic Hazard Assessment. Front. Earth Sci. 9:744655. doi: 10.3389/feart.2021.744655*

## 1 INTRODUCTION

Characterizing potential volcanic eruption hazard scenarios involves many factors. In many cases, potential scenarios have been encapsulated in hazard maps for particular volcanoes, some of which have been constructed using modern computational simulations of volcanic flows (Calder et al., 2015). Such maps can suffer from their static nature, being difficult to adapt to changing eruption situations, or unforeseen eruption scenarios. Use of computer simulations to construct the maps presents one pathway to readily updating them. Although deterministic simulation tools are available for modeling evolving or unforeseen volcanic hazard scenarios, including those that involve dangerous pyroclastic

flows and ash clouds (Stein et al., 2015; Takarada, 2017), in most cases, parameters and initial conditions for the governing equations will be poorly constrained and must be treated as random variables to be sampled (Dalbey, 2009). For the construction of hazard maps based on the resulting ensembles of deterministic computer runs, accurate outputs, obtained through careful consideration of input and parameter ranges, and propagation of the resulting uncertainty to output quantities of interest, are needed to properly estimate probabilities (Spiller et al., 2014; Bayarri et al., 2015). While there exist several current efforts at making simulation tools available online for use by volcanologists (Takarada et al., 2014; Woodhouse et al., 2021), none support the complexity required by the uncertainty quantification processes, thereby restricting access to such analysis to specialists reducing their routine use in effective hazard management.

Characterizing the output uncertainty due to parametric and input boundary value uncertainty simultaneously involves using ensemble based methods to fully explore the parameter and input spaces. Complex tasks, such as running thousands of instances of a deterministic model with parameter and input uncertainty, need to be well-defined and repetitive to make them good candidates for automation (Rohit et al., 2014). We have programmed a workflow of tasks, executing ensemble simulations of pyroclastic flows and ash clouds to run in parallel and analyze the simulations outputs, leading to twin computational challenges of managing large amounts of data and performing CPU intensive processing. The resulting flow of work requires complex sequences of tasks, interactions, and exchanges of data, hence automatic management of the workflow is essential to producing orderly, usable and timely output.

Here we discuss the computer workflow, which is based on a well-established scientific infrastructure (McLennan and Kennell, 2010), as well as a methodology that enables scientists and other members of the volcanology research community to construct conditional probabilistic hazard assessments given potential eruption scenarios at any volcano in the world. In exploring potential hazardous volcanic flows with models and computer simulations, we have designed the workflow to seek answers to questions such as "What is the probability of flow depth reaching a critical value at a particular location during a volcanic eruption?" or "What is the probability of having an ash cloud at a particular location within a specified height range following a volcanic eruption?" Such questions need to be explored by geoscientists and policy makers, often under short timelines during an evolving crisis, making it essential that the answers are available using the best science, but not requiring complicated and slow manual processes. With the workflows introduced herein, we facilitate timely answers to critical hazard analysis questions using tools to provide online access to automated workflows for volcanic hazard assessment.

# 2 MATERIALS AND METHODS

## 2.1 Hazard Map Workflow Architecture

Volcanic probabilistic hazard map workflow development requires expertise and collaboration between diverse volcanology research scientists and cyberinfrastructure experts. Scientific HUBs provide the perfect platform for fostering this collaboration. The VHub science HUB, provides an online resource for modeling and analysis in volcanology research and risk mitigation. To make volcanic hazard analysis easier for the end researcher to access, VHub portal based access to computational workflows for pyroclastic flows and ash clouds transports have been developed. These workflows are based on the Pegasus Workflow Management System (WMS) architecture which is integrated into the HUBzero framework. A high level overview of the underlying workflow architecture is shown in **Figure 1A**. In this section, details of the workflow architecture are described. In **Section 2.2**, two implementations of this workflow architecture are presented.

### 2.1.1 Computer Infrastructure Platform

VHub is hosted at the San Diego Supercomputer Center and is built on the HUBzero platform for Scientific Collaboration. An advantage of using the HUBzero platform is that users can launch software tools with a web browser without having to download, compile, or install code on local systems (McLennan and Kennell, 2010).

The VHub portals are accessible to the volcanological and meteorological community from anywhere in the world. The portals provide user-friendly access to the advanced scientific resources using a web browser. Using the portals, researchers and operational scientists can execute models of hazards from volcanic debris avalanches to atmospheric ash transport without direct participation of an array of computational scientists and computing professionals.

VHub's architecture consists of a database server and webserver; an execution host that runs software containers for computational tools; and middleware—software that coordinates the container sessions with user sessions (Sperhac et al., 2021). HUBzero System Administrators handle user accounts and interaction, including registering and subsequently authenticating users, controlling access to tools and other hosted resources.

### 2.1.2 Workflow Tools

Users interface with VHub by running computational tools. When a user runs a computational tool on VHub, a virtual container is started on the execution host. Each tool container has been configured to support specific computational needs, such as memory or disk space. Additional execution host servers may be deployed to scale up either the number of users supported, the resource footprint for tool sessions, or both. Finally, tools needing additional resources or parallel execution can submit jobs to a remote host's compute cluster. VHub enables members of the volcanology research community to deploy hazard map workflow tools that a user can interact with. VHub tools are maintained *via* a development lifecycle which guides users through a framework for publishing their tools on VHub; subversion control, testing, verification and review by domain scientists and HUBzero System Administrators prior to publication on the VHub website (Sperhac et al., 2021).

An important consideration for the development of a hazard map workflow tool is to abstract the complexity of

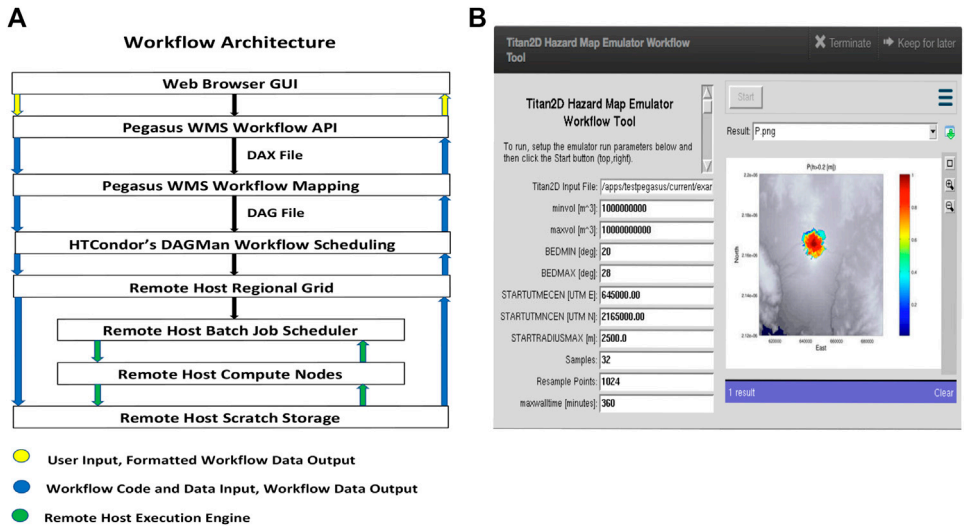


**FIGURE 1 | (A)** Workflow using multiple hardware and system software units, and **(B)** graphical user interface of workflow for a hazard map based on Titan2D tool.

the workflow from users. A user friendly graphical user interface (GUI) (**Figure 1B**) gives the user control over each analysis, and hides the complexities of the workflow implementation from the user, such as controlling the bounds of uncertainty for each simulation run. The GUI also provides the user with easy access to output of workflows. Ultimately, the results could provide a path forward for the routine construction of probabilistic, spatio-temporal pyroclastic flow and ash cloud hazard maps.

### 2.1.3 Workflow Management

The Pegasus Workflow Management System (WMS) (Deelman et al., 2015) provides the structured platform required for implementing the workflows. The Pegasus WMS automates and manages the execution of the jobs required to run the workflows, including staging the jobs, distributing the work, submitting the jobs to run on a remote host, as well as handling data flow dependencies and overcoming job failures. The integration of the Pegasus WMS into the HUBzero framework has brought the power of automated workflows to many more users (McLennan et al., 2015). The Pegasus WMS consists of Pegasus and its workflow engine, the directed acyclic graph manager (DAGMan) within HTCondor (Couvares et al., 2007; Deelman et al., 2015). HTCondor is a workload scheduling system for computational jobs. HTCondor provides a job queuing mechanism and resource monitoring capabilities. DAGMan is a meta-scheduler for HTCondor, which is a service for executing multiple jobs with dependencies among them; it manages dependencies between jobs at a higher level than does the HTCondor scheduler (University of Wisconsin–Madison Center for High Throughput Computing, 2021). Pegasus uses DAGMan and the rest of the HTCondor stack to execute the workflows (**Figure 1A**).

Pegasus workflows are described in an abstract format *via* abstract workflow (DAX) files which are directed acyclic graphs in XML format. The abstract format means that the description does not include data and software locations; these are looked up at planning time, enabling portability of the workflows. A DAX generating Application Programming Interface (API) is used to create the DAX file for a workflow. For the workflows described herein, a python script is invoked. The DAX file provides the primary input to Pegasus and defines the jobs required for executing the workflow, the job dependencies, and the input and output files for each job. With the HUBzero submit tool, a simple submit command verifies that the jobs pass HUBzero security checks and dispatches the workflow to the Pegasus WMS for execution (McLennan et al., 2015).

The Pegasus WMS is flexible and supports a wide variety of execution environments (Deelman et al., 2015). For the Titan2D Hazard Emulator and Bent-Hysplit Workflow tools, Pegasus jobs are submitted to the University at Buffalo Center for Computational Research's (CCR's) generally accessible academic compute cluster, UB-HPC, *via* a UB-HPC regional grid (Neeman et al., 2010). Pegasus takes the abstract description and determines where to execute the jobs and where to access the data. Pegasus augments the DAX with data movement directives and compiles a directed acyclic graph (DAG). The resulting DAG is then given to HTCondor's DAGMan. DAGMan, as directed by the DAG, orders the jobs according to their dependencies, and submits the jobs ready for execution to the remote host, UB-HPC. At the remote host, the SLURM (Simple Linux Utility for Resource Management) Workload Manager provides the framework for queuing jobs, allocating compute nodes, and starting the execution of jobs. A challenge for executing the Pegasus jobs on VHub is the limited home disk space each user has. To overcome this challenge, Pegasus scratch directories are located in CCR's high performance global

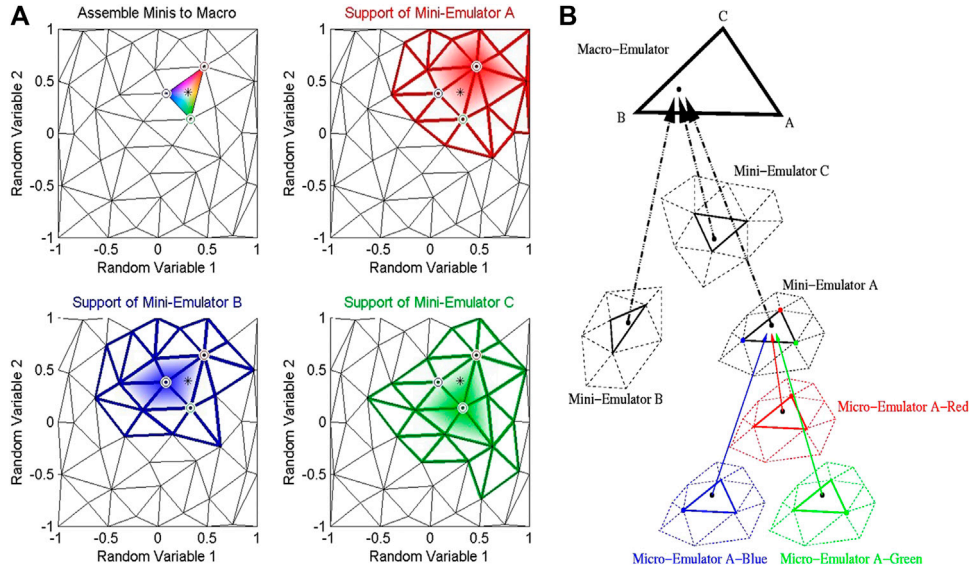


**FIGURE 2 |** Example mini-emulators. **(A)** Tessellation of the input parameter space showing micro-emulator support of mini-emulators. **(B)** Assembly of the hierarchy of emulators to produce the macro-emulator (Dalbey, 2009).

**TABLE 1 |** Titan2D hazard map workflow parallelization strategy.

| | |
|---|---|
| Step 1 | Create required parameters for evaluating sample uncertainty using Latin Hypercube Sampling. |
| Step 2 | Modify the Titan2D Input File for each sample. Run Titan2D in parallel for each sample. |
| Step 3 | Down sample the flow depth (pile height) records output by Titan2D in parallel. Requires all output from the previous step for each sample. |
| Step 4 | Construct the macro-emulator and mini-emulators in parallel. Requires all output from the previous step. |
| Step 5 | Setup for re-sampling the macro-emulator and create the initial probabilistic hazard map. Requires all output from the previous step. |
| Step 6 | Aggregate mini-emulators into a macro-emulator in parallel and re-sample the macro-emulator to create the conditional probabilistic hazard map. Requires all output from the previous step. |

scratch space which is accessible from all UB-HPC compute nodes.

System level implementation details for Pegasus, including setting up the mapping *via* the site and transformation catalogs that Pegasus requires, are abstracted from workflow developers; Steven Clark, HUBzero, and Steven Gallo, CCR, set up the Pegasus WMS lower level interfaces for the workflows.

When a SLURM job execution completes, the final status of the finished job is returned to Pegasus. If the final status indicates a job failure, Pegasus will retry re-executing the job. For the current VHub Pegasus implementation, Pegasus will retry to execute a failed job no more than two times.

A working directory for either the Titan2D Hazard Map Emulator or Bent-Hysplit Workflow tool is created in the user's VHub home folder's data/sessions directory when the tool is launched. Workflow input files generated by the GUI are stored in this work directory. When a workflow execution is started, input files required by the workflow and specified in the DAX, are uploaded by Pegasus to the Pegasus scratch directory. When a workflow's execution is complete, output files generated by the workflow and specified in the DAX, are downloaded by Pegasus from the Pegasus scratch directory to the tool's work directory. In addition, Pegasus status and analysis information is returned in a file called pegasus.analysis. If workflow errors occurs, the pegasus.analysis file will contain details for the errors. For the Bent-Hysplit Workflow tool, output files are moved from the work directory to a dated run created when the workflow's execution is started.

## 2.2 Hazard Map Workflow Tools

Two tools were developed using the computer infrastructure and methodology outlined in the previous section. Both tools are currently published on the VHub website, these are the Titan2D Hazard Map Emulator Workflow Tool for Volcanic Pyroclastic Flow Transport Hazards and the Bent-Hysplit Workflow Tool for Volcanic Ash Cloud Transport Hazards. In this section, details of these workflow tools are described.

### 2.2.1 Volcanic Mass Flow Hazard Map

Titan2D (Patra et al., 2005) is a computer program for simulating granular avalanches over digital elevation models of natural terrain. The program is designed for simulating geological mass flows such as pyroclastic flows, debris flows, debris avalanches and landslides. Titan2D combines numerical

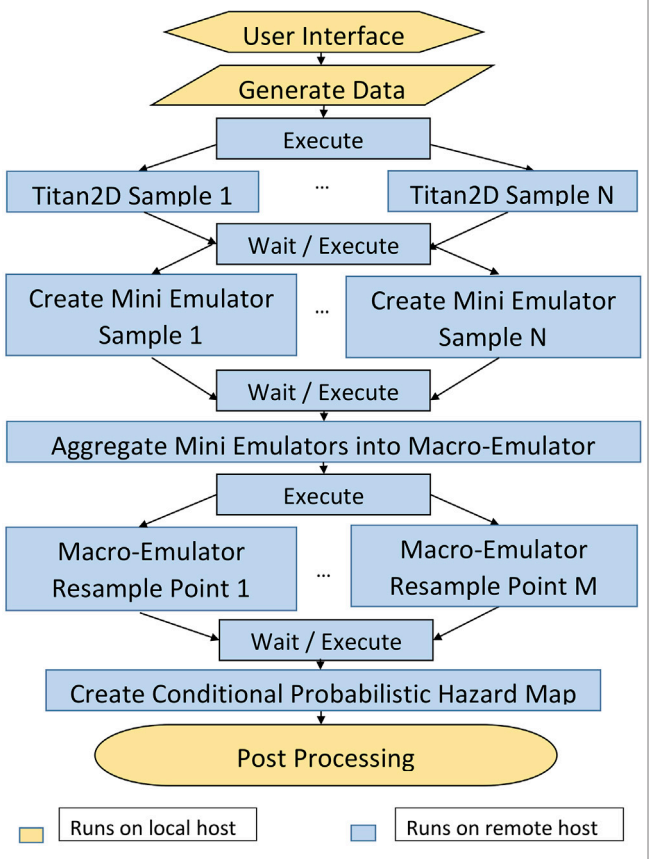


**FIGURE 3 |** Titan2D hazard map workflow tasks for pyroclastic flows and other surficial mass flows. Pegasus monitors the completion of task executions by determining when required output files are created by the tasks.

simulations of a flow with digital elevation data of natural terrain supported through a Geographical Information System (GIS) interface.

The Titan2D program is based upon a depth-averaged model of an incompressible continuum, a "shallow-water" granular flow. The conservation equations for mass and momentum are solved with different rheological properties modeling the interactions between the grains of the medium and one another, an interstitial fluid or the basal surface. The resulting hyperbolic system of equations is solved using a parallel, adaptive mesh, Godunov scheme.

The shallow-water model conservation equations solved by Titan2D are given by:

$$U_t + F(U)_x + G(U)_y = S(U) \tag{1}$$

where, $U$ is a vector of conserved state variables, $F$ is a vector of mass and momentum fluxes in the $x$-direction, $G$ is a vector of mass and momentum fluxes in the $y$-direction, and, $S$ is a vector of driving and dissipative force terms.

The Titan2D tools solve **Eq. 1** numerically for flow depth and a depth-averaged velocity at every grid point in the mesh. To run Titan2D, a digital elevation map (DEM) of the region of interest is read into the computer, together with flow-specific parameters such as the material friction angles, initial volume, initial direction and initial velocity.

For the construction of the Titan2D hazard map, the flow-specific parameters and the DEM may be poorly characterized, and should be viewed as uncertain (Stefanescu et al., 2012).

One way to quantify the uncertainty is to use Monte Carlo type sampling, which requires multiple runs of the Titan2D simulator. Each run of Titan2D takes 20 min or more on a single processor, so Monte Carlo type sampling is considered too expensive.

To make the hazard map construction more accessible (Dalbey, 2009), created estimates of expectation and associated uncertainty, for given locations and sparse guiding data, using a statistical surrogate model called the Bayes Linear Method developed by Goldstein (Goldstein, 1995). Sets of flow-specific and DEM parameters are generated using Latin Hypercube Sampling and Titan2D simulations at these inputs are performed. Latin Hypercube Sampling requires fewer design points to fill a design space as compared to Monte Carlo. The data is used to create a statistical surrogate Bayes linear emulator, which attempts to fit a piecewise polynomial and an error model through the available numerical data from the simulator. The emulator $s(\mathbf{x})$ may be written as:

$$s(\mathbf{x}) = \beta^T \mathbf{x} + \epsilon, \tag{2}$$

where $s\mathbf{x}$ is a quantity of interest (e.g., maximum flow depth attained at a location, $\beta$ are least square coefficients, $\mathbf{x}$ is the vector of input variables and the error $\epsilon$ is modeled as Gaussian with 0 mean normal distribution with variance $\sigma$. (Dalbey, 2009) carefully lays out a process for adapting the work of Goldstein (Goldstein, 1995) to adjust the expectation and variance implicit in the model above with data from the numerical simulator. The emulator acts as a fast surrogate of the simulator. To surmount the cost of emulator construction for full field simulations where the correlation structures lead to the need for inverting very large matrices, a localized approximation is used [in a process quite similar to the well studied Gaussian Markov random fields (Rue and Held, 2005)]. This is key to constructing a multi-level Bayesian hierarchical emulator from an ensemble of training simulations. The hierarchical nature allows the emulator components to be constructed and evaluated concurrently (**Figure 2A**). However, this leads to much greater complexity in the workflow, and challenges in automation.

As implemented, the hierarchical emulator is an ensemble of smaller emulators, each covering a portion of the uncertain input space. Using Delaunay triangulation, tessellation of sample points is performed to generate a set of triangles whose nodes are sample sites in the input space. A mini-emulator centered about each sample is constructed using only those samples in the neighborhood of the central sample. The adjusted mean and variance of the mini-emulators are calculated for arbitrary re-sample points. The adjusted means and variances of the mini-

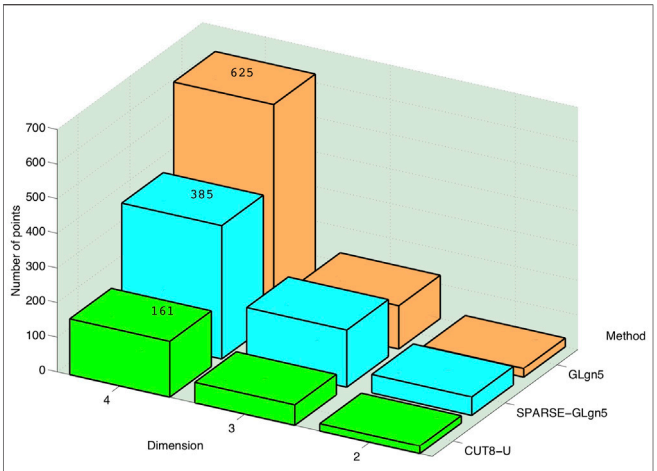


**FIGURE 4 |** Points needed to find $8^{th}$ order moment in 2–4 dimensions using different sampling techniques.

emulators are combined in a weighted sum. The mini-emulators are then aggregated into a macro-emulator (**Figure 2B**). The macro-emulator is re-sampled to produce the conditional probabilistic hazard map.

The steps required to implement the workflow and the parallelization strategy are highlighted in **Table 1**.

The speed-up provided by the parallel workflow is n-fold over the corresponding sequential processing. The actual speed-up is dependent on machine considerations. For example, sharing compute nodes with other programs may reduce the speed-up. Usage and performance of UB-HPC cluster nodes resources are monitored *via* UB CCR's Open XDMoD tool (Sperhac et al., 2020). When a workflow's execution is complete, the XDMoD user interface enables workflow developers to view important information about a workflow's task execution on a CCR compute node such as the executable information and summary statistics.

The VHub Titan2D Hazard Map Emulator Workflow Tool extends capability provided by the VHub Titan2D Mass-Flow Simulation Workflow Tool and produces ASCII formatted and Portable Network Graphics files containing information on the conditional probability of a Titan2D flow depth reaching a critical height over a period of time following a volcanic eruption, given a user defined eruption scenario. Titan2D and Matlab/Octave scripts developed by Dalbey (2009), provide the base software required to implement this tool. A GUI is displayed when the tool is launched. The GUI provides the user interface for defining the eruption scenario and for controlling and running a Titan2D Hazard Map Emulator workflow. This tool was developed based on the HUBzero Pegasus tutorial (pegtut) and presents a HUBzero Rappture (Rapid application Infrastructure) interface. Rappture is a toolkit within the HUBzero platform that makes it easy to develop a graphical user interface for scientific modeling tools (McLennan, 2009).

A python input file contains the parameters for running Titan2D. An ensemble of Titan2D executions provide sample data for this tool. Users enter the name of a python input file for running Titan2D into the GUI's Titan2D Input File text box.

The Titan2D Hazard Map Emulator Workflow tool handles uncertainty in input parameters given ranges for these parameters specified *via* GUI text boxes. These are minimum volume (minvol), maximum volume (maxvol), minimum bed friction (BEDMIN), maximum bed friction (BEDMAX), starting center coordinate in easting and northing (STARTUTMECEN, STARTUTMNCEN), and starting mass radius (STARTRADIUSMAX). Sets of flow-specific and DEM parameters are generated using Latin Hypercube Sampling in conjunction with the specified ranges these parameters. The generated parameter sets are used to modify the user specified python input file for each Titan2D ensemble execution.

The GUI processes the user input and determines the executable jobs, job dependencies, and the input and output files for each job required to implement the workflow tasks displayed in **Figure 3**, calls Pegasus WMS API functions to create a DAX file, and, submits the workflow to Pegasus for execution (**Figure 1A** and **Section 2.1.3**).

### 2.2.2 Volcanic Ash Cloud Transport Hazard Map

Bent is a theoretical model of a volcanic eruption plume developed by (Bursik, 2001; Pouget et al., 2016), based on applying the equations of motion for a non-Boussinesq, particle-laden source in a plume-centered coordinate system. Bent outputs plume trajectories and rise heights, as well as pyroclast loadings as a function of height, and provides input for the Air Resources Laboratory volcanic ash transport and dispersion model (VATD), HYSPLIT. The Bent and HYSPLIT models require input data on volcanic source conditions as well as the wind field; the NCEP/NCAR Reanalysis model is currently the default in use for wind speed, although this can easily be changed to a higher resolution model. As this is a non-federal implementation of HYSPLIT, forecast wind fields cannot be used[1]. HYSPLIT is used to propagate ash particles in the windfield. The Bent-Hysplit workflow comprises a coupling of the Bent, HYSPLIT and Reanalysis models.

Some of the source parameters for the Bent and HYSPLIT models, specifically vent radius, vent source velocity, both of which affect plume height, and mean and standard deviation of ejecta grain size, which affect the distance carried, may be poorly characterized, and should be viewed as uncertain (Madankan et al., 2014).

The Bent-HYSPLIT workflow automates previous work for uncertainty in predictions from a model of volcanic ash transport in the atmosphere arising from uncertainty in both eruption source parameters and the model wind field (Stefanescu et al., 2014). Previous work used PUFF as the VATD model, and Weather Research and Forecasting (WRF) as the wind field model.

[1]Alternate versions of the tools with the unrestricted tool PUFF from Univ of Alaska-Fairbanks may also be used with forecast versions of numerical weather prediction models

**TABLE 2 |** Bent hysplit workflow parallelization strategy.

| | |
|---|---|
| Step 1 | Create the PCQ/CUT sample points. |
| Step 2 | Modify the puffin input file for each sample. Run puffin in parallel for each sample. |
| Step 3 | Run Hysplit in parallel for each sample. Requires all output from the previous step for each sample. |
| Step 4 | Convert SRM file output by Hysplit to NetCDF in parallel. Requires all output from the previous step. |
| Step 5 | Run UQ analysis for each time in parallel. Requires all output from the previous step. |
| Step 6 | Create the conditional probabilistic hazard map. Requires all output from the previous step. |

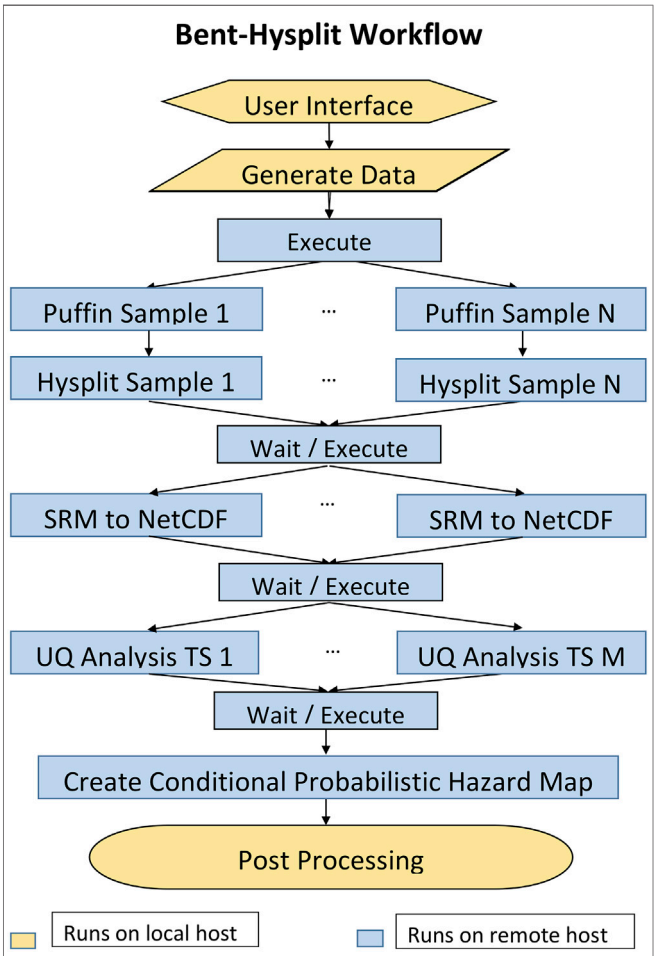


**FIGURE 5 |** Bent-Hysplit workflow tasks for ash clouds. Pegasus monitors the completion of task executions by determining when required output files are created by the tasks.

To implement the Bent-HYSPLIT-Reanalysis coupling, a quantity of interest is considered, for example, ash concentration at a specific location through time. Let the quantity of interest be represented as a random variable, $\boldsymbol{x}_k$, whose time evolution is given by HYSPLIT:

$$\dot{\boldsymbol{x}} = \mathbf{f}(t, \boldsymbol{x}, \boldsymbol{\Theta}, \mathcal{W}) \tag{3}$$

In **Eq. 3**, $\boldsymbol{\Theta} = \{\theta_1, \theta_2, \ldots\}$ represents uncertain initial conditions or system parameters such as the vent radius, eruption velocity, mean grain size and grain size variance, and $\mathcal{W}$ is a given wind field from a numerical weather prediction (NWP) model, such as reanalysis. Weighted samples from the random variables in the eruption source parameter space are drawn using the Conjugate Unscented Transform (CUT) (Madankan et al., 2014) and can be used to effectively estimate integral moments (means, variances) or even construct a surrogate using the underlying basis functions that define the polynomial approximation of the probability distribution for the quantities of interest. The main idea of the CUT approach is to select specific structures for symmetric points, rather than taking a tensor product of 1-D points as in the Gauss quadrature scheme. As a result, the quadrature points still exactly integrate polynomials of total degree $2N - 1$ in $n$-dimensional uncertainty space, while the number of points is much less than $N^n$ where $N$ represents the number of quadrature points needed to solve a one-dimensional integral (according to the Gaussian quadrature scheme).

**Figure 4**, adapted from (Madankan et al., 2014), displays a comparison for the number of points needed to find the $8^{th}$ order moment in four dimensions using Clenshaw-Curtis points [$9^4$ (6561)], Gauss-Legendre points [$5^4$ (625)], and CUT points (161 CUT points). The CUT points are very efficient relative to other quadrature driven sampling schemes and are used in our workflow here. Using the CUT points, the output moments are approximated as a weighted sum of the output of simulation runs at these carefully selected values of uncertain parameters.

The conditional probability of having ash at a specific height is then given by:

$$P(h) = \int_{\Omega} P(h|W)p(W)dW \approx \frac{1}{N_W}\sum_{i=1}^{N_W} P(h|W_i) \tag{4}$$

where, $w_i$ are the weights associated with the wind field ensemble, while $w_q$ are those obtained from using the CUT or generalized polynomial chaos (gPC) expansion (Marcus et al., 2012).

The expected value of ash at a given height is then:

$$\begin{aligned} E[h] &= \int hP(h)dh \\ &= \int h(\theta, W)\Big(\int P(h|W)p(W)dW\Big)dh \\ &= \iint h(\theta, W)P(h|W)p(W)dWdh \\ &= \sum_{i=1}^{N_W} w_i \sum_{q=1}^{N_{CUT}} w_q h\big(\theta_q, W_i\big) \end{aligned} \tag{5}$$

Sets of uncertain input values generated using polynomial chaos quadrature (PCQ), CUT sampling and Bent simulations of the inputs are performed. Control files are created using the

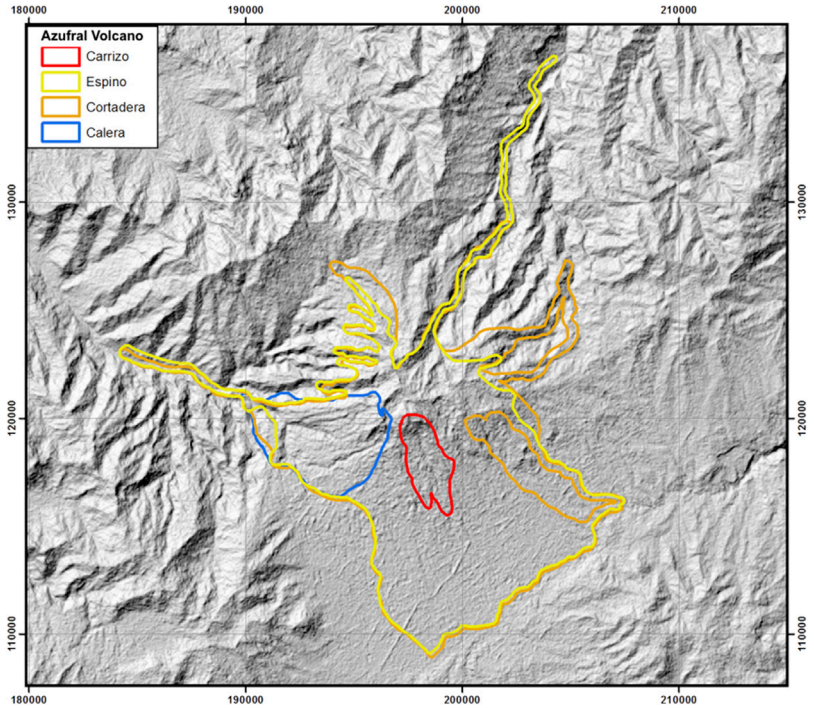


**FIGURE 6 |** Map showing mapped pyroclastic flow deposits for Azufral Volcano (Williams, 2015). Outline is known extent of each named deposit.

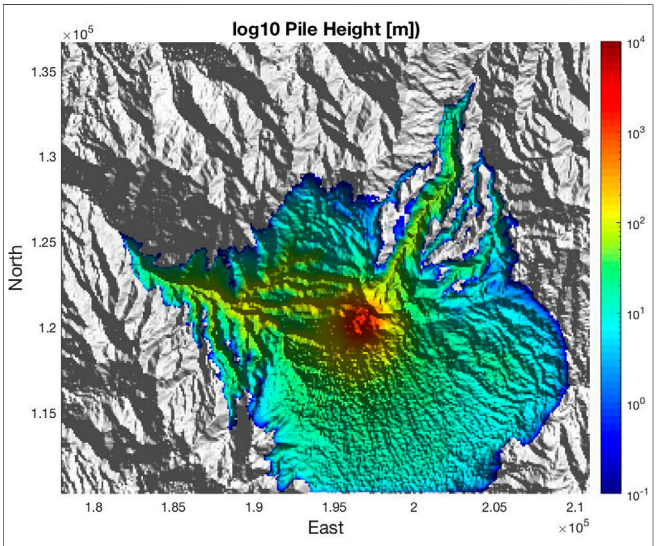


**FIGURE 7 |** Titan2D simulation of a flow at Azufral Volcano showing spread of flow widely in unchannelized areas, and confinement to valleys in channelized areas. Volume used similar to that of Espino and Cortadera flows in **Figure 6**, producing similar runout distance or extent.

Bent output, which are used as input to HYSPLIT; and HYSPLIT simulations are performed. The resulting HYSPLIT ensemble is used to construct a surrogate model, which in turn is sampled to create a conditional probabilistic hazard map. Ensemble methods that explore full parameter space are crucial

**TABLE 3 |** Titan2D eruption source parameters for Azufral volcano, Colombia.

| Titan2D parameter | Value |
|---|---|
| Pile UTM Zone | 18 North |
| Pile X Coordinate UTM E | 196,672.7 |
| Pile Y Coordinate UTM N | 120,213.0 |
| Pile Height (m) | 1,389.5 |
| Pile Major Radius (m) | 1,389.5 |
| Pile Minor Radius (m) | 1,389.5 |
| Pile Rotation Angle | 0.0 |
| Pile Flow Speed | 0.0 |
| Pile Flow Direction | 0.0 |
| Bed Friction Angle | 15 |
| Internal Friction Angle | 20 |

to obtaining good probabilistic estimates and insights into the potential for hazardous flow. The steps required to implement the workflow are shown in **Table 2**. The ability to parallelize these steps are exploited in the workflow construction.

The VHub Bent-Hysplit Workflow Tool extends capabilities of the VHub puffin tool and produces a netCDF formatted file containing information on the conditional probability of ash concentrations at specific heights, times and locations following a volcanic eruption, given a user defined eruption scenario. A GUI is displayed when the tool is launched. The GUI provides the user interface for defining the eruption scenario, for controlling and running a Bent-Hysplit workflow, and, for streamlining access to other websites for obtaining information required by the workflow.

Bent requires column formatted radiosonde files containing atmospheric parameters for the currently selected volcano

**TABLE 4 |** Eruption PHM Scenarios for Azufral volcano, Colombia.

| PHM scenario | Min bed friction | Max bed friction | Min vol $m^3$ | Max vol $m^3$ |
|---|---|---|---|---|
| 1 | 12 | 35 | $10^4$ | $10^6$ |
| 2 | 8 | 4 | $10^6$ | $10^8$ |
| 3 | 7 | 10 | $10^8$ | $10^{10}$ |

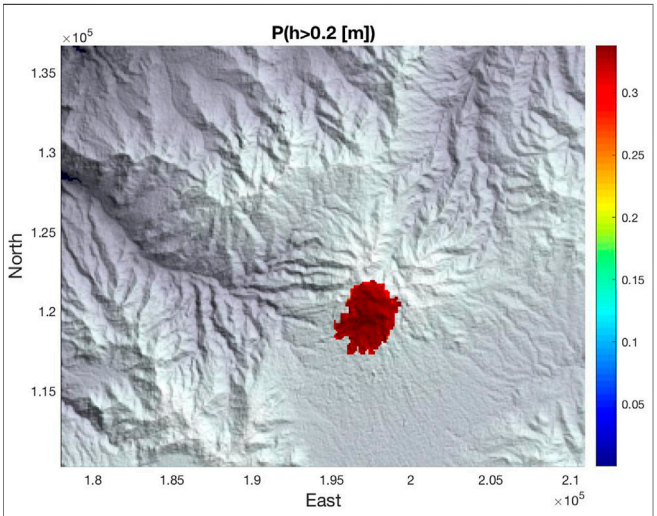


**FIGURE 8 |** Titan2D emulator based probability of exceeding 0.2 m flows in Scenario 1.

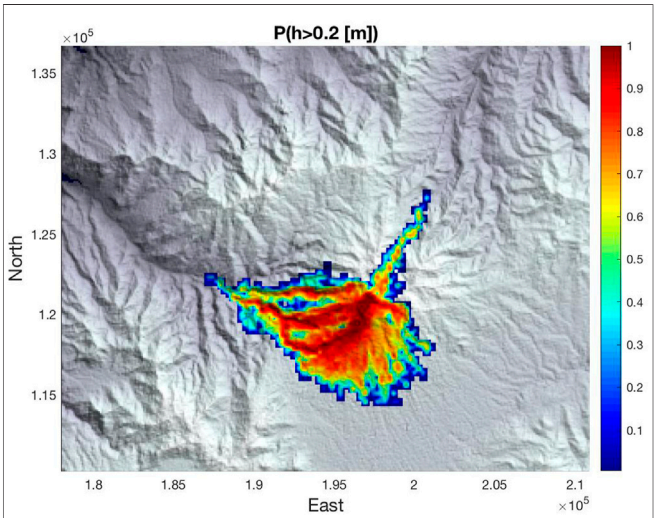


**FIGURE 9 |** Titan2D emulator based probability of exceeding 0.2 m flows in Scenario 2. Note similarity of probability of noticeable flow extent to mapped extent of Carrizo and Calera flows.

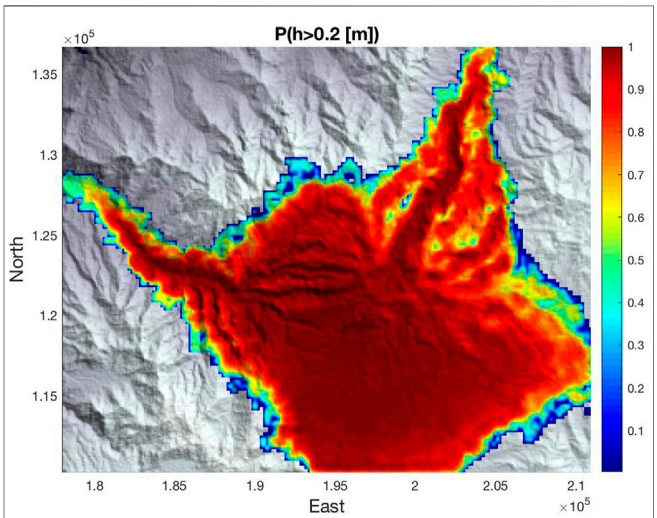


**FIGURE 10 |** Titan2D emulator based probability of exceeding 0.2 m flows in Scenario 3. Note similarity of probability of noticeable flow extent to mapped extent of Cortadera and Espino flows.

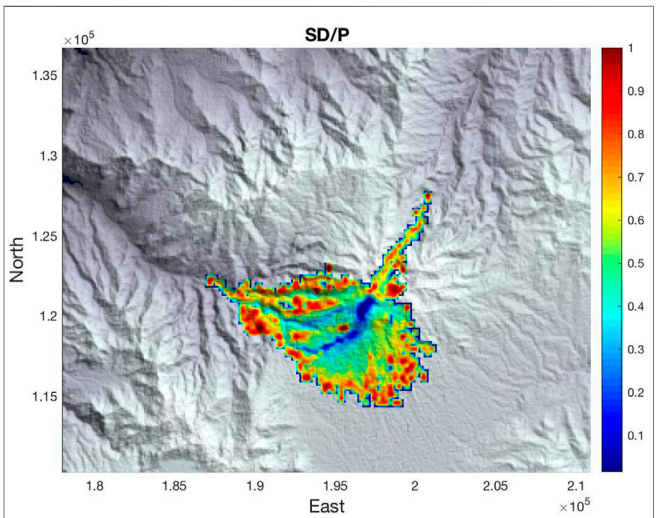


**FIGURE 11 |** Titan2D estimate of non-confidence in emulator based probability assessment for Scenario 2, using the ratio of standard deviation and probability. Lower SD/P is better, showing that near vent, confidence in model output is higher.

eruption date and time. The GUI provides the ability to automatically download weather balloon radiosonde files obtained in HTML format from the University of Wyoming Weather Web webpage. The software searches a master location identifier database to determine World Meteorological Organization (WMO) stations closest to the volcano, and then an attempt is made to retrieve a radiosonde file from the closest WMO station for the selected

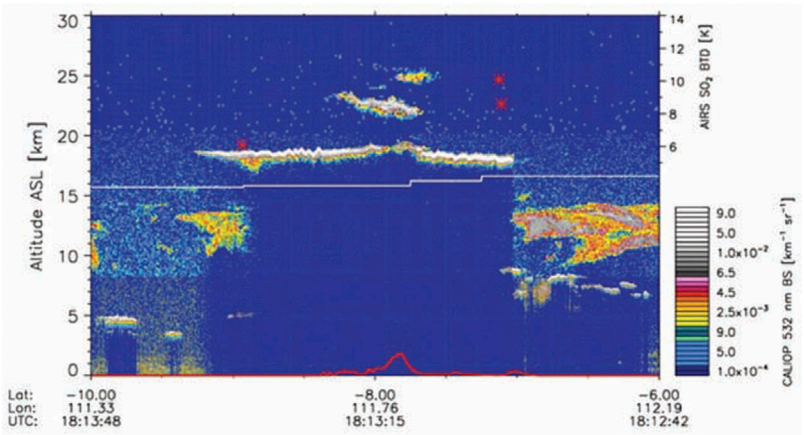


**FIGURE 12 |** CALIOP cross-section through Kelut volcanic cloud from data acquired on 14 February 2014. Top of plume imaged near center; note top of umbrella spreading region at height above 18 km, and compactness of cloud. Lower bright areas near edges are nonvolcanic water-vapor clouds. (Global Volcanism Program, 2014).

**TABLE 5 |** Eruption source parameters for a hypothetical eruption of Kelut volcano.

| Parameter | Value range |
|---|---|
| Vent radius (m) | 65.0–150.0 |
| Vent velocity (m/s) | 45.0–124.0 |
| Grain mean ($\varphi = -\log_2$ mm) | 3.5–7.0 |
| Grain standard deviation ($\varphi = -\log_2$ mm) | 0.5–3.0 |
| Eruption temperature (K) | 1,200 |
| Erupted water mass fraction (%) | 0.017 |
| Eruption duration (hours) | 1.0 |

eruption date and time. HYSPLIT requires NOAA Air Resources Laboratory (ARL) NCEP/NCAR Reanalysis meteorological data files. The GUI provides the ability to automatically download ARL files from the NCEP/NCAR Reanalysis website "NCEP/NCAR Reanalysis" for the selected eruption date. The GUI also provides the ability to view volcano conditions from the Volcanic Cloud Monitoring—NOAA/CIMSS webpage for the selected volcano.

The Bent-Hysplit Workflow tool handles uncertainty in column (eruption plume) rise height through the Vent Radius and Vent Velocity configuration parameters, which together control mass eruption rate (MER), and uncertainty in the grain size, fine-grain fraction and potential ash accretion through the Grain Mean and Grain Standard Deviation configuration parameters. Polynomial Chaos Quadrature (PCQ) sample points, generated using the Conjugate Unscented Transform method, are used in conjunction with ranges for these parameters specified on the GUI's Run Control tab to create sets of Bent input values for the parameters. Running Bent with a particular set of input values for these parameters is considered a sample run of Bent. Bent output from each member of the sample run is used in conjunction with other configuration parameters specified on the Run Control tab to create CONTROL and SETUP.CFG files for HYSPLIT; running HYSPLIT with these CONTROL and SETUP. CFG files is considered a sample run of HYSPLIT. HYSPLIT output from all HYSPLIT sample run members is used as input to the tool's uncertainty quantification analysis software. The output of the tool's uncertainty quantification analysis software is a NetCDF formatted file, probmap.nc, containing probabilities of ash concentrations greater than specific levels at specific times and locations. In all, 161 sample runs of Bent and HYSPLIT are performed at CUT points, requiring an ensemble of Bent, HYSPLIT and uncertainty quantification analysis tasks, which are encapsulated and executed as a workflow.

The GUI processes the user input and determines the executable jobs, job dependencies, and the input and output files for each job required to implement the workflow tasks displayed in **Figure 5**, calls Pegasus WMS API functions to create a DAX file, and, submits the workflow to Pegasus for execution (**Figure 1A** and **Section 2.1.3**).

From previous work, the Bent model has been improved to use either radiosonde or different types of NWP data directly to get atmospheric parameters. An inverse model was added to update source parameter estimates; simulation of collapse behavior and low fountain development was formalized; modules for water were added; double-precision and adaptive step size were added; and umbrella cloud flow and pyroclast fallout completed.

# 3 RESULTS

## 3.1 Volcanic Pyroclastic Flow Transport Hazard Map

Azufral, Colombia, is a stratovolcano (1.09°N, 77.72°W/UTM Zone 18N, 197 272 UTM°E, 120615 UTM°N) with a summit elevation of 4,050 m. Mapped pyroclastic flow deposits for the Azufral volcano are shown in **Figure 6**. These polygons were determined by thorough mapping by the Servicio Geologico Colombiano. If we assume the eruption units were erupted as single events, and the pyroclastic surges and flows are separated into different density currents, the eruption units can be modeled using Titan2D (Williams, 2015).

Results for running one simulation of a likely flow using Titan2D are displayed in **Figure 7**. A circular sampling area

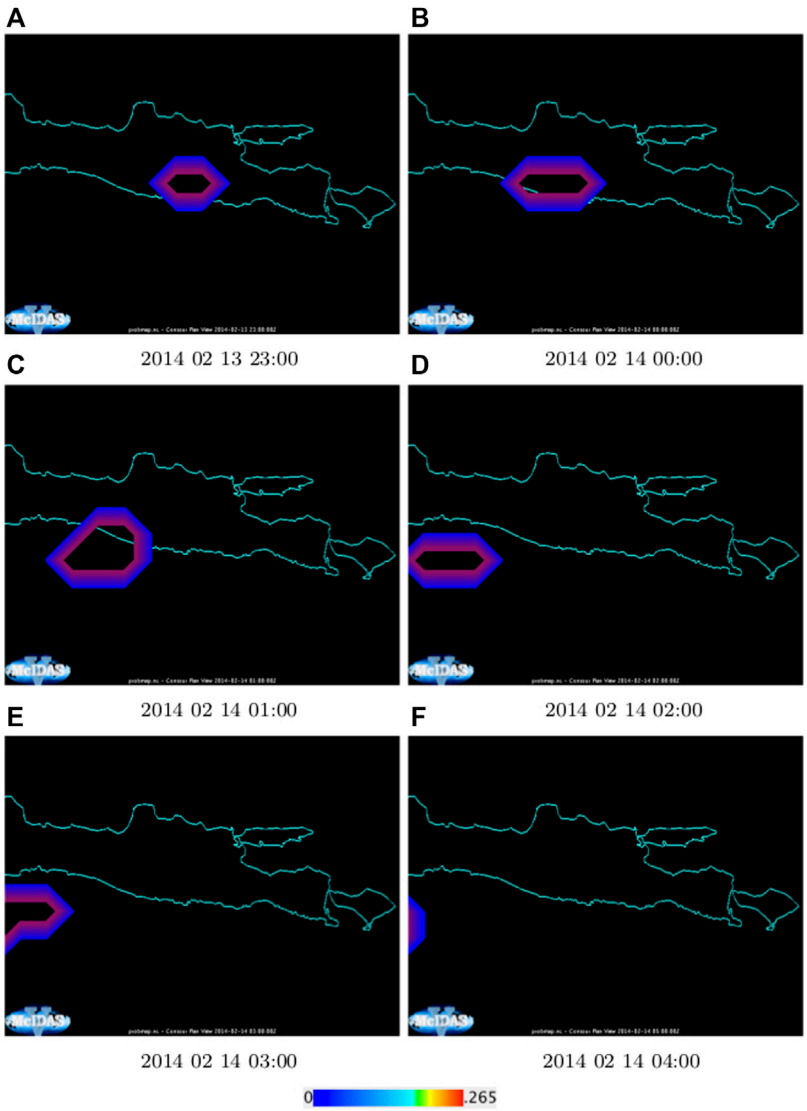


**FIGURE 13 | (A–F)** Conditional probability of ash at height c. 17 km for 6 h following the Kelut volcano eruption February 13, 2014. Plots were created with a low resolution grid. Higher resolution grids may be used *via* the tool's Select Meteo Data File input option.

from which the X and Y coordinate points for source vent centers was chosen. This area encompasses that inside the crater of Azufral. The simulation parameters for running Titan2D are displayed in **Table 3**. As indicated in **Table 3**, we assume that the origin of flow is near the crater.

For Azufral volcano, the initial volume, bed (also known as basal) friction angle and DEM are poorly characterized and Titan2D Hazard Map Workflow software was used to produce conditional probabilistic hazard maps (PHMs). Three separate PHM eruption scenarios were created based on binned volume and apparent basal friction angles for the PDCs derived in Bursik et al. (2005), and Williams (2015). The ranges for the volume and bed friction angle are shown in **Table 4**. A uniform distribution is used to model the variability of the volume and bed friction angle, as each value in the range of values for these are equally likely to occur.

Results for the three scenarios are shown in **Figures 8**–**10**. The spatially varying hazard criterion that we chose was whether or not the flow depth exceeds 0.2 m during a particular event. The workflow was run with 32 simulated samples of Titan2D.

Results for Scenario 1 show that due to high bed friction angle values and low volumes, hazards are limited to the area near the crater. Results for Scenario 2 show that flow becomes more probable towards the southern half of the volcanic complex, and potential for flow remains confined to valleys to the west and north. Results for Scenario 3 show that the highest probabilities occur close to the summit of Azufral volcano, on the southern flanks of the volcano and in the bottom of valleys to the west and north.

For the Espino and Cortadera units shown in **Figure 6** following (Williams et al., 2017), the magnitude of the eruptions are reasonably within the volume sampling boundary conditions of

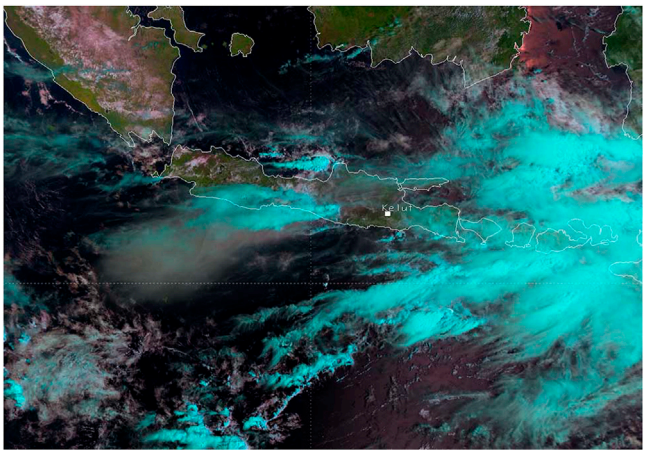


**FIGURE 14 |** Natural color RGB image of Kelut ash cloud (diffuse gray area), taken c. 2 h after the eruption, shows WSW drifting of cloud, consistent with probabilistic estimate of workflow. (EUMESTAT, 2021).

Scenario 3 (**Figure 10**). The PDC conditions are highly probable as the Scenario 3 PHM encompasses likely scenarios given a positive correlation with the deposits of Espino and Cortadera.

The standard deviation divided by the probability of hazard, is a measure of the non-confidence in the statistics due to insufficient re-sampling. This measure is displayed for Scenario 2 (**Figure 11**). The measure cannot be used to directly evaluate the quality of the emulator, although it is possible to obtain a measure of this with some minor modifications and re-evaluations of the re-sample inputs (Dalbey, 2009).

## 3.2 Volcanic Ash Cloud Transport Hazard Map

Kelut (or Kelud), Indonesia, is a stratovolcano (7.93°S, 112.308°E/ UTM Zone 49S, 644 177 UTM E, 9123 214 UTM N) with a summit of 1,731 (m) located in the province of East Java. On February 13, 2014, the Indonesian National Board for Disaster Management (Badan Nasional Penanggulangan Bencana-BNPB) reported that a major eruption occurred at Kelut (Global Volcanism Program, 2014). The plume reached a maximum height of 26 km and an umbrella cloud spreading height of around 16–17 km (**Figure 12**) (Bear-Crozier et al., 2020).

We have conducted tests with the Kelut eruption to create a conditional probabilistic hazard map for this event. The potential vent radius, velocity of ejection from the vent, grain mean size and standard deviation are poorly characterized. The ranges for these parameters as well as other eruption source parameters are listed in **Table 5**. A uniform distribution is used to model the variability of the vent radius, initial velocity, grain mean and standard deviation, as each value in the range of values for these are as equally likely to occur. **Figure 13** displays results of analyzing the netCDF formatted probability of ash at height greater and 17,000 m for the 6 h following the eruption on 13 February 2014. The plots were created using the (external) McIDAS software package, from the netCDF file returned by the workflow. The natural color RGB image of the eruption cloud, **Figure 14**, shows that ash drifted WSW after 2 h. **Figure 13** shows that an ash cloud at height near 17 km would have the same WSW drift in movement.

For this exercise, the workflow downloaded the windfield data from the NOAA Air Resources Laboratory (ARL) Gridded Meteorological Archives. The tool also provides the capability for the user to use a windfield data file stored in the user's home directory on VHub.

# 4 CONCLUSION

Workflow hazard map development is generally complex and very inefficient and prone to errors when performed manually. The software modules that are required to run in parallel on multiple processors makes hazard map development inaccessible to many people. The process of downloading and verifying required field data is handled using a simple GUI interface.

This paper presents a computing infrastructure and methodology which enables scientists and other members of the volcanology research community to automate and use complex workflows for construction of probabilistic hazard maps. The work addresses a major scientific challenge; making sophisticated, probabilistic computational hazard map development accessible to a range of potential users. The steps towards usability through use of a web-interface to parameterize and initialize computations is a valuable contribution to the volcanology research community.

Two geologic flow-transport modelling systems applicable to volcanic eruptions, the computational models, the ways of using these models, and the use of Pegasus as a WMS for controlling the execution of these models are presented. The results of two realistic case studies as a means of preliminary evaluation are denoted in the **Section 3** and support the viability of this computer infrastructure and methodology for the construction of probabilistic hazard maps.

# DATA AVAILABILITY STATEMENT

The original contributions presented in the study are included in the article/Supplementary Material, further inquiries can be directed to the corresponding author.

# AUTHOR CONTRIBUTIONS

All authors contributed to the workflow conceptual design. RJ developed workflow software and ran the simulations. All authors verified and validated the computational results and contributed to writing the manuscript.

# FUNDING

This work was supported by National Science Foundation awards OAC/2125974 and OAC/2004302.

## REFERENCES


Bayarri, M. J., Berger, J. O., Calder, E. S., Patra, A. K., Pitman, E. B., Spiller, E. T., et al. (2015). Probabilistic Quantification of Hazards: A Methodology Using Small Ensembles of Physics-Based Simulations and Statistical Surrogates. *Int. J. Uncertaintyquantification* 5 (4), 297–325. doi:10.1615/int.j.uncertaintyquantification.2015011451

Bear-Crozier, A., Pouget, S., Bursik, M., Jansons, E., Denman, J., Tupper, A., et al. (2020). Automated Detection and Measurement of Volcanic Cloud Growth: towards a Robust Estimate of Mass Flux, Mass Loading and Eruption Duration. *Nat. Hazards* 101 (1), 1–38. doi:10.1007/s11069-019-03847-2

Bursik, M. (2001). Effect of Wind on the Rise Height of Volcanic Plumes. *Geophys. Res. Lett.* 28, 3621–3624. doi:10.1029/2001gl013393

Bursik, M., Patra, A., Pitman, E. B., Nichita, C., Macias, J. L., Saucedo, R., et al. (2005). Advances in Studies of Dense Volcanic Granular Flows. *Rep. Prog. Phys.* 68 (2), 271–301. doi:10.1088/0034-4885/68/2/r01

Calder, E., Wagner, K., and Ogburn, S. E. (2015). Volcanic hazard Maps. *Glob. volcanic hazards Risk*, 335–342. doi:10.1017/cbo9781316276273.022

Couvares, P., Kosar, T., Roy, A., Weber, J., and Wenger, K. (2007). *Workflow Management in Condor*. London: Springer London, 357–375.

Dalbey, K. (2009). *Predictive Simulation and Model Based Hazard Maps of Geophysical Mass Flows*. PhD Thesis. Buffalo, NY: Department of Mechanical and Aerospace Engineering, University at Buffalo.

Deelman, E., Vahi, K., Juve, G., Rynge, M., Callaghan, S., Maechling, P. J., et al. (2015). Pegasus, a Workflow Management System for Science Automation. *Future Generation Comp. Syst.* 46, 17–35. doi:10.1016/j.future.2014.10.008

Eumestat (2021). Kelut Volcano Eruption. Available at: https://www.eumetsat.int/kelut-volcano-eruption (accessed November, , 2021).

Global Volcanism Program (2014). "Report on Kelut," in *Bulletin of the Global Volcanism Network*. Editor R. Wunderman (Indonesia: Smithsonian Institution), 39, 2.

Goldstein, M. (1995). *Bayes Linear Methods I - Adjusting Beliefs: Concepts and Properties*. Durham: University of Durham.

Madankan, R., Pouget, S., Singla, P., Bursik, M., Dehn, J., Jones, M., et al. (2014). Computation of Probabilistic hazard Maps and Source Parameter Estimation for Volcanic Ash Transport and Dispersion. *J. Comput. Phys.*, 39–59. doi:10.1016/j.jcp.2013.11.032

Marcus, B., Jones, M., Carn, S., Dean, K., Patra, A., Pavolonis, M., et al. (2012). Estimation and Propagation of Volcanic Source Parameter Uncertainty in an Ash Transport and Dispersal Model: Application to the Eyjafjallajökull Plume of 14–16 April 2010. *Bull. volcanology* 74 (10), 2321–2338.

McLennan, M. (2009). Introducing the Rappture Toolkit.

McLennan, M., Clark, S., Deelman, E., Rynge, M., Vahi, K., McKenna, F., et al. (2015). HUBzero and Pegasus: Integrating Scientific Workflows into Science Gateways. *Concurrency Computat.: Pract. Exper.* 27 (2), 328–343. doi:10.1002/cpe.3257

McLennan, M., and Kennell, R. (2010). HUBzero: A Platform for Dissemination and Collaboration in Computational Science and Engineering. *Comput. Sci. Eng.* 12 (2), 48–53. doi:10.1109/mcse.2010.41

Neeman, A. G., Gallo, S. M., and Efstathiadis, E. (2010). Collaborative Research in a Regional Grid. *Gateway Comput. Environments Workshop*, 1–11. doi:10.1109/gce.2010.5676131

Patra, A. K., Bauer, A. C., Nichita, C. C., Pitman, E. B., Sheridan, M. F., Bursik, M., et al. (2005). Parallel Adaptive Numerical Simulation of Dry Avalanches over Natural Terrain. *J. Volcanology Geothermal Res.* 139 (1-21–21). doi:10.1016/j.jvolgeores.2004.06.014

Pouget, S., Bursik, M., Singla, P., and Singh, T. (2016). Sensitivity Analysis of a One-Dimensional Model of a Volcanic Plume with Particle Fallout and Collapse Behavior. *J. Volcanology Geothermal Res.* doi:10.1016/j.jvolgeores.2016.02.018

Rohit, S., Patra, A., and Chaudhary, V. (2014). Integrating Data and Compute-Intensive Workflows for Uncertainty Quantification in Large-Scale Simulation: Application to Model-Based hazard Analysis. *Int. J. Comp. Math.* 91 (4), 730–747. doi:10.1080/00207160.2013.844337

Rue, H., and Held, L. (2005). Gaussian Markov Random Fields: Theory and Applications. *Gaussian Markov Random Fields* 104, 02.

Sperhac, J., DeLeon, R. L., White, J. P., Jones, M., Andrew, E. B., Jones Ivey, R., et al. (2020). Towards Performant Workflows, Monitoring and Measuring. In 2020 29th International Conference on Computer Communications and Networks, 1–9. doi:10.1109/icccn49398.2020.9209647

Sperhac, J. M., Poinar, P., Jones-Ivey, R., Briner, J., Csatho, B., Nowicki, S., et al. (2021). GHub: Building a Glaciology Gateway to Unify a Community. *Concurrency Comput. Pract. Experience* 33 (19), e6130.

Spiller, E. T., Bayarri, M. J., Berger, J. O., Calder, E. S., Patra, A. K., Pitman, E. B., et al. (2014). Automating Emulator Construction for Geophysical Hazard Maps. *Siam/asa J. Uncertainty Quantification* 2 (1), 126–152. doi:10.1137/120899285

Stefanescu, E. R., Bursik, M., Cordoba, G., Dalbey, K., Jones, M. D., Patra, A. K., et al. (2012). Digital Elevation Model Uncertainty and hazard Analysis Using a Geophysical Flow Model. *Proc. R. Soc. Lond. A: Math. Phys. Eng. Sci.* 468, 1543–1563.

Stefanescu, E. R., Patra, A. K., Bursik, M. I., Madankan, R., Pouget, S., Jones, M., et al. (2014). Temporal, Probabilistic Mapping of Ash Clouds Using Wind Field Stochastic Variability and Uncertain Eruption Source Parameters: Example of the 14 April 2010 Eyjafjallajökull Eruption. *J. Adv. Model. Earth Syst.* 6 (4), 1173–1184. doi:10.1002/2014ms000332

Stein, A. F., Draxler, R. R., Rolph, G. D., Stunder, B. J. B., Cohen, M. D., and Ngan, F. (2015). NOAA's HYSPLIT Atmospheric Transport and Dispersion Modeling System. *Bull. Am. Meteorol. Soc.* 96 (12), 2059–2077. doi:10.1175/bams-d-14-00110.1

Takarada, S., Bandibas, J. C., and Ishikawa, Y.Ever Promotion Team, G (2014). Global Earthquake and Volcanic Eruption Risk Management Activities, Volcanic hazard Assessment Support System and Asia-pacific Region hazard Mapping Project in G-EVER. *Episodes* 37, 321–328. doi:10.18814/epiiugs/2014/v37i4/014

Takarada, S. (2017). The Volcanic Hazards Assessment Support System for the Online Hazard Assessment and Risk Mitigation of Quaternary Volcanoes in the World. *Front. Earth Sci.* 5, 102. doi:10.3389/feart.2017.00102

University of Wisconsin–Madison Center for High Throughput Computing (2021). *HTCondor Manual*. University of Wisconsin–Madison.

Williams, M., Bursik, M. I., Cortes, G. P., and Garcia, A. M. (2017). Correlation of Eruptive Products, Volcán Azufral, Colombia: Implications for Rapid Emplacement of Domes and Pyroclastic Flow Units. *J. Volcanology Geothermal Res.* 341, 21–32. doi:10.1016/j.jvolgeores.2017.05.001

Williams, M. (2015). *Eruption History and Pyroclastic Flow Modeling at Azufral Volcano, Colombia*. Master Thesis. Buffalo, NY: Department of Geology, University at Buffalo.

Woodhouse, M., Hogg, A., and Phillips, J. Laharflow. Available at: https://www.laharflow.bristol.ac.uk/help/userguide/FrontPage.php (accessed October, 2021).


**Conflict of Interest:** The authors declare that the research was conducted in the absence of any commercial or financial relationships that could be construed as a potential conflict of interest.

**Publisher's Note:** All claims expressed in this article are solely those of the authors and do not necessarily represent those of their affiliated organizations, or those of the publisher, the editors and the reviewers. Any product that may be evaluated in this article, or claim that may be made by its manufacturer, is not guaranteed or endorsed by the publisher.

frontiers in Earth Science

ORIGINAL RESEARCH
published: 25 January 2022
doi: 10.3389/feart.2021.757618

# The Sensitivity of Tsunami Impact to Earthquake Source Parameters and Manning Friction in High-Resolution Inundation Simulations

*Steven J. Gibbons[1]*, Stefano Lorito[2], Marc de la Asunción[3], Manuela Volpe[2], Jacopo Selva[4], Jorge Macías[3], Carlos Sánchez-Linares[3], Beatriz Brizuela[2], Malte Vöge[1], Roberto Tonini[2], Piero Lanucara[5], Sylfest Glimsdal[1], Fabrizio Romano[2], Jan Christian Meyer[6] and Finn Løvholt[1]*

[1]The Norwegian Geotechnical Institute (NGI), Oslo, Norway, [2]Istituto Nazionale di Geofisica e Vulcanologia (INGV), Roma, Italy, [3]Análisis Matemático, Estadística e Investigación Operativa y Matemática Aplicada, Universidad de Málaga, Málaga, Spain, [4]Istituto Nazionale di Geofisica e Vulcanologia (INGV), Bologna, Italy, [5]CINECA SuperComputing Applications and Innovation, Roma, Italy, [6]Department of Computer Science, Faculty of Information Technology and Electrical Engineering, Norwegian University of Science and Technology (NTNU), Trondheim, Norway

OPEN ACCESS

**Edited by:**
*Mark Bebbington, Massey University, New Zealand*

**Reviewed by:**
*Qi Yao, Institute of Earthquake Forecasting, China*
*Jacob Stolle, Université du Québec, Canada*

***Correspondence:**
*Steven J. Gibbons*
*steven.gibbons@ngi.no*

**Specialty section:**
*This article was submitted to Geohazards and Georisks, a section of the journal Frontiers in Earth Science*

**Received:** *12 August 2021*
**Accepted:** *23 December 2021*
**Published:** *25 January 2022*

**Citation:**
*Gibbons SJ, Lorito S, de la Asunción M, Volpe M, Selva J, Macías J, Sánchez-Linares C, Brizuela B, Vöge M, Tonini R, Lanucara P, Glimsdal S, Romano F, Meyer JC and Løvholt F (2022) The Sensitivity of Tsunami Impact to Earthquake Source Parameters and Manning Friction in High-Resolution Inundation Simulations. Front. Earth Sci. 9:757618. doi: 10.3389/feart.2021.757618*

In seismically active regions with variable dominant focal mechanisms, there is considerable tsunami inundation height uncertainty. Basic earthquake source parameters such as dip, strike, and rake affect significantly the tsunamigenic potential and the tsunami directivity. Tsunami inundation is also sensitive to other properties such as bottom friction. Despite their importance, sensitivity to these basic parameters is surprisingly sparsely studied in literature. We perform suites of systematic parameter searches to investigate the sensitivity of inundation at the towns of Catania and Siracusa on Sicily to changes both in the earthquake source parameters and the Manning friction. The inundation is modelled using the Tsunami-HySEA shallow water code on a system of nested topo-bathymetric grids with a finest spatial resolution of 10 m. This GPU-based model, with significant HPC resources, allows us to perform large numbers of high-resolution tsunami simulations. We analyze the variability of different hydrodynamic parameters due to large earthquakes with uniform slip at different locations, focal depth, and different source parameters. We consider sources both near the coastline, in which significant near-shore co-seismic deformation occurs, and offshore, where near-shore co-seismic deformation is negligible. For distant offshore earthquake sources, we see systematic and intuitive changes in the inundation with changes in strike, dip, rake, and depth. For near-shore sources, the dependency is far more complicated and co-determined by both the source mechanisms and the coastal morphology. The sensitivity studies provide directions on how to resolve the source discretization to optimize the number of sources in Probabilistic Tsunami Hazard Analysis, and they demonstrate a need for a far finer discretization of local sources than for more distant sources. For a small number of earthquake sources, we study systematically the inundation as a function of the Manning coefficient. The sensitivity of the inundation to this parameter varies greatly for different earthquake sources and topo-bathymetry at the coastline of interest. The friction greatly affects the velocities and momentum flux and to a

lesser but still significant extent the inundation distance from the coastline. An understanding of all these dependencies is needed to better quantify the hazard when source complexity increases.

**Keywords: tsunami, inundation, HPC, earthquakes, numerical simulations**

## INTRODUCTION

Earthquake tsunamis pose a significant hazard to coastal communities, and account for approximately 80% of tsunami events globally (e.g. NCEI, 2021). A strong component of the global earthquake tsunami hazard is the one induced by large subduction zone events (e.g. Løvholt et al., 2012a; Løvholt et al., 2014; Davies et al., 2018) where sources are aligned along well known tectonic interfaces along the Pacific Ring of Fire and Sunda Trench in the Indian Ocean. On the other hand, in regions where the tectonic setting is more complex, the dominant tsunamigenic structures are less well known, and the tsunamigenesis and hazard is consequently subject to much larger uncertainty. Examples of such complex areas include for instance eastern Indonesia and the Philippines (Løvholt et al., 2012b; Horspool et al., 2014), the Caribbean (Parsons and Geist, 2008; Harbitz et al., 2012), and the Mediterranean Sea (Lorito et al., 2008; Selva et al., 2016; Basili et al., 2021; Lorito et al., 2021; Selva et al., 2021). This large source uncertainty poses a challenge for modelling the hazard, with accurate and efficient numerical modelling required for simulating tsunami generation, propagation, and inundation. Estimating the tsunami hazard that a given coastal region is exposed to requires an understanding of the likelihood and variability of virtually all possible seismic sources, the generation and propagation of the tsunami, and the coastal inundation, necessitating Probabilistic Tsunami Hazard Analysis (PTHA). A comprehensive review is provided by Grezio et al. (2017). We hence need to understand better the basic relationship between fault parameters and tsunamigenic strength to more efficiently sample the source variability and in turn correctly determine the hazard.

While there is increasing understanding that spatially variable slip on ruptures can be critical in determining the tsunami impact (Geist, 2002; McCloskey et al., 2007; Davies et al., 2015; Li et al., 2016; Murphy et al., 2016; Davies, 2019; Scala et al., 2020), it still remains essential to understand the source sensitivity from the simpler constant slip models on tsunami inundation (see also An et al., 2018). In addition to the heterogeneity of the slip, also the fault geometry may affect the tsunami modeling, as shown recently by a sensitivity analysis for subduction earthquakes in the same region of this study by Tonini et al. (2020). However, as stressed above, for many tsunamigenic earthquake scenarios, we may not have a good model of the fault geometry. Moreover, large earthquakes with complex rupture geometries are typically modelled as slip on multiple fault segments with simpler geometry. It is important to understand well the variability due to simpler uniform-slip models in its own right, also as a basis for more complex slip realizations. The model typically applied is that of Okada (1985) which computes analytically through a complex set of equations the seabed surface deformation resulting from a uniform dislocation (slip) occurring along a rectangular fault plane embedded into a homogeneous linear elastic half-space. In this approach the earthquake source, in addition to the position, is parameterised through its size (length and width of the rectangle), its orientation (strike and dip angles), and two kinematic rupture parameters (the slip and its direction in the fault plane, the rake angle). Several sensitivity studies using Okada's source formulation have been performed. Geist (1998) reviews the basic tsunamigenic principles due to co-seismic slip. Gica et al. (2007) and Burbidge et al. (2015) perform systematic parameter sweeps to determine the sensitivity of the maximum offshore wave-height at a given location to the characteristics of the earthquake source as specified by the Okada parameters. Løvholt et al. (2012c) investigated sensitivity to slip distribution for different dip angles and depth for variable slip. However, none of the above studies performed a broad sensitivity analysis with focus on inundation; this is partly expected as this requires large computational resources.

Recent advances in efficient GPU (Graphical Processing Unit) shallow water-type tsunami models, combined with advances in High Performance Computing facilities, have now made it feasible to perform very large numbers of tsunami simulations with inundation modelled at high spatial resolution (down to a few meters). If further source down-sampling is still necessary due to limited computational resources, there are several techniques for limiting the number of simulations calculated (Lorito et al., 2015; Volpe et al., 2019; Williamson et al., 2020). Gibbons et al. (2020) performed a comprehensive PTHA for the town of Catania on the Eastern coast of Sicily comprising over 32,000 tsunami simulations for different earthquake sources in the Mediterranean Sea. The calculations were performed using the GPU-based Tsunami-HySEA code (de la Asunción et al., 2013; Macías et al., 2016, 2017). Each simulation in that study took approximately 30 min on an NVIDIA V-100 GPU, modelling the tsunami wave from source to inundation on a numerical Digital Elevation Model (DEM) with 10 m lateral resolution. However, a rather rough discretization of source parameters has been applied to reduce the computational effort, inherited from regional studies from which scenarios have been selected (see Selva et al., 2016; Basili et al., 2021). For such local studies, a finer discretization of earthquake sources, both spatially and with regards to source mechanism, can instead help improving the accuracy of the hazard analysis. To this end, a systematic sensitivity study on its impact of hazard is still required, to define efficient strategies for source description.

The accuracy of tsunami hazard estimates depends also upon the accuracy of the tsunami numerical models themselves for a fixed set of source parameters. Their accuracy will depend in turn

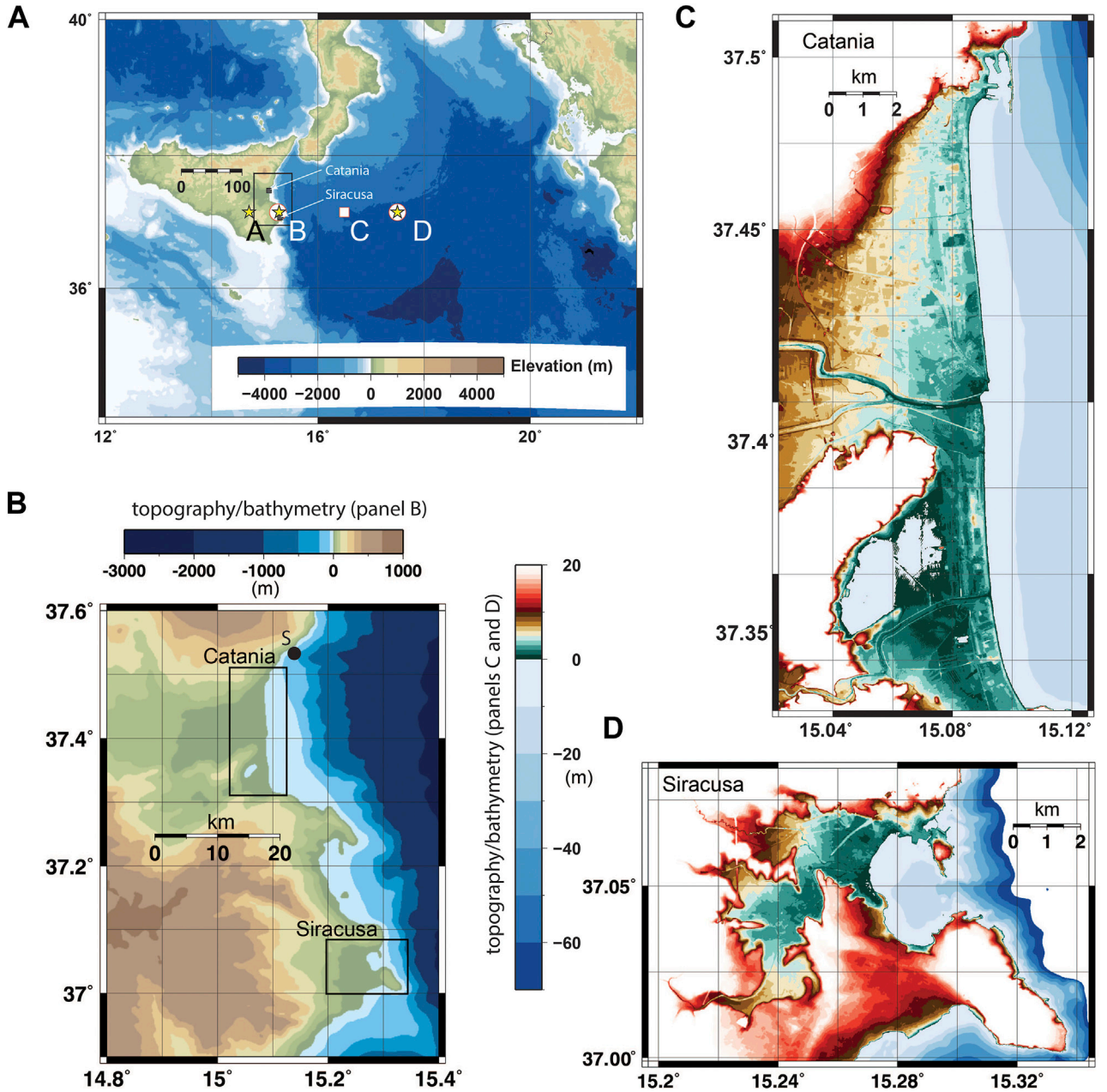


**FIGURE 1 |** Maps at different scales for the earthquake sources and tsunami inundation. **(A)** shows the fault centers for all earthquake scenarios considered. Points A, B, C, and D are all at latitude 37.15°, with longitudes 14.70°, 15.25°, 16.50°, and 17.50° respectively. Yellow asterisks mark the locations of epicenters for scenarios where we examine the effect of the Manning friction coefficient. White circles are locations for which we conduct a fine scan of strike and dip parameters. The white square marks the epicenter of sources where we search the strike, dip, and depth parameter. Panels **(B–D)** show higher resolution maps of the regions surrounding the towns of Catania and Siracusa, where the tsunami inundation is to be evaluated. The black circle labelled S in panel **(B)** is the location 37.5368°N, 15.1333°E for which the sea height time-series are displayed later.

both upon the fidelity of the DEM (e.g. Griffin et al., 2015) and on how well the resistance that surface friction, vegetation, and infrastructure provides is represented (e.g. Kaiser et al., 2011). In the numerical model used to perform the calculations described here, the combined friction effects are often described with the Manning equation where the bottom friction is proportional to the velocity squared through the Manning coefficient $n$. The significance of the choice of $n$ for run-up and inundation was demonstrated by Gayer et al. (2010) who applied both spatially varying and uniform friction to tsunami simulations for Bali, Sumatra, and Java. Bricker et al. (2015) argue that values of $n$ typically applied in tsunami

simulations are too low, in particular for urban and highly vegetated areas. Here, for a limited number of earthquake scenarios, we systematically vary this parameter while keeping the earthquake source definition constant to estimate the influence of $n$ on inundation extent and other properties of the flow. The intention is also to provide insight into the degree to which typical inundation estimates (e.g. those used in Gibbons et al., 2020) were determined by the choice of this parameter.

Here, we study inundation for the stretches of coastline surrounding the towns of Catania and Siracusa in Eastern Sicily, each represented numerically in the simulations with a system of nested grids. Based on Gibbons et al. (2020), we select a subset of the relevant parameters for which we investigate the sensitivity of model parameters on the inundation. **Figure 1A** displays the topo-bathymetric model of the region of the Mediterranean Sea in which the numerical tsunami simulations are performed. With the four earthquake locations in **Figure 1**, we can study earthquakes both offshore and with significant crustal deformation at the coast of interest. In section *Numerical Simulations of Earthquake Generated Tsunamis off the Coast of Sicily* we provide more comprehensive details about the sequences of simulations performed. In section *Sensitivity of Inundation to the Manning Friction* we discuss the sequence of calculations performed to investigate the sensitivity of inundation to the Manning friction coefficient and in section *Sensitivity of Inundation to Earthquake Source Parameters* we discuss the sequences of calculations performed to explore the sensitivity to earthquake source parameters. In section *Conclusion and Discussion* we draw conclusions.

## NUMERICAL SIMULATIONS OF EARTHQUAKE GENERATED TSUNAMIS OFF THE COAST OF SICILY

In this paper, we have carried out sensitivity tests by performing 1,516 separate tsunami simulations to understand how coastal inundation at high spatial resolution varies as a function of several key parameters. For these simulations, we employ the shallow water model Tsunami-HySEA (de la Asunción et al., 2013; Macías et al., 2016, 2017). The shallow water model assumes that the wave length is much longer than the water depth and hence neglects higher order characteristics such as frequency dispersion that is important for some types of tsunamis (e.g. Glimsdal et al., 2013; Løvholt et al., 2013). Manning friction terms, which assume that the bottom friction is proportional to the Manning number $n$ and the squared current velocity, are added to the to the momentum terms in the shallow water equation system. Instantaneous earthquake deformations assuming planar uniform slip using the Okada (1985) model are provided as initial conditions to the simulations. Tsunami-HySEA solves the non-linear shallow water equations through a Finite Volume scheme by means of Riemann solvers, with shock-capturing properties that ensure that wave-breaking is incorporated and with wetting and drying processes necessary for capturing inundation. Further details of the specific Tsunami-HySEA implementation of friction are provided in de la Asunción et al. (2013). Finally, we note that Tsunami-HySEA includes a telescopic grid functionality that allow the modeller to couple coarsely resolved wave propagation over an ocean scale with high-resolution inundation simulations in a local domain. The simulations are performed with a system of four telescopic nested grids. The coarsest grid has the spatial extent displayed in **Figure 1A** and a spatial resolution of 640 m. The others have progressively finer resolutions of 160, 40, and 10 m. The inundation is modelled for the regions surrounding the towns of Catania and Siracusa on the East coast of Sicily (see also Tonini et al., 2021).

All tsunamis simulated are generated by hypothetical earthquakes whose epicenters are located at the positions A, B, C, and D in **Figure 1A**. These earthquake epicenters are based on a subset of the earthquake sources considered in the probabilistic earthquake model of the TSUMAPS-NEAM (NEAMTHM18) Tsunami Hazard Model (Basili et al., 2021). The NEAMTHM18 model consists of a discretization of tsunamigenic earthquake scenarios covering the entire NEAM (North East Atlantic and Mediterranean) region with different magnitudes, depths, fault orientations, and slip distributions. Here, we identified two crustal earthquake scenarios from the NEAMTHM18 model which had resulted in the greatest inundation in the bay of Catania in the tsunami simulations from Gibbons et al. (2020). Both were associated with hypothetical Mw 8.0 earthquakes with fault ruptures of length 183.5 km and width 38.1 km, and with slip of 7.5 m. Both had epicenters on the coast (point B in **Figure 1**), or inland (close to point A in **Figure 1**), and both earthquakes had resulted in significant crustal deformation both onshore and offshore. The coseismic deformations resulting from these two earthquakes are displayed in **Figure 2** (panels A and C). These scenarios are in the low-probability and high-consequence end of the source discretization.

**Figure 1B** displays the locations of the numerical grids with the highest spatial resolution (10 m) and **Figures 1C,D** detail the high-resolution topo-bathymetry with a colour scale chosen to emphasize spatial differences in elevation in the zero to 20-m range of greatest relevance for tsunami inundation and consequence for human life and infrastructure. Regions with elevation over sea-level in the range 0–5 m are coloured green, regions with elevation in the range 5–10 m are coloured brown, and regions with elevation exceeding 10 m coloured red with the colour fading as rising topography takes land and infrastructure above the tsunami threat. Details of the Digital Elevation Model (DEM) are provided in Gibbons et al. (2020) and the sources are listed in the Data Availability Statement. The DEM does not include buildings but, even at a 10-m resolution, some choices have been made regarding built infrastructure with, for example, raised road constructions visible in **Figure 1**. In the DEM and Tsunami-HySEA inundation modelling, these provide a barrier to the incoming water.

The first part of the analysis in the present study is dedicated to exploring systematically how the inundation varies with the choice of the Manning friction parameter. To this end, we perform a suite of tsunami simulations considering four different earthquake sources and 19 values of $n$ (76 scenarios in total). A constant value of the Manning $n$ value for the entire

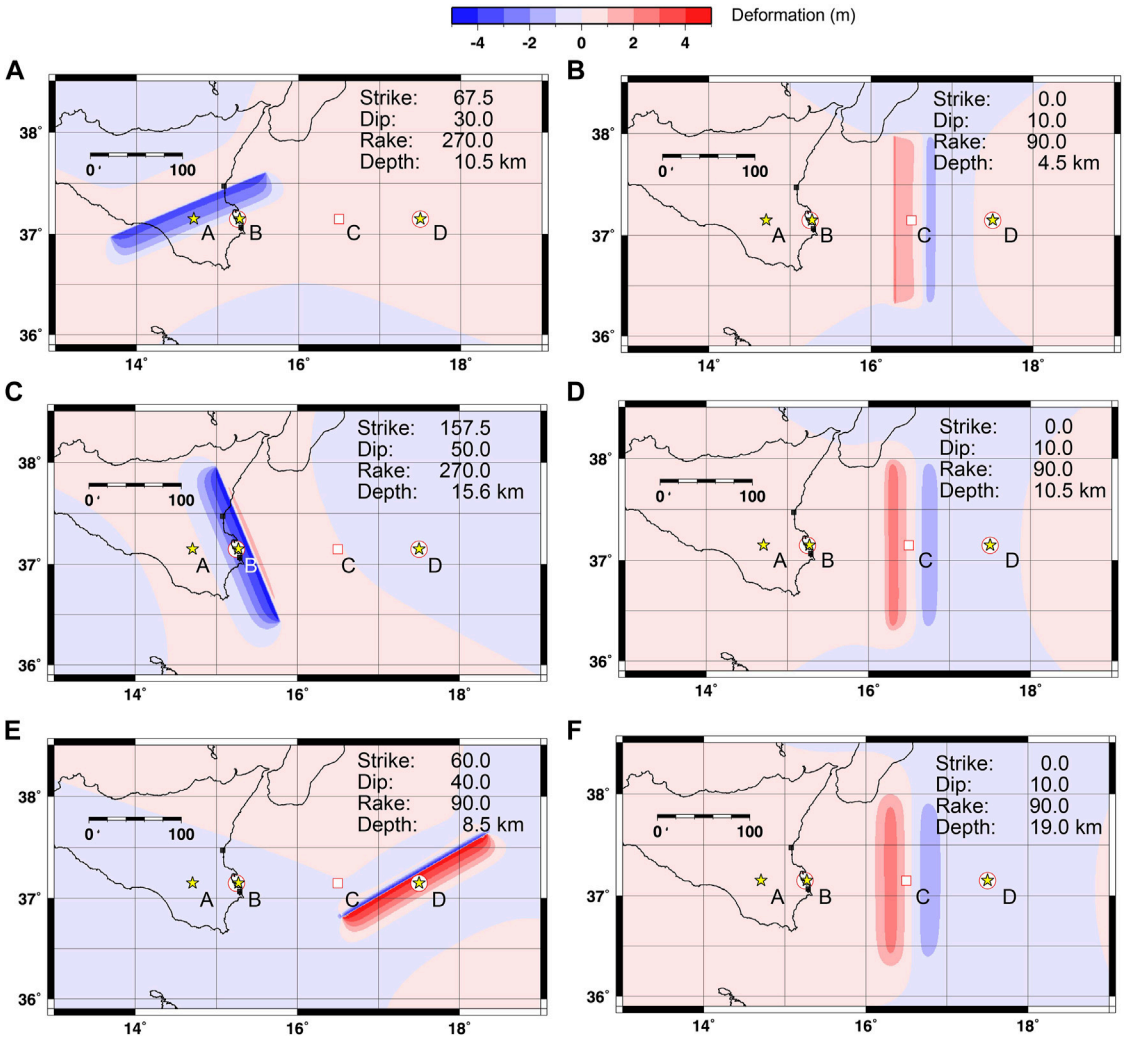


**FIGURE 2 |** Sea floor deformation using the Tsunami-HySEA code with Okada sources with strike, dip, rake, and depth parameters as indicated. All sources have length 183.5 km, width 38.1 km, and slip 7.5 m. Red and blue indicate a raising and a sinking of the ocean floor respectively. The Depth quoted here is the depth of the fault plane centroid. The sea floor displacements in panels **(A,C)** correspond to scenarios based on definitions in the NEAMTHM18 model (subsequently labelled M1 and M2 respectively). The remaining panels **(B,D–F)** show non-NEAMTHM18 scenario definitions considered in this study.

domain is assumed for simplicity. Such an approach is common practice in tsunami simulations even though this does not resolve spatially dependent friction properties of the Earth's surface. We justify it here on the grounds that we want to examine inundation over varying topography as a function of this parameter. A spatially varying $n$ here would represent a vast number of parametric choices and would complicate interpretation. Results from our uniform $n$ parameter searches will hopefully provide guidance in experiment design for studies with spatially varying $n$. The second part of the study explores the dependency of the tsunami inundation on the variability of fault orientation (i.e. strike and dip angles), the slip direction (i.e. the rake angle), and the depth of the source; in that case we analyse a suite of 1,440 tsunami simulations. **Figure 2** shows the sea floor deformation resulting from six different specifications of earthquake parameters selected from the total set of combinations. We adopt for each scenario a uniform slip value along the fault plane and all simulations were run for a total of 4 h following the earthquake.

## SENSITIVITY OF INUNDATION TO THE MANNING FRICTION

Testing the sensitivity of the inundation to the Manning friction was performed for four hypothetical earthquake scenarios, M1, M2, M3, and M4. Two of them, labelled M1 and M2, are almost identical to scenarios from the NEAMTHM18 model, changed only in the exact coordinates of the earthquake fault centers. Scenarios M3 and M4 have the same Okada parameters as scenarios M1 and M2 respectively, except for the epicenters that are moved

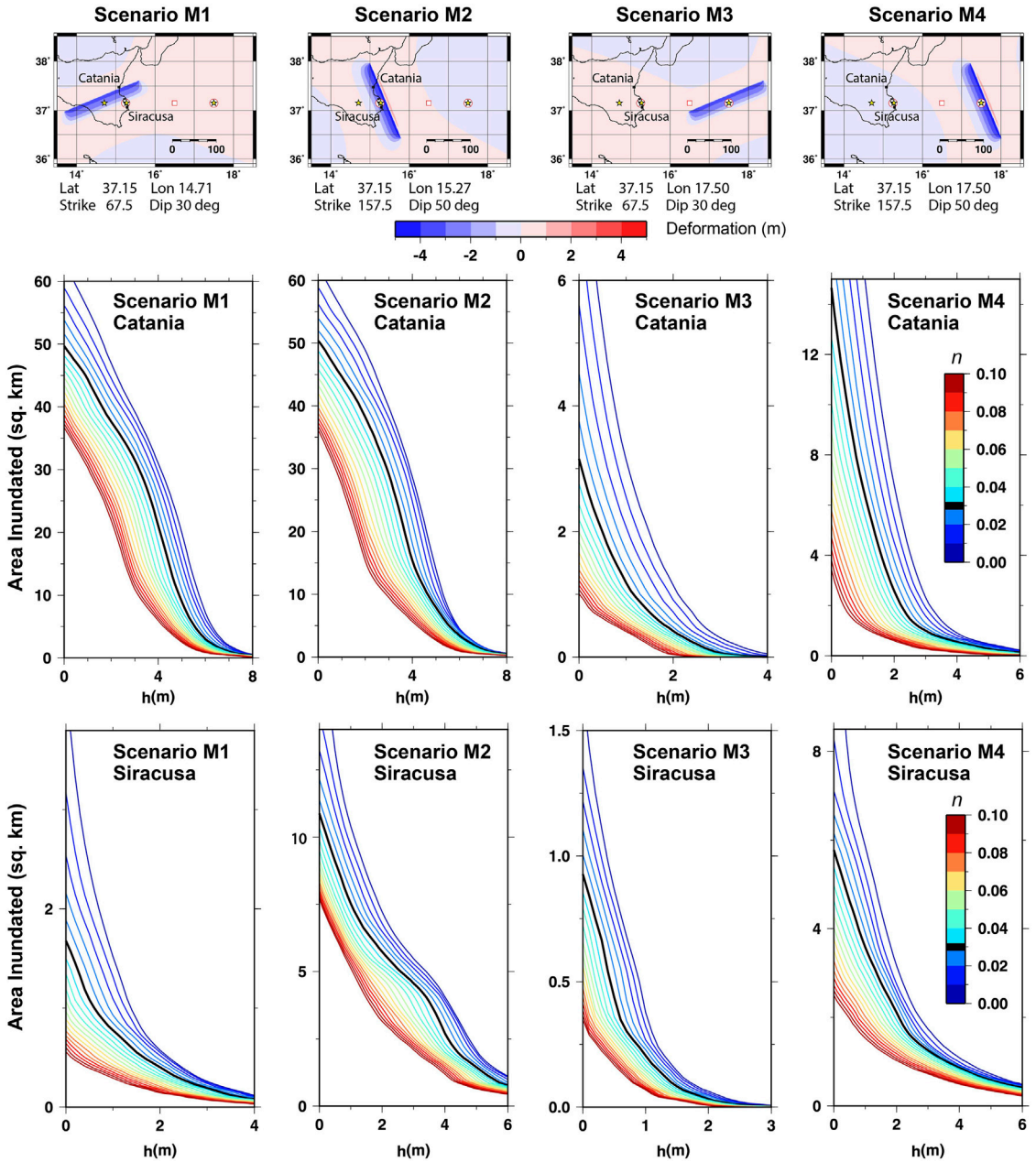


**FIGURE 3 |** Cumulative inundation area plots for Catania and Siracusa for the scenarios M1, M2, M3, and M4. For a given value of h, the curve indicates the area of land that was dry prior to the event which has experienced a maximum flow depth exceeding h m. The 19 curves in each panel cover values of the Manning friction, n, between 0.05 and 0.95 in intervals of 0.005. The curves for n = 0.03 are highlighted and coloured black to mark that this was the value used for all calculations in Gibbons et al. (2020).

significantly offshore to point D to model the sensitivity of a more distal earthquake. These scenarios were selected since the corresponding models from NEAMTHM18 had demonstrated inundation at significant distances inland from the shoreline, such that changes in the degree of inundation due to changes in the friction would be easy to visualize. Out of the subset of scenarios simulated in Gibbons et al. (2020) which generated high inundation, the selection for the friction study here is otherwise quite arbitrary. The seafloor displacements for all four scenarios are displayed in **Figure 3** together with the areas of inundations at Catania and Siracusa resulting from the generated tsunamis.

Inundation scenarios are obtained for Catania and Siracusa for each of the four earthquakes considered and each of the 19 values of $n$, covering the range from 0.005 to 0.095 in increments of 0.005. The value $n$ = 0.03 (which is widely used in operational

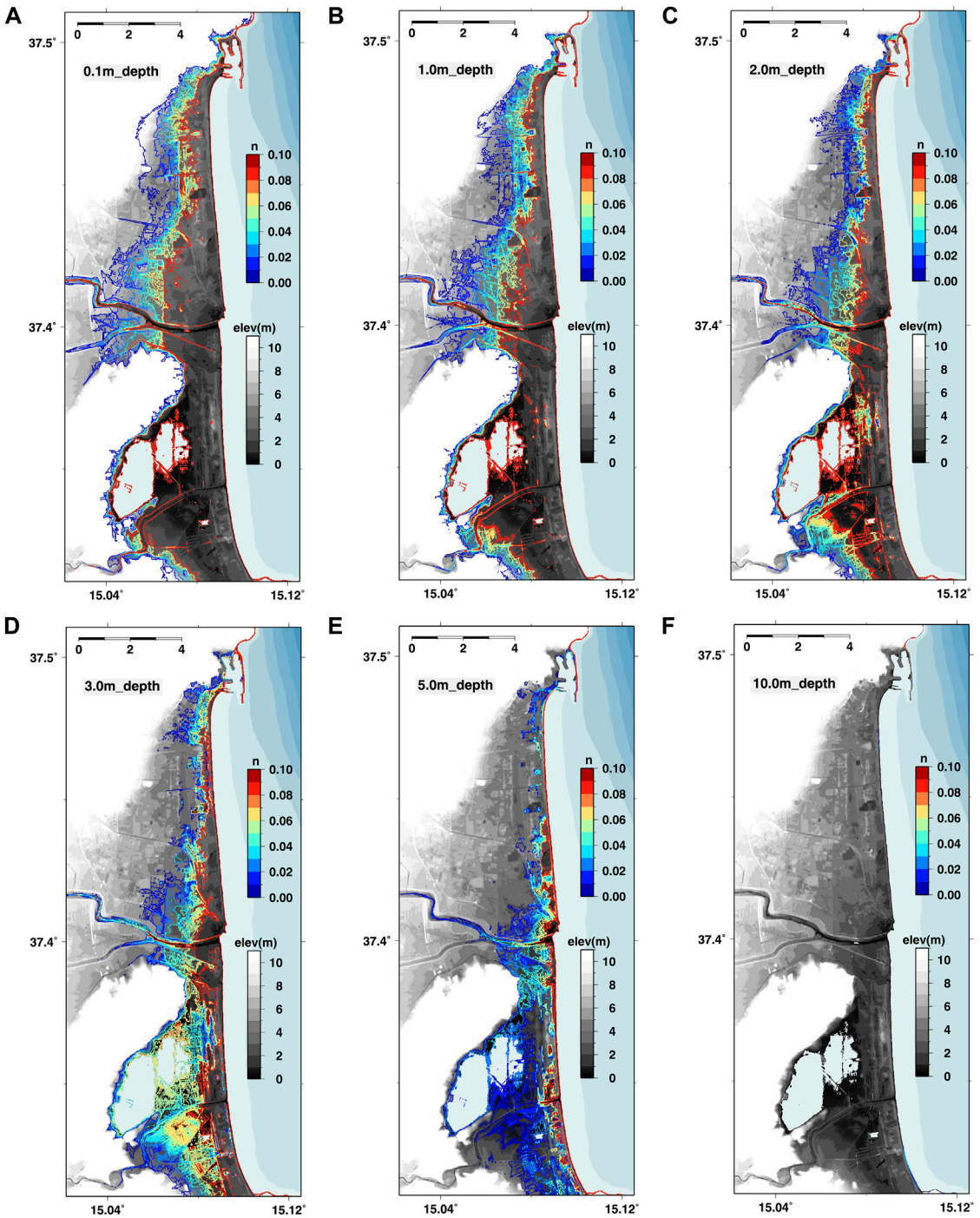


**FIGURE 4 |** Inundation regions for Catania given earthquake scenario M1 for flow depth as indicated for different values of the Manning friction, n. We note that n applies both in onshore and offshore regions and that high n in very shallow offshore water may dissipate some energy in the tsunami before it reaches the shore. Panels **(A–F)** show respectively the maximum extent of inundation for a flow depth of 0, 1, 1.0, 2.0, 3.0, 5.0, and 10.0 m.

tsunami modelling) is highlighted in **Figure 3** as this was the value applied uniformly to all calculations in Gibbons et al. (2020). In all cases, a constant value of n for the entire domain is assumed for simplicity. The Tsunami-HySEA code calculates the tsunami propagation on the bathymetry and topography as deformed by the earthquake and records, for each grid location, the highest water level (relative to the undisturbed sea surface) attained over the entire simulation. The flow depth for a given location is obtained in post-processing by subtracting the deformed topography from this

value. The flow-depth is therefore sensitive to the onshore co-seismic displacement which varies from scenario to scenario, in addition to the water displacement offshore. We consider only areas that were above sea-level prior to the earthquake. **Figure 3** displays, for a given height, $h$, the area of land (in square kilometers) for which the maximum flow depth exceeds $h$. We note that both the horizontal and vertical scales vary from panel to panel in **Figure 3**. Each set of panels corresponds to a different earthquake scenario, and the curves for that scenario are reported for all the 19 $n$ coefficient values. We compare directly only the shapes of the curves for the different values of $n$. All scales were chosen to optimize the resolution of the relationships between the different curves, even though this is at the expense of direct comparison between curves in different panels.

The space between the curves in the $y$-direction gives a measure of the sensitivity of inundation to the $n$ parameter. If the lines are very close together, it means that the inundated area is not highly sensitive to the parameter for the given flow depth. If the lines are far apart, it means that the modelled inundation varies greatly for different values of the friction. The ratio between the value of a curve for a given $h$ and the value of the same curve at $h = 0$ indicates the proportion of the inundated land experiencing the indicated flow depth or higher. That the curves diminish towards zero indicates that relatively small regions experience the maximum flow depths calculated for each scenario. For smaller flow depths, the lines diverge. Simulations with very low values of $n$ model inundation that covers far wider regions than simulations with much higher values.

The results are evaluated for both Catania and Siracusa. We see, in **Figure 1**, three fundamental differences between the regions exposed to inundation at Catania and Siracusa. First, that there is far less low-lying land at Siracusa than at Catania. Second, that the Bay of Catania has almost 20 km of exposed coastline compared with an inlet less than 2 km wide at Siracusa. Thirdly, much of the Bay of Catania has several km of relatively shallow water (less than 100 m deep) separating the coast from the deep sea. At Siracusa, a large shallow bay is partially protected by a large sea wall and the sea floor falls to great depth within a far shorter distance than at Catania.

For the Bay of Catania, the inundation area vs $n$ curves are similar for scenarios M1 and M2. While the epicenters and angle of strike for the two cases differ somewhat, both result in comparable co-seismic subsidence in the region where the inundation is measured. The curves for offshore earthquake scenarios M3 and M4 also display somewhat similar shapes, but the inundation is several times greater for scenario M4 than for scenario M3. Scenarios M3 and M4 differ in the choice of both the strike and dip angles. The strike angle for scenario M4 ($157^o$) makes the rupture more parallel to the coastline than is the case for scenario M3 (strike = $67^o$), and the angle of dip for case M4 ($50^o$) is greater than for case M3 ($30^o$). Both these factors may contribute to the higher inundation for scenario M4. Scenarios M1 (strike = $67^o$) and M2 (strike = $157^o$) differ similarly in orientation to scenarios M3 and M4. However, being far closer to shore and with significant co-seismic displacement within the coastal zone, the tsunami generation relative to the shore is more complicated than for the more distant sources. There are many factors affecting the inundation area metrics for scenarios M1 and M2 and the similarity in the inundated extents may be quite coincidental.

For Siracusa, the two scenarios M2 and M4 (both with strike = $157^o$) result in significantly greater inundation than either scenarios M1 or M3 (both with strike = $67^o$). That the inundation for scenario M4 significantly exceeds the inundation for scenario M3 at Siracusa is, as for Catania, likely the result of the strike angle being more aligned with the coastline, resulting in an unfavourable directivity of the tsunami. The corresponding difference between scenarios M1 and M2 is likely exacerbated by the significant co-seismic subsidence at Siracusa for scenario M2 which does not happen in scenario M1 (see uppermost panel of **Figure 3**).

**Figure 4** illustrates what the inundation curves mean in terms of the spatial pattern of the inundation for scenario M1 at Catania (as shown in the top left panel of **Figure 3**). We focus on the pre-earthquake topography between zero and 10 m with a greyscale indication of elevation. A sequence of coloured lines marks the maximum extent of inundation for each of the specified levels of flow depth as a function of the Manning friction. The Southernmost part of the Bay of Catania is low-lying land bounded by a steep rise in topography. Panel A shows that the inundation of the low-lying region is stopped only by topography for all but the highest (and least physical) values of $n$. In the Northern part of the bay, the topography rises somewhat more gradually. The extent of the inundation increases steadily further inland for lower values of $n$. In this northern part, the extent of inundation with the high friction parameter of $n = 0.09$ is approximately 50% of the extent of inundation with the respective low value of $n = 0.01$ with intermediate (and more realistic) values resulting in inundation extents between these extremes. Greater flow depths (panels B through F) are increasingly restricted to the near-shore region. In the more sloping northern part of the bay, the limit of inland reach approaches the coast steadily for each increase in flow depth considered. In the far flatter southern part of the bay, the area of inundation is less sensitive to $n$. For flow depths of 0–2 m (panels A–C, only the very highest values of $n$ prevent almost total inundation of the low-lying region. For a flow depth of 5 m (panel E), only at the lowest values of $n$ is there inundation significantly inland. As expected from the inundation curves in **Figure 3**, a flow depth of 10 m is recorded only close to the shoreline to the north of the harbour wall (panel F).

**Figure 5** displays the maximum momentum flux attained as a function of location for each of the scenarios and for three chosen values of $n$: 0.01, 0.03, and 0.05. This measure of the tsunami impact changes more significantly with $n$ than the spatial extent of the inundation. The wave period of the incident wave is in the order of 10 min; this gives rise to a positive wave forcing on the coastline that lasts for several minutes. This will feed the inland wave over a long time before the wave can retreat. In the lower lying regions, the inundation will continue until stopped by an ultimate topographic barrier. The flow depth, and consequently the momentum flux, will decrease more with distance from the sea for higher values of $n$. For areas with gently increasing topography, the reduction in flow depth with distance

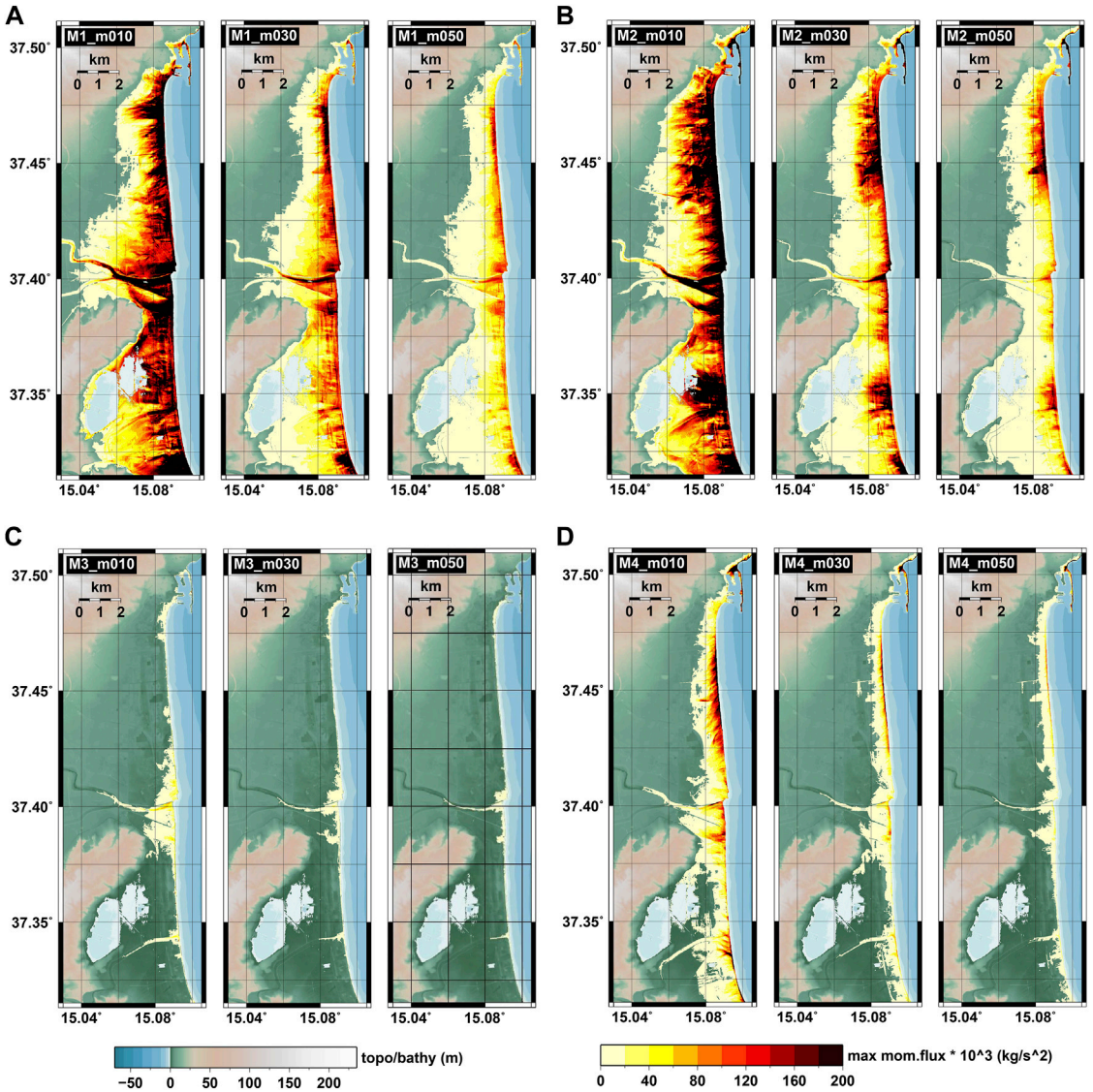


**FIGURE 5 |** Maximum momentum flux recorded as a function of position in the Bay of Catania for earthquake scenarios M1, M2, M3, and M4 in panels **(A–D)** respectively. Each panel shows the results of the simulations with Manning friction values 0.01, 0.03, and 0.05 as indicated.

resulting from the higher *n* will lead to a corresponding reduction in the inundation distance.

**Figure 6** displays corresponding patterns of maximum momentum flux but for the region surrounding Siracusa. Whereas the inundation in the Bay of Catania is very similar for scenarios M1 and M2 (**Figures 5A,B**), the inundation at Siracusa for scenario M1 (**Figure 6A**) is significantly lower than that for scenario M2 (**Figure 6B**). This is easy to understand in relation to the fault specifications (**Figure 3**). Both scenarios have significant downward displacement along the Catania coastline but only scenario M2 results in ground displacement directly at Siracusa. Even though the inundation for scenario M1 is significantly less at Siracusa, there are clear differences in both the extent of inundation and in the maximum momentum flux for the different values of *n*. In all cases, the inundation is greatest for the town of Siracusa (at the northern end of the bay) although inundation penetrates several km inland along the lowest-lying ground both for scenarios M2 and M4.

## SENSITIVITY OF INUNDATION TO EARTHQUAKE SOURCE PARAMETERS

We perform four different sweeps of parameters, with one being described in each of the following four sections. The first of these sweeps considers sensitivity to the angle of rake. The second and third sweeps scan jointly the parameters strike and dip, considering separately the far offshore and the near-shore earthquake sources. The fourth and final sweep investigates the dependency on strike, dip, and depth.

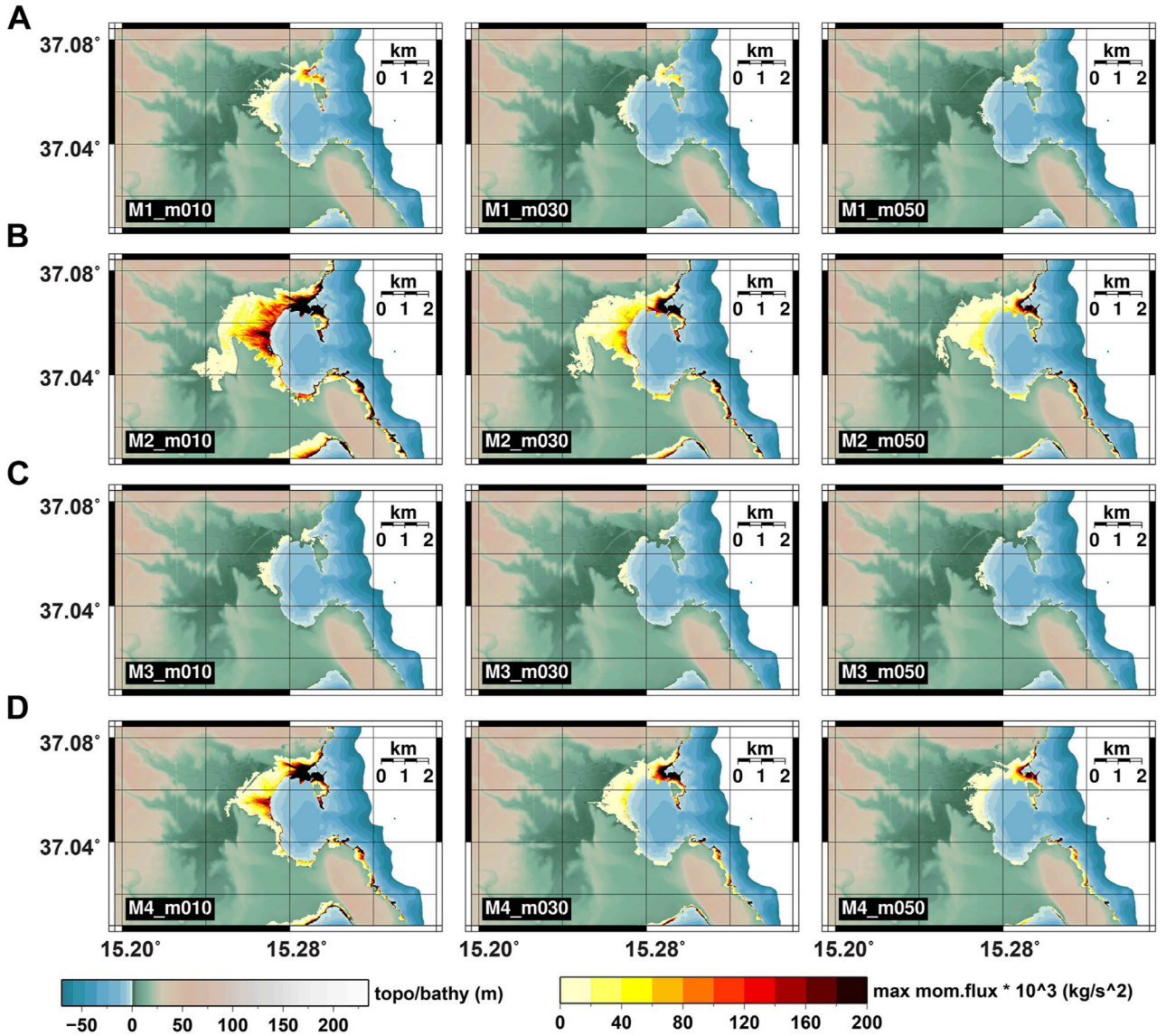


**FIGURE 6 |** Maximum momentum flux recorded as a function of position around Siracusa for earthquake scenarios M1, M2, M3, and M4 in panels **(A–D)** respectively. Each panel shows the results of the simulations with Manning friction values 0.01, 0.03, and 0.05 as indicated.

## Sensitivity to the Angle of Rake

The angle of rake gives the relative direction in which the hanging wall moves over the foot wall. A rake angle of zero or 180° is a strike-slip fault, in which there is no vertical slip. A rake angle of +90° is a reverse thrusting fault, where the hanging wall moves upwards relative to the foot wall. A rake angle of 270° or −90° is a normal fault in which the hanging wall moves downwards relative to the foot wall. All other angles of rake indicate some form of oblique faulting. The eastern coast of Sicily is approximately North-South aligned such that a tsunami generated by an earthquake to the East of Sicily will likely have greatest impact if the rupture has a North-South strike angle. We also anticipate that an dip angle of around 45–50°, accompanied by dip-slip faulting (rake around 90° or −90°), will likely have the greatest effect (Kajiura, 1980; Geist, 1998). We ran 48 simulations, with strike angles of both 0° and 180° and the full range of rake angles in increments of 15°. The epicenter for all the earthquake sources selected was set to the point labelled D in **Figure 1**; this ensured that no co-seismic displacement occurred on or close to land at the coastline of interest.

In addition to the inundation maps, we also save time-series of tsunami surface elevations at several offshore points of interest from the numerical tsunami simulations. **Figure 7** displays these time-series for each of the 48 simulations, evaluated at a single location offshore Catania: synthetic marigrams. **Figure 7B** is for strike = 0°, where the fault dips to the East and away from Sicily,

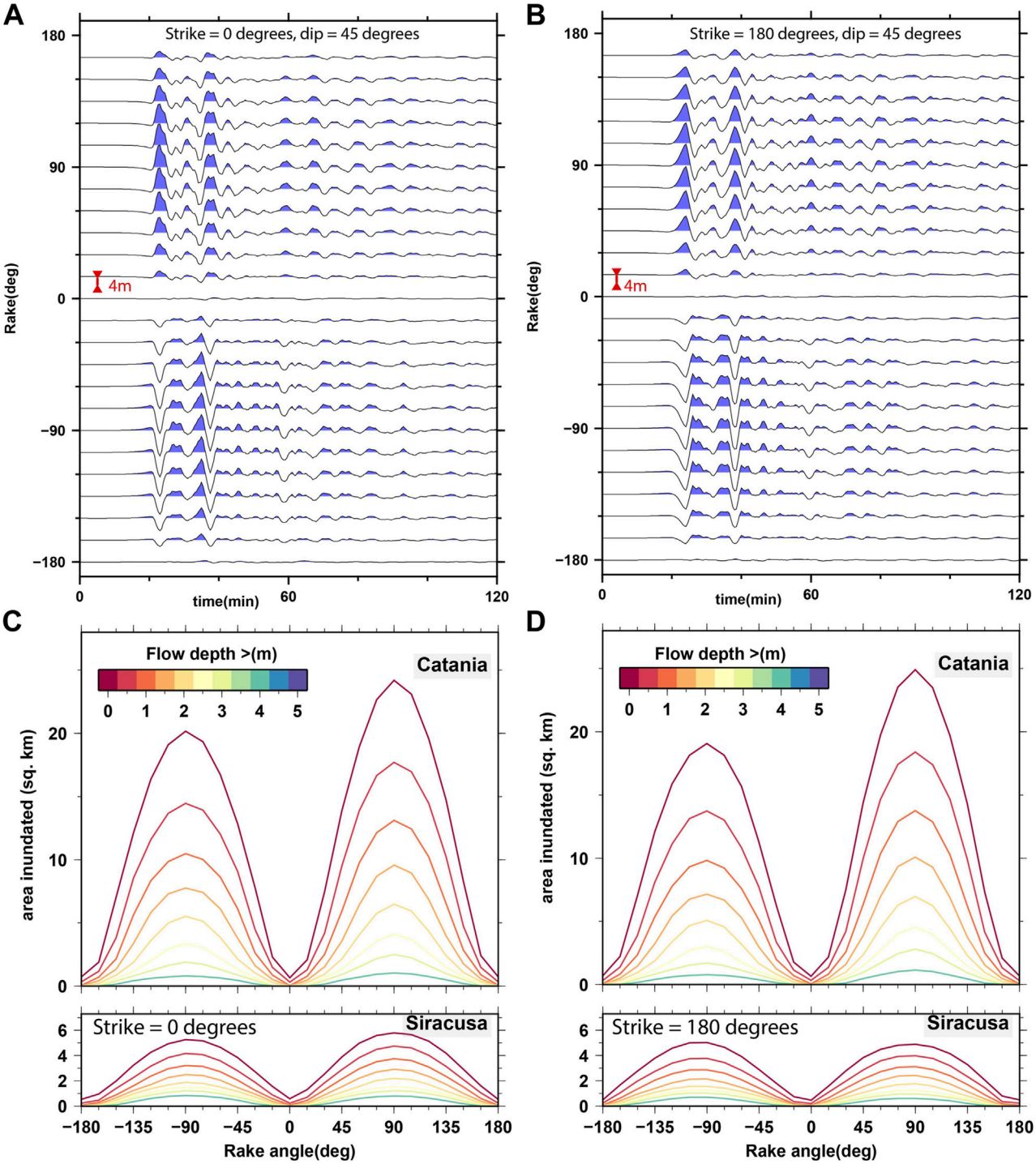


**FIGURE 7 |** Varying the angle of rake. **(A,B)** Offshore surface elevation time-series generated by the Tsunami-HySEA code for the location 37.5368°N, 15.1333°E, offshore of the Bay of Catania on Sicily as a function of minutes after the earthquake origin time. All channels are displayed to the same vertical scale with the red scale bar indicating a vertical displacement of 4 m **(C,D)** Area of land inundated with a flow depth exceeding the value indicated by the colour for the tsunamis generated by the earthquakes in the scenarios as indicated. The areas measured for Catania are within the region displayed in **Figure 1C** and the areas measured for Siracusa are within the region displayed in **Figure 1D**. The curves are displayed for the following values of the height, h: 0.01, 0.5, 1.0, 1.5, 2.0, 2.5, 3.0, and 4.0 m.

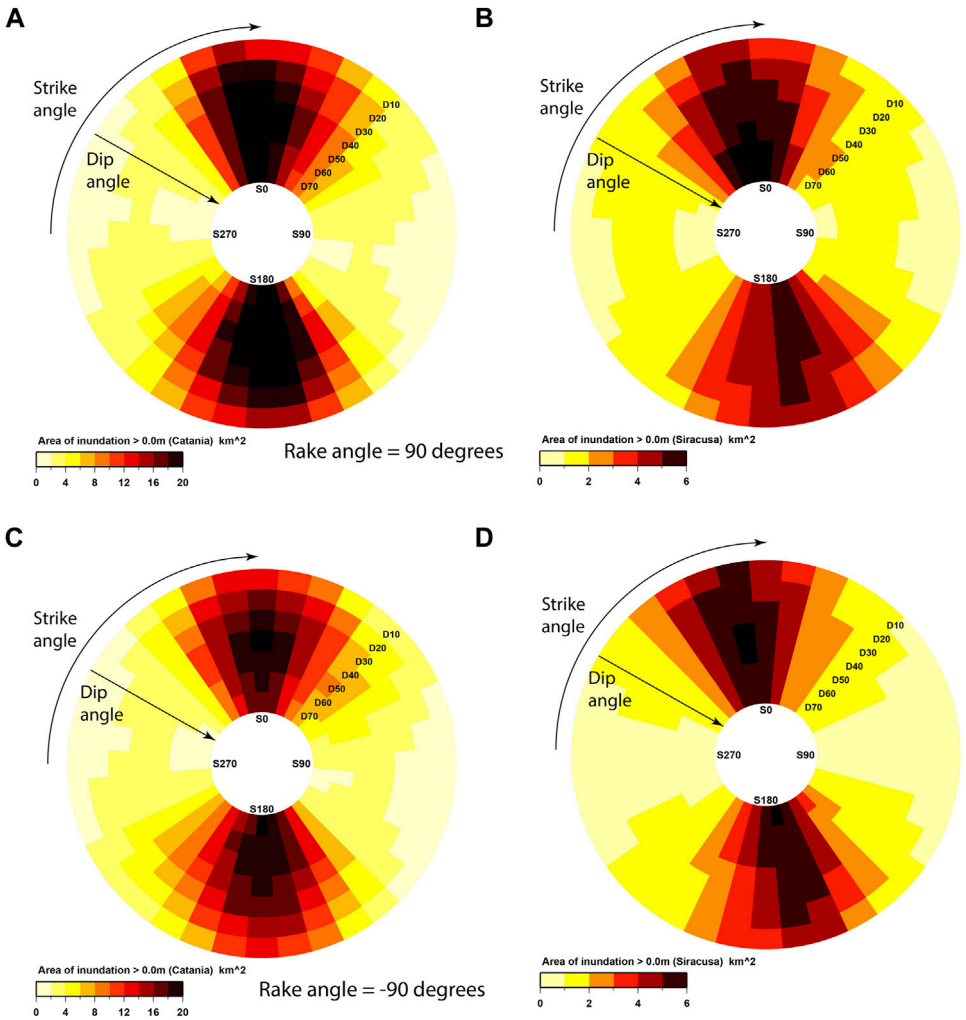


**FIGURE 8 |** Area of tsunami inundation in km$^2$ for Catania **(A,C)** and Siracusa **(B,D)** for earthquake scenarios with fault centers at point D (significantly offshore). Panels **(A,B)** display inundation for rake = 90$^o$ (reverse faulting) and panels **(C,D)** for rake = –90$^o$ (normal faulting). The colour scales differ for the two locations, reflecting the areas subject to inundation, but are identical for the normal and reverse sources at both locations.

and panel (B) is for strike = 180$^o$, where the fault dips to the West and towards Sicily. As expected, the greatest amplitudes are observed for the pure reverse faulting (rake = 90$^o$) and the pure normal faulting (rake = −90$^o$) whereas the strike-slip faulting results in very small wave-heights. As is quite well established, the oblique faulting scenarios result in very similar waveforms to the purely reverse and normal faulting scenarios, just at lower amplitudes, as the faulting style controls the proportion between horizontal and vertical coseismic sea floor displacement; dip-slip faulting provokes a larger amount of the more tsunamigenic vertical displacement.

The choice between strike 0$^o$ and strike 180$^o$ has a second order effect on the amplitudes, affecting the shape of the waves more than their amplitude. For the strike = 0$^o$ simulations (fault dipping away from Sicily: **Figure 7A**), reverse faulting (rake > 0$^o$) results in a small initial drop in the offshore sea elevation, around 15 min after the earthquake, followed by a rapid increase, for which the global maximum is achieved about 20 min after the origin time. For the normal faulting earthquakes (rake < 0$^o$) the opposite occurs; a small increase is followed by a significant decrease with maximum inundation happening some 20 min after the initial wave arrival. For the strike = 180$^o$ simulations (fault dipping towards Sicily: **Figure 7B**), with reverse faulting, the maximum sea elevation still happens on the first upward wave but with a somewhat slower rise. For the normal faulting sources, the offshore elevation is somewhat lower than both the reverse faulting sources and the normal faulting sources for the strike = 0$^o$ case.

**Figures 7C,D** shows the dependence of the inundation features to the faulting parameters. We choose several discrete target flow depth values, $h$, and for each we plot, as a function of the rake angle, a curve of the area of land inundated with maximum flow depth greater than $h$. This is done separately for Catania and Siracusa, and for strike = 0$^o$ and strike = 180$^o$, as indicated. For both Catania and Siracusa, and both strike = 0$^o$ and strike = 180$^o$, there is an approximate order of magnitude scaling

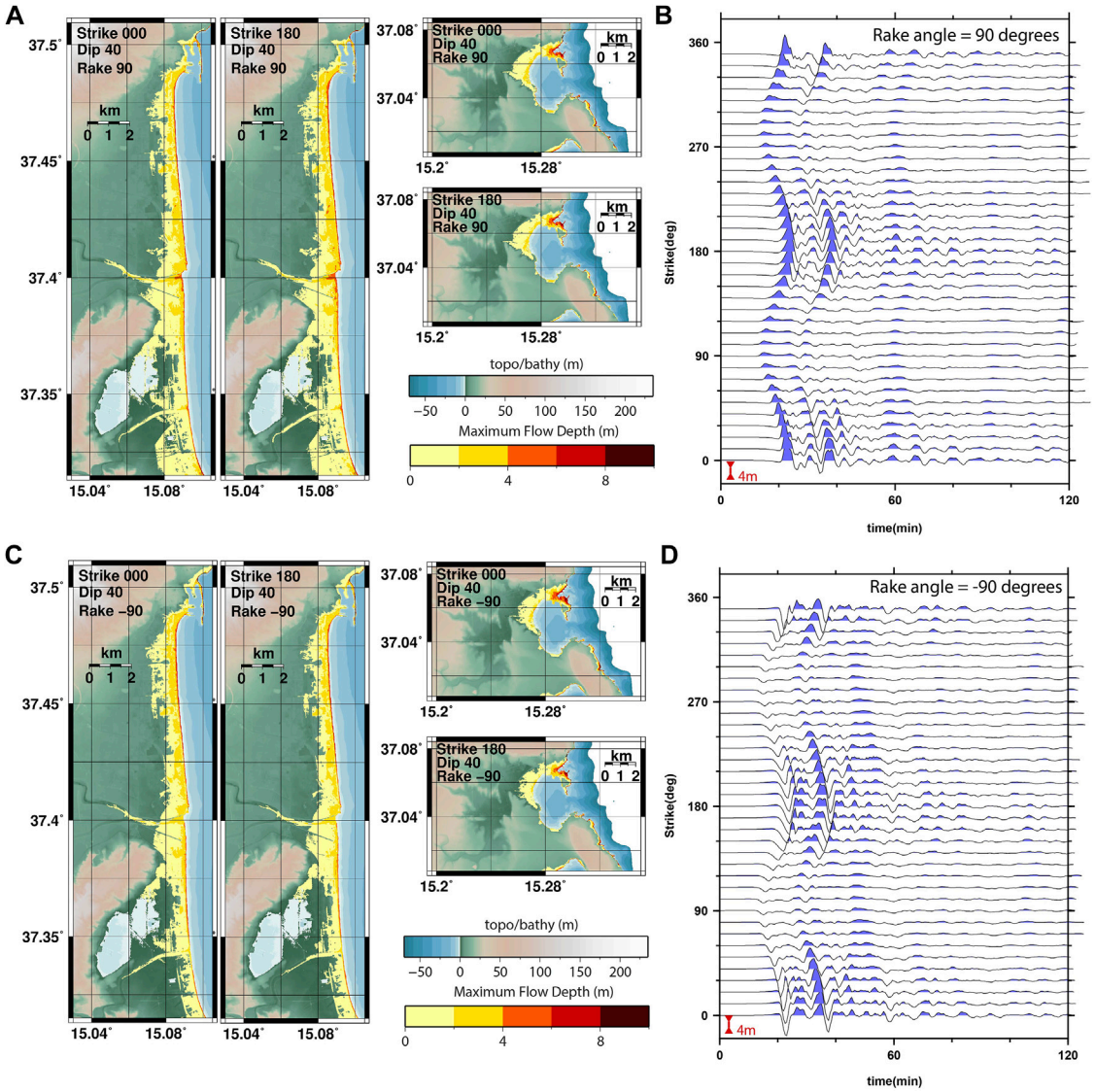


**FIGURE 9 |** Inundation maps for Catania and Siracusa for the relatively distant offshore earthquakes as indicated together with surface elevation time-series as simulated at the location 37.5368°N, 15.1333°E. Panels **(A,B)** display inundation maps and time-series for rake = 90°, panels **(C,D)** for rake = −90°. The time-series are all for the dip = 50° scenarios. Vertical surface elevation scales and colour scales are identical for all panels.

factor between the inundated area given a normal or reverse thrust fault movement (rake = 90° or -90°) and the inundated area given a purely strike-slip fault. For Catania, the reverse thrusting faults generate a 20–25% greater inundation than the corresponding normal faults, which reflects the ratio between the positive and negative offshore amplitudes (**Figures 7A,B**). For Siracusa, there is less of a difference. As expected there is a quite simple relation between the rake angle and the area of inundation, supporting the assumption that we can limit our parameter searches in PTHA earthquake scenarios to the cases 180°, 90°, 0°, and −90° (as with e.g. Selva et al., 2016; Basili et al., 2021) and estimate from calibration curves what the inundation would be for oblique faulting. We appreciate that there may be situations in more complicated topo-bathymetry where the angle of rake and severity of inundation could have a more complicated relationship.

## Sensitivity to the Fault Strike and Dip (Far Offshore Case)

For the second sweep of earthquake parameters, we stay at the further offshore source location (**Figure 1D**) and vary the angles of strike and dip while assuming rake angles of +90° or −90°. We cover the full range of strike angles in intervals of 10° and consider dip angles in the range 10°–70°, also in intervals of 10°. **Figure 8** displays the inundated area in the Bay of Catania (panels A and C) and at Siracusa (panels B and D) as a function of strike and dip using intensity of colour in a wheel; the sources

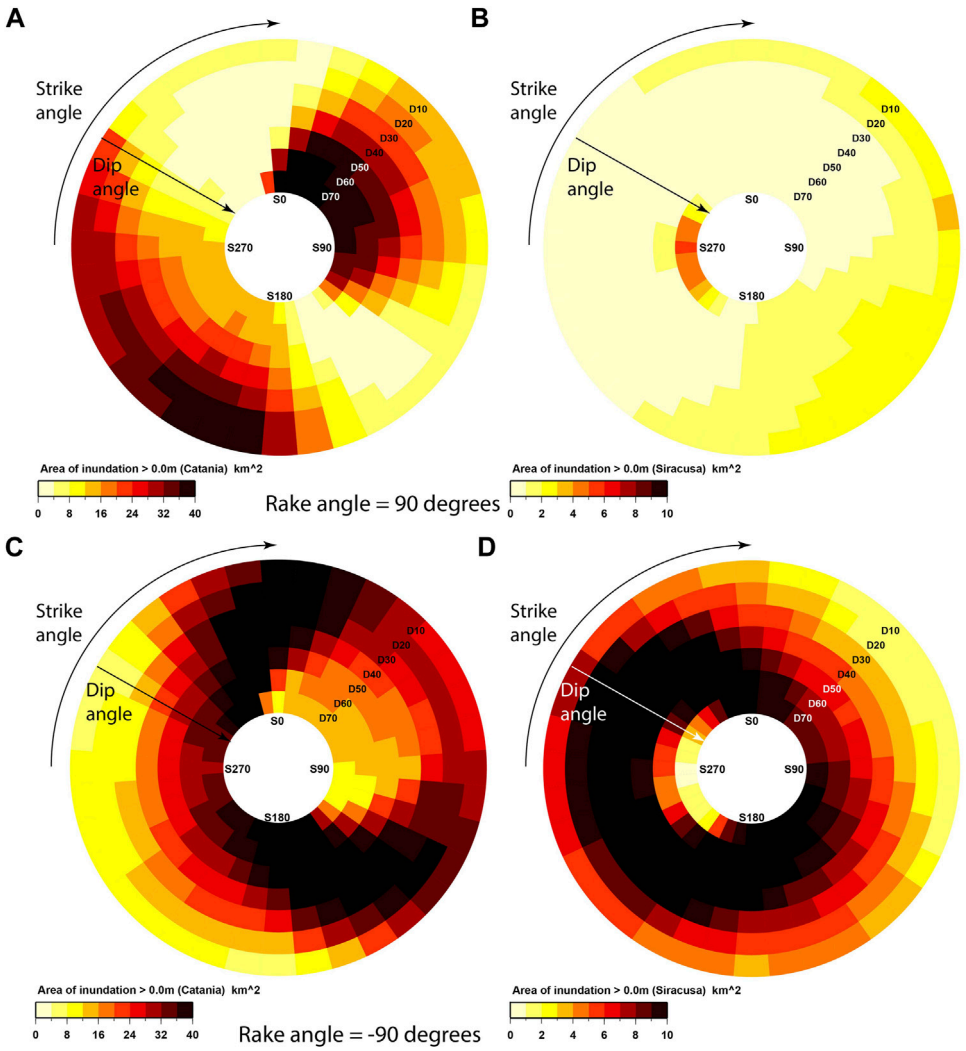


**FIGURE 10 |** Area of tsunami inundation in km$^2$ for Catania and Siracusa for the earthquake scenarios with fault centers at point B (near-shore). Panels **(A,B)** display inundation for rake = 90°, panels **(C,D)** for rake = –90°. The colour scales differ for the two locations, reflecting the areas subject to inundation, but are identical for the normal and reverse sources at both locations.

with shallow dip angles (dip = 10°) are displayed in the outer ring and sources with increasingly steep dip angles displayed progressively closer to the center. The upper panels (A and B) are for reverse thrust faulting earthquakes and the lower panels (C and D) are for normal earthquake sources.

Strike and dip seem to influence the inundation area almost independently, with the peaks induced by the dip at intermediate angles that modulate the trend imposed by the strike angle. The strongest dependence is with the strike angle with by far the greatest inundation for sources with strike angles in an approximately North-South direction. The strike angles resulting in the most significant inundation differ slightly for the two coastal stretches, matching almost perfectly the corresponding coastline orientations at the two locations (see **Figure 1B**). A strike angle differing from this direction by 30° or more results in a significant decrease in the inundation area.

The dip angle dependence is weaker than the strike angle dependence. Maximum inundation typically occurs for a dip angle around 45° degrees although there are exceptions. The steeper dip angle sources result in greater inundation for some strike angles (at Siracusa in particular) and only for the shallowest dip angles (e.g. 10°) is the inundation extent significantly lower than for the steeper angles. There is significant symmetry between the inundation areas resulting from the reverse fault earthquakes (**Figures 8A,B**) and the corresponding normal counterparts (**Figures 8C,D**). Inundation varies relatively smoothly with both strike and dip and it appears that the chosen discretization is sufficiently fine that no qualitatively different inundation patterns have been omitted. Each of the rose diagrams in **Figure 8** contains the results from 252 calculations such that, with this sampling density, 504 scenarios are required to cover the strike, dip, and rake parameters alone for a single location, depth, dimensions,

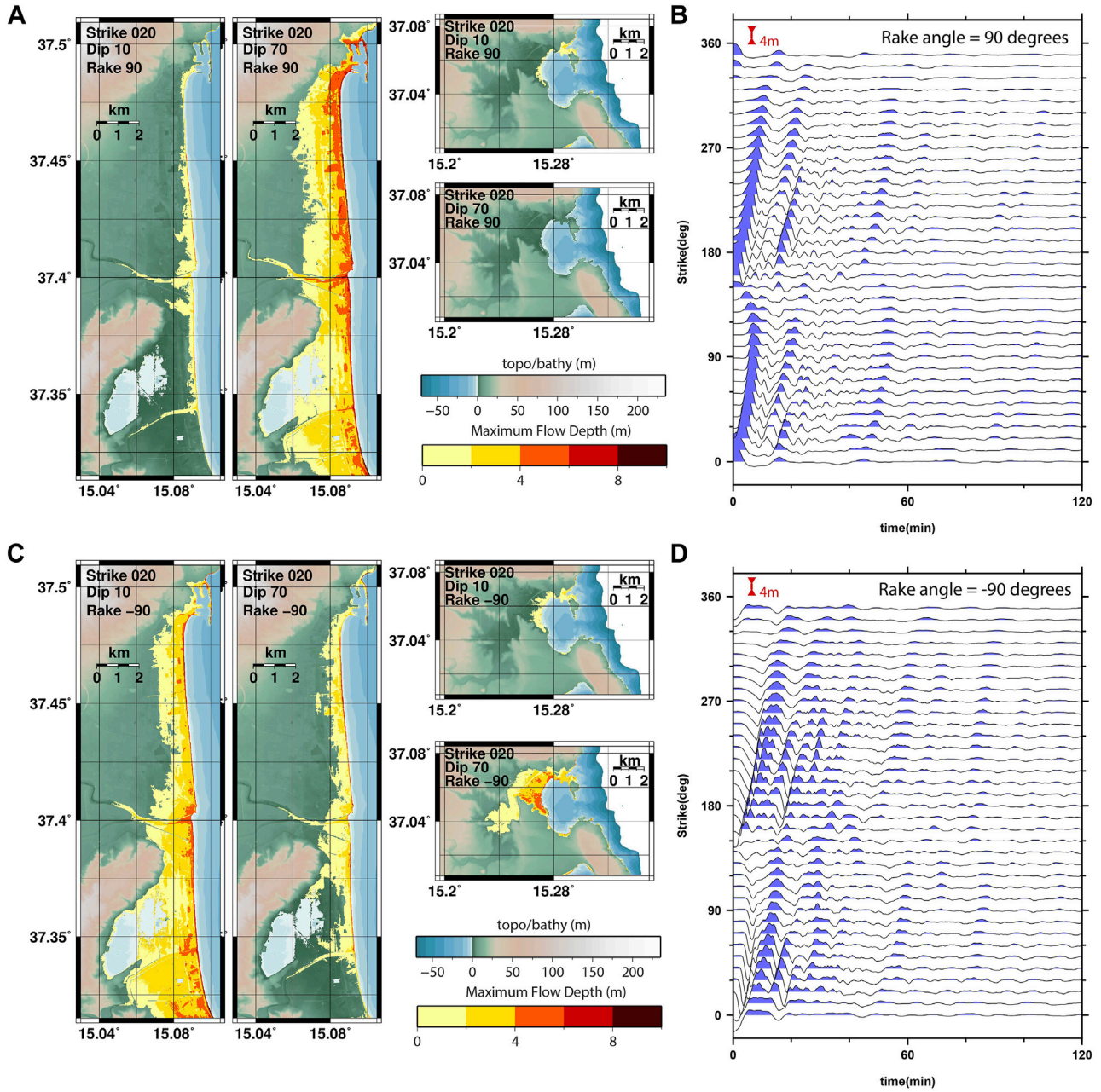


**FIGURE 11 |** Inundation maps for Catania and Siracusa for the relatively distant offshore earthquakes as indicated together with surface elevation time-series as simulated at the location 37.5368°N, 15.1333°E. Panels **(A,B)** display inundation maps and wave height for rake = 90°, panels **(C,D)** for rake = −90°. The time-series are all for the dip = 50° scenarios. Vertical surface elevation scales and colour scales are identical for all panels.

and slip specifications. In a PTHA, where many fault centers, magnitudes, and slip specifications need to be covered, we would ideally like to reduce the sampling density for these angles. Given the relatively small range of the strike angles resulting in the greatest inundation, it seems necessary to have 30-degree intervals or finer for the angle of strike for resolving this parameter space in hazard analysis. The smaller sensitivity to the dip angle would suggest that the sampling interval in dip could be reduced without fear of introducing significant bias in inundation quantification.

**Figures 9A,C** show maximum flow depth maps at both Catania and Siracusa for four of the scenarios displayed in **Figure 8** resulting in the greatest inundation areas. All scenarios have a dip angle of 40° and we consider strike = 0° and 180° for both normal and reverse earthquake mechanisms. The patterns of maximum inundation are relatively consistent for

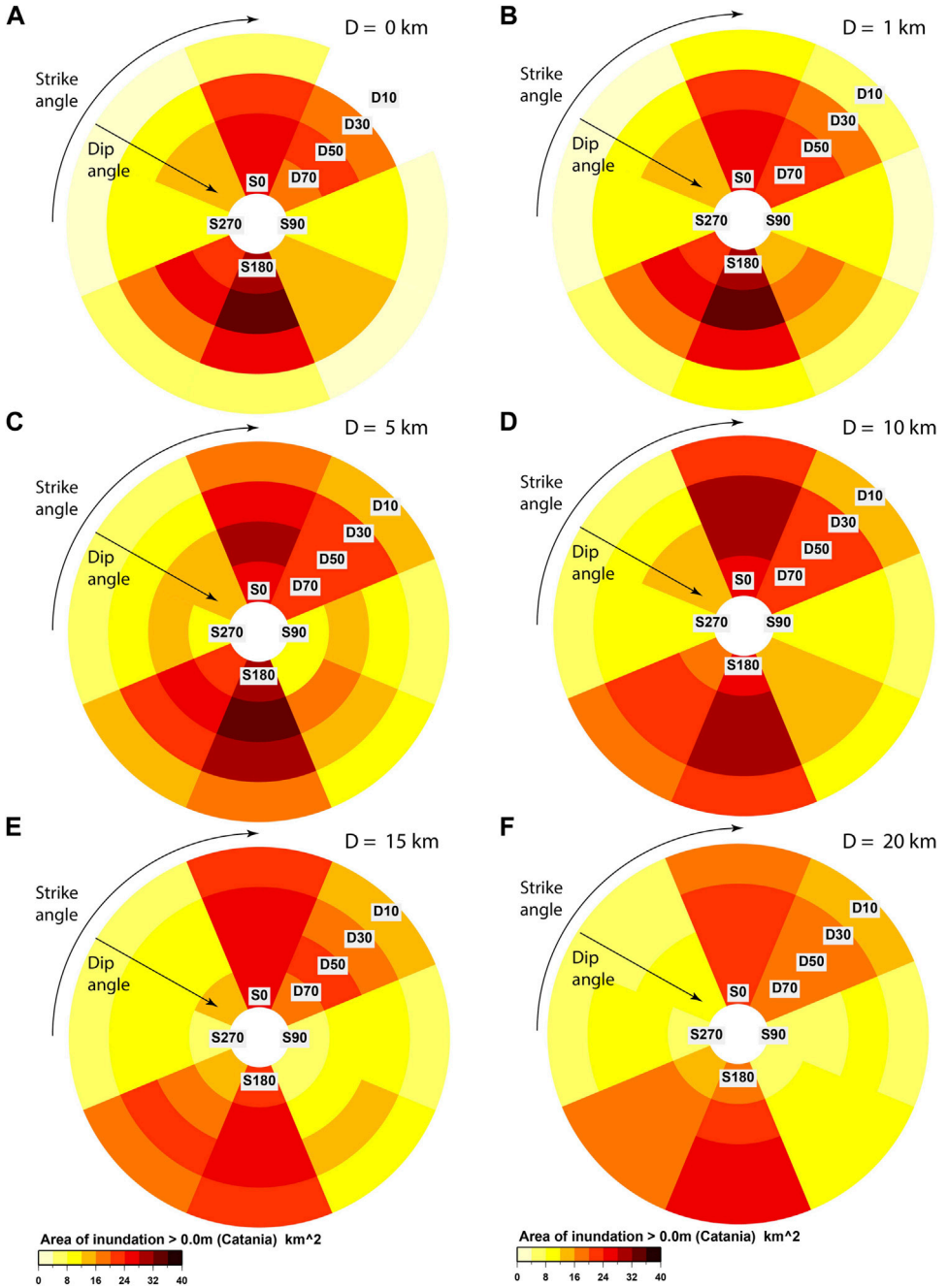


**FIGURE 12 |** Area of inundation in the bay of Catania as a function of strike, dip, and depth for tsunamis with the earthquake sources with rake = 90°. Panels **(A–F)** indicate respectively inundation resulting from earthquakes with depths 0, 1, 5, 10, 15, and 20 km.

all scenarios with no qualitative differences observed. Panels B and D shows synthetic marigrams at the same offshore point as displayed in **Figure 7** for each of the calculations with dip = 50°. Whereas the wave arrival time was almost identical for all the traces in **Figure 7**, with a fixed strike angle and varying rake, there is an almost sinusoidally varying arrival time for the traces in **Figure 9**. The East-West striking sources result in weaker inundation but an earlier arriving wave, as part of the seafloor displacement occurs closer to the sensor. The maximum surface elevations achieved for strike = 0° and strike = 180° are similar although there are subtle differences in the shape of the waveform. The gradual change in the shape of the wavelet with the 10° increment in the strike angle is again a good indication that the applied parameter sampling density is sufficient for a qualitative understanding of the behaviour over the full range of strike angles. We note that these single-point

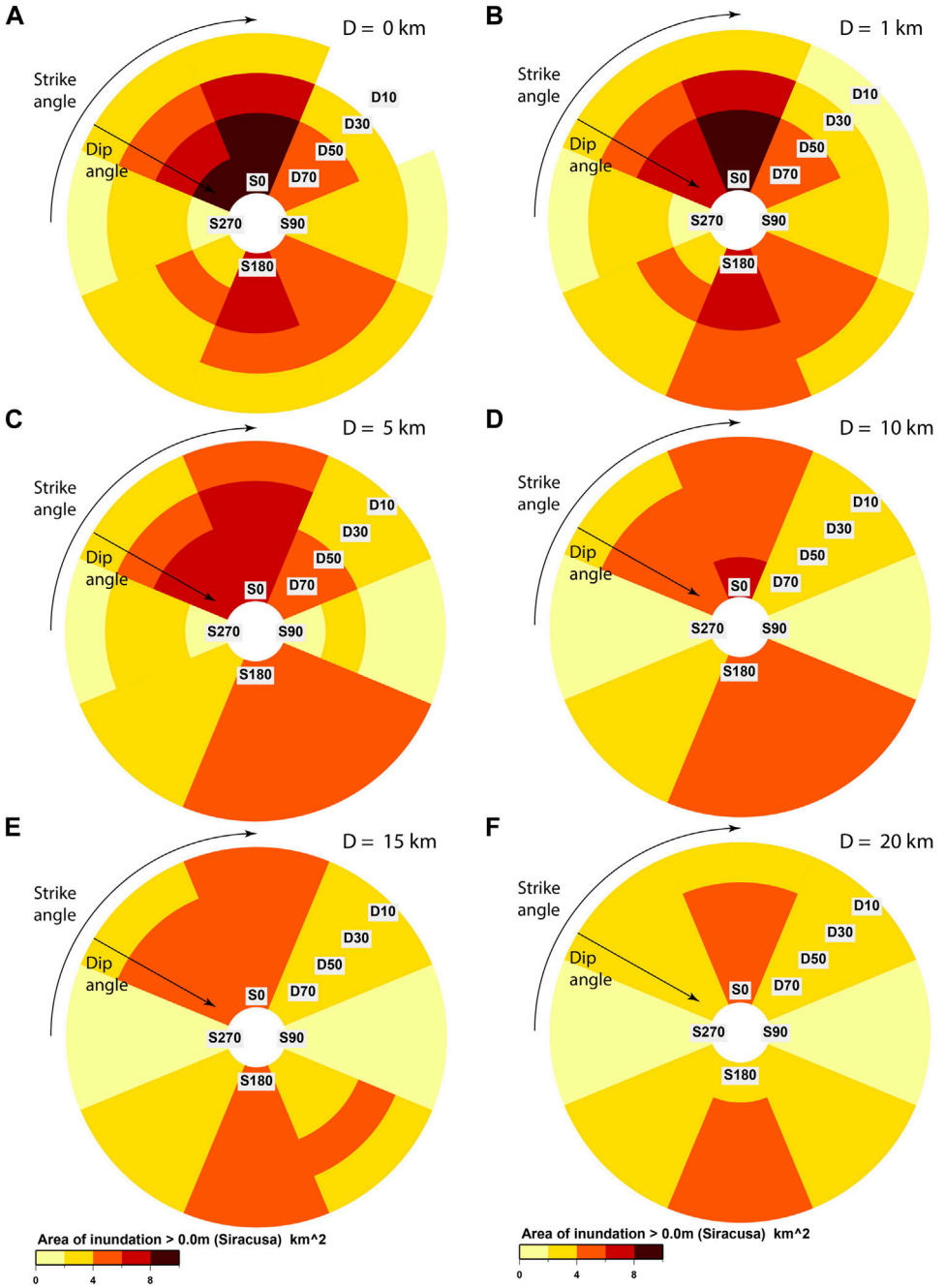


**FIGURE 13 |** Area of inundation in the bay of Siracusa as a function of strike, dip, and depth for tsunamis with the earthquake sources with rake = 90°. Note that the colour scales in **Figures 12**, **13** are different with lower areas of inundation for the smaller bay at Siracusa. Panels **(A–F)** indicate respectively inundation resulting from earthquakes with depths 0, 1, 5, 10, 15, and 20 km.

offshore time-series do not provide any information about the directionality of the wave. The offshore wave amplitudes are lower for the East-West striking sources than for the North-South striking sources and the oblique directivity of the incoming wave will likely reduce the inundation further.

The simulated offshore marigrams in **Figures 9B,D** indicate the most significant differences between the normal and reverse faulting sources. For the reverse mechanisms (**Figure 9B**), the maximum surface elevation is attained on the first peak; the corresponding times in the traces for the normal mechanism earthquakes (**Figure 9D**) has a negative peak with similar amplitude. Along the wavetrain, there is considerable symmetry between each trace for the reverse thrusting earthquake in **Figure 9B** and the negative of the

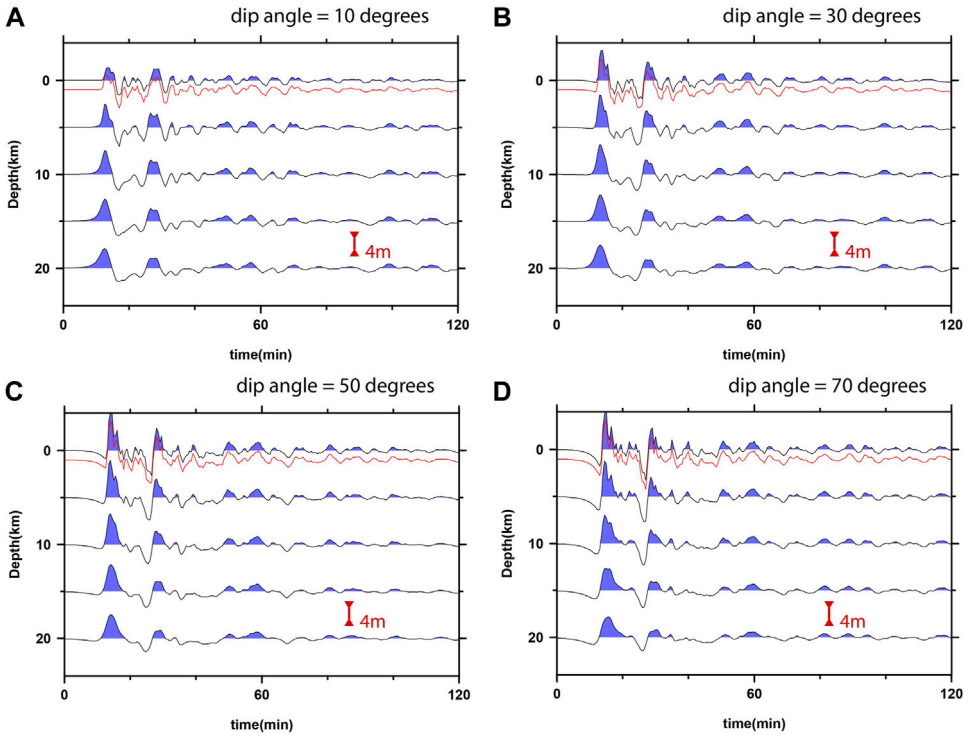


**FIGURE 14 |** Offshore time-series of tsunami surface elevation as a function of dip angle and depth for tsunamis from earthquake sources with rake = 90°and strike = 0°. The scenario with the top of the fault at 1 km depth is displayed in red and was included first and foremost as a check that there was no fundamental or qualitative difference between having the top of the fault plane at zero or close to zero. Panels **(A–D)** show the results using dip angles of 10°, 30°, 50°, and 70° respectively.

corresponding trace for the corresponding normal source in **Figure 9D**. As we observed for the normal faulting sources in **Figure 7**, the first major peak in amplitude is downwards and the maximum upward offshore wave-height arrives some 20 min later.

## Sensitivity to the Fault Strike and Dip (Near-Shore Case)

We repeat an identical set of calculations to those in the previous section, with the significant difference that all sources here have an epicenter at the point B: the one closest to the shore of interest. **Figure 10** displays the exact analogies of the quantities displayed in the panels of **Figure 8** but for the near-shore earthquakes. Almost every symmetrical feature in **Figure 8** is replaced by an asymmetric (or antisymmetric) feature in **Figure 10**. For the significantly offshore earthquake sources (**Figure 8**), there is a relatively simple relationship between the inundation area and the strike angle, for a given dip angle, and similarly between the inundation area and the dip, for a given strike angle. (The functions of strike have maxima near 0° and 180° and minima near 90° and 270°; the functions of dip have maxima close to 45°.) For the close-to-shore earthquakes, there are also trends indicating significant dependencies of inundation on the specific combination of strike and dip.

The patterns of inundation area for the distal reverse faulting sources (**Figures 8A,B**) are almost identical to the corresponding patterns for the distal normal faulting sources (**Figures 8C,D**). All panels of **Figure 10** show complicated patterns of dependence upon the strike and dip angles with non-linear dependencies on the two different parameters. The inundation rose plots for the near-shore reverse faulting sources (**Figures 10A,B**) are almost inverse images of the corresponding plots for the near-shore normal faulting sources (**Figures 10C,D**). The relationship between the land orientation and the source orientation varies greatly from case to case for the near-shore earthquakes, with the exact spatial form of the uplift or subsidence depending strongly on both angles of strike and slip. From the present analysis, we cannot determine the causative reason for this parametric control on the inundated area, but we note the following aspects that can provide a substantial influence: First, the rake angle controls the displaced volume of water and the depth of generation, this provides two different proxies for the tsunamigenic strength. The displaced volume and distribution of the initial wave naturally influences this strength and the depth influences the relative contribution of shoaling. Second, the source orientation influences the relative orientation towards the shoreline, influencing the wave directivity. Third, as the angle of rake determines either upward or downward displacement, the complementary nature of panels (A, B) and (C, D) in **Figure 10** indicate that the co-seismic displacement on land can influence the spatial extent of the tsunami inundation for these sources. These trends are

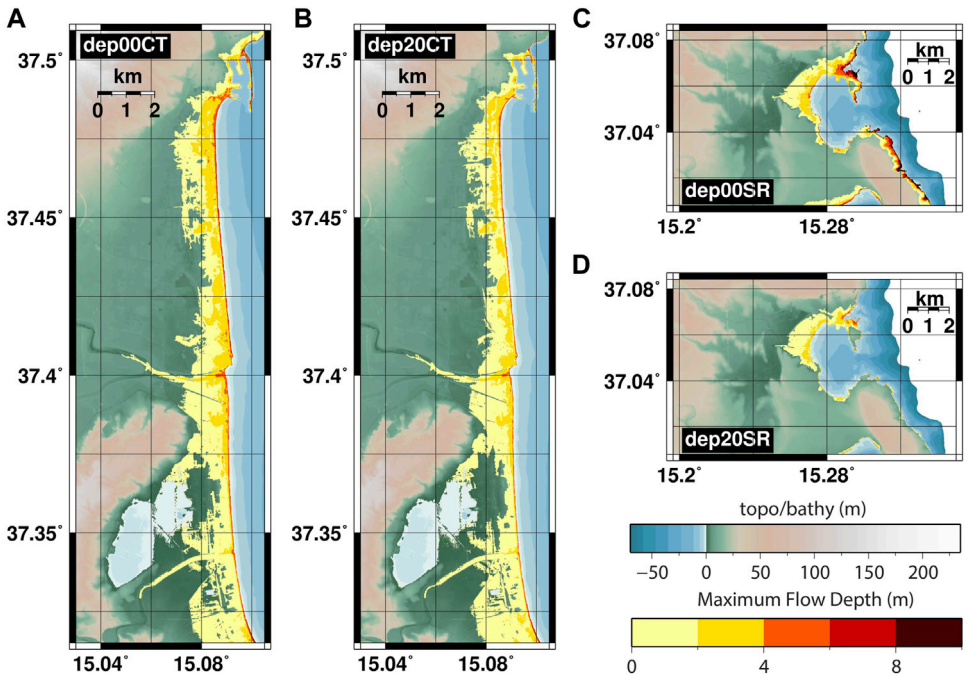


**FIGURE 15 |** Maximum flow-depth in meters recorded for simulations with strike = 0°, rake = 90°, and dip = 70° with depth 0 km (panels **(A,C)**) and depth 20 km (panels **(B,D)**).

difficult to predict and to be generalized. Therefore, for a PTHA, a rather fine discretization of the parameters seems to be required for near-field sources.

**Figure 11** shows corresponding inundation areas for Catania and Siracusa for four selected earthquake scenarios. All these sources have strike angle 20° but differ in dip and rake angles and show very different inundation patterns on both stretches of coastline. **Figure 11A** shows inundation maps for two reverse thrusting earthquakes with dip angles 10° and 70°. The shallow dip reverse fault earthquake results in moderate inundation at both Catania and Siracusa whereas the steep dip earthquake results in severe inundation at Catania and exceptionally little at Siracusa. The maps in **Figure 11A** provide an interpretation of the relative colour scales in **Figures 10A,B**. For the normal fault earthquakes with the same dip angles (**Figure 11C**), the situation is the exact reverse. There is severe inundation at Catania for the shallow dip source and less for the steep dip source. The opposite is also seen at Siracusa; there is far greater inundation for the steep dip earthquake than for the shallow dip source.

The surface elevation time-series (**Figures 11B,D**) are also distinctly different from the corresponding traces in **Figure 9**. For the offshore sources (**Figure 9**), there is a delay of between 10 and 20 min between the time of the earthquake and the water wave reaching the sensor; the exact time of arrival varies near-sinusoidally with the angle of strike. For the near-shore sources (**Figure 11**), the displacement of water at the location of the sensor is immediate or almost immediate after the earthquake.

## Sensitivity to the Earthquake Depth

Our final parameter sweep explores the sensitivity of the inundation to the depth of the earthquake, in addition to the angles of strike and dip. The fault centers of all earthquakes are located at point C in **Figure 1**. As it is primarily depth we are focusing on, we present a coarser discretization of the angles of strike and dip. The earthquakes are located such that little or no co-seismic displacement is to be expected at the coast. However, the distance between the extremes of the fault plane and the coast becomes relatively small for values of the strike close to 90 or 270°. **Figure 12** displays the inundation rose plots for the bay of Catania for the reverse thrusting scenarios at six different depths. The depth displayed is that of the top of the fault, such that one adds half the product of the fault width and the sine of the angle of dip to get the depth of the fault center.

**Figures 12A–C**, for the shallowest events, all display quite similar rose plots. The inundation is strongest for the strike = 0° and strike = 180° scenarios, although the inundation for the 45° and 225° scenarios is more significant than for the more distant earthquakes displayed in **Figure 10**. The dependence upon the dip angle is quite strong with significant inundation for dip = 50° and very little inundation for dip = 10°. However, this dependency is significantly influenced by the depth of the source; the deeper the source, the weaker the dip-dependence becomes. Indeed, **Figures 12D–F** show the dip and strike dependence for progressively deeper earthquakes and, while the strike-dependence remains quite constant, the variability with the angle of dip diminishes. For the deepest earthquakes (panel F), the dependence is almost purely a function of strike alone.

This is interpreted as an effect of the deeper earthquakes providing more smoothing of the initial seabed displacement, which reduces the tsunami variability. **Figure 13** shows the inundation area at Siracusa for the same set of scenarios displayed in **Figure 12** for Catania. The severity of tsunami inundation varies with strike angle somewhat differently for the two locations. However, the first order observations are consistent; the inundation is most significant for North-South striking earthquake sources and the dependence upon the angle of dip diminishes with greater depth. For PTHA, the trend is quite smooth. Thus, the consideration of different depth is very important, but a rough discretization may be sufficient to cover the natural variability of tsunami inundation.

**Figure 14** displays offshore surface elevation time-series with the panels (A), (B), (C), and (D) showing the time-series as a function of depths for the angles of dip for the panels as indicated. For the sources closest to the surface, the surface elevation is very sensitive to the angle of dip with the uppermost traces in panels (A), (B), (C), and (D) increasing in amplitude. The lowest amplitude wave-heights for the dip = $10^{o}$ case is consistent with the minimum area of inundation displayed in **Figures 12A**, **13A**. Like with the inundation areas in **Figures 12**, **13**, the surface elevation time-series displayed in **Figure 14** become more and more similar for the different angles of dip as the depth decreases.

The maximum flow depths recorded in the simulations for which the time-series are displayed in **Figure 14D** (uppermost and lowermost traces) are mapped out in **Figure 15**. The shallow source results in a higher amplitude wavetrain with shorter period waves than the deeper source. The inundation maps for the Bay of Catania (**Figures 15A,B**) for the two scenarios are very similar, the greatest differences being observed to the North where the near-shore water is deepest. The difference in the maximum flow depth for Siracusa is much greater with far higher flow depths recorded for the shallow source than the deep source.

## CONCLUSION AND DISCUSSION

We have performed multiple numerical simulations modelling earthquake-generated tsunamis in the Mediterranean Sea, where the inundation at the towns of Catania and Siracusa on the island of Sicily is estimated on 10 m by 10 m resolution grids. The non-linear shallow water Tsunami-HySEA model was used with a system of nested grids, with a scale of four increase in cell dimensions for each level. All earthquake sources were modelled using uniform slip on a single rectangular fault segment, modelling large earthquakes centered at four different locations. We performed parameter sweeps studying how the inundation at Catania and Siracusa varied with the Manning friction, $n$, and different combinations of the geometrical Okada fault parameters. We have performed both an analysis of the dependence of the inundation characteristic to the input parameter variation (seismic parameters) and to the model parameterization (Manning coefficient), but we also briefly discussed the sensitivity to the adopted discretization, that is to say how densely the allowed parameter ranges are sampled. Just as Burbidge et al. (2015) demonstrated that offshore tsunami height is a complex function of earthquake parameters, we demonstrate significant differences in the intensity and extent of onshore inundation both as a function of source and friction parameters.

We confirm that the Manning friction, $n$, is a significant parameter in determining the extent of inundation in numerical tsunami simulations. The sensitivity of the inundation to the choice of this parameter is dependent upon the amplitude of the incoming wave and on the topography of the coastal region. In our study of the inundation of the Bay of Catania in Sicily, we showed that the sensitivity of the inundation area to the Manning coefficient is likely greatest when the topography increases gently. While increasing $n$ reduces the geographical extent of the inundation, the reduction in the momentum flux is likely far larger. This metric may have greater significance as a hazard indicator than the tsunami flow depth. When PTHA is focused on quantifying inundation area, the results of our test show that there is a significant dependency of the results on the selected Manning coefficient. This means that more attention should be devoted in future local PTHA analyses to constraining the arising epistemic uncertainty, which may significantly impact the overall results.

For PTHA, we need a meaningful discretization of all potential earthquake tsunami sources. To make a PTHA computationally feasible, and calculable in a time-frame of interest, we want the minimum number of scenario definitions possible, while adequately covering the expected aleatory variability and related parameter space, and eventually different parameterizations or ranges stemming from the description of the epistemic uncertainty. In this study, we have considered only uniform slip on faults of a single dimension and only a single value of the slip. In addition, we have greatly restricted the number of earthquake locations. These limitations have allowed us to cover the angles of strike, dip, and rake using a fine discretization. Knowing how finely the source parameter space needs to be discretized is not possible, or is highly subjective, without a comprehensive sensitivity study. Or, seen the other way around, the risk is to adopt a too fine discretization to avoid undersampling. We wish for a discretization of each parameter such that no scenarios with significantly different tsunami impact are missed. In other words, the tsunami impact for a scenario with a given value of one parameter can be reasonably well predicted from the tsunami impact resulting from scenarios with neighbouring values of that parameter. Our goal is that the behaviour at arbitrarily specified points in our parameter space can be well interpolated from the behaviour at the points in our discretization.

We see examples of relatively smoothly varying behaviour as a function of the angle of rake (**Figure 7**) and the angles of strike and dip (**Figure 8**) for significantly offshore earthquakes. The continuity of the inundation metrics and the shapes of the offshore time-series with changes in these parameters give us confidence that the number of simulations performed can be limited to relatively few points in this parameter space for a given fault size and epicenter. In practice, this means for offshore earthquakes that we can probably consider only rake = $90^{o}$ and rake = $-90^{o}$, angles of strike in 30-degree increments, and 3 or 4 different values of the dip angle. For scenarios similar to those studied here, the tsunami impact from earthquakes with

intermediate parameters can likely be well estimated using a relatively sparse set of scenarios. When the earthquake sources are far closer to the shore where inundation occurs, a far finer discretization of the hazard may be needed. The spatial distribution and intensity of the inundation is also greatly influenced by the co-seismic deformation (c.f. Volpe et al., 2019). We found that the impact of far offshore earthquakes was very similar for normal and reverse faulting, despite significant differences in the wave height time-series and implied consequences for the time before maximum inundation (**Figure 9**). For near-shore earthquakes, the impact metrics for normal faulting (rake = $-90^{o}$) are almost an inverse of the impact metrics for reverse faulting (rake = $90^{o}$).

Finally, in a more limited sweep of strike and dip angles for offshore earthquakes, we demonstrate that the dependency upon the angle of dip decreases for deeper sources. For earthquakes close to the sea floor, shorter period waves are generated and there are significant changes in the tsunami intensity as we change both angles of strike and dip. For deeper earthquakes, only the longer period waves are excited and the tsunami intensity becomes less affected by the angle of dip. The strike angle is still significant for deeper earthquakes.

Despite the large number of simulations performed in this study, only a tiny fraction of parameter space has been covered. It is first noted that only two small stretches of coast have been studied, with a relatively simple relation between orientation of the coast to the locations of the prescribed earthquakes. Stretches of coastline with other geometries will likely experience tsunami impact which varies with source parameters in different ways. Some of the asymmetries displayed in this study are likely related to specific characteristics of the topo-bathymetry combined with the source orientations. These complications will increase as more complicated source geometries and more realistic models of heterogeneous slip are employed. Serra et al. (2021), for example, recently studied the sensitivity of tsunami height along the Iberian coast as a function of complex fault geometry and variable slip and find significant variability in the tsunami impact for different realizations. Such offshore studies illustrate how the relationship between slip distribution and bathymetric features influences near-shore wave height for extensive coastal stretches. However, the inundation problem represents an enormous increase in the computational cost and yet remains essential for assessing long term local tsunami hazard.

There may be several strategies for predicting onshore tsunami impact from offshore models. Davies et al. (2021) apply efficient Monte-Carlo sampling to estimate onshore PTHA from offshore. Liu et al. (2021) apply different Machine Learning (ML) techniques to predict tsunami amplitude at forecast points based upon short-term time-series at more offshore observation points; it is conceivable that an extension of such ideas will allow realistic inundation forecasts with high spatial resolution based upon offshore models and ML with a sufficient set of training data. For both ideas, simulated high-resolution inundation as a function of finely resolved parameter spaces will provide good validation of model forecasts. As PTHA with high-resolution inundation simulations becomes increasingly feasible for vast numbers of tsunamigenic scenarios, we seek a tsunami hazard quantification that is converged with respect to the granularity of the source discretization and modelling parameters. This work is a step in that direction.

## DATA AVAILABILITY STATEMENT

Publicly available datasets were analyzed in this study. This data can be found here: The Tsunami-HySEA code can be obtained from https://edanya.uma.es/hysea/index.php/models/tsunami-hysea (last accessed January 2022). The Digital Elevation Model used was constructed at INGV using data obtained from the following sources: https://www.gebco.net/ (GEBCO, accessed January 2022) https://www.ingv.it/it/monitoraggio-e-infrastrutture-per-la-ricerca/laboratori/laboratorio-geologia-e-geotecnologia (The Geological and Geotechnical Laboratory, INGV, last accessed January 2022) https://sextant.ifremer.fr/record/18ff0d48-b203-4a65-94a9-5fd8b0ec35f6/ (EMODnet Digital Bathymetry, DTM2018, last accessed January 2022) http://dati.protezionecivile.it/geoportalDPC/catalog/main/home.page (Dipartimento della Protezione Civile, Italy, last accessed January 2022).

## AUTHOR CONTRIBUTIONS

SG designed the experiment, performed the calculations, generated figures, and prepared the manuscript. SL, MVolpe, JS, BB, RT, and FR designed the calculation framework and computational grids, and contributed to interpretation of results. MdlA, JM, and CS-L extensively rewrote the Tsunami-HySEA code for this set of calculations. MVöge and SGli designed and tested the procedure for generating the input for the simulations and automating the procedure on HPC facilities. PL assisted with installing and implementing the procedure on Marconi-100 at CINECA. JCM assisted with installing and implementing the procedure on SAGA at the Norwegian University of Science and Technology. FL supervised the project, contributed to interpretation of the results, and prepared the manuscript. All authors contributed to review, revision, and quality control of the manuscript.

## FUNDING

This work is partially funded by the European Union's Horizon 2020 Research and Innovation Program under grant agreement No 823844 (ChEESE Center of Excellence, www.cheese-coe.eu). Additional funding was received from the Research Council of Norway under grant 322236 (INITIATOR). Computational resources made available through Sigma2/UNINETT on Saga at NTNU, Trondheim, Norway (in project nn5008 k) and through PRACE on Marconi-100 at CINECA, Rome, Italy (through a PRACE grant with project number 2020225386: Pra21_5,386/TsuHazAP). Some authors also received funding from the project "Assessment of Cascading Events triggered by the Interaction of Natural Hazards and Technological Scenarios involving the release of Hazardous Substances," funded by the Italian

Ministry MIUR PRIN (Progetti di Ricerca di Rilevante Interesse Nazionale) 2017—Grant 2017CEYPS8. This work benefited of the agreement between Istituto Nazionale di Geofisica e Vulcanologia and the Italian Presidenza del Consiglio dei Ministri, Dipartimento della Protezione Civile (DPC). This paper does not necessarily represent DPC official opinion and policies.

## ACKNOWLEDGMENTS

Maps and tsunami intensity plots were created using GMT software (Wessel et al., 2019). We gratefully acknowledge the contribution of three reviewers whose comments made significant improvements to the manuscript.

## REFERENCES

An, C., Liu, H., Ren, Z., and Yuan, Y. (2018). Prediction of Tsunami Waves by Uniform Slip Models. *J. Geophys. Res. Oceans* 123, 8366–8382. doi:10.1029/2018JC014363

Basili, R., Brizuela, B., Herrero, A., Iqbal, S., Lorito, S., Maesano, F. E., et al. (2021). The Making of the NEAM Tsunami Hazard Model 2018 (NEAMTHM18). *Front. Earth Sci.* 8, 1–29. doi:10.3389/feart.2020.616594

Bricker, J. D., Gibson, S., Takagi, H., and Imamura, F. (2015). On the Need for Larger Manning's Roughness Coefficients in Depth-Integrated Tsunami Inundation Models. *Coastal Eng. J.* 57, 1550005-1–1550005–13. doi:10.1142/S0578563415500059

Burbidge, D., Mueller, C., and Power, W. (2015). The Effect of Uncertainty in Earthquake Fault Parameters on the Maximum Wave Height from a Tsunami Propagation Model. *Nat. Hazards Earth Syst. Sci.* 15, 2299–2312. doi:10.5194/nhess-15-2299-2015

Davies, G., Griffin, J., Løvholt, F., Glimsdal, S., Harbitz, C., Thio, H. K., et al. (2018). A Global Probabilistic Tsunami hazard Assessment from Earthquake Sources. *Geol. Soc. Lond. Spec. Publications* 456, 219–244. doi:10.1144/SP456.5

Davies, G., Horspool, N., and Miller, V. (2015). Tsunami Inundation from Heterogeneous Earthquake Slip Distributions: Evaluation of Synthetic Source Models. *J. Geophys. Res. Solid Earth* 120, 6431–6451. doi:10.1002/2015JB012272

Davies, G. (2019). Tsunami Variability from Uncalibrated Stochastic Earthquake Models: Tests against Deep Ocean Observations 2006-2016. *Geophys. J. Int.* 218, 1939–1960. doi:10.1093/gji/ggz260

Davies, G., Weber, R., Wilson, K., and Cummins, P. (2021). From Offshore to Onshore Probabilistic Tsunami hazard Assessment via Efficient Monte-Carlo Sampling. *earthArXiv*. doi:10.31223/X5J04W

de la Asunción, M., Castro, M. J., Fernández-Nieto, E. D., Mantas, J. M., Acosta, S. O., and González-Vida, J. M. (2013). Efficient GPU Implementation of a Two Waves TVD-WAF Method for the Two-Dimensional One Layer Shallow Water System on Structured Meshes. *Comput. Fluids* 80, 441–452. doi:10.1016/j.compfluid.2012.01.012

Gayer, G., Leschka, S., Nöhren, I., Larsen, O., and Günther, H. (2010). Tsunami Inundation Modelling Based on Detailed Roughness Maps of Densely Populated Areas. *Nat. Hazards Earth Syst. Sci.* 10, 1679–1687. doi:10.5194/nhess-10-1679-2010

Geist, E. L. (2002). Complex Earthquake Rupture and Local Tsunamis. *J. Geophys. Res.* 107, 2086. doi:10.1029/2000JB000139

Geist, E. L. (1998). Local Tsunamis and Earthquake Source Parameters. *Adv. Geophys.* 39, 117–209. doi:10.1016/S0065-2687(08)60276-9

Gibbons, S. J., Lorito, S., Macías, J., Løvholt, F., Selva, J., Volpe, M., et al. (2020). Probabilistic Tsunami Hazard Analysis: High Performance Computing for Massive Scale Inundation Simulations. *Front. Earth Sci.* 8, 1–20. doi:10.3389/feart.2020.591549

Gica, E., Teng, M. H., Liu, P. L.-F., Titov, V., and Zhou, H. (2007). Sensitivity Analysis of Source Parameters for Earthquake-Generated Distant Tsunamis. *J. Waterway, Port, Coastal, Ocean Eng.* 133, 429–441. doi:10.1061/(asce)0733-950x(2007)133:6(429)

Glimsdal, S., Pedersen, G. K., Harbitz, C. B., and Løvholt, F. (2013). Dispersion of Tsunamis: Does it Really Matter? *Nat. Hazards Earth Syst. Sci.* 13, 1507–1526. doi:10.5194/nhess-13-1507-2013

Grezio, A., Babeyko, A., Baptista, M. A., Behrens, J., Costa, A., Davies, G., et al. (2017). Probabilistic Tsunami Hazard Analysis: Multiple Sources and Global Applications. *Rev. Geophys.* 55, 1158–1198. doi:10.1002/2017RG000579

Griffin, J., Latief, H., Kongko, W., Harig, S., Horspool, N., Hanung, R., et al. (2015). An Evaluation of Onshore Digital Elevation Models for Modeling Tsunami Inundation Zones. *Front. Earth Sci.* 3. doi:10.3389/feart.2015.00032

Harbitz, C. B., Glimsdal, S., Bazin, S., Zamora, N., Løvholt, F., Bungum, H., et al. (2012). Tsunami hazard in the Caribbean: Regional Exposure Derived from Credible Worst Case Scenarios. *Continental Shelf Res.* 38, 1–23. doi:10.1016/j.csr.2012.02.006

Horspool, N., Pranantyo, I., Griffin, J., Latief, H., Natawidjaja, D. H., Kongko, W., et al. (2014). A Probabilistic Tsunami hazard Assessment for Indonesia. *Nat. Hazards Earth Syst. Sci.* 14, 3105–3122. doi:10.5194/nhess-14-3105-2014

Kaiser, G., Scheele, L., Kortenhaus, A., Løvholt, F., Römer, H., and Leschka, S. (2011). The Influence of Land Cover Roughness on the Results of High Resolution Tsunami Inundation Modeling. *Nat. Hazards Earth Syst. Sci.* 11, 2521–2540. doi:10.5194/nhess-11-2521-2011

Kajiura, K. (1980). "Some Statistics Related to Observed Tsunami Heights along the Coast of Japan," in *Tsunamis: Their Science and Engineering* (Dordrecht: Springer Netherlands), 131–145. doi:10.1007/978-94-009-7172-1_11

Li, L., Switzer, A. D., Chan, C.-H., Wang, Y., Weiss, R., and Qiu, Q. (2016). How Heterogeneous Coseismic Slip Affects Regional Probabilistic Tsunami hazard Assessment: A Case Study in the South China Sea. *J. Geophys. Res. Solid Earth* 121, 6250–6272. doi:10.1002/2016JB013111

Liu, C. M., Rim, D., Baraldi, R., and LeVeque, R. J. (2021). Comparison of Machine Learning Approaches for Tsunami Forecasting from Sparse Observations. *Pure Appl. Geophys.* 178, 5129–5153. doi:10.1007/s00024-021-02841-9

Lorito, S., Alessandro, A., Cugliari, L., Romano, F., Tonini, R., Valbonesi, C., et al. (2021). Tsunami hazard, Warning, and Risk Reduction in Italy and the Mediterranean Sea: State of the Art, Gaps, and Future Solutions. *Turkish J. Earth Sci.* 30, 882–897. doi:10.3906/yer-2110-7

Lorito, S., Selva, J., Basili, R., Romano, F., Tiberti, M. M., and Piatanesi, A. (2015). Probabilistic Hazard For Seismically Induced Tsunamis: Accuracy And Feasibility Of Inundation Maps. *Geophys. J. Int.* 200, 574–588. doi:10.1093/gji/ggu408

Lorito, S., Tiberti, M. M., Basili, R., Piatanesi, A., and Valensise, G. (2008). Earthquake-generated Tsunamis in the Mediterranean Sea: Scenarios of Potential Threats to Southern Italy. *J. Geophys. Res.* 113, B01301. doi:10.1029/2007JB004943

Løvholt, F., Glimsdal, S., Harbitz, C. B., Horspool, N., Smebye, H., de Bono, A., et al. (2014). Global Tsunami hazard and Exposure Due to Large Co-seismic Slip. *Int. J. Disaster Risk Reduction* 10, 406–418. doi:10.1016/j.ijdrr.2014.04.003

Løvholt, F., Glimsdal, S., Harbitz, C. B., Zamora, N., Nadim, F., Peduzzi, P., et al. (2012a). Tsunami hazard and Exposure on the Global Scale. *Earth-Science Rev.* 110, 58–73. doi:10.1016/j.earscirev.2011.10.002

Løvholt, F., Kühn, D., Bungum, H., Harbitz, C. B., and Glimsdal, S. (2012b). Historical Tsunamis and Present Tsunami hazard in Eastern Indonesia and the Southern Philippines. *J. Geophys. Res.* 117, 1–19. doi:10.1029/2012JB009425

Løvholt, F., Lynett, P., and Pedersen, G. (2013). Simulating Run-Up on Steep Slopes with Operational Boussinesq Models; Capabilities, Spurious Effects and Instabilities. *Nonlin. Process. Geophys.* 20, 379–395. doi:10.5194/npg-20-379-2013

Løvholt, F., Pedersen, G., Bazin, S., Kühn, D., Bredesen, R. E., and Harbitz, C. (2012c). Stochastic Analysis of Tsunami Runup Due to Heterogeneous Coseismic Slip and Dispersion. *J. Geophys. Res. Ocean.* 117, n/a. doi:10.1029/2011JC007616

Macías, J., Castro, M. J., Ortega, S., Escalante, C., and González-Vida, J. M. (2017). Performance Benchmarking of Tsunami-HySEA Model for NTHMP's Inundation Mapping Activities. *Pure Appl. Geophys.* 174, 3147–3183. doi:10.1007/s00024-017-1583-1

Macías, J., Mercado, A., González-Vida, J. M., Ortega, S., and Castro, M. J. (2016). Comparison and Computational Performance of Tsunami-HySEA and MOST

Models for LANTEX 2013 Scenario: Impact Assessment on Puerto Rico Coasts. *Pure Appl. Geophys.* 173, 3973–3997. doi:10.1007/s00024-016-1387-8

McCloskey, J., Antonioli, A., Piatanesi, A., Sieh, K., Steacy, S., Nalbant, S. S., et al. (2007). Near-field Propagation of Tsunamis from Megathrust Earthquakes. *Geophys. Res. Lett.* 34, L14316. doi:10.1029/2007GL030494

Murphy, S., Scala, A., Herrero, A., Lorito, S., Festa, G., Trasatti, E., et al. (2016). Shallow Slip Amplification and Enhanced Tsunami hazard Unravelled by Dynamic Simulations of Mega-Thrust Earthquakes. *Sci. Rep.* 6, 35007. doi:10.1038/srep35007

NCEI (2021). National Geophysical Data Center/World Data Service: NCEI/WDS Global Historical Tsunami Database. doi:10.7289/V5PN93H7

Okada, Y. (1985). Surface Deformation Due to Shear and Tensile Faults in a Half-Space. *Bull. Seismol. Soc. Am.* 75, 1135–1154. doi:10.1785/bssa0750041135

Parsons, T., and Geist, E. L. (2008). Tsunami Probability in the Caribbean Region. *Pure Appl. Geophys.* 165, 2089–2116. doi:10.1007/s00024-008-0416-7

Scala, A., Lorito, S., Romano, F., Murphy, S., Selva, J., Basili, R., et al. (2020). Effect of Shallow Slip Amplification Uncertainty on Probabilistic Tsunami Hazard Analysis in Subduction Zones: Use of Long-Term Balanced Stochastic Slip Models. *Pure Appl. Geophys.* 177, 1497–1520. doi:10.1007/s00024-019-02260-x

Selva, J., Amato, A., Armigliato, A., Basili, R., Bernardi, F., Brizuela, B., et al. (2021). Tsunami Risk Management for Crustal Earthquakes and Non-seismic Sources in Italy. *Riv. Nuovo Cim.* 44, 69–144. doi:10.1007/s40766-021-00016-9

Selva, J., Tonini, R., Molinari, I., Tiberti, M. M., Romano, F., Grezio, A., et al. (2016). Quantification of Source Uncertainties in Seismic Probabilistic Tsunami Hazard Analysis (SPTHA). *Geophys. J. Int.* 205, 1780–1803. doi:10.1093/gji/ggw107

Serra, C. S., Martínez-Loriente, S., Gràcia, E., Urgeles, R., Gómez de la Peña, L., Maesano, F. E., et al. (2021). Sensitivity of Tsunami Scenarios to Complex Fault Geometry and Heterogeneous Slip Distribution: Case-Studies for SW Iberia and NW Morocco. *J. Geophys. Res. Solid Earth* 126. doi:10.1029/2021JB022127

Tonini, R., Basili, R., Maesano, F. E., Tiberti, M. M., Lorito, S., Romano, F., et al. (2020). Importance of Earthquake Rupture Geometry on Tsunami Modelling: the Calabrian Arc Subduction Interface (Italy) Case Study. *Geophys. J. Int.* 223, 1805–1819. doi:10.1093/gji/ggaa409

Tonini, R., Di Manna, P., Lorito, S., Selva, J., Volpe, M., Romano, F., et al. (2021). Testing Tsunami Inundation Maps for Evacuation Planning in Italy. *Front. Earth Sci.* 9. doi:10.3389/feart.2021.628061

Volpe, M., Lorito, S., Selva, J., Tonini, R., Romano, F., and Brizuela, B. (2019). From Regional to Local SPTHA: Efficient Computation of Probabilistic Tsunami Inundation Maps Addressing Near-Field Sources. *Nat. Hazards Earth Syst. Sci.* 19, 455–469. doi:10.5194/nhess-19-455-2019

Wessel, P., Luis, J. F., Uieda, L., Scharroo, R., Wobbe, F., Smith, W. H. F., et al. (2019). The Generic Mapping Tools Version 6. *Geochem. Geophys. Geosyst.* 20, 5556–5564. doi:10.1029/2019GC008515

Williamson, A. L., Rim, D., Adams, L. M., LeVeque, R. J., Melgar, D., González, F. I., et al. (2020). A Source Clustering Approach for Efficient Inundation Modeling and Regional Scale Probabilistic Tsunami Hazard Assessment. *Front. Earth Sci.* 8, 1–22. doi:10.3389/feart.2020.591663

**Conflict of Interest:** The authors declare that the research was conducted in the absence of any commercial or financial relationships that could be construed as a potential conflict of interest.

**Publisher's Note:** All claims expressed in this article are solely those of the authors and do not necessarily represent those of their affiliated organizations, or those of the publisher, the editors and the reviewers. Any product that may be evaluated in this article, or claim that may be made by its manufacturer, is not guaranteed or endorsed by the publisher.

frontiers in Earth Science

ORIGINAL RESEARCH
published: 03 February 2022
doi: 10.3389/feart.2021.760773

# High-Performance Computing of 3D Magma Dynamics, and Comparison With 2D Simulation Results

*Deepak Garg* and Paolo Papale*

*Istituto Nazionale di Geofisica e Vulcanologia, Sezione di Pisa, Pisa, Italy*

The dynamics of magma is often studied through 2D numerical simulations because 3D simulations are usually complex and computationally expensive. However, magmatic systems and physical processes are 3D and approximating them in 2D requires an evaluation of the information which is lost under different conditions. This work presents a physical and numerical model for 3D magma convection dynamics. The model is applied to study the dynamics of magma convection and mixing between andesitic and dacitic magmas. The 3D simulation results are compared with corresponding 2D simulations. We also provide details on the numerical scheme and its parallel implementation in C++ for high-performance computing. The performance of the numerical code is evaluated through strong scaling exercises involving up to >12,000 cores.

**Keywords: magma dynamics, 3D numerical simulations, Rayleigh-Taylor instability, incompressible-compressible multicomponent flow, VMS finite element method, strong-scaling, 3D-2D comparison**

OPEN ACCESS

***Edited by:***
*Sara Barsotti,*
*Icelandic Meteorological Office, Iceland*

***Reviewed by:***
*Zhipeng Qin,*
*Guangxi University, China*
*Giuseppe La Spina,*
*Istituto Nazionale di Geofisica e Vulcanologia (INGV), Italy*

****Correspondence:***
*Deepak Garg*
*deepak.garg@ingv.it*

***Specialty section:***
*This article was submitted to Volcanology, a section of the journal Frontiers in Earth Science*

***Received:*** *18 August 2021*
***Accepted:*** *17 December 2021*
***Published:*** *03 February 2022*

***Citation:***
*Garg D and Papale P (2022) High-Performance Computing of 3D Magma Dynamics, and Comparison With 2D Simulation Results. Front. Earth Sci. 9:760773. doi: 10.3389/feart.2021.760773*

## 1 INTRODUCTION

Understanding magma transport in the crust is one of the major challenges in modern volcanology. Current models depict magmatic systems as an interconnected network of compositionally heterogeneous magmas, involving multiple chambers and dikes that extend from shallow to deep levels in the crust (Gudmundsson, 1995; Gudmundsson, 2011; Blundy and Annen, 2016).

Magma chambers are the main engines of active volcanoes and serve as a storage region for magma ascent and its chemical evolution (DePaolo, 1981; Bachmann and Bergantz, 2003). The pressure in the chamber may vary largely over time due to a variety of processes, including fractional crystallization, volatile exsolution and magma recharge, potentially leading towards an eruption (Sparks and Huppert, 1984; Folch and Marti, 1998; Gudmundsson, 2012; Edmonds and Wallace, 2017; Papale et al., 2017; Cassidy et al., 2018). Therefore, studying magma dynamics in a chamber is of utmost importance and has become a mainstream theme over the recent years (Bergantz, 2000; Couch et al., 2001; Gutiérrez and Miguel, 2010; Karlstrom et al., 2010; Bergantz et al., 2015; Garg et al., 2019) as the ongoing flow dynamics and associated surface signals can depict the current state of the volcano and its possible evolutions (Gottsmann et al., 2011; Longo et al., 2012a; Bagagli et al., 2017; Sparks and Cashman, 2017; Carrara, 2019; Lieto et al., 2020).

Typically, buoyancy instabilities develop when a low-density, volatile-rich, primitive, hot magma ascends in the crust and interacts with previously stored, more chemically evolved, partially degassed and denser magma in shallow chambers (Semenov and Polyansky, 2017; Garg et al., 2019). There are multiple pieces of evidence of eruptions shortly preceded by interaction of compositionally different magmas at shallow depths (Tomiya et al., 2013; Sides et al., 2014; Perugini et al., 2015; Sundermeyer et al., 2020). The degree of magma mixing, which spans a continuum from mechanical mingling to complete chemical homogenisation,

depends upon the magma properties, the driving forces, and the time available for mixing (Garg et al., 2019).

Recently a number of authors [e.g., (Sparks and Cashman, 2017), and references therein] have been hypothesizing that although usually not seen among the erupted volcanic products, a crystal-rich mush may constitute a large dominant portion of the magmatic plumbing system, with dominantly liquid magma possibly being an ephemeral occurrence driven by melt segregation and contributing to characterize the unrest and eruption states of the volcano. Clear evidence from active magmatic systems is not available yet, as volcanic plumbing systems continue to be hidden from direct observation. A few accidental encounters with buried shallow magma bodies during geothermal drilling do not appear to support the presence of important layers of mushy magma across the rock-magma transition (Eichelberger, 2020). More is needed before we get to a clear, robust picture of active magmatic systems, justifying substantial efforts to overcome the current limitations in directly observing, measuring and sampling underground magma (https://www.kmt.is). Here we focus on either dominantly liquid reservoirs, or on the dominantly liquid core region of mushy magma reservoirs, over time scales that are typical of individual magma convection events, likely much less than the time scales associated with the existence of ephemeral liquid-dominated magmatic bodies.

Over the years significant efforts have been invested to study several aspects of the magma physics relevant to understand the volcano dynamics and anticipate their evolution. The physics of magma mixing has been studied through numerical simulations and experiments with both synthetic and natural compositions (Campbell and Turner, 1986; Huppert et al., 1986; Jellinek and Kerr, 1999; Michioka and Sumita, 2005; Sato and Sato, 2009; De Campos et al., 2011; Laumonier et al., 2014; Morgavi et al., 2015; Perugini et al., 2015; Bergantz et al., 2015; Schleicher et al., 2016; Garg et al., 2019). Usually, numerical simulations are simplified by referring to a 2D geometrical configuration, because 3D dynamics can be very complex and are extremely expensive in terms of required computational resources. Even 2D magma mixing simulations need extremely refined meshes to capture the flow features down to the dm (or lower) scales that are sometimes required, e.g., at the intersection between feeding dykes and chambers (Longo et al., 2012a; Papale et al., 2017). Solving such problems in 3D on a single computer is practically impossible. Nowadays the simulations are usually run over clusters of cores providing high speed data processing capability. In high performance computing (HPC) paradigm, many processors work simultaneously to produce exceptional computational power and to significantly reduce the total computational time (Dowd and Charles, 2010; Flanagan et al., 2020). High performance is achieved through parallel computing in which large computational domains are subdivided into smaller, interconnected ones, which can be solved at the same time (Gottlieb, 1989; Asanovic et al., 2006).

So far the numerical simulations performed for magma mixing in the literature are in 2D (Bergantz, 2000; Longo et al., 2012a; Papale et al., 2017; Garg et al., 2019). However, strictly speaking, 2D calculations apply only to flows that are inherently two-dimensional, and can be extended to real 3D systems only under restricted conditions whereby any change in physical quantities over the third dimension can be neglected. Real magmatic systems are commonly such that 2D simplifications can only be introduced with some arbitrariness, typically with the objective of extracting zero-order approximations of more complex 3D processes and dynamics. In most cases, however, the loss of information due to 2D simplification is unknown.

The purpose of this work is that of 1) presenting a physical and numerical model for transient 3D magma dynamics, including its parallel implementation and scaling performance, 2) applying the model to 3D magma chamber convection dynamics in an initially stratified, gravitationally unstable magma chamber, and 3) comparing the 3D simulation results with the 2D case.

## 2 MAGMA FLOW MODEL

Natural magmas are composed of crystals, melt oxides and volatiles, with the latter that can be dissolved in the liquid phase or exsolved in a gas phase with proportions depending on local pressure (p), temperature (T), and composition (Y). Flow conditions span wide ranges from essentially incompressible to largely compressible, including supersonic flow during eruptions. In magmas where the volatiles are largely dissolved, and the Mach number is $\ll 1$, the flow remains weakly compressible. In this work we are specifically interested in modelling the flow dynamics inside magma chambers where two compositionally different magmas interact with each other. The model that we present is however general, and can be applied to transonic flow as well.

We model compressible/incompressible flow of multi-component magma with GALES (Longo et al., 2012b; Garg et al., 2018a; Garg et al., 2018b; Garg et al., 2021). The numerical scheme and parallel implementation in GALES are described in **Appendixes A, B**. GALES has been validated on a number of 2D/3D benchmarks for multi-component compressible/incompressible flows (Longo et al., 2012b), single-component compressible/incompressible flows (Garg et al., 2018a), free surface flows (Garg et al., 2018b) and fluid-structure interaction (Garg et al., 2021). Additional validation tests for compressible and incompressible flows with 3D geometries are reported in the **Supplementary Material**.

The properties of each magma component in GALES are computed from local conditions including composition in terms of ten major oxides plus the two major volatile species $H_2O$ and $CO_2$. The mixture is assumed to be in chemical, mechanical and thermodynamic equilibrium. The flow is governed by the following equations:

$$\frac{\partial \rho}{\partial t} + \boldsymbol{\nabla} \cdot (\rho \boldsymbol{v}) = 0 \tag{1}$$

$$\frac{\partial (\rho \boldsymbol{v})}{\partial t} + \boldsymbol{\nabla} \cdot (\rho \boldsymbol{v} \otimes \boldsymbol{v}) = \boldsymbol{\nabla} \cdot \boldsymbol{\sigma} + \rho \boldsymbol{b}, \tag{2}$$

$$\frac{\partial(\rho E)}{\partial t} + \nabla \cdot (\rho E \boldsymbol{v}) = \nabla \cdot (\boldsymbol{\sigma v} - \boldsymbol{q} - (\boldsymbol{h}'\boldsymbol{J})') + \rho(\boldsymbol{b} \cdot \boldsymbol{v}), \quad (3)$$

$$\frac{\partial \rho Y_k}{\partial t} + \nabla \cdot (\rho \boldsymbol{v} Y_k) = -\nabla \cdot \boldsymbol{J}_k \qquad k = 1, 2, \ldots, n \quad (4)$$

**Equations 1–3** represent mass, momentum and energy conservation of the mixture, while **Eq. 4** is mass conservation of the $k$th component in the $n$-component mixture. The equations are same as in (Garg et al., 2019) with a three-dimensional extension of vector and tensor quantities. In the above equations, $Y_k$ is the mass fraction of the $k$th component, with $\sum_k Y_k = 1$. This implies that for given $n$ components, only $n - 1$ components are independent and require each one expression of **Eq. 4**. For an $n$-component mixture, the density ($\rho$) is given by:

$$\frac{1}{\rho} = \frac{Y_1}{\rho_1} + \frac{Y_2}{\rho_2} + \cdots + \frac{Y_n}{\rho_n} \quad (5)$$

where $\rho_k$ is the density of the $k$th component which depends on local p-T and composition; $\boldsymbol{v}$ is the velocity; $\boldsymbol{b}$ is body force vector per unit mass; $E = c_v T + |\boldsymbol{v}|^2/2$ is total specific energy, with $c_v$ being the specific heat capacity at constant volume; $T$ is temperature; $\boldsymbol{h}$ is the vector of specific enthalpies for the components.

The mass diffusion flux is modelled with Fick's law as

$$\boldsymbol{J}_k = -\rho \boldsymbol{D} \nabla Y_k \quad (6)$$

where $\boldsymbol{D}$ is the mass diffusion coefficient matrix. Viscous flux is modelled as

$$\begin{aligned} \boldsymbol{\sigma} &= \mu(\nabla \boldsymbol{v} + (\nabla \boldsymbol{v})') - \frac{2}{3}\mu(\nabla \cdot \boldsymbol{v})\boldsymbol{I} - p\boldsymbol{I} \\ &= \boldsymbol{\tau} - p\boldsymbol{I} \end{aligned} \quad (7)$$

where $p$ is pressure, $\mu$ is the viscosity of the mixture and $\boldsymbol{\tau}$ is the viscous stress tensor. The heat flux is modelled by Fourier's law:

$$\boldsymbol{q} = -\kappa \nabla T \quad (8)$$

where $\kappa$ is thermal conductivity.

**Equations 1–4** are written in the conservative form and describe fully compressible flow. The incompressible flow equations are merely a simplification of the above equations by referring to a constant density. We remark that although in magma reservoirs the Mach number is usually very low, the density of the magmatic mixture varies, mostly as a response to phase changes of volatile components. Therefore, considering the flow as fully incompressible would miss many important flow features of gas-bearing magmas.

In magma reservoirs, and over the time scale of individual convection events analysed here, phase separation is of minimum importance. In our previous works (Longo et al., 2012a; Papale et al., 2017; Garg et al., 2019) we have estimated that flow Stokes number $St = t_0 v_0 / l_0$, where $t_0$ is the relaxation time of the crystal, $v_0$ is the flow velocity and $l_0$ is the diameter of the crystal, remains very low, of order $10^{-4}$ for crystals up to cm size. The same is true for gas bubbles. Based on the typical gas volume fractions obtained in our previous works and assumed bubble number density as low as $10^{14}\ m^{-3}$ (Cashman, 2000), the value of St remains less than $10^{-4}$. The low value of St indicates that mechanical phase separation is negligible, and the relative velocity terms describing phase separation can be safely ignored.

The physical properties of magma are modelled as a function of local pressure, temperature and composition in the space-time domain, as they evolve during magma convection and mixing. Throughout this paper the word "mixing" refers to the scale of our analysis, whereby the smallest elements in the computational domain have linear dimension of order 1 m. At such a scale many orders of magnitude larger than the scale of molecules, and for the employed computational times of order a few hours, chemical mixing is unresolved and likely to be poorly effective. Therefore, we refer only to mechanical mixing whereby both magma types are present within individual computational elements, with no reference to physical processes occurring at the molecular scale.

As components for use in **Eq. 4** above, we refer here to the magma types involved in convection and mixing (e.g., "andesite", "rhyolite", etc.), each expressed in terms of oxides including volatile species. Accordingly, each component is modeled as a mixture of 1) silicate melt including the dissolved volatiles and 2) exsolved volatiles. Non-reactive crystals can be added and their effects in modifying the mechanical and thermal properties of magma can be accounted for (for simplicity, however, we have neglected crystals in the computations illustrated below). The density of the volatile free silicate melt is modelled according to (Lange, 1994) and the effects on the density by dissolved $H_2O$ is computed by the model of (Burnham et al., 1969). For the gas phase, we use the ideal gas equation as the equation of state. For each magma, the phase distribution of volatiles is computed by multi-component ($H_2O$ + $CO_2$) gas-melt equilibrium modelling (Papale et al., 2006). The viscosity of each magma component is modelled as a function of oxide composition, dissolved $H_2O$ and temperature (non-Arrhenian) as described in (Giordano et al., 2008), with the effect of non-deformable gas bubbles accounted for by the model of (Ishii and Zuber, 1979) and strain-rate dependent non-Newtonian rheology due to the presence of crystals and of deforming bubbles (Caricchi et al., 2007; Pal, 2003). The viscosity of the two-component mixture is modelled as $\mu = \sum_k x_k \mu_k$, where $x_k$ and $\mu_k$ are, respectively, the mole fraction and the viscosity of the $k$th mixture component (again, in our case, "andesite", "rhyolite", etc.). The specific heat capacity at constant pressure for the melt is computed as $c_p = \sum_j x_j c_{pj}$, where $c_{pj}$ and $x_j$ are, respectively, the specific heat capacity at constant pressure and mole fraction for the $j$th oxide subcomponent [**Table 1** in (Garg et al., 2019)]. The specific heat capacity at constant volume, $c_v$ is computed as $c_v = c_p - \alpha^2 T/(\beta\rho)$, where $\alpha$ and $\beta$ are isobaric expansion coefficient and isothermal compressibility coefficient, respectively. In this work we use a constant thermal conductivity, $\kappa = 1.2\ Wm^{-1}K^{-1}$ (Garg et al., 2019).

The numerical scheme and the stabilization terms employed for the solution of the set of **Eqs 1–4** above, are reported in the **Appendix**.

**TABLE 1 |** Composition of magmas and list of simulations. For consistency with the corresponding 2D cases in (Garg et al., 2019), we keep the same simulations numbering here.

| | $SiO_2$ | $TiO_2$ | $Al_2O_3$ | $Fe_2O_3$ | FeO | MnO | MgO | CaO | $Na_2O$ | $K_2O$ |
|---|---|---|---|---|---|---|---|---|---|---|
| Andesite | 58.70 | 0.88 | 17.24 | 3.31 | 4.09 | 0.14 | 3.37 | 6.88 | 3.53 | 1.64 |
| Dacite | 65.98 | 0.59 | 16.15 | 2.47 | 2.33 | 0.09 | 1.81 | 4.38 | 3.85 | 2.20 |

| Simulation | Andesite | | Dacite | | Viscosity | Simulated time |
|---|---|---|---|---|---|---|
| | $H_2O$ wt% | $CO_2$ wt% | $H_2O$ wt% | $CO_2$ wt% | ($10^3$ Pa s) | (h) |
| 1 | 4 | 2 | 4 | 0.1 | 6.2–32.0 | 1.25 |
| 3 | 4 | 2 | 4 | 0.1 | 62.9–320.8 | 2.0 |

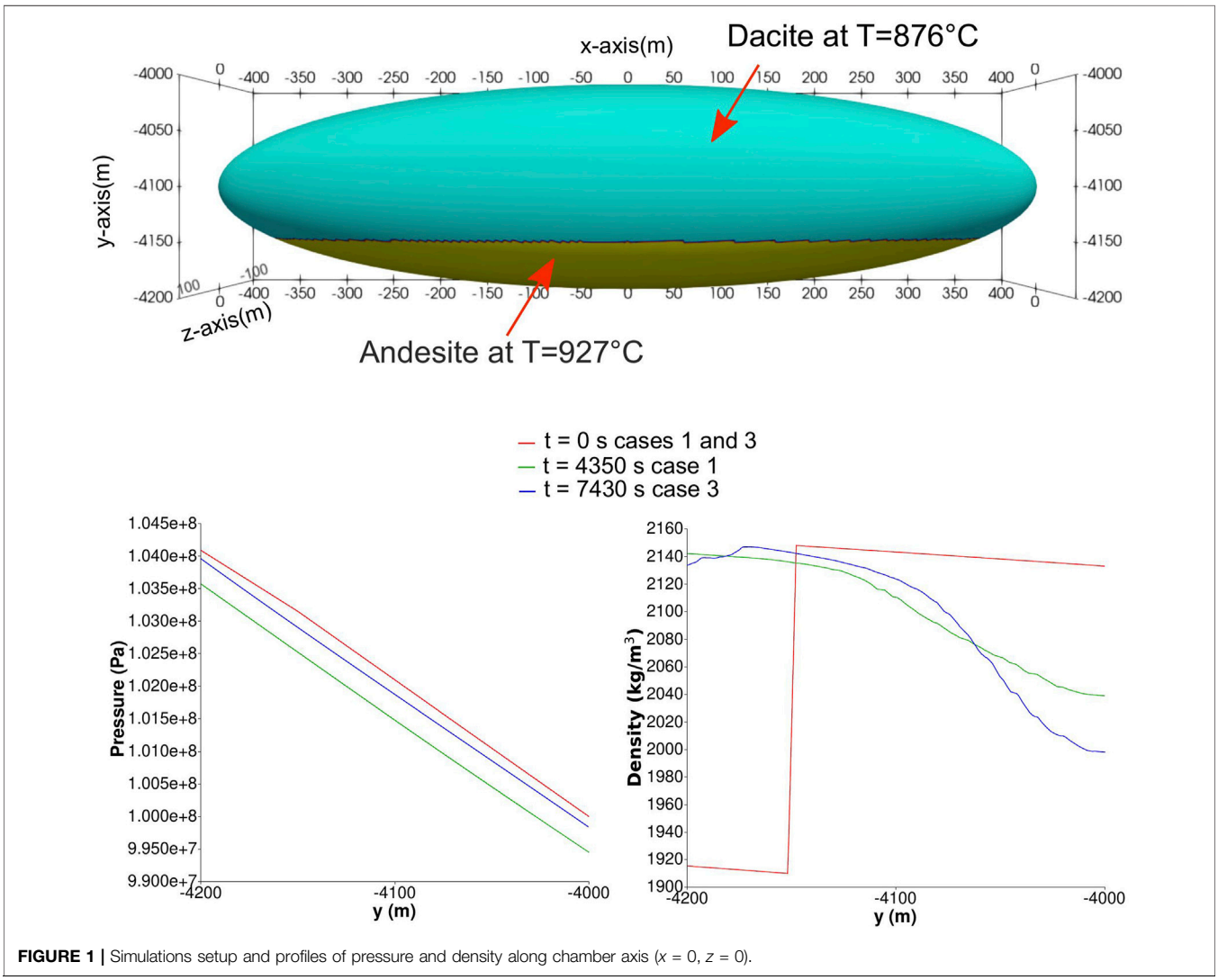


**FIGURE 1 |** Simulations setup and profiles of pressure and density along chamber axis ($x = 0$, $z = 0$).

## 3 APPLICATIONS TO MAGMA MIXING DYNAMICS

As discussed above, magmatic systems often consist of multiple heterogeneous magmas stored in a network of interconnected sills and dykes. Magma mixing is understood as one of many possible mechanisms for triggering an eruption (Sparks et al., 1977). Petrology and geochemistry analysis indicates that multiple intrusions of mafic to intermediate magma in more chemically evolved magmas stored at shallow depths may produce hybrid melts with zoned crystals. Sometimes the ejecta contain abundant inter-mingled hybrid magmas, suggesting efficient stirring and mingling in the reservoir as a result of replenishment and convection dynamics (Turner and

Campbell, 1986; Petrelli et al., 2011; Longo et al., 2012a; Garg et al., 2019).

Arc volcanoes are known for their dominantly explosive character. Their erupted products span the so-called andesitic magmatic suite, ranging from basaltic andesite to rhyolite. The occurrence of repeated pre-eruptive mixing events involving andesitic and dacitic melts is often recognized in the discharged magmas [e.g., (Tamura et al., 2003; Shane et al., 2008; Conway et al., 2020)].

Here we employ the 3D physical model described above to study the physics of mixing between andesite and dacite magmas. We use these magmas because arc-volcanism emits mainly the andesitic suite of magmas. The objective is to study magma dynamics for this suite of magmas through numerical simulations and extract some geologically meaningful information. We remark that the model and numerical scheme employed here is applicable on any suite of magmas. In particular we model the convection dynamics emerging from a gravitationally unstable stratification of andesite and dacite magmas in a shallow reservoir. We refer to a set up that represents a 3D extension of the one employed in previous work (Garg et al., 2019), allowing us to also compare between 2D and 3D dynamics.

## 3.1 Simulation Setup

The computational domain represents a prolate ellipsoid with longer axis in the $x$ direction (**Figure 1**). The centre of the ellipsoid is placed at 4.1 km depth. The lengths of the semi-axes in x, y, and z directions are 400, 100 and 100 m respectively. With respect to the 2D setup in (Garg et al., 2019), the third dimension added here ($z$-axis) is short enough to cause significant deviation from 2D conditions (approximated when the neglected dimension is much longer than the considered ones). We perform two simulations which correspond to run cases #1 and #3 in (Garg et al., 2019). For consistency with the corresponding 2D cases in (Garg et al., 2019), we keep the same numbering throughout in this work (**Table 1**). In the simulations, andesite at a temperature of 927°C is placed at the bottom of the domain, while the upper part is filled with dacite at a temperature of 876°C. A horizontal interface, separating the two magmas, is set at 4,150 m depth (**Figure 1**). The chemical composition of the two magmas and their volatile contents are reported in **Table 1**. The two cases differ for only magma viscosity, with case #1 corresponding to locally defined, space-time dependent viscosity computed as described above, and case #3 equal to case #1 with the viscosity arbitrarily multiplied by a factor 10 everywhere in space and time. The effects of varying the amount of volatile contents in the 2D setup were studied in (Garg et al., 2019). While such a viscosity increase may approximate the effect of non-reactive crystals, which affect viscosity much more than other properties including density, the aim here is mostly that of evaluating the 3D dynamics and comparing with the 2D case, over a range of viscosities thus of dynamic time scales; as well as that of evaluating the 3D code performance in terms of computational time and scalability. The initial pressure distribution is computed by considering the lithostatic load at the chamber roof (average rock density = 2,500 kg/m$^3$) and a horizontally uniform magmastatic profile. The bottom panel of **Figure 1** (red lines) displays the initial pressure and density profiles along the chamber axis. No-slip adiabatic conditions are employed at the chamber walls. The numerical scheme presented in the **Appendix A** is employed with 2.6 million linear tetrahedral elements. The side length of the computational elements ranges 1–4 m. The numerical integrals are computed with four Gauss quadrature points. The unstructured tetrahedral mesh results in uneven interface providing the initial perturbations that destabilize the interface between the two magma types. The simulations are run on an HP cluster system at INGV Pisa, composed of 432 Intel Xeon 2.3 GHz cores distributed over six nodes connected through a low latency 100 Gbps Infiniband network. Scaling tests reported below and involving up to thousands cores for a much shorter computational time are run instead on the supercomputing facilities at the Barcelona Supercomputing Center.

# 4 RESULTS

We present the results of the numerical simulations by first analysing the 3D convection dynamics, then comparing with the 2D case in (Garg et al., 2019).

## 4.1 3D Dynamics

The 3D dynamics are illustrated here mostly through comparison between the two simulation cases 1 and 3 in **Table 1**, with the latter being identical to the former, except for the computed viscosity which is everywhere in space and time arbitrarily multiplied by a factor 10. We anticipate that as for the 2D case (Garg et al., 2019), the more viscous situation corresponds to slower convection dynamics, lower number of buoyant plumes of andesite-rich magma rising through the dacite, and finally lower mixing efficiency. **Figure 2** illustrates well such differences. The figure shows the evolution of the isosurface corresponding to a mass fraction of andesite equal to 0.5 (which at time zero corresponds to the interface between the two magma types) for cases 1 and 3. The differences are striking: after 100 s case 1 shows a highly dynamic state with a complex structure made of several inter-digitized rising plumes interacting with each other and occupying the entire chamber; while at the same time, only minor perturbations appear on the interface initially separating the two dacitic and andesitic magmas. At a later time when the dynamics are well developed also for case 3, this case displays a much simpler overall structure with many less plumes, each one on average much bigger than for case 1. The 0.5 mass fraction isosurface for the more viscous case 3 is conserved within the chamber over a much longer time, and it is still visible after more than 2 h from start of the simulation. On the contrary, the same isosurface is completely lost in case 1 after only 5 min, as a consequence of much faster and more intense magma mixing for this lower viscosity case.

**Figure 3** highlights the differences in plume structure for the two cases, through a planar view of the interface at an early stage of its destabilization. The higher the viscosity (case 3),

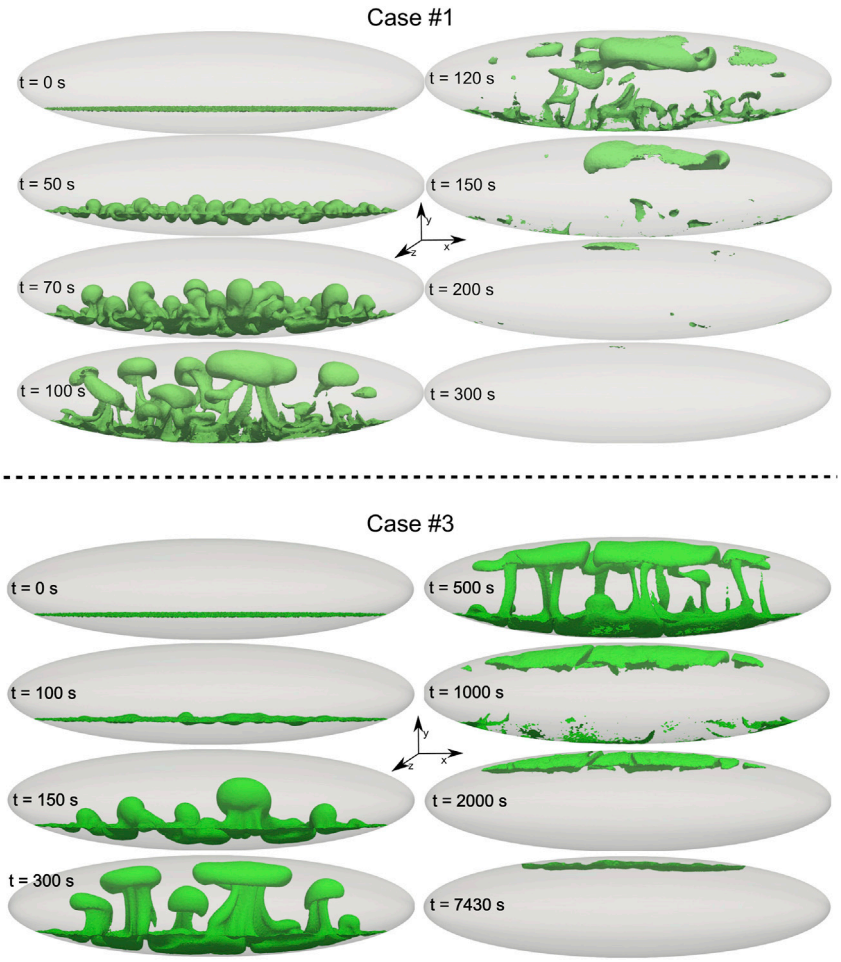


**FIGURE 2 |** Temporal evolution of isosurfaces of mass fraction $Y = 0.5$.

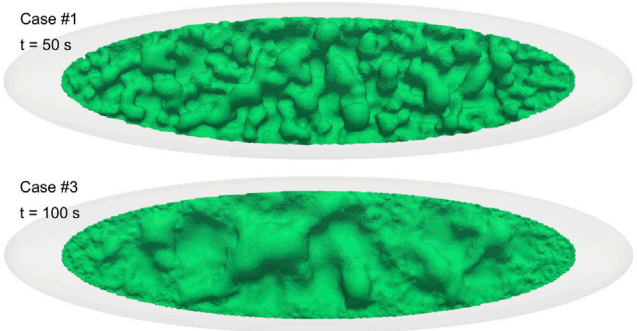


**FIGURE 3 |** Plume structure looking at the interface from the top. The interface is depicted by isosurfaces of mass fraction $Y = 0.5$.

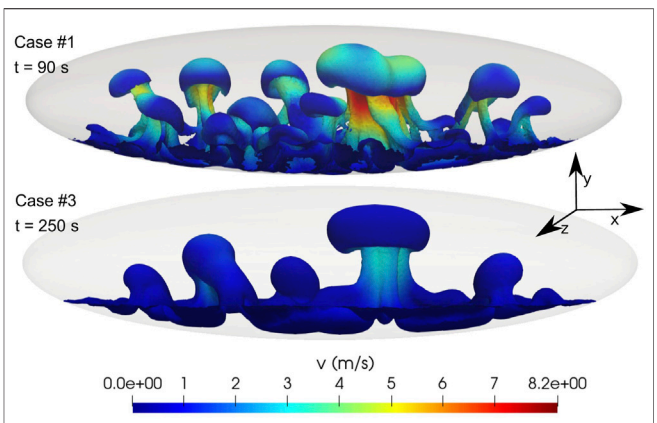


**FIGURE 4 |** Velocity distribution of uprising plumes when the maximum value is reached.

the lower the number density (and the larger the average size) of the rising plumes formed as a consequence of Rayleigh-Taylor Instabilities. **Figure 4** shows instead the distribution of velocity in the uprising plumes, at the two times (90 and 250 s, respectively) at which the maximum velocity is attained for the two cases 1 and 3. That maximum velocity corresponds to 8.2 m/s in case 1, while it is only 3.5 m/s for the more viscous case 3.

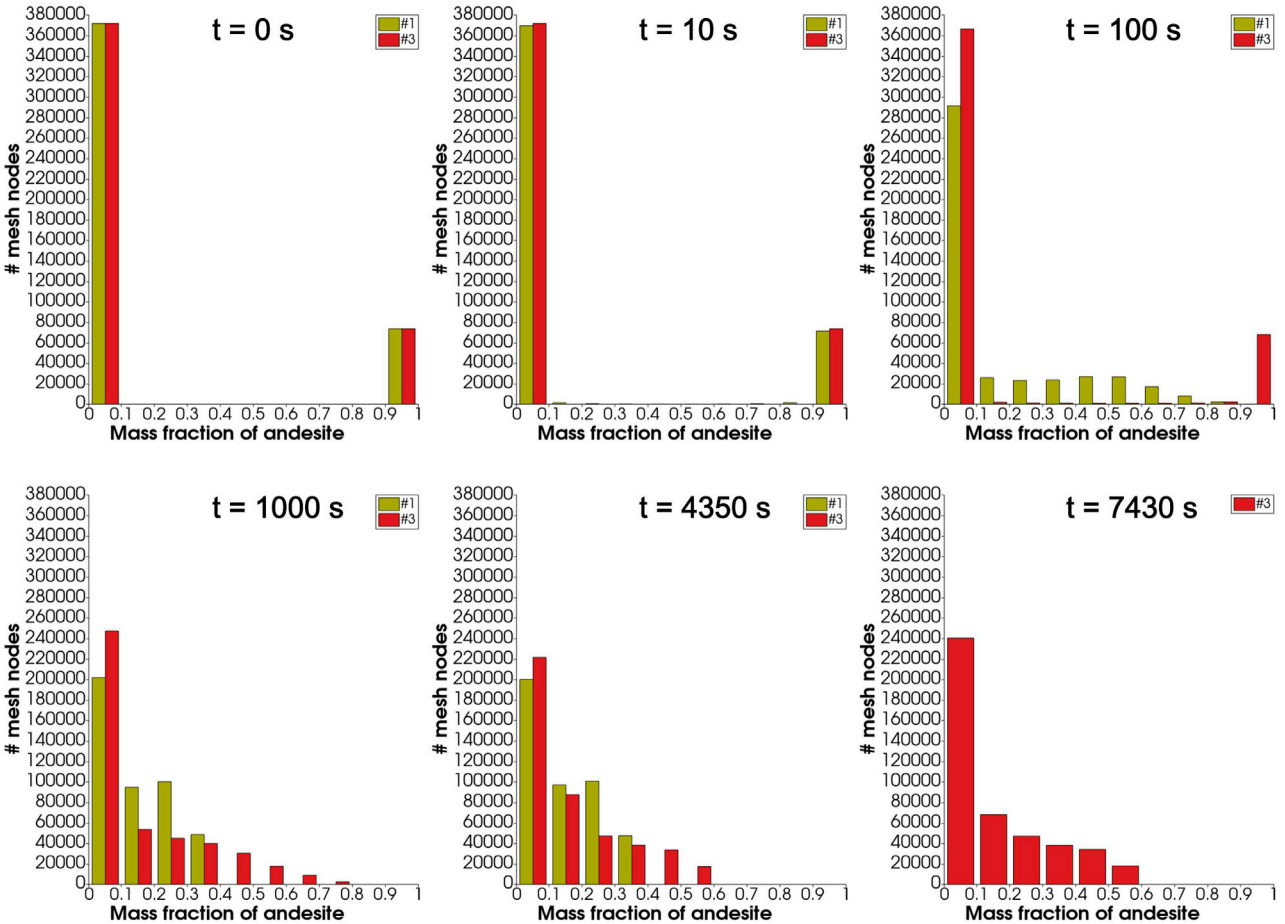


**FIGURE 5 |** Distribution of composition across mesh nodes. Simulation case 1 was run up to 4,350 s. Therefore, at 7,430 s, only #3 is displayed.

**Figure 5** illustrates the evolution of mixing throughout the computational domain. Case 1 corresponds to viscosity computed by model described in (Giordano et al., 2008) and case 3 is with tenfold increase in viscosity than case 1. Initially, for both cases 1 and 3 the computational nodes host either pure dacite or pure andesite. In both cases the less viscous, less abundant andesitic end-member quickly vanishes as a pure component (at the scale of the resolution of the present simulations, which is of order 1 m), whereas nearly pure dacite continues to be largely present in the system at the latest simulation times. Faster and more efficient mixing for case 1 is clearly visible as an earlier decrease of the maximum length of the compositional bars (that is, faster decrease of the number of nodes hosting pure dacite) as well as narrower compositional interval span inside the chamber at latest simulation times, when efficient convection is terminated in both cases (further illustrated below). For the more viscous case 3 the andesite can be seen to constitute at most about 50% of individual computational nodes, whereas for case 1 the maximum proportion of andesite in individual computational nodes at process end is only about 30%.

In both cases 1 and 3 by the latest times, the system is decompressed throughout by 6 and 2 bars, respectively, and the density evolves from an initial step profile to a smooth one (**Figure 1**). For both simulation cases 1 and 3, pressure and temperature distributions along $z = 0$ and $x = 0$ planes is provided in the **Supplementary Material**. We also display the profiles of scaled temperature and composition along the chamber axis in the **Supplementary Material**.

## 4.2 Comparison Between 3D and 2D Simulation Results

As it is explained above, the present 3D simulation cases correspond to previous 2D simulations in (Garg et al., 2019), so to confidently explore the effects of 3D vs. 2D simulation setup. In particular, the numerical code and the physical and numerical setup in the 2D and 3D cases are the same, except for the specific aspects defining 2D vs. 3D simulated dynamics. The average length of computational elements across the initial compositional interface is of order 1 m in both cases, and the number of elements in the 2D cases and along domain-centered 2D slides in the 3D cases are of order $10^5$ in both cases.

One of the major results from the simulation of 2D magma convection dynamics was the achievement of a stable dynamic

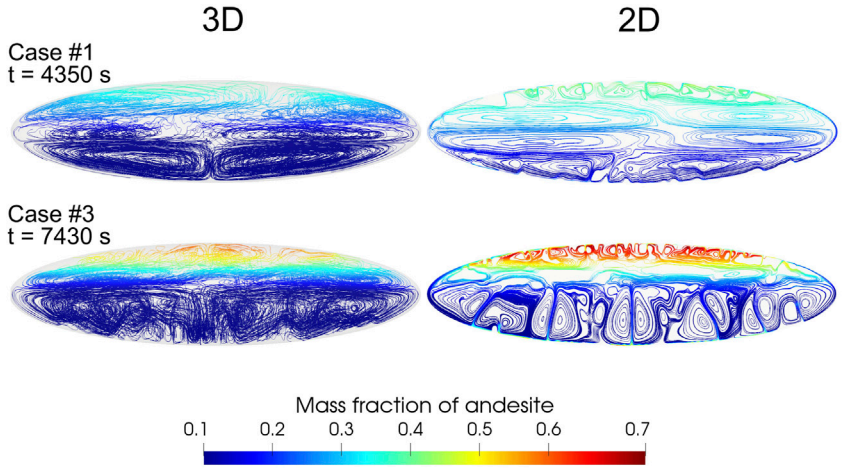


**FIGURE 6 |** Streamline structure with composition colorbar.

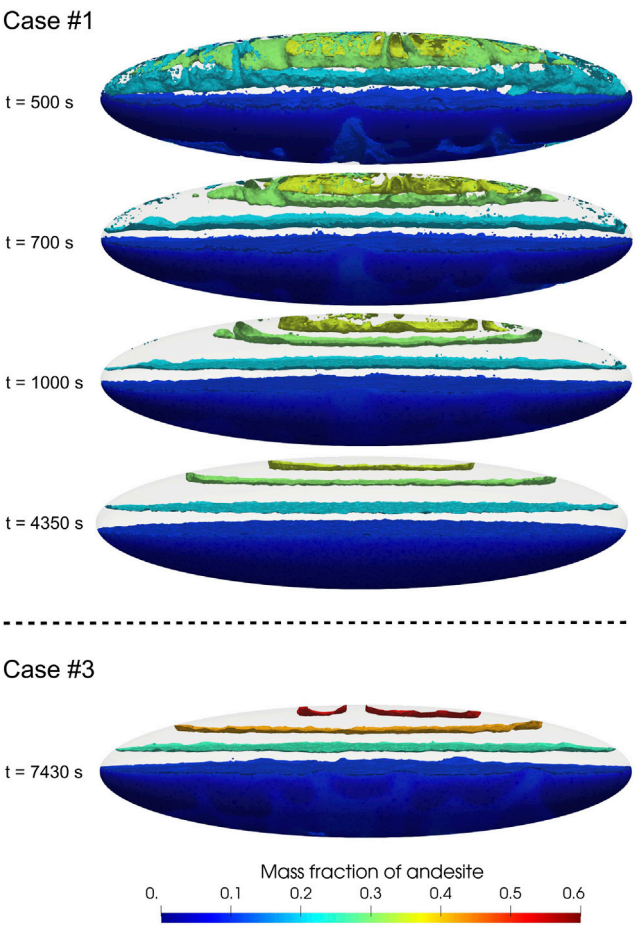


**FIGURE 7 |** Temporal evolution of isosurfaces of mass fraction of andesite.

state characterized by separate convective regions effectively impeding further mechanical mixing (Garg et al., 2019). **Figure 6** shows that such a major result is confirmed by 3D numerical simulations: dynamically stable, largely closed circulation patterns separating regions with different composition emerge, explaining the long-term maintenance of the heterogeneities at advanced times in **Figure 5**. In fact, the circulation patterns in **Figure 6** give rise to a stable, dynamic layering inside the magma chamber (**Figure 7**). The details of the circulation patterns are not easy to compare, as those patterns are intimately three-dimensional for the 3D simulations, therefore, comparing a slice cut with the 2D case, e.g. as in **Figures 8**, **9** below, would not make any sense. Here we stress the overall first order agreement between the 2D and 3D simulation cases with respect to the major conclusion that magma chamber overturning and associated convection and mixing dynamics lead to the achievement of a stable dynamic state preserving compositional heterogeneities over the long term. We discuss in (Garg et al., 2019) some major consequences for the interpretation of compositional heterogeneities in magmas erupted during individual eruptions.

A more direct comparison between the simulated 2D and 3D dynamics is displayed in **Figures 8**, **9** for the simulation cases 1 and 3, respectively. For the 2D case each panel in the figures represents the entire computational domain, with the third neglected dimension (perpendicular to the sheet) assumed much longer than the two simulated ones so as to satisfy the 2D approximation. On the contrary, for the 3D case each panel reports a vertical slice cut across the center of the 3D computational domain, with the third dimension, simulated but not visible from the slice cut, being equal in size to the vertical dimension (**Figure 1**).

At first sight, the 3D and 2D dynamics in **Figures 8**, **9** appear quite similar, especially in light of the different evolutions characterizing the less and more viscous cases, respectively, one and 3. That may appear surprising, considering the small length of the third chamber dimension in the present 3D simulations. However, such qualitative similarities are consistent with previous findings, e.g., (Young et al., 2001; Cabot, 2006) (although those authors investigate high-Re

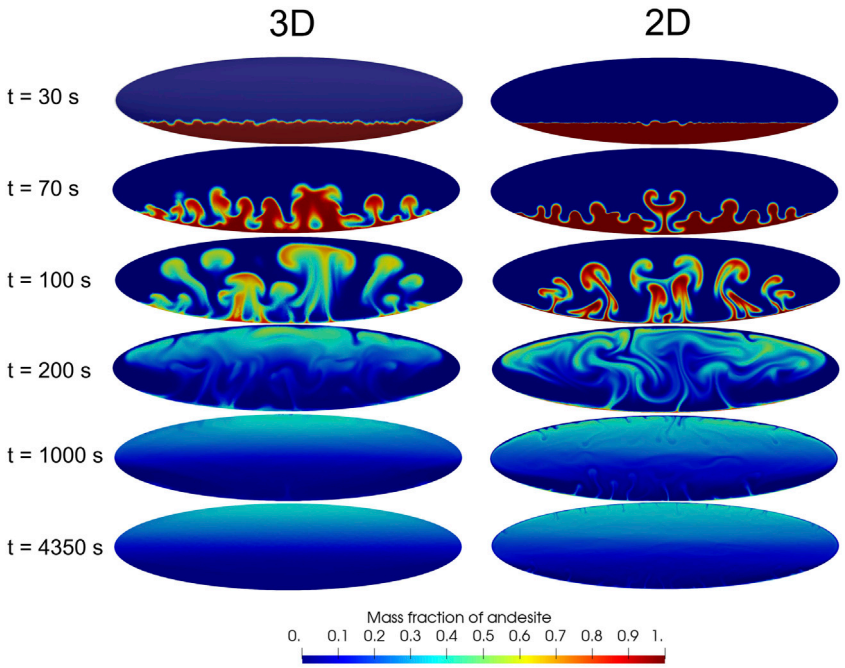


**FIGURE 8 |** Comparison between 2D simulation and a vertical slice at $z = 0$ from the 3D simulation #1.

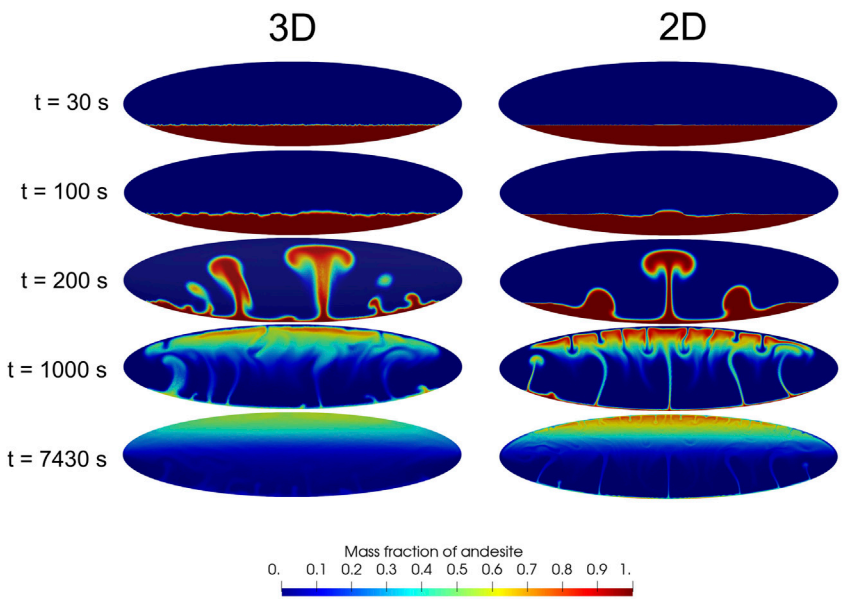


**FIGURE 9 |** Comparison between 2D simulation and a vertical slice at $z = 0$ from the 3D simulation #3.

incompressible flows), and as for those cases, we show here that the differences are also relevant.

The comparison shows that the interface destabilization time in the two 3D and 2D cases is very similar [while it is significantly influenced, as any other aspect of the overall dynamics, by magma viscosity. The role of viscosity—and of volatile contents—is however described in (Garg et al., 2019), and it is only marginally considered here]. However, the 3D geometry of the interface appears to result in more complex perturbation structure comprising a broad range of scales, compared to the geometrically much simpler 2D perturbations. At later times such a richer 3D structure is visible as a much less symmetric geometry

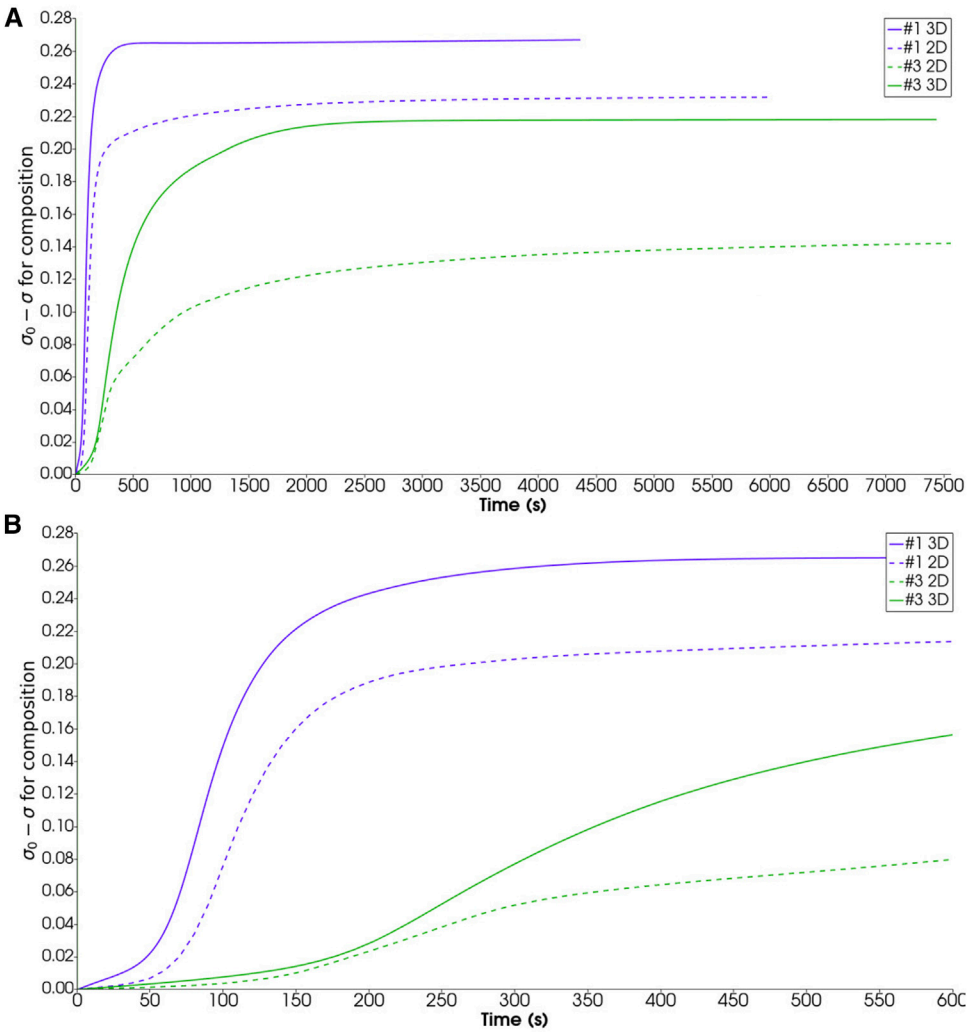


**FIGURE 10 |** Panel **(A)**: Evolution of overall compositional heterogeneities. $\sigma$ is overall compositional standard deviation and $\sigma_0$ is the same quantity at time zero. Panel **(B)**: Zoom view of first 600 s.

of the rising plumes, and more widespread plume size range. The plumes in the 3D cases also appear to rise faster, and are more mixed than for the 2D cases. That is well evident at time 100 s for case 1 (**Figure 8**) or time 200 s for case 2 (**Figure 9**): the 2D plumes maintain a much larger proportion of nearly pure andesite (dark red), which is instead much less represented (**Figure 9**), or practically absent (**Figure 8**), in the 3D cases at the same time. At the latest simulation times corresponding to achievement of a stable dynamic stratification as discussed above, the more viscous case in **Figure 9** shows that andesite-rich (70–80 wt%) magma concentrates close to magma chamber top in the 2D case, whereas only < 60 wt% andesitic magma occupies the same chamber region in the 3D case.

The faster, more efficient mixing dynamics found for the 3D case are best highlighted in **Figure 10**. Here, to establish a measure of mixing, we refer to progressive reduction of the overall compositional heterogeneity inside the chamber. As a quantitative measure of such heterogeneity we compute the standard deviation ($\sigma$) of the mass fraction of andesite in the overall computational domain. For any time we first determine the mean value of the composition in the entire domain, then use that value to compute ($\sigma$), which measures the extent of dispersion of the composition around its mean value. The larger the value of ($\sigma$), the lower the extent of mixing:

$$\sigma = \sqrt{\frac{1}{N}\sum_{i=1}^{N}\left(x_{i,and} - \bar{x}_{and}\right)^2} \tag{9}$$

where $N$ is the total number of nodes in the computational domain, $x$ is mass fraction, and the horizontal bar indicates the mean value over the entire computational domain.

The computed evolutions of $\sigma$ in **Figure 10** for the 2D and 3D simulations evidence the different stages of the overturning process (Garg et al., 2019), starting in all cases with a low slope section corresponding to the initial phase 1 of

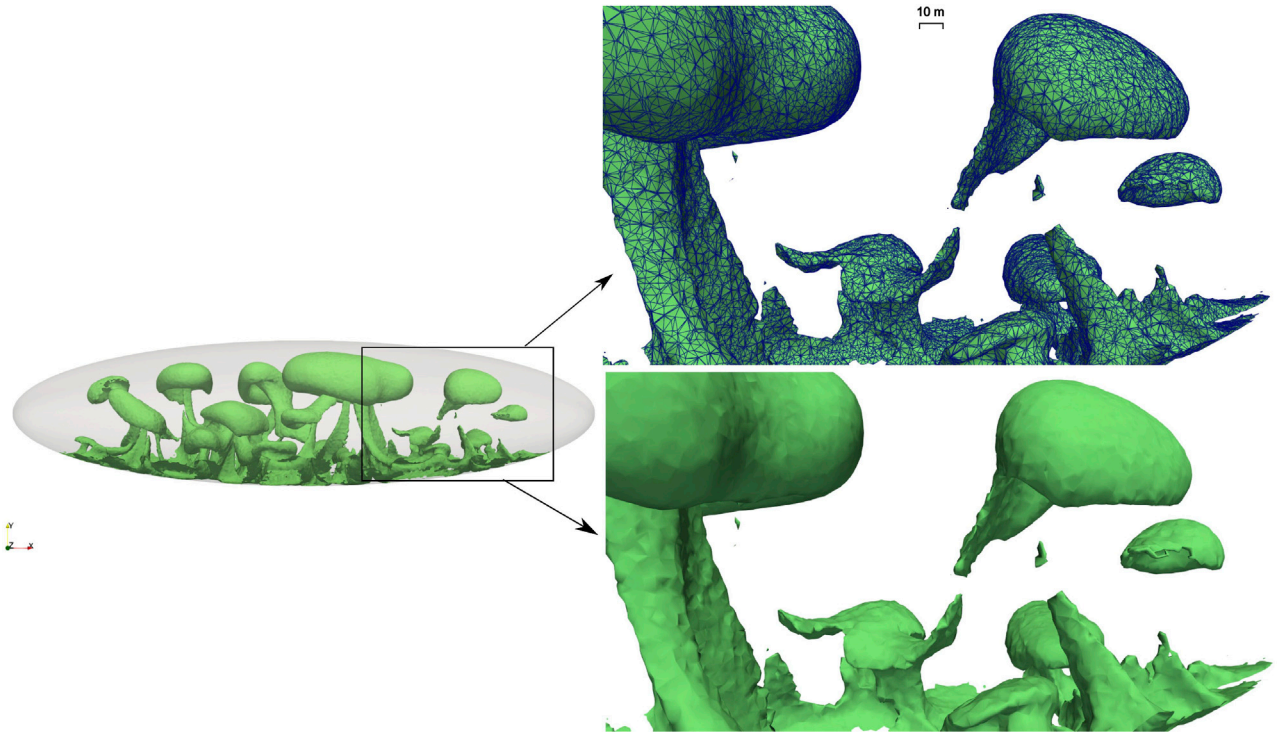


**FIGURE 11 |** Zoom view of the computational mesh and isosurfaces $Y$ = 0.5 at t = 100 s for case #1.

development of the Rayleigh-Taylor instability, followed by a high slope section corresponding to highly efficient mixing during the convective phase of plume rise and vortex formation (phase 2), and terminating with an essentially flat section (phase 3) when the final stable dynamic state described above, preventing significant further mixing, is achieved. Faster development of the Rayleigh-Taylor instability and transition to phase 2 (efficient plume rise) is highlighted in the zoom view of **Figure 10B**. Similarly, faster overall dynamics and more efficient mixing for the 3D case translate in earlier achievement of the flat section corresponding to phase 3. Note that for the high-viscosity case 3, the 2D simulation never attains a completely flat section, indicating that some mixing continues to be effective up to the last simulated time > 2 h. That suggests that constraining the magma circulation patterns over a 2D plane (or better, assuming zero gradient of any flow variable including velocity along the neglected dimension as it is implicit in 2D simulations) may cause the flow streamlines to distort to an extent sufficient to break the closed circulation patterns in **Figure 6**, resulting in further mixing not seen at such late times from the 3D simulations. Finally, and mostly relevant, the final extent of homogenization (that is, the overall change in $\sigma$) is significantly larger for the 3D simulation cases, reflecting enhanced convection and mixing efficiency with respect to the 2D case. The difference is important, amounting to 18% of the total $\sigma$ change computed from the 2D simulation for case 1, and as large as 55% of that change for case 3. Therefore, not only mixing and homogenization in the magma chamber are significantly enhanced when considering the flow dynamics in a more realistic 3D environment; also, the extent of such enhancement depends substantially on the specific conditions. While the less viscous case 1 leads to more homogenization, the extent of change when moving from 2D to 3D turns out to be larger for the more viscous case 3. In other words, it seems plausible, based on our first 3D simulations and comparison with the corresponding 2D cases, to suggest that the errors and approximations introduced by neglecting more realistic 3D dynamics may vary substantially depending on the conditions considered, and may increase in relevance with increasing magma viscosity.

## 5 CODE PERFORMANCE

As we mention above, the 3D simulation results presented above make use of 2.6 million tethrahedral elements in order to resolve the 3D Rayleigh-Taylor flow structure determined by the adopted initial unstable configuration. **Figure 11** shows a zoom view of one isosurface distribution from **Figure 2**. In particular, superposition of the computational mesh illustrates well the resolution level achieved, and the kind of details that are resolved.

To check the parallel performance of GALES, we conduct a strong scaling test which is widely used to check the ability of a software to deliver results in less time when the amount of resources is increased. The parallel performance is quantified by comparing the actual speedup with the ideal speedup for a

**TABLE 2 |** Mesh models for strong scaling test.

| Test | #Nodes | #Elements | #dofs | r | N |
|---|---|---|---|---|---|
| 1 | 175001 | 1004750 | 1050006 | 96 | 96–1,536 |
| 2 | 1951658 | 11782329 | 11709948 | 192 | 192–6,144 |
| 3 | 7802061 | 47581941 | 46812366 | 384 | 384–12,288 |

given set of processors. The actual speedup and the ideal speedup are defined as

$$\text{Actual speedup} = \frac{t_r}{t_N} \qquad r < N \tag{10}$$

$$\text{Ideal speedup} = \frac{N}{r} \tag{11}$$

where $t_r$ and $t_N$ are the computational times taken by $r$ processors and $N$ processors, respectively. Parallel efficiency is computed as the ratio of the actual speedup and the ideal speedup for a given number of processors:

$$\text{Efficiency} = \frac{t_r}{t_N}.\frac{r}{N} \tag{12}$$

An ideal scalable software should result in a linear speedup. However, this is hardly achieved in real situations. For a given

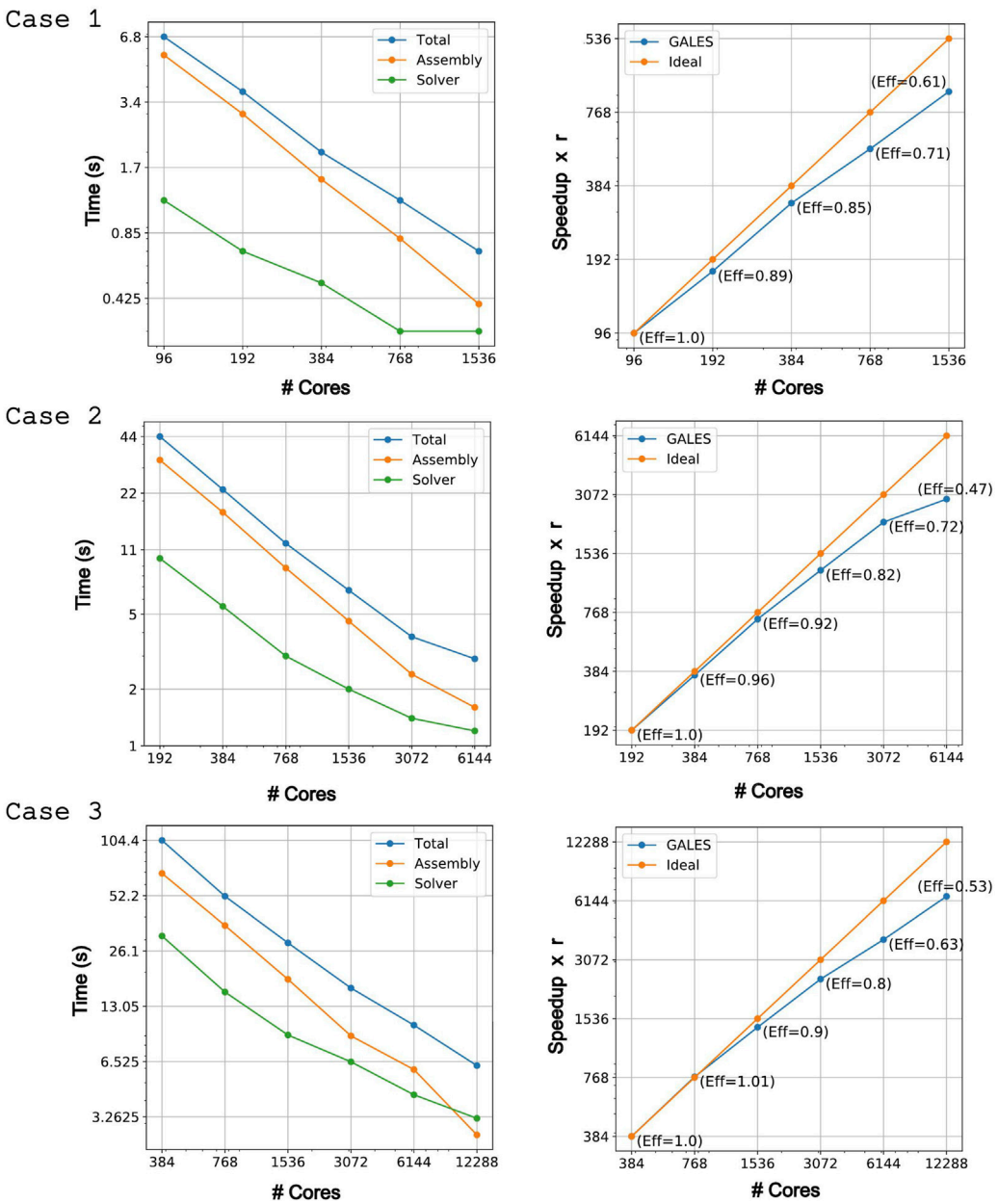


**FIGURE 12 |** Strong scaling results for test cases in **Table 2**.

**TABLE 3 |** Partitioning statistics for test case 3 in Table 2. The second column reports the average number of elements per core. The third column reports the average percentage of nodes lying on inter-processor boundaries.

| #Cores | #Elements | Boundary nodes (in percentage) | Scaling efficiency |
|---|---|---|---|
| 384 | 123911 | 19 | 1.0 |
| 768 | 61,955 | 23 | 1.0 |
| 1,536 | 30,977 | 30 | 0.91 |
| 3,072 | 15,488 | 35 | 0.80 |
| 6,144 | 7,744 | 42 | 0.63 |
| 12,288 | 3,872 | 50 | 0.53 |

mesh the parallel efficiency decreases as we increase the number of processors, mostly as a consequence of increased time spent in communication among processors. The scaling tests are performed on the Marenostrum supercomputer at the Barcelona Supercomputing Centre (BSC) (https://www.bsc.es/marenostrum/marenostrum/technical-information) within the project GALES-3D (2010PA5625) in the frame of a PRACE preparatory access A (https://prace-ri.eu/).

The scaling tests were run on three different meshes with progressively increasing size. The mesh models are listed in **Table 2**. The simulations use the same setup as described in **Section 3.1**. The adopted numerical methods and the parallelization strategy employed are illustrated in detail in **Appendixes A,B**. Here we only recall the monolithic approach to solve the linearized system of equations describing the space-time system dynamics, which is effective in reducing data transfer in parallel computing implementations (Dowd and Charles, 2010).

**Figure 12** shows the strong scaling results for each test case. The left panels in the figure display the time taken by the assembly procedure, the linear solver and the total time. We report here the average time taken for a non-linear iteration over 10 time steps (the observed standard deviation being $2 \times 10^{-2}$ s). The right panels in the figure plot the speedup and the efficiency as a function of number of cores.

Overall, the scaling behavior of GALES is quite satisfactory in the explored range of computational elements and cores (a parallel efficiency of 0.6 or greater is taken here as satisfactory). The left panels in **Figure 12** show that most of the computational time is spent in the assembly of the linearized system of equations. The solution time is only a fraction of the assembly time, increasing in relevance with increasing number of cores thus (right panels) with decreasing parallel efficiency. The total computational time decays nearly linearly (in the log scale of the figures) with increasing number of cores, and the parallel efficiency (right panels) is seen to decrease below satisfactory only for the largest number of cores employed for each different mesh size.

Parallel performance primarily depends on load balancing and inter-processor communication. Our linear solvers are distributed and use peer-to-peer communication to solve the system. **Table 3** displays the partition statistics for test case 3 in **Table 2**, and illustrates well the reasons and conditions under which the parallel efficiency becomes less than satisfactory. Specifically, we display the average number of elements on a processor and the average percentage of inter-processor boundary nodes, computed from the load balanced partitions generated by the Metis software (see the **Appendix B** for further details). Load balance when increasing the computational resources reduces the overall execution time. However, by increasing the number of processors the percentage of boundary nodes lying at inter-processor boundaries also increases, implying that the processors need to communicate more data. This translates into increased communication time and works towards decreased parallel efficiency. In other words, for any specific problem there is an optimal balance between decreasing load per core and increasing core inter-communication when increasing the overall computational resources. The results in **Figure 12** show that for GALES, and in the range of the strong scaling exercise described here, a one order of magnitude decrease in total computational time is allowed before such a balancing condition is achieved.

## 6 DISCUSSION AND CONCLUSION

In this paper we present a 3D parallel code for computing compressible to incompressible multi-component magma dynamics, compare numerical simulations of 3D vs. 2D dynamics for a simple test case represented by the development of Rayleigh-Taylor instability in a stratified, idealized magma chamber, and illustrate code performance by analyzing the results of a strong scaling test involving up to nearly 50 million computational elements and up to >12,000 computational cores. The computational speedup is close to ideal and above satisfactory levels as long as the element/core ratio is sufficiently large so as to limit boundary nodes to less than half total nodes. The demonstrated parallel efficiency is such as to guarantee efficient use of HPC resources in 3D applications to more realistic magmatic configurations including geometrically complex multiple chamber, dike and conduit systems, likely requiring a number of computational elements exceeding the maximum employed here. Recent extension of GALES to include fluid-structure interaction and coupling with solid elasto-dynamics (Garg et al., 2021) further extends the accessible computational domains requiring exploration of the potential towards exascale computing (e.g., as in the ChEESE European Center of Excellence, www.cheese-coe.eu).

The numerical simulations performed here, designed to compare with previous 2D simulations, illustrate the 3D dynamics of magma chamber overturning due to gravitationally unstable initial conditions and development and evolution of Rayleigh-Taylor instability. The numerical results illustrate to a high resolution level the 3D dynamics of development and growth of the instability, the formation and reciprocal interaction of buoyant plumes of magma, the complexities of the associated vorticity patterns and associated magma mixing, and the evolution towards a stable dynamic state preserving compositional heterogeneities and resulting in a dynamic layering of the magma chamber.

Remarkably, the much simpler 2D simulation approach is found to reproduce the more realistic 3D dynamics on a zero/

first-order level, showing similar overall dynamics occurring over comparable time scales, and similar overall effects due to increased magma viscosity. On a more quantitative level, the 3D dynamics show however important differences, and in particular they produce faster plumes leading to more efficient magma mixing than for the corresponding 2D approximation. These results are in general consistent with those from the engineering literature (Young et al., 2001; Cabot, 2006) where similar overall qualitative consistency but important quantitative differences between 2D and 3D simulations are evidenced, although for high Re incompressible flows. In particular, our results suggest that the extent of approximation introduced by the 2D simplification may depend on the specific conditions, and may be smaller for low viscosity conditions. That could be relevant in light of the substantial computational efforts required by the solution of 3D dynamics, and we deserve to evaluate it further, e.g., for more complex geometrical systems over a range of magmatic compositions.

## DATA AVAILABILITY STATEMENT

The raw data supporting the conclusion of this article will be made available by the authors, without undue reservation.

## AUTHOR CONTRIBUTIONS

DG and PP designed the study, analysed and discussed the results, and wrote the article, DG carried out the numerical simulations and postprocessed the results.

## ACKNOWLEDGMENTS

We gratefully acknowledge the reviewers for their comments, which improve the quality of the manuscript. We acknowledge that the results on the code performance have been achieved using the PRACE Research Infrastructure resource MareNostrum based in Spain at Barcelona Supercomputing Centre (BSC). One of us (D.G.) was supported by an EPOS-IT grant.

## SUPPLEMENTARY MATERIAL

The Supplementary Material for this article can be found online at: https://www.frontiersin.org/articles/10.3389/feart.2021.760773/full#supplementary-material

## REFERENCES

Asanovic, K., Bodik, R., Gebis, J., Husbands, P., Keutzer, K., Shalf, J., et al. (2006). Technical report. Berkeley: EECS Department, University of California. The Landscape of Parallel Computing Research: A View from berkeley.

Bachmann, O., and Bergantz, G. W. (2003). Rejuvenation of the Fish canyon Magma Body: A Window into the Evolution of Large-Volume Silicic Magma Systems. *Geol.* 31 (9), 789–792. doi:10.1130/g19764.1

Bagagli, M., Montagna, C. P., Papale, P., and Longo, A. (2017). Signature of Magmatic Processes in Strainmeter Records at Campi Flegrei (italy). *Geophys. Res. Lett.* 44, 718–725. doi:10.1002/2016gl071875

Bavier, E., Hoemmen, M., Rajamanickam, S., and Thornquist, H. (2012). Amesos2 and Belos: Direct and Iterative Solvers for Large Sparse Linear Systems. *Scientific Programming* 20 (3), 241–255. doi:10.1155/2012/243875

Bazilevs, Y., Calo, V., Cottrell, J. A., Hughes, T., Reali, A., Scovazzi, G., et al. (2007). Variational Multiscale Residual-Based Turbulence Modeling for Large Eddy Simulation of Incompressible Flows. *CMAME* 197 (1), 173–201. doi:10.1016/j.cma.2007.07.016

Bergantz, G. W. (2000). On the Dynamics of Magma Mixing by Reintrusion: Implications for Pluton Assembly Processes. *J. Struct. Geology* 22 (22), 1297–1309. doi:10.1016/s0191-8141(00)00053-5

Bergantz, G. W., Schleicher, J. M., and Burgisser, A. (2015). Open-system Dynamics and Mixing in Magma Mushes. *Nat. Geosci.* 8, 793–796. doi:10.1038/ngeo2534

Blundy, J. D., and Annen, C. J. (2016). Crustal Magmatic Systems from the Perspective of Heat Transfer. *Elements* 12 (2), 115–120. doi:10.2113/gselements.12.2.115

Burnham, C. W., Holloway, J. R., and Davis, N. F. (1969). Thermodynamic Properties of Water to 1,000° C and 10,000 Bars. *Geol. Soc. America Spec. Pap.* 132, 1–96. doi:10.1130/spe132-p1

Cabot, W. (2006). Comparison of Two- and Three-Dimensional Simulations of Miscible Rayleigh-taylor Instability. *Phys. Fluids* 18, 1–9. doi:10.1063/1.2191856

Campbell, I. H., and Turner, J. S. (1986). The Influence of Viscosity on Fountains in Magma chambers. *J. Petrology* 27, 1–30. doi:10.1093/petrology/27.1.1

Caricchi, L., Burlini, L., Ulmer, P., Gerya, T., Vassalli, M., and Papale, P. (2007). Non-newtonian Rheology of crystal-bearing Magmas and Implications for Magma Ascent Dynamics. *Earth Planet. Sci. Lett.* 264, 402–419. doi:10.1016/j.epsl.2007.09.032

Carrara, A. (2019). Numerical Modeling of the Physical Processes Causing the Reawakening of a Magmatic Chamber and of the Associated Geophysical Signals Theses Grenoble: Université Grenoble Alpes.

Cashman, C. (2000). *Encyclopedia of Volcanoes*. Academic Press.

Cassidy, M., Manga, M., Cashman, K., and Bachmann, O. (2018). Controls on Explosive-Effusive Volcanic Eruption Styles. *Nat. Commun.* 9 (2839), 1–16. doi:10.1038/s41467-018-05293-3

Conway, C. E., Chamberlain, K. J., Harigane, Y., Morgan, D. J., and Wilson, C. J. N. (2020). Rapid Assembly of High-Mg Andesites and Dacites by Magma Mixing at a continental Arc Stratovolcano. *Geology* 48, 1033–1037. doi:10.1130/g47614.1

Couch, S., Sparks, R. S. J., and Carroll, M. R. (2001). Mineral Disequilibrium in Lavas Explained by Convective Self-Mixing in Open Magma chambers. *Nature* 411, 1037–1039. doi:10.1038/35082540

De Campos, C. P., Perugini, D., Ertel-Ingrisch, W., Dingwell, D. B., and Poli, G. (2011). Enhancement of Magma Mixing Efficiency by Chaotic Dynamics: an Experimental Study. *Contrib. Mineral. Petrol.* 161, 863–881. doi:10.1007/s00410-010-0569-0

DePaolo, D. J. (1981). Trace Element and Isotopic Effects of Combined Wallrock Assimilation and Fractional Crystallization. *Earth Planet. Sci. Lett.* 53 (2), 189–202. doi:10.1016/0012-821x(81)90153-9

Dowd, K., and Charles, S. (2010). *High Performance Computing*. Texas: Rice University.

Edmonds, M., and Wallace, P. J. (2017). Volatiles and Exsolved Vapor in Volcanic Systems. *Elements* 13 (1), 29–34. doi:10.2113/gselements.13.1.29

Eichelberger, J. (2020). Distribution and Transport of thermal Energy within Magma–Hydrothermal Systems. *Geosciences* 10, 1–26. doi:10.3390/geosciences10060212

Flanagan, J., Davies, G. H., Boy, F., and Doneddu, D. (2020). A Review of a Distributed High Performance Computing Implementation. *J. Inf. Technology Case Appl. Res.* 22 (3), 142–158. doi:10.1080/15228053.2020.1812803

Folch, A., and Marti, J. (1998). The Generation of Overpressure in Felsic Magma chambers by Replenishment. *Earth Planet. Sci. Lett.* 163 (1), 301–314. doi:10.1016/s0012-821x(98)00196-4

Franco, R., and Rafael Saavedra, G. Z. (2006). A Stabilized Finite Element Method Based on Sgs Models for Compressible Flows. *Computer Methods Appl. Mech. Eng.* 196 (1), 652–664.

Garg, D., Papale, P., Colucci, S., and Longo, A. (2019). Long-lived Compositional Heterogeneities in Magma chambers, and Implications for Volcanic hazard. *Sci. Rep.* 9 (3321), 1–13. doi:10.1038/s41598-019-40160-1

Garg, D., Longo, A., and Papale, P. (2018a). Computation of Compressible and Incompressible Flows with a Space-Time Stabilized Finite Element Method. *Comput. Mathematics Appl.* 75, 4272–4285. doi:10.1016/j.camwa.2018.03.028

Garg, D., Longo, A., and Papale, P. (2018b). Modeling Free Surface Flows Using Stabilized Finite Element Method. *Math. Probl. Eng.* 2018 (6154251), 1–9. doi:10.1155/2018/6154251

Garg, D., Papale, P., and Longo, A. (2021). A Partitioned Solver for Compressible/incompressible Fluid Flow and Light Structure. *Comput. Mathematics Appl.* 100, 182–195. doi:10.1016/j.camwa.2021.09.005

Giordano, D., Russell, J. K., and Dingwell, D. B. (2008). Viscosity of Magmatic Liquids: a Model. *Earth Planet. Sci. Lett.* 271, 123–134. doi:10.1016/j.epsl.2008.03.038

Gottlieb, A. (1989). *Highly Parallel Computing*. Redwood City, CA: Benjamin-Cummings Publishing Co., Inc..

Gottsmann, J., De Angelis, S., Fournier, N., Van Camp, M., Sacks, S., Linde, A., et al. (2011). On the Geophysical Fingerprint of Vulcanian Explosions. *Earth Planet. Sci. Lett.* 306 (1), 98–104. doi:10.1016/j.epsl.2011.03.035

Gudmundsson, A. (2011). Deflection of Dykes into Sills at Discontinuities and Magma-Chamber Formation. *Tectonophysics* 500 (1), 50–64. doi:10.1016/j.tecto.2009.10.015

Gudmundsson, A. (1995). Infrastructure and Mechanics of Volcanic Systems in iceland. *J. Volcanology Geothermal Res.* 64 (1), 1–22. doi:10.1016/0377-0273(95)92782-q

Gudmundsson, A. (2012). Magma chambers: Formation, Local Stresses, Excess Pressures, and Compartments. *J. Volcanology Geothermal Res.* 237-238, 19–41. doi:10.1016/j.jvolgeores.2012.05.015

Gutiérrez, F., and Miguel, A. (2010). Parada. Numerical Modeling of Time-dependent Fluid Dynamics and Differentiation of a Shallow Basaltic Magma Chamber. *J. Petrology* 51 (3), 731–762.

Hauke, G., and Hughes, T. J. R. (1998). A Comparative Study of Different Sets of Variables for Solving Compressible and Incompressible Flows. *CMAME* 153 (1–2), 1–44. doi:10.1016/s0045-7825(97)00043-1

Hauke, G., and Hughes, T. J. R. (1994). A Unified Approach to Compressible and Incompressible Flows. *CMAME* 113 (3), 389–395. doi:10.1016/0045-7825(94)90055-8

Hauke, G. (2001). Simple Stabilizing Matrices for the Computation of Compressible Flows in Primitive Variables. *CMAME* 190 (51–52), 6881–6893. doi:10.1016/s0045-7825(01)00267-5

Hughes, T. J. R., Feijoo, G., Mazzei, L., and Quincy, J. B. (1998). The Variational Multiscale Method—A Paradigm for Computational Mechanics. *Computer Methods Appl. Mech. Eng.* 166 (1), 3–24. doi:10.1016/s0045-7825(98)00079-6

Hughes, T. J. R. (1995). Multiscale Phenomena: Green's Functions, the Dirichlet-To-Neumann Formulation, Subgrid Scale Models, Bubbles and the Origins of Stabilized Methods. *Computer Methods Appl. Mech. Eng.* 127 (1), 387–401. doi:10.1016/0045-7825(95)00844-9

Huppert, H. E., Sparks, R. S. J., Whitehead, J. A., and Hallworth, M. A. (1986). Replenishment of Magma chambers by Light Inputs. *J. Geophys. Res.* 91, 6113–6122. doi:10.1029/jb091ib06p06113

Ishii, M., and Zuber, N. (1979). Drag Coefficient and Relative Velocity in Bubbly, Droplet or Particulate Flows. *Aiche J.* 25, 843–855. doi:10.1002/aic.690250513

Jellinek, A. M., and Kerr, R. C. (1999). Mixing and Compositional Stratification Produced by Natural Convection: 2. Applications to the Differentiation of Basaltic and Silicic Magma chambers and Komatiite Lava Flows. *J. Geophys. Res.* 104, 7203–7218. doi:10.1029/1998jb900117

Karlstrom, L., Dufek, J., and Manga, M. (2010). Magma Chamber Stability in Arc and continental Crust. *J. Volcanology Geothermal Res.* 190 (3), 249–270. doi:10.1016/j.jvolgeores.2009.10.003

Karypis, G., and Kumar, V. (1999). A Fast and High Quality Multilevel Scheme for Partitioning Irregular Graphs. *SIAM J. Scientific Comput.* 20 (1), 359–392.

Lange, R. A. (1994). Chapter 9. The Effect of $H_20$, $CO_2$ and F on the Density and Viscosity of Silicate Melts. *Rev. Mineralogy* 30, 331–370. doi:10.1515/9781501509674-015

Laumonier, M., Scaillet, B., Pichavant, M., Champallier, R., Andujar, J., and Arbaret, L. (2014). On the Conditions of Magma Mixing and its Bearing on Andesite Production in the Crust. *Nat. Commun.* 5 (1–12), 5607. doi:10.1038/ncomms6607

Lieto, B. D., Romano, P., Scarpa, R., and Linde, A. T. (2020). Strain Signals before and during Paroxysmal Activity at Stromboli Volcano, Italy. *Geophys. Res. Lett.* 47, 1–9. doi:10.1029/2020gl088521

Longo, A., Barsanti, M., Cassioli, A., and Papale, P. (2012). A Finite Element Galerkin/Least-Squares Method for Computation of Multicomponent Compressible-Incompressible Flows. *Comput. Fluids* 67, 57–71. doi:10.1016/j.compfluid.2012.07.008

Longo, A., Papale, P., Vassalli, M., Saccorotti, G., Montagna, C. P., Cassioli, A., et al. (2012). Magma Convection and Mixing Dynamics as a Source of Ultra-long-period Oscillations. *Bull. Volcanol.* 74, 873–880. doi:10.1007/s00445-011-0570-0

Michioka, H., and Sumita, I. (2005). Rayleigh-taylor Instability of a Particle Packed Viscous Fluid: Implications for a Solidifying Magma. *Geophys. Res. Lett.* 32 (3), 1–4. doi:10.1029/2004gl021827

Morgavi, D., Petrelli, M., Vetere, F. P., González-García, D., and Perugini, D. (2015). High-temperature Apparatus for Chaotic Mixing of Natural Silicate Melts. *Rev. Scientific Instr.* 86, 105108. doi:10.1063/1.4932610

Pal, R. (2003). Rheological Behavior of Bubble-Bearing Magmas. *Earth Planet. Sci. Lett.* 207 (1), 165–179. doi:10.1016/s0012-821x(02)01104-4

Papale, P., Montagna, C. P., and Longo, A. (2017). Pressure Evolution in Shallow Magma chambers upon Buoyancy-Driven Replenishment. *Geochem. Geophys. Geosyst.* 18, 1214–1224. doi:10.1002/2016gc006731

Papale, P., Moretti, R., and Barbato, D. (2006). The Compositional Dependence of the Saturation Surface of $H_2O$+$CO_2$ Fluids in Silicate Melts. *Chem. Geology* 229, 78–95. doi:10.1016/j.chemgeo.2006.01.013

Perugini, D., De Campos, C. P., Petrelli, M., and Dingwell, D. B. (2015). Concentration Variance Decay during Magma Mixing: a Volcanic Chronometer. *Sci. Rep.* 5 (14225), 1–10. doi:10.1038/srep14225

Petrelli, M., Perugini, D., and Poli, G. (2011). Transition to Chaos and Implications for Time-Scales of Magma Hybridization during Mixing Processes in Magma Chambers. *Lithos* 125 (1), 211–220. doi:10.1016/j.lithos.2011.02.007

Rispoli, F., Delibra, G., Venturini, P., Corsini, A., Saavedra, R., and Tezduyar, T. E. (2015). Particle Tracking and Particle-Shock Interaction in Compressible-Flow Computations with the V-SGS Stabilization and $Y\ Z\ \beta$ Shock-Capturing. *Comput. Mech.* 55, 1201–1209. doi:10.1007/s00466-015-1160-3

Sato, E., and Sato, H. (2009). Study of Effect of Magma Pocket on Mixing of Two Magmas with Different Viscosities and Densities by Analogue Experiments. *J. Volcanology Geothermal Res.* 181 (1–2), 115–123. doi:10.1016/j.jvolgeores.2009.01.005

Schleicher, J. M., Bergantz, G. W., Breidenthal, R. E., and Burgisser, A. (2016). Time Scales of crystal Mixing in Magma Mushes. *Geophys. Res. Lett.* 43, 1543–1550. doi:10.1002/2015gl067372

Semenov, A. N., and Polyansky, O. P. (2017). Numerical Modeling of the Mechanisms of Magma Mingling and Mixing: A Case Study of the Formation of Complex Intrusions. *Russ. Geology Geophys.* 58, 1317–1332. doi:10.1016/j.rgg.2017.11.001

Shakib, F., Hughes, T., and Johan, Z. (1991). A New Finite Element Formulation for Computational Fluid Dynamics: X. The Compressible Euler and Navier-Stokes Equations. *CMAME* 89 (1–3), 141–219. doi:10.1016/0045-7825(91)90041-4

Shane, P., Doyle, L. R., and Nairn, I. A. (2008). Heterogeneous Andesite-Dacite Ejecta in 26-16.6 Ka Pyroclastic Deposits of Tongariro Volcano, New Zealand: the Product of Multiple Magma-Mixing Events. *Bull. Volcanol.* 70, 517–536. doi:10.1007/s00445-007-0152-3

Sides, I., Edmonds, M., Maclennan, J., Houghton, B. F., Swanson, D. A., Maclnnis, M. J., et al. (2014). Magma Mixing and High Fountaining during the 1959 Kīlauea Iki Eruption, Hawai'i. *Earth Planet. Sci. Lett.* 400, 102–112. doi:10.1016/j.epsl.2014.05.024

Sparks, R. S. J., and Cashman, K. V. (2017). Dynamic Magma Systems: Implications for Forecasting Volcanic Activity. *Elements* 13, 35–40. doi:10.2113/gselements.13.1.35

Sparks, R. S. J., and Huppert, H. E. (1984). Density Changes during the Fractional Crystallization of Basaltic Magmas: Fluid Dynamic Implications. *Contr. Mineral. Petrol.* 85, 300–309. doi:10.1007/bf00378108

Sparks, S. R. J., Sigurdsson, H., and Wilson, L. (1977). Magma Mixing: a Mechanism for Triggering Acid Explosive Eruptions. *Nature* 267, 315–318. doi:10.1038/267315a0

Sundermeyer, C., Gätjen, J., Weimann, L., and Worner, G. (2020). Timescales from Magma Mixing to Eruption in Alkaline Volcanism in the Eifel Volcanic fields,

Western germany. *Contrib. Mineral. Petrol.* 175, 1–23. doi:10.1007/s00410-020-01715-y

Tamura, Y., Yuhara, M., Ishii, T., Irino, N., and Shukuno, H. (2003). Andesites and Dacites from Daisen Volcano, Japan: Partial-To-Total Remelting of an Andesite Magma Body. *J. Petrology* 44 (12), 2243–2260. doi:10.1093/petrology/egg076

Tezduyar, T. E., and Senga, M. (2006). Stabilization and Shock-Capturing Parameters in Supg Formulation of Compressible Flows. *Computer Methods Appl. Mech. Eng.* 195 (13), 1621–1632. doi:10.1016/j.cma.2005.05.032

The Belos Project Team (2021). *The BELOS Project Website*.

The Epetra Project Team (2021). *The EPETRA Project Website*.

The Trilinos Project Team (2021). *The Trilinos Project Website*.

Tomiya, A., Miyagi, I., Saito, G., and Geshi, N. (2013). Short Time Scales of Magma-Mixing Processes Prior to the 2011 Eruption of Shinmoedake Volcano, Kirishima Volcanic Group, Japan. *Bull. Volcanol.* 75, 1–19. doi:10.1007/s00445-013-0750-1

Turner, J. S., and Campbell, I. H. (1986). Convection and Mixing in Magma chambers. *Earth-Science Rev.* 23 (4), 255–352. doi:10.1016/0012-8252(86)90015-2

Vollaire, C., Nicolas, L., and Nicolas, A. (1998). Parallel Computing for the Finite Element Method. *Eur. Phys. J. Appl. Phys.* 1, 305–314.

Xu, F., Moutsanidis, G., Kamensky, D., Hsu, M.-C., Murugan, M., Ghoshal, A., et al. (2017). Compressible Flows on Moving Domains: Stabilized Methods, Weakly Enforced Essential Boundary Conditions, Sliding Interfaces, and Application to Gas-Turbine Modeling. *Comput. Fluids* 158, 201–220. doi:10.1016/j.compfluid.2017.02.006

Young, Y.-N., Tufo, H., Dubey, A., and Rosner, R. (2001). On the Miscible Rayleigh-Taylor Instability: Two and Three Dimensions. *J. Fluid Mech.* 447, 377–408. doi:10.1017/s0022112001005870

**Conflict of Interest:** The authors declare that the research was conducted in the absence of any commercial or financial relationships that could be construed as a potential conflict of interest.

**Publisher's Note:** All claims expressed in this article are solely those of the authors and do not necessarily represent those of their affiliated organizations, or those of the publisher, the editors and the reviewers. Any product that may be evaluated in this article, or claim that may be made by its manufacturer, is not guaranteed or endorsed by the publisher.

# APPENDIX A NUMERICAL METHOD

The system of **Eqs (1–4)** can be written and solved in a fully coupled monolithic manner as a single transport system (Hauke and Hughes, 1998; Longo et al., 2012b; Garg et al., 2018a):

$$\boldsymbol{U}_{,t} + \boldsymbol{F}^a_{i,i} - \boldsymbol{F}^d_{i,i} - \boldsymbol{S} = 0 \tag{13}$$

where the vectors are given by

$$\boldsymbol{U} = \begin{bmatrix} \rho \\ \rho \boldsymbol{v} \\ \rho E \\ \rho Y_k \end{bmatrix} \qquad \boldsymbol{F}^a_i = \begin{bmatrix} \rho v_i \\ \rho v_i \boldsymbol{v} + \boldsymbol{\delta_i} p \\ \rho v_i E + v_i p \\ \rho v_i Y_k \end{bmatrix}$$
$$\boldsymbol{F}^d_i = \begin{bmatrix} 0 \\ \boldsymbol{\tau_i} \\ \tau_{ij} v_j - q_i - \sum_k h_{ki} J_{ki} \\ \boldsymbol{J}_{ki} \end{bmatrix} \qquad \boldsymbol{S} = \begin{bmatrix} 0 \\ \rho \boldsymbol{b} \\ \rho b_i v_i \\ 0 \end{bmatrix}. \tag{14}$$

In the above equations the following notions are used: $\boldsymbol{\delta}_i = \boldsymbol{\delta e}_i$ and $\boldsymbol{\tau}_i = \boldsymbol{\tau e}_i$, where $\boldsymbol{e}_i$ is the unit vector in the $i^{\text{th}}$ direction and $\boldsymbol{\delta} = [\delta_{ij}]$ is the Kronecker delta. The sub-indexes $i$ and $j$ stand for spatial coordinates, *i.e. i, j*=1,2,3; while $k$ stands for the mixture component. For spatial coordinates the Einstein summation convention of repeated indexes is used throughout.

**Equation (13)** can be rewritten for any independent set of variables **X** (Shakib et al., 1991; Hauke and Hughes, 1994) as

$$\boldsymbol{A}_0 \boldsymbol{X}_{,t} + \boldsymbol{A}_i \boldsymbol{X}_{,i} - \left(\boldsymbol{K}_{ij} \boldsymbol{X}_{,j}\right)_{,i} - \boldsymbol{S} = 0, \tag{15}$$

where $\boldsymbol{A}_0 = \boldsymbol{U}_{,\boldsymbol{X}}, \boldsymbol{A}_i = \boldsymbol{F}^a_{i,\boldsymbol{X}}$ is the $i$th Euler Jacobian matrix and $\boldsymbol{K} = [\boldsymbol{K}_{ij}]$ is the diffusivity matrix with $\boldsymbol{K}_{ij}\boldsymbol{X}_{,j} = \boldsymbol{F}^d_i$.

The monolithic approach used in this work has several advantages over segregated approaches in terms of simplicity of the formulation, robustness of the solution approach, and smaller data transfer when doing parallel programming. In the present study, the vector $\boldsymbol{X}$ has been chosen as the set of pressure primitive variables, i.e. $\boldsymbol{X} = [p, \boldsymbol{v}, T, Y_k]$, which allows modelling of both compressible and incompressible flows by a unified formulation (Hauke and Hughes, 1994; Hauke and Hughes, 1998; Longo et al., 2012b; Xu et al., 2017; Garg et al., 2018a; Garg et al., 2018b; Garg et al., 2021).

The boundary value problem can be expressed as below. Consider an open spatial domain $\Omega$ with boundary $\Gamma$, such that $\Gamma = \Gamma_G \cup \Gamma_H$ and $\Gamma_G \cap \Gamma_H = \phi$, where $\Gamma_G$ and $\Gamma_H$ are the Dirichlet and Neumann parts of the boundary, respectively. The strong form of the problem consists of finding the solution vector $\boldsymbol{X} : \Omega \rightarrow \mathbb{R}^{n_{eq}}$, where $n_{eq}$ is the number of equations of the system, such that for the given essential boundary conditions $\boldsymbol{X}_G$ and the natural boundary conditions $\boldsymbol{X}_H$, the following equations are satisfied:

$$\begin{aligned} \boldsymbol{\mathcal{R}}(\boldsymbol{X}) = \boldsymbol{\mathcal{L}}\boldsymbol{X} - \boldsymbol{S} = 0 \quad & \text{in} \quad \Omega \\ \boldsymbol{X} = \boldsymbol{X}_G \quad & \text{on} \quad \Gamma_G \\ \left(\boldsymbol{F}^a_i - \boldsymbol{F}^d_i\right)\boldsymbol{n}_i = \boldsymbol{X}_H \quad & \text{on} \quad \Gamma_H \end{aligned} \tag{16}$$

where $\boldsymbol{\mathcal{R}}(\boldsymbol{X})$ is the residual of the equations and $\boldsymbol{\mathcal{L}}$ represents the transient-advective-diffusive operator such that

$$\begin{aligned} \boldsymbol{\mathcal{L}}\boldsymbol{X} &= \boldsymbol{A}_0 \boldsymbol{X}_{,t} + \boldsymbol{A}_i \boldsymbol{X}_{,i} - \left(\boldsymbol{K}_{ij} \boldsymbol{X}_{,j}\right)_{,i} \\ &= \boldsymbol{U}_{,t} + \boldsymbol{F}^a_{,i} - \boldsymbol{F}^d_{,i} \end{aligned} \tag{17}$$

The weak form of the above equations can be expressed as: given a trial function space $\mathcal{T} = \{\boldsymbol{X} \mid \boldsymbol{X} \in (\boldsymbol{H}^1)^{n_{eq}}, \ \boldsymbol{X} = \boldsymbol{X}_G \text{ on } \Gamma_G\}$ and weighting function space $\Gamma = \{\boldsymbol{W} \mid \boldsymbol{W} \in (\boldsymbol{H}^1)^{n_{eq}}, \ \boldsymbol{W} = 0 \text{ on } \Gamma_G\}$ find $\boldsymbol{X} \in \mathcal{T}$ such that $\forall\ \boldsymbol{W} \in \Gamma$

$$(\boldsymbol{W}, \ \boldsymbol{\mathcal{R}}(\boldsymbol{X}))_\Omega = \int_\Omega \boldsymbol{W} \cdot \boldsymbol{\mathcal{R}}(\boldsymbol{X}) = 0 \tag{18}$$

which by substituting the definition of $\boldsymbol{\mathcal{R}}(\boldsymbol{X})$, integrating by parts and applying the boundary conditions, can be written as

$$(\boldsymbol{W}, \ \boldsymbol{U}(\boldsymbol{X})_{,t} - \boldsymbol{S})_\Omega + \left(\boldsymbol{W}_{,i}, \ \boldsymbol{F}^d_i - \boldsymbol{F}^a_i\right)_\Omega + (\boldsymbol{W}, \ \boldsymbol{X}_H)_{\Gamma_H} = 0 \tag{19}$$

## A.1 Variational Multiscale Formulation

We consider the transport operator $\boldsymbol{\mathcal{L}}$ in Eq. 17 as quasi-linear and solve Eq. 13 by variational multiscale method (VMS) (Hughes, 1995; Hughes et al., 1998; Bazilevs et al., 2007). The VMS method has been successfully used for compressible flows (Franco and Rafael Saavedra, 2006; Rispoli et al., 2015) and turbulent flows (Bazilevs et al., 2007) without employing any *ad hoc* terms such as eddy viscosities. In the VMS method the solution vector $\boldsymbol{X}$ is decomposed into the resolved (coarse, grid-scale) finite element solution $\bar{\boldsymbol{X}}$ and unresolved (fine, sub-grid) error $\boldsymbol{X}'$,

$$\boldsymbol{X} = \bar{\boldsymbol{X}} + \boldsymbol{X}' \tag{20}$$

Similarly $\boldsymbol{W}$ is decomposed as

$$\boldsymbol{W} = \bar{\boldsymbol{W}} + \boldsymbol{W}' \tag{21}$$

The VMS method consists of substituting the above splitting into the weak form and solving the following two subproblems for coarse-scale and fine-scale:

$$(\bar{\boldsymbol{W}}, \ \boldsymbol{\mathcal{R}}(\boldsymbol{X}))_\Omega = 0 \tag{22}$$
$$(\boldsymbol{W}', \ \boldsymbol{\mathcal{R}}(\boldsymbol{X}))_\Omega = 0 \tag{23}$$

The essence of VMS method is to solve for the coarse scale solution numerically and compute the fine scale part either analytically or approximate it through an algebraic expression. With this aim, using adjoint duality, **Eq. 22** can be written as

$$(\bar{\boldsymbol{W}}, \ \boldsymbol{\mathcal{R}}(\bar{\boldsymbol{X}}))_\Omega + (\boldsymbol{\mathcal{L}}^* \bar{\boldsymbol{W}}, \ \boldsymbol{X}')_\Omega = 0 \tag{24}$$

where

$$\boldsymbol{\mathcal{L}}^* \bar{\boldsymbol{W}} = -\boldsymbol{A}_0 \bar{\boldsymbol{W}}_{,t} - \boldsymbol{A}_i \bar{\boldsymbol{W}}_{,i} - \left(\boldsymbol{K}_{ij} \bar{\boldsymbol{W}}_{,j}\right)_{,i} \tag{25}$$

Assuming $\boldsymbol{X}' = 0$ on element boundaries, **Eq. 23** can be expressed as:

$$\left(\boldsymbol{W}', \ \boldsymbol{U}(\boldsymbol{X}')_{,t} - \boldsymbol{S}'\right)_\Omega + \left(\boldsymbol{W}'_{,i}, \ \boldsymbol{F}^{d'}_i - \boldsymbol{F}^{a'}_i\right)_\Omega = (\boldsymbol{W}', \boldsymbol{\mathcal{R}}(\bar{\boldsymbol{X}})) \tag{26}$$

The solution of the above equation can be represented as a function $f$ of $\bar{\boldsymbol{X}}$ and $\boldsymbol{\mathcal{R}}(\bar{\boldsymbol{X}})$:

$$\boldsymbol{X}' = f\left(\bar{\boldsymbol{X}}, \boldsymbol{\mathcal{R}}\left(\bar{\boldsymbol{X}}\right)\right) \tag{27}$$

To obtain a simple, basic and computationally efficient method, the VMS formulation relies on approximating $\boldsymbol{X}'$ with the product of element-wise algebraic stabilisation operator $\boldsymbol{P}$ and the coarse scale residual, $\boldsymbol{\mathcal{R}}(\bar{\boldsymbol{X}})$ (Bazilevs et al., 2007),

$$\boldsymbol{X}' = -\boldsymbol{P}\,\boldsymbol{\mathcal{R}}\left(\bar{\boldsymbol{X}}\right) \tag{28}$$

Complete VMS formulation along with the discontinuity capturing operator (see below) (Tezduyar and Senga, 2006) can be expressed as:

$$\begin{aligned}\int_{\Omega} \boldsymbol{W}^h \cdot \left(\boldsymbol{A}_0 \bar{\boldsymbol{X}}^h_{,t} - \boldsymbol{S}\right) + \boldsymbol{W}^h_{,i} \cdot \left(\boldsymbol{F}^d_i\left(\bar{\boldsymbol{X}}^h\right) - \boldsymbol{F}^a_i\left(\bar{\boldsymbol{X}}^h\right)\right) d\Omega + \int_{\Gamma_H} \boldsymbol{W}^h \cdot \boldsymbol{H}^h \, d\Gamma \\ + \sum_{e=1}^{n_{el}} \int_{\Omega^e} \left(\boldsymbol{A}_0 \boldsymbol{W}^h_{,t} + \boldsymbol{A}_i \boldsymbol{W}^h_{,i} + \left(\boldsymbol{K}_{ij} \boldsymbol{W}^h_{,j}\right)_{,i}\right) \boldsymbol{P} \cdot \boldsymbol{\mathcal{R}}\left(\bar{\boldsymbol{X}}^h\right) d\Omega \\ + \sum_{e=1}^{n_{el}} \int_{\Omega^e} \nu_{\mathrm{dc}} \boldsymbol{W}^h_{,i} \cdot \boldsymbol{A}_0 \bar{\boldsymbol{X}}^h_{,i} \, d\Omega = 0\end{aligned} \tag{29}$$

## A.2 Stabilization Operator

In the present work we follow the same design for the $\boldsymbol{P}$ matrix as it was developed in (Hauke, 2001) and extended to multi-component conditions in (Longo et al., 2012b). We first design $\boldsymbol{P_U}$ for the conservation variables and then transform it into the pressure-primitive-variable formulation ($\boldsymbol{P_X}$) using the following expression

$$\boldsymbol{P} = \boldsymbol{P}_X = \boldsymbol{X}_{,U} \boldsymbol{P}_U \tag{30}$$

$\boldsymbol{P_U}$ is given as:

$$\boldsymbol{P}_U = \mathrm{diag}\left(P_c, P_m, P_m, P_m, P_E, P_{Y_k}\right) \tag{31}$$

where the diagonal entries are given by

$$P_c = \min\left(\frac{\Delta t}{2}, \frac{h^e}{2\left(|\boldsymbol{v}| + c\right)} + \frac{h^e}{2|\boldsymbol{v}|}\right) \tag{32}$$

$$P_m = \min\left(\frac{\Delta t}{2}, \frac{h^e}{2\left(|\boldsymbol{v}| + c\right)} + \frac{h^e}{2|\boldsymbol{v}|}, \frac{\rho (h^e)^2}{12\mu}\right) \tag{33}$$

$$P_E = \min\left(\frac{\Delta t}{2}, \frac{h^e}{2\left(|\boldsymbol{v}| + c\right)} + \frac{h^e}{2|\boldsymbol{v}|}, \frac{\rho c_v (h^e)^2}{12\kappa}\right) \tag{34}$$

$$P_{Y_k} = \min\left(\frac{\Delta t}{2}, \frac{h^e}{2\left(|\boldsymbol{v}| + c\right)} + \frac{h^e}{2|\boldsymbol{v}|}, \frac{(h^e)^2}{12 d_k}\right) \tag{35}$$

where $\Delta t$ is the time step, $h^e$ is the element size along the streamline direction, $c$ is the local sound speed and $d_k$ is the mass diffusion coefficient of $k$th component.

To handle incompressibility the entry of the first row of the $\boldsymbol{P}$ matrix is modified as

$$\boldsymbol{P}_c = \left(\boldsymbol{P}_c^{-1} + \left(\rho \boldsymbol{P}_m{}^{\star}\left(\boldsymbol{g} \cdot \boldsymbol{g}\right)\right)^{-1}\right)^{-1} \tag{36}$$

where $\boldsymbol{P}_c$ and $\boldsymbol{P}_m$ are the diagonal entries of $\boldsymbol{P}$ matrix corresponding to the continuity and the momentum equations, and

$$\boldsymbol{g} = \{g_i\}, \qquad g_i = \sum_{j=1}^{3} \frac{\partial \xi_j}{\partial x_i} \qquad \text{and} \qquad \boldsymbol{g} \cdot \boldsymbol{g} = \sum_{i=1}^{3} g_i g_i \tag{37}$$

## A.3 Discontinuity Capturing Operator

The discontinuity capturing operator is implemented as in (Tezduyar and Senga, 2006). The parameter $\nu_{\mathrm{dc}}$ is defined as

$$\nu_{\mathrm{dc}} = \|\boldsymbol{U}_{\mathrm{ref}}^{-1} \boldsymbol{Z}\| \left(\sum_{i=1}^{3} \|\boldsymbol{U}_{\mathrm{ref}}^{-1} \boldsymbol{U}_{,i}\|^2\right)^{\frac{\beta}{2}-1} \|\boldsymbol{U}_{\mathrm{ref}}^{-1} \boldsymbol{U}\|^{1-\beta} \left(\frac{h_{dc}}{2}\right)^{\beta} \tag{38}$$

where $\boldsymbol{U}_{\mathrm{ref}}$ is a diagonal scaling matrix constructed from the reference values of the components of $\boldsymbol{U}$ and $\boldsymbol{Z} = \boldsymbol{U}_{,t} + \boldsymbol{A}_i \boldsymbol{U}_{,i}$. The parameter $\beta$ determines the sharpness of the discontinuity and is set as $\beta = 1$ for smoother solution and $\beta = 2$ to retain sharp discontinuity. $h_{dc}$ is defined as

$$h_{dc} = 2\left(\sum_{i=1}^{n_{en}} \left|\frac{\boldsymbol{\nabla}\rho}{\|\boldsymbol{\nabla}\rho\|} \cdot \boldsymbol{\nabla} N_a\right|\right)^{-1} \tag{39}$$

## A.4 Numerical Discretization and Solver

The weight functions ($\boldsymbol{W}^h$), the solution variables ($\boldsymbol{X}^h$), and their time derivatives ($\boldsymbol{X}^h_{,t}$) are expanded in terms of piece-wise linear basis functions. The integrals in **Eq. 29** are then evaluated using Gauss quadrature resulting in a system of non-linear ordinary differential equations:

$$\boldsymbol{R}\left(\boldsymbol{X}, \dot{\boldsymbol{X}}\right) = 0 \tag{40}$$

where $\boldsymbol{R}$ is the residual vector, $\boldsymbol{X}$ is the vector of unknowns and $\dot{X}$ is its time derivative. To solve **Eq. 40** a predictor-corrector method is used (Shakib et al., 1991). The temporal discretization is done by implicit Euler method. Given the solution at time instance $n$, the algorithm is written as:

Predictor:

$$\boldsymbol{X}^{(i)}_{n+1} = \boldsymbol{X}_n \tag{41}$$

Corrector:
Construct Jacobian matrix:

$$\boldsymbol{M}^{(i)}_{n+1} = \frac{\partial \boldsymbol{R}^{(i)}_{n+1}}{\partial \boldsymbol{X}^{(i)}_{n+1}} \tag{42}$$

Solve for $\Delta \boldsymbol{X}$:

$$\boldsymbol{M}^{(i)}_{n+1} \, \Delta \boldsymbol{X}^{(i)} = -\boldsymbol{R}^{(i)}_{n+1} \tag{43}$$

Update the solution:

$$\boldsymbol{X}^{(i+1)}_{n+1} = \boldsymbol{X}^{(i)}_{n+1} + \Delta \boldsymbol{X}^{(i)} \tag{44}$$

Within a time step, the iteration loop ends if either the maximum prespecified corrector passes are reached or one of the following convergence criteria is met:

$$\|\boldsymbol{R}^{(i)}\| < 10^{-5} \qquad \text{or} \qquad \frac{\|\boldsymbol{R}^{(i)}\|}{\|\boldsymbol{R}^{(0)}\|} < 10^{-8} \tag{45}$$

The linear system of **Eq. 43** is solved with the GMRES method from the Belos package of Trilinos (Bavier et al., 2012; The Belos Project Team, 2021). GMRES is a Krylov subspace-based iterative method that minimizes the residual of the linear system and is best known for its robustness and efficiency in solving large and sparse systems of equations. The GMRES solver requires to specify an initial guess of the solution, the subspaces number, restarts, iterations and the tolerance for the relative residual. For all numerical tests in this study we set these numbers as subspaces = 200, restarts = 5, iterations = 300 and residual tolerance = $10^{-6}$. The GMRES method often requires a good preconditioner which could effectively lower the condition number of the matrix and achieve convergence with reasonable computational effort. We use the incomplete lower-upper factorization (ILU) preconditioned version of the GMRES method. The preconditioner is generated from the ifpack package of Trilinos.

## A.5 Time Step Control

As described in the previous subsection, we use an implicit method which does not bring about any stability requirement on time step. Nevertheless, a control on time step is needed. In fact an arbitrarily large time step results in ill-conditioned linear system of equations which is computationally expensive to solve. Whereas, a very small time step takes too many time iterations to reach to the predefined final time and hence needs a long time to finish the simulation. An implicit method combined with a suitable time adaptive method reduces the total compute time. In this work we control the time step through a prespecified value of the Courant number (Cr): before each time iteration, the time step ($\Delta t$) is computed as (Shakib et al., 1991):

$$\Delta t = \frac{\mathrm{Cr}}{\frac{2}{h^2}\ max\left(\frac{2\mu}{\rho}, \frac{\kappa}{\rho c_v}, d_k\right) + \frac{\sqrt{\|v\|^2+2c^2+c\sqrt{4\|v\|^2+c^2}}}{h}} \tag{46}$$

Since the numerical method is implicit, Cr is not constrained to be smaller than 1. However, we fix Cr = 1 in this study and adapt the time step accordingly.

# APPENDIX B PARALLEL IMPLEMENTATION

GALES is written in object-oriented C++ and is parallelized using OpenMpi for parallel computing. In the framework of the FEM, computations are carried out at the element level which is well suited for parallelization as the computational load can be well balanced by distributing almost equally weighted elements on different processors (Vollaire et al., 1998). Typically, an FEM solver spends most of its time in the following two steps:

1. Element level computations and assembly of the linear system of equations
2. Solution of the linear system of equations

Both steps can be performed in parallel. In GALES, prior to the simulation, the computational mesh is partitioned into multiple parts. Each part is assigned to a processor (process) that carries out all of the numerical operations corresponding to that part of the mesh. We use the element based domain partition strategy, in which each element is assigned to a unique processor, but nodes can belong to multiple processors if they belong to the element lying on the boundary between different subdomains. For mesh partitioning we use METIS, which uses the multilevel heuristic graph partitioning approach and assigns a balanced number of elements to processors (Karypis and Kumar, 1999). That is crucial for load-balancing and performance. For the element level computations, we construct vectors and matrices from the boost library which has a rich variety of optimized functions for vector and matrix arithmetics and is very convenient in the frame of FEM.

The distribution of degrees of freedom (DOFs) across the processors is taken care of by suitable mappings. In GALES we construct maps with the *Epetra_Map* class (The Epetra Project Team, 2021) of the Trilinos library (The Trilinos Project Team, 2021). The maps encapsulate the details of distributing data over MPI processors. We create two different distributed maps that we call shared map and non-shared map. The shared map is based on the element distribution. We use it to initialize the vector of DOFs and to carry the solution forward in transient problems. The non-shared map is based on the uniquely assigned mesh nodes. Before creating the map each node lying on inter-processor boundaries is assigned uniquely to an owner processor. This is to ensure that the aggregate of DOFs over owner PIDs is equal to the total DOFs of the computational mesh and is independent of the mesh parts. The maps themselves are distributed and do not store all data on a single processor to ensure memory scalability.

The global sparse tangent matrix, solution vector and the right-hand side vectors of the linear system of **Eq. (43)** are constructed as distributed objects whose entries lie across multiple processors. To define them, we use the *FE_CrsMatrix* and *FE_Vector* classes of the Epetra package. The classes automatically handle the details about the data layout, the storage format, and the number of the ghost nodes and their corresponding location. The data entries in *FE_CrsMatrix* are stored in a compressed row format. The element level data can be added to the global linear system through three functions, *InsertGlobalValues, ReplaceGlobalValues* and *SumIntoGlobalValues*. The objects of the classes are created by passing the DOFs distribution described by the non-shared map. The assembly procedure is completed by calling the *GlobalAssemble* function, which gathers any shared data into the non-overlapping partitioning defined by the non-shared map. *GlobalAssemble* is a collective method that reorganizes the data to be classified as off-processor, on-processor and on inter-processor boundaries. Accordingly, the communication patterns are established to transfer the data from a non-owner processor to the owner as specified by the non-shared map. The reorganized data structure is further used for the matrix-vector product in the linear solver. Finally, the linear solver is solved with parallel GMRES solver implemented in the Belos package which is proved to be scalable up to several hundred thousands of processors (The Belos Project Team, 2021).

frontiers in Earth Science

ORIGINAL RESEARCH
published: 09 March 2022
doi: 10.3389/feart.2022.762768

# Performance Assessment of the Cloud for Prototypical Instant Computing Approaches in Geoscientific Hazard Simulations

*Jörn Behrens*[1]*, *Arne Schulz*[2] and *Konrad Simon*[1]

[1]Department of Mathematics/CEN, Universität Hamburg, Hamburg, Germany, [2]Axtrion GmbH & Co. KG, Bremen, Germany

Computing forecasts of hazards, such as tsunamis, requires fast reaction times and high precision, which in turn demands for large computing facilities that are needed only in rare occasions. Cloud computing environments allow to configure largely scalable on-demand computing environments. In this study, we tested two of the major cloud computing environments for parallel scalability for relevant prototypical applications. These applications solve stationary and non-stationary partial differential equations by means of finite differences and finite elements. These test cases demonstrate the capacity of cloud computing environments to provide scalable computing power for typical tasks in geophysical applications. As a proof-of-concept example of an instant computing application for geohazards, we propose a workflow and prototypical implementation for tsunami forecasting in the cloud. We demonstrate that minimal on-site computing resources are necessary for such a forecasting environment. We conclude by outlining the additional steps necessary to implement an operational tsunami forecasting cloud service, considering availability and cost.

**Keywords: cloud computing, natural hazard, instant computing, tsunami, parallel performance**

OPEN ACCESS

***Edited by:***
*Manuela Volpe,*
*Istituto Nazionale di Geofisica e Vulcanologia (INGV), Italy*

***Reviewed by:***
*Iyan E. Mulia,*
*RIKEN, Japan*
*José Manuel González-Vida,*
*University of Malaga, Spain*

***Correspondence:**
*Jörn Behrens*
*joern.behrens@uni-hamburg.de*

***Specialty section:***
*This article was submitted to Geohazards and Georisks, a section of the journal Frontiers in Earth Science*

***Received:*** *22 August 2021*
***Accepted:*** *10 February 2022*
***Published:*** *09 March 2022*

***Citation:***
*Behrens J, Schulz A and Simon K (2022) Performance Assessment of the Cloud for Prototypical Instant Computing Approaches in Geoscientific Hazard Simulations. Front. Earth Sci. 10:762768. doi: 10.3389/feart.2022.762768*

## 1 INTRODUCTION

Tsunami forecasting and hazard assessment procedures require modeling as one integral part. As an example, the accreditation of tsunami service providers in the North-East Atlantic, Mediterranean, and Connected Seas region requires model-based forecasting of tsunami hazard information (NEAMTWS, 2016).

In operational tsunami forecasting, either pre-computed scenario based hazard assessment or online simulation based approaches are common [see e.g., Behrens et al. (2010), Løvholt et al. (2019)]. Another approach—so far not operationally implemented—is statistical emulation, in which a relatively small number of true offline scenarios is used to populate a statistical interpolation (emulation) function for deriving forecasts including uncertainty values for real events (Sarri et al., 2012).

An optimal workflow for tsunami forecasting—both in near and in far field hazard forecasting—would consist of a reliable source determination followed by an integrated tsunami propagation and inundation simulation with an instant visualization and dissemination of results (Wei et al., 2013). This case would require large and scalable computing resources in case of an event for the simulation part involved in the workflow. Depending on budget and facilities, this requirement could pose unacceptable restrictions or would impose inefficient use of limited resources (since the computing resources would mostly idle, waiting for the event).

Since very flexible and large scalability is available in cloud computing environments, a straight forward strategy is to utilize the cloud for an instant computing framework for tsunami forecasting. An accepted definition for cloud computing reads (Mell and Grance, 2011):

> Cloud computing is a model for enabling ubiquitous, convenient, on-demand network access to a shared pool of configurable computing resources (e.g., networks, servers, storage, applications, and services) that can be rapidly provisioned and released with minimal management effort or service provider interaction.

It is this minimal management effort and flexibility that lead scientists to explore possibilities and evaluate performance of cloud computing environments for scientific computing applications early on [e.g., Foster et al. (2009); Zhang et al. (2010); Fox (2011)].

Utilizing cloud computing environments for tsunami hazard assessment not only enables great scalability in an early warning setting, but allows for deployment of modeling capabilities to users who do not have direct access to corresponding facilities. In fact other groups have started to provide tsunami forecasting services via web services, even calling their service "cloud." For example, the TRIDEC cloud is an online service providing simulation capabilities for tsunami forecasting (Hammitzsch, 2021). Implementing a similar workflow as the approach documented here and funded from the EU FP7 project *ASTARTE*, the IH-TsuSy tsunami simulation system obtains earthquake parameters from USGS, computes a tsunami wave propagation, based on corresponding sources and provides graphical information about the maximum wave height and arrival times (IH Cantabria, 2016). However, both services are strictly speaking no cloud computing efforts, since the computing devices are located at the hosting institute's premises. A server, available to the public and capable of instantly computing tsunami scenarios, however manually triggered, is the TAT server, maintained by the Joint Research Center of the European Commission in Ispra (European Commission, 2022 Security and Migration Directorate—JRC Ispra Site). The services are provided by web interfaces and as such could be considered as a so-called platform as a service (PaaS) model. These services are not configurable and call for provider interaction to be used.

Other possible cloud computing utilization for geoscientific applications are possible and will be further discussed in the next section. This report aims at assessing performance and feasibility of cloud computing in particular for tsunami hazard modeling. The service accessed in the cloud is a so-called infrastructure as a service (IaaS) model. We document a preliminary assessment of computational performance for scientific computing on two of the major cloud computing platforms, i.e., the Amazon Web Services (AWS) and Microsoft Azure. Additionally, a prototypical implementation of an early warning modeling framework, using a Python script for controlling the workflow and utilizing Amazon Web Services (AWS) cloud computing facilities is described. The prototype demonstrates the ease of use and cost effectiveness of such cloud computing environments for online tsunami forecasting simulations. We stress, however, that the demonstrator is by far not fit for operational services, since more optimization of the tsunami model, more fine-tuning of the required data, quality control, and testing would be necessary, which is outside of the scope of this study.

## 2 MOTIVATION

As described in the introduction (**Section 1**), one of the main motivations for an instant computing framework using cloud instances is to perform online tsunami forecast simulations efficiently and reliably in the event of a tsunamogenic earthquake. This section intends to motivate the use of such facilities in some more detail and strives to assess the strengths and weaknesses of the approach.

One of the first motivations for using the cloud for tsunami modeling in case of early warning use cases was the cost effectiveness of cloud computing. In fact, an hour of CPU time on a reasonably sized cloud device costs approximately 2.00 USD. This includes investment, energy, cooling, maintenance and administration, as well as utility costs and needs to be spent only if used. Some additional costs are to be allocated for storage and network traffic, however this is very difficult to assess, since it depends very much on the actual situation and usage. Therefore, we will compare very coarse estimates in the following. We are aware of the preliminary character of this assessment, but think it is nevertheless useful as a guiding example.

Let us compare a cloud computing approach to on-premise computing for a usual deprecation period (for computing hardware) of 3 years and let us assume a (relatively high) number of processed tsunami events of 50 per year (or roughly 1 per week). In the cloud, every event needs computing time, so we assume approx. ten aggregated CPU hours of computing time per event. An appropriate medium size general purpose Amazon EC2 instance of 32 vCPUs (virtual CPUs), 128 GB of RAM and approx. 1,000 GB SSD intermediate storage costs (e.g., m5.8xlarge[1]) approx. 2.00 USD per hour or 20.00 USD per event, totaling to 3,000.00 USD over the period of 3 years. The same applies to an Azure D32 v3 instance[2], comprising also 32 CPUs, 128 GB of RAM, and 800 GB of local storage. We might need to add some cost for implementation and testing, but since this can be done on smaller instances, the cost should not exceed approx. 1,000.00 USD. Furthermore, we assume approx. 50.00 USD per month for storage and data transfer, amounting to a total of 1,800.00 USD over the period of 3 years.

For the on-premise cost comparison we assume a reasonable server of 64 GB main memory, similar number of cores as for the cloud instances (e.g., 4 nodes of 8 cores each), and an appropriate hard drive installation totaling an investment of approximately 10,000.00 USD. Furthermore, such device consumes approx. one kilo Watt of electrical power per hour and we assume the cost for

[1]According to https://aws.amazon.com/de/ec2/pricing/on-demand/, last accessed 2022-01-21.

[2]According to https://azure.microsoft.com/de-de/pricing/calculator/, last accessed 2022-01-21.

**TABLE 1 |** Cost comparison of cloud and on-premise computing.

| | Cloud (AWS/Azure) | On-premise |
|---|---|---|
| Investment | — | 10,000.00 USD |
| Energy | — | 5,200.00 USD |
| Cooling | — | 5,200.00 USD |
| Maintenance | — | 22,500.00 USD |
| Preparation/testing cost | 1,000.00 USD | — |
| Storage/data transfer | 1,800.00 USD | — |
| Event computing cost | 3,000.00 USD | — |
| Total | 5,800.00 USD | 42,900.00 USD |

energy with 20 cents per kWh. Furthermore, we need to provide cooling, which we have assumed of the same order as the energy costs. Maintenance can be achieved by assuming one 10th of a full time equivalent of a technician, costing approx. 7,500 USD per year. We neglect utility costs and costs for repairs for now. A summary of these estimations can be found in **Table 1**. All in all, the cost for on-premise computing can be estimated with 42,900.00 USD versus costs for on-demand cloud computing of 5,800.00 USD. We repeat at this point that these numbers are very preliminary and may vary substantially with location, since labor costs as well as energy costs are quite different in different parts of the world.

An important argument for keeping computing facilities on-premise is the availability. In order to have a redundant computing environment that is fail-save in case of emergency, two computing devices would be necessary and in principle, these should be maintained at different locations. With cloud computing devices, the location can be everywhere. The above mentioned Amazon EC2 instance is available in more than 20 locations worldwide on all continents (except Antarctica). The service level agreement of the Amazon EC2 guarantees 99.95% availability for one of the locations. When assuming (as stated in the agreement) a month of 30 days, the system may fail for up to 21 min. However, in this case yet another of the locations could be reached. It is hard to achieve such low failure rate with an on-premise service, in particular in less developed areas.

Of course, a communication network needs to be in place. But again, it can readily be argued that in times of abundant redundant mobile communication networks, establishing a communication to a cloud server might be more reliable than an on-premise solution. Even in case of failed local communication, ad-hoc peer-to-peer networks of mobile devices are ready to be established (ASTARTE Project, 2017b).

One particular advantage of a cloud computing solution is its accessibility from everywhere. Even in remote areas, where maintaining compute infrastructures may not be feasible, a communication (e.g., via satellite link) to a cloud computing device could be established and would allow for scalable modern computing capabilities. Additionally, the cloud instance can be accessed from mobile devices.

Since the cloud infrastructure is easily scalable, it is possible to run several computations in parallel. A common practice in numerical weather forecasting—namely ensemble forecasts—could be established in tsunami modeling for capturing the uncertainty and quantifying it by varying the source parameters (Selva et al., 2021).

Access to the cloud infrastructure works with web interfaces and secure shell access. Web interfaces are used to start, control, and stop the cloud instance, which in our demonstration cases are always stored as virtual Linux machines. While the cloud instance is not running, storage of these several tens of gigabyte large files generates costs of the order of a few dollars per month. The virtual machine is pre-configured with compiled versions of the simulation code, repositories for bathymetry and topography data, post-processing tools, and possibly visualization pipelines. In the presented prototype, the sources are computed from moment tensor solutions available by web service from the GEOFON web page (GEOFON, 2021). Bathymetry and topography data are prepared and stored in the virtual machine, but could potentially also be retrieved on demand. In our case, visualization is performed on a local personal computer, but it would also be possible to configure a second cloud instance especially dedicated for high-performance visualization such that the results can readily be obtained by mobile devices such as smart phones or public projection screens.

Looking beyond hazard computing, cloud computing enables researchers and institutions without funding for large investments access to large scale computing facilities. Since cloud computing instances can be tailored and scaled to the requirements during development and production phases on demand, cost efficiency can be achieved and large computations are accessible with low budgets. Even in research environments, where larger budgets are generally available, it may be difficult to allocate investments into large computing infrastructures. In that case cloud computing costs can be accounted to research project material expenses and do not necessitate any investments.

Another important advantage goes beyond the application of tsunami hazard assessment. The cost efficient availability of cloud computing infrastructure would allow countries without locally available large-scale computing resources to run local hazard assessments in case of, e.g., potentially severe weather events where devastating effects of such events have greater human impact than in industrial countries with advanced computing and warning infrastructure that run their own weather services.

Last but not least, large on-premise computing hardware has a significant disadvantage in countries, where energy costs are high, such as in central Europe or in very warm countries. An enormous amount of energy is required for cooling. Cloud computing hardware can be placed anywhere. As an example, in Iceland cloud computing facilities can be run and cooled using geothermal energy only. Thus the impact of running cloud computing hardware on the environment can be minimized in contrast to on-premise solutions.

## 3 PERFORMANCE ASSESSMENT

In order to assess the feasibility of large scale geoscientific computing in cloud infrastructures, we perform benchmark tests representing numerical operations typically occurring in applications such as tsunami simulations, shown in the next section, as well as other geoscientific applications with high computational demands. We employ different sets of benchmarks in different cloud computing environments. Our tests were performed on the AWS cloud, employing a Fortran program for solving an elliptic partial differential equation by classical iteration, parallelized alternatively with OpenMP or

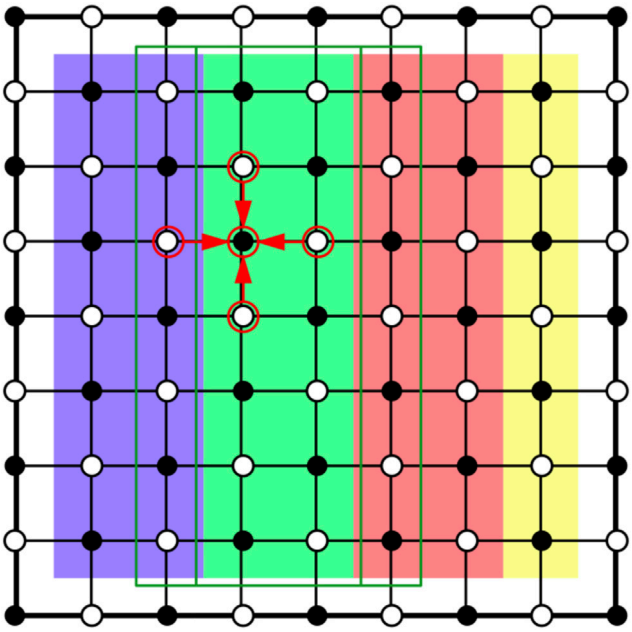

**FIGURE 1 |** Access pattern and domain decomposition of the red-black relaxation method used in the algorithm for performance testing in **Section 3.1**. Underlying colors indicate the distribution to processors, only interior nodes are processed. The access stencil is indicated by arrows. Green lines indicate the region, where read access to neighboring nodes is necessary.

MPI. These tests were performed in a comparison with an on-premise computer in the context of the ASTARTE project (ASTARTE Project, 2017a) and documented in an internal report. They are reported here for reference and for a better comparison and understanding.

The second set of benchmarks is performed using a mixed OpenMP-MPI parallelized C/C++ implementation of advection-diffusion type partial differential equations. These types of equations are typical for all kinds of geoscientific phenomena and are often used as a first representation for the development of numerical algorithms in this application field. Tsunamis can be represented by a non-linear generalization of such equation type. This benchmark will be tested on a number of differently sized instances of the Azure cloud computing platform.

## 3.1 Description of Elliptic PDE Benchmark—AWS Cloud

The elliptic partial differential equation solved in this benchmark represents a simple Poisson equation in two spatial dimensions:

$$\begin{aligned} -\Delta u &= f \quad \text{in } \Omega = [0,1]^2 \subset \mathbb{R}^2, \\ u &= g \quad \text{on } \Gamma = \delta\Omega. \end{aligned}$$

We use $f(x, y) = 2(x + y - x^2 - y^2)$ and $g \equiv 0$. $u(x, y) \in \mathbb{R}$ is an unknown potential. The domain $\Omega$ is discretized by a uniform equidistant grid $(x_i, y_j) = (i\Delta x, j\Delta x)$, with $\Delta x = \frac{1}{n}$, $i, j = 0: n$, of $(n + 1) \times (n + 1)$ grid points, and $\delta\Omega$ is the boundary of $\Omega$. Discretizing this equation by a finite difference operator and solving by an iterative Gauß-Seidel procedure results in an inner loop operation of the form

$$u^{[k+1]}(i,j) = \frac{1}{4}\Big(u^{[k+1]}(i-1,j) + u^{[k]}(i+1,j) + u^{[k+1]}(i,j-1) + u^{[k]}(i,j+1) + \Delta x^2 f(i,j)\Big), \quad (1)$$

where $u(i, j) = u(x_i, y_j)$, and $k$ represents the iteration count. The discrete form requires an access pattern to the nearest neighbors. When ordering the grid points in a white-black checkerboard pattern, the white and the black points can be processed in parallel and only one barrier synchronization is necessary within each iteration. The access pattern is visualized in **Figure 1**. The unknowns are distributed to processors in equal sized areas with full columns. Each processor has read access to one column to the left and right of its own domain, so that after each iteration these rows need to be communicated among neighbors, when local memory message passing (MPI) is employed. Computation of white nodes and black nodes is completely independent and could also be distributed in a different way. Within each iteration a synchronization is necessary, when switching from black to white nodes. A five point stencil is marked for the access pattern in **Equation 1**.

## 3.2 Description of Elliptic PDE Benchmark—Azure Cloud

The same model as in **Section 3.1** is tested in Microsoft's Azure cloud environment with a modified right hand side:

$$f(x,y) = \begin{cases} 1 & \text{if } y < \frac{1}{2} + \frac{1}{4}\sin(4\pi x), \\ -1 & \text{otherwise.} \end{cases} \quad (2)$$

It is a modified version of an example within the Deal.II library ("step 40"). We solve the model using a computationally more demanding adaptive finite element method (FEM) in 2D on a distributed mesh with parallel linear algebra. The solver is implemented using the Deal.II library (Arndt et al., 2020).

Essentially, this is the same test case that has been conducted in Bangerth et al. (2012) on an on-site high-performance cluster to show the scalability of certain functionality within Deal.II whereas we exploit this well tested high-performance computing software to show the suitability of scalable cloud environments. Note that the right-hand side constitutes a discontinuous forcing. This causes the solution to display large gradients at the discontinuity and hence the mesh is expected to be refined there allowing us to test the performance in a sequence of refinement cycles that constitute different problem sizes. The test is conducted on two cluster settings:

### 3.2.1 Small Setup

This setup consists of a small sized master node that does not participate in the actual computation but serves as a load balancer running a SLURM scheduler (Yoo et al., 2003). This master node distributes the MPI-parallel computation across ten compute

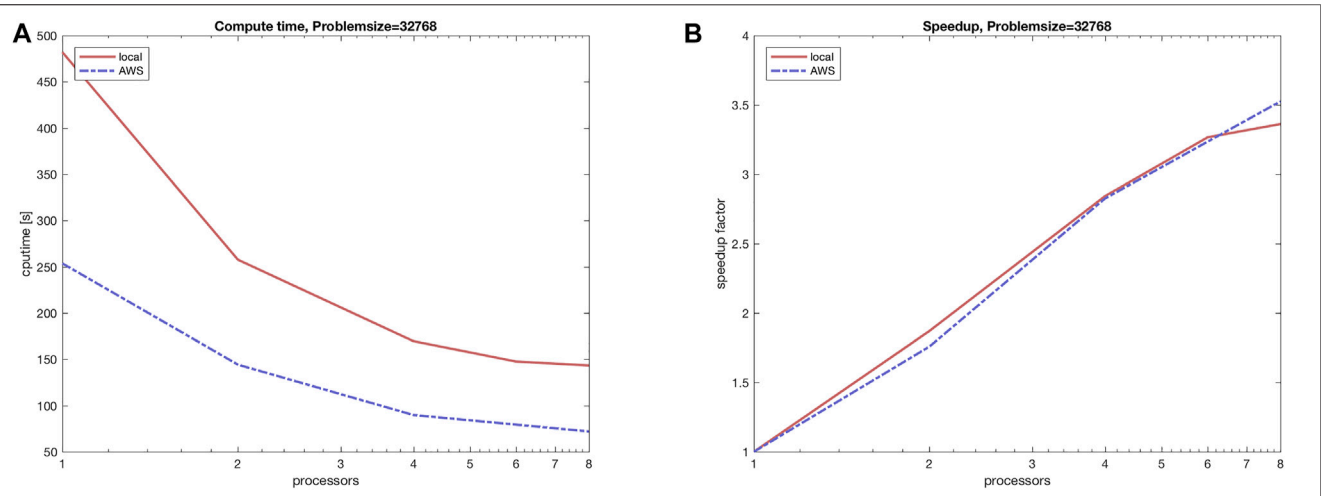


**FIGURE 2 | (A)** Compute time comparison for parallel execution of benchmark program in **Section 3.1** on an on-premise computer in comparison with AWS EC2 cloud instances. **(B)** The speedup (strong scaling) of the corresponding benchmark tests.

nodes each equipped with an Intel® Xeon® Platinum 8272CL, 2.1 GHz, with 2 cores and 8 GB of RAM. This is also the setup for the master node. The nodes are connected in a fast and modern Infiniband network which facilitates a high communication throughput. A shared SSD data storage of 256 GB was mounted on each of the compute nodes.

### 3.2.2 Large Setup

The same load balancer as in the *small setup* is reused with ten compute nodes each equipped with an Intel® Xeon® Platinum 8168, 3.4 GHz, with 32 CPU cores (16 physical and 16 virtual) and 64 GB of fast main memory.

## 3.3 Description of Bouyancy-Boussinesq PDE Benchmark

This test case is the basis for the large scale framework ASPECT (Bangerth et al., 2015) that serves the purpose of the simulation of convection processes inside the earth mantle. As in **Section 3.2** we run it with essentially the same parameter configuration as in Bangerth et al. (2012) but yet, again, to demonstrate the feasibility of well tested high performace software for cloud computations. The model is essentially a temperature feedback driven incompressible Stokes model with an advection-diffusion equation for the temperature variable. The model equations are given by

$$\begin{cases} -\nabla\cdot\left(2\eta\epsilon(u)\right)+\nabla p &= \rho\left(T,T_{\text{ref}},\rho_{\text{ref}}\right)ge_r,\\ \epsilon(u) &= \frac{1}{2}\left(\nabla u+\nabla u^T\right),\\ \nabla\cdot u &= 0,\\ \partial_t T+u\cdot\nabla T &= \nabla\left(\mu\nabla T\right)+f. \end{cases} \tag{3}$$

Here, $u$ is the velocity, $T$ the temperature, $p$ the pressure, $\rho$ a density, $\mu$ is a thermal conductivity of the medium, $\epsilon$ ist the symmetric gradient (strain), $g$ the gravitational constant, $e_r$ the outward normal vector, $T_{\text{ref}}$ and $\rho_{\text{ref}}$ reference temperature and density, respectively. The implementation uses $H^1$-conformal linear finite elements for velocity and temperature and $L^2$-conformal (discontinuous) elements for the pressure and is again a modified version of an example of the Deal.II library ("step 32").

## 3.4 AWS Benchmark Results

While the elliptic test problem does not cover all different computational aspects of a tsunami simulation—in particular not with the discontinuous Galerkin approach, used in the prototypical implementation in **Section 4**—it is suited to give a good first impression of the computational capabilities of cloud instances in real life application scenarios. In order to assess the expected performance of a cloud instance in comparison with an on-premise compute server tests with up to 8 processors are conducted. It turns out that the test program does not scale very well, but it is not the purpose of this test to see optimal parallel performance but to be able to compare cloud vs. on-premise computing devices. Parallelization is implemented by the Message Passing Interface (MPI) parallel programming model, and no specific action is taken to optimize parallel efficiency. Note that these tests were performed some time ago and are included in this report for reference.

The tests are performed with the following configurations. The on-premise computer is a 2 node 2.67 GHz Xeon X5650 server with 12 cores, which is used with up to 16 processes (hyperthreading). It is equipped with 32 GB of main memory. The AWS EC2 cloud instances are of type c3.8xlarge, which is a Xeon E5-2680 based architecture with 32 virtual processors, 60 GB of main memory, and 10 GBit high speed networking. The performance results are shown in **Figure 2**. It can be seen from the figure that the local on-premise computation is a factor of 2 slower due to different processor generations, but the parallel scaling shows approximately the same behavior for the cloud as well as for the on-premise servers.

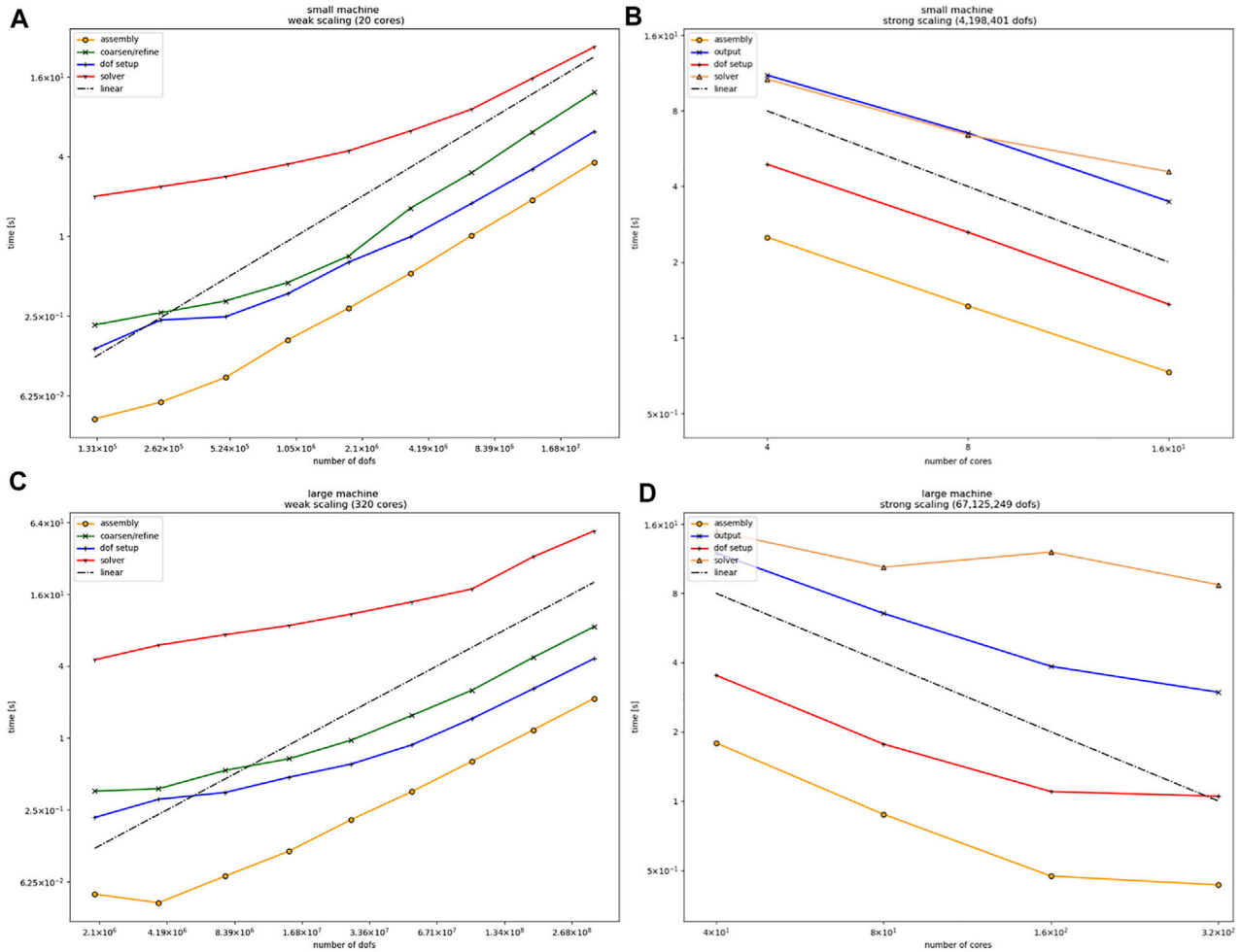


**FIGURE 3 | (A)** Weak scaling in the *small setup* for the test case in **Section 3.2** computed on 20 distributed CPUs with up to 17 million degrees of freedom. **(B)** Strong scaling for selected parts of the algorithm for the *small setup* with 4.2 million degrees of freedom on up to 16 distributed cores. **(C)** Weak scaling in the *large setup* for the test case in **Section 3.2** computed on 320 distributed CPUs with up to 270 million degrees of freedom. **(D)** Strong scaling for the *large setup* with 67 million degrees of freedom on up to 320 distributed cores. Both weak scaling plots do not show timings for the data output since its overhead becomes dominant at around $10^8$ Dofs. Both strong scaling plots do not time coarsening and refinement since the runs are not adaptive.

As a preliminary conclusion, it can be stated that the same kind of performance can be expected from an on-premise server as well as from a cloud instance. Performance-wise there is no specific advantage using an on-premise computer. In particular looking at the cost comparison of the previous chapter 2, the cloud instance can be regarded as the advantageous architecture.

## 3.5 Azure Benchmark Results

### 3.5.1 Elliptic PDE Benchmark

We perform weak and strong scaling tests, i.e., we take timings with fixed allocated hardware and gradually increase the problem size (weak scaling) as well as timing tests, where we fix the problem size and gradually allocate more compute resources (strong scaling). Both scaling tests are performed on the *small* and the *large setup* as described in **Section 3.2**. Although both our *small* and *large setup* are rather small compared to the cluster setup used in Bangerth et al. (2012), allowing only qualitative comparisons, similar (linear) scaling effects for differently sized problems are clearly visible for weak and strong scaling, see **Figure 3**. The scaling tests show timings of the main building blocks of adaptive FEMs which are essentially the setup of the mesh and the distribution of the degrees of freedom (*dof setup*), the assembly of the (sparse) system (*assembly*), the conjugate gradient solver preconditioned with algebraic multigrid (*solver*), a posteriori error estimation and adaptive coarsening and refinement of the mesh including rebalancing the mesh (*coarsen/refine*), and the data output (*output*). **Figure 4** additionally shows the partitioning of the adaptive mesh among 20 MPI processes.

Remark. We pass on timing the output in the weak scaling tests **Figures 3A,C** in our parallel setting since its overhead becomes very dominant for problem sizes with a number of degrees of freedom at a magnitude $10^8$ and higher and simply does not fit nicely in the plot of (**Figure 3C**). Also, **Figures 3B,D** do not show

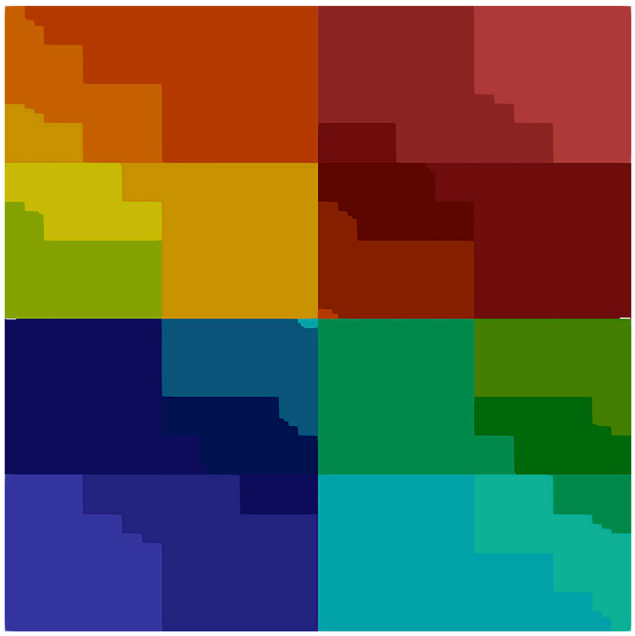

**FIGURE 4 |** Distributed mesh (20 CPUs on 10 nodes, small setup) for the test case in **Section 3.2**. Each color indicates a different processor owning a part of the mesh.

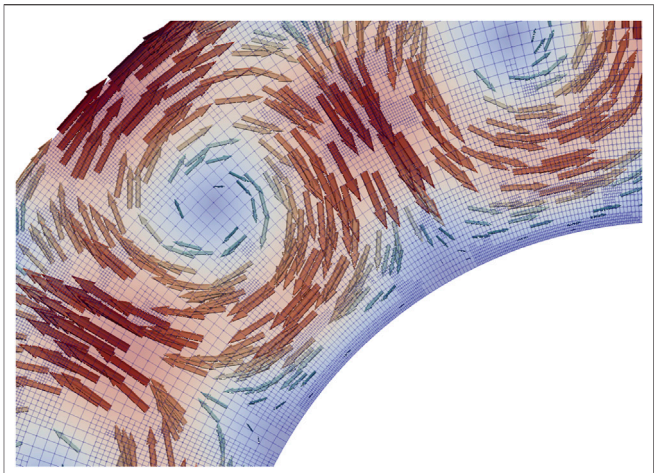

**FIGURE 5 |** Snapshot of the solution of the Boussinesq test case of **Section 3.3**. A crossection of the earth's mantle is shown with the adaptively refined mesh. Arrows indicate the flow direction and speed. Color also indicates flow speed.

timings of refinement and coarsening, because it was disabled for the strong scaling setup since we used a fixed number of degrees of freedom and only increased the number of processors.

### 3.5.2 Bouyancy-Boussinesq PDE Benchmark

This is an example of a massively parallel implementation since idle cores on each node will also be used for local shared memory parallelism. Thus for a substantial test of strong scalability taking full control over local threading and carefully choosing the balance of participating compute nodes versus the number of local cores on each node and the accessibility of memory banks is necessary. We pass on this and only show weak scaling results on 160 CPU cores on all ten machines. Note that the remaining virtual cores are used for threading the assembly of the system matrices and right-hand sides. Also note that we do not scale to the same large number of DoFs as in the test of **Section 3.2** since the problem is numerically much more challenging. **Figure 5** shows a snapshot of the Bouyancy-Boussinesq problem applied to mantle convection applications. **Figure 6** shows the weak scaling effects on 160 cores in the *large setup* for 100 time steps and increasing problem sizes due to adaptive mesh refinement. Note that coarsening and refinement includes re-balancing the mesh, and that the solvers scale slightly better than linearly since the solution at the preceding time step is used as an initial guess. The overall solution times for each iteration show slightly better scaling than linear, most likely because we are not in the asymptotic regime.

Overall, these scaling examples demonstrate the capacity of cloud facilities for typical numerical computation primitives. Scaling as well as absolute performance indicators are similar to on-premise computing facilities, at least for reasonably sized computers. The software environments of cloud instances are very similar to on-premise computing facilities, since the cloud instances can be configured analogously, providing Linux operating systems with the usual libraries and compilers, and even specialized libraries can be installed into the virtual machines running in the cloud environments.

## 4 EXAMPLE WORKFLOW FOR TSUNAMI HAZARD COMPUTING

A prototypical workflow for an instant computing scenario in tsunami early warning could be given by the following sequence:

1. Trigger: Earthquake detected through network of seismometers and suitable processing, information available *via* web service [e.g., GEOFON (2021)]
2. Gather Boundary Data: Bathymetry/topography data (possibly pre-) processed from online resources for the computational domain of interest.
3. Derive Initial Data: Obtain rupture parameters (Okada parameters) from earthquake parameters, e.g., through scaling laws (Mansinha and Smylie, 1971; Okada, 1985; Kanamori and Brodsky, 2004).
4. Simulation: Run tsunami forecasting simulation with initial conditions (Okada) and boundary data from previous two steps.
5. Deploy/visualize results: Visualize simulation results, and deploy additional products through web services from data, which were generated and stored in files during the simulation.

This workflow is given in **Figure 7** as a flow diagram.

In order to implement a prototypical realization of this workflow, several pre-fabricated tools were available and have

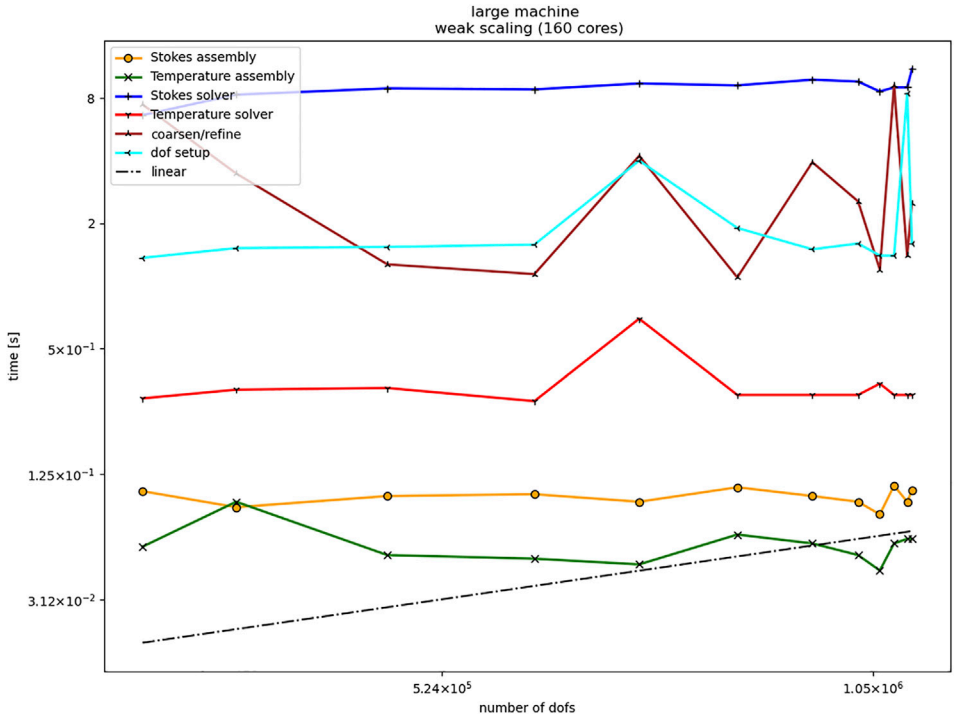


**FIGURE 6 |** Weak scaling on 160 CPU cores with local threading on ten nodes for the test in **Section 3.3** (large setup).

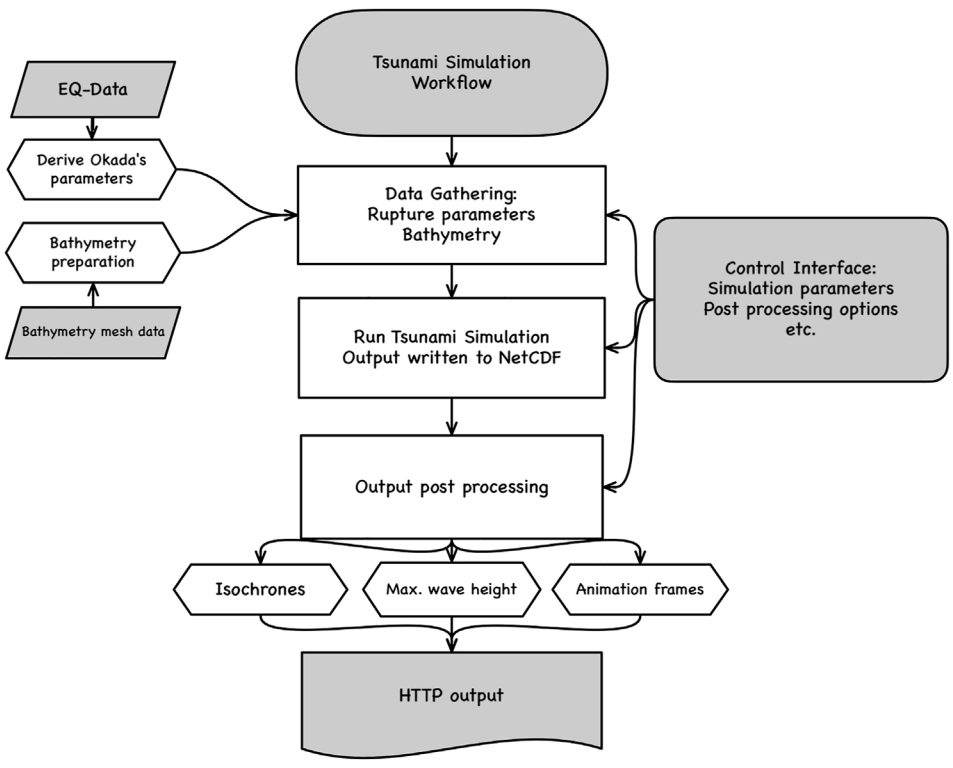


**FIGURE 7 |** Prototypical workflow for tsunami forecasting.

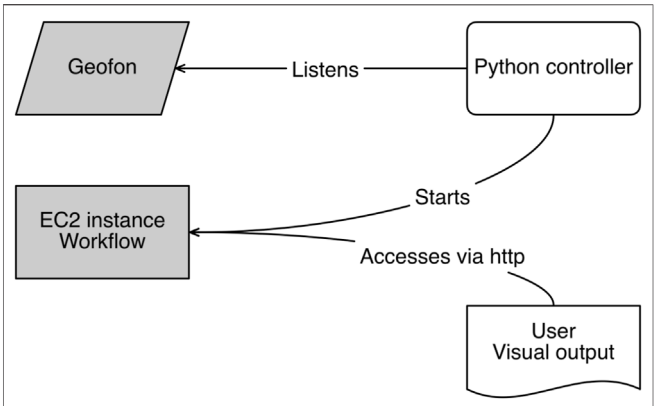


**FIGURE 8 |** Architecture of the prototypical cloud based tsunami forecasting system.

been used. As a first step, however, a well configured AWS EC2 virtual machine instance needs to be generated. Since the EC2 instances are scalable, the configuration concerns in particular the connectivity of the cloud machine. In our case access to the machine is established *via* secure shell (SSH) on port 22, and the (secure) HTTP/HTTPS protocols *via* ports 80 and 443 respectively. Corresponding keys need to be generated and stored appropriately.

The workflow is implemented by a 250 line Python script. In order to be able to achieve this brevity, several pre-fabricated libraries are used. The Boto library (Amazon Web Services, 2021) helps to start and configure the EC2 instance out of the python run-time environment. To simplify the interaction with the EC2 instance via SSH the Paramico library (Forcier, 2021) is used.

The general architecture of the implementation is shown in **Figure 8**. The Python controller script can run either on a very small/weak cloud instance or on any computer on-premise. It uses hardly any resources and will just listen to incoming mail from the triggering earthquake alert service. When the workflow is triggered by an earthquake alert message, the controller starts the EC2 instance, which is stored as a pre-fabricated and configured virtual machine. This consists of a current Debian Linux operating system, a repository of bathymetry/topography data for the region of interest (in our case the western Mediterranean), a compiled simulation program (StormFlash2d, see below) with all necessary libraries, and post-processing tools. Once the EC2 instance is running, it provides an HTTP-interface for clients, including mobile devices, to retrieve simulation results.

In this prototypical implementation the trigger for activating the workflow is an email sent by the GEOFON server (GEOFON, 2021) in case of an earthquake. The alerting email contains information on the earthquake's epicenter location, time, source parameters, and a unique event identifier. For reasonably significant earthquakes moment tensor parameters are automatically computed and can be accessed via web interfaces. The python controller parses relevant values from the text file containing the moment tensor parameters and derives the corresponding input to be used in the Okada model for tsunami sources (Okada, 1985). The empirical formulas are taken from Pranowo (2010) and are based on Kanamori and Brodsky (2004); Mansinha and Smylie (1971) and others.

Once the Okada parameters are derived, the corresponding source serves as initial condition for starting the simulation. Other boundary conditions (bathymetry/topography) are obtained from previously prepared and stored data. The propagation and inundation is computed by the simulation software StormFlash2D, an adaptive discontinuous Galerkin non-linear shallow water model (Vater et al., 2015, 2019). The output of StormFlash2D—wave height and velocity on adaptively refined triangular meshes—is stored in NetCDF files (Unidata, 2021), following the UGRID conventions (Jagers, 2018). These files are then further processed and visualized, utilizing the pyugrid Python library (Barker et al., 2021). Post-processing can then be applied to the stored files, in order to derive forecasting products, such as arrival time maps, mareograms, etc.

In this prototypical implementation that serves mainly the purpose of demonstrating feasibility, we use parameters similar to

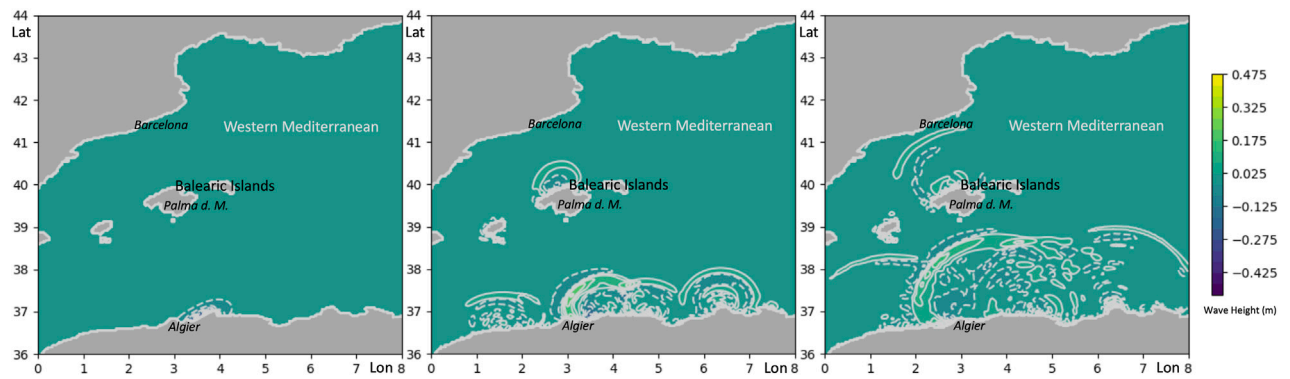


**FIGURE 9 |** Three snapshots of an animation result from the prototypical cloud based tsunami simulation. *x*- and *y*-axis represent degrees East longitude and North latitude, colors/contour lines indicate wave amplitude in meters. This is a scenario with a synthetic source of an earthquake tsunami originating in the North Algerian subduction zone. The images cover a map area reaching from approximately Valencia/Spain in the West to Monaco in the East and from a little South of Algier/Algeria in the South to Montpellier/France in the North.

the 2003 Zemmouri-Bourmedes tsunami event at the coast of Algeria in the Mediterranean (Alasset et al., 2006). The example email triggering the workflow contains the earthquake magnitude (MW 6.8) and location data (epicenter 36.83 N, 3.65 E, and depth 8 km). Further local tensor data are assumed to be strike 54°, dip 50° and rake 90°. Applying the above mentioned empirical scaling laws to the earthquake magnitude, we set a slip of little less than 1 m, a length of the Okada plate of 30.2 km and a width of 15.1 km. A single plate is assumed.

The only product delivered to a potential user in this feasibility study is a short animation of waves propagating over the ocean area of interest (see **Figure 9**). This sequence is computed using standard gebco bathymetry GEBCO (2014), which is interpolated linearly to the triangular mesh. The mesh for this computation was not adapted, but used in a uniformly refined version with 16 refinement levels, corresponding to a grid of approx. 260,000 grid cells or to a resolution of approx. 1,300 m. Note that in the visualization, there are some numerical artifacts (secondary waves) caused by a somewhat sloppy implementation of the interpolation of the Okada initial conditions (computed on a rectangular mesh) to the triangular computational mesh of StormFlash2d.

The above steps, i.e., listening to incoming email, parsing data into files controlling the execution of the tsunami model, and collecting output data, are performed by a small Python script on a local laptop or desktop computer. Starting the EC2 AWS instance takes less than 30 s. Run time for this serial computation on one node of the AWS instance takes approx. 100 s, the time for output being less than 1% of the total computing time.

While this proves the feasibility of implementing such workflow in IaaS type cloud services, it is by no means useful for real world operations. The adaptive tsunami simulation—while potentially efficient and accurate—is not applied to local resolutions of 10 s of meters for usefully precise forecast information. If this was the aim, additional resources and performance optimizations would be necessary. Additionally, a more diverse and more quality controlled post-processing pipeline would be necessary. Usually, wave arrival time maps, wave height maps, possibly inundation maps, and even flow speed assessments would be of practical interest.

## 5 SUMMARY AND CONCLUSION

In this study we assess the feasibility of on-demand cloud computing for tsunami hazard assessment as well as other demanding geophysical applications. On the one hand, we test the capacity of cloud computing environments to provide scalable high-performance computing capabilities. A number of advantages of such cloud-based computing facilities motivate us to further investigate their usability for more practical applications. Therefore, we propose a simple workflow that can be implemented in a cloud environment. While we are aware that there exist similar workflows in tsunami hazard assessment, they are all based on remotely accessible, but local on-premise computing environments.

A simplified prototypical workflow, utilizing cloud instances is implemented and demonstrates the overall feasibility of our approach. More work needs to be invested to empower this approach for operational use:

- Some manual work is required to obtain quality controlled bathymetry/topography data.
- A permanent control process needs to be instantiated in order to listen to relevant trigger data (such as earthquake portals) and compute robust and useful sources from earthquake parameters. The prototypical application is much too simple for operational purposes.
- More relevant output formats and better visualization needs to be implemented to interact with the instant computing workflow.
- The simulation software StormFlash2D needs thorough parallelization and optimization to be used in an operational environment.
- It would be desirable to also include other operational models for assessing the uncertainty in the forecast, related to the modeling technique.
- Instantiating several on-demand computations with a variation in the earthquake parameters within the data uncertainty, would create an ensemble of forecasts, allowing for probabilistic forecasts such as those proposed by Selva et al. (2021).

By conducting the scalability tests with selected benchmarks we could show that cloud computing environments are capable of providing the required performance for many geoscientific applications at reasonable costs. Therefore further exploration and development of standardized interfaces for managing and controlling the cloud computing infrastructure is worthwhile.

## DATA AVAILABILITY STATEMENT

The raw data supporting the conclusion of this article will be made available by the authors, without undue reservation.

## AUTHOR CONTRIBUTIONS

JB wrote main parts of the article, coordinated the project, and raised funding. AS provided and configured the necessary cloud infrastructure, and performed early benchmark tests on the AWS cloud. KS configured the software environment and ran most of the tests in the Azure cloud.

## FUNDING

Parts of this research were conducted in the framework of the ASTARTE project with funding from the European Unions Seventh Program for research, technological development and demonstration under grant agreement No. 603839. Additional funding was obtained by the Deutsche Forschungsgemeinschaft (DFG, German Research Foundation) under Germany's Excellence Strategy—EXC 2037 'CLICCS—Climate, Climatic Change, and Society'—Project Number: 390683824, contribution to the Center for Earth System Research and Sustainability (CEN) of Universität Hamburg.

## ACKNOWLEDGMENTS

The authors gratefully acknowledge the following individual contributions. Development of the tsunami demonstrator was mainly conducted by JB's student Mathias Widok, who implemented the Python code and configured AWS instances for the demonstrator application. Stefan Vater, post-doc in JB's research group, together with Michel Bänsch, student assistant, provided the tsunami simulation software StormFlash2D and configured it to be used in the western Mediterranean. Assistance in benchmarking and performance assessment of the benchmark AWS cloud instances was provided by the Andreas Oetken for Axtrion.

## REFERENCES

Alasset, P.-J., Hébert, H., Maouche, S., Calbini, V., and Meghraoui, M. (2006). The Tsunami Induced by the 2003 Zemmouri Earthquake (Mw= 6.9, Algeria): Modelling and Results. *Geophys. J. Int.* 166, 213–226. doi:10.1111/j.1365-246x.2006.02912.x

Amazon Web Services (2021). Boto 3 Docs 1.17.53 Documentation. Available at: https://boto3.readthedocs.io/en/latest/. Accessed: 2021--04-18.

Arndt, D., Bangerth, W., Blais, B., Clevenger, T. C., Fehling, M., Grayver, A. V., et al. (2020). The deal.II Library, Version 9.2. *J. Numer. Maths.* 28, 131–146. doi:10.1515/jnma-2020-0043

ASTARTE Project (2017a). Assessment, Strategy and Risk Reduction for Tsunamis in Europe. Available at: https://cordis.europa.eu/project/id/603839/reporting. Accessed: 2022-02-04.

ASTARTE Project (2017b). Find platform, fundação da faculdade de ciências da universidade de lisboa. Available at: http://accessible-serv.lasige.di.fc.ul.pt/~find/. Accessed: 2017-05-13.

Bangerth, W., Burstedde, C., Heister, T., and Kronbichler, M. (2012). Algorithms and Data Structures for Massively Parallel Generic Adaptive Finite Element Codes. *ACM Trans. Math. Softw. (Toms)* 38, 1–28.

Bangerth, W., Dannberg, J., Fraters, M., Gassmoeller, R., Glerum, A., Heister, T., et al. (2015). Aspect v1.5.0: Advanced Solver for Problems in Earth's Convection. *Comput. Infrastructure Geodynamics*. doi:10.5281/zenodo.344623

Barker, C., Calloway, C., and Signell, R. (2021). Pyugrid 0.3.1: A Package for Working with Triangular Unstructured Grids, and the Data on Them. Available at: https://pypi.python.org/pypi/pyugrid. Accessed: 2021-06-27

Behrens, J., Androsov, A., Babeyko, A. Y., Harig, S., Klaschka, F., and Mentrup, L. (2010). A New Multi-Sensor Approach to Simulation Assisted Tsunami Early Warning. *Nat. Hazards Earth Syst. Sci.* 10, 1085–1100. doi:10.5194/nhess-10-1085-2010

European Commission (2022). Space, Security and Migration Directorate - JRC Ispra Site. Tsunami analysis tool (tat) Available at: https://webcritech.jrc.ec.europa.eu/TATNew_web/ (Accessed 01, 19).2022.

Forcier, J. (2021). Paramico - a python Implementation of Sshv2. Available at: http://docs.paramiko.org/en/2.1/. Accessed: 2021-06-27.

Foster, I., Zhao, Y., Raicu, I., and Lu, S. (2008). Cloud Computing and Grid Computing 360-degree Compared. *IEEE Xplore*. doi:10.1109/GCE.2008.4738445

Fox, A. (2011). Cloud Computing-What's in it for Me as a Scientist? *Science* 331, 406–407. doi:10.1126/science.1198981

GEBCO (2014). The Gebco_2014 Grid, version 20150318.Available at: https://www.gebco.net. Accessed: 2022-01-19.

GEOFON (2021). Geofon Homepage. Available at: http://geofon.gfz-potsdam.de. Accessed: 2021-06-27.

Hammitzsch, M. (2021). Tridec Cloud for Tsunamis, Gfz German Research center for Geosciences. Available at: http://tridecloud.gfz-potsdam.de/. Accessed: 2021-06-27.

Cantabria, I. H. (2016). Ih-tsunamis System (Ihtsusy) an Online Real-Time Tsunami Simulation and Notification Application. Available at: https://ihcantabria.com/en/specialized-software/ih-tsusy/. Accessed: 2021-06-27.

Jagers, B. (2018). Ugrid Conventions (v1.0). Available at: http://ugrid-conventions.github.io/ugrid-conventions/. Accessed: 2021-06-27.

Kanamori, H., and Brodsky, E. E. (2004). The Physics of Earthquakes. *Rep. Prog. Phys.* 67, 1429–1496. doi:10.1088/0034-4885/67/8/r03

Lovholt, F., Lorito, S., Macias, J., Volpe, M., Selva, J., and Gibbons, S. (2019). "Urgent Tsunami Computing," in *IEEE/ACM HPC for Urgent Decision Making (UrgentHPC)* (Denver, CO; USA: IEEE), 45–50. doi:10.1109/UrgentHPC49580.2019.00011

Mansinha, L., and Smylie, D. E. (1971). The Displacement fields of Inclined Faults. *Bull. Seismological Soc. America* 61, 1433–1440. doi:10.1785/bssa0610051433

Mell, P. M., and Grance, T. (2011). *The NIST Definition of Cloud ComputingSpecial Publication 800-145*. Gaithersburg, MD: NIST - National Institute of Standards and Technology.

Neamtws, I. (2016). NEAMTWS Procedures for the Accreditation of TSPs. Available at: https://oceanexpert.org/document/16615. Accessed: 2022-02-04.

Okada, Y. (1985). Surface Deformation Due to Shear and Tensile Faults in a Half-Space. *Bull. Seismological Soc. America* 75, 1135–1154. doi:10.1785/bssa0750041135

Pranowo, W. S. (2010). Ph.D. thesis. Bremen, Germany: Universität Bremen. Available at: http://nbn-resolving.de/urn:nbn:de:gbv:46-diss000120084. Adaptive Mesh Refinement Applied to Tsunami Modeling: TsunaFLASH.

Sarri, A., Guillas, S., and Dias, F. (2012). Statistical Emulation of a Tsunami Model for Sensitivity Analysis and Uncertainty Quantification. *Nat. Hazards Earth Syst. Sci.* 12, 2003–2018. doi:10.5194/nhess-12-2003-2012

Selva, J., Lorito, S., Volpe, M., Romano, F., Tonini, R., Perfetti, P., et al. (2021). Probabilistic Tsunami Forecasting for Early Warning. *Nat. Commun.* 12, 1–14. doi:10.1038/s41467-021-25815-w

Unidata (2021). Network Common Data Form (Netcdf).Available at: https://www.unidata.ucar.edu. Accessed: 2021-04-19.

Vater, S., Beisiegel, N., and Behrens, J. (2015). A Limiter-Based Well-Balanced Discontinuous Galerkin Method for Shallow-Water Flows with Wetting and Drying: One-Dimensional Case. *Adv. Water Resour.* 85, 1–13. doi:10.1016/j.advwatres.2015.08.008

Vater, S., Beisiegel, N., and Behrens, J. (2019). A Limiter-based Well-balanced Discontinuous Galerkin Method for Shallow-water Flows with Wetting and Drying: Triangular Grids. *Int. J. Numer. Meth Fluids* 91, 395–418. doi:10.1002/fld.4762

Wei, Y., Chamberlin, C., Titov, V. V., Tang, L., and Bernard, E. N. (2013). Modeling of the 2011 japan Tsunami: Lessons for Near-Field Forecast. *Pure Appl. Geophys.* 170, 1309–1331. doi:10.1007/s00024-012-0519-z

Yoo, A. B., Jette, M. A., and Grondona, M. (2003). "Slurm: Simple Linux Utility for Resource Management," in *Job Scheduling Strategies for Parallel Processing*. Editors D. Feitelson, L. Rudolph, and U. Schwiegelshohn (Berlin, Heidelberg: Springer Berlin Heidelberg), 44–60. doi:10.1007/10968987_3

Zhang, Q., Cheng, L., and Boutaba, R. (2010). Cloud Computing: State-Of-The-Art and Research Challenges. *J. Internet Serv. Appl.* 1, 7–18. doi:10.1007/s13174-010-0007-6

**Conflict of Interest:** Author AS was employed by the Axtrion GmbH & Co. KG.

The remaining authors declare that the research was conducted in the absence of any commercial or financial relationships that could be construed as a potential conflict of interest.

The handling Editor declared a past co-authorship with the authors JB.

frontiers | Frontiers in Earth Science

ORIGINAL RESEARCH
published: 07 April 2022
doi: 10.3389/feart.2022.743860

# A Statistical Approach Towards Fast Estimates of Moderate-To-Large Earthquake Focal Mechanisms

*Marisol Monterrubio-Velasco*[1]*, *Jose C. Carrasco-Jimenez*[1], *Otilio Rojas*[1,2], *Juan E. Rodríguez*[1], *Andreas Fichtner*[3] and *Josep De la Puente*[1]

[1]Barcelona Supercomputing Center - Centro Nacional de Supercomputación, Barcelona, Spain, [2]Escuela de Computación, Facultad de Ciencias, Universidad Central de Venezuela, Caracas, Venezuela, [3]Institute of Geophysics, ETH Zurich, Zurich, Switzerland

Emerging high-performance computing systems, combined with increasingly detailed 3-D Earth models and physically consistent numerical wave propagation solvers, are opening up new opportunities for urgent seismic computing. This may help, for instance, to guide emergency response teams in the wake of large earthquakes. A key component of urgent seismic computing is the early availability of source mechanism estimates, well before conventional and time-consuming moment tensor inversions are carried out and published. Here, we introduce a methodology that rapidly estimates focal mechanisms (FM) for moderate and large earthquakes ($M_w$ > 4.0) by means of statistical and clustering algorithms. The fundamental rationale behind the method is that events of a certain size tend to be similar to other events of similar size in similar locations. In this work, two different strategies are used to provide different FM solutions: the first is based only in spatial considerations including statistical analysis, and the other one is based on a data clustering algorithm. We exemplify our methodology with six different subsets of the open-access Global Centroid Moment Tensor (GCMT) catalog. Specifically, our study datasets include events from Japan, New Zealand, California, Mexico, Iceland, and Italy, which represent six seismically active regions, with a large FM variability. Our results show a 70–85% agreement between our fast FM estimates and inversion results, depending on the particular tectonic region, dataset size, and magnitude threshold. In addition, our FM estimation strategies only spend few seconds for processing, since they are totally independent of seismic record retrieval and inversion. Albeit not meant to be a substitute for CMT inversions, our methodologies can bridge the time gap between earthquake detection and FM inversion.

**Keywords: focal mechanism, fast-response, urgent computing, GCMT catalog, DBSCAN clustering, source parameters**

OPEN ACCESS

***Edited by:***
*Alice-Agnes Gabriel, Ludwig Maximilian University of Munich, Germany*

***Reviewed by:***
*Wenhuan Kuang, Southern University of Science and Technology, China*
*Stefania Tarantino, University of Naples Federico II, Italy*

***Correspondence:**
*Marisol Monterrubio-Velasco*
*marisol.monterrubio@bsc.es*

***Specialty section:***
*This article was submitted to Geohazards and Georisks, a section of the journal Frontiers in Earth Science*

***Received:*** *19 July 2021*
***Accepted:*** *18 February 2022*
***Published:*** *07 April 2022*

***Citation:***
*Monterrubio-Velasco M, Carrasco-Jimenez JC, Rojas O, Rodríguez JE, Fichtner A and Puente JDl (2022) A Statistical Approach Towards Fast Estimates of Moderate-To-Large Earthquake Focal Mechanisms. Front. Earth Sci. 10:743860. doi: 10.3389/feart.2022.743860*

## 1 INTRODUCTION

Fast earthquake magnitude and focal mechanism (FM) estimates are key information for rapid emergency response applications, including urgent post-event seismic simulations. Few hours after the occurrence of a large-magnitude earthquake, these simulations aim to map ground shaking in the affected region to show areas of high intensity motion, which may host potential structural damages. An FM solution describes the fault-plane orientation and directions of principal stresses in the area

where the earthquake occurred (Udias and Buforn 2017; Maeda 1992). The FM is given by three angles, two of them, the strike $\phi$ and dip $\delta$ angles, geometrically define the fault plane, and the third angle, the rake $\lambda$ measures the direction of fault slip. Thus, an FM is used for the mathematical description of seismic sources in terms of the moment tensor (MT) equivalent body forces. The most general approach to determine an FM solution is by computing the centroid moment tensor (CMT). For moderate-to-large magnitude earthquakes, CMTs are usually obtained from waveform or spectral data inversions (Dziewonski et al., 1981; Dziewonski and Woodhouse 1983). Although, approaches to estimate earthquake location and magnitude are consolidated and extremely fast, automatic solutions for FM estimates are not always provided by the seismological agencies, or are only available at later times after waveform inversions have been completed (Tarantino et al., 2019). However, it is worth noting that significant efforts have been made towards almost real-time determination of FM (or CMT) by using different methods and algorithms. For example, Lin et al. (2019) and Melgar et al. (2012) exploit GPS networks, while other works use source inversion algorithms based on modelling of the W-phase, a very long-period phase (100–1,000 s) arriving at the same time as the P-wave (see, e.g., Duputel et al., 2012). Another approach relies on the azimuthal distribution of early P-wave peaks in displacement, velocity and acceleration traces (Tarantino et al., 2019). Moreover, several packages have been developed for automatic MT determination, such as Scisola (open-source software developed by Triantafyllis et al., 2016) or Gisola (Triantafyllis et al., 2021). Scisola is an open source Python based software for automatic MT calculation that combines two platforms, ISOLA (Sokos and Zahradnik 2008) and SeisComP3 (Weber et al., 2007). Gisola is an evolved version of Scisola that applies enhanced algorithms for waveform data filtering. However, the response times of most aforementioned techniques are constrained by the retrieval times of their input data, i.e., seismic records of the recent earthquakes (Melgar et al., 2012; Scognamiglio et al., 2010, and ref. there in). Therefore, the development of alternative approaches for fast FM estimations, independent of seismic records, may serve as temporary replacement until inversions have finished. This work explores statistical approaches, with the assistance of clustering algorithms, to estimate FM solutions for a new earthquake based on the similarity of $\phi$, $\delta$ and $\lambda$ with respect to past events. The historical databases are gathered by the open-access Global Centroid Moment Tensor (GCMT) catalog (GCMT, Ekström et al., 2012). As input data, our methodologies only require the hypocentral location and magnitude of the new earthquake. This information is promptly provided by different seismological agencies with a latency of few seconds after earthquake occurrence. Once triggered, our methodologies can provide FM estimates within seconds, thereby enabling real-time affectation analyses before FM inversions become available. Our results can be potentially used to add directivity information into fast shaking assessment estimates, shortly after the earthquake is recorded, because it is precise for large events which have damaging potential. The method, however, is not universal, because it behaves worse if smaller magnitude events are used. Hence it is no substitute for CMT inversion, but a provider of fast estimates.It is important to acknowledge that the methodology results not in one single best-fitting result, but in a collection of results among which is a good-fitting result. For shaking assessment (see, e.g., Wald et al., 1999, Wald et al., 2008) this is not a strong limitation, as few scenarios can be computed using all CMT estimates and the best fit can be assessed a posteriori. Last but not least, the methodology has a potential for probabilistic seismic hazard (PSHA, see e.g. Baker 2008; Mulargia et al., 2017) studies, especially those taking into account CMT information in their attenuation relationships or seismic modelling components. When populating hypothetical future earthquakes, in the so-called earthquake rupture forecast, CMTs could be estimated using our method, thus not necessarily restricting such earthquakes to mapped faults and their prescribed tectonic regimes. In fact, using catalog information (i.e. our CMT estimate) to make assessments about a hypothetical scenario is at the very core of PSHA. Nevertheless a seismic scenario computed using our CMT estimates would lack any kind of probabilistic component: it would be a deterministic scenario with associated uncertainties inherent to the CMT estimation methodology. The proposed methodology for FM estimation exploits information on hypocenters and magnitudes of catalogued neighboring events. Specifically, we employ conventional statistical analysis and the automatic DBSCAN clustering algorithm (Ester et al., 1996). To measure distance between two FM solutions, we use the Minimum Rotated Angle (MRA) metrics Kagan (2007) that quantify similarities between two double-couple (DC) sources in absolute angle degrees. It is worth noting that non-DC components, typically associated with volcanic activity and fluid-related earthquakes, are not the focus of our work because they do not typically produce large-magnitude, i.e. highly damaging, events (Stierle 2015; Wang et al., 2018). We assess the accuracy of the methodology through statistical comparisons of our FM results with published GCMT inversion solutions. For validation, we select six seismically active regions with large variability of the rupture mechanisms for the selected historical earthquakes used as estimation basis. These regions are Japan, New Zealand, California, Mexico, Iceland, and Italy.

# 2 BACKGROUND

## 2.1 Global Centroid Moment Tensor Catalog and Input Datasets

We obtained the datasets used in this work from the GCMT catalog (Dziewonski et al., 1981; Ekström et al., 2012), available through the Searchable Product Depository (SPUD) of the Incorporated Research Institutions for Seismology (IRIS) (Trabant et al., 2012). Global Centroid-Moment-Tensors from the GCMT project at Lamont-Doherty Earth Observatory are available through SPUD within minutes after their publication. Initial quick-CMT solutions are shown and are later updated to GCMT solutions when updates arrive. At present, the GCMT catalog contains more than 40,000 earthquakes. From the queried catalog we use the Event information which includes the

**TABLE 1 |** Filters applied to the GCMT database to extract six regional datasets. We list the total amount of events in each dataset. Databases have been queried from IRIS "https://ds.iris.edu/spud/momenttensor"

| Subset | Latitude (°) | Longitude (°) | Depth (km) | Event count | Magnitude ($M_w$) | Date |
|---|---|---|---|---|---|---|
| New Zealand | [-46.02, -34.42] | [166.1, 178.71] | [0, 518] | 273 | [4.8, 7.8] | [1965, 2018] |
| Japan | [30.03, 46.3] | [128.84, 147.1] | [0, 588] | 2652 | [4.6, 9.1] | [1967, 2019] |
| California | [29.72, 44.77] | [-129.76, -110.36] | [0, 30] | 460 | [4.4, 7.3] | [2010, 2019] |
| México | [10, 33] | [-120, -90] | [0, 251.1] | 1705 | [4.5, 8.2] | [1967, 2020] |
| Iceland | [63.06, 66.94] | [-24.43, -16.58] | [0, 33] | 124 | [4.6, 6.5] | [1976, 2018] |
| Italy | [34.95, 47.94] | [5.18, 21.0] | [0, 502] | 692 | [3.9, 6.9] | [1976, 2015] |

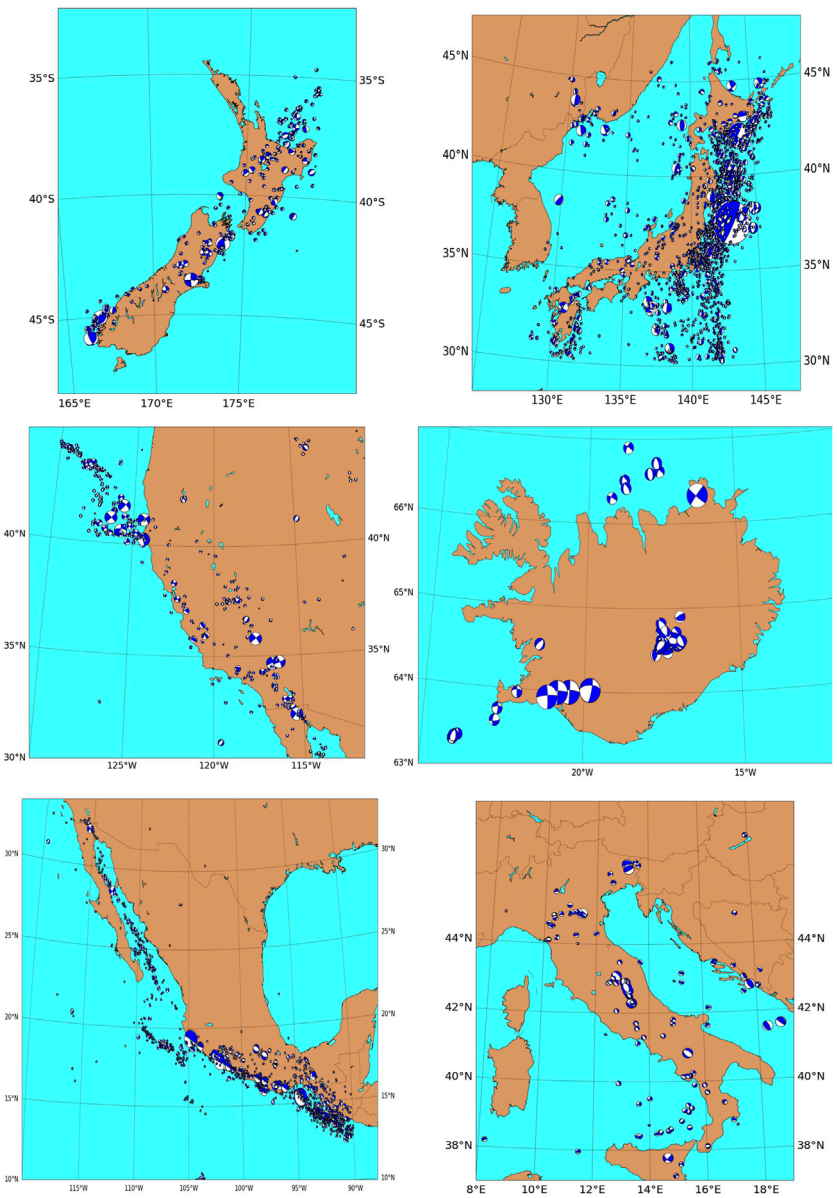


**FIGURE 1 |** GCMT datasets used in this study (see **Table 1**), the epicentral locations, and the FM solutions are shown.

hypocenter location, earthquake magnitude, Date-Time UCT, faulting geometry, and the FM solution of moderate to large events with magnitude M ≥ 4.5. Is worth to highlight that in this work we only use the hypocenter location of the Event information to give the coherence of the first information registered after an earthquake occurs.

In this study, we consider six data subsets associated with six study regions: New Zealand, Japan, California, Mexico, Iceland, and Italy. Each subset is defined by the ranges of hypocentral locations, magnitudes and event times (**Table 1**). **Figure 1** shows each regions and FM solutions, represented as beach balls. The beach ball sizes are proportional to the event magnitude.

## 2.2 Minimum Rotated Angle Metric to Measure Similarity Between Two Focal Mechanisms

In this work, we assess the accuracy of our FM solutions by means of the MRA metric, proposed by Kagan (2007). This metric measures the distance between two double-couple (DC) solutions in absolute angular terms, and it enables a comparison between two DC solutions obtained by different methods, as well as variations of earthquake FMs in space and time. Moreover, the MRA has been used widely, thereby allowing us to compare methodologies of different authors.

MRA requires computing the matrix eigenvectors **t**, **p** and **b**, which belong to $\mathbb{R}^3$ and represent the three orthogonal axes describing the radiation of P-waves from a DC point source (Frohlich 1996; Aki and Richards 2002). To compute the MRA, we consider the eigenvector components in terms of the strike $\phi$, dip $\delta$, and rake $\lambda$ angles,

$$\begin{aligned}
t_1 &= \left(-\sin\phi\sin\delta + \cos\phi\cos\lambda + \sin\phi\cos\delta\sin\lambda\right)/\sqrt{2}\\
t_2 &= \left(\cos\phi\sin\delta + \sin\phi\cos\lambda - \cos\phi\cos\delta\sin\lambda\right)/\sqrt{2}\\
t_3 &= \left(-\cos\delta - \sin\delta\sin\lambda\right)/\sqrt{2}\\
p_1 &= \left(-\sin\phi\sin\delta - \cos\phi\cos\lambda - \sin\phi\cos\delta\sin\lambda\right)/\sqrt{2}\\
p_2 &= \left(\cos\phi\sin\delta - \sin\phi\cos\lambda + \cos\phi\cos\delta\sin\lambda\right)/\sqrt{2}\\
p_3 &= \left(-\cos\delta + \sin\delta\sin\lambda\right)/\sqrt{2}\\
b_1 &= \cos\phi\sin\lambda - \sin\phi\cos\delta\cos\lambda\\
b_2 &= \sin\phi\sin\lambda + \cos\phi\cos\delta\cos\lambda\\
b_3 &= \sin\delta\cos\lambda
\end{aligned} \tag{1}$$

The MRA $\Phi$, as defined in Kagan (2007), is given by

$$\Phi = \arccos\left[\frac{1}{2}\left(|\mathbf{t}'\cdot\mathbf{t}''| + |\mathbf{p}'\cdot\mathbf{p}''| + |\mathbf{b}'\cdot\mathbf{b}''| - 1\right)\right] \tag{2}$$

Where **t'**, **p'** and **b'**, are the eigenvectors associated to one FM solution, while a second FM solution has **t"**, **p"** and **b"** as eigenvectors.

Following the formulation in Kagan (2007), **Eq. 2** yields the correct value of the rotation angle for $\Phi < 90^\circ$. However, if **Eq. 2** results in $\Phi > 90^\circ$ then a more general equation should be applied to compute $\Phi$. For $\Phi > 90^\circ$ to obtain the minimum rotation angle $\Phi$ **Eq. 3** is applied, in those cases the smallest absolute value dot product should be negative, and the other products should be positive (further details see Kagan (2007).)

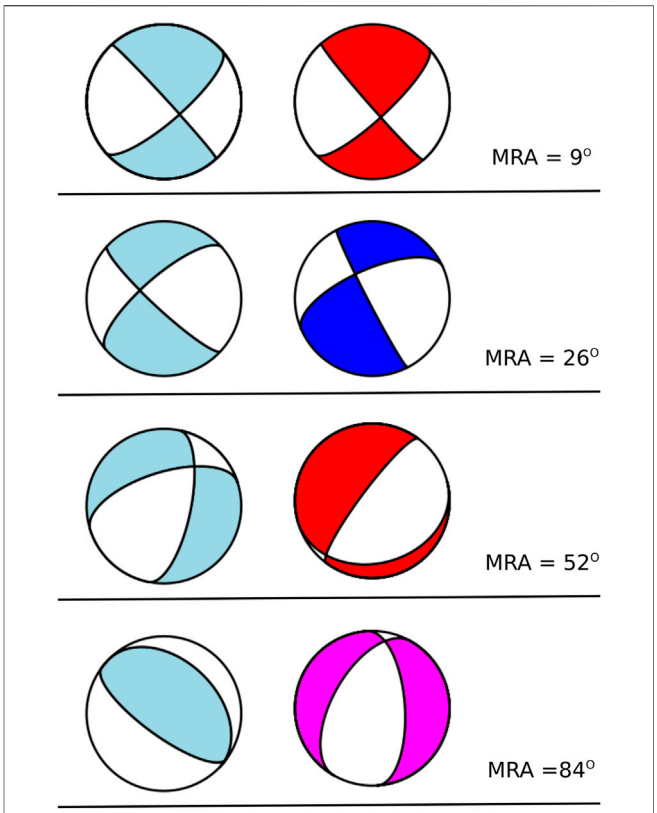


**FIGURE 2 |** Example of the MRA metric comparing two FM solutions.

$$\Phi = \arccos\left[\frac{1}{2}\left(\mathbf{t}'\cdot\mathbf{t}'' + \mathbf{p}'\cdot\mathbf{p}'' + \mathbf{b}'\cdot\mathbf{b}'' - 1\right)\right] \tag{3}$$

**Figure 2** depicts some examples of different MRA values computed from the shown FM solutions.

Different research results conclude that an acceptable agreement between two FM solutions is given by angle differences of the order of a few tens of degrees, while a strong variance corresponds to an angle difference greater than 50° (or 60°) (Vannucci et al., 2004; Triantafyllis 2014; Triantafyllis et al., 2016). Triantafyllis et al. (2013) found an average error between manual and the automatic FM solutions computed using Scisola of $\Phi \approx 37^\circ$. Moreover, based on heuristic analyses from our statistical results, in this work we assume a similarity threshold $\Phi_{th} < 30^\circ$. Therefore, we suggest that two FM solutions with $\Phi > \Phi_{th}$ are not comparable.

## 2.3 DBSCAN Clustering Algorithm

Class identification in spatial databases can be accomplished through the exploitation of clustering algorithms. Cluster analysis is developed under the assumption that spatial data has an implicit structure that can be uncovered by clustering algorithms. The clusters must comply with two characteristics: internal cohesion, also known as homogeneity, and external isolation, also known as separation. Thus, clustering techniques seek to summarize meaningfully different pattern

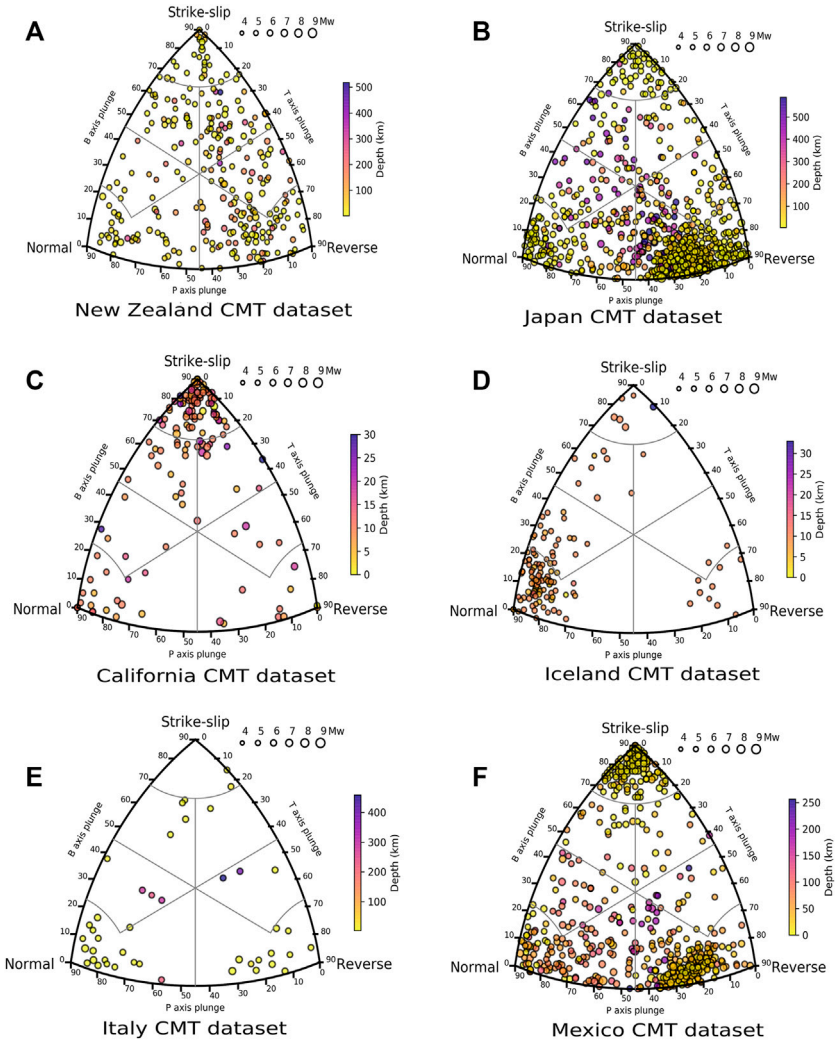


**FIGURE 3 |** Kaverina's diagrams for selected six regions: **(A)** New Zealand $M \geq 4.8$, **(B)** Japan $M \geq 5.5$, **(C)** California $M \geq 4.4$, **(D)** Iceland $M \geq 4.6$, **(E)** Italy $M \geq 4.6$, and **(F)** Mexico $M \geq 5.5$.

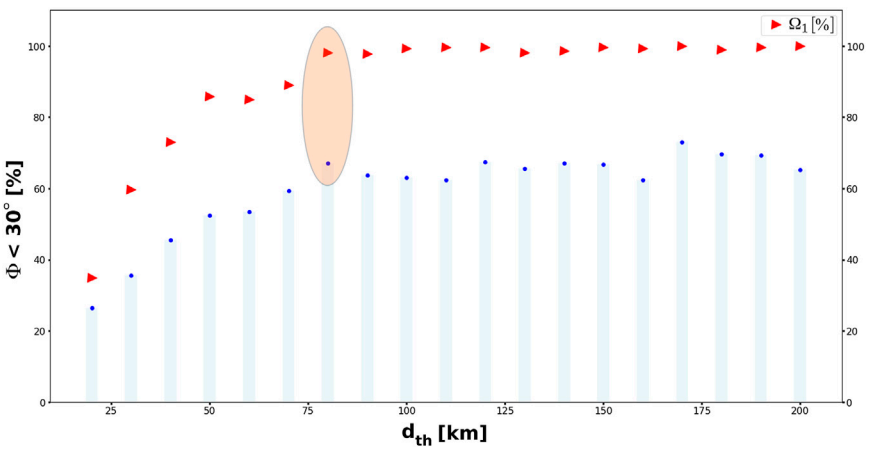


**FIGURE 4 |** Example of the selection process of the optimal *d*th parameter. Red markers show the percentage of events with at least one neighbor inside the sphere ($\Omega_1$). Blue marks indicate the percentage of events with at least one FM solution with $\Phi < 30^{\circ}$. Ellipse indicates the optimum *d*th considered in the study as the inflection point in both curves.

**TABLE 2 |** Results of the methodology proposed in this work: *d***th** is the neighborhood radius size in kilometers; *M***th** the minimum magnitude considered in the study; Number of events the total number of earthquakes with a magnitude larger or equal than *M*th; $\Omega_1$ and $\Omega_3$ are the number of events with at least one or three neighbors inside the sphere of radius *d*th respectively; and $\Phi_{(30,\Omega_1)}$ and $\Phi_{(30,\Omega_3)}$ depicts the percentage of events with at least one solution with a $\Phi < 30$ computed from the Statistical method or DBSCAN algorithm respectively.

| Region | *d*th [*km*] | *M*th | Number of events | Nearest Neighbors | DBCAN |
|---|---|---|---|---|---|
| | | | | $\Omega_1$ $\Phi_{(30,\ 1)}$ | $\Omega_3$ $\Phi_{(30,\ 3)}$ |
| **New Zealand** | 80 | 4.8 | 273 | 220 73% | 154 82% |
| **Japan** | 80 | 5.0 | 2263 | 2085 77% | 1771 79% |
| **Japan** | 110 | 5.5 | 937 | 816 80% | 621 81% |
| **Japan** | 150 | 6.0 | 331 | 261 85% | 196 88% |
| **California** | 80 | 5.0 | 363 | 328 83% | 301 79% |
| **Mexico** | 60 | 5.0 | 1,426 | 1,302 86% | 938 86% |
| **México** | 80 | 5.5 | 588 | 542 87% | 361 89% |
| **Mexico** | 130 | 6.0 | 203 | 178 83% | 101 89% |
| **Italy** | 80 | 4.8 | 114 | 66 85% | 38 92% |
| **Iceland** | 70 | 4.6 | 124 | 122 77% | 113 83% |

profiles by identifying segments of points in which observations within the same cluster exhibit high degrees of similarity (homogeneity) while differing in some respects from observations in other clusters (separation). In this work, a density-based method, namely Density-based Spatial Clustering of Applications with Noise (DBSCAN) Ester et al. (1996) is used to identify geological or structural profiles, which are depicted by the clusters uncovered by the algorithm. DBSCAN relies on two parameters: a distance threshold $\epsilon$, which indicates the maximum distance between two observations, and the minimum number of observations $n$ to form a cluster. The first step is to describe each observation, i.e., an earthquake with a focal mechanism, using a multi-dimensional real-valued vector representation described by the hypocentral location, strike, dip and rake. The set of observations is fed to the DBSCAN algorithm to uncover the intrinsic geological or structural profiles. In order to obtain the optimal number of profiles (i.e. clusters), the distance threshold and the minimum number of samples, both of which parameters have an effect on the number of clusters. The distance threshold $\epsilon$ is estimated using the strategy based on knee/elbow methodology (Satopaa et al., 2011). And the minimum number of samples $n$ are set equal to two

## 3 STATISTICAL AND CLUSTERING METHODOLOGY FOR FAST ESTIMATING FOCAL MECHANISMS

In the following subsection we provide a general description of the proposed method. Subsequently, we present its application to several regions of interest.

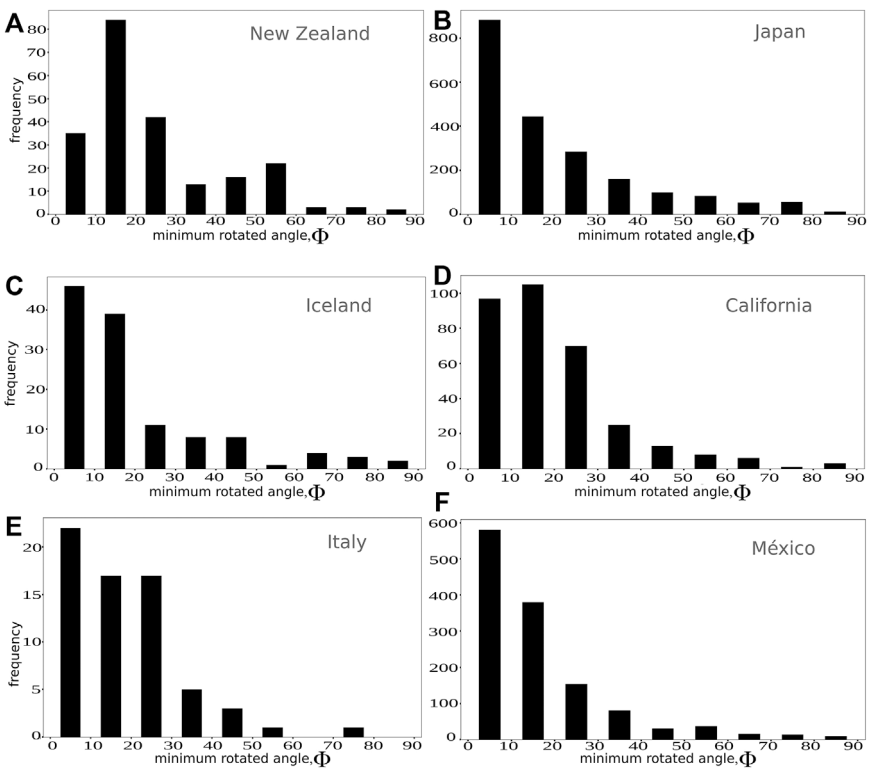


**FIGURE 5 |** Histogram distribution of Φ values obtained by the comparison between each new event and its nearest neighbors (*k1*, *k2*, *k3*, *k4*, *k median*). The values represented in the plot are the minimum Φ obtained in the nearest neighbor comparison.

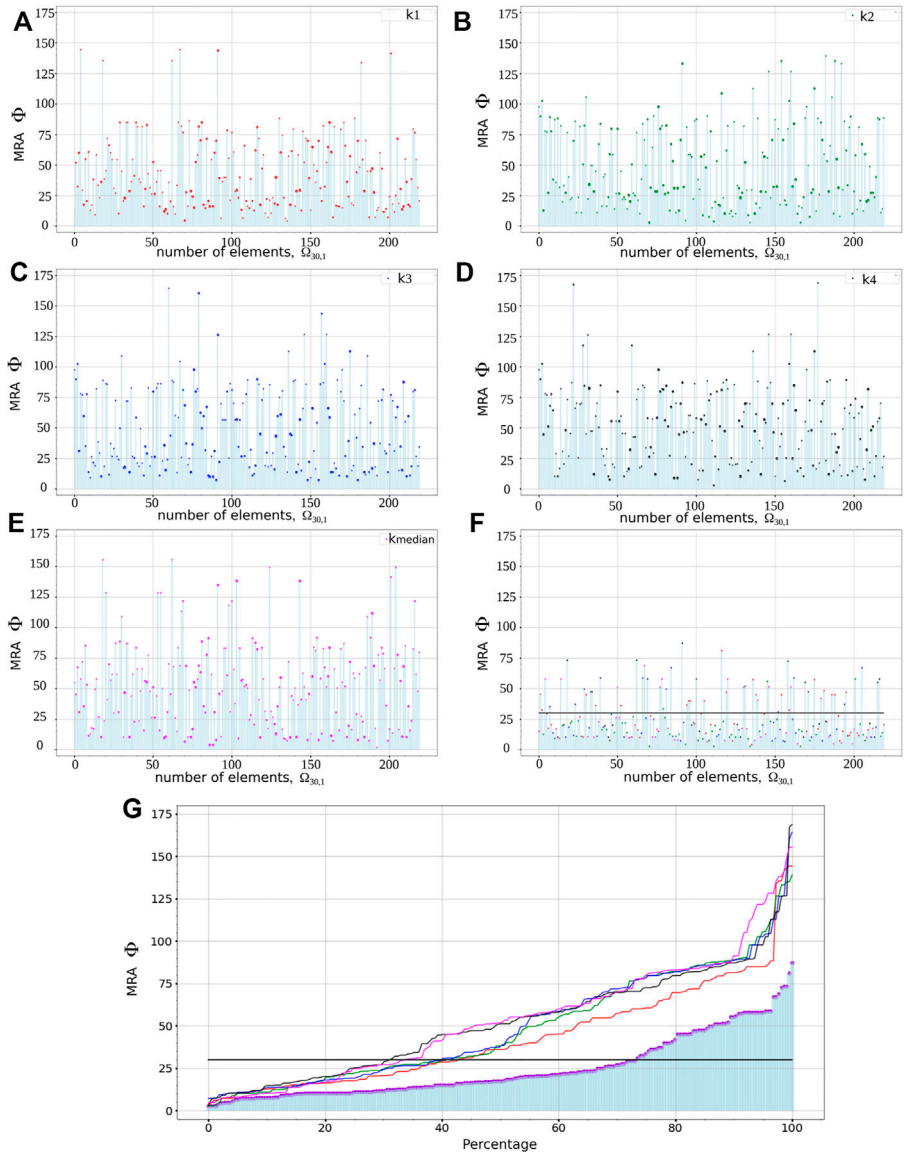


**FIGURE 6 |** Statistical metrics results in the New Zealand region. Each subplot depicts the Φ computed for each *new*-event *vs*. the four nearest neighbors *k1* **(A)**, *k2* **(B)**, *k3* **(C)**, *k4* **(D)**, and *k*-Median **(E)**. The minimum values between these five statistical solutions are depicted in subplot **(F)** where the horizontal line indicates the threshold $\Phi < 30^{\circ}$. **(G)** shows the ordered values of the other subplots in same colors except the dark-violet that corresponds to the minimum value in subplot **(F)**.

## 3.1 Methodology at a Glance

The proposed methodology to estimate an FM solution is based on spatial properties. Thus, once the hypocentral location of the new event with an unknown FM solution is available, we select a spherical neighborhood centered at its hypocentral location. Previous events inside this neighborhood will then be used to suggest different FM solutions. In this work we propose two different methods for this:

(a) The first method is based on spatial assumptions and uses the hypocentral Euclidean distance Δ as a metric to quantify the distance between the new event and each of its neighbors. To measure it, we apply the Haversine formula that determines the great circle distance between two points (Sinnott 1984),

$$d = 2R \arcsin\left(\sqrt{\sin^2\frac{(\psi_2-\psi_1)}{2} + \cos(\psi_1)\cos(\psi_2)\sin^2\frac{(\lambda_2-\lambda_1)}{2}}\right) \tag{4}$$

Where $R$ is the radius of the Earth, and $\psi_1, \psi_2$, and $\lambda_1, \lambda_2$ are the latitude and longitude coordinates of two points, respectively. Once $d$ is computed, the Euclidean distance from the new event to

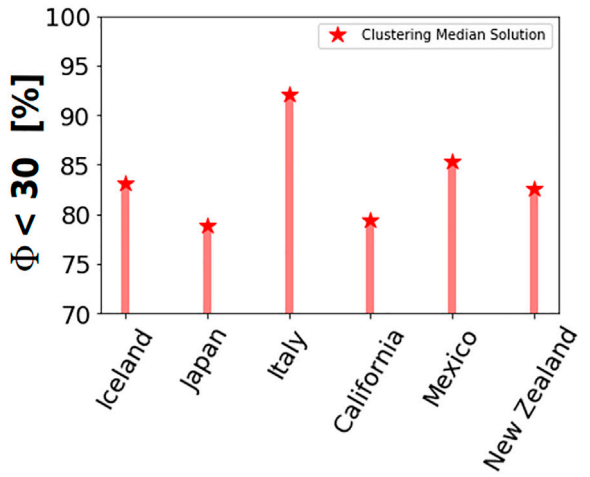


**FIGURE 7 |** Statistical results of the DBSCAN algorithm. The percentage considers the subset $\Omega_3$ where the median FM from at least one predicted cluster has $\Phi < 30^{\circ}$.

each neighbor is given by $\Delta = \sqrt{d^2 + z^2}$, where $z$ is the difference in depth. Therefore, we select the four nearest neighbors (hereafter denoted as $k1$, $k2$, $k3$, $k4$) from the closest to the farthest, respectively. Here, we assume that these four nearest earthquakes could have occurred under similar geological and tectonic conditions or under similar faulting type. Therefore, this method gives four FM solutions coming from the solutions of the four closest neighbors. The number four is an empirically motivated choice, found to produce useful results in the statistical analyses presented later. Additionally, we compute a median FM solution from all neighbors in the sphere. This median value is computed using the three angles $\phi_i$, $\delta_i$, and $\lambda_i$, where $i$ is related to each the $i$-neighbors. This fifth FM solution, named $k - median$ could be related with a "typical" faulting type in that region. To apply this method we consider a minimum of one neighbor ($n = 1$) inside the sphere.

(b) The second method is based on the DBSCAN clustering algorithm. To apply this algorithm, we select four features, the distance from each neighbor to the hypocenter of the new event, and also the three angles of the FM of each neighbor. Once the algorithm automatically detects the clusters, we compute the position of each centroid, as well as the FM solution from the median of $\phi_x$, $\delta_x$, and $\lambda_x$ from the events that belong to each $x$ cluster. The number of solutions depends on the number of clusters detected in the DBSCAN algorithm. It is worth noting that a minimum number of neighbors to apply the cluster algorithm should be assumed. Hence, in this application we take a minimum of three neighbors ($n = 3$). The clusters automatically detected could reflect information about different regional tectonic features.

**TABLE 3 |** Earthquakes analyzed using the statistical methodology proposed in this work (see. **section 4**).

| Region | $M_w$ | Date | Hypocentral Location (lon,lat,depth) | $d$th [km] |
|---|---|---|---|---|
| New Zealand | 5.0 | 30/11/2018 4:17 | 166.12, -45.57, 31.5 km | 80 |
| Japan | 5.2 | 1/6/2011 3:14 | 143.84, 39.79, 14.4 km | 80 |
| California | 5.3 | 28/10/2019 11:01 | -125.9, 41.91, 15.0 km | 80 |
| Iceland | 4.8 | 29/5/2009 21:33 | -22.52, 63.82, 12.7 km | 70 |
| Italy | 5.2 | 20/5/2012 13:18 | 11.49, 44.81, 12 km | 80 |
| Mexico | 7.4 | 23/6/2020 15:29 | -96.06, 16.04, 20 km | 60 |

## 3.2 Methodology Application

To apply the methods described in the previous subsection we follow a step-by-step process

The first step is the compilation of suitable datasets. For this, we access moment tensor information of each selected region, summarized in **Table 1**, through the IRIS-SPUD website 1 (Trabant et al., 2012). We perform an exploratory study to visualise the statistical FM distribution using Kaverina diagrams (Kaverina et al., 1996) which classify events according to their double-couple (DC) rupture type. **Figure 3** shows the Kaverina diagrams for each study region using the visualizing tool developed in (Álvarez-Gómez 2019). Clearly dominant rupture types are observed in some regions, for example, strike-slip events in California, or normal faulting in Iceland. Other regions, such as New Zealand, Mexico and Japan, depict a larger variety of rupture types. The main purpose of visualizing historical datasets in Kaverina diagrams is to know the rupture-type at each region. This information is useful for the interpretation of results in the following section.

In the second step, we perform a statistical analyses using the two methods described in the previous subsection. This statistical evaluation aims to test the proposed methodology using each earthquake in the dataset as an independent observation, considering them as a hypothetical new event with unknown FM. Moreover, the statistical analysis allows us to quantify the accuracy of the proposed methodology by means of the MRA computed between the proposed and the original solution. In this work, we choose an MRA threshold value of $\Phi_{th} = 30^{\circ}$ (Triantafyllis 2014; Kagan 2007), below which two FM solutions are deemed sufficiently similar, suggesting that the proposed one may indeed be used as a first guess for the new earthquake with unknown FM solution. This value is motivated by earlier studies on the similarity between FM solutions (Triantafyllis et al., 2013, Triantafyllis et al., 2016; Altunel and Pinar 2021), and by the observation that differences between FM solutions for an earthquake provided by different agencies are typically below $\Phi = 30^{\circ}$. From this point of view both methods described in the previous subsection can be considered supervised

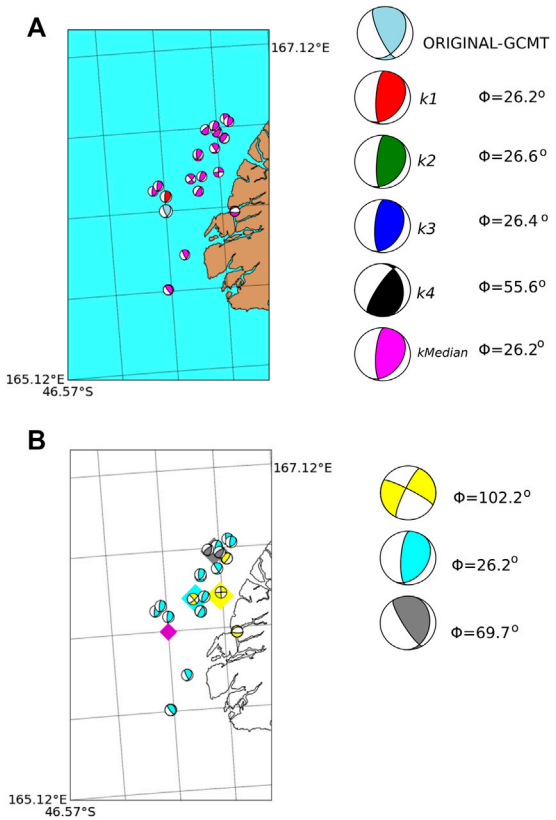


**FIGURE 8 | (A)** Nearest neighbor solutions for a particular example in New Zealand (see **Table 3**). The map shows the location and focal mechanism of the test event (light-blue) and its neighbors. From closer to farther solutions, *k*1 (red beachball), *k*2 (green), *k*3 (dark-blue), *k*4 (black), and *k* – *median* (magenta). The MRA values Φ, listed to the right, measure the differences between each neighbor and the test event solution. **(B)** DBSCAN results for the same earthquake of **Figure 8A** in light-blue. The magenta diamond indicates its epicentral location. The beach balls with the same color belong to the same cluster defined by the DBSCAN algorithm. The centroids of each cluster are shown in diamond markers of the corresponding color. Those centroids are computed as the mean value of the latitude, longitude and depth from each event in the cluster. At the right side the median FM solutions computed in each cluster are shown. The MRA value Φ relative to the test-event is also indicated.

techniques, because the FM solution for the *new*-event is already known.

As previously mentioned, each method requires a minimum number of neighbors around the new event. At least three neighbors, $n = 3$, for the DBSCAN algorithm, and one neighbor, $n = 1$, for the hypocentral Euclidean distance. In the following, we will denote by $\Omega_n$ the number of events in the dataset that fulfill the requirement of having a minimum of $n$ neighbors.

In the third, step we optimize the neighborhood size. Trying to find an optimal size, we modify the radius $d$th of the spherical neighborhood. To find the optimum $d$th, we repeat the previous step, increasing the neighborhood radius after testing all the events in the dataset. We start with a radius of 20 km, and increase up to 200 km in 10 km steps. An optimum $d$th value must satisfy two conditions:

(1) a large number of events in the dataset with at least one neighbor inside the sphere, that is, a large $\Omega_1$,
(2) and a large percentage of events with at least one neighbor with $\Phi < 30^{\circ}$.

In **Figure 4**, we exemplify this search for an optimal $d$th. Blue bars indicate the percentage of events with at least one solution with $\Phi < 30^{\circ}$. The red triangles depict the percentage of events in the dataset considered in the analysis, i.e., events with at least one neighbor inside the sphere ($\Omega_1$). For all regions, as the neighborhood size increases, the percentage of spheres with at least one neighbor increases until an inflection point, beyond which it remains constant. We consider this inflection point as the threshold size $d$th. This indicates that, although the neighborhood size increases (and thus the number neighbors), the similarities between FM solutions are not further improved. Therefore, the optimal radius of the sphere maximizes both percentages at the same time, as indicated by the orange ellipse in **Figure 4**.

To study how the minimum magnitude $M$th in a dataset modifies the threshold radius $d$th, we repeat the same analysis considering different $M$th values. However, this analysis is possible only for large catalogs, such as for the Japan and Mexico datasets. **Table 2** depicts the selected $d$th values for each region.

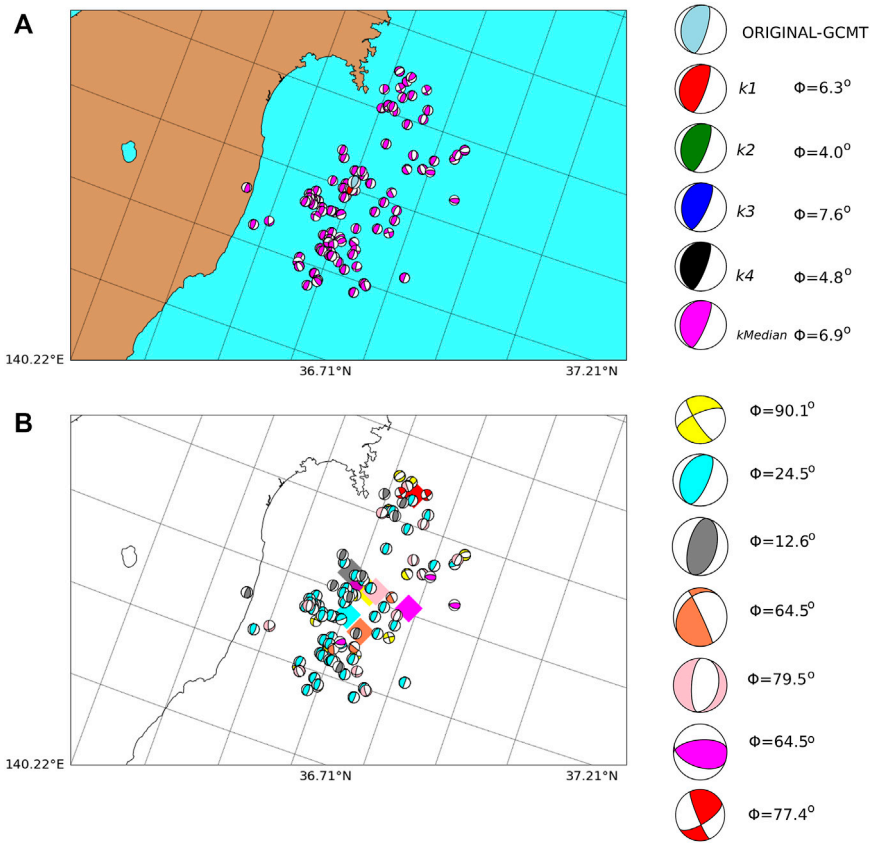


**FIGURE 9 |** Same as **Figure 8** for an $M_w$ = 5.2 Japanese earthquake (see **Table 3**).

## 4 STATISTICAL AND CLUSTERING RESULTS

In the first part of this section we present the results of the two methods applied to the selected regions. This will be followed in the second part by specific examples for selected earthquakes in each region.

**Table 2** shows the main results of the statistical analysis for each region. It is worth noting that for a similar *M*th the radius *d*th is similar to with few tens of kilometers for different regions. Also, as *M*th increases, the radius *d*th becomes larger. The statistical results indicate that around 70–85% of the tested events have an FM solution similar to those computed in the GCMT catalog ($\Phi < 30$). This percentage range is accomplished for both, the clustering algorithm and the spatial metrics. Moreover in the regions with similar rupture types, such as California, Mexico, Japan or Iceland (**Figure 3**), this percentage increases. On the other hand, this similarity decreases in regions where the faulting types are more diverse, including New Zealand and Italy. In the datasets with few events such Italy, performance of both methods is lower because the neighborhood tends to have scarce data, thereby preventing improvements of the statistics.

**Figures 5A–F** shows the MRA histograms for each region, obtained with the statistical metrics ($\Omega_{th,1}$). We observe that the MRA distribution is clearly skewed towards low MRA values, mostly reaching $\Phi < 30$.

In **Figure 6**, a detailed plot shows the behavior of $\Phi_{(30,\ 1)}$ considering the nearest neighbors and the median statistical solution for New Zealand. **Figure 6G** shows the ordered $\Omega$ values obtained in the (a-f) subplots. In dark-violet the minimum value between *k*1, *k*2, *k*3, *k*4 and *k* − *median* is depicted, from there is easy to observe how the FM solutions is improved.

In general, the nearest neighbor, *k*1, is the most likely to provide a similar FM solution. This is expected because nearby earthquakes are likely to rupture the same fault or under similar tectonic regimens. However, we also observe that the median FM solution produce MRA of $\Phi < 30^{\circ}$. In those cases, most neighbors have similar rupture types than the new-event. Moreover, in some cases, also another neighbors (*k*2, *k*3, *k*4), show a smaller $\Phi$ than *k*1. This could be related to hypocenter location uncertainties.

Statistical results of the DBSCAN algorithm are shown in **Figure 7** for each region. The percentages shown in this figure consider that at least one FM solution computed using the median values in each cluster has $\Phi < 30^{\circ}$, for events with at least three neighbors ($\Omega_3$). The median FM solutions are computed by using the events belonging to each automatically detected cluster. We observe that the DBSCAN algorithm

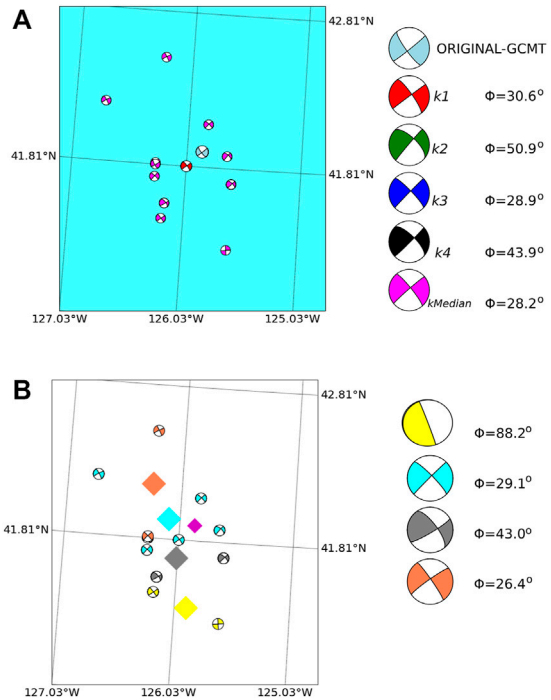


**FIGURE 10 |** Same as **Figure 8** for an $M_w$ = 5.3 Californian earthquake (see **Table 3**).

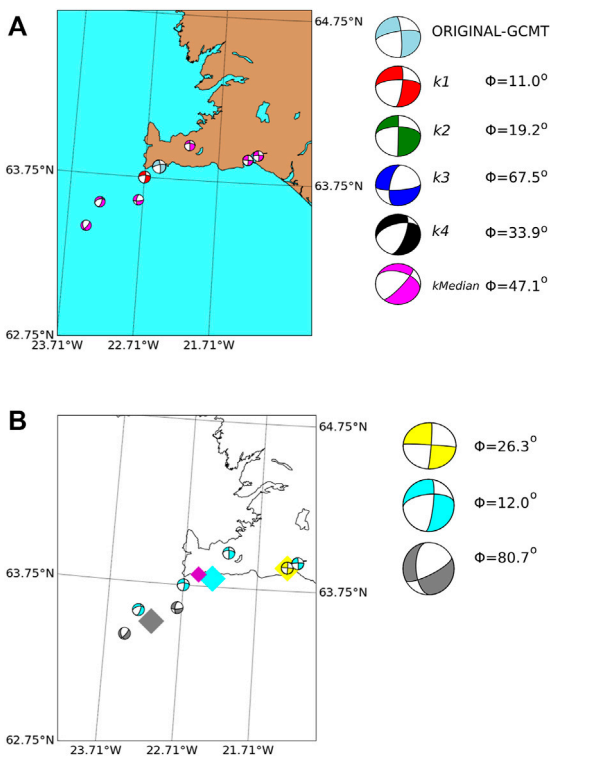


**FIGURE 11 |** Same as **Figure 8** for an $M_w$ = 4.8 Icelandic earthquake (see **Table 3**).

computes similar percentages to the nearest neighbors statistics for those events that fulfill the number of neighbors $\Omega_3$.

## 4.1 Examples of the Methodology for Selected Regions

In this section, we apply the method presented above to specific earthquakes in different regions. From the databases we randomly choose one test event with at least three neighbors inside the sphere of size *d*th. The selected earthquakes are listed in **table 3**.

New Zealand **Figure 8A** shows the spatial epicentral locations and focal mechanisms of the test event, it neighbors inside the sphere, and the median event. and their focal mechanism in magenta color is plotted. The closest neighbor is shown in red. In this example, we obtain MRA values of $\Phi < 30^{\circ}$ for the three nearest events *k*1, *k*2 and *k*3, and for the median event *k* – *median*.

The DBSCAN clustering results are presented in **Figure 8B**. The different colors indicate the clusters detected in the DBSCAN algorithm and the diamonds mark their respective cluster-centroid locations. In this particular example, the smallest cluster has the more similar FM solution to the test event.

Japan The dataset of the Japan region is the largest in our analysis. We also choose randomly an earthquake with more than three neighbors inside a sphere of radius *d*th = 80 *km* size. Our threshold magnitude in this example is 5.0.

The hypocentral locations and focal mechanisms of the test event and its four nearest neighbors are displayed in **Figure 9**. In this example, the similarity is high for all neighbors. This is also

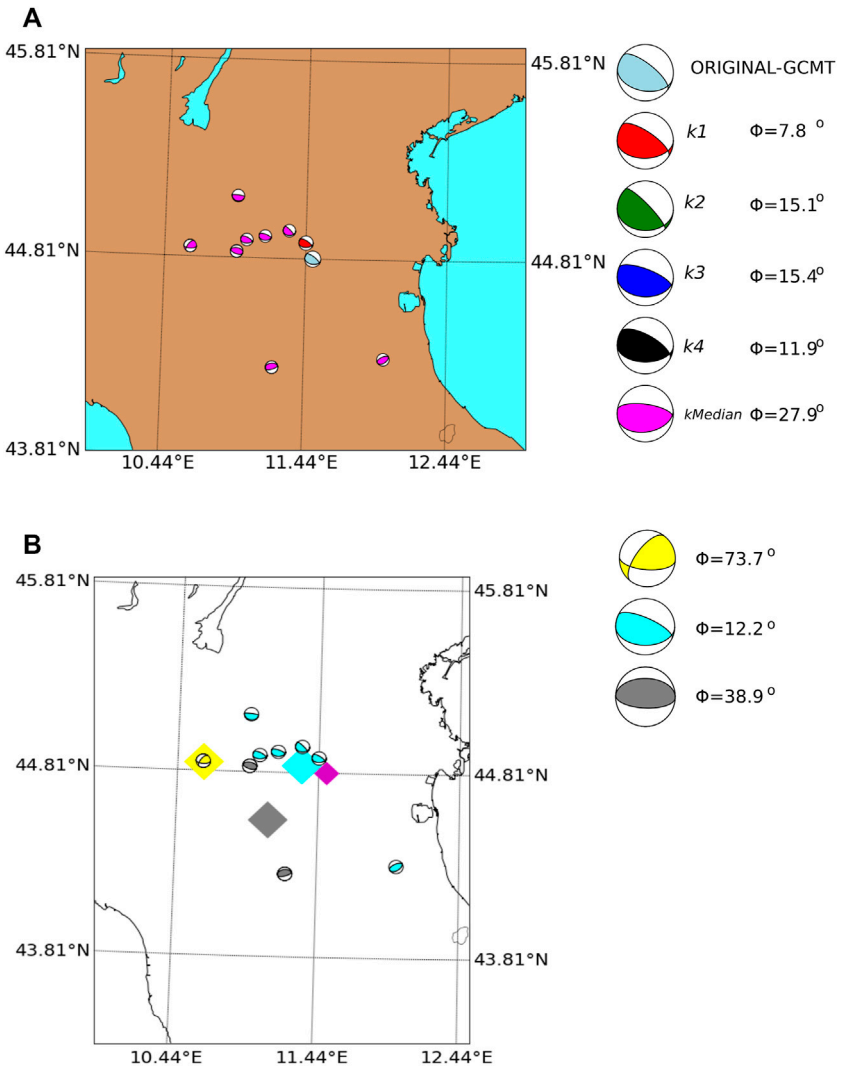


**FIGURE 12 |** Same as **Figure 8** for an $M_w$ = 5.2 Italian earthquake (see **Table 3**).

reflected in the clustering algorithm which detects three clusters. Is worth to note that the clustering algorithm joins in the yellow cluster different event solutions. Let us keep in mind that the objective of cluster analysis is to generalize the solution model, thus, some individual events may be misclassified, which does not diminish the contribution of the solution. The generalization seeks to have good classification of spatial events in the general population of events, and low error rates do not mean perfect classification. However, it is important to note that the rest of the clusters in **Figure 9** share many similarities between their elements reflecting a good clustering selection by the DBSCAN. The most similar median FM solution is for the larger cluster. These results could indicate similar geological patterns in that region, producing events with similar FM solutions.

California The California region shows a predominant strike-slip rupture style, as seen in **Figure 3**. The results of our method, displayed in **Figure 10**, reveal a similarity close to $\Phi < 30^{\circ}$. In this example, the $k$-median is the event with the lowest MRA. The cluster analysis gives three groups, with the largest cluster being the one with the closest centroid and the smallest median MRA.

Iceland In this example, the nearest neighbors metric offers a better solution for the closest neighbor $k1$ (see **Figure 11**). The clustering results also provide a good solution for the cluster with the closest centroid to the test event, thus indicating short-range similar tectonics over distances of few kilometers).

Italy The Italian region shows a predominantly normal and reverse rupture type distribution (**Figure 3**). However, this database has only 118 earthquakes, and so we consider all events provided in the GCMT catalog. In the example shown in **Figure 12**, we observe a large similarity between the selected earthquake and its neighbors, with the lowest MRA for the nearest neighbor $k1$. The results from the clustering algorithm

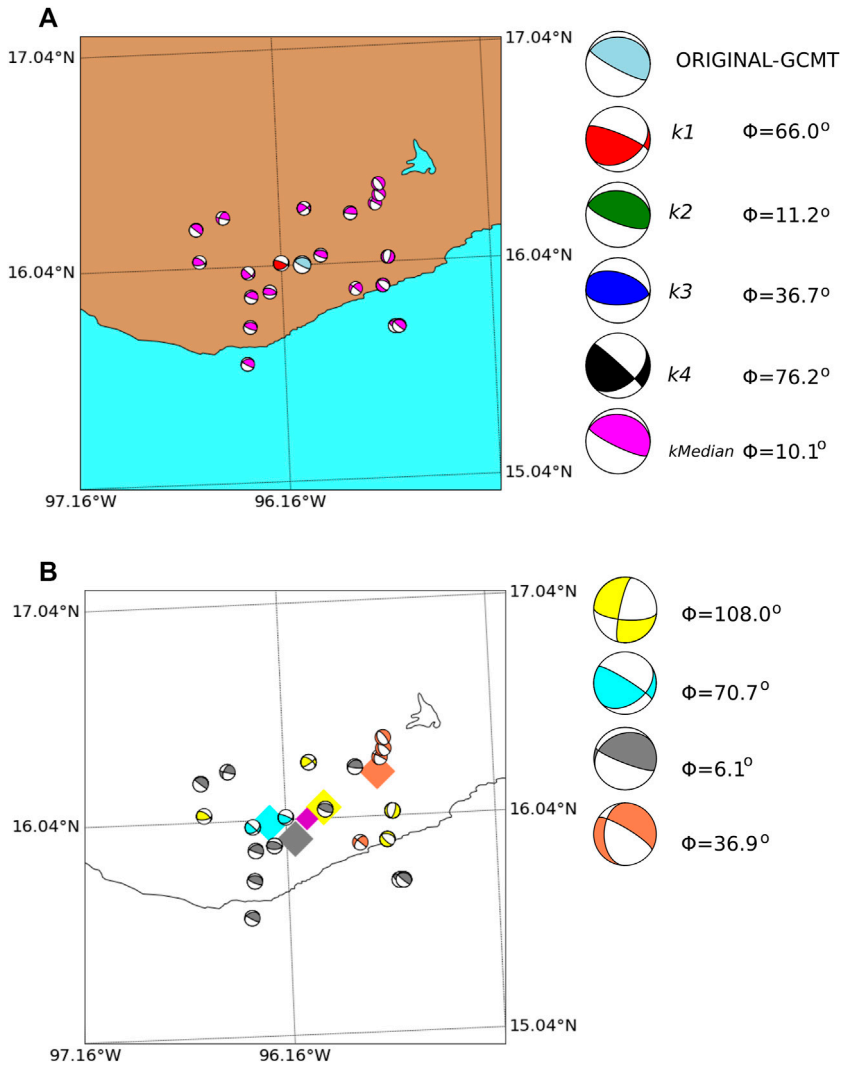


**FIGURE 13 |** Same as **Figure 8** for an $M_w$ = 7.4 Mexican earthquake (see **Table 3**).

also provide a similar solution for the larger cluster with the closest centroid.

Mexico The Mexican region has one of the largest datasets. The statistical results provide one event with $\Phi < 30^{\circ}$. In this particular example, we observe that the $k-$*median* neighbor gives the largest similarity (**Figure 13**). Moreover, the median FM of the largest cluster provides the most similar solution to the test event.

## 5 DISCUSSION AND CONCLUSION

In this work we propose an inversion-free approach to the fast estimation of FM solutions, primarily intended to serve as input for urgent seismic simulations or similar problems with computation deadlines. Within this context, the rapid estimation of source parameters is highly relevant. Moreover, the predictive power of historical datasets represents an opportunity that is worth being exploited. In particular, in this work we develop a methodology for the estimation of FM solutions that is based purely on past earthquakes. After statistically validating the experiments, we find some important advantages of this statistical estimation tool.

Firstly, the method is extremely fast, with time to solution at < 10 s. In terms of accuracy, comparing our results to those provided in Triantafyllis (2014) by the Scisola software, we observe similar statistics in the Kagan diagrams (**Figure 5**). We have used a threshold $\Phi \leq 30^{\circ}$ for MRA which is similar to the differences between various FM inversion results and published by different agencies. For example, in Scognamiglio et al. (2010), the authors estimated the FM solution for the 2009/04/06 Mw = 6.1 L'Aquila earthquake as [$\theta = 139$, $\delta = 48$, $\lambda = -87$] for nodal plane 1, and [$\theta = 314$, $\delta = 42$, $\lambda = -94$] for nodal plane 2. In contrast, the FM solution for the same earthquake given in the GCMT catalog was [$\theta = 120$, $\delta = 54$, $\lambda = -113$] for nodal plane 1, and [$\theta = 336$, $\delta = 42$, $\lambda = -62$] for nodal plane 2. In this case the MRA is $\Phi \approx 21^{\circ}$ for both nodal planes. The threshold of $\Phi \leq 30^{\circ}$

was also used in Triantafyllis (2014), where the authors mention that an acceptable agreement between FM solutions corresponds to MRA values of few tens of degrees. Nevertheless, we remark that the lowest MRA between the test event and the neighbors is not always provided by the closest event ($k1$). In fact, we observe that other neighbors, including the median event, may provide a better solution in terms of MRA.

Among the advantages of our method, it relies on catalog information about past events. This is in contrast to more traditional methods based on waveform analysis, hence our method is significantly faster. Among its disadvantages, with respect to classical CMT inversion, we can only estimate CMT from large events, which are more likely to behave similarly to other similar events in the catalog. For smaller events our approach loses precision. Moreover, non-DC components are ignored in our study, which is not very relevant for large earthquakes but definitely relevant for smaller-event catalogs. In addition, we acknowledge that the method relies in similarity among large earthquakes recorded in a particular region. If events are few or too dissimilar, our method would fail. Nevertheless, the predictive capacity of our method can be analyzed a priori for such a region and thus we can establish the method's suitability for the region beforehand.

As a conclusion, our method can provide with suitable CMT estimates, with statistically relevant accuracy, shortly after a large event is recorded. This enables the possibility or urgent computing of seismic hazard by means of physical simulations where directivity may be a significant component. We have tested our method in several regional contexts and analyzed its accuracy. The precision that can be attained depends strongly on the statistical distribution of large events in our study region's catalog but produces a starting point for analysis prior to the latter determination of the CMT by means of inversion, which supersedes our result.

In future works we will study the impact of CMT accuracy in ground motion values and intensity measures such as peak ground accelerations resulting from simulations. Similarly we will analyze means to improve the method's predictive capabilities by narrowing the choice of final CMT candidates.

## 5.1 Permission to Reuse and Copyright



## DATA AVAILABILITY STATEMENT

The datasets presented in this study can be found in online repositories. The names of the repository/repositories and accession number(s) can be found below: http://ds.iris.edu/spud/momenttensor.

## AUTHOR CONTRIBUTIONS

MM-V, JC-J, AF, and JP, contributed to conception and design of the study. MM-V, OR, and JR wrote the first draft of the manuscript. All authors contributed to manuscript revision, read, and approved the submitted version.

## FUNDING

The research leading to these results has received funding from the European Union's Horizon 2020 research and innovation programme under the grant agreement no. 823844, the Center of Excellence for Exascale in Solid Earth (ChEESE CoE Project).

## ACKNOWLEDGMENTS

MM-V, JR, OR, AF, JP, thank the ChEESE CoE Project.

## REFERENCES

Aki, K., and Richards, P. G. (2002). *Quantitative Seismology the City*. 2nd ed. Sausalito, CA: University Science Books.

Altunel, E., and Pinar, A. (2021). Tectonic Implications of the Mw 6.8, 30 October 2020 Kuşadası Gulf Earthquake in the Frame of Active Faults of Western Turkey. *Turkish J. Earth Sci.* 30, 436–448. doi:10.3906/yer-2011-6

Álvarez-Gómez, J. A. (2019). FMC-earthquake Focal Mechanisms Data Management, Cluster and Classification. *SoftwareX* 9, 299–307. doi:10.1016/j.softx.2019.03.008

Baker, J. W. (2008). An Introduction to Probabilistic Seismic hazard Analysis (Psha). *White paper*, 72. version 1.

Duputel, Z., Rivera, L., Kanamori, H., and Hayes, G. (2012). W Phase Source Inversion for Moderate to Large Earthquakes (1990-2010). *Geophys. J. Int.* 189, 1125–1147. doi:10.1111/j.1365-246x.2012.05419.x

Dziewonski, A. M., Chou, T.-A., and Woodhouse, J. H. (1981). Determination of Earthquake Source Parameters from Waveform Data for Studies of Global and Regional Seismicity. *J. Geophys. Res.* 86, 2825–2852. doi:10.1029/jb086ib04p02825

Dziewonski, A. M., and Woodhouse, J. H. (1983). An experiment in Systematic Study of Global Seismicity: Centroid-Moment Tensor Solutions for 201 Moderate and Large Earthquakes of 1981. *J. Geophys. Res.* 88, 3247–3271. doi:10.1029/jb088ib04p03247

Ekström, G., Nettles, M., and Dziewoński, A. M. (2012). The Global CMT Project 2004-2010: Centroid-Moment Tensors for 13,017 Earthquakes. *Phys. Earth Planet. Interiors* 200-201, 1–9. doi:10.1016/j.pepi.2012.04.002

Ester, M., Kriegel, H.-P., Sander, J., and Xu, X. (1996). A Density-Based Algorithm for Discovering Clusters in Large Spatial Databases with Noise. *Kdd* 96, 226–231.

Frohlich, C. (1996). Cliff's Nodes Concerning Plotting Nodal Lines for P, Sh and Sv. *Seismological Res. Lett.* 67, 16–24. doi:10.1785/gssrl.67.1.16

Kagan, Y. Y. (2007). Simplified Algorithms for Calculating Double-Couple Rotation. *Geophys. J. Int.* 171, 411–418. doi:10.1111/j.1365-246x.2007.03538.x

Kaverina, A. N., Lander, A. V., and Prozorov, A. G. (1996). Global Creepex Distribution and its Relation to Earthquake-Source Geometry and Tectonic Origin. *Geophys. J. Int.* 125, 249–265. doi:10.1111/j.1365-246x.1996.tb06549.x

Lin, J.-T., Chang, W.-L., Melgar, D., Thomas, A., and Chiu, C.-Y. (2019). Quick Determination of Earthquake Source Parameters from Gps Measurements: a Study of Suitability for Taiwan. *Geophys. J. Int.* 219, 1148–1162. doi:10.1093/gji/ggz359

Maeda, N. (1992). A Method of Determining Focal Mechanisms and Quantifying the Uncertainty of the Determined Focal Mechanisms for Microearthquakes. *Bull. Seismological Soc. America* 82, 2410–2429.

Melgar, D., Bock, Y., and Crowell, B. W. (2012). Real-time Centroid Moment Tensor Determination for Large Earthquakes from Local and Regional Displacement Records. *Geophys. J. Int.* 188, 703–718. doi:10.1111/j.1365-246x.2011.05297.x

Mulargia, F., Stark, P. B., and Geller, R. J. (2017). Why Is Probabilistic Seismic hazard Analysis (Psha) Still Used? *Phys. Earth Planet. Interiors* 264, 63–75. doi:10.1016/j.pepi.2016.12.002

Satopaa, V., Albrecht, J., Irwin, D., and Raghavan, B. (2011).Finding a" Kneedle" in a Haystack: Detecting Knee Points in System Behavior. In 2011 31st international conference on distributed computing systems workshops. IEEE, 166–171. doi:10.1109/icdcsw.2011.20

Scognamiglio, L., Tinti, E., Michelini, A., Dreger, D. S., Cirella, A., Cocco, M., et al. (2010). Fast Determination of Moment Tensors and Rupture History: What Has Been Learned from the 6 April 2009 L'Aquila Earthquake Sequence. *Seismological Res. Lett.* 81, 892–906. doi:10.1785/gssrl.81.6.892

Sinnott, R. W. (1984). Virtues of the Haversine. *Sky Telesc* 68, 159.

Sokos, E. N., and Zahradnik, J. (2008). Isola a Fortran Code and a Matlab Gui to Perform Multiple-point Source Inversion of Seismic Data. *Comput. Geosciences* 34, 967–977. doi:10.1016/j.cageo.2007.07.005

Stierle, E. (2015). *Non-Double-Couple Components in Moment Tensors of Aftershock Seismicity and Laboratory Earthquakes*. Ph.D. thesis.

Tarantino, S., Colombelli, S., Emolo, A., and Zollo, A. (2019). Quick Determination of the Earthquake Focal Mechanism from the Azimuthal Variation of the Initial P-Wave Amplitude. *Seismological Res. Lett.*

Trabant, C., Hutko, A. R., Bahavar, M., Karstens, R., Ahern, T., and Aster, R. (2012). Data Products at the Iris Dmc: Stepping Stones for Research and Other Applications. *Seismological Res. Lett.* 83, 846–854. doi:10.1785/0220120032

Triantafyllis, N. (2014). *Scisola: Automatic Moment Tensor Solution for SeisComP3*. Master's thesis. Patras: School of Engineering, Computer Engineering Informatics Departme.

Triantafyllis, N., Sokos, E., and Ilias, A. (2013). Automatic Moment Tensor Determination for the Hellenic Unified Seismic Network. *Bull. Geol. Soc. Greece* 47, 1308–1315.

Triantafyllis, N., Sokos, E., and Ilias, A. (2016). Scisola: Real-Time Moment Tensor Monitoring for Seiscomp3. *Bull. Geol. Soc. Greece* 50, 1120–1129.

Triantafyllis, N., Venetis, I., Fountoulakis, I., Pikoulis, E.-V., Sokos, E., and Evangelidis, C. (2021). *Gisola: Real-Time Moment Tensor Computation Optimized for Multicore and Manycore Architectures. Tech. Rep.* Copernicus Meetings.

Udias, A., and Buforn, E. (2017). *Principles of Seismology*. Cambridge University Press.

Vannucci, G., Pondrelli, S., Argnani, A., Morelli, A., Gasperini, P., and Boschi, E. (2004). An Atlas of Mediterranean Seismicity. *Ann. Geophys.* 47.

Wald, D. J., Quitoriano, V., Heaton, T. H., Kanamori, H., Scrivner, C. W., and Worden, C. B. (1999). Trinet "Shakemaps": Rapid Generation of Peak Ground Motion and Intensity Maps for Earthquakes in Southern california. *Earthquake Spectra* 15, 537–555. doi:10.1193/1.1586057

Wald, D., Lin, K.-W., Porter, K., and Turner, L. (2008). Shakecast: Automating and Improving the Use of Shakemap for post-earthquake Decision-Making and Response. *Earthquake Spectra* 24, 533–553. doi:10.1193/1.2923924

Wang, R., Gu, Y. J., Schultz, R., and Chen, Y. (2018). Faults and Non-double-couple Components for Induced Earthquakes. *Geophys. Res. Lett.* 45, 8966–8975. doi:10.1029/2018gl079027

Weber, B., Becker, J., Hanka, W., Heinloo, A., Hoffmann, M., Kraft, T., et al. (2007). Seiscomp3—automatic and Interactive Real Time Data Processing. *Geophys. Res. Abstr.* 9, 219.

**Conflict of Interest:** The authors declare that the research was conducted in the absence of any commercial or financial relationships that could be construed as a potential conflict of interest.

**Publisher's Note:** All claims expressed in this article are solely those of the authors and do not necessarily represent those of their affiliated organizations, or those of the publisher, the editors and the reviewers. Any product that may be evaluated in this article, or claim that may be made by its manufacturer, is not guaranteed or endorsed by the publisher.

frontiers | Frontiers in Earth Science

TYPE Original Research
PUBLISHED 23 September 2022
DOI 10.3389/feart.2022.941789



OPEN ACCESS

EDITED BY
Mark Bebbington,
Massey University, New Zealand

REVIEWED BY
Alberto Armigliato,
Alma Mater Studiorum—Università di Bologna, Italy
Karoly Nemeth,
Massey University, New Zealand

*CORRESPONDENCE
Beatriz Martínez Montesinos,
beatriz.martinez@ingv.it

SPECIALTY SECTION
This article was submitted to Geohazards and Georisks, a section of the journal Frontiers in Earth Science

RECEIVED 11 May 2022
ACCEPTED 22 August 2022
PUBLISHED 23 September 2022

CITATION
Montesinos BM, Luzón MT, Sandri L, Rudyy O, Cheptsov A, Macedonio G, Folch A, Barsotti S, Selva J and Costa A (2022), On the feasibility and usefulness of high-performance computing in probabilistic volcanic hazard assessment: An application to tephra hazard from Campi Flegrei. *Front. Earth Sci.* 10:941789. doi: 10.3389/feart.2022.941789



# On the feasibility and usefulness of high-performance computing in probabilistic volcanic hazard assessment: An application to tephra hazard from Campi Flegrei

Beatriz Martínez Montesinos[1]*, Manuel Titos Luzón[2], Laura Sandri[1], Oleksandr Rudyy[3], Alexey Cheptsov[3], Giovanni Macedonio[4], Arnau Folch[5,6], Sara Barsotti[2], Jacopo Selva[1] and Antonio Costa[1]

[1]Istituto Nazionale di Geofisica e Vulcanologia, Bologna, Italy, [2]Icelandic Met Office, Reykjavík, Iceland, [3]High-Performance Computing Center Stuttgart, Stuttgart, Germany, [4]Istituto Nazionale di Geofisica e Vulcanologia, Naples, Italy, [5]Barcelona Supercomputing Center, Barcelona, Spain, [6]Geociencias Barcelona (GEO3BCN), CSIC, Barcelona, Spain

For active volcanoes, knowledge about probabilities of eruption and impacted areas becomes valuable information for decision-makers to develop short- and long-term emergency plans, for which probabilistic volcanic hazard assessment (PVHA) is needed. High-resolution or spatially extended PVHA requires extreme-scale high-performance computing systems. Within the framework of ChEESE (Center of Excellence for Exascale in Solid Earth; www.cheese-coe.eu), an effort was made to generate exascale-suitable codes and workflows to collect and process in some hours the large amount of data that a quality PVHA requires. To this end, we created an optimized HPC-based workflow coined PVHA_HPC-WF to develop PVHA for a volcano. This tool uses the Bayesian event tree methodology to calculate eruption probabilities, vent-opening location(s), and eruptive source parameters (ESPs) based on volcano history, monitoring system data, and meteorological conditions. Then, the tool interacts with the chosen hazard model, performing a simulation for each ESP set or volcanic scenario (VS). Finally, the resulting information is processed by proof-of-concept-subjected high-performance data analytics (HPDA) scripts, producing the hazard maps which describe the probability over time of exceeding critical thresholds at each location in the investigated geographical domain. Although PVHA_HPC-WF can be adapted to other hazards, we focus here on tephra (i.e., lapilli and ash) transport and deposition. As an application, we performed PVHA for Campi Flegrei (CF), Italy, an active volcano located in one of the most densely inhabited areas in Europe and under busy air traffic routes. CF is currently in unrest, classified as being in an attention level by the Italian Civil Protection. We consider an approximate 2,000 × 2,000 × 40 km computational domain with 2 km grid resolution in the horizontal and 40 vertical levels, centered in

CF. To explore the natural variability and uncertainty of the eruptive conditions, we consider a large number of VSs allowing us to include those of low probability but high impact, and simulations of tephra dispersal are performed for each of them using the FALL3D model. Results show the potential of HPC to timely execute a vast range of simulations of complex numerical models in large high-resolution computational domains and analyze great volumes of data to obtain quality hazard maps.

KEYWORDS

**HPC, probabilistic volcanic hazard assessment, ash dispersal, exascale computing, Bayesian event tree, performance optimization and productivity, workflow manager, Campi Flegrei**

# 1 Introduction

Volcanic eruptions can cause a wide variety of hazardous phenomena, with impacts ranging from proximal to global scales. For instance, during explosive eruptions (Newhall and Hoblitt, 2002; Jenkins et al., 2014), volcanoes can inject large volumes of fragmented pyroclasts (tephra), which disperse into the atmosphere under the effects of turbulence and prevailing winds, and deposit up to thousands of km from the volcano (Martin and Nemeth, 2007). Pyroclasts can range in size from several cm to a few μm. Depending upon their size, they can persist in the atmosphere for a few seconds or for several days and can represent a serious threat when an eruption occurs near inhabited areas or to air traffic routes in very distal regions. The finest fraction of tephra (i.e., PM10, with a diameter smaller than 10 μm) can be inhaled by humans and animals, and the fraction with a diameter smaller than 4 μm (called respirable) can be breathed into the alveolar region of the lung and has the greatest toxic potential (Horwell and Baxter, 2006). Exposure to high concentrations of fine tephra can have serious implications for human health and represents a serious hazard to consider in the presence of explosive volcanoes (Damby et al., 2013). Eventually, tephra fallout may affect a variety of infrastructures that are essential for our daily lives all over the world. Examples are the road network, where a few-mm thick tephra deposit can create dangerous driving conditions (Blake et al., 2017); power plants and powerline transmissions (Wilson et al., 2012); transportation systems in general (Guffanti et al., 2010); contamination of water reservoirs and vegetation (Ágústsdóttir, 2015); telecommunication networks (Wilson et al., 2012). The adverse effect of volcanic ash (i.e., tephra smaller than 2 mm in size) on aircraft gas turbine engines is well known (Prata and Tupper, 2009; Chen and Zhao, 2015) and recently described more quantitatively (Clarkson et al., 2016). Fine ash can travel for thousands of km, extending the potential impact of explosive eruptions beyond borders and continents.

The quantification of tephra hazard is particularly relevant for volcanoes located close to large urban centers and/or to air traffic routes; the Neapolitan area in Southern Italy is one of those. Field-based hazard maps obtained from the study of the deposits of past eruptions and the eruptive history of specific volcanoes represent important information to assess volcanic hazards (Lirer et al., 2001; Alberico et al., 2002; Orsi et al., 2004). However, since volcanic processes are complex, that is, governed by many degrees of freedom (the number of independent parameters that define their state), their outcome is intrinsically unpredictable in terms of temporal occurrence and eruption parameters. For this reason, a probabilistic approach, that is able to integrate the uncertainty due to intrinsic stochasticity (aleatory uncertainty) and due to our limited knowledge of chemical-physical processes and system conditions (epistemic uncertainty), is more suitable than a deterministic approach, where randomness or uncertainty are not considered (Budnitz et al., 1997; Bonadonna et al., 2005; Macedonio et al., 2008; Marti et al., 2008; Neri et al., 2008; Folch et al., 2009; Marzocchi et al., 2010; Biasse et al., 2014; Marzocchi and Jordan, 2014; Barsotti et al., 2018; Selva et al., 2018; Marzocchi et al., 2021). PVHA is indeed the main tool for hazard and risk mitigation plans, as well as the main input to quantitative risk assessment (Spence et al., 2004; Zuccaro, 2008; Jenkins et al., 2014). Depending on the application, PVHA may be performed in the long-term by forecasting the hazard over long time windows (e.g., 50 years) as well as in the short-term by forecasting the hazard over shorter time windows (e.g., few hours). Long-term PVHA is the primary tool for long-term mitigation actions like evacuation plans or regulatory aspects of buildings (Marzocchi et al., 2008, 2010), while short-term PVHA (Selva et al., 2014) is more suitable for actions such as evacuation or air traffic management (for example, airport closure and rerouting).

PVHA can be defined as the quantification of the potential impact of a volcanic hazardous phenomenon generated by any possible volcanic eruption, evaluated at specific geographical points around the volcano, and quantified by the exceedance probability of a selected set of thresholds (e.g., tephra load at the ground or ash concentration at flight levels in case of tephra hazard) in a given time window (hours/days for short-term analyses or years/tens-of-years for long-term analyses). This information allows estimation of, for instance, the probability that the tephra deposit accumulated during an eruption exceeds

the critical condition that causes building collapse/failure, the probability that the ash cloud concentration exceeds the critical values for flight safety and with what persistence, or the probability that airports or important assets will be affected by the presence of ash (Sulpizio et al., 2012).

The performance of PVHA with physics-based fully resolved numerical models (e.g., FALL3D) is computationally expensive, as it ideally involves thousands to millions of simulation runs exploring the full natural variability of the source (eruption magnitude, intensity, vent position, etc.) and of the propagation conditions (wind distribution), also considering the epistemic uncertainty (alternative databases, alternative models, etc.). This problem has typically been solved by restricting the exploration of natural variability (e.g., with representative scenarios) or simplifying the modeling strategy (e.g., with analytical models or with restricted target grids), potentially introducing unwanted biases in the hazard estimates (Bonadonna et al., 2005; Sandri et al., 2016; Selva et al., 2018).

Advances at the computational level, particularly in high-performance computing (HPC) and high-performance data analytics (HPDA), already permit PVHA in a reasonable time (hours), with a sufficient level of detail to help civil protection officials and society for reliable risk ranking and assessment. Several works have been carried out in this direction. For instance, Folch and Sulpizio (2010) performed a long-term probabilistic assessment of volcanic ash hazard for Somma–Vesuvius (Italy) using a specific range of eruption parameters, and Titos et al. (2022) developed a long-term hazard assessment of ash dispersion at relevant flight levels for Jan Mayen (Norway) exploring a large set of possible combinations of eruptive parameters.

Herein, we present the probabilistic volcanic hazard assessment workflow (PVHA_HPC-WF) developed within the ChEESE project (www.cheese-coe.eu), an optimized numerical tool for developing short-term to long-term PVHA for a specific volcano. We then apply it to the Campi Flegrei caldera (CFc), Italy, considering a wide number of VSs for demonstrating the feasibility and potential usefulness of PVHA_HPC-WF to produce robust and unbiased tephra PVHA for end users such as civil protection agencies, aviation stakeholders, and other scientific institutions. To this end, first, the probabilistic methodology on which this study is based is outlined in Section 2. Section 3, then describes PVHA_HPC-WF in which this methodology is accommodated and illustrates how the workflow manager system light (WMS-light) and the performance optimization and productivity (POP) process have helped to make optimized codes and workflows. The test cases at Campi Flegrei are discussed in Section 4. Finally, the results are discussed, and some conclusions are drawn in Section 5. Although we also briefly explore the volcanological background, this work focuses on the probabilistic and computational methodology.

## 2 Probabilistic volcanic hazard analysis

The chain of processes leading to a volcanic eruption is complex (Marzocchi et al., 2004, 2008), implying that there are substantial and non-negligible uncertainties, stemming both from the intrinsic natural variability of such processes (so-called aleatory variability) and from the limitations of our models and observations (epistemic uncertainty). Probabilistic volcanic hazard analysis defines a set of variables, called intensity measures $X$, that describe the intensity of a given hazardous phenomenon $h$ and quantifies the so-called hazard curves $\theta$, which report the probability that $X$ exceeds the interest intensity values (thresholds) $x$ at a specific target point $\vec{a}$ = (latitude, longitude, altitude) at least once in a period of time $\Delta T$:

$$\theta^{(h,\vec{a},\Delta T)}(x) = P^{(h,\vec{a},\Delta T)}(X \geq x).$$

Statistically, this exceedance probability curve is a survivor function, describing the natural variability of the phenomenon at the site, that is, the aleatory uncertainty.

With the total probability theorem, hazard curves can be evaluated considering the contribution of a set of volcanic scenarios, that is,

$$\begin{aligned}\theta^{(h,\vec{a},\Delta T)}(x) &= P(\Delta T, E)\int_{\Omega} P(vs|E)\cdot P^{(h,\vec{a},\Delta T)}(X \geq x|vs)\mathrm{d}vs \\ &\approx P(\Delta T, E) \cdot \sum_{i}^{N}\left[P(VS_i|E)\cdot P^{(h,\vec{a},\Delta T)}(X \geq x|VS_i)\right],\end{aligned} \tag{1}$$

where $P(\Delta T, E)$ represents the probability of the occurrence of a general event eruption $E$ during the period of time $\Delta T$, and $\Omega$ represents the infinite set of possible source (vs) (e.g., magnitude and location) combinations that can be approximated with a finite set of $N$ specific volcanic scenarios. The factor $P^{(h,\vec{a},\Delta T)}(X \geq x|VS_i)$ evaluates the potential impact at the site $\vec{a}$ of each VS based on the model and thus is often called the propagation factor (in the insurance industry, this is normally known as the *footprint generator* because each realization of the model (propagator) generates a so-called *footprint*). As explained in the next section, the dependence of this factor on $\Delta T$ is related to the fact that the evaluation of this probability may change for smaller/larger $\Delta T$ (days vs. years). The other factors instead deal with the variability of the source, and they are thus collectively called source factors.

This representation is possible only if such scenarios represent a set of mutually exclusive and collectively exhaustive representations of the general event $E$, that is,

$$\sum_{i}^{N} P(VS_i|E) = 1,$$

which is approximately achieved by using as many randomly selected volcanic configurations as possible within the known ranges for each volcano. This formulation assumes that the

TABLE 1 Parameters of Gaussian functions used for Nodes 1 to 4 for the application of the PVHA_HPC-WF in Campi Flegrei.

| Node | Parameter | Value | Source |
|---|---|---|---|
| 1—unrest | Prior probability | 0.5 | Selva et al. (2012a) |
| | Lambda | 1 | |
| | Past data suc./tot | 7.4/306 | |
| 2—magmatic | Prior probability | 0.5 | Selva et al. (2012a) |
| | Lambda | 1 | |
| | Past data suc./tot | 0/0 | |
| 3—eruption | Prior probability | 0.33 | Selva et al. (2012a) |
| | Lambda | 1 | |
| | Past data suc./tot | 0/3.7 | |
| 4—vents | Number of vents | 40 | Selva et al. (2012b) |
| | Lambda | 2 | |
| | Prior probabilities | See Supplementary Material | |
| | Past data suc./tot | See Supplementary Material | |

probability of observing more than one eruption in $\Delta T$ is negligible and, under this condition, it holds for both long- and short-term PVHA.

The hazard curves are often computed conditional on the event $E$, in which case only the summation in Eq. 1 is evaluated, neglecting the temporal component $P$ ($\Delta T$, $E$). The obtained conditional volcanic hazard (cVH) curves have direct application to planning short-term risk mitigation actions during a volcanic crisis, such as the definition of evacuation areas.

In all cases, hazard curves are usually quantified on a set of points within the geographic area under study, and hazard/probability maps are produced to show the exceeded thresholds/probability distribution by cutting at a probability/critical-intensity value.

The evaluation of Eq. 1 involves studying the statistics (aleatory uncertainty) of the source (i.e., eruption scenarios) and the propagation of the hazard from the source to the target point (e.g., tephra dispersion). Multiple alternative models can be formulated, leading to alternative quantifications of $\theta^{(h,\vec{a},\Delta T)}(x)$. This uncertainty, named epistemic, is typically modeled by quantifying the variability of the hazard curves under a reasonable range of scientifically acceptable scientific models (Budnitz et al., 1997; Marzocchi and Jordan, 2014; Marzocchi et al., 2021).

## 2.1 Short-term and long-term probabilistic volcanic hazard assessment

PVHA can be focused on different scales for $\Delta T$ depending on the time horizon in which significant variations are expected in the activity of the volcano under study and on the type of potentially risk-reducing actions. We focus here on two different time scales: the short-term (ST) PVHA and the long-term (LT) PVHA. ST PVHA refers to a time window ranging from hours to weeks and is useful for crisis management during volcanic unrest (Sandri et al., 2012; Selva et al., 2014). LT PVHA considers years to decades and is interesting, for example, in the case of a quiescent volcano for land-use planning (Marti et al., 2008; Neri et al., 2008; Selva et al., 2010; Titos et al., 2022). The methods adopted in ST/LT PVHA are inherently linked to different sources of information used to issue an eruption forecast or to model the hazard (Marzocchi et al., 2008). For LT assessments, PVHA mostly relies on the historical and/or geological records of the volcano under study (or from analog volcanoes) and on expert opinion (e.g., Aspinall, 2006), as well as on the statistics for propagation conditions of the hazard we are assessing. For ST assessment, PVHA considers the actual and updated information coming from the monitoring system and other short-term forecast systems (e.g., weather).

Also, the information used to constrain propagation conditions may change for ST and LT PVHA. In the case of tephra hazard, ST and LT PVHAs rely on different information for the wind data: for the former, the present wind forecast is used to run the tephra dispersion model; for the latter, the climatology of wind over tens of years is used instead. This impacts the quantification of $p^{(h,a,\Delta T)}(X \geq x|V\,S_i))$ in Eq. 1, which in fact explicitly depends on $\Delta T$. Actually, the difference between ST and LT is the potential variability of the wind to be accounted for in the $\Delta T$. In the ST (few days), the possible meteorological scenarios (propagators) are strictly connected to wind forecasts, and only a rather small set of wind scenarios have practically non-zero probability, resulting in a smaller N. As $\Delta T$ increases, their variability necessarily increases because we move from forecast to seasonal climatology and finally to annual averages, and N should increase accordingly.

## 2.2 Probabilistic volcanic hazard assessment through Bayesian event tree analysis

The Bayesian event tree (BET) method can be used to calculate the long- and short-term probabilities of any volcanic phenomena

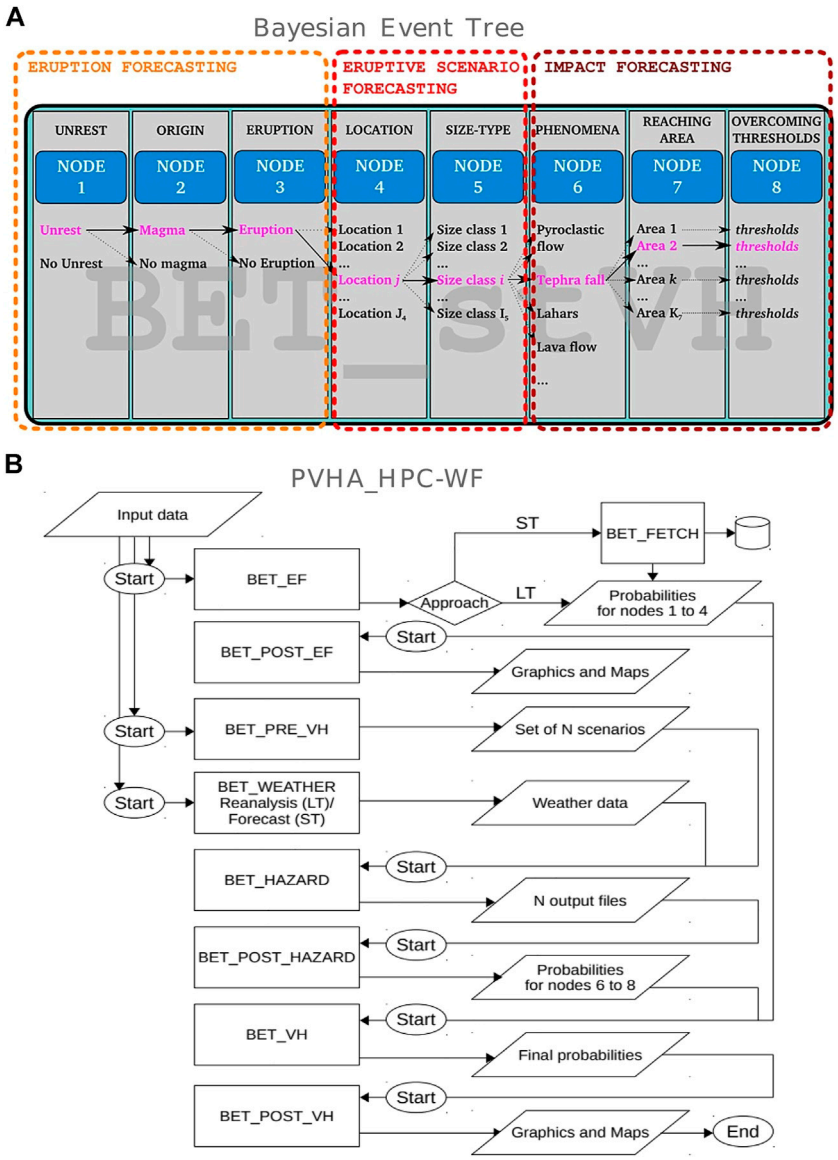


FIGURE 1
**(A)** Graphical representation of the Bayesian event tree methodology (BET) used in this work [image from Selva et al. (2014)]. **(B)** Flow diagram of the PVHA_HPC-WF.

(Eq. 1) by applying a Bayesian inference procedure (Newhall and Hoblitt, 2002; Marzocchi et al., 2004, 2008; Lindsay et al., 2010; Selva et al., 2010, 2014). Using a structured event tree, each volcanic event is represented by an individual branch which splits up into a set of possible subsequent events whose probabilities and uncertainties are estimated from prior information available from the volcanological information obtained from the history of a volcano, empirical and theoretical models, and monitoring observations.

Figure 1A shows a graphical representation of the BET used in this work (Selva et al., 2014). This event tree describes the possible evolution of an eruption in eight steps (nodes). Node 1 indicates the probability of unrest or not unrest within the time interval $\Delta T$, Node 2 gives the probability that, in the case of unrest, it is due to magma or to other causes, and Node 3 provides the probability that, in the case of unrest due to magma, the magma will trigger an eruption or not. The final eruption probability, representing the eruptive forecasting (EF), will then be calculated by a combination of Nodes 1, 2, and 3. Nodes 4 and 5 handle the VSs, dealing with variability in potential vent positions and size, respectively. Node 6 expresses the probability of generating or not generating a specific hazardous phenomenon $h$, Node 7 expresses the probability to reach or not to reach a site $\vec{a}$ by the hazardous phenomenon, and Node 8 provides the probability of

TABLE 2 PDFs and value ranges of the main eruptive parameters for CFc. Bounds on mass eruption rate (MER) values are a consequence of the sampling procedure for total erupted volume (TEV) and duration of the fallout phase described in this work. For the total grain size distribution (TGSD), we selected three different kinds of particles: juveniles, lithics, and crystals. To describe juvenile particle, we used a bi-Gaussian (in Φ) distribution where both $\mu$ and $\sigma$ were sampled from the distribution detail and whose degree of mixing is given by the TGSD probabilities of juveniles. Lithics and crystals were described using a Gaussian distribution.

| Parameter | Eruption size | PDF type and ranges |
|---|---|---|
| TEV ($kg^a$) | Low | Uniform on [$10^{10}$;$10^{11}$] |
| | Medium | Uniform on [$10^{11}$;$10^{12}$] |
| | High | Uniform on [$10^{12}$;$10^{13}$] |
| Duration of fallout (hours) | Low | Uniform on [3.48; 27.36] |
| | Medium | Uniform on [1.95; 3.48] |
| | High | Uniform on [1.92; 1.95] |
| MER (kg/s) | Low | Uniform on [1.5*$10^6$;1.2*$10^8$] |
| | Medium | Uniform on [1.2*$10^8$;2.1*$10^9$] |
| | High | Uniform on [2.1*$10^9$;2.2*$10^{10}$] |
| TGSD juveniles (Φ units) | All types | Beta on [2.7; 4] for $\mu$1 |
| | | Beta on [4.9; 5.4] for $\mu$2 |
| | | Beta on [0.9; 1.5] for $\sigma_1$ |
| | | Beta on [3.5; 5.5] for $\sigma_2$ |
| TGSD probabilities of juveniles (%) | Low | Beta on [0.3; 0.5] |
| | Medium | Beta on [0.2; 0.4] |
| | High | Beta on [0; 0.3] |
| TGSD lithics (Φ units) | All types | Beta on [-2; -0.5] for $\mu$ |
| | | Beta on [1.4; 1.7] for $\sigma$ |
| TGSD crystals (Φ units) | All types | Beta on [0.1; 0.6] for $\mu$ |
| | | Beta on [0.7; 1.2] for $\sigma$ |
| Initial density of juveniles $\rho_0$ | All types | Beta on [500; 1,000] |
| Maximum juvenile density ($kg/m^3$) | All types | 2,500 |
| Density of juveniles (%) | Low | Beta on [1; 1.5] for $\alpha$ |
| | | Beta on [0.3; 0.6] for $r$ |
| | Medium | Beta on [1.5; 2] for $\alpha$ |
| | | Beta on [0.4; 0.7] for $r$ |
| | High | Beta on [2; 4.5] for $\alpha$ |
| | | Beta on [0.5; 1] for $r$ |
| Density of tephra particles ($kg/m^3$) | All types | Lithics: 2,500 |
| | | Crystals: 2,800 |
| Particle proportion ($kg/m^3$) | All types | Dirichlet on [2.01; 0.66; 0.33] |
| Tephra mass fraction (%) | All types | 25 |
| Density of particle aggregates ($kg/m^3$) | All types | Accretionary lapilli: [1,000; 2,000] |
| | | Other aggregates: [100; 600] |
| Diameter of particle aggregates (Φ units) | All types | Accretionary lapilli: 2,000 |
| | | Other aggregates: 200 |
| Particle proportion aggregates (%) | Low | Uniform on [10; 30] |
| | Medium | Uniform on [30; 60] |
| | High | Uniform on [60; 90] |
| Particle proportion lapilli (%) | All types | Uniform on [0; 20] |

exceeding a critical threshold $x$ in the target site in the event of an eruption with a given VS. Nodes 6–8 deal with the impact of each VS, that is, collectively evaluate the propagation factor of Eq. 1, whose probability values are calculated by BET by analyzing the results of the propagation model (in our case, FALL3D) (Selva et al., 2010).

The event tree factorizes Eq. 1 into a set of conditional probabilities $\theta_i$, with $i$ from 1 to 8. The probability at each node is evaluated with a Bayesian method, quantifying the epistemic uncertainty as a distribution for $\theta_i$, hereinafter indicated as $[\theta_i]$. In this way, Eq. 1 can be expressed as

$$\left[\theta^{(h,\vec{a},\Delta T)}(X>x)\right] = \left[\theta_{123}^{\text{Eruption}}\right] \cdot \sum_{j\in J}\sum_{k\in K}\left[\left[\theta_4^j\right]\cdot\left[\theta_5^k\right]\cdot\left[\theta_6^h\right]\cdot\left[\theta_7^{h,\vec{a}}\right]\left[\theta_8^{h,\vec{a},X>x}\right]\right], \quad (2)$$

where

$$\left[\theta_{123}^{\text{Eruption}(\Delta T)}\right] = \left[\theta_1^{\text{Unrest}}\right]\cdot\left[\theta_2^{\text{Magma|Unrest}}\right]\cdot\left[\theta_3^{\text{Eruption|Magmatic unrest}}\right]$$

is the probability that an eruption occurs in the time window $\Delta T$, and $X$ is the random variable that describes the intensity measure associated with the hazard $h$ at the point $\vec{a}$. $J$ is the set of potential vent-opening locations, and $K$ is the set of possible VSs for each vent location in $J$.

A critical role in the definition of PVHA hazard curves through Eqs. 1 and 2 is played by the definition of volcanic scenarios (VSs). A VS is defined as an eruption of a given size in a given vent location. At Nodes 4 and 5, often a generic definition of VS is applied, defining a set of VS classes, each class often modeled with representative scenarios. However, Sandri et al. (2016) demonstrated the importance of modeling the intra-class variability (i.e., eruptive size difference within a class). To this end, it is important to create a consistent stratified sampling of the VSs in order to represent the entire variability of the eruptive source parameters (ESPs). To this end, a four-step procedure may be proposed. First, the possible eruptive size classes may be defined, for example, based on the volcanic explosivity index (VEI) (Newhall and Self, 1982) or preferably on eruption magnitude and intensity (Mason et al., 2004; Pyle, 2015). Each eruptive size class will be characterized by a series of ESPs such as the total erupted mass (TEM), the column height, and the duration of tephra fallout phases, as well as any known parameters that may influence the modeling of the volcanic hazard. The parameters used for the modeling of tephra dispersal by means of FALL3D in Campi Flegrei are listed in Table 2. Such size classes and ESPs will be in turn fully described by probability density functions (PDFs) fixed on the basis of the knowledge of the volcano. Next, within an eruptive size class, a value should be sampled from each ESP's PDF, characterizing this set as the ESPs of the VS. Then, the vent location has to be estimated from historical or monitoring data. Finally, the propagation conditions (e.g., wind distribution) have to be associated with the VS. For example, for an ST tephra PVHA, the sampled scenarios would be associated with the forecast meteorological conditions, while for an LT tephra PVHA, each scenario would have different weather conditions chosen randomly from the meteorological data of a period of time.

# 3 Probabilistic volcanic hazard assessment HPC workflow

To accommodate the methodology described in the previous section, we built the software package PVHA_HPC-WF (Probabilistic Volcanic Hazard Assessment HPC Workflow) based on the prototype tool BET@OV (Perfetti et al., 2021). BET@OV was created by researchers at Istituto Nazionale di Geofisica e Vulcanologia (INGV, Italy) to compute eruption forecasting and probabilistic tephra fallout hazard assessment at CFc by combining the Bayesian event tree method and the FALL3D tephra dispersal model (Costa et al., 2006; Folch et al., 2009). In particular, BET@OV was designed to compute 1) the probability of eruption at CFc ($[\theta_{1,2,3}^{Eruption(\Delta T)}]$) with $\Delta T$ = 1, 2, 3 days, 2) the conditional vent-opening probability map ($[\theta_4]$), and 3) the probability $[\theta^{(h,\vec{a},\Delta T)}]$ by using three fixed VSs in terms of eruptive sizes, that is, low, medium, and high explosive according to Orsi et al. (2009). To achieve new goals, we increased the BET@OV modeling capabilities so that it can generate PVHA, overcoming current computational limitations in terms of time/space domain size, resolution, and the number of representative VSs. In particular, to simulate tephra fallout and ash concentration at flight levels, PVHA_HPC-WF interacts with the model FALL3D-8.0 (Folch et al., 2020; Prata et al., 2021).

## 3.1 Workflow architecture

PVHA_HPC-WF is made up of a set of Python modules (see Figure 1B) in charge of calculating each of the BET nodes described earlier in Subsection 2.2 as well as performing the post-processing and visualization of results. The workflow tasks are managed by the ChEESE workflow management system *WMS-light*, and to consolidate the data and keep history, the PostgreSQL LISTEN exchange is used. The next section describes how the workflow is managed by WMS-light and how the optimization has been carried out. A description of each of the Python modules can be found in the Supplementary Material.

## 3.2 Workflow implementation

The PVHA_HPC-WF is a classic workflow-based application, in which the data-interconnected components are executed in a synchronized order according to the application logic, as depicted in Figure 1B. Running such applications on IT infrastructures, including diverse HPC systems with their distributed computing and storage components or their respective different resource access and application execution strategies, is a challenging task. In practice, running application workflows on the on-demand parallel and distributed infrastructures often impose the following issues:

- Automation of distributed control flow. The workflow components that are running on different parts of the physically distributed infrastructure resources have to employ sophisticated synchronization strategies in order to be able to track the progress of the interdependency of tasks.
- Heterogeneous deployment configurations. Depending on the infrastructure availability and the application's non-

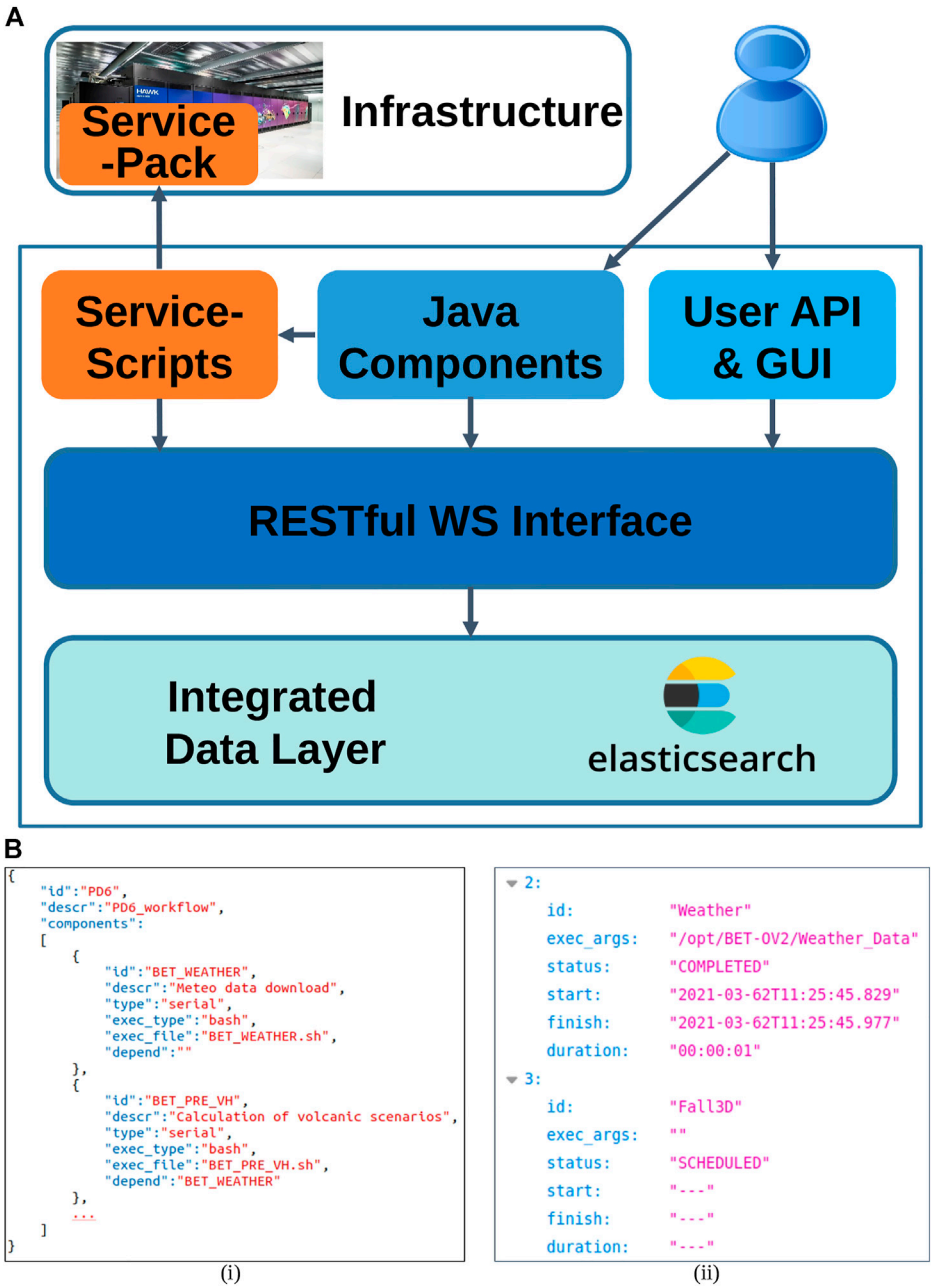


FIGURE 2
**(A)** Architecture of WMS-light workflow management system. **(B)** WMS-light specifications: i) workflow and ii) monitoring information.

functional requirements, it might be necessary for application components to be executed on different infrastructure sites, which can change from one deployment (execution) to the next one. In such cases, the application will have to deal with different access policies (e.g., certificate-based authorization instead of the user's login and password), job execution strategies (different job managers like *PBS/Torque* or *SLURM*), organization of the storage, and many other site-specific settings that have zero or little relevance to the application itself.

- Distributed data access. The application components are interchained not only by the control but also by the data flow. The data dependencies can be implemented in several different ways, depending on the concrete (and, generally, deployment-specific) properties of the infrastructure

resources that are hosting the components, such as with the classic *FTP* and *SCP*, but also with the throughput-optimized grid protocols such as *GridFTP*.
- Dynamic scaling of components. Depending on the availability of the infrastructure resources, the application components might need to scale up or down to saturate the maximal capacity of the assigned hardware in order to increase the performance and/or optimize non-functional properties. As the available resource size might be unknown at the time of the application workflow submission, the scaling has to be performed dynamically at the runtime of the application instance.

In order to address the abovementioned issues during the development and execution of the application workflow, the PVHA_HPC-WF application employs a workflow management system *WMS-light*, which was developed in the context of the ChEESE project (see a basic introduction in Cheptsov and Beljaev, 2020). *WMS-light* is a lightweight middleware that supports developers of the application workflows that are to be run in distributed, parallel, and heterogeneous computing environments and have dynamic deployment properties. The *WMS-light* support generally includes the synchronized execution of components on distributed hosts (serial, parallel, HPC), the realization of data dependencies, and the tracking of execution properties (across several applications and/or their instances) and requires minimal to zero changes in the original application components' code due to a non-intrusive programming model of *WMS-light*. Non-intrusiveness is a key property of *WMS-light* and applies not only to the applications but also to the infrastructure. Unlike the majority of well-established workflow managers, *WMS-light* requires only a minimal set of software that has to be installed in the user's space and does not require any special administrative privileges. *WMS-light* is designed in a modular and highly transparent way (see Figure 2A). The core of *WMS-light* is constituted by a set of Java components and service bash scripts, which makes it portable to almost any architecture, from a small edge-server to the largest HPC system. All data related to the execution of instances (runs) of the application workflows are stored in the intelligent data layer and made available to the users and system middleware components by means of a rich-functional *RESTful* web service interface. All specifications, including the workflow definition (see Figure 2Bi), are made in the flexible *JSON* format. *WMS-light* allows live-tracking of the workflow execution status for each of the submitted instances (Figure 2Bii).

## 3.3 Workflow performance optimization

Within the framework of the EU Performance Optimization and Productivity Center of Excellence in HPC (POP CoE), critical parts of the PVHA workflow were analyzed because of their initial poor performance. More specifically, the analysis of volcanic hazard probabilities from FALL3D capability simulations became a concerning bottleneck due to long capability workflow execution times (note that this optimization does not concern single FALL3D model instances, but the capability workflow resulting from the aggregation of many independent instances). Thus, we applied the POP's profiling and optimization cycle. First, we identified through a performance assessment what was causing such bad workflow performance. Second, we addressed with a proof-of-concept (PoC) each individual problem.

### 3.3.1 Workflow performance assessment

With a performance assessment, we discovered that the part of the code that was slowing down the workflow was the analysis of the many instances of FALL3D, and we figured out what factors were responsible. Using Extrae (Center, 2022), we traced the application in various strong scalability tests up to 1,024 ranks MPI (Message Passing Interface). Then, with Paraver (Pillet et al., 1995), we analyzed the traces and generated a set of metrics giving us insights into the application's efficiency. For example, Figure 3A displays a Paraver trace showing qualitatively what regions of the program are being run in one execution with 48 MPI ranks. In Figure 3B, we can see the quantitative results of one strong scalability test. Thanks to these POP performance metrics (POP, 2022) we could identify that PVHA_HPC-WF suffered mainly from two problems. First, it suffered from load-balancing problems. For instance, with 192 MPI ranks (four compute nodes in this setup), the load balance is already below 80%. Second, it presented a low serial performance as indicated by the average IPC (instructions per cycle). With 4 MPI ranks, the average IPC is 0.98, which is already low since a good IPC would be 2–3 for an application. However, from here, it only gets worse until an average IPC of 0.36 with 1,024 MPI ranks.

Given the previous analysis, we identified why the workflow performed badly and the reasons for load imbalance and poor CPU (central processing unit) utilization. Indeed, we realized that the different processor performances between ranks and one non-parallel region were causing load balance problems. Regarding low IPC, we attributed it to poorly optimized Python code. In addition to all that, we also saw that MPI usage could be improved.

### 3.3.2 Proof-of-concept

Once we discovered what could be improved, we started working on optimizations in a proof-of-concept. On one hand, we addressed load balance issues by equally mapping data to every processor, keeping NUMA (non-uniform memory access) awareness in mind and parallelizing a region of serial code. On the other hand, we improved the poor workflow serial performance by optimizing the main nested loops of the

A


B

| MPI Ranks | 4 | 16 | 24 | 32 | 48 | 192 | 576 | 1024 |
|---|---|---|---|---|---|---|---|---|
| Nodes | 1 | 1 | 1 | 1 | 1 | 4 | 12 | 22 |
| Global efficiency | 91 | 47 | 33 | 33 | 32 | 25 | 16 | 11 |
| -Parallel efficiency | 91 | 89 | 95 | 80 | 90 | 71 | 46 | 31 |
| -Load Balance | 93 | 93 | 95 | 86 | 91 | 71 | 46 | 32 |
| -Communication efficiency | 98 | 96 | 99 | 94 | 99 | 100 | 98 | 99 |
| -Serialization efficiency | 100 | 100 | 100 | 100 | 100 | 100 | 100 | 100 |
| -Transfer efficiency | 98 | 96 | 100 | 94 | 99 | 100 | 98 | 99 |
| -Computational Scaling | 100 | 53 | 35 | 41 | 35 | 35 | 35 | 35 |
| -IPC Scaling | 100 | 53 | 35 | 41 | 35 | 35 | 35 | 37 |
| -Instruction Scaling | 100 | 100 | 100 | 100 | 100 | 100 | 99 | 96 |
| -CPU Frequency Scaling | 100 | 100 | 100 | 100 | 100 | 100 | 99 | 98 |
| Speedup | 1,00 | 2,05 | 2,19 | 2,87 | 4,16 | 13,02 | 25,01 | 31,01 |
| Average IPC | 0,98 | 0,52 | 0,34 | 0,40 | 0,34 | 0,34 | 0,34 | 0,36 |
| Average frequency (GHz) | 3,37 | 3,35 | 3,36 | 3,36 | 3,36 | 3,36 | 3,34 | 3,31 |

FIGURE 3
**(A)** PVHA_HPC-WF Paraver trace. The x-axis shows the program's execution time in microseconds, while the y-axis displays each one of the 48 parallel MPI ranks. Colors indicate what part of the application is being run at a time. **(B)** POP metrics table of a PVHA_HPC-WF strong scalability test. Colored values are in percentage.

Python code. The outcome of these optimizations improved the workflow's time-to-solution by 588 times.

We first optimized the serial computation loops. After some experiments, we found that the best performance was achieved using Numpy vectorization. Thanks to Numpy we replaced all Python for-loops with calls to Numpy vector operations, which yielded a maximum speedup of 775 times in the execution of that part of the code compared to the original workflow version. Listings 1 and 2 show an example of a change made to the code, which is to replace matrix multiplication in plain Python with matrix multiplication using Numpy vectorization. We also fixed a memory access pattern that was not exploiting the spatial locality of cache memory well.

**Listing 1.** Matrix multiply in plain Python.

```
product = np.zeros ((n, m), dtype = 'int')

for i in range (n):
for j in range (m):
for z in range (k):
product [i, j] += matrix1 [i, z] * matrix2 [z, j]
```

**Listing 2.** Matrix multiply using Numpy vectorization.

```
import numpy as np
product = np.matmul (matrix1, matrix2)
```

After the first optimization, all processors had the same amount of data to compute and the same memory access latency, so one balancing problem was already gone. The second problem was a sequential workflow region that took 2/3 of the execution time. Therefore, we parallelized this part with MPI, which reduced the total execution time by 2.3 times. Figure 4A shows the result of this parallelization. In the window at the bottom, the master rank is doing useful computation (in blue) for the last 2/3 of the window, while all the other processors are idle (in black) waiting. In the window at the top, the master rank is spending 2.3 times less execution time running sequential code. It seems that there is still room for improvement, as the application presents large serial parts. However, those parts belong mostly to the I/O operations of pre and post processing.

The final results of this PoC are displayed in Figure 4B, where we compare the base version versus our PoC version running with different number of ranks. Thanks to our

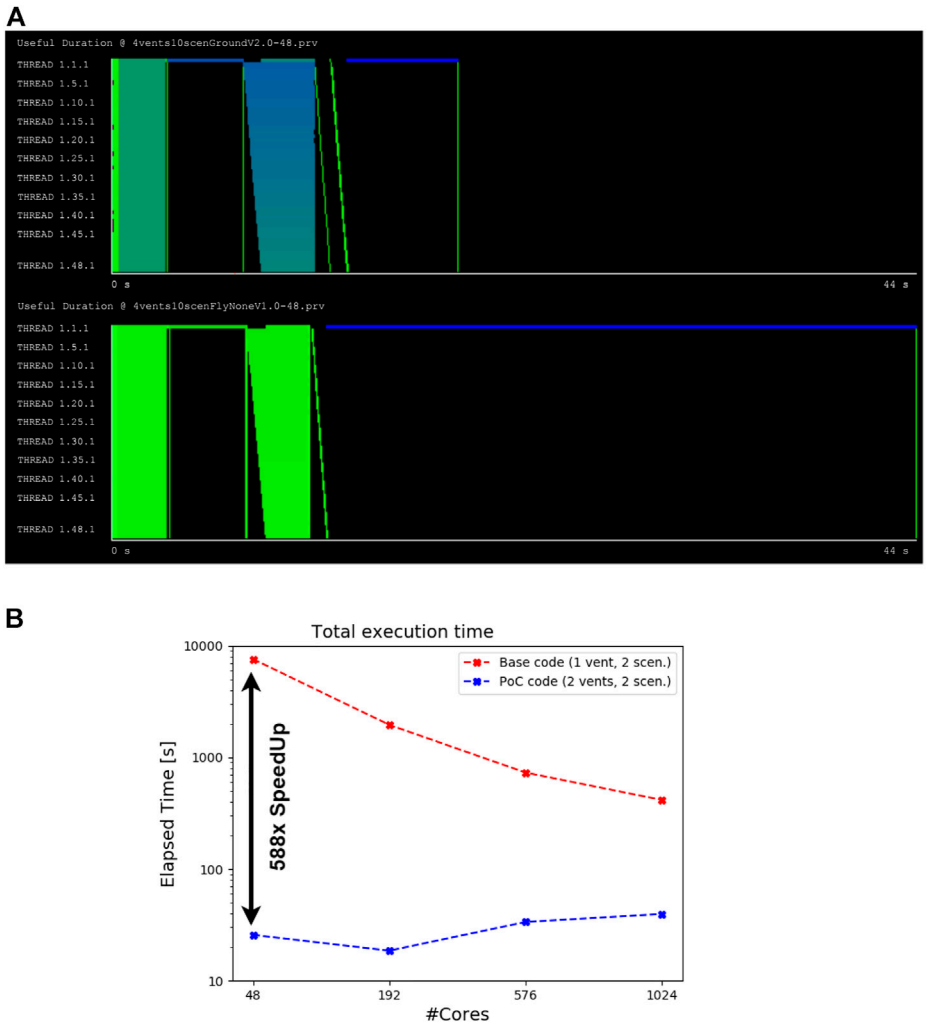


FIGURE 4
**(A)** Paraver traces showing useful duration (computation) of two executions with 48 MPI ranks. Both windows have the same duration. The trace at the bottom is the application with the expensive sequential region. The trace at the top is the same application but with that region parallelized. Ignore the color gradient, only notice that the execution at the bottom takes 44s to finish, while the execution at the top takes a bit less than half of the time. Black means threads are not running the program. **(B)** PVHA_HPC-WF execution time comparison between the original code (in red color) and the proof-of-concept version (in blue color) for the FL050 case.

changes; we were able to reduce the application's runtime by up to 588 times on average. Usage of Numpy vectorization was the main source of this large improvement and after that the parallelization with MPI of the sequential region.

## 4 Test case: Tephra probabilistic volcanic hazard assessment for Campi Flegrei

The metropolitan area of Naples (more than three million inhabitants, www.cittametropolitana.na.it) is under the threat of three active and well-studied volcanoes: Somma-Vesuvius, Campi Flegrei, and Ischia. The PVHA of these volcanoes is based on several multidisciplinary studies (Costa et al., 2009; Selva et al., 2010; Sandri et al., 2016; Macedonio and Costa, 2018; Selva et al., 2018, 2021). In this study, we focused on the Campi Flegrei volcanic system, although the presented methodology can be applied to other volcanoes as well. The Campi Flegrei caldera (CFc) resulted from at least two major collapses from the Campanian Ignimbrite (Ort et al., 2003) and the Neapolitan Yellow Tuff (Deino et al., 2004) eruptions, 37,000 and 12,000 years BP, respectively. More recent volcanism was concentrated in epochs of intense activity (i.e., eruptions occurred at time intervals of a few tens of years), alternating with periods of quiescence (Costa et al.,

2022). Subsection 4.2 provides information on eruption probabilities, styles, intensity, and vent locations in CF. CFc is located in one of the most densely populated areas in Europe, so an eruption would have a tremendous impact, not only on air traffic but also on people and infrastructure. INGV is the reference scientific institution for the Italian government in the field of volcanic monitoring and hazards and operates in close synergy with the Italian Civil Protection authorities at the national and local levels. The surveillance system of Osservatorio Vesuviano of INGV continuously monitors, among others, volcano seismicity, ground deformations, and gas emissions and performs tephra dispersion simulations driven by this information and the ARPA-SIM meteorological data for forecasting plume evolution in the Campania region. A short-term PVHA is currently run twice daily for tephra fallout and is based on three representative scenarios over a 250 km × 200 km geographic area at 1 km grid spacing due to the high computational cost of simulating the eruptive variability on local servers (Perfetti et al., 2021).

Herein, we improve the assessment of the tephra hazard associated with an eruption at Campi Flegrei in order to better answer important questions such as

1. In the short term, what are the probabilities of eruption and vent-opening locations?
2. In the short and long term, what is the probability, both absolute and conditional on the occurrence of an eruption, that the cumulative tephra deposit will exceed critical thresholds known to cause issues, such as building collapse/failure or traffic disruption after a certain number of hours from the eruption onset?
3. In the short and long term, what is the probability, both absolute and conditional on the occurrence of an eruption, that the ash cloud concentration will exceed critical conditions and hazardous temporal persistence known for safe flights within a certain number of hours since the beginning of the eruption, and which levels (FLs) are likely to be most predominantly affected?
4. In the short and long term, what is the expected time for ash concentration to reach a critical value at a specific geographical point and flight level?

The PVHA_HPC-WF presented here allows us to answer these questions by conducting a hazard assessment related not only to tephra ground load but also to ash concentration at various FLs over a surveillance area large enough to track the evolution of ash clouds, and considering a large number of VSs, thus reducing the uncertainty in the eruptive parameters and meteorological conditions.

In this application case, we generated both LT and ST tephra PVHA for Campi Flegrei. For an LT assessment, we have considered 1,500 VSs for each of the three explosive eruption sizes at Campi Flegrei, that is, low (L), medium (M), high (H) size, and meteorological conditions during 20 years of reanalysis from Copernicus Climate Change Service ERA5. As examples of ST, we developed the PVHA for December 5, 6, and 7, 2019, when seismic activity was more energetic than usual with a magnitude 3.1 intracaldera earthquake: in the present example, we consider 180 VSs for each explosive eruption size and day and the monitoring data from the Osservatorio Vesuviano surveillance system recorder on those days. All the studies were carried out in a regional-scale domain of 2,000 km × 2,000 km at a 2 km horizontal resolution, approximately, and a vertical resolution ranging from 0.5 to 1 km, considering eight flight levels from FL050 to FL400, 5,000 ft (1.5 km) to 40,000 ft (12.2 km) altitude, approximately. The simulations for each of the 6,120 VSs (1,500 VSs × 3 sizes +180 VSs × 3 sizes × 3 days) have been carried out by running the FALL3D-8.0 model on the French Joliot-Curie supercomputer, while the eruptive forecast (EF) has been calculated on the CENERI server of the Osservatorio Vesuviano of INGV, and the workflow manager system has been launched in the ADA cluster at INGV-Bologna.

An introduction to the monitoring system is given in the next Subsection 4.1. Subsection 4.2 describes the configuration of the model adopted for this test case and the parameters used to calculate each of the BET nodes, and a detailed explanation of the VS generation process is shown in Subsection 4.3. In Subsection 4.4, it is specified how the meteorological data have been obtained. Subsection 4.5 is dedicated to the specification of the computational resources and performance of the PVHA_HPC-WF. Finally, the presentation of results and a sample of the graphs and maps obtained are shown in Subsection 4.6.

## 4.1 Monitoring system

Monitoring data, necessary for ST assessment, are provided by the Osservatorio Vesuviano's surveillance system (Bianco et al., 2022). Seismic data are collected from the seismological database SERENADE (SEismic Restful ENAbled DatabasE), which was developed to manage multiple locations for each event in order to unify the data source for automatic, preliminary, and revised locations (Peluso, 2014). The PostgreSQL database server is the internal engine of SERENADE and allows requests to be made using standard HTTP commands. On the other hand, from the network of permanent GPS stations operating in the CFc, we obtained the deformation data for these studies (De Martino et al., 2021). Other data, such as anomalies in gas fluxes or compositions, can also be accounted for as user-specified parameters.

## 4.2 Model setup

Here, we describe the parameters at each of the BET nodes and the computational domains used for this test case.

The BET_EF settings used to calculate Nodes 1, 2, and 3 rely on the work of Selva et al. (2012a) and are reported in the first three

rows of Table 1 and in Figure 5A regarding the probability of unrest, magmatic unrest, and eruption, respectively. For the LT, a Poisson distribution over time has been assumed, and the results of which are compatible with the works of Sandri et al. (2018) and Bevilacqua et al. (2017).

The considered eruptive area for Node 4, based on the geodynamical structures and the position of past eruptive vents within the CF caldera (Selva et al., 2012b), consists of 40 potential vent-opening locations distributed equidistantly in a geographical area encompassed between 40.775°N and 40.875°N latitude and 14.05°E to 14.225°E longitude, whose locations and prior (LT) probabilities are indicated in Table 1 and displayed in Figure 5B. Short-term maps are built by integrating the position of observed anomalies, such as seismic activity and deformation, as in Marzocchi et al. (2008). Although part of the CFc is under the sea, since the most likely opening vent areas are in shallow waters and the effects are generally negligible at relatively large distances (Selva et al., 2018), we do not consider the effects of the sea on the formation of eruptive columns. The reader who wants to go deeper into the effects over sea water on the eruptions at CFc, including tsunamis, can consult, for example, Tonini et al. (2015), Selva et al. (2018), Paris et al. (2019), and Grezio et al. (2020).

Based on the eruptive record of Campi Flegrei (Orsi et al., 2009), we consider four eruption sizes: an effusive (E) size and three explosive ones, which are the low (L) (e.g., Averno 2), the medium (M) (e.g., Astroni 6), and the high (H) (e.g., Agnano-Monte Spina) sizes. The probabilities of occurrence for each size are defined in Table 1 and graphically represented in Figure 5C (Sandri et al., 2016). Then, as we already mentioned earlier, for each explosive size, we build 1,500 VSs for LT assessment, 180 VSs for ST, and for 5, 6, and 7 December 2019, totaling 6,120 VSs. In Subsection 4.3, we provide the details on the creation of the volcanic scenarios.

Regarding Node 6, we study tephra fallout hazard at ground and ash concentration hazard at eight flight levels (FL050–FL400) during the 24 and 48 h after the eruption by running FALL3D-8.0 for each VS in a computational domain spanning from 31°N to 50°N latitude and from 3°E to 28°E longitude at 0.025° resolution (2 km, approximately). Due to the flat topography of the CFc (that does not affect significantly the pattern of ash dispersal), to the proximity of the volcanic vents with respect to the size of the simulation grid, and to the resolution of the meteorological data, we do not repeat the tephra dispersion simulations for each of the vent locations but instead translate the output of simulations to each of the 40 vent positions (Selva et al., 2010).

For Node 7, we examined the target area from 34°N to 50°N latitude and 3°E to 28°E longitude (Figure 5D) at 0.025° resolution and the eight flight levels from FL050 to FL400. The reason this target area is slightly smaller than the FALL3D area is to have the same number of simulation outputs in each target area cell after translating the simulations over the 40 vent locations.

With respect to Node 8, we examine 23 critical thresholds, from 0.01 to 16.0 kPa, for the ground load hazard (Wilson et al., 2012) and the thresholds of 0.2, 2, and 4 mg/m$^3$ for the airborne ash concentration, as well as the temporal persistence of 1, 3, 6, 12, 18, and 24 h.

These input parameters are collected in a configuration file called BET.CFG, which is the input file to the PVHA_HPC-WF (see Supplementary Material).

## 4.3 Generation of volcanic scenarios

As explained in previous sections, we adopt a probabilistic approach that merges the results of a large number of numerical simulations, each of them corresponding to a potential VS, to fully explore the natural variability associated with volcanic phenomena and to take into account the impact of low-probability but high-consequence events. The probabilistic approach adopted follows Sandri et al. (2016) based on the definition of three broad eruptive size classes (low-, medium-, and high-explosive, respectively): L, M, and H. Each eruptive explosive size is fully described by a set of ESPs sampled from PDFs previously defined. The PDF shape and parameters are defined on the basis of previously published articles in agreement with field observations (Sandri et al., 2016; Mele et al., 2020) and compiled in Table 2. The methodology followed to generate a potential eruptive scenario is reported in the Supplementary Material.

## 4.4 Meteorological data

To fully explore the natural variability of weather conditions, each VS was randomly assigned weather conditions corresponding to a time period between 1 January 1999 and 1 January 2019 for the tephra dispersal simulations for the long-term assessment. For the short-term assessment, the meteorological data corresponding to each of the days 5, 6, and 7 December 2019 have been used. All these data have been obtained from the Copernicus Climate Change Service ERA5 reanalysis with a temporal resolution of 3 h at a spatial resolution of 0.25°. Details for downloading and handling these data are attached in the Supplementary Material.

## 4.5 Computational resources and performance

The PVHA_HPC-WF has been distributed into three clusters:

- ADA. HPC-MASTER-Computing Cluster, 140 cores × node, INGV Section of Bologna;

**A** **Nodes 1, 2, 3 - Eruption probabilities**

| Node | Probability of | 5% | mean | 90% |
|---|---|---|---|---|
| 1 | unrest in the next month (assuming no anomalies) | 0.016 | 0.027 | 0.039 |
| 2 | unrest magmatic given an unrest | 0.128 | 0.500 | 0.897 |
| 3 | eruption given a magmatic unrest | 0.004 | 0.118 | 0.299 |
| 123 | eruption in 50 years | 0.005 | 0.618 | 0.998 |

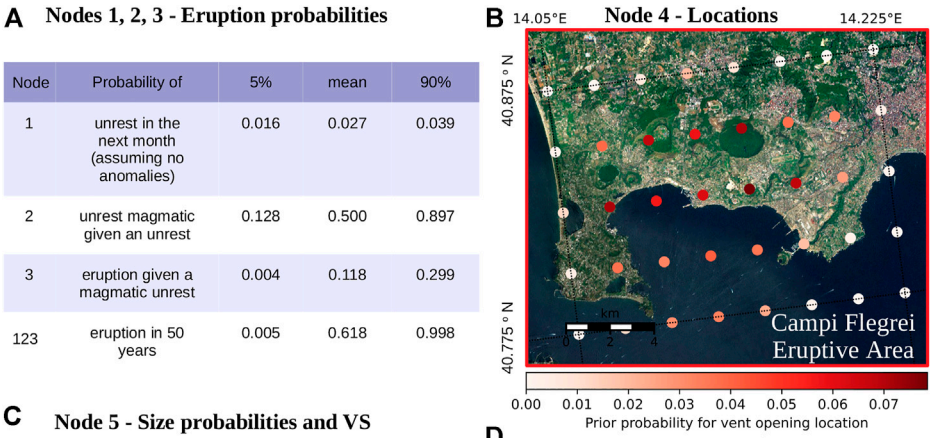


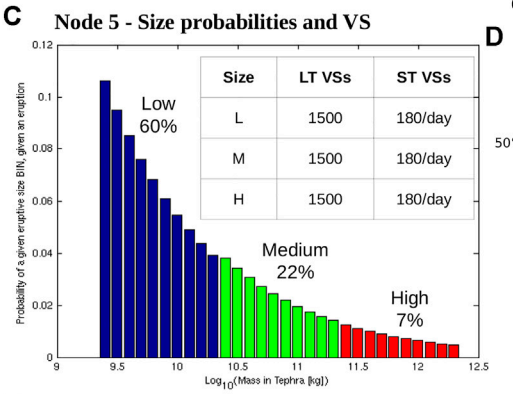


| Size | LT VSs | ST VSs |
|---|---|---|
| L | 1500 | 180/day |
| M | 1500 | 180/day |
| H | 1500 | 180/day |

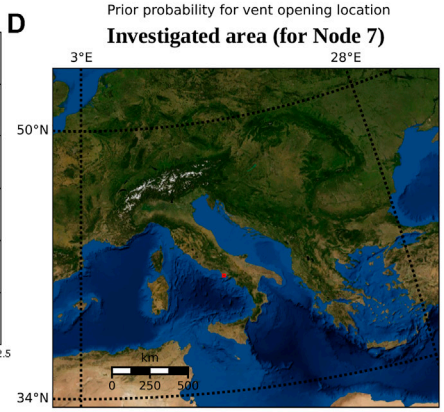


**E** **Nodes 6 and 8 – Hazards and Thresholds**

| Hazard | Thresholds |
|---|---|
| Thephra load (kPa) | 0.01, 0.1, 0.2, 0.3, 0.4, 0.5, 0.6, 0.7, 0.8, 0.9, 1.0, 1.5, 2.0, 2.5, 3, 3.5, 4.0, 6.0, 8.0, 10.0, 12.0, 14.0, 16.0 |
| Ash concentration ($mg/m^3$) | 0.2, 2, 4 |

| | Min / Max / Resolution |
|---|---|
| Lon | 3° / 28° / 0.025° |
| Lat | 34° / 50° / 0.025° |
| FL | 50 / 400 / 8 ( ≈ 5000 ft / 40000 ft / 50 ft) |

FIGURE 5
CF model setup. **(A)** reports the probability of unrest (Node 1), magmatic unrest (Node 2), and eruption (Node 3) and the combination of the three nodes. **(B)** is the Campi Flegrei eruptive area where the 40 vent-opening locations considered in this study and their respective prior probabilities are indicated. **(C)** shows the probability density function for the size of the eruption at Campi Flegrei and the number of scenarios considered for each of them. **(D)** indicates the geographical area studied in this work (upper image) and the resolution and coordinates of the computational domain (lower table). **(E)** specifies the thresholds set for each hazard.

- CENERI. Debian GNU/Linux, Osservatorio Vesuviano in INGV Section of Naples;
- IRENE-SKYLAKE. Bi-processor with 24 cores per node, TGCC, France.

The workflow management system was installed and launched on ADA which interacted with CENERI, IRENE, and with itself. The BET_EF and BET_FETCH modules, in charge of interrogating the monitoring database and calculating the probabilities of eruption, were serially executed on the CENERI server, lasting less than 1 min. Also, the BET_PRE_VH was run in series on ADA, generating the set of VSs in a few seconds for the LT and the ST. The module BET_TEPHRA, responsible for executing the simulations of volcanic tephra transport and deposition *via* FALL3D-8.0 for each of the 6,120 VSs generated, was executed in parallel on IRENE using an average of 16 nodes and 3 h, approximately, of elapsed time for each simulation. The analysis of the FALL3D simulations, through the BET_POST_TEPHRA module, has been carried out in parallel in IRENE using 1 node and less than 20 min, approximately, for each set of simulations corresponding to each of the three eruptive sizes. Also in IRENE, the module BET_VH was executed utilizing 12 nodes and 15 min, approximately, for each desired combination of altitude level/persistency/period of time. In total, approximately $11{\cdot}10^6$ h of CPU time was used in Irene for the

TABLE 3 Computational performance for PVHA at Campi Flegrei. Herein, we use the abbreviation PERS for temporal persistence and TP for period of time.

| LT | Number of runs | Cluster | CPUs per run | Nodes per run | Average elapsed time per run |
|---|---|---|---|---|---|
| BET_EF | 1 | CENERI | Serial | - | < 1 min |
| BET_POST_EF | 1 | CENERI | Serial | - | < 1 min |
| BET_WEATHER | 20 | ADA | Serial | - | 90 min |
| BET_PRE_VH | 1 | IRENE | | | |
| BET_TEPHRA | 4,500 | IRENE | 768 | 16 | 3 h |
| BET_POST_TEPHRA | | | | | |
| Exceedance probability | 6 (3 sizes × 2 TPs) | IRENE | 48 | 1 | 20 min |
| Arrival time | 3 (3 sizes) | IRENE | 48 | 1 | 15 min |
| BET_VH | (1 × GROUND, 1 × FL × PERS) × TP | IRENE | 576 | 12 | 15 min |
| BET_POST_VH | | | | | |
| Exceedance probability | 1 × GROUND × TP | ADA | Serial | - | 8 min |
| Exceedance probability | 1 × FL × PERS × TP | ADA | Serial | - | 5 min |
| Arrival time | 1 × FL × size × TP | ADA | Serial | - | 2 min |
| **ST** | **Number of runs** | **Cluster** | **CPUs per run** | **Nodes per run** | **Average elapsed time per run** |
| BET_FETCH | 1 | CENERI | Serial | - | < 1 min |
| BET_EF | 1 | CENERI | Serial | - | < 1 min |
| BET_POST_EF | 1 | CENERI | Serial | - | < 1 min |
| BET_WEATHER | 1 × day | ADA | Serial | - | 30 min |
| BET_PRE_VH | 1 | IRENE | | | |
| BET_TEPHRA | 1,620 | IRENE | 768 | 16 | 3 h |
| BET_POST_TEPHRA | | | | | |
| Exceedance probability | 6 (3 sizes × 2 TPs) | IRENE | 48 | 1 | 10 min |
| Arrival time | 3 (3 sizes) | IRENE | 48 | 1 | 15 min |
| BET_VH | (1 × GROUND, 1 × FLxPERS) × TP | IRENE | 576 | 12 | 15 min |
| BET_POST_VH | | | | | |
| Exceedance probability | 1 × GROUND × TP | ADA | Serial | - | 8 min |
| Exceedance probability | 1 × FL × PERS × TP | ADA | Serial | - | 5 min |
| Arrival time | 1 × FL × size × TP | ADA | Serial | - | 2 min |

LT, and $125{\cdot}10^4$ for each of the ST days. Finally, the final hazard curves and figures were generated serially in ADA by BET_POST_VH, requiring approximately 8 min. All this information is compiled in Table 3.

## 4.6 Results

A large portfolio of results from the workflow can be extracted and mapped. Herein, we show some of the results that may answer the questions posed in the second paragraph of Section 4, following the numbering of those questions.

For LT analysis, the workflow can provide:

1. probability maps with uncertainty showing the 50-year forecast absolute probability and the probability conditional on the occurrence of an eruption exceeding the previously defined critical tephra fallout thresholds after 24 and 48 h from the beginning of an eruption,
2. probability maps with uncertainty showing the 50-year forecast absolute probability and the probability conditional on the occurrence of an eruption exceeding the critical ash concentration thresholds of 0.2, 2, and 4 mg/m$^3$ for at least 1, 3, 6, 12, 18, and 24 of the hours after 24 and 48 h from the beginning of an eruption at eight flight levels from FL050 to FL400,
3. maps of the time required to exceed the ash concentration thresholds corresponding to each explosive eruption size.

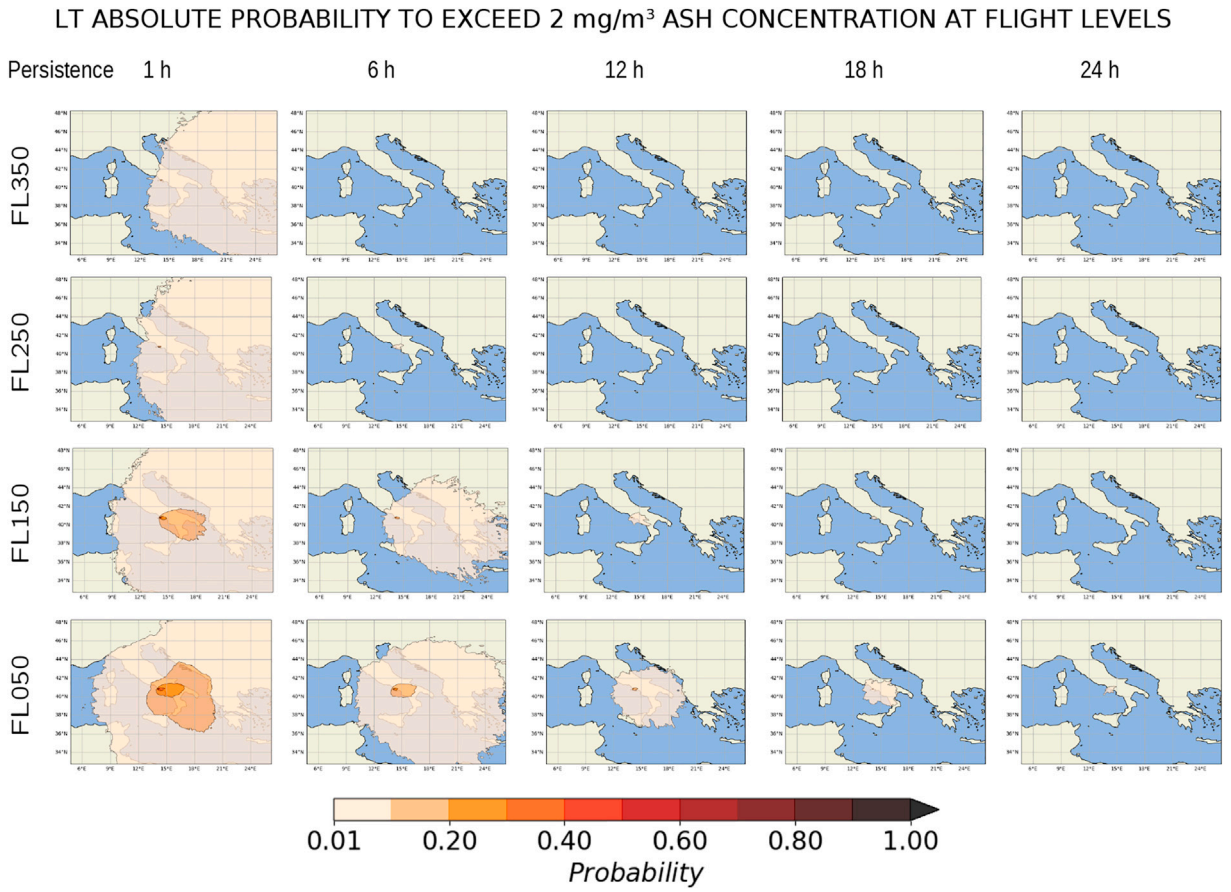


FIGURE 6
Probability maps showing the long-term mean absolute probability that the 50-year forecast ash will exceed a concentration of 2 mg/m$^3$ with persistence of 1, 6, 12, 18, and 24 h (left to right columns) during a period of time of 48 h in FL050, FL150, FL250, and FL350 (bottom to top columns). We can see that the probability for the next 50 years of exceeding 2 mg/m$^3$ for at least 1 of the 48 h observed is greater than 1% at all flight levels. FL050 would be the most affected where the critical threshold could be exceeded for at least 24 out of the 48 h studied. We can also observe that the spread pattern is toward the east and slightly south.

For ST analysis corresponding to each of December 5, 6, and 7, 2019, the workflow can provide:

1. eruption probabilities and vent-opening location maps,
2. probability maps with uncertainty showing the absolute probability and the probability conditional on the occurrence of an eruption exceeding the critical tephra fallout thresholds after 24 and 48 h from the beginning of an eruption,
3. probability maps with uncertainty showing the absolute probability and the probability conditional on the occurrence of an eruption exceeding the previously defined critical ash concentration thresholds for at least 1, 3, 6, 12, 18, and 24 of the hours after 24 and 48 h from the beginning of an eruption at eight flight levels from FL050 to FL400, and
4. maps showing the time required to exceed the ash concentration thresholds corresponding to each explosive eruption size.

We show here only a small sample of the large number of maps generated. Other maps can be found in the Supplementary Material, including those corresponding to each of the seasons of the year.

### 4.6.1 Long-term analysis

As an example of probability maps, Figure 6 presents the 50-year forecast absolute probability that the ash concentration at FL050, FL150, FL250, and FL350 exceeds the critical concentration of 2 mg/m$^3$ with persistency of 1, 6, 12, 18, and 24 h in the 48 h following an eruption onset. We can observe that the probability for the next 50 years of exceeding 2 mg/m$^3$ for at least 1 of the 48 h observed is greater than 1% at all flight levels. FL050, especially interesting because it is the aircraft takeoff and landing flight level, would be the most affected where the critical threshold could be exceeded for at least 24 out of the 48 h

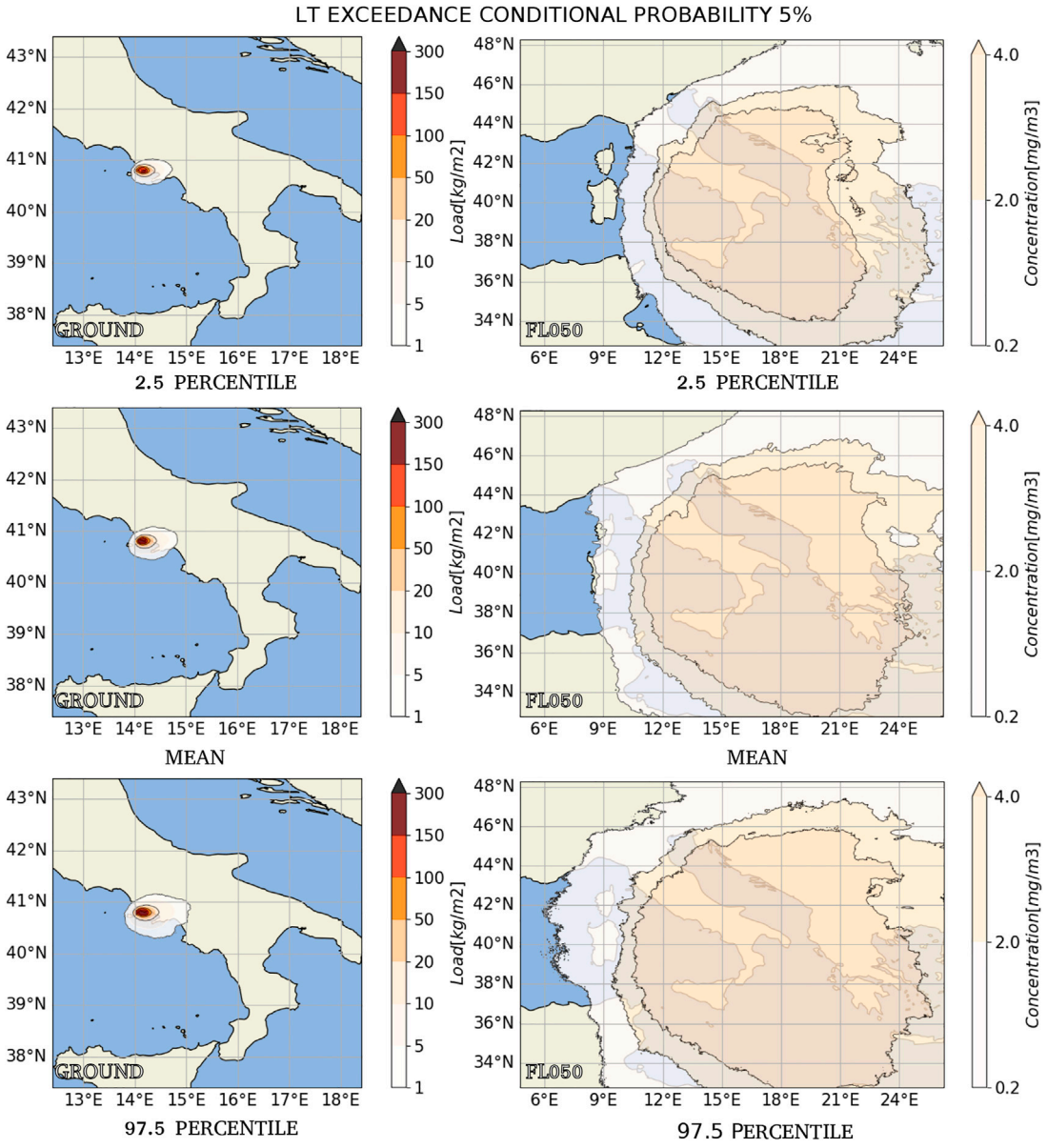


FIGURE 7
Long-term hazard maps relative to the 5% probability threshold conditional on an eruption event provide a graphical representation of epistemic uncertainty for tephra fallout (left column) and ash concentration at FL050 (right column). For each hazard intensity value (color bar label), the maps show the areas where that value will be exceeded with a probability greater than 0.05 in the event of an eruption within 48 h from eruption onset. We can see that in the case of an eruption, a large part of the Campania region would be affected for tephra load with a probability greater than 5%. Also, an eruption would affect air traffic with an exceedingly high ash concentration above 4 mg/m$^3$ throughout a large area with a spread pattern to the east and slightly south.

studied. As a sample of intensity hazard maps, Figure 7 shows the tephra ground load and the ash concentration at FL050 within 48 h from eruption onset, both the mean values and those corresponding to the 2.5 and 97.5 percentiles, relative to the 5% probability conditional on an eruption event. We can see that in the case of an eruption, a large part of the Campania region would be affected by tephra load above 1 kg/m$^2$ with a probability greater than 5%, even exceeding thresholds above 300 kg/m$^2$ in the areas closest to the volcano. Also, an eruption would affect air traffic in extensive areas with exceedingly high ash concentrations above 4 mg/m$^3$. Both Figures 6 and 7

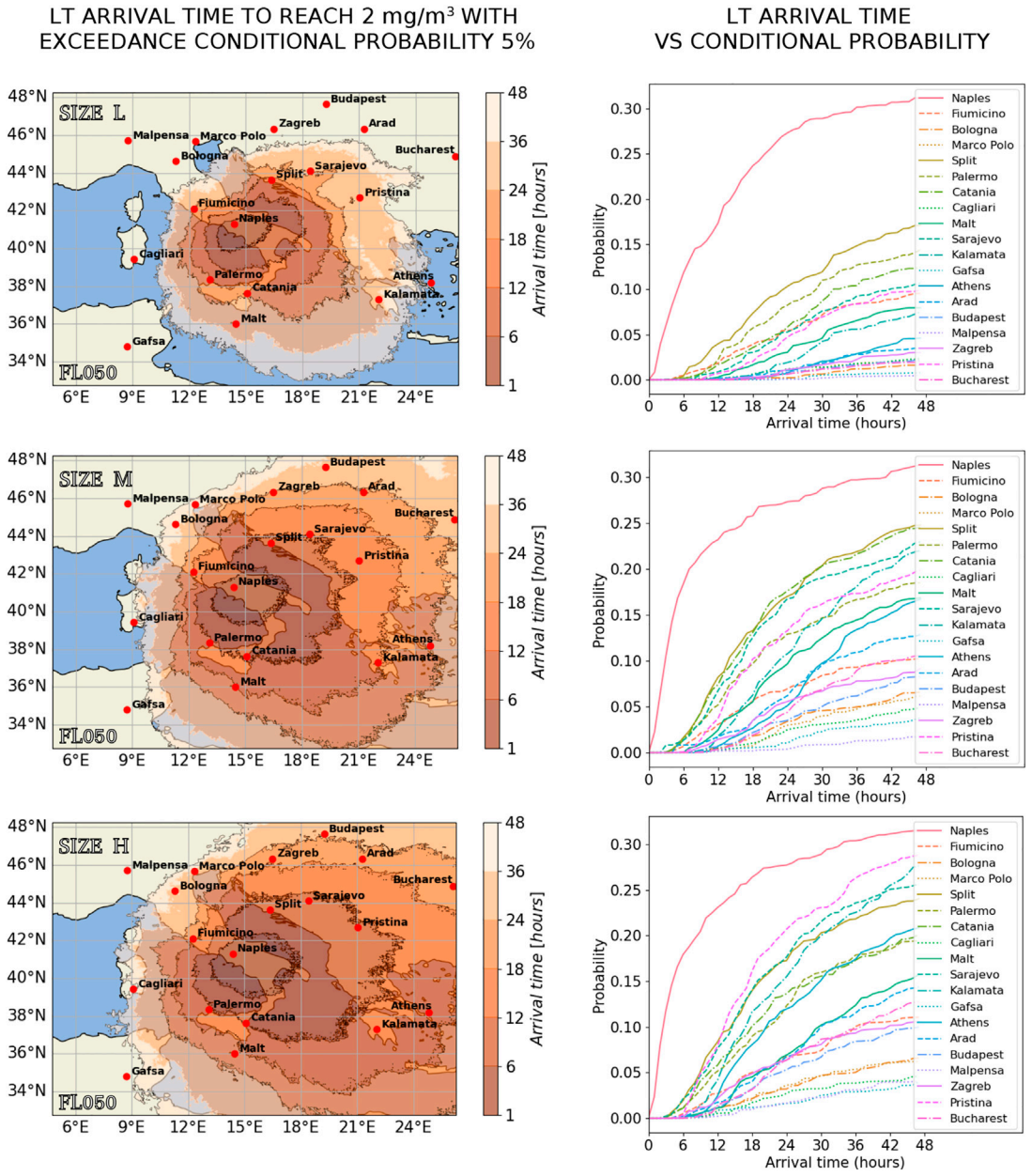


FIGURE 8
Long-term arrival time maps. Left column shows, from top to bottom, the expected time in which the ash concentration at FL050 will reach the critical threshold of 2 mg/m$^3$ with a probability of 5% in the event of a low-, medium-, and high-sized eruption at Campi Flegrei, respectively. The right column shows the probabilities to reach 2 mg/m$^3$ at FL050 above some of the surrounding airports in each of the hours following the eruption.

show the trend of the ash to spread to the east and slightly to the south, following the most common wind patterns in that area. As for the arrival time maps, Figure 8 shows, for each eruption size, the expected time to reach the critical ash concentration threshold of 2 mg/m$^3$ at FL050 with a probability of 5% in the event of an eruption and, for some of the airports around Campi Flegrei, arrival time values versus their probability values. Most airports would be affected in less than 48 h in case of an explosive eruption with a probability of 5%. We can observe that the arrival time to exceed the critical threshold of ash concentration in the different airports is less the greater the size of the eruption. Examples for other flight levels and persistence can be found in the Supplementary Material.

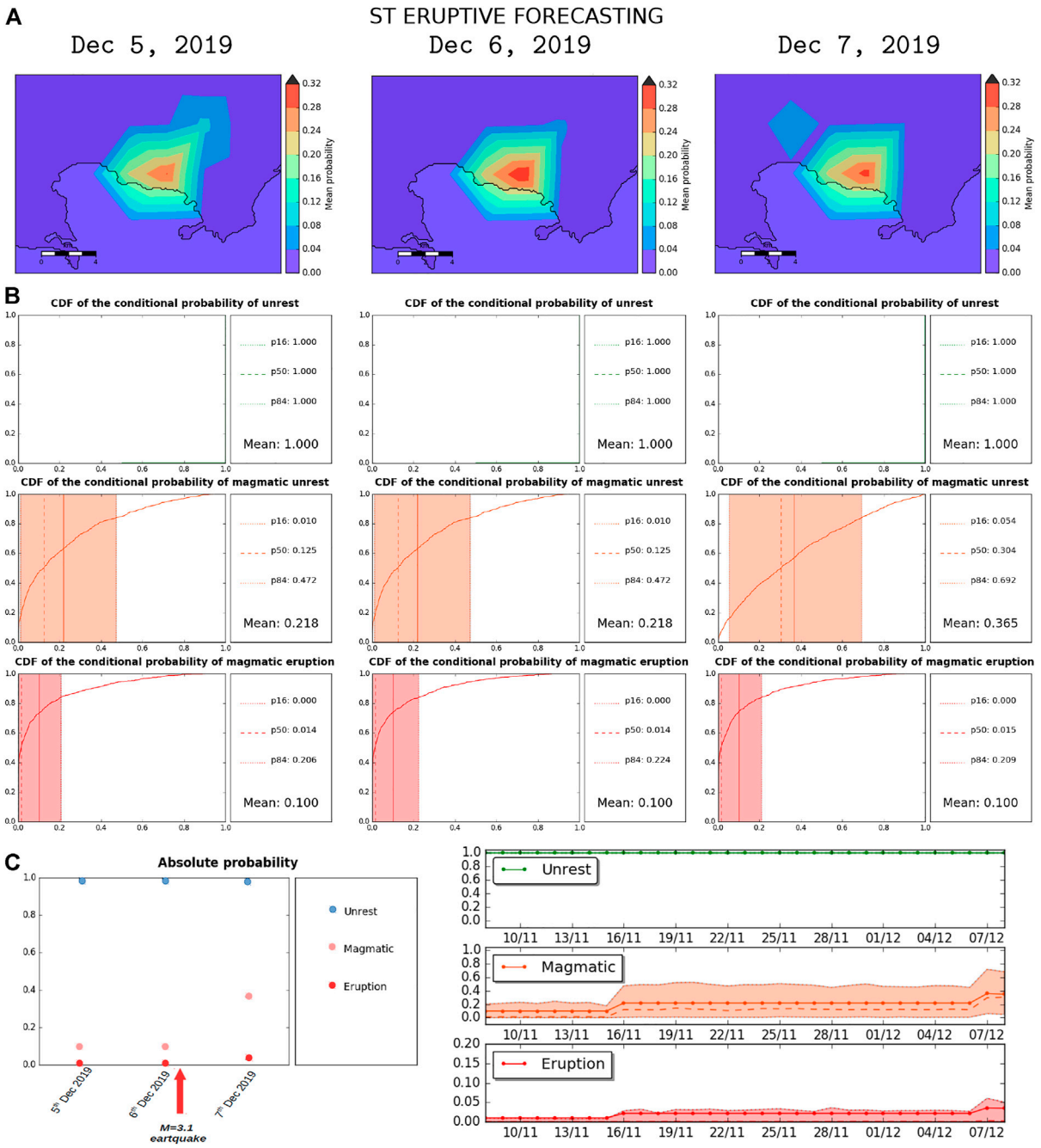


FIGURE 9
ST eruptive forecasting (EF) for December 5, 6, and 7, 2019. **(A)** is the temporal evolution during the 3 days of the vent-opening probability map, conditional to eruption occurrence. **(B)** shows the temporal evolution of the CDF of unrest, magmatic unrest, and magmatic eruption. **(C)** displays the temporal evolution of the mean values of the probability density function of unrest (blue circles), magmatic unrest (pink circles), and eruption (red circles) in the 3 days of application, where the occurrence of a magnitude 3.1 earthquake is marked by the red arrow.

### 4.6.2 Short-term analysis for days 5, 6, and 7 December 2019

Figure 9 is a compilation of the eruption forecasting (EF) for 5, 6, and 7 December 2019. As we have explained previously, EF is independent of the hazard we are modeling, and it is based mainly on the information from the monitoring system. Regarding the location of the eruption, Figure 9A presents the temporal evolution of the mean conditional probability of the eruption occurring at each of the 40 potential vent locations. Figure 9B shows the

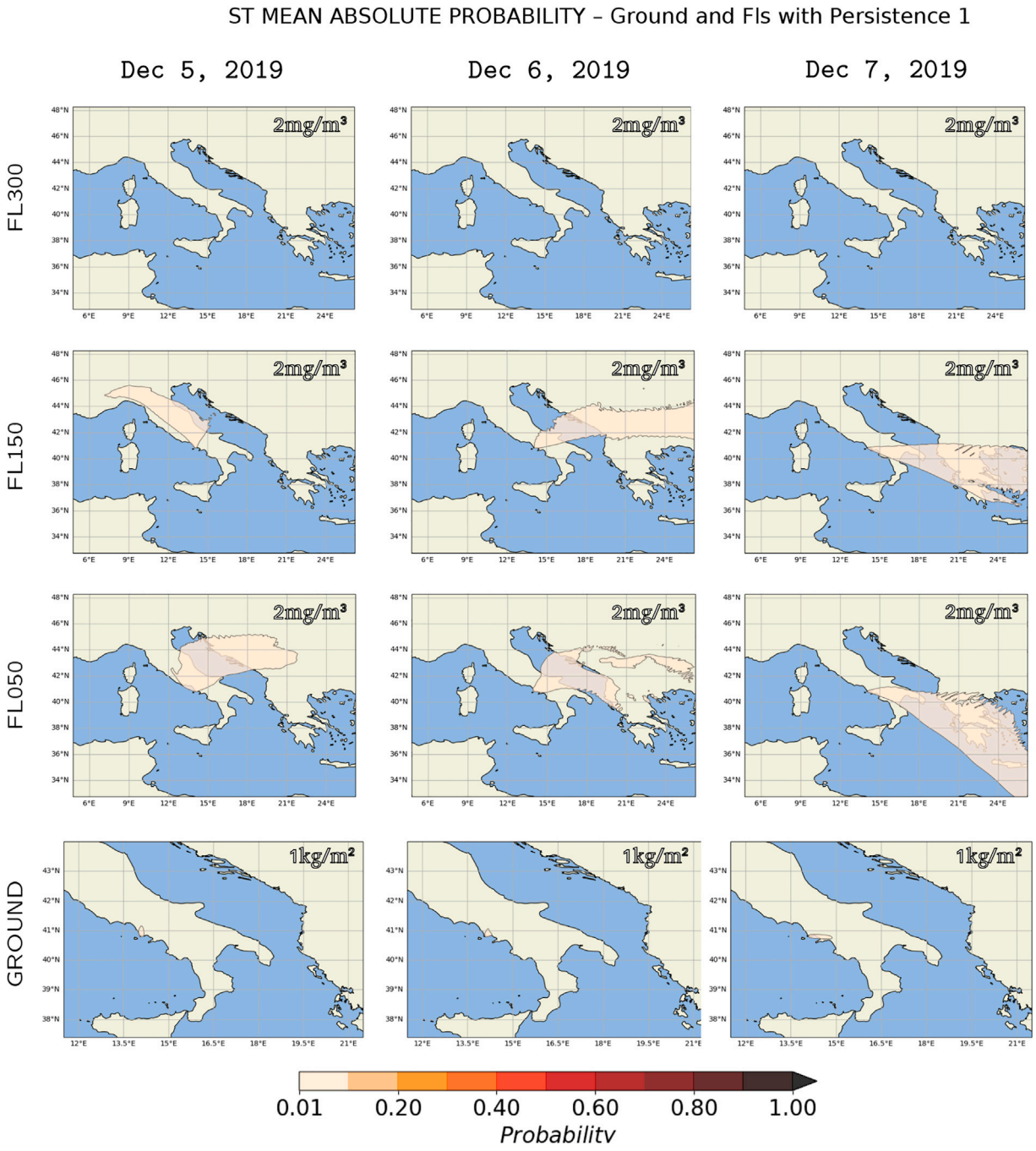


FIGURE 10
Maps showing the short-term mean absolute probability for December 5, 6, and 7, 2019. The last row shows the probability of exceeding the 1 kg/m$^2$ tephra load, while rows from 1 to 3 show the probability of exceeding the 2 mg/m$^3$ ash concentration at FL300, FL150, and FL050, respectively, with the persistence of 1 h.

temporal evolution of the mean and the 16, 50, and 84 percentiles of the conditional probability density function (CDF) of unrest, magmatic unrest, and magmatic eruption (those percentiles are equal to two standard deviations ($2\sigma$), that is, 68% confidence interval). Figure 9C, left panel, displays the temporal evolution of the mean values of the probability density function of unrest, magmatic unrest, and eruption in the 3 days of application, where the occurrence of a magnitude 3.1 earthquake is marked by the red arrow on the left

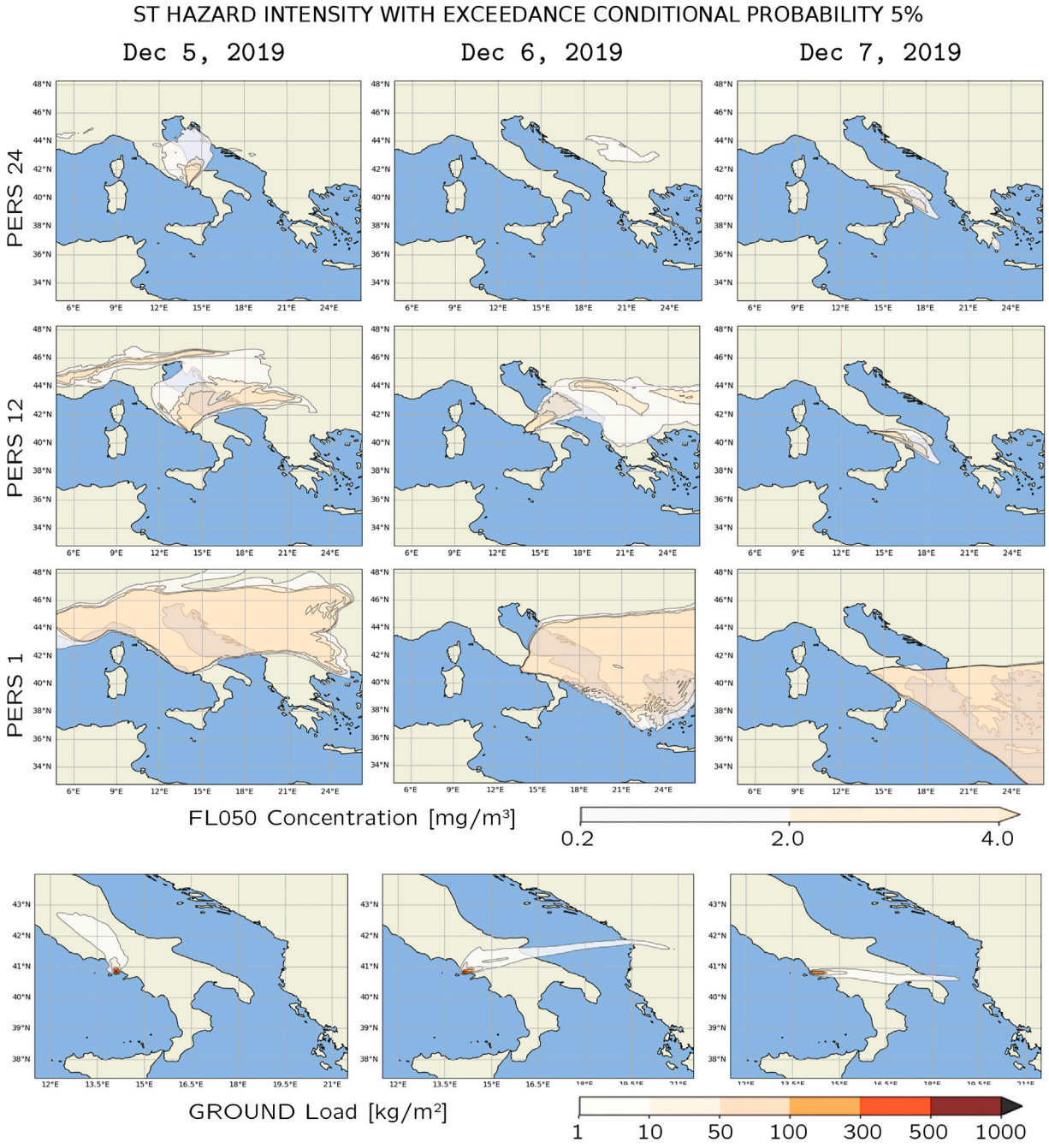


FIGURE 11
Short-term hazard maps relative to the 5% probability threshold conditional on an eruption event providing in the first four rows the tephra concentration at FL050 with persistence 1, 12, and 24, respectively. The last row shows the ground load. For each hazard intensity value (color bar label), the maps show the areas where that value will be exceeded with a probability greater than 5% in the event of an eruption within 48 h of the observed time.

panel. The right panel shows the time trend in the probability of unrest, magmatic unrest, and eruption in the previous days, where shaded areas indicate the 10th–90th percentile confidence band. As a sample of ST probability maps, Figure 10 presents the mean absolute probability for each of the days of exceeding the tephra load of 1 kg/m$^2$ at the ground and that of exceeding an ash concentration of 2 mg/m$^3$ at FL050, FL150, and FL300, respectively, for at least 1 hour in the 48 h following the eruption onset. The most affected flight level would have been FL050, closely followed

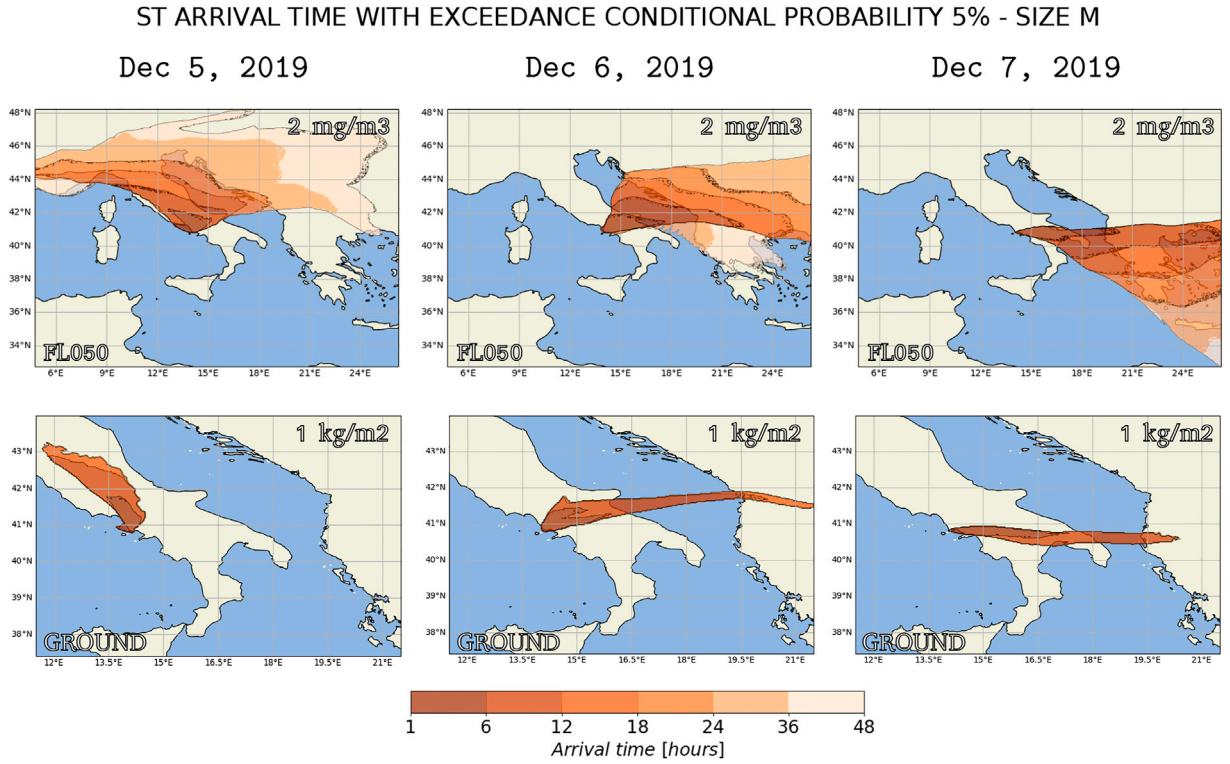


FIGURE 12
Short-term arrival time maps for medium (M) size for December 5, 6, and 7, 2019. The bottom and top rows show the expected time for tephra ground load and for ash concentration at FL050 to reach the critical thresholds of 1 kg/m$^2$ and 2 mg/m$^3$, respectively, with a probability of 5% in the event of a medium-sized eruption at Campi Flegrei.

by FL150, while at FL300, this critical threshold would have not been exceeded. Figure 11 shows ST hazard maps with tephra load and ash concentration at FL050 with a probability of 5%. Note, for example, that the day 6 eruption could have produced a tephra load beyond the Albanian coast. The arrival time of exceeding the threshold of 1 kg/m$^2$ and 2 mg/m$^3$ at the ground and at FL050, respectively, with a probability of 5% in the case of a medium-size eruption, is displayed in Figure 12. In all the images, the wind field pointed predominantly to the north on day 5, to the east on day 6, and to the southeast on day 7, which illustrated the influence of meteorological variability and the need to develop a daily evaluation of the tephra hazard in a wide geographical area.

## 5 Conclusion

This study highlights the feasibility and usefulness of HPC-integrated PVHA. In particular, we have shown that HPC integrated into PVHA can provide quantitative hazard results capable of answering some of the questions that decision-makers have to face in case of volcanic unrest possibly evolving toward an eruption (short-term) or in planning land use or air traffic development (long-term) over a large-scale and high-resolution domain.

We have implemented the Probabilistic Volcanic Hazard Assessment HPC Workflow (PVHA_HPC-WF) to calculate the short-term (ST) and the long-term (LT) probabilistic volcanic hazard assessment (PVHA) for a specific volcano based on the Bayesian event tree (BET) methodology and starting from the existing prototype tool BET@OV. We have subjected the code to a performance and productivity audit and have optimized it following a proof-of-concept process, thanks to which the execution time of some of the most critical parts of the workflow has been reduced by up to 588 times. Through the workflow manager system light (WMS-light), we have given the PVHA_HPC-WF the ability to interact with different machines to distribute tasks and exchange data.

We have tested the LT PVHA_HPC-WF by performing a long-term tephra hazard assessment of the Campi Flegrei (CF) volcanic caldera, Italy, on the ground and at eight flight levels in a geographic area of approximately 2,000 km ×

2,000 km. To this end, we have used the FALL3D-8.0 model to perform ash dispersion simulations at a horizontal resolution of 0.025° (approximately 2 km) for 4,500 different volcanic scenarios (VS), also including those of low probability but high impact, and considering 20 years of meteorological data from ERA5. The workflow tasks have been distributed into three clusters, the ADA, HPC-MASTER Super Computing Cluster in the INGV Section of Bologna (Italy), the CENERI, Cluster at the Osservatorio Vesuviano in the INGV Section of Naples (Italy), and the IRENE-SKYLAKE, in the Computing Center TGCC (France), using approximately 576 h of CPU time in ADA, some minutes in CENERI, and $11{\cdot}10^6$ h of CPU time in IRENE, demonstrating that the entire process could be carried out in a real time within 4.5 h if resources are available to execute the independent tasks simultaneously.

We have also tested the ST PVHA_HPC-WF by performing the short-term tephra hazard assessment of CF for December 5, 6, and 7, 2019, with the same model configuration used for LT but using, for each of the days, 540 VS and its corresponding meteorological data also from ERA5. For this, we have used approximately, for each date, 576 h of CPU time in ADA, some minutes in CENERI, and $125{\cdot}10^4$ h of CPU time in IRENE, showing that a daily process considering 540 VSs could run in 4.25 h if resources are available. We note that this time could be improved for real-time crisis management if specific location targets are provided (e.g., a specific FL).

## Data availability statement

The raw data supporting the conclusions of this article will be made available by the authors, without undue reservation.

## Author contributions

Conceptualization: LS, ACo, JS, GM, AF. Methodology: BMM,MTL, LS, ACo, JS, AF, GM, SB. Software: BMM, MTL, OR (Performance Optimization), ACh (development of WMS-light and adaptation to PVHA HPC-WF) Writing – original draft: BMM Writing – review and editing: BMM, MTL, LS, ACo, JS, AF, GM, SB, OR, and ACh. Supervision and coordination: ACo. Funding: ACo.

## Funding

The research leading to these results has been supported by the European Commission's CORDIS [ChEESE (grant no. 823844)]. Part of this work was supported by European Community's Horizon 2020 POP project under grant agreements (no. 824080). Multi-year PRACE Project Access "Volcanic ash hazard and forecast" (ID 2019215114). This work was granted access to the HPC/AI resources of TGCC under the allocation 2020-RA2020235114 made by GENCI.

## Acknowledgments

We thank the European Union's Horizon 2020 research and innovation program. We thank the PRACE partnership. We thank TGCC France. We thank Copernicus Climate Change Service (C3S) (2017): ERA5: Fifth generation of ECMWF atmospheric reanalyses of the global climate. Copernicus Climate Change Service Climate Data Store (CDS) date of access for the access to the meteorological data. We thank SERENADE—SEismic Restful ENAbled DatabasE—for the provision of the seismic data of the Campi Flegrei area. We thank Paolo Perfetti and Roberto Tonini for early support at the beginning of the study with help on BET@OV basics. We thank Stefano Cacciaguerra (INGV) for its technical support in the use of the computer clusters. We also acknowledge the MIUR project Premiale Ash-RESILIENCE.

## Conflict of interest

The authors declare that the research was conducted in the absence of any commercial or financial relationships that could be construed as a potential conflict of interest.

## Publisher's note



## Supplementary material

The Supplementary Material for this article can be found online at: https://www.frontiersin.org/articles/10.3389/feart.2022.941789/full#supplementary-material

# References


Ágústsdóttir, A. M. (2015). Ecosystem approach for natural hazard mitigation of volcanic tephra in Iceland: Building resilience and sustainability. *Nat. Hazards (Dordr).* 78, 1669–1691. doi:10.1007/s11069-015-1795-6

Alberico, I., Lirer, L., Petrosino, P., and Scandone, R. (2002). A methodology for the evaluation of long-term volcanic risk from pyroclastic flows in campi flegrei (Italy). *J. Volcanol. Geotherm. Res.* 116, 63–78. doi:10.1016/s0377-0273(02)00211-1

Aspinall, W. (2006). Structured elicitation of expert judgment for probabilistic hazard and risk assessment in volcanic eruptions. *Statistics Volcanol.* 1, 15–30.

Barsotti, S., Di Rienzo, D. I., Thordarson, T., Björnsson, B. B., and Karlsdóttir, S. (2018). Assessing impact to infrastructures due to tephra fallout from öræfajökull volcano (Iceland) by using a scenario-based approach and a numerical model. *Front. Earth Sci. (Lausanne).* 6, 196. doi:10.3389/feart.2018.00196

Bevilacqua, A., Neri, A., Bisson, M., Esposti Ongaro, T., Flandoli, F., Isaia, R., et al. (2017). The effects of vent location, event scale, and time forecasts on pyroclastic density current hazard maps at Campi Flegrei caldera (Italy). *Front. Earth Sci. (Lausanne).* 5, 72. doi:10.3389/feart.2017.00072

Bianco, F., Caliro, S., De Martino, P., Orazi, M., Ricco, C., Vilardo, G., et al. (2022). "The permanent monitoring system of the Campi Flegrei Caldera, Italy," in *Campi Flegrei. A restless caldera in a densely populated area. Active volcanoes of the world*. Editors G. Orsi, M. D'Antonio, and L. Civetta (Berlin, Heidelberg: Springer), 219–237. doi:10.1007/978-3-642-37060-1_8

Biasse, S., Bagheri, G., Aeberhard, W., and Bonadonna, C. (2014). Terror: towards a better quantification of the uncertainty propagated during the characterization of tephra deposits. *Stat. Volcanol.* 1, 1–27. doi:10.5038/2163-338x.1.2

Blake, D. M., Deligne, N. I., Wilson, T. M., Lindsay, J. M., and Woods, R. (2017). Investigating the consequences of urban volcanism using a scenario approach ii: Insights into transportation network damage and functionality. *J. Volcanol. Geotherm. Res.* 340, 92–116. doi:10.1016/j.jvolgeores.2017.04.010

Bonadonna, C., Connor, C. B., Houghton, B. F., Connor, L., Byrne, M., Laing, A., et al. (2005). Probabilistic modeling of tephra dispersal: Hazard assessment of a multiphase rhyolitic eruption at Tarawera, New Zealand. *J. Geophys. Res.* 110, B03203. doi:10.1029/2003JB002896

Budnitz, R., Apostolakis, G., and Boore, D. M. (1997). *Recommendations for probabilistic seismic hazard analysis: guidance on uncertainty and use of experts*. Tech. rep. Washington, DC (United States): US Nuclear Regulatory Commission NRC, Div.

Center, B. S. (2022). *Extrae instrumentation package*. [Dataset]. Available at: https://tools.bsc.es/extrae.

Chen, W., and Zhao, L. (2015). Review–volcanic ash and its influence on aircraft engine components. *Procedia Eng.* 99, 795–803. doi:10.1016/j.proeng.2014.12.604

Cheptsov, A., and Beljaev, O. (2020). "A microservices approach for parallel applications design: A case study for cfd simulation in geoscience domain," in The twelfth international conference on advanced geographic information systems, applications, and services, Valencia, Spain, November 21–25, 2020 (IARIA), 25–30.

Clarkson, R. J., Majewicz, E. J., and Mack, P. (2016). A re-evaluation of the 2010 quantitative understanding of the effects volcanic ash has on gas turbine engines. *Proc. Institution Mech. Eng. Part G J. Aerosp. Eng.* 230, 2274–2291. doi:10.1177/0954410015623372

Costa, A., Macedonio, G., and Folch, A. (2006). A three-dimensional eulerian model for transport and deposition of volcanic ashes. *Earth Planet. Sci. Lett.* 241, 634–647. doi:10.1016/j.epsl.2005.11.019

Costa, A., Dell'Erba, F., Di Vito, M. A., Isaia, R., Macedonio, G., Orsi, G., et al. (2009). Tephra fallout hazard assessment at the Campi Flegrei caldera (Italy). *Bull. Volcanol.* 71, 259–273. doi:10.1007/s00445-008-0220-3

Costa, A., Di Vito, M. A., Ricciardi, G. P., Smith, V. C., and Talamo, P. (2022). The long and intertwined record of humans and the Campi Flegrei volcano (Italy). *Bull. Volcanol.* 84, 5–27. doi:10.1007/s00445-021-01503-x

Damby, D., Horwell, C., Baxter, P., Delmelle, P., Donaldson, K., Dunster, C., et al. (2013). The respiratory health hazard of tephra from the 2010 Centennial eruption of Merapi with implications for occupational mining of depositsMerapi eruption. *J. Volcanol. Geotherm. Res.* 261, 376–387. doi:10.1016/j.jvolgeores.2012.09.001

De Martino, P., Dolce, M., Brandi, G., Scarpato, G., and Tammaro, U. (2021). The ground deformation history of the neapolitan volcanic area (campi flegrei caldera, somma–vesuvius volcano, and ischia island) from 20 years of continuous GPS observations (2000–2019). *Remote Sens.* 13, 2725. doi:10.3390/rs13142725

Deino, A. L., Orsi, G., Piochi, M., and de Vita, S. (2004). The age of the Neapolitan Yellow Tuff caldera-forming eruption (Campi Flegrei caldera-Italy) assessed by $^{40}$ar/$^{39}$ar dating method. *J. Volcanol. Geotherm. Res.* 133, 157–170. doi:10.1016/s0377-0273(03)00396-2

Folch, A., and Sulpizio, R. (2010). Evaluating long-range volcanic ash hazard using supercomputing facilities: application to somma-vesuvius (Italy), and consequences for civil aviation over the central mediterranean area. *Bull. Volcanol.* 72, 1039–1059. doi:10.1007/s00445-010-0386-3

Folch, A., Costa, A., and Macedonio, G. (2009). Fall3d: A computational model for transport and deposition of volcanic ash. *Comput. Geosci.* 35, 1334–1342. doi:10.1016/j.cageo.2008.08.008

Folch, A., Mingari, L., Gutierrez, N., Hanzich, M., Macedonio, G., and Costa, A. (2020). FALL3D-8.0: a computational model for atmospheric transport and deposition of particles, aerosols and radionuclides – part 1: Model physics and numerics. *Geosci. Model Dev.* 13, 1431–1458. doi:10.5194/gmd-13-1431-2020

Grezio, A., Cinti, F. R., Costa, A., Faenza, L., Perfetti, P., Pierdominici, S., et al. (2020). Multisource bayesian probabilistic tsunami hazard analysis for the gulf of naples (Italy). *J. Geophys. Res. Oceans* 125, e2019JC015373. doi:10.1029/2019jc015373

Guffanti, M., Casadevall, T. J., and Budding, K. E. (2010). *Encounters of aircraft with volcanic ash clouds: A compilation of known incidents, 1953-2009*. U.S. Geological Survey Data Series 545, ver. 1.0, 12 p.. Reston, VA: U.S. Geological Survey. Available at: https://pubs.usgs.gov/ds/545/.

Horwell, C. J., and Baxter, P. J. (2006). The respiratory health hazards of volcanic ash: a review for volcanic risk mitigation. *Bull. Volcanol.* 69, 1–24. doi:10.1007/s00445-006-0052-y

Jenkins, S., Spence, R., Fonseca, J., Solidum, R., and Wilson, T. (2014). Volcanic risk assessment: Quantifying physical vulnerability in the built environment. *J. Volcanol. Geotherm. Res.* 276, 105–120. doi:10.1016/j.jvolgeores.2014.03.002

Lindsay, J., Marzocchi, W., Jolly, G., Constantinescu, R., Selva, J., and Sandri, L. (2010). Towards real-time eruption forecasting in the auckland volcanic field: application of BET_EF during the New Zealand national disaster exercise 'ruaumoko. *Bull. Volcanol.* 72, 185–204. doi:10.1007/s00445-009-0311-9

Lirer, L., Petrosino, P., Alberico, I., and Postiglione, I. (2001). Long-term volcanic hazard forecasts based on Somma-Vesuvio past eruptive activity. *Bull. Volcanol.* 63, 45–60. doi:10.1007/s004450000121

Macedonio, G., and Costa, A. (2018). "Mappe di pericolosità per la dispersione di cenere a larga scala per lo scenario medio del Vesuvio," in *Relazione per il Dipartimento della Protezione Civile e il Centro di Competenza Plinivs* (Istituto Nazionale di Geofisica e Vulcanologia).

Macedonio, G., Costa, A., and Folch, A. (2008). Ash fallout scenarios at vesuvius: numerical simulations and implications for hazard assessment. *J. Volcanol. Geotherm. Res.* 178, 366–377. doi:10.1016/j.jvolgeores.2008.08.014

Marti, J., Spence, R., Calogero, E., Ordoñez, A., Felpeto, A., and Baxter, P. (2008). Estimating building exposure and impact to volcanic hazards in Icod de los Vinos, Tenerife (Canary Islands). *J. Volcanol. Geotherm. Res.* 178, 553–561. doi:10.1016/j.jvolgeores.2008.07.010

Martin, U., and Nemeth, K. (2007). *Practical volcanology-Lecture notes for understanding volcanic rocks from field based studies*. Budapest: Geological Institute of Hungary.

Marzocchi, W., and Jordan, T. H. (2014). Testing for ontological errors in probabilistic forecasting models of natural systems. *Proc. Natl. Acad. Sci. U. S. A.* 111, 11973–11978. doi:10.1073/pnas.1410183111

Marzocchi, W., Sandri, L., Gasparini, P., Newhall, C., and Boschi, E. (2004). Quantifying probabilities of volcanic events: the example of volcanic hazard at mount vesuvius. *J. Geophys. Res.* 109, B11201. doi:10.1029/2004jb003155

Marzocchi, W., Sandri, L., and Selva, J. (2008). BET_EF: a probabilistic tool for long-and short-term eruption forecasting. *Bull. Volcanol.* 70, 623–632. doi:10.1007/s00445-007-0157-y

Marzocchi, W., Sandri, L., and Selva, J. (2010). BET_VH: a probabilistic tool for long-term volcanic hazard assessment. *Bull. Volcanol.* 72, 705–716. doi:10.1007/s00445-010-0357-8

Marzocchi, W., Selva, J., and Jordan, T. H. (2021). A unified probabilistic framework for volcanic hazard and eruption forecasting. *Nat. Hazards Earth Syst. Sci.* 21, 3509–3517. doi:10.5194/nhess-21-3509-2021

Mason, B. G., Pyle, D. M., and Oppenheimer, C. (2004). The size and frequency of the largest explosive eruptions on Earth. *Bull. Volcanol.* 66, 735–748. doi:10.1007/s00445-004-0355-9

Mele, D., Costa, A., Dellino, P., Sulpizio, R., Dioguardi, F., Isaia, R., et al. (2020). Total grain size distribution of components of fallout deposits and implications for magma fragmentation mechanisms: examples from campi flegrei caldera (Italy). *Bull. Volcanol.* 82, 31–12. doi:10.1007/s00445-020-1368-8

Neri, A., Aspinall, W. P., Cioni, R., Bertagnini, A., Baxter, P. J., Zuccaro, G., et al. (2008). Developing an event tree for probabilistic hazard and risk assessment at Vesuvius. *J. Volcanol. Geotherm. Res.* 178, 397–415. doi:10.1016/j.jvolgeores.2008.05.014

Newhall, C., and Hoblitt, R. (2002). Constructing event trees for volcanic crises. *Bull. Volcanol.* 64, 3–20. doi:10.1007/s004450100173

Newhall, C. G., and Self, S. (1982). The volcanic explosivity index (vei) an estimate of explosive magnitude for historical volcanism. *J. Geophys. Res.* 87, 1231–1238. doi:10.1029/jc087ic02p01231

Orsi, G., Di Vito, M. A., and Isaia, R. (2004). Volcanic hazard assessment at the restless campi flegrei caldera. *Bull. Volcanol.* 66, 514–530. doi:10.1007/s00445-003-0336-4

Orsi, G., Di Vito, M. A., Selva, J., and Marzocchi, W. (2009). Long-term forecast of eruption style and size at Campi Flegrei caldera (Italy). *Earth Planet. Sci. Lett.* 287, 265–276. doi:10.1016/j.epsl.2009.08.013

Ort, M., Orsi, G., Pappalardo, L., and Fisher, R. V. (2003). Emplacement processes in a far-traveled dilute pyroclastic current: anisotropy of magnetic susceptibility studies of the campanian ignimbrite. *Bull. Volcanol.* 65, 55–72. doi:10.1007/s00445-002-0241-2

Paris, R., Ulvrova, M., Selva, J., Brizuela, B., Costa, A., Grezio, A., et al. (2019). Probabilistic hazard analysis for tsunamis generated by subaqueous volcanic explosions in the campi flegrei caldera, Italy. *J. Volcanol. Geotherm. Res.* 379, 106–116. doi:10.1016/j.jvolgeores.2019.05.010

Peluso, R. (2014). *Il database sismico serenade: un sistema rest per la gestione delle localizzazioni sismiche*. Roma: MISCELLANEA INGV 46.

Perfetti, P., Tonini, R., and Selva, J. (2021). [Dataset]. perfettp/BET-Tephra: v0.2017.04. Zenodo. doi:10.5281/zenodo.4638667

Pillet, V., Labarta, J., Cortes, T., and Girona, S. (1995). "Paraver: A tool to visualize and analyze parallel code," in Proceedings of WoTUG-18: transputer and occam developments (Citeseer), 17–31.44

POP (2022). *POP standard metrics for parallel performance analysis*. [Dataset]. Available at: https://pop-coe.eu/node/69.

Prata, A., and Tupper, A. (2009). *Aviation hazards from volcanoes: the state of the science*. [Dataset].

Prata, A. T., Mingari, L., Folch, A., Macedonio, G., and Costa, A. (2021). FALL3D-8.0: a computational model for atmospheric transport and deposition of particles, aerosols and radionuclides – Part 2: Model validation. *Geosci. Model Dev.* 14, 409–436. doi:10.5194/gmd-14-409-2021

Pyle, D. M. (2015). "Sizes of volcanic eruptions," in *The encyclopedia of volcanoes* (Elsevier), 257–264.

Sandri, L., Jolly, G., Lindsay, J., Howe, T., and Marzocchi, W. (2012). Combining long-and short-term probabilistic volcanic hazard assessment with cost-benefit analysis to support decision making in a volcanic crisis from the Auckland Volcanic Field, New Zealand. *Bull. Volcanol.* 74, 705–723. doi:10.1007/s00445-011-0556-y

Sandri, L., Costa, A., Selva, J., Tonini, R., Macedonio, G., Folch, A., et al. (2016). Beyond eruptive scenarios: assessing tephra fallout hazard from neapolitan volcanoes. *Sci. Rep.* 6, 24271–24313. doi:10.1038/srep24271

Sandri, L., Tierz, P., Costa, A., and Marzocchi, W. (2018). Probabilistic hazard from pyroclastic density currents in the Neapolitan area (Southern Italy). *J. Geophys. Res. Solid Earth* 123, 3474–3500. doi:10.1002/2017jb014890

Selva, J., Costa, A., Marzocchi, W., and Sandri, L. (2010). BET_VH: exploring the influence of natural uncertainties on long-term hazard from tephra fallout at campi flegrei (Italy). *Bull. Volcanol.* 72, 717–733. doi:10.1007/s00445-010-0358-7

Selva, J., Marzocchi, W., Papale, P., and Sandri, L. (2012a). Operational eruption forecasting at high-risk volcanoes: the case of campi flegrei, naples. *J. Appl. Volcanol.* 1, 5–14. doi:10.1186/2191-5040-1-5

Selva, J., Orsi, G., Di Vito, M. A., Marzocchi, W., and Sandri, L. (2012b). Probability hazard map for future vent opening at the Campi Flegrei caldera, Italy. *Bull. Volcanol.* 74, 497–510. doi:10.1007/s00445-011-0528-2

Selva, J., Costa, A., Sandri, L., Macedonio, G., and Marzocchi, W. (2014). Probabilistic short-term volcanic hazard in phases of unrest: A case study for tephra fallout. *J. Geophys. Res. Solid Earth* 119, 8805–8826. doi:10.1002/2014jb011252

Selva, J., Costa, A., De Natale, G., Di Vito, M. A., Isaia, R., and Macedonio, G. (2018). Sensitivity test and ensemble hazard assessment for tephra fallout at Campi Flegrei, Italy. *J. Volcanol. Geotherm. Res.* 351, 1–28. doi:10.1016/j.jvolgeores.2017.11.024

Selva, J., Azzaro, R., Taroni, M., Tramelli, A., Alessio, G., Castellano, M., et al. (2021). The seismicity of ischia island, Italy: An integrated earthquake catalogue from 8th century bc to 2019 and its statistical properties. *Front. Earth Sci. (Lausanne).* 9, 629736. doi:10.3389/feart.2021.629736

Spence, R. J., Baxter, P. J., and Zuccaro, G. (2004). Building vulnerability and human casualty estimation for a pyroclastic flow: a model and its application to vesuvius. *J. Volcanol. Geotherm. Res.* 133, 321–343. doi:10.1016/s0377-0273(03)00405-0

Sulpizio, R., Folch, A., Costa, A., Scaini, C., and Dellino, P. (2012). Hazard assessment of far-range volcanic ash dispersal from a violent strombolian eruption at somma-vesuvius volcano, naples, Italy: Implications on civil aviation. *Bull. Volcanol.* 74, 2205–2218. doi:10.1007/s00445-012-0656-3

Titos, M., Martínez Montesinos, B., Barsotti, S., Sandri, L., Folch, A., Mingari, L., et al. (2022). Long-term hazard assessment of explosive eruptions at Jan Mayen (Norway) and implications for air traffic in the North Atlantic. *Nat. Hazards Earth Syst. Sci.* 22, 139–163. doi:10.5194/nhess-22-139-2022

Tonini, R., Sandri, L., Costa, A., and Selva, J. (2015). Brief Communication: The effect of submerged vents on probabilistic hazard assessment for tephra fallout. *Nat. Hazards Earth Syst. Sci.* 2, 7181–7196. doi:10.5194/nhessd-2-7181-2014

Wilson, T. M., Stewart, C., Sword-Daniels, V., Leonard, G. S., Johnston, D. M., Cole, J. W., et al. (2012). Volcanic ash impacts on critical infrastructure. *Phys. Chem. Earth, Parts A/B/C* 45, 5–23. doi:10.1016/j.pce.2011.06.006

Zuccaro, G. (2008). "A probabilistic model for the evaluation of the impact of explosive eruption scenarios at Vesuvius,". *Urban habitat constructions under catastrophic events: COST Action C26*. Editors F. M. Mazzolani, E. Mistakidis, R. P. Borg, M. Byfield, G. De Matteis, and E. Dubina (Malta: University of Malta), 476, 486–70.

## Glossary

**BET** Bayesian event tree

**CDF** conditional probability density function

**CF** Campi Flegrei

**CFc** Campi Flegrei caldera

**ChEESE** Center of Excellence for Exascale in Solid Earth

**CPU** central processing unit

**E** effusive

**EF** eruptive forecasting

**ESP** eruptive source parameter

**ESPs** eruptive source parameters

**FL** flight level

**H** high

**HPC** high-performance computing

**HPDA** high-performance data analytics

**INGV** Istituto Nazionale di Geofisica e Vulcanologia

**IPC** instructions per cycle

**L** low

**LT** long term

**M** medium

**MER** mass eruption rate

**MPI** Message Passing Interface

**NUMA** non-uniform memory access

**PDF** probability density function

**PoC** proof of concept

**POP** performance optimization and productivity

**POP CoE** EU Performance Optimization and Productivity Center of Excellence in HPC

**PVHA** probabilistic volcanic hazard assessment

**PVHA_HPC-WF** Probabilistic Volcanic Hazard Assessment Workflow

**SERENADE** SEismic Restful ENAbled DatabasE

**ST** short term

**TEM** total erupted mass

**TEV** total erupted volume

**TGSD** total grain size distribution

**VEI** volcanic explosivity index

**VS** volcanic scenario

**WMS-light** workflow manager system light.

# Frontiers in Earth Science

**Investigates the processes operating within the major spheres of our planet**

Advances our understanding across the earth sciences, providing a theoretical background for better use of our planet's resources and equipping us to face major environmental challenges.

---

## Discover the latest Research Topics

See more →


**Frontiers**

Avenue du Tribunal-Fédéral 34
1005 Lausanne, Switzerland
frontiersin.org

**Contact us**

+41 (0)21 510 17 00
frontiersin.org/about/contact